Acta Physica Hungarica

VOLUME 67 · NUMBERS 1–2, 1990

Akadémiai Kiadó, Budapest

ACTA PHYS. HUNG. APAHAQ 67 (1–2) 3–243 (1990) HU ISSN 0231–4428

ACTA PHYSICA HUNGARICA

A JOURNAL OF THE HUNGARIAN ACADEMY OF SCIENCES

EDITED BY
I. KOVÁCS

Acta Physica publishes original papers on subjects in physics. Papers are accepted in English, French, German and Russian.

Acta Physica is published in two yearly volumes (4 issues each) by

AKADÉMIAI KIADÓ
Publishing House of the Hungarian Academy of Sciences
H-1117 Budapest, Prielle Kornélia u. 19–35

Subscription information

Orders should be addressed to

KULTURA Foreign Trading Company
1389 Budapest P.O. Box 149

or to its representatives abroad.

Acta Physica Hungarica is abstracted/indexed in Chemical Abstracts, Mathematical Reviews, Scienc Abstracts, Physics Briefs, Risk Abstracts

ACTA PHYSICA HUNGARICA

VOLUME 67

AKADÉMIAI KIADÓ, BUDAPEST
1990

CONTENTS

Volume 67

FLUIDS, PLASMAS AND ELECTRIC DISCHARGES

CONDENSED MATTER

CROSS-DISCIPLINARY

CONTENTS

ELEMENTARY PARTICLES AND FIELDS

NUCLEAR PHYSICS

ATOMIC AND MOLECULAR PHYSICS

FLUIDS, PLASMAS AND ELECTRIC DISCHARGES

CONDENSED MATTER

Manuscript received by Akadémiai Kiadó:
21 December 1988
Manuscript received by TYPOTEX GT
for TEX typesetting: 2 June 1989

Date of publication: 10 July 1990

PRINTED IN HUNGARY

Akadémiai Kiadó és Nyomda Vállalat, Budapest

Acta Physica Hungarica 67 (1-2), pp. 3-26 (1990)

SEMIEMPIRICAL DETERMINATION OF ELECTRONIC-VIBRO-ROTATIONAL RADIATIVE TRANSITION PROBABILITIES IN DIATOMIC MOLECULES I. THEORY*

B. P. LAVROV and V. I. USTIMOV

Institute of Physics, Leningrad State University, Leningrad 198904, USSR

(Received 24 September 1988)

The theory of electronic-vibro-rotational radiative transitions is considered within the framework of the perturbation theory. For the case of regular (monotonic) perturbations caused by relatively far lying terms of the molecule the simple analytical expressions for the line strengths of the $^{2S+1}\Lambda' \rightarrow {}^{2S+1}\Lambda''$ transitions are derived in the second order of the perturbation theory. Most distributed schemes of angular momenta coupling — Hund's cases "a" and "b" — are considered. It is shown that the line strengths can be expressed in terms of a finite number (usually small) of the parameters (certain combinations of matrix elements describing the effects of perturbations and vibration–rotation interaction) which may be determined either from the experimental data in a semiempirical approach or from numerical calculations of adiabatic electronic and vibrational wave functions.

Preface

Several years ago we have had the honour and the pleasure of working together with Prof. I. Kovács on one particular case of perturbations in rovibronic line intensities of Fulcher-α band system of H_2 [1]. This work stimulated our interest in further studies of electronic–vibro-rotational (rovibronic) radiative transition probabilities. The aim of the present paper (devoted to Prof. I. Kovács' 75^{th} birthday) is to introduce some simple analytical formulas which may be used both in "ab initio" calculations and in semiempirical procedures of determination of the transition probabilities in diatomic molecules when regular perturbations due to the electronic–rotational interaction are sufficient.

1. Introduction

The investigation of radiative transition probabilities not only extends our knowledge of molecular structure but is also necessary for various applications in molecular spectroscopy, physics and diagnostics of ionized gases, plasma chemistry, aeronomy and astrophysics, rarefied gas dynamics and laser physics.

*Presented at the Conference on High Resolution Electronic Spectroscopy of Molecules, Tihany, Hungary, 19-24 September 1988

In the optically thin plasma the intensity[1] of the electronic–vibro-rotational line belonging to the spontaneous emission band spectra $I^{n'v'J'M'}_{n''v''J''M''}$ is connected with the population density of upper level $N_{n'v'J'M'}$ and corresponding transition probability $A^{n'v'J'M'}_{n''v''J''M''}$ by well-known expression

$$I^{n'v'J'M'}_{n''v''J''M''} = N_{n'v'J'M'} \cdot A^{n'v'J'M'}_{n''v''J''M''}. \tag{1.1}$$

Here n denotes set of quantum numbers describing electronic states of the molecule (including spin of electrons[2]), v-vibrational quantum number, J and M-total angular momentum of molecule and its projection on the certain direction marked out in space. The magnitudes pertaining to initial and final states of the transition are marked with single and double primes, respectively.

The probabilities of electric dipole transition are connected with the matrix element of the dipole moment operator $\mathbf{d}$ over the wave functions of the electronic-vibro-rotational states by

$$A^{n'v'J'M'}_{n''v''J''M''} = \frac{64\pi^4}{3h}\left(\nu^{n'v'J'M'}_{n''v''J''M''}\right)^3 |\langle n''v''J''M''|\mathbf{d}|n'v'J'M'\rangle|^2, \tag{1.2}$$

where usual Dirac's notation for the wave functions is used, ν is the wave number of the line in cm^{-1}, and π, h are known constants.

Usually the total line intensity summarised over fine structure is detected in an experiment:

$$I^{n'v'J'}_{n''v''J''} = \sum_{M'} N_{n'v'J'M'} \sum_{M''} A^{n'v'J'M'}_{n''v''J''M''}. \tag{1.3}$$

As can be seen from formula (1.3) $I^{n'v'J'}_{n''v''J''}$ is not strictly connected with total population density of upper electronic-vibro-rotational level

$$N_{n'v'J'} \equiv \sum_{M'} N_{n'v'J'M'}. \tag{1.4}$$

But when in the light source there is no marked out direction due to external fields then Zeeman sublevels with various M' are to be populated uniformly

$$N_{n'v'J'M'} = \frac{N_{n'v'J'}}{(2J'+1)} \tag{1.5}$$

and supposing approximately

$$\left(\nu^{n'v'J'M'}_{n''v''J''M''}\right)^3 \approx \left(\nu^{n'v'J'}_{n''v''J''}\right)^3$$

[1]By the intensity of spectral line here and further on we understand the number of quanta belonging to the transition under study and emitted by the unit volume in unit time throughout all directions.

[2]It will be often more convenient to write down explicitly the quantum number Λ of the projection of resultant electronic (orbital) angular momentum $\mathbf{L}$ about internuclear axis. Then the remaining quantum numbers characterizing the electronic state of the molecule will be lettered γ.

one obtains

$$I^{n'v'J'}_{n''v''J''} = N_{n'v'J'} \cdot A^{n'v'J'}_{n''v''J''}, \tag{1.6}$$

where

$$A^{n'v'J'}_{n''v''J''} = \frac{64\pi^4}{3h}\left(\nu^{n'v'J'}_{n''v''J''}\right)^3 \frac{S^{n'v'J'}_{n''v''J''}}{(2J'+1)}. \tag{1.7}$$

The line strength $S^{n'v'J'}_{n''v''J''}$ is expressed in terms of matrix elements of dipole moment as

$$S^{n'v'J'}_{n''v''J''} = \sum_{M',M''} |\langle n''v''J''M''|\mathbf{d}|n'v'J'M'\rangle|^2. \tag{1.8}$$

When the total wave functions of both states may be represented as the product of electronic ψ, vibrational χ and rotational ϕ wave functions (see e.g. Herzberg [2])

$$\Psi = \psi \cdot \chi \cdot \phi, \tag{1.9}$$

then the so-called rotational line strength $S^{J'}_{J''}$ can be factorized and

$$S^{n'v'J'}_{n''v''J''} = \left|R^{n'v'J'}_{n''v''J''}\right|^2 \cdot S^{J'}_{J''}. \tag{1.10}$$

Magnitudes $S^{J'}_{J''}$ appear in (1.10) as a result of integrating over angular variables. For pure types of angular momentum coupling they are simple analytical functions of rotational quantum numbers depending only on the type of electronic transition: $\Sigma - \Sigma, \Sigma - \Pi, \Pi - \Delta$, etc. (Often they are also called Hönl–London factors). A most complete set of such expressions for transitions of various multiplicity is presented in Kovács [3].

Matrix elements $R^{n'v'J'}_{n''v''J''}$ are the result of integrating over coordinates of the electrons and internuclear distance R. In principle they depend on the rotational quantum numbers due to J-dependence of the vibrational wave functions χ (so-called effect of vibration–rotation interaction). This dependence is usually weak and often may be neglected (see e.g. Villarejo et al [4])[3]. Then the formula (1.7) is reduced to

$$A^{n'v'J'}_{n''v''J''} = \frac{64\pi^4}{3h}\left(\nu^{n'v'J'}_{n''v''J''}\right)^3 \left|R^{n'v'}_{n''v''}\right|^2 \frac{S^{J'}_{J''}}{(2J'+1)}. \tag{1.11}$$

As a rule in spectroscopical applications the formula (1.11) with Hönl–London factors is used for the determination of the distributions of population density

[3]Born-Oppenheimer separation of variables (formula (1.9)) leaves the possibility of relatively slow R-dependences of electronic wave functions ψ and the electronic transition moment $\langle\psi_{n''}|\mathbf{d}|\psi_{n'}\rangle$. In the Franck–Condon approximation this effect is neglected and the term in formula (1.10) connected with electronic transition probability may be also factorized. The effects of vibration–rotation interaction and R-dependency of $\langle\psi_{n''}|\mathbf{d}|\psi_{n'}\rangle$ are independent of each other. Only in the case when both effects can be neglected the expression for line strengths has most simple form – the product of three factors depending on electronic, vibrational and rotational quantum numbers respectively, (see e.g. Kirbjat'eva et al [5]).

among rotational levels of excited electronic-vibrational states. It should be underlined that this expression is based on several assumptions, namely:

1) applicability of an adiabatic approximation;
2) neglecting the perturbations among the adiabatic electronic states of the molecule;
3) neglecting the effect of the vibration–rotation interaction;
4) pure and known type of angular momenta coupling (Hund's cases "a", "b", "c").

These assumptions seriously restrict the field of validity of the formula (1.11) making it applicable only in some particular cases.

In more complicated but much more distributed situations of regular and unregular perturbations, transitional types of angular momenta coupling and sufficient vibration–rotation interaction these theoretical formulas are not valid and the application can lead to serious errors in relative population densities of rotational levels (It was firstly noticed by Ginsburg and Dieke [6]).

Rigorous quantum-mechanical calculations of the probabilities as well as pure experimental solution of the problem are difficult to overcome nowadays. Therefore, the aim of the present series of papers is to propose and realize the semi-empirical approach to the determination of the electronic–vibro-rotational radiative transition probabilities in diatomic molecules.

The basic idea of our approach is that more or less general theoretical analysis will make it possible to express the probability of arbitrary vibro-rotational transition as a function of rotational quantum number of the initial state and certain magnitudes (constants or quite weak, practically linear functions of J') describing the perturbations and vibration–rotation interaction. Then the parameters entering the theoretical formulas may be obtained from a finite volume of experimental data on the relative transition probabilities for pairs of emission spectral lines starting from the same upper rotational level and belonging to the same electronic-vibrational band. The first attempt of such approach have been earlier presented in our studies of the intensity anomalies in Fulcher-α bands of the H_2 molecule (Kovács et al [1]).

The goal of the present paper is to produce a detailed analysis of non-adiabatic theory (free from the above mentioned restricting assumptions) of electronic–vibro-rotational transitions in diatomic molecules and to derive for their probabilities the certain simple analytical expressions which can be used for further analysis of experimental data on the relative transition probabilities or life times and the semi-empirical determination of $S^{n'v'J'}_{n''v''J''}$ line strengths.

We restricted ourselves to considering the transitions between the states belonging to Hund's limiting cases "a" and "b" most frequently met in practice.

The review of earlier works and the bibliography can be found in Herzberg [2] and Kovács [3].

2. Construction of non-adiabatic wave functions

The total wave functions $\Psi \equiv |\mathbf{r}, \mathbf{R}\rangle$ appearing in formula (1.8) have to satisfy Schrödinger's equation which may be written as

$$\hat{H}\,|\mathbf{r}, \mathbf{R}\rangle = E\,|\mathbf{r}, \mathbf{R}\rangle\,, \tag{2.1}$$

where $\mathbf{r}$ denotes coordinates of electrons and $\mathbf{R}$ the internuclear vector.

After the separation of the mass center movement (in the body-fixed frame) the Hamilton operator for the diatomic molecule (see e.g. Kołos and Wolniewicz [7])

$$\hat{H} = -\frac{1}{2m}\sum_{j=1}^{N_e}\Delta_{\mathbf{r}_j} - \frac{1}{2\mu}\Delta_{\mathbf{R}} - \frac{1}{8\mu}\left(\sum_{j=1}^{N_e}\nabla_{\mathbf{r}_j}\right)^2 - \frac{1}{2\mu_a}\nabla_{\mathbf{R}}\sum_{j=1}^{N_e}\nabla_{\mathbf{r}_j} + V. \tag{2.2}$$

Here m is the electron mass, μ is reduced mass of the molecule, $\mu_a = M_1 \cdot M_2(M_1 - M_2)^{-1}$, M_1 and M_2 are masses of nuclei, N_e is the number of electrons in the molecule, V is the interaction potential. The relativistic terms in the Hamiltonian (2.2) are omitted whereas electron spin may be taken into account if one will require the coordinate part of total wave function $|\mathbf{r}, \mathbf{R}\rangle$ to satisfy certain symmetry properties (to be an eigenfunction of total angular momentum, including the angular momentum of nuclei, orbital and spin momenta of electrons).

For the separation of the molecular axis rotation in space-fixed frame let us expand $|\mathbf{r}, \mathbf{R}\rangle$ in the series of Wigner functions $D^j_{mm'}(\alpha, \beta, 0)$ depending on an orientation of internuclear axis (Varshalovich et al [8]). The angles α and β coincide with the first two Euler angles which describe the orientation of the body-fixed frame and the third one is equated to zero (Ostrovsky and Ustimov [9]). Independent of the angles the coefficients in the series are the functions of $\mathbf{R}$ and $\mathbf{r}$. They may be also represented as an expansion over a complete set of functions. For this purpose it is convenient to choose the sets of electronic $|\gamma, \Lambda, \mathbf{r}, R\rangle_0 \equiv |\gamma, \Lambda\rangle_0$ and vibrational $|\gamma, \Lambda, v, R\rangle_0 \equiv |\gamma, \Lambda, v\rangle_0$ wave functions, obtained for the same molecule in an adiabatic approximation. Then the expression for total wave function is presented as:

$$|\mathbf{r}, \mathbf{R}\rangle = \\ = \sum_{\gamma,\Lambda,v}\sum_{N,M_N} G\,(\gamma, \Lambda, v|N, M_N)\sqrt{\frac{4\pi}{2N+1}}\,|\gamma, \Lambda\rangle_0\,|\gamma, \Lambda, v\rangle_0\,D^N_{-M_N-\Lambda}\,(\alpha, \beta, 0)\,, \tag{2.3}$$

where M_N is a projection of total angular momentum of the molecule excluding the spin of electrons N on any fixed axis in space-fixed frame.

The explicit form of the coefficients $G(\gamma, \Lambda, v|N, M_N)$ depends on the type of angular momenta coupling and in particular it is connected with total electronic spin S.

Substituting expressions (2.2) and (2.3) into the Eq. (2.1) and making the integration over angular variables one can obtain the following system of equations for the coefficients G (Kołos and Wolniewicz [7])

$$\begin{aligned}\left(\hat{H}_{\Lambda\Lambda} - E\right)\sum_{\gamma,v} G(\gamma,\Lambda,v|N,M_N)\,|\gamma,\Lambda\rangle_0|\gamma,\Lambda,v\rangle_0 + \\ + \hat{H}_{\Lambda\Lambda-1}\sum_{\gamma,v} G(\gamma,\Lambda-1,v|N,M_N)\,|\gamma,\Lambda-1\rangle_0|\gamma,\Lambda-1,v\rangle_0 + \\ + \hat{H}_{\Lambda\Lambda+1}\sum_{\gamma,v} G(\gamma,\Lambda+1,v|N,M_N)\,|\gamma,\Lambda+1\rangle_0|\gamma,\Lambda+1,v\rangle_0 = 0,\end{aligned} \tag{2.4}$$

where

$$\begin{aligned}\hat{H}_{\Lambda\Lambda} = -\frac{1}{2m}\sum_{j=1}^{N_e}\langle\Lambda|\Delta_{\mathbf{r}_j}|\Lambda\rangle_0 + V + \frac{1}{8\mu}\langle\Lambda|\mathbf{P}^2|\Lambda\rangle_0 - \\ - \frac{1}{2\mu}\left(\frac{\partial^2}{\partial R^2} + \frac{2}{R}\frac{\partial}{\partial R} - \frac{N(N+1)-\Lambda(\Lambda+1)}{R^2} - \frac{1}{R^2}\langle\Lambda|L^+L^-|\Lambda\rangle_0\right) - \\ - \frac{i}{2\mu_a}\left(P_z\frac{\partial}{\partial R} + \frac{1}{2R}\langle\Lambda|P^+L^- - P^-L^+|\Lambda\rangle_0\right),\end{aligned} \tag{2.5}$$

$$\begin{aligned}\hat{H}_{\Lambda\Lambda-1} = \\ = \sqrt{(N+\Lambda)(N-\Lambda+1)}\left(\frac{1}{2\mu R^2}\langle\Lambda|L^+|\Lambda-1\rangle_0 - \frac{i}{4\mu_a R}\langle\Lambda|P^+|\Lambda-1\rangle_0\right),\end{aligned} \tag{2.6}$$

$$\begin{aligned}\hat{H}_{\Lambda\Lambda+1} = \\ = \sqrt{(N-\Lambda)(N+\Lambda+1)}\left(\frac{1}{2\mu R^2}\langle\Lambda|L^-|\Lambda+1\rangle_0 + \frac{i}{4\mu_a R}\langle\Lambda|P^-|\Lambda+1\rangle_0\right).\end{aligned} \tag{2.7}$$

Here $\mathbf{P}$ and $\mathbf{L}$ are the operators of momentum and angular momentum of the electrons. Correspondingly $P_x, P_y, P_z, L_x, L_y, L_z$ are their projections about the axes of rotating system of coordinates (body-fixed frame) the direction of Z axis coinciding with internuclear vector; $P^{\pm} = P_x \pm iP_y$ and $L^{\pm} = L_x \pm iL_y$.

Adiabatic electronic wave functions $|\gamma,\Lambda\rangle_0$ are to be obtained from the Schrödinger equation for fixed nuclei. It can be deduced from the Eq. (2.4) by turning the masses of nuclei M_1 and M_2 to infinity:

$$\left(-\frac{1}{2m}\sum_{j=1}^{N_e}\langle\Lambda|\Delta_{\mathbf{r}_j}|\Lambda\rangle_0 + V - \varepsilon_{\gamma|\Lambda|}(R)\right)|\gamma,\Lambda\rangle_0 = 0. \tag{2.8}$$

Eigenvalues $\varepsilon_{\gamma|\Lambda|}(R)$ (adiabatical electronic terms) depend on internuclear distance R as a parameter.

Multiplying the Eq. (2.4) by ${}_0\langle\gamma,\Lambda|$ and making an integration over coordinates of the electrons one obtains the following system of equations for the factors G and vibrational wave functions $|\gamma,\Lambda,v\rangle_0$

$$\left[-\frac{1}{2\mu}\left(\frac{\partial^2}{\partial R^2}+\frac{2}{R}\frac{\partial}{\partial R}-\frac{\langle\gamma,\Lambda|(L-N)^2|\gamma,\Lambda\rangle_0}{R^2}\right)+\varepsilon_{\gamma|\Lambda|}(R)-E\right]\cdot$$
$$\cdot\sum_v G(\gamma,\Lambda,v|N,M_N)\,|\gamma,\Lambda,v\rangle_0+ \tag{2.9}$$
$$+\sum_{\gamma',v}\sum_{\Lambda'=|\Lambda-1|}^{\Lambda+1}\hat{\mathcal{L}}_{\gamma\Lambda}^{\gamma'\Lambda'}(N)G(\gamma',\Lambda',v|N,M_N)\,|\gamma',\Lambda',v\rangle_0=0,$$

where

$$\hat{\mathcal{L}}_{\gamma\Lambda}^{\gamma'\Lambda}(N)=\frac{1}{8\mu}\langle\gamma,\Lambda|P^2|\gamma',\Lambda\rangle_0-$$
$$-\frac{1}{2\mu}\left(\langle\gamma,\Lambda\left|\frac{\partial^2}{\partial R^2}\right|\gamma',\Lambda\rangle_0+\frac{2}{R}\langle\gamma,\Lambda\left|\frac{\partial}{\partial R}\right|\gamma',\Lambda\rangle_0\right)-$$
$$-\frac{i}{2\mu_a}\left(\gamma,\Lambda\left|P_Z\frac{\partial}{\partial R}\right|\gamma',\Lambda\rangle_0+\frac{1}{2R}\langle\gamma,\Lambda\,|P^+L^--P^-L^+|\,\gamma',\Lambda\rangle_0\right)-$$
$$-\frac{1}{\mu}\langle\gamma,\Lambda\left|\frac{\partial}{\partial R}\right|\gamma',\Lambda\rangle_0\frac{\partial}{\partial R}-\frac{i}{2\mu_a}\langle\gamma,\Lambda\,|P_Z|\,\gamma',\Lambda\rangle_0\frac{\partial}{\partial R}, \tag{2.10}$$

$$\hat{\mathcal{L}}_{\gamma\Lambda}^{\gamma'\Lambda-1}(N)=\sqrt{(N+\Lambda)(N-\Lambda+1)}$$
$$\left(\frac{1}{2\mu R^2}\langle\gamma,\Lambda|L^+|\gamma',\Lambda-1\rangle_0-\frac{i}{4\mu_a R}\langle\gamma,\Lambda|P^+|\gamma',\Lambda-1\rangle_0\right), \tag{2.11}$$

$$\hat{\mathcal{L}}_{\gamma\Lambda}^{\gamma'\Lambda+1}(N)=\sqrt{(N-\Lambda)(N+\Lambda+1)}$$
$$\left(\frac{1}{2\mu R^2}\langle\gamma,\Lambda|L^-|\gamma',\Lambda+1\rangle_0+\frac{i}{4\mu_a R}\langle\gamma,\Lambda|P^-|\gamma',\Lambda+1\rangle_0\right), \tag{2.12}$$

Vibrational wave functions $|\gamma,\Lambda,v\rangle_0$ are to be found from the equation

$$\left[-\frac{1}{2\mu}\left(\frac{\partial^2}{\partial R^2}+\frac{2}{R}\frac{\partial}{\partial R}-\frac{\langle\gamma,\Lambda|(L-N)^2|\gamma,\Lambda\rangle_0}{R^2}\right)+\right.$$
$$\left.+\,\epsilon_{\gamma|\Lambda|}(R)-E^{(0)}_{\gamma|\Lambda|v}\right]|\gamma,\Lambda,v\rangle_0=0. \tag{2.13}$$

The adiabatic electronic term earlier obtained in (2.8) is used in Eq. (2.13) as potential energy. The term $\langle\gamma,\Lambda|(L-N)^2|\gamma,\Lambda\rangle_0\cdot R^{-2}$ describes the rotation of nuclei. It should be noted that the electronic–vibro-rotational term $E^{(0)}_{\gamma|\Lambda|v}$ depends on the rotational quantum numbers as well as the wave functions $|\gamma,\Lambda,v\rangle_0$ (vibration–rotation interaction).

Multiplying the Eq. (2.9) by ${}_0\langle\gamma, \Lambda, v|$ and integrating it over internuclear distance one can get an infinite system of algebraic equations for factors G

$$\left(E^{(0)}_{\gamma|\Lambda|v} - E\right) G(\gamma, \Lambda, v|N, M_N) + \sum_{\gamma', v'} \sum_{\Lambda'=|\lambda-1|}^{\Lambda+1} \mathcal{M}^{\gamma'\Lambda'v'}_{\gamma\Lambda v}(N) \cdot G(\gamma, \Lambda, v|N, M_N) = 0, \tag{2.14}$$

where

$$\mathcal{M}^{\gamma'\Lambda'v'}_{\gamma\Lambda v}(N) = \langle\gamma, \Lambda, v|\mathcal{L}^{\gamma'\Lambda'}_{\gamma\Lambda}(N)|\gamma', \Lambda', v'\rangle_0. \tag{2.15}$$

If the adiabatic wave functions are known the matrix elements $\mathcal{M}^{\gamma'\Lambda'v'}_{\gamma\Lambda v}(N)$ can be calculated and the obtained system of equations may be solved numerically by the method of reductions leaving a finite number of the equations in the system. However, the realization of this approach is hardly probable nowdays due to sufficient difficulties of calculation of electronic wave functions and the matrix elements. Let us distinguish two limit cases when the analytical expressions for the factors G can be obtained:

1) The electronic–vibrational state under study is perturbed by a single electronic–vibrational state due to the strong interaction between them (like in the case of Fermi resonance). Then the interaction with other states of the molecule can be neglected and only two equations remain in the system (2.14). One particular case of such irregular perturbations (${}^3\Pi(b) \rightarrow {}^3\Sigma(b)$) was recently considered in Kovács et al [1].

2) The electronic–vibrational state under study interacts with an indefinite number of relatively far lying terms. Then the perturbation theory can be applied for the solution of the system (2.14). The case is usually known as that of regular perturbations.

In the first mentioned case of strong interaction between the levels (resonance perturbation) not only sufficient derivations of term disposition from their adiabatic values exist. Certain changes in spectral line intensities from those predicted by formulas (1.11) are usually observed as well. Some lines may even disappear under background noise. In the situations an identification of spectral lines and the intensity measurements become a difficult problem from the experimental point of view. Therefore we restrict ourselves to regular perturbations which are much more distributed molecular spectra and certainly more important for various applications. This case may be treated in the framework of the second order of the perturbation theory.

3. The line strengths in second order of perturbation theory

Let us represent the coefficients $G(\gamma, \Lambda, v|N, M_N)$ and the perturbed term values $E_{\gamma\Lambda v}$ in the form of the sums of decreasing items (Landau and Lifshitz [10])

$$G(\gamma, \Lambda, v|N, M_N) = G^{(0)} + G^{(1)} + G^{(2)} + \ldots \tag{3.1}$$

and

$$E_{\gamma\Lambda v} = E^{(0)} + E^{(1)} + E^{(2)} + \dots \tag{3.2}$$

where $G^{(0)}$ and $E^{(0)}$ are the adiabatic (unperturbed) values, $G^{(1)}$ and $E^{(1)}$ are the smaller terms of the same order of magnitude as the perturbation term in the Hamiltonian (the first order) and $G^{(2)}$ and $E^{(2)}$, the second order perturbation terms.

Then, substituting (3.1) and (3.2) into the system of equations (2.14), equating the terms of the same order of smallness and limiting to the second order terms one can get the following expression for the energy

$$E_{\gamma\Lambda v} = E^{(0)}_{\gamma|\Lambda|v} + \mathcal{M}^{\gamma\Lambda v}_{\gamma\Lambda v}(N) + {\sum_{\gamma',v'}}' \sum_{\Lambda'=|\Lambda-1|}^{\Lambda+1}{}' \frac{\mathcal{M}^{\gamma'\Lambda'v'}_{\gamma\Lambda v}(N)\,\mathcal{M}^{\gamma\Lambda v}_{\gamma'\Lambda'v'}(N)}{E^{(0)}_{\gamma|\Lambda|v} - E^{(0)}_{\gamma'|\Lambda'|v'}}, \tag{3.3}$$

where the prime noted by the sign of summation means that when summing up over γ', Λ', v' the terms corresponding to $\gamma' = \gamma;\ \Lambda' = \Lambda;\ v' = v$ have to be omitted.

It should be noted that the wave functions $|\gamma, \Lambda\rangle_0$ entering in the matrix elements $\mathcal{M}$ in formula (3.3) must be properly symmetrized by Eq. (3.6).

In the second order of the perturbation theory the corresponding wave function $|\gamma, \Lambda, v, \Gamma\rangle$ (where Γ is the set of rotational quantum numbers) may be written as

$$\begin{aligned}
&|\gamma, \Lambda, v, \Gamma\rangle = \\
&= \sum_{N, M_N} \sqrt{\frac{4\pi}{(2N+1)}}\, G^{(0)}(\gamma, \Lambda, v|N, M_N)\Big[|\gamma, \Lambda\rangle_0 |\gamma, \Lambda, v\rangle_0 \mathcal{D}^N_{-M_N-\Lambda}(\alpha, \beta, 0) + \\
&\sum_{\gamma', \Lambda'} \sum_{\Lambda'=|\Lambda-1|}^{\Lambda+1} \Big(\sqrt{N+\Lambda)(N-\Lambda+1)}\,\delta_{\Lambda'\Lambda-1} + \sqrt{(N-\Lambda)(N+\Lambda+1)} \\
&\delta_{\Lambda'\Lambda+1} + \delta_{\Lambda'\Lambda}\Big) \cdot \Theta^{\gamma\Lambda v}_{\gamma'\Lambda'v'} \times |\gamma', \Lambda'\rangle_0 |\gamma', \Lambda', v'\rangle_0 \mathcal{D}^N_{-M_N-\Lambda'}(\alpha, \beta, 0)\Big],
\end{aligned} \tag{3.4}$$

where

$$\begin{aligned}
&\Theta^{\gamma\Lambda v}_{\gamma'\Lambda'v'} = \\
&= \Big(\sqrt{N+\Lambda)(N-\Lambda+1)}\,\delta_{\Lambda'\Lambda-1} + \sqrt{(N-\Lambda)(N+\Lambda+1)}\,\delta_{\Lambda'\Lambda+1} + \delta_{\Lambda'\Lambda}\Big)^{-1} \cdot \\
&\cdot \frac{\mathcal{M}^{\gamma\Lambda v}_{\gamma'\Lambda'v'}(N)}{E^{(0)}_{\gamma|\Lambda|v} - E^{(0)}_{\gamma'|\Lambda'|v'}},
\end{aligned} \tag{3.5}$$

and $\delta_{ki} = \begin{cases} 1 \text{ for } k=i \\ 0 \text{ for } k\neq i \end{cases}$ is the Kronecker delta function.

The matrix elements of the perturbation operator $\Theta^{\gamma\Lambda v}_{\gamma'\Lambda'v'}$ derived in the form of (3.5) can depend on the rotational quantum numbers only due to the J-dependences of the vibrational wave functions and differences between adiabatic

term values of perturbed and perturbing states of the molecule. Taking into account the weakness of the vibration-rotation interaction and the smallness of the rotational energy differences in comparison with those for electronic–vibrational states (for regular perturbations) the dependence of $\Theta^{\gamma\Lambda v}_{\gamma'\Lambda'v'}$ on the rotational quantum numbers is expected often to be very weak.

The zero order, adiabatic values $G(0)$ must be chosen so that the wave functions $|\gamma, \Lambda, v, \Gamma\rangle$ would correspond to a certain type of angular momentum coupling. Then the wave functions of diatomic molecules must possess certain symmetry for the reflection of the electron coordinates in the plane crossing the internuclear axis. If the operator $\hat{I}$ corresponds to this transformation, then

$$|\gamma, \Lambda, v, \Gamma; \eta\rangle = \frac{1}{\sqrt{2(1+\delta_{\Lambda 0})}} \left(|\gamma, \Lambda, v\rangle + \eta \hat{I}|\gamma, \Lambda, v\rangle\right), \tag{3.6}$$

where the symbols η adopt values $\pm$ in the spectroscopic notation corresponding to the values ± 1 in the formula. Unperturbed electronic wave functions of Σ states already have certain "+" or "−" symmetry. Therefore in this case it is enough to put the value η in the formula (3.6) equal to unity for both "+" and "−" states.

After substituting (3.4) into (3.6) the non-adiabatic wave functions are represented as

$$\begin{aligned}
|\gamma, \Lambda, v, \Gamma; \eta\rangle = \sqrt{\frac{\pi}{(1+\delta_{\Lambda 0})}} \sum_{N, M_N} (2N+1)^{-1} \Big[\big(G^{(0)}(\gamma, \Lambda, v|N, M_N)|\gamma, \Lambda\rangle_0 \cdot \\
\cdot \mathcal{D}^N_{-M_N -\Lambda}(\alpha, \beta, 0) + \eta G^{(0)}(\gamma, -\Lambda, v|N, M_N)|\gamma, -\Lambda\rangle_0 \mathcal{D}^N_{-M_N \Lambda}(\alpha, \beta, 0)\big)|\gamma, \Lambda, v, \rangle_0 + \\
\sum_{\gamma', v'} \sum_{\Lambda' = |\Lambda - 1|}^{\Lambda+1} \Big(\sqrt{N+\Lambda)(N-\Lambda+1)}\delta_{\Lambda'\Lambda-1} + \sqrt{(N-\Lambda)(N+\Lambda+1)} \\
\delta_{\Lambda'\Lambda+1} + \delta_{\Lambda'\Lambda}\Big) \cdot \cdot \Theta^{\gamma\Lambda v}_{\gamma'\Lambda' v'} \cdot \big(G^{(0)}(\gamma, \Lambda, v|N, M_N)|\gamma', \Lambda'\rangle_0 \mathcal{D}^N_{-M_N -\Lambda'}(\alpha, \beta, 0) + \\
\eta G^{(0)}(\gamma, -\Lambda, v|N, M_N)|\gamma', -\Lambda'\rangle_0 \mathcal{D}^N_{-M_N -\Lambda'}(\alpha, \beta, 0)\big)\gamma', \Lambda', v'\rangle_0 \Big].
\end{aligned} \tag{3.7}$$

Constructed in such a way non-adiabatic total wave functions can be used for derivation of the expressions for the line strengths. Substituting the wave functions (3.7) for initial and final states of the transition into the formula (1.8) and taking into account the normalization of the wave functions one obtains

$$S^{\gamma'\Lambda' v' \Gamma' \eta'}_{\gamma''\Lambda'' v'' \Gamma'' \eta''} = \sum_{M'_J, M''_J} |\langle \gamma'', \Lambda'', v'', \Gamma''; \eta''|\mathbf{d}|\gamma', \Lambda', v', \Gamma'; \eta'\rangle|^2. \tag{3.8}$$

For the calculation of the matrix elements the dipole moment of fixed nuclei molecule $\mathbf{d} = e\sum_{j=1}^{N_e} r_j$ is convenient to be represented in the form of spherical vector

$$f_{10} = i d_z \tag{3.9a}$$

$$f_{1\pm 1} = \mp \frac{i}{\sqrt{2}} (d_x \pm i d_y). \tag{3.9b}$$

When the coordinate system is turning its components are to be transformed as spherical functions. It means that certain projections of the vector in the space-fixed frame $\overline{f}_{1q}$ and in the body-fixed frame f_{1q} are connected by the following relation

$$\overline{f}_{1q} = \sum_{q'} \mathcal{D}^1_{q'q} f_{1q'}, \tag{3.10}$$

where $\mathcal{D}^1_{q'q}$ are the Wigner functions.

The expression (3.10) may be used for making the integration in (3.8) over angular variables in an explicit form. But on this step it is necessary to take into consideration the concrete scheme of angular momenta coupling. It is natural to use Hund's limiting cases "a" and "b" in the further analysis because of their prevalence and importance for spectroscopical applications. The next three paragraphs are devoted to "b"→ "b", "a"→ "a", and "a"→ "b" transitions respectively.

4. "b"→ "b" transitions

Let us begin with the case when the energy of the spin-orbit interaction is negligibly small in comparison with the rotational levels separation (Hund's case "b"). Then the molecule can be characterised by definite total momentum excluding the spin of electrons N_0. Therefore in the formula (3.7) the summation over N is eliminated by the Kronecker delta function and the expression for $G^{(0)}_{(b)}$ is reduced to (Nikolsky [11], Ostrovsky and Ustimov [9])

$$G^{(0)}_{(b)} = \frac{1}{4\pi}\sqrt{(2J+1)}\sum_{M_S}(-1)^{N-\Lambda+S-M_S}\begin{pmatrix} J & N & S \\ M_J & -M_N & -M_S \end{pmatrix}\delta_{NN_0}, \tag{4.1}$$

where $\begin{pmatrix} j_1 & j_2 & j_3 \\ m_1 & m_2 & m_3 \end{pmatrix}$ is 3-j symbol (Landau and Lifshitz [10]).

Introducing adiabatic electronic–vibro-rotational wave functions[4]

$$|\nu,\Lambda,S,v,J,N,M_J;\eta\rangle_0 =$$
$$= \sqrt{\frac{(2J+1)(2N+1)}{8\pi(1+\delta_{\Lambda 0})}}\sum_{M_N,M_S}(-1)^{N+S-M_S}\begin{pmatrix} J & N & S \\ M_J & -M_N & -M_S \end{pmatrix}\times$$
$$\times\left[|\nu,\Lambda,S\rangle_0 \mathcal{D}^N_{-M_N-\Lambda}(\alpha,\beta,0) + \eta|\nu,-\Lambda,S\rangle_0 \mathcal{D}^N_{-M_N\Lambda}(\alpha,\beta,0)\right]|\nu,\Lambda,S,v,N\rangle_0 \tag{4.2}$$

[4]For further analysis it is necessary to mark out S-dependences in explicit form. Therefore we will use ν for the set of quantum numbers describing the electronic state of the molecule excluding Λ and S i.e. $\gamma \equiv \{\nu, S\}$.

the expression for non-adiabatic wave function in the first order of the perturbation theory (the formula (3.7)) is represented in the form

$$|\nu, \Lambda, S, v, J, N, M_J; \eta\rangle = |\nu, \Lambda, S, v, J, N, M_J; \eta\rangle_0 +$$
$$\sum_{\overline{\nu}\overline{v}} \sum_{\overline{\Lambda}=|\Lambda-1|}^{\Lambda+1} \left(\sqrt{(N+\Lambda)(N-\Lambda+1)}\delta_{\overline{\Lambda}\Lambda-1} + \sqrt{(N-\Lambda)(N+\Lambda+1)}\delta_{\overline{\Lambda}\Lambda+1} + \delta_{\overline{\Lambda}\Lambda}\right)$$
$$\times \Theta^{\nu\Lambda Sv}_{\overline{\nu}\overline{\Lambda}S\overline{v}} |\overline{\nu}, \overline{\Lambda}, S, \overline{v}, J, N, M_J; \eta\rangle_0. \tag{4.3}$$

Then the matrix element of the dipole moment entering into the expression for line strengths (3.8) may be represented as the sum of matrix elements calculated on adiabatic wave functions:

$$\begin{aligned}
&\langle \nu'', \Lambda'', S, v'', J'', N'', M''_J; \eta''|\mathbf{d}|\nu', \Lambda', S, v', J', N', M'_J; \eta'\rangle = \\
&= \langle \nu'', \Lambda'', S, v'', J'', N'', M''_J; \eta''|\mathbf{d}|\nu', \Lambda', S, v', J', N', M'_J; \eta'\rangle_0 + \\
&+ \sum_{\overline{\nu}', \overline{v}'} \sum_{\overline{\Lambda}'=|\overline{\Lambda}'-1|}^{\Lambda'+1} \left(\sqrt{(N'+\Lambda')(N'-\Lambda'+1)}\delta_{\overline{\Lambda}'\Lambda'-1} + \right. \\
&\qquad \left. + \sqrt{(N'-\Lambda')(N'+\Lambda'+1)}\delta_{\overline{\Lambda}'\Lambda'+1} + \delta_{\overline{\Lambda}'\Lambda'}\right) \times \\
&\times \Theta^{\nu'\Lambda' Sv'}_{\overline{\nu}'\overline{\Lambda}'S\overline{v}'} \langle \nu'', \Lambda'', S, v'', J'', N'', M''_J; \eta''|\mathbf{d}|\nu', \Lambda', S, v', J', N', M'_J; \eta'\rangle + \\
&+ \sum_{\overline{\nu}'', \overline{v}''} \sum_{\overline{\Lambda}''=|\overline{\Lambda}''-1|}^{\Lambda''+1} \left(\sqrt{(N''+\Lambda'')(N''-\Lambda''+1)}\delta_{\overline{\Lambda}''\Lambda''-1} + \right. \\
&\qquad \left. + \sqrt{(N''-\Lambda'')(N''+\Lambda''+1)}\delta_{\overline{\Lambda}''\Lambda''+1} + \delta_{\overline{\Lambda}''\Lambda''}\right) \times \\
&\times \Theta^{\nu''\Lambda'' Sv''}_{\overline{\nu}''\overline{\Lambda}''S\overline{v}''} \langle \nu'', \Lambda'', S, v'', J'', N'', M''_J; \eta''|\mathbf{d}|\nu', \Lambda', S, v', J', N', M'_J; \eta'\rangle_0.
\end{aligned} \tag{4.4}$$

Using the formula (3.10) it is possible to make integration over angular variables in the adiabatic matrix elements, then one obtains the following expression

$$\begin{aligned}
&\langle \nu'', \Lambda'', S, v'', J'', N'', M''_J; \eta''|\overline{f}_{1q}|\nu', \Lambda', S, v', J', N', M'_J; \eta'\rangle_0 = \\
&= \left[\frac{(2J'+1)(2J''+1)(2N'+1)(2N''+1)}{(1+\delta_{\Lambda'0})(1+\delta_{\Lambda''0})}\right]^{\frac{1}{2}} \cdot \\
&\cdot \sum_{M'_N, M''_N} \sum_{M'_S, M''_S} (-1)^{N'-\Lambda-M'_S-N''+M''_N+M''_S} \begin{pmatrix} J'' & N'' & S \\ M''_J & -M''_N & -M''_S \end{pmatrix} \times \\
&\times \begin{pmatrix} J' & N' & S \\ M'_J & -M'_N & -M'_S \end{pmatrix} \begin{pmatrix} N' & 1 & N'' \\ -M'_N & q & M''_N \end{pmatrix} \times \\
&\times \begin{pmatrix} N' & 1 & N'' \\ -\Lambda' & \Lambda'-\Lambda'' & \Lambda'' \end{pmatrix} R^{\nu'\Lambda' Sv'N'}_{\nu''\Lambda'' Sv''N''},
\end{aligned} \tag{4.5}$$

where electronic transition moment

$$R^{\nu'\Lambda'Sv'N'}_{\nu''\Lambda''Sv''N''} =$$

$$= \frac{\xi}{2\left[(1+\delta_{\Lambda'0})(1+\delta_{\Lambda''0})\right]^{\frac{1}{2}}} \langle \nu'', \Lambda'', S, v'', N'' | \left(\langle \nu'', \Lambda'', S | f_{1q} | \nu', \Lambda', S \rangle_0 + \right. \tag{4.6}$$

$$\left. + \langle \nu'', -\Lambda'', S | f_{1q} | \nu', -\Lambda', S \rangle_0 \right) | \nu', \Lambda', S, v', N' \rangle_0,$$

$$\xi = \begin{cases} 1 \text{ for } \Lambda' \text{ and } \Lambda'' \neq 0, \\ 2 \text{for } \Lambda' \text{ or } \Lambda'' = 0. \end{cases}$$

It should be noted that electric dipole transitions are going on between molecular states of opposite symmetry about the inversion of the particles relative to the middle of internuclear axis (opposite sign of the levels). Therefore

$$\eta'\eta''(-1)^{N'+N''+1} = 1.$$

Substituting (4.4), (4.5), (4.6) into (3.8) and summing over M'_J, M''_J the general expression for the line strength in the second order of the perturbation theory is obtained

$$S^{\nu'\Lambda'Sv'J'N'\eta'}_{\nu''\Lambda''Sv''J''N''\eta''} = (2J'+1)(2J''+1)(2N'+1)(2N''+1) \begin{Bmatrix} J' & S & N' \\ N'' & 1 & J'' \end{Bmatrix}^2$$

$$\left| \left[\begin{pmatrix} N' & 1 & N'' \\ -\Lambda' & \Lambda'-\Lambda'' & \Lambda'' \end{pmatrix} R^{\nu'\Lambda'Sv'N'}_{\nu''\Lambda''Sv''N''} + \right.\right.$$

$$+ \sum_{\overline{v}',\overline{v}'} \sum_{\overline{\Lambda}'=|\overline{\Lambda}'-1|}^{\Lambda'+1} \left(\sqrt{(N'+\Lambda')(N'-\Lambda'+1)}\,\delta_{\overline{\Lambda}'\Lambda'-1} + \right.$$

$$\left. + \sqrt{(N'-\Lambda')(N'+\Lambda'+1)}\,\delta_{\overline{\Lambda}'\Lambda'+1} + \delta_{\overline{\Lambda}'\Lambda'} \right) \begin{pmatrix} N' & \overline{1} & N'' \\ -\overline{\Lambda}' & \overline{\Lambda}'-\Lambda'' & \Lambda'' \end{pmatrix} \times$$

$$\times \Theta^{\nu'\Lambda'Sv'}_{\overline{v}'\overline{\Lambda}'S\overline{v}'} R^{\overline{v}'\overline{\Lambda}'S\overline{v}'N'}_{\nu''\Lambda''Sv''N''} +$$

$$+ \sum_{\overline{v}'',\overline{v}''} \sum_{\overline{\Lambda}''=|\overline{\Lambda}''-1|}^{\Lambda''+1} \left(\sqrt{(N''-\Lambda'')(N''+\Lambda''+1)}\,\delta_{\overline{\Lambda}''\Lambda''-1} + \right.$$

$$\left. + \sqrt{(N''-\Lambda'')(N''+\Lambda''+1)}\,\delta_{\overline{\Lambda}''\Lambda''+1} + \delta_{\overline{\Lambda}''\Lambda''} \right) \times$$

$$\left. \left. \begin{pmatrix} N' & 1 & N'' \\ -\Lambda' & \Lambda'-\overline{\Lambda}'' & \overline{\Lambda}'' \end{pmatrix} \Theta^{\nu''\Lambda''Sv''}_{\overline{v}''\overline{\Lambda}''S\overline{v}''} R^{\nu'\Lambda'Sv'N'}_{\overline{v}''\overline{\Lambda}''S\overline{v}''N''} \right] \right|^2, \tag{4.7}$$

where $\begin{Bmatrix} j_1 & j_2 & j_3 \\ j_4 & j_5 & j_6 \end{Bmatrix}$ is 6-j symbol (Landau and Lifshitz [10]).

This expression is sufficiently simplified after summing over J''. Taking into account the expression (Landau and Lifshitz [10])

$$\sum_j (2j+1)(2j'+1) \begin{Bmatrix} j_1 & j_2 & j' \\ j_3 & j_4 & j \end{Bmatrix} \begin{Bmatrix} j_3 & j_2 & j \\ j_1 & j_4 & j'' \end{Bmatrix} = \delta_{j'j''}, \tag{4.8}$$

it may readily be shown that

$$S^{\nu'\Lambda'Sv'J'N'\eta'}_{\nu''\Lambda''Sv''N''\eta''} \equiv \sum_{J''} S^{\nu'\Lambda'Sv'J'N'\eta'}_{\nu''\Lambda''Sv''J''N''\eta''} = (2J'+1)(2N''+1)\cdot$$

$$\left|\left[\begin{pmatrix} N' & 1 & N'' \\ -\Lambda' & \Lambda'-\Lambda'' & \Lambda'' \end{pmatrix} R^{\nu'\Lambda'Sv'N'}_{\nu''\Lambda''Sv''N''} + \right.\right.$$

$$+ \sum_{\overline{\nu}',\overline{v}'} \sum_{\overline{\Lambda}'=|\overline{\Lambda}'-1|}^{\Lambda'+1} \left(\sqrt{(N'+\Lambda')(N'-\Lambda'+1)}\,\delta_{\overline{\Lambda}'\Lambda'-1} + \right.$$

$$\left. + \sqrt{(N'-\Lambda')(N'+\Lambda'+1)}\,\delta_{\overline{\Lambda}'\Lambda'+1} + \delta_{\overline{\Lambda}'\Lambda'}\right) \begin{pmatrix} N' & 1 & N'' \\ -\overline{\Lambda}' & \overline{\Lambda}'-\Lambda'' & \Lambda'' \end{pmatrix} \times$$

$$\times \Theta^{\nu'\Lambda'Sv'}_{\overline{\nu}'\overline{\Lambda}'S\overline{v}'} R^{\overline{\nu}'\overline{\Lambda}'S\overline{v}'N'}_{\nu''\Lambda''Sv''N''} +$$

$$+ \sum_{\overline{\nu}'',\overline{v}''} \sum_{\overline{\Lambda}''=|\overline{\Lambda}''-1|}^{\Lambda''+1} \left(\sqrt{(N''+\Lambda'')(N''-\Lambda''+1)}\,\delta_{\overline{\Lambda}''\Lambda''-1} + \right.$$

$$\left. + \sqrt{(N''-\Lambda'')(N''+\Lambda''+1)}\,\delta_{\overline{\Lambda}''\Lambda''+1} + \delta_{\overline{\Lambda}''\Lambda''}\right) \times$$

$$\left.\begin{pmatrix} N' & 1 & N'' \\ -\Lambda' & \Lambda'-\overline{\Lambda}'' & \overline{\Lambda}'' \end{pmatrix} \Theta^{\nu''\Lambda''Sv''}_{\overline{\nu}''\overline{\Lambda}''S\overline{v}''} R^{\nu'\Lambda'Sv'N'}_{\overline{\nu}''\overline{\Lambda}''S\overline{v}''N''}\right]\Bigg|^2 . \tag{4.9}$$

Neglecting the effect of perturbing interactions by equating the matrix elements Θ to zero in formula (4.7) one obtains the expression for adiabatic line strengths for $\Lambda'(b) \to \Lambda''(b)$ transitions

$$S^{\nu'\Lambda'Sv'J'N'\eta'}_{\nu''\Lambda''Sv''J''N''\eta''} = \left|R^{\nu'\Lambda'Sv'N'}_{\nu''\Lambda''Sv''N''}\right|^2 S^{J'N'}_{J''N''}, \tag{4.10}$$

where the expression for rotational line strengths (Hönl–London factors)

$$S^{J'N'}_{J''N''} = (2J'+1)(2J''+1)(2N'+1)(2N''+1) \begin{Bmatrix} J' & S & N' \\ N'' & 1 & J'' \end{Bmatrix}^2 \begin{pmatrix} N' & 1 & N'' \\ -\Lambda' & \Lambda'-\Lambda'' & \Lambda'' \end{pmatrix}^2 . \tag{4.11}$$

For particular cases this formula gives simple analytical expressions for $S^{J'N'}_{J''N''}$ coinciding with those listed in Kovács [2]. The simple sum rule valid for $S^{J'N'}_{J''N''}$:

$$\sum_{J'',N''} S^{J'N'}_{J''N''} = (2J'+1). \tag{4.12}$$

The general formula (4.7) may be sufficiently simplified for certain cases interesting in applications. As an example we list below the expressions for

$^{2S+1}\Sigma' \to {}^{2S+1}\Sigma''$ transitions where only two branches P $(\Delta N = N'' - N' = +1)$ and R $(\Delta N = -1)$ take place:

P-branch

$$S^{\nu' 0 S v' J' N' \eta'}_{\nu'' 0 S v'' J'' N'+1 \eta''} = (2J'+1)(2J''+1) \begin{Bmatrix} J' & S & N' \\ N'+1 & 1 & J'' \end{Bmatrix}^2 (N'+1)$$

$$\left| R^{\nu' 0 S v' N'}_{\nu'' 0 S v'' N'+1} \right|^2 \times$$

$$\times \left| 1 + \gamma^{\nu' 0 S v' N'}_{\nu'' 0 S v'' N'+1}(\Sigma - \Sigma) - N' \gamma^{\nu' 0 S v' N'}_{\nu'' 0 S v'' N'+1}(\Sigma' - \Pi) - \right. \tag{4.13}$$

$$\left. - (N'+2) \gamma^{\nu' 0 S v' N'}_{\nu'' 0 S v'' N'+1}(\Sigma'' - \Pi) \right|^2 ,$$

R-branch

$$S^{\nu' 0 S v' J' N' \eta'}_{\nu'' 0 S v'' J'' N'-1 \eta''} = (2J'+1)(2J''+1) \begin{Bmatrix} J' & S & N' \\ N'-1 & 1 & J'' \end{Bmatrix}^2 N'$$

$$\left| R^{\nu' 0 S v' N'}_{\nu'' 0 S v'' N'-1} \right|^2 \times$$

$$\times \left| 1 + \gamma^{\nu' 0 S v' N'}_{\nu'' 0 S v'' N'-1}(\Sigma - \Sigma) - (N'+1) \gamma^{\nu' 0 S v' N'}_{\nu'' 0 S v'' N'-1}(\Sigma' - \Pi) + \right. \tag{4.14}$$

$$\left. + (N'-1) \gamma^{\nu' 0 S v' N'}_{\nu'' 0 S v'' N'-1}(\Sigma'' - \Pi) \right|^2 .$$

Here

$$\gamma^{\nu' 0 S v' N'}_{\nu'' 0 S v'' N''}(\Sigma - \Sigma) = \left(R^{\nu' 0 S v' N'}_{\nu'' 0 S v'' N''} \right)^{-1}$$

$$\left[\sum_{\overline{\nu}', \overline{v}'} \Theta^{\nu' 0 S v'}_{\overline{\nu}' 0 S \overline{v}'} R^{\overline{\nu}' 0 S \overline{v}' N'}_{\nu'' 0 S v'' N''} + \sum_{\overline{\nu}'', \overline{v}''} \Theta^{\nu'' 0 S v''}_{\overline{\nu}'' 0 S \overline{v}''} R^{\nu' 0 S v' N'}_{\overline{\nu}'' 0 S \overline{v}'' N''} \right] , \tag{4.15a}$$

$$\gamma^{\nu' 0 S v' N'}_{\nu'' 0 S v'' N''}(\Sigma' - \Pi) = \left(R^{\nu' 0 S v' N'}_{\nu'' 0 S v'' N''} \right)^{-1} \sum_{\overline{\nu}', \overline{v}'} \Theta^{\nu' 0 S v'}_{\overline{\nu}' 0 S \overline{v}'} R^{\overline{\nu}' 0 S \overline{v}' N'}_{\nu'' 0 S v'' N''} (\sqrt{2})^{-1}, \tag{4.15b}$$

$$\gamma^{\nu' 0 S v' N'}_{\nu'' 0 S v'' N''}(\Sigma'' - \Pi) = \left(R^{\nu' 0 S v' N'}_{\nu'' 0 S v'' N''} \right)^{-1} \sum_{\overline{\nu}'', \overline{v}''} \Theta^{\nu'' 0 S v''}_{\overline{\nu}'' 0 S v''} R^{\nu' 0 S v' N'}_{\overline{\nu}'' 0 S \overline{v}'' N''} (\sqrt{2})^{-1}. \tag{4.15c}$$

The magnitudes $\gamma(\Sigma' - \Pi)$ and $\gamma(\Sigma'' - \Pi)$ describe the perturbation of Σ', v' and Σ'', v'' states respectively due to their interaction with all possible $\Pi, \overline{v}$ electronic-vibrational states of the molecule. The factor $\gamma(\Sigma - \Sigma)$ corresponds to the perturbation of the states under study by all $\Sigma, \overline{v}$ states.

It is interesting now to study the conditions which are necessary for derivation in the second order of perturbation theory of the simple sum rules (for line strengths

of all possible transitions starting from or coming to the same rotational level) analogous to those obtained in adiabatic theory, e.g. formula (4.12) (see also the discussion in Kuznetzova et al [12]). For simplicity let us consider the concrete example of ${}^{2S+1}\Sigma', v', J' \to {}^{2S+1}\Sigma'', v'', J''$ transitions. Then we must take the sum of the line strengths for transitions in P and R branches (formulas (4.13) and (4.14)) starting from upper level with rotational quantum number J' and make summing up over J''. Neglecting J-dependences of : i) vibrational wave functions and ii) term differences between perturbed and perturbing levels one obtains

$$\begin{aligned}
&\sum_{J''}\left(S^{\nu'0Sv'J'N'\eta'}_{\nu''0Sv''J''N'+1\eta''}S^{\nu'0Sv'J'N'\eta'}_{\nu''0Sv''J''N'-1\eta''}\right)=\left|R^{\nu'0Sv'}_{\nu''0Sv''}\right|^2\times\\
&\times\Bigg[(2J'+1)\left(1+\gamma^{\nu'0Sv'}_{\nu''0Sv''}(\Sigma-\Sigma)\right)^2\\
&-\frac{(2J'+1)(N'+1)}{(2N'+1)}\gamma^{\nu'0Sv'}_{\nu''0Sv''}(\Sigma''-\Pi)\left(1+\gamma^{\nu'0Sv'}_{\nu''0Sv''}(\Sigma-\Sigma)\right)-\\
&-2(2J'+1)N'(N'+1)\gamma^{\nu'0Sv'}_{\nu'0Sv''}(\Sigma'-\Pi)\gamma^{\nu'0Sv'}_{\nu''0Sv''}(\Sigma''-\Pi)+\\
&(2J'+1)\left[(N')^2+N'+4\right]\left(\gamma^{\nu'0Sv'}_{\nu'0Sv''}(\Sigma''-\Pi)\right)^2+\\
&+(2J'+1)N'(N'+1)\left(\gamma^{\nu'0Sv'}_{\nu''0Sv''}(\Sigma'-\Pi)\right)^2\Bigg].
\end{aligned}\tag{4.16}$$

It can be seen from the formula (4.16) that the sum rule (4.12) is not generally valid in the case of sufficient perturbations of the levels. The interaction between the states with the same Λ (in our case with $\Lambda=0$) does not prevent derivation of the sum rule analogous to the formula (4.12).

When we propose the final electronic state to be unperturbed and assume the perturbation effect in initial state of the transition to be weak enough for neglecting the terms containing squares of γ, then the sum rule (4.16) is reduced to

$$\sum_{J''}\left(S^{\nu'0Sv'J'N'\eta'}_{\nu''0Sv''J''N'+1\eta''}+S^{\nu'0Sv'J'N'\eta'}_{\nu''0Sv''J''N'-1\eta''}\right)=(2J'+1)f^{\nu'0Sv'}_{\nu''0Sv''},\tag{4.17}$$

where

$$f^{\nu'0Sv'}_{\nu''0Sv''}=\left|R^{\nu'0Sv'}_{\nu''0Sv''}\right|^2\left(1+2\gamma^{\nu'0Sv'}_{\nu''0Sv''}(\Sigma-\Sigma)\right)\tag{4.18}$$

being independent of J', J''.

From this the useful relation follows

$$\frac{\sum_{J''}\left(S^{\nu'0Sv'J'N'\eta'}_{\nu''0Sv''J''N'+1\eta''}+S^{\nu'0Sv'J'N'\eta'}_{\nu''0Sv''J''N'-1\eta''}\right)}{\sum_{\overline{J}''}\left(S^{\nu'0Sv'\overline{J}'N'\eta'}_{\nu''0Sv''\overline{J}''N'+1\eta''}+S^{\nu'0Sv'\overline{J}'N'\eta'}_{\nu''0Sv''\overline{J}''N'-1\eta''}\right)}=\frac{(2J'+1)}{(2\overline{J}'+1)}.\tag{4.19}$$

As appears from the above in the second order of perturbation theory simple sum rules such as (4.18) analogous to the adiabatic ones (formula (4.12)) are valid only under certain conditions, namely:

1) negligible vibration–rotation interaction in vibrational wave functions,

2) negligible J-dependency of term differences between perturbed and perturbing electronic–vibro-rotational levels,

3) electronic–vibrational state chosen for summing up over rotational quantum numbers J (in the above consideration it is the final state of the transition (in emission) and $\overline{J} = J''$) have to be unperturbed[5] It is obvious that this result illustrated here on the concrete example of ${}^{2S+1}\Sigma' \to {}^{2S+1}\Sigma''$ transitions has to be valid in the general case also.

5. "a"→ "a" transitions

In Hund's case "a" the energy of spin-internuclear axis interaction exceeds essentially values of rotational levels separation. The well-defined quantum numbers are total angular momentum J and total spin of electrons S, their projections on the internuclear axis Ω and Σ, resultant electronic angular momentum about internuclear axis Λ and the projection of J about certain axis fixed in space M_J. The expression for factors $G^{(0)}_{(a)}$ may be written as (Nikolsky [11], Ostrovsky and Ustimov [9]):

$$G^{(0)}_{(a)} = \frac{1}{4\pi}\sqrt{(2J+1)(2N+1)} \sum_{M_S}(-1)^{M_S-\Sigma}\begin{pmatrix} J & N & S \\ M_J & -M_N & -M_S \end{pmatrix}\begin{pmatrix} J & N & S \\ \Omega & -\Lambda & -\Sigma \end{pmatrix}. \tag{5.1}$$

Non-adiabatic wave functions $|\nu, \Lambda, \Omega, S, v, J, M_J; \eta\rangle$ in the first order of perturbation theory are represented as

$$|\nu, \Lambda, \Omega, S, v, J, M_J; \eta\rangle = \sum_N \Bigg[|\nu, \Lambda, \Omega, S, v, J, M_J; \eta\rangle_0 + \sum_{\overline{\nu v}} \sum_{\overline{\Lambda}=|\Lambda-1|}^{\Lambda+1} \begin{pmatrix} J & N & S \\ \Omega & -\Lambda & -\Sigma \end{pmatrix}\begin{pmatrix} J & N & S \\ \overline{\Omega} & -\overline{\Lambda} & -\overline{\Sigma} \end{pmatrix}^{-1} \left(\sqrt{(N+\Lambda)(N-\Lambda+1)}\delta_{\overline{\Lambda}\Lambda-1} + \sqrt{(N-\Lambda)(N+\Lambda+1)}\delta_{\overline{\Lambda}\Lambda+1} + \delta_{\overline{\Lambda}\Lambda}\right) \cdot \Theta^{\nu\Lambda\Omega S v}_{\overline{\nu}\overline{\Lambda}\overline{\Omega}S\overline{v}} |\overline{\nu}, \overline{\Lambda}, \overline{\Omega}, S, \overline{v}, J, N, M_J; \eta\rangle_0 \Bigg], \tag{5.2}$$

[5] If one is interested in the sum rules for the transition probabilities instead of those for the line strengths then the additional assumption of negligible J-dependency of ν^3 is necessary.

where

$$|\nu,\Lambda,\Omega,S,v,J,N,M_J;\eta\rangle_0 = \sqrt{\frac{(2J+1)}{8\pi(1+\delta_{\Lambda 0})}}\sum_{M_N}\sum_{M_S}(-1)^{M_S}(2N+1)\times$$
$$\times\begin{pmatrix} J & N & S \\ M_J & -M_N & -M_S\end{pmatrix}\begin{pmatrix} J & N & S \\ \Omega & -\Lambda & -\Sigma\end{pmatrix}\Big[|\nu,\Lambda,\Omega,S\rangle_0 \mathcal{D}^N_{-M_N-\Lambda}(\alpha,\beta,0)+$$
$$+\eta(-1)^{J+N+S}\times|\nu,-\Lambda,-\Omega,S\rangle_0\mathcal{D}^N_{-M_N\Lambda}(\alpha,\beta,0)\Big]|\nu,\Lambda,\Omega,S,v,J\rangle_0. \tag{5.3}$$

Notice that in Hund's case "a" the adiabatic vibrational wave functions (and consequently the matrix elements Θ) depend on J. Moreover, from the beginning we have to take into account spin–spin and spin–orbit interactions in potential V entering the Hamiltonian (2.2). These interactions may change the value of Σ (i.e. corresponding matrix elements are not equal to zero). The effect is taken into account by summing over Σ in the formula (5.2). It is included in summing over ν characterizing the electronic state of molecule.

Substituting (5.1)-(5.3) into (3.8) and integrating over angular variables one obtains the following formula for the line strengths:

$$S^{\nu'\Lambda'\Omega'Sv'J'\eta'}_{\nu''\Lambda''\Omega''Sv''J''\eta''} =$$
$$(2J'+1)(2J''+1)\sum_{N',N''}\sum_{\overline{N}',\overline{N}''}(2N'+1)(2N''+1)(2\overline{N}'+1)(2\overline{N}''+1)\cdot$$
$$\cdot\begin{pmatrix} J' & N' & S \\ \Omega' & -\Lambda' & -\Sigma\end{pmatrix}\begin{pmatrix} J' & \overline{N}' & S \\ \Omega' & -\Lambda' & -\Sigma\end{pmatrix}\cdot\cdot\begin{pmatrix} J'' & N'' & S \\ \Omega'' & -\Lambda'' & -\Sigma\end{pmatrix}\begin{pmatrix} J'' & \overline{N}'' & S \\ \Omega'' & -\Lambda'' & -\Sigma\end{pmatrix}\cdot$$
$$\cdot\begin{Bmatrix} J' & S & N' \\ N'' & 1 & J''\end{Bmatrix}\begin{Bmatrix} J' & S & \overline{N}' \\ \overline{N}'' & 1 & J''\end{Bmatrix}\times\Bigg[\begin{pmatrix} N' & 1 & N'' \\ -\Lambda' & \Lambda'-\Lambda'' & \Lambda''\end{pmatrix}R^{\nu'\Lambda'\Omega'Sv'J'}_{\nu''\Lambda''\Omega''Sv''J''}+$$
$$+\sum_{\overline{\nu}'\overline{v}'}\sum_{\overline{\Lambda}'=|\Lambda'-1|}^{\Lambda'+1}\Bigg(\sqrt{(N'+\Lambda')(N'-\Lambda'+1)}\delta_{\overline{\Lambda}'\Lambda'-1}+\sqrt{(N'-\Lambda')(N'+\Lambda'+1)}\cdot$$
$$\cdot\ \delta_{\overline{\Lambda}'\Lambda'+1}+\delta_{\overline{\Lambda}'\Lambda'}\Bigg)\begin{pmatrix} N' & 1 & N'' \\ -\overline{\Lambda}' & \overline{\Lambda}'-\Lambda'' & \Lambda''\end{pmatrix}\Theta^{\nu'\Lambda'\Omega'Sv'}_{\overline{\nu}'\overline{\Lambda}'\overline{\Omega}'S\overline{v}'}R^{\overline{\nu}'\overline{\Lambda}'\overline{\Omega}'Sv'J'}_{\nu''\Lambda''\Omega''Sv''J''}+$$
$$+\sum_{\overline{\nu}''\overline{v}''}\sum_{\overline{\Lambda}''=|\Lambda''-1|}^{\Lambda''+1}\Bigg(\sqrt{(N''+\Lambda'')(N''-\Lambda''+1)}\delta_{\overline{\Lambda}''\Lambda''-1}+$$
$$+\sqrt{(N''-\Lambda'')(N''+\Lambda''+1)}\cdot$$
$$\cdot\ \delta_{\overline{\Lambda}''\Lambda''+1}+\delta_{\overline{\Lambda}''\Lambda''}\Bigg)\begin{pmatrix} N' & 1 & N'' \\ -\Lambda' & \Lambda'-\overline{\Lambda}'' & \overline{\Lambda}''\end{pmatrix}\Theta^{\nu''\Lambda''\Omega''Sv''}_{\overline{\nu}'\overline{\Lambda}''\overline{\Omega}''S\overline{v}''}R^{\nu'\Lambda'\Omega'Sv'J'}_{\overline{\nu}''\overline{\Lambda}''\overline{\Omega}''S\overline{v}''J''}\Bigg]$$

$$\left[\begin{pmatrix} \overline{N}' & 1 & \overline{N}'' \\ -\Lambda' & \Lambda' - \Lambda'' & \Lambda'' \end{pmatrix} R^{\nu'\Lambda'\Omega' S v' J'}_{\nu''\Lambda''\Omega'' S v'' J''} + \right.$$

$$+ \sum_{\overline{\nu}'\overline{v}'} \sum_{\overline{\Lambda}'=|\Lambda'-1|}^{\Lambda'+1} \left(\sqrt{(\overline{N}' + \Lambda')(\overline{N}' - \Lambda' + 1)}\, \delta_{\overline{\Lambda}'\Lambda'-1} + \sqrt{(N' - \Lambda')(N' + \Lambda' + 1)} \cdot \right.$$

$$\left. \cdot\ \delta_{\overline{\Lambda}'\Lambda'+1} + \delta_{\overline{\Lambda}'\Lambda'} \right) \times \begin{pmatrix} \overline{N}' & 1 & \overline{N}'' \\ -\overline{\Lambda}' & \overline{\Lambda}' - \Lambda'' & \Lambda'' \end{pmatrix} \Theta^{\nu'\Lambda'\Omega' S v'}_{\overline{\nu}'\overline{\Lambda}'\overline{\Omega}' S \overline{v}'} R^{\overline{\nu}'\overline{\Lambda}'\overline{\Omega}' S \overline{v}' J'}_{\nu''\Lambda''\Omega'' S v'' J''} +$$

$$+ \sum_{\overline{\nu}''\overline{v}''} \sum_{\overline{\Lambda}''=|\Lambda''-1|}^{\Lambda''+1} \left(\sqrt{(\overline{N}'' + \Lambda'')(\overline{N}'' - \Lambda'' + 1)}\, \delta_{\overline{\Lambda}''\Lambda''-1} \right.$$

$$+ \sqrt{(N'' - \Lambda'')(N'' + \Lambda'' + 1)} \cdot$$

$$\left. \left. \cdot\ \delta_{\overline{\Lambda}''\Lambda''+1} + \delta'_{\overline{\Lambda}''\Lambda} \right) \times \begin{pmatrix} \overline{N}' & 1 & \overline{N}'' \\ -\overline{\Lambda}' & \overline{\Lambda}' - \Lambda'' & \Lambda'' \end{pmatrix} \Theta^{\nu''\Lambda''\Omega'' S v''}_{\overline{\nu}'\overline{\Lambda}''\overline{\Omega}'' S \overline{v}''} R^{\nu'\Lambda'\Omega' S v' J'}_{\overline{\nu}''\overline{\Lambda}''\overline{\Omega}'' S \overline{v}'' \overline{J}''} \right]^* . \tag{5.4}$$

Using the known expression for $3-j$ symbols (Edmonds [13])

$$\begin{aligned} &\sqrt{J(J+1) - M(M+1)} \begin{pmatrix} j_1 & j_2 & J \\ m_1 & m_2 & -M \end{pmatrix} \\ &+ \sqrt{j_1(j_1+1) - m_1(m_1+1)} \begin{pmatrix} j_1 & j_2 & J \\ m_1+1 & m_2 & -M-1 \end{pmatrix} \\ &+ \sqrt{j_2(j_2+1) - m_2(m_2+1)} \begin{pmatrix} j_1 & j_2 & J \\ m_1 & m_2+1 & -M-1 \end{pmatrix} = 0 \end{aligned} \tag{5.5}$$

and the connection of $6-j$ and $3-j$ symbols

$$\begin{pmatrix} j_1 & j_2 & j_3 \\ m_1 & m_2 & m_3 \end{pmatrix} \begin{Bmatrix} j_1 & j_2 & j_3 \\ J_1 & J_2 & J_3 \end{Bmatrix} = \sum_{M_1, M_2, M_3} (-1)^{J_1+J_2+J_3+M_1+M_2+M_3} \times$$

$$\times \begin{pmatrix} J_1 & J_2 & j_3 \\ M_1 & -M_2 & m_3 \end{pmatrix} \begin{pmatrix} J_2 & J_3 & j_1 \\ M_2 & M_3 & m_1 \end{pmatrix} \begin{pmatrix} J_3 & J_1 & j_2 \\ M_3 & -M_1 & m_2 \end{pmatrix} \tag{5.6}$$

the summation over $N', \overline{N}', N''$ and $\overline{N}''$ can be made in general form and the expression for the line strengths (independent of the spin S in explicit form) is reduced to

$$S^{\nu'\Lambda'\Omega' S v' J' \eta'}_{\nu''\Lambda''\Omega'' S v'' J'' \eta''} = (2J'+1)(2J'+1) \left| \left[\begin{pmatrix} J' & 1 & J'' \\ -\Omega' & \Omega' - \Omega'' & \Omega'' \end{pmatrix} R^{\nu'\Lambda'\Omega' S v' J'}_{\nu''\Lambda''\Omega'' S v'' J''} + \right. \right.$$

$$+\sum_{\overline{\nu}'\overline{v}'}\sum_{\overline{\Lambda}'=|\Lambda'-1|}^{\Lambda'+1}\sum_{\overline{\Omega}'=|\Omega'-1|}^{\Omega'+1}\Big(\sqrt{(J'+\Omega')(J'-\Omega'+1)}\delta_{\overline{\Omega}'\Omega'-1}+$$

$$+\sqrt{(J'-\Omega')(J'+\Omega'+1)}\delta_{\overline{\Omega}'\Omega'+1}+\delta_{\overline{\Omega}'\Omega'}\Big)\times$$

$$\times\begin{pmatrix}J' & 1 & J''\\ -\overline{\Omega}' & \overline{\Omega}'-\Omega'' & \Omega''\end{pmatrix}\Theta^{\nu'\Lambda'\Omega' S v'}_{\overline{\nu}'\overline{\Lambda}'\overline{\Omega}' S\overline{v}'}R^{\overline{\nu}'\overline{\Lambda}'\overline{\Omega}' S\overline{v}' J'}_{\nu''\Lambda''\Omega'' S v'' J''}+$$

$$+\sum_{\overline{\nu}''\overline{v}''}\sum_{\overline{\Lambda}''=|\Lambda''-1|}^{\Lambda''+1}\sum_{\overline{\Omega}''=|\Omega''-1|}^{\Omega''+1}\Big(\sqrt{(J''+\Omega'')(J''-\Omega''+1)}\delta_{\overline{\Omega}''\Omega''-1}+ \tag{5.7}$$

$$+\sqrt{(J''-\Omega'')(J''+\Omega''+1)}\delta_{\overline{\Omega}''\Omega''+1}+\delta_{\overline{\Omega}''\Omega''}\Big)\times$$

$$\times\begin{pmatrix}J' & 1 & J''\\ -\Omega' & \Omega'-\overline{\Omega}'' & \overline{\Omega}''\end{pmatrix}\Theta^{\nu''\Lambda''\Omega'' S v''}_{\overline{\nu}''\overline{\Lambda}''\overline{\Omega}'' S\overline{v}''}R^{\nu'\Lambda'\Omega' S v' J'}_{\overline{\nu}''\overline{\Lambda}''\overline{\Omega}'' S\overline{v}''\overline{J}''}\Big]\Big|^2 .$$

In the case of negligible effects of the perturbation and vibration–rotation interaction the matrix elements Θ may be equated to zero and the rotational line strength $S^{J'}_{J''}$ is factorized. Then from the formula (5.7) one can obtain usual adiabatic formulas for Hönl–London factors for "a"→"a" transitions

$$S^{J'}_{J''}=(2J'+1)(2J''+1)\begin{pmatrix}J' & 1 & J''\\ -\Omega' & \Omega'-\Omega'' & \Omega''\end{pmatrix}^2 \tag{5.8}$$

coinciding with those listed in Kovács [3] (see table 3.1 on p. 121).

In the second order of the perturbation theory the sum rule for "a"→"a" transitions is the same as that for "b"→"b" ones and it is valid under the same restricting conditions (see above §4).

It should be noted that the variables describing spin in wave functions (5.2) are considered in the space-fixed frame. If one considers the spin in the body-fixed frame then in Hund's case "a" the rotation of the molecule may be described by only one Wigner function $\mathcal{D}^J_{-M_J-\Omega}(\alpha,\beta,0)$ and the expression (5.7) can be derived in a much simpler way.

But wave functions (5.2) have their own advantages, for example non-adiabatic wave functions for Hund's case "b" (formula (4.3)) may be easily constructed from adiabatic wave functions (5.2) by:

i) leaving in the sum over N the single term corresponding to the total angular momentum without spin;

ii) making the normalization procedure (then the 3-j symbol

$$\begin{pmatrix}J & N & S\\ \Omega & -\Lambda & -\Sigma\end{pmatrix}$$

describing summing over S and N into total angular momentum J will vanish).

In the same manner the expression for the line strengths of "b"→"b" transitions may be obtained from that for "a"→"a" transitions.

6. "b"⇌"a" transitions

Finally, from the formula (5.4) one gets the expression for the line strengths when one of the states of the transition belongs to Hund's case "b" whereas another corresponds to Hund's case "a". For example one can obtain the following expression for the line strengths of "a"→"b" transitions

$$
\begin{aligned}
&S^{\nu'\Lambda'\Omega'Sv'J'\eta'}_{\nu''\Lambda''Sv''J''N''\eta''} = \\
&= (2J'+1)(2J''+1)(2N''+1)\begin{pmatrix} J'' & N'' & S \\ \Omega'+\Lambda''-\Lambda' & -\Lambda'' & -\Omega'+\Lambda' \end{pmatrix}^2 \times \\
&\times \Bigg| \Bigg[\begin{pmatrix} J' & 1 & J'' \\ -\Omega' & \Lambda'-\Lambda'' & \Omega''-\Lambda'+\Lambda'' \end{pmatrix} R^{\nu'\Lambda'\Omega'Sv'J'}_{\nu''\Lambda''Sv''N''} + \\
&+ \sum_{\overline{\nu}'\overline{v}'} \sum_{\overline{\Lambda}'=|\Lambda'-1|}^{\Lambda'+1} \sum_{\overline{\Omega}'=|\Omega'-1|}^{\Omega'+1} \Big(\sqrt{(J'+\Omega')(J'-\Omega'+1)}\,\delta_{\overline{\Omega}'\Omega'-1} \\
&\qquad + \sqrt{(J'-\Omega')(J'+\Omega'+1)}\,\delta_{\overline{\Omega}'\Omega'+1} + \delta_{\overline{\Omega}'\Omega'} \Big) \times \\
&\times \begin{pmatrix} J' & 1 & J'' \\ -\overline{\Omega}' & \overline{\Lambda}'-\Lambda'' & \overline{\Omega}''-\overline{\Lambda}'+\Lambda'' \end{pmatrix} \Theta^{\nu'\Lambda'\Omega'Sv'}_{\overline{\nu}'\overline{\Lambda}'\overline{\Omega}'S\overline{v}'} R^{\overline{\nu}'\overline{\Lambda}'\overline{\Omega}'S\overline{v}'J'}_{\nu''\Lambda''Sv''N''} \\
&+ \sum_{\overline{\nu}''\overline{v}''} \sum_{\overline{\Lambda}''=|\Lambda''-1|}^{\Lambda''+1} \Big(\sqrt{(N''-\Lambda'')(N''+\Lambda''+1)}\,\delta_{\overline{\Lambda}''\Lambda''-1} + \\
&\qquad + \sqrt{(N''+\Lambda'')(N''-\Lambda''+1)}\,\delta_{\overline{\Lambda}''\Lambda''+1} + \delta_{\overline{\Lambda}''\Lambda''} \Big) \times \\
&\times \begin{pmatrix} J' & 1 & J'' \\ -\Omega' & \Lambda'-\overline{\Lambda}'' & \Omega'-\Lambda'+\overline{\Lambda}'' \end{pmatrix} \Theta^{\nu''\Lambda''Sv''}_{\overline{\nu}''\overline{\Lambda}''S\overline{v}''} R^{\nu'\Lambda'\Omega'Sv'J'}_{\overline{\nu}''\overline{\Lambda}''S\overline{v}''N''} \Bigg] \Bigg|^2 .
\end{aligned}
\tag{6.1}
$$

Neglecting the perturbations among the adiabatic electronic states of the molecule the rotational line strengths $S^{J'}_{J''N''}$ are expressed as

$$
\begin{aligned}
S^{J'}_{J''N''} = (2J'+1)(2J''+1)(2N''+1) &\begin{pmatrix} J'' & N'' & S \\ \Omega'+\Lambda''-\Lambda' & -\Lambda'' & -\Omega'+\Lambda' \end{pmatrix}^2 \\
&\begin{pmatrix} J' & 1 & J'' \\ -\Omega' & \Lambda'-\Lambda'' & \Omega'-\Lambda'+\Lambda'' \end{pmatrix}^2
\end{aligned}
\tag{6.2}
$$

and the sum rule analogous to formula (4.12) must be fulfilled.

7. Discussion

In principle the matrix elements Θ and R entering the formulas for the line strengths may be obtained from the numerical calculations of electronic and vibrational wave functions in an adiabatic approximation. Such pure theoretical determination of the radiative transition probabilities seems to be hardly realizable nowadays even for the simplest molecules due to computation difficulties.

Therefore we propose the semiempirical approach to be much more fruitful for determining the electronic–vibro-rotational radiative transition probabilities in diatomic molecules[6] . The theoretical formulas of the present paper may be used for this purpose if one considers the matrix elements Θ and R (or their combinations) as fitting parameters which are to be derived from experimental data about relative line strengths or radiative lifetimes. For example in the case of $\Sigma \to \Sigma$ transitions such combinations of matrix elements were denoted above as γ.

It is important that in the formulas for the line strengths the main part of their dependences on rotational quantum numbers is extracted and written in an explicit form. The remainder part, J-dependences of matrix elements Θ and R, is connected with vibration–rotation interaction in vibrational wave functions (matrix elements Θ can also depend on the rotation through term differences between perturbed and perturbing adiabatic states of the molecule). The dependences are usually quite weak and the matrix elements as well as their combinations may often be regarded as approximately constants[7]. Then the expression for the line strengths is sufficiently simplified. For instance in the case of $\Sigma \to \Sigma$ transitions only three parameters γ remain for each pair of initial and final electronic–vibrational states. Further decrease of a number of fitting parameters may be achieved by a consideration of more detailed models. In particular, in the Franck–Condon approximation for perturbation and radiative processes the matrix elements are proportional to the values of corresponding overlap intergrals of vibrational wave functions, which can be calculated numerically if the potential curves of the states are known (see e.g. Lavrov et al [14]).

The perturbations are traditionally investigated by experimental studies of wave numbers of the spectral lines and analysis of electronic–vibro-rotational term dispositions. The proposed theoretical description of radiative transition probabilities makes it possible to consider regular perturbations of intensity distributions in the rotational structure of emission and adsorption bands (apparently the first

[6]It should be noted that this approach is widely disseminated in the studies of electronic-vibrational transitions (see e.g. Kuznetzova et al [12]).

[7]Taking into account the weaknesses of these dependences they may be also represented in the form of power series

$$R = R_0 + R_1 J' + R_2 (J')^2 + \dots$$

and

$$\Theta = \Theta_0 + \Theta_1 J' + \Theta_2 (J')^2 + \dots$$

where R_0, R_1, R_2 and $\Theta_0, \Theta_1, \Theta_2$ do not depend on rotational quantum numbers. Then, in analysing experimental data one can omit higher order terms and in the expansions only one, two or three first terms remain.

successful example of this kind — studies of the intensity anomalies in R and P branches of hydrogen Fulcher-α bands — has been shown in our recent work: Kovács et al [1]).

In the next paper of this series the general theoretical scheme of the present work is illustrated by the application to the semiempirical determination of the radiative transition probabilities for the bands starting from the levels of the triplet $3p$-complex of the H_2 molecule — $d^3\Pi_u^{\pm}, v', N' \to a^3\Sigma_g^+, v'', N''$ and $e^3\Sigma_u^+, v', N' \to a^3\Sigma_g^+, v'', N''$ transitions.

The results obtained in the present work appear to be able to extend the possibilities in studies of electronic–vibro-rotational collisional transitions by including into consideration widely disseminated cases of regular (monotonic) perturbations and noticeable vibration–rotational interaction. Thus, an inclusion of non-adiabatic wave functions composed in the form (3.7) into the theoretical scheme developed in Ostrovsky and Ustimov [9] and Lavrov et al [15] makes it possible to give and adequate description of the collisional transitions between perturbed states of the molecule. From the other side the values of the transition probabilities which can be obtained semiempirically on the basis of the formulas of the present paper may be used then for the determination of the population densities of the electronic–vibro-rotational states (from measured spectral line intensities) inside the collision chamber in crossed beams and gas-beam experiments (see e.g. Lavrov et al [16]).

The formulas presented in the present work for electric dipole transitions may be easily rewritten for radiative transitions of higher multipolarity. For that the angular momentum equal to unity in $6j$ and $3j$ symbols of formulas (4.7), (5.7) and (6.1) have to be changed for the angular momentum corresponding to the order of the multipolarity. For example the unity used for dipole transitions must be replaced by two for electric quadrupole transitions.

Acknowledgements

The authors are indebted to Professor I. Kovács, Professor V. N. Ostrovsky and Professor T. K. Rebane for helpful discussions.

References

1. I. Kovács, B. P. Lavrov, V. V. Tyutchev and V. I. Ustimov, Acta Phys. Hung., *54*, 161, 1983.
2. G. Herzberg, Spectra of Diatomic Molecules, Van Nostrand, New York, 1950.
3. I. Kovács, Rotational Structure in the Spectra of Diatomic Molecules, Adam Hilger, London, Akadémiai Kiadó, Budapest, 1969.
4. D. Villarejo, R. Stockbauer and M. G. Inghram, J. Chem. Phys., *50*, 1754, 1969.
5. T. V. Kirgjat'eva, B. P. Lavrov, V. N. Ostrovsky, M. V. Tyutchev and V. I. Ustimov, Opt. Spectrosk., *52*, 39, 1982.
6. N. Ginsburg and G. H. Dieke, Phys. Rev., *59*, 632, 1941.
7. W. Kołos and L. Wolnievicz, Rev. Mod. Phys., *35*, 473, 1963.
8. D. A. Varshalovich, A. N. Moskalev and V. K. Khersonsky, Kvantovaja teorija uglovogo momenta (in Russian: Quantum theory of angular momentum), Nauka, Leningrad, 1975.

9. V. N. Ostrovsky and V. I. Ustimov, J. Phys. B: At. Mol. Phys., *14*, 1139, 1981.
10. L. D. Landau and E. M. Lifshitz, Quantum Mechanics, Addison-Wesley, Reading, Mass., 1965.
11. K. V. Nikolsky, Kvantovaja Mehanika Molekuli (in Russian: Quantum Mechanics of Molecules) GTTI, Leningrad-Moscow, 1934, p. 411.
12. L. A. Kuznetzova, N. E. Kuz'menko, Yu. Ya. Kuzyakov and Yu. A. Plastinin, Veroyatnosty Opticheskih Perehodov Dvuhatomnih Molekul (in Russian: Optical Transition Probabilities in Diatomic Molecules), Nauka, Moscow, 1980.
13. A. R. Edmonds, Angular Momentum in Quantum Mechanics, Princeton, 1957.
14. B. P. Lavrov, M. V. Tyutchev, V. I. Ustimov, Opt. Spectrosk., *64*, 1251, 1988.
15. B. P. Lavrov, V. N. Ostrovsky and V. I. Ustimov, J. Phys. B: At. Mol Phys., *14*, 4389, 1981.
16. B. P. Lavrov, V. N. Ostrovsky and V. I. Ustimov, J. Phys. B: At. Mol Phys., *14*, 4701, 1981.

Acta Physica Hungarica 67 (1-2), pp. 27-45 (1990)

RECENT ADVANCES AT NASA IN CALCULATING THE ELECTRONIC SPECTRA OF DIATOMIC MOLECULES*

ELLIS E. WHITING

ELORET Institute[a], Sunnyvale, California 94087 USA

and

JOHN A. PATERSON

NASA Ames Research Center, Moffett Field, California 94035 USA

(Received 24 September 1988)

Advanced entry vehicles, such as the proposed Aero-assisted Orbital Transfer Vehicle, provide new and challenging problems for spectroscopy. Large portions of the flow field about such vehicles will be characterized by chemical and thermal nonequilibrium. Only by considering the actual overlap of the atomic and rotational lines emitted by the species present can the impact of the radiative transport within the flow field be assessed correctly. To help make such an assessment, a new computer program is described that can generate high-resolution, line-by-line spectra for any spin-allowed transitions in diatomic molecules. The program includes the matrix elements for the rotational energy and distortion to fourth order, the spin–orbit, spin–spin, and spin–rotation interactions to first order, and the lambda splitting by a perturbation calculation. An overview of the Computational Chemistry Branch at Ames Research Center is also presented.

Introduction

It is indeed a great pleasure for me to be here at Tihany and to participate in this Conference dedicated to Professor Kovács. His dedicated and creative research of over 50 years has brought order and clarity to the study of diatomic spectroscopy and has provided us with an incredible array of practical and elegant formulae that enable us to calculate realistic spectra. His work has certainly been the basis for much of my own work. His book [12] on the "Rotational Structure in the Spectra of Diatomic Molecules" presents the theory in a logical step-by-step way and the results in an easy to use format. Professor Kovács, I am sure that all of us here have been, and will continue to be, influenced greatly by your accomplishments. We thank you very sincerely, and we wish you continued success in your life and research.

*Presented at the Conference on High Resolution Electronic Spectroscopy of Molecules, Tihany, Hungary, 19-24 September 1988

[a]Mailing address: NASA Ames Research Center, Moffett Field, CA 94035, USA

I am also pleased to be here as an unofficial representative of NASA. The coming year (1989) after nearly 3 years of pain, soul-searching, and redesign, will see the rebirth of the Shuttle program and at least two launches of great scientific and spectroscopic interest: the placing of the Hubble telescope in Earth orbit and the launch of the Galileo Jupiter-entry mission. The Hubble telescope will see farther back into time than ever before possible, and the Jupiter entry probe will provide direct in situ measurements in the atmosphere of this mysterious giant. We expect that the new discoveries made by these missions to greatly increase our understanding of the universe and they will, I am sure, provide a vast array of new puzzles to be solved. Unfortunately, we will need to be very patient for results from the Galileo mission, as the transit time to Jupiter will be approximately 7 long years.

The U.S.S.R. is also planning several exciting space launches in 1989 and will land two probes on the surface of the small, 30-km-oblong, Martian moon Phobos. NASA will be cooperating in this mission by providing deep space tracking information to the U.S.S.R. We all hope for world peace, and I believe that the expansion of such cooperative scientific efforts help to achieve our true destiny as one people, one world.

The emphasis of this paper, however, is not on current scientific missions, but instead is focused on some of the ways that spectroscopy will help in building the knowledge base needed to design future advanced atmospheric entry vehicles. A perspective for this work is provided by a brief description of the proposed National Aero-Space Plane (NASP) and the Aero-assisted Orbital Transfer Vehicle (AOTV) concepts and a description of the Aero-assist Flight Experiment (AFE) project. As a part of this perspective, the importance of assessing the impact of radiative transport on an AOTV is described and a new computer program for calculating high-resolution spectra needed for making this assessment is discussed. The last section of the paper highlights the Computational Chemistry Branch at Ames Research Center, and some of its latest results are presented to illustrate the present state of theoretical spectroscopic research.

Overview of NASP and AOTV

The proposed NASP and AOTV have produced a renaissance in atmospheric entry studies after a hiatus of nearly 15 years. They have reopened old areas of study and placed new demands on the technology base.

An artist's conception of what the NASP might look like is shown in Fig. 1. The NASP represents an ultimate aero-space plane that would take off from a traditional runway, fly through the atmosphere at high speed, and proceed on into near-Earth space. It is conceived as a possible follow-on to the Shuttle vehicle and would function as a resupply and cargo vehicle for the space station. An alternate version of the NASP may not have a space capability, but instead will function as an intercontinental passenger aircraft, which would fly in the upper reaches of the

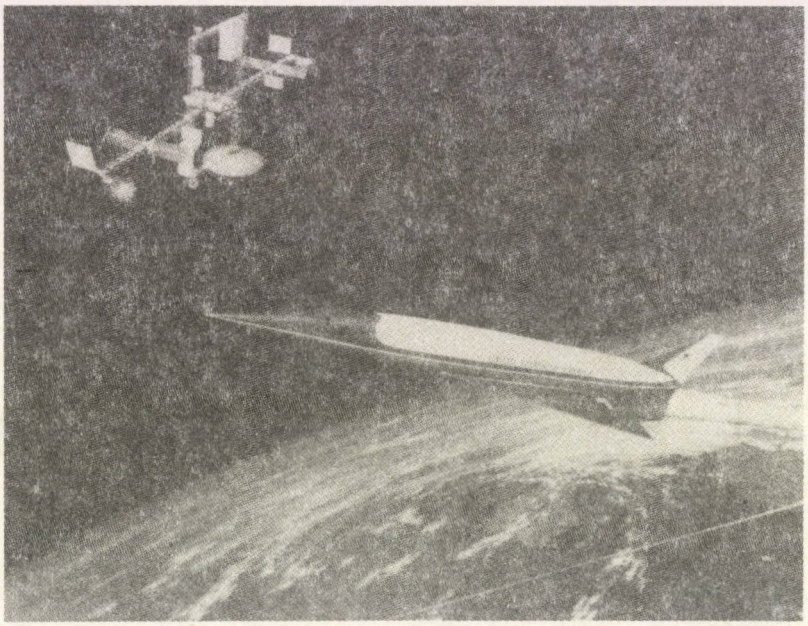

Fig. 1. Artist's conception of National Aero-Space Plane (NASP)

atmosphere and be able to travel from Los Angeles to Tokyo in about two hours.

A possible design of an AOTV is shown in Fig. 2. This spacecraft is intended to ferry people and cargo between geosynchronous orbit and low Earth orbit or between the moon and low Earth orbit. The payload of an orbital transfer vehicle can be approximately doubled if the Earth's atmosphere, rather than a retrorocket, is used to dissipate the kinetic energy of such a vehicle after it has returned from a high orbit and before it is inserted into a low Earth orbit.

The NASP and AOTV differ from previous entry vehicles, such as Apollo and Space Shuttle, in that they are intended to fly at high altitude and high speed for considerable periods of time. Under these conditions the air flowing around them will be characterized by extensive regions that are not in either chemical or thermal equilibrium, i.e., the collision rate in the reacting flow field is too low to promote equilibrium before the gas flows through a significant portion of the flow field.

One important result of these flight conditions is that the radiative heating of the vehicle will be greatly enhanced. Thus, the design of safe and efficient vehicles requires that the radiative heating from the nonequilibrium flow field around the vehicles must be known accurately. This situation provides an important impetus to spectroscopic research and to the development of engineering methods based on spectroscopic techniques and results.

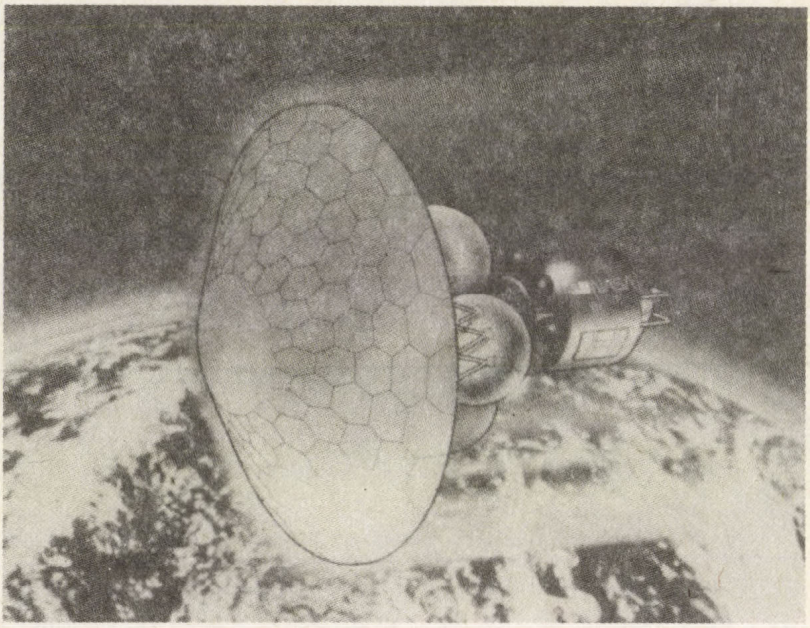

Fig. 2. Artist's conception of a possible design for the Aero-assisted Orbital Transfer Vehicle (AOTV)

Flow-field solutions must be developed that couple fluid mechanics, chemical reactions, other relaxation phenomena, and radiative transport. The radiative portion of the problem requires knowledge of the excitation state, the high-temperature properties, and the spectroscopic parameters of the species present in the flow field, as well as the availability of computational tools necessary to calculate the radiative transport to a high degree of precision.

The technology base necessary to design NASP and AOTV vehicles is being developed. However, because of the increase in knowledge necessary in many scientific and engineering disciplines, it is quite likely that intermediate test vehicles will be flown before an actual vehicle is designed. The NASP program has not yet advanced to the stage of having an approved test vehicle program. The AOTV has reached this stage of development, and the test program is called the Aero-assist Flight Experiment (AFE).

The AFE test vehicle for AOTV is shown in Fig. 3 as it might appear as it enters the Earth's atmosphere. A tentative mission profile for the AFE is shown in Fig. 4. This profile shows the vehicle being launched from the Shuttle, being propelled toward the Earth to simulate return from a geosynchronous orbit, flying through the Earth's upper atmosphere at an altitude of about 70 km, leaving the atmosphere, and being recovered by the Shuttle.

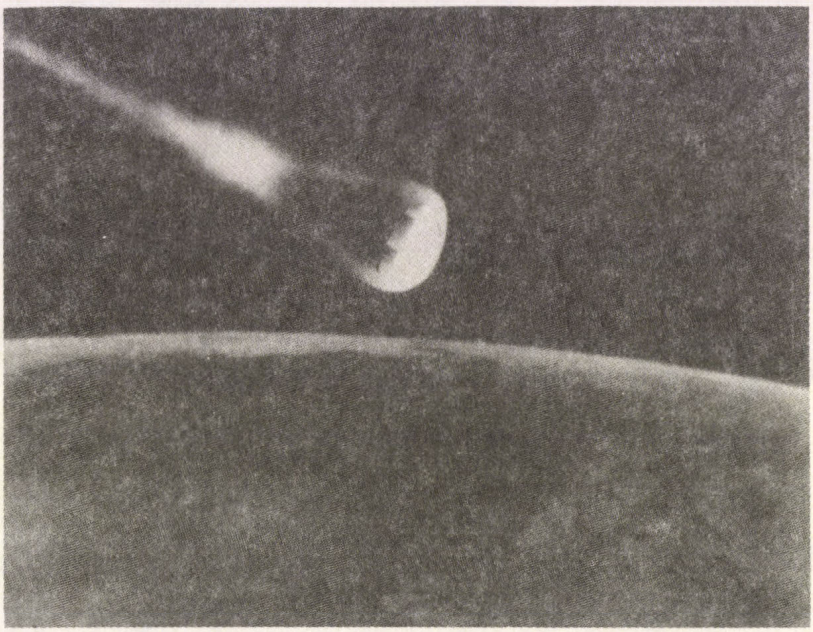

Fig. 3. Aero-assist Flight Experiment (AFE) vehicle as it enters the Earth's atmosphere

A large amount of high- and low-resolution spectroscopic, pressure, acceleration, and temperature data will be recorded during the flight through the atmosphere. These data will provide a realistic data base for a reasonably large vehicle against which predictions and predictive techniques can be evaluated, and will lead to the development of a more advanced and reliable computational capability. Some important aspects of the AFE project that are directly related to the base of spectroscopic knowledge are discussed in the following Section.

AFE and radiative transport

The radiometric data taken during the AFE flight is crucial in helping to understand the chemistry and excitation mechanisms taking place in the flow field. Interpreting these data will involve a complex interplay of predictions based on various flow-field, chemical, excitation, and radiation models. The signal recorded by each radiometric instrument will be an integral of all optical effects taking place within the view field and optical bandpass of that instrument. The principal tool of interpreting these data will be the flow-field solution being developed by the

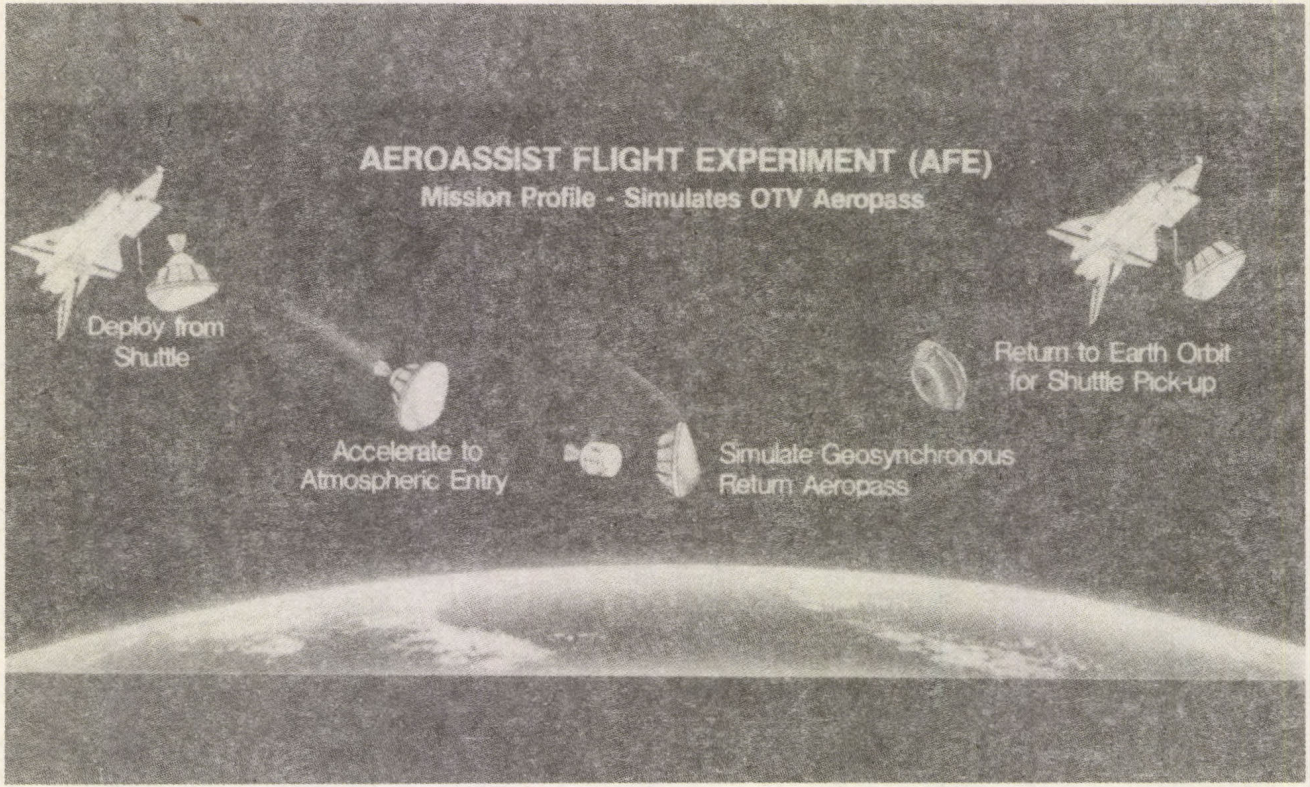

Fig. 4. A tentative mission profile for the AFE

people on the project team who are expert in various aspects of computational fluid dynamics.

The accuracy of the flow-field solution will depend upon realistic chemical and excitation models, and upon accurate reaction rates, cross sections, partition functions, transport properties, and transition moments in gases characterized by multiple temperatures, some of which are well above the temperatures at which reliable experimental data are available.

Dr. Chul Park at Ames Research Center, and a member of the AFE team, has developed a two-temperature (TTv) model of the reacting flow and a quasi-steady state (QSS) model of the electronic excitation of the atomic and molecular species in the nonequilibrium flow field. The TTv model equates the kinetic temperature of the atoms and molecules and the rotational temperature. It also equates the vibrational, electronic excitation and electron kinetic temperatures. The QSS model assumes that the resultant population of an electronic state changes much more slowly than the separate rates for populating and depopulating the state.

The TTv model greatly simplifies the flow-field solution, and the QSS models the calculation of radiative intensities. These models appear to give reasonable results when compared to available experimental data for compressive flow, such as those on the front surface of an entry vehicle, but they may not be valid for the expanding flow from the outer edge of the vehichle into the wake region.

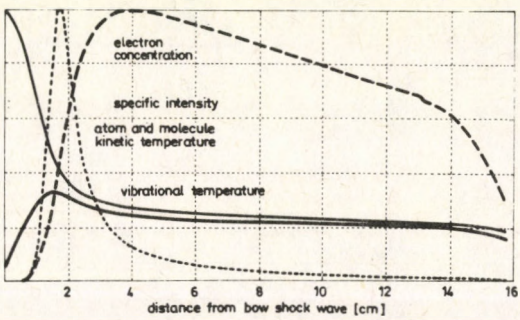

Fig. 5. Flow-field properties along AFE stagnation streamline near peak heating

Computer programs for the one-dimensional reacting flow behind a normal shock wave and along the stagnation streamline between a normal shock wave and a blunt body have been written by Dr. Park using the TTv and QSS models. Some sample results generated by the stagnation streamline program for conditions appropriate for the AFE flight trajectory are shown in Fig. 5. Only a qualitative description of the flow field is given, as all reference to flight and thermodynamic conditions have been removed from the figure.

Figure 5 shows that the heavy-particle kinetic temperature jumps to a high value directly behind the shock wave where the vibrational temperature is still close to the free-stream value. As the flow continues, collisions begin to dissociate the

molecules and excite the internal states of the atoms and molecules. These processes lower the heavy-particle kinetic temperature and cause the vibrational temperature to rise. At some point the vibrational temperature reaches a peak value and begins to follow the kinetic temperature as equilibrium is approached. Also, at some point a significant number of electrons begin to be produced and they play a major role in the electronic excitation process.

The total specific intensity of the gas from 200 to 1000 nm is also presented in Fig. 5. The specific intensity rises to a peak value and then begins to drop substantially as the flow relaxes toward equilibrium. The large nonequilibrium overshoot in the radiation is due to the high temperatures and the species present in the reacting region of the shock layer. The radiation above 200 nm is produced primarily by diatomic species that exist in the reacting region, but disappear as equilibrium is approached, under the AFE entry conditions. Below a wavelength of 200 nm the radiation is produced principally by atomic nitrogen and oxygen.

The radiation emitted by the shock layer alters the energy distribution in the shock layer, heats the vehicle, and produces the signal levels for the radiometric measurements. Thus, the impact of the radiation on the flow field, the vehicle, and the signal levels must be carefully assessed. Under the flight conditions of the AFE trajectory, the radiative heating load is expected to be a significant fraction of the total heat load.

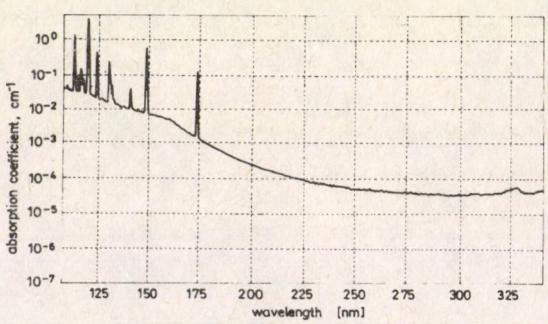

Fig. 6. Calculated absorption coefficient at a point on the AFE stagnation streamline

The problem of radiative energy transport is greatly simplified for two special situations: (1) the gas is optically thick so that the photons are absorbed very close to the point where they are emitted and (2) the gas is optically thin so that all photons emitted are lost from the flow field. In the case of an optically thick gas, neither significant energy redistribution nor radiative transport occurs. In the case of an optically thin gas, the radiation acts as a simple energy sink at each point in space, and vehicle heating can be calculated in a straightforward manner by line-of-sight methods.

If the flow field on the AFE does not fall into either of these simple cases, then the very difficult general radiative transport problem, which couples each point in the flow field to all other points, must be solved or adequately approximated.

The absorption coefficient of the gas in the flow field gives a qualitative assessment of the importance of radiative transport on the flow-field solution and the radiative heating of a vehicle. Fig. 6 shows the calculated absorption coefficient for the spectral region from about 110 to 340 nm, at a point on the stagnation streamline shown in Fig. 5, near the peak of the specific intensity curve. The absorption coefficient at longer wavelengths does not change the conclusions that follow. The line width used in these calculations was 0.5 nm in order to cover a wide wavelength range. The actual line width, however, is about 0.005 nm. Thus, peak absorption coefficient values shown here must be increased by about a factor of 100 to correspond to the actual peak absorption coefficients.

Multiplying the values plotted in Fig. 6 by 100 still leaves the maximum absorption coefficients in the region above 200 nm less than 0.01 cm^{-1}. This value indicates that the flow field above 200 nm is expected to be nearly optically thin, as the shock layer thickness is only about 15 cm.

The calculated absorption coefficients shown here below 200 nm are produced principally by atomic lines with a background of free–bound and free–free transitions. Across each atomic line the absorption coefficient varies by several orders of magnitude. Near the line center where the radiation is most intense the absorption coefficients, after again being multiplied by a factor of 100, are about 10.0 cm^{-1} or greater. This calculation indicates that below 200 nm the gas is probably optically thick. The radiation emitted in this spectral region, however, is so intense that even if only a small fraction of it reaches the vehicle surface, it could produce a significant contribution to the total heat load. Therefore, the radiative transport in this region of the spectrum must be examined in far greater detail to assess the importance of radiative transfer on vehicle heating and on the energy redistribution in the shock layer.

A. Allowed transitions

1.	$b'\ ^1\Sigma_u^+ - X\ ^1\Sigma_g^+$	First Birge – Hopfield
2.	$b\ ^1\Pi_u - X\ ^1\Sigma_g^+$	Second Birge – Hopfield

B. Forbidden transitions

1.	$A\ ^3\Sigma_g^+ - X\ ^1\Sigma_g^+$	Vegard – Kaplan
2.	$B\ ^3\Pi_g - X\ ^1\Sigma_g^+$	Wilkinson
3.	$W^3\Delta_u - X\ ^1\Sigma_g^+$	Saum – Benesch
4.	$B'\ ^3\Sigma_u^- - X\ ^1\Sigma_g^+$	Ogawa – Tanaka – Wilkinson
5.	$a\ ^1\Pi_g - X\ ^1\Sigma_g^+$	Lyman – Birge – Hopfield
6.	$w\ ^1\Delta_u - X\ ^1\Sigma_g^+$	Tanaka
7.	$a'\ ^1\Sigma_u^- - X\ ^1\Sigma_g^+$	Ogawa – Tanaka – Wilkinson – Mulliken

Fig. 7. N_2 band systems involving the ground state

Future radiative transport calculations will be improved in two important ways: (1) by including the N_2 band systems that transition to the ground state

and emit significant radiation, and (2) by using more accurate, higher-resolution spectral calculations. Most of the important N_2 band systems that transition to the ground state are shown in Fig. 7. Two of these systems, the first and second Birge–Hopfield systems, are allowed transitions and will be included in future calculations. In addition, some of the stronger forbidden transitions may also be included, such as the Vegard–Kaplan and Lyman–Birge–Hopfield systems.

The inclusion of these N_2 band systems will increase the specific intensity emitted by the gas below 200 nm. However, because they involve the ground state of the N_2 molecule and because the N_2 concentration is always fairly high under AFE flight conditions, it is expected that their contributions to the absorption coefficient will be large and that they will cause the radiative transport to decrease.

By using more realistic line shapes and an improved method of calculating the wavelengths of rotational lines, the radiative transport calculations will be improved by increasing the spectral resolution. High-resolution calculations are necessary to ensure that the actual overlap of rotational and atomic lines occurring in the flow field is handled correctly. The line width and shape under the AFE flight conditions are determined principally by Doppler broadening. However, a range of line shapes, including some with strong wings, will be explored to determine the sensitivity of the calculations to this parameter.

Accurate energy levels, or, equivalently, wavelengths or wavenumbers, will be calculated by direct diagonalization of the Hamiltonian matrices for the upper and lower states. The computer program developed to make these calculations at high spectral resolution is discussed in the following Section.

Computer program for high-resolution spectral calculations

The computer program for calculating high-resolution spectra is based on direct diagonalization of the Hamiltonian matrix, which includes the matrix elements shown in Fig. 8. The matrix elements included are those for the rotational energy and rotational distortion up to fourth order and first-order spin–orbit; spin–spin, and spin–rotation interactions. The expressions shown are derived in Kovács [12], except for the H_v and F_v rotational terms. The general form of the rotational terms is given by Murai and Shimauchi [14]. The spin–spin interaction between the lambda components of $^3\Pi_0$ substates has not been included in the Hamiltonian matrix, but is included indirectly in the perturbation calculation of the lambda splitting, to be discussed later.

The Hamiltonian matrix is developed for a single electronic state in Hund's case (a) basis functions. That is, both Λ and Σ are defined in the basis set, which is a realistic basis for the nonrotating molecule. The transition from Hund's case (a) to case (b) as molecular rotation increases is produced by the off-diagonal terms in the Hamiltonian matrix. Diagonalization of the Hamiltonian matrix gives the energy levels and the proper mix of the basis functions that defines the corresponding wave functions.

For: Single state (Σ, Π, Δ, etc.)
$\Delta\Lambda = 0$
Hund's case (a)

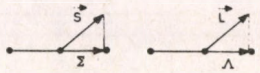

$\Omega_1 = \Lambda + \Sigma$
$\Omega_2 = \Lambda + \Sigma - 1$
$\vdots$
$\Omega_{2S+1} = \Lambda - \Sigma$

$H_{ij} \equiv H(\Lambda\Sigma_i;\Lambda\Sigma_j) = \langle \Lambda S\Sigma_i; J\Omega_i|H|J\Omega_j;\Lambda S\Sigma_j\rangle$
Spin–orbit: $H^{so}(\Lambda\Sigma;\Lambda\Sigma) = A\Lambda\Sigma$
Spin–spin: $H^{ss}(\Lambda\Sigma;\Lambda\Sigma) = \epsilon[3\Sigma^2 - S(S+1)]$
Spin–rotation: $H^{sr}(\Lambda\Sigma;\Lambda\Sigma) = \gamma[\Sigma^2 - S(S+1)]$
$H^{sr}(\Lambda\Sigma;\Lambda\Sigma \pm 1) = -\frac{\gamma}{2}[S(S+1) - \Sigma(\Sigma \pm 1)]^{1/2}[J(J+1) - \Omega(\Omega \pm 1)]^{1/2}$
Rotational energy and distortion:
$H^{P}(\Lambda\Sigma_i;\Lambda\Sigma_j) = B_v M - D_v M^2 + H_v M^3 + F_v M^4 + \cdots$
where:
$M(\Lambda\Sigma;\Lambda\Sigma) = J(J+1) - \Omega^2 + S(S+1) - \Sigma^2$
$M(\Lambda\Sigma;\Lambda\Sigma \pm 1) = [S(S+1) - \Sigma(\Sigma \pm 1)]^{1/2}[J(J+1) - \Omega(\Omega \pm 1)]^{1/2}$
$M^2 = M \bullet M$
$M^3 = M^2 \bullet M$
$M^4 = M^3 \bullet M$
(etc.)

Fig. 8. Hamiltonian matrix elements

Lambda splitting of the energy levels is included in the analysis as a perturbation calculation, as shown in Fig. 9. This calculation provides an estimate of the actual lambda splitting without having to build a Hamiltonian matrix that involves several electronic states. The calculation uses the matrix S that diagonalizes the Hamiltonian matrix and the parameters C_0, C_1, C_2, and C_3 that are usually determined experimentally. The expression for the lambda splitting of triplet states is given here, which is taken from Dixon [6]. Kovács [12] contains this expression without the C_3 term, and similar expressions for the singlet, doublet, and quartet cases.

The new computer program includes the Hamiltonian matrix as outlined above, the program by Whiting [19] to calculate the rotational line intensity factors of diatomic molecules, and the program by Whiting, Arnold, and Lyle [18] to generate a line-by-line spectrum for atoms and diatomic molecules. The new program accurately calculates wavelengths and intensity factors for any spin-allowed transition, generates a synthetic spectrum to high resolution, and plots the resultant spectrum. The extension to the spin-forbidden case should be straightforward with due consideration to the cases in which the lambda components are not of equal intensity.

The new program was tested by calculating the high-resolution spectrum of the (0,0) band of the $A\,^3\Pi \rightarrow X\,^3\Sigma^-$ transition of the NH molecule and comparing the calculated wavenumbers for the rotational lines with the experimental data of Funke [8–9] and Dixon [6]. The difference between the calculated and experimental

values is shown in Fig. 10 for the P_1 branch. The cutoff in the spectrum at a rotational number of about 34 is due to rotational dissociation in the upper state.

$$\Delta\nu^F_{e-f}(J) = C_0 S^2_{1,F} + C_1 S_{1,F} S_{2,F}\sqrt{2J(+1)}$$
$$+[C_2 + C_3 J(J+1)]\left[S^2_{2,F} J(J+1) + 2S_{1,F}S_{3,F}\sqrt{(J-1)J(J+1)(J+2)}\right]$$

where:

$F + 1, 2$ or 3 indicates spin substate

$\Delta\nu^F_{e-f}$ = Lambda doubling in F substate

$= E^F_e - E^F_f$

$S_{i,F}$ = Matrixelements of the matrix S that diagonalizes the Hamiltonian Matrix i.e., $E = S^{-1}HS$

Fig. 9. Perturbation expression for lambda splitting in triplet states (Dixon [6])

The calculated results were made using the spectroscopic parameters determined by Dixon [6], Murai and Shimauchi [14], and the present work. Notice the large change in scale for the y-axis when using Dixon's parameters. For high rotational values the calculated results of both Murai and Shimauchi and the present work deviate from the experimental data. This is due to the contributions of the higher-order rotational constants (H_v and F_v) and lambda splitting parameters (C_2 and C_3), which are each quite large, about 15 to 20 cm^{-1}. Slight changes in these parameters can produce improved agreement in any selected branch, but they degrade the agreement between the theory and experiment in at least some of the other branches. Generally, the agreement between the calculated and experimental values is good when using the parameters determined by Murai and Shimauchi and by the present work.

The parameters used in the calculations are shown in Table I. Dixon's values were based on the rotational distortion produced only by the diagonal D_v matrix elements. Murai and Shimauchi determined improved rotational constants, and in the present work we have made slight adjustments to the combined parameters of Dixon and Murai and Shimauchi. Veseth [16] also analyzed this transition, and his parameters are shown in Table I. His parameters, however, were determined using a more complete Hamiltonian matrix which included both the $A\,^3\Pi$ and $X\,^3\Sigma^-$ states simultaneously. Thus, his "true" parameters are not appropriate for the single-state Hamiltonian matrix used here, and also used by Dixon and Murai and Shimauchi. Introducing his parameters into the present program produces an error of about 25 cm^{-1} at N'' values near 30. The single-state parameters are considered to be "effective" parameters.

Three plots of the (0,0) NH band generated using the parameters from the present work are shown in Fig. 11. All 27 branches are introduced in these plots, and some of the weak satellite branches can be seen in the logarithmic plots.

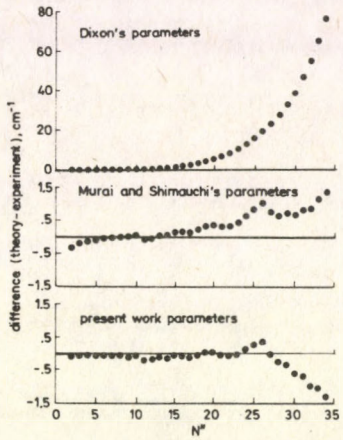

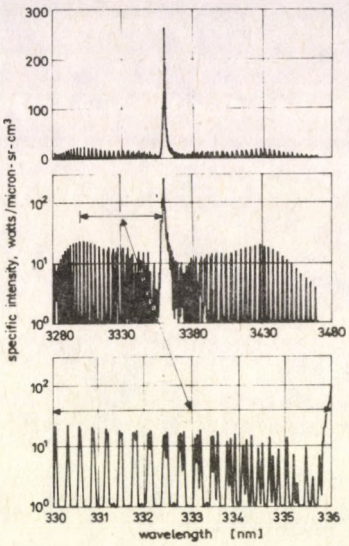

Fig. 10. Difference between calculated and experimental wavenumbers for the rotational lines in the (0,0) band of the $A\ ^3\Pi \rightarrow X\ ^3\Sigma^-$ transition in NH. Experimental data from Dixon [6]

Fig. 11. Calculated spectrum of the (0,0) band of the $A\ ^3\Pi \rightarrow X\ ^3\Sigma^-$ transition in NH, using parameters from present work

The new program provides a powerful computational tool for generating high-resolution spectra for any allowed transition and will be used to help understand the radiative transport in the AFE flow field from 100 to 200 nm. However, spectral programs such as this one still depend on the availability of accurate spectroscopic parameters (e.g., the parameters discussed above for the energy levels and those needed for absolute intensity calculations, such as the transition moments).

Previously, most spectroscopic parameters have come principally from experimental measurements. However, a revolution in spectroscopy has occurred in the past 5 to 10 years and now many of these parameters are calculated to high accuracy by theoretical methods. The reasons for this change have been the development of high-speed, large-memory supercomputers and the highly sophisticated computer programs for solving the Schrödinger equation for diatomic and triatomic molecules. One of the groups that make such calculations is the Computational Chemistry Branch at Ames Research Center. This group and some of its results are highlighted in the following Section.

Table I
Spectroscopic parameters for NH $A\ ^3\Pi \rightarrow X\ ^3\Sigma^-$ transition used in calculations shown in Figures 10 and 11, values in cm^{-1}

Parameter	Dixon [6]	Murai and Shimauchi [14]	Veseth [16]	Present
		$A\ ^3\Pi$ STATE		
B_0	16.3221	16.3181	16.3018	16.3181
D_0	17.58×10^{-4}	17.78×10^{-4}	17.80×10^{-4}	17.78×10^{-4}
H_0	–	7.80×10^{-8}	9.9×10^{-8}	7.80×10^{-8}
F_0	–	–	-13.0×10^{-12}	-1.30×10^{-12}
A	-35.02	Dixon	-34.79	-34.72-.007J(J+1)
ε	–	–	-0.149	0.
γ	0.04	Dixon	0.0063	0.04
C_0	-2.63	Dixon	Dixon	-2.75
C_1	-0.005	Dixon	Dixon	-0.005
C_2	0.0318	Dixon	Dixon	0.0318
C_3	-1.30×10^{-5}	Dixon	Dixon	-1.30×10^{-5}
		$A\ ^3\Sigma^-$ STATE		
B_0	16.3454	16.3447	16.3748	16.3447
D_0	16.85×10^{-4}	16.99×10^{-4}	17.097×10^{-4}	16.99×10^{-4}
H_0	–	10.48×10^{-8}	10.47×10^{-8}	10.48×10^{-8}
F_0	–	–	-7.0×10^{-12}	0
ε	0.618	Dixon	0.557	0.618
γ	-0.053	Dixon	-0.0114	-0.053
Band Origin	29777.09	–	–	29777.50

Computational chemistry at Ames Research Center

The research effort in computational chemistry at Ames Research Center was initiated in 1973 and was organized as a separate research branch in 1985. This work continues to receive strong management support because the research closely supports the Center's major thrust in computational fluid dynamics, particularly at high temperatures, and because of its unique scientific capability within NASA. The Computational Chemistry Branch is a major user of the computational resources at the center. These resources include a Cray X-MP in the Center's central computer facility and two Cray-2's in the Numerical Aerodynamic Simulation (NAS) facility, which is a national facility for research in computational fluid dynamics located at Ames.

The Computational Chemistry Branch carries out research in the two broad discipline areas shown in Table II. These areas are gas-phase and gas-surface interactions. The gas-phase work is further subdivided into molecular properties; reaction

rates and scattering, and transport properties and cross sections. The gas-surface work is subdivided into metallic and polymer surfaces. For each of these subdisciplines, selected molecular systems or reactions that have been studied recently are listed to illustrate the broad range of topics covered. Some of the work listed has not yet appeared in the literature.

Table II

Computational chemistry branch at Ames Research Center
with selected systems that have been examined recently

Gas phase

1. Atomic and molecular properties

N_2^+	H_2O	N_iN_2	Si_2
NO_7	Al_2	$N_i(N_2)_4$	FeH
OH	AlC	N_iCO	Cu_2
N_2	AlH	$N_i(CO)_4$	Cu_3
CN	AlN	F	F^-

2. Reaction rates and scattering

$Ca+HF \rightarrow CaF+H$
$N+O_2 \rightarrow NO+O$
$O+N_2 \rightarrow NO+O$
$H_2+H+H \rightarrow H_2+H_2$

$e+N_2(v) \rightarrow e+N_2(v^*)$
$e+N_2(X\ ^1\Sigma_g^+) \rightarrow e+N_2(B^3\Pi_g, A^3\Sigma_u^+, W^3\Delta_u, a^1\Pi_g)$
$N_2(v)+N_2(v') \rightarrow N_2(v^*)^2+N+N$
$\rightarrow N_2(v^*)+N_2(v'^*)$

3. Transport properties and cross sections

N^+-N
O^+-O
$N-O$
Air

Gas–surface interactions

1. Metallic surface

Be_{13} Be_{55}
Small Al Clusters
$(C_5H_5V)_2C_8H_8$

2. Polymer surface

Polycarbonate (100,000 segments)
Polyethylene
Polyimide
$O(^3P)+C_3H_8 \rightarrow C_3H_8O^*$
$\rightarrow C_3H_7+OH(\ ^2\Pi)$

A detailed study of the accuracy of the molecular properties calculated, based on the approximations used, has been made by the Ames researchers. The problem of which configurations to include in the calculation (the correlation problem) can now be examined in depth because the Cray-2 memory permits full configuration interaction (CI), benchmark calculations to be made. For example, a full CI calculation on the H_2O molecule made by Bauschlicher and Taylor [1], included 28 million determinants and 7 million configurations, which required about 70 million words of fast memory. This calculation required about 10 hours of CPU time. Such benchmark calculations enable the results from approximate methods to be evaluated. Some are found to give very reliable results and also reduce the CPU time required to less than 0.1% of that required for a full CI calculation.

The full CI benchmark calculations have also clearly identified limitations in previous basis sets and have led to the development of improved basis sets based

on atomic natural orbitals. These new basis sets lead to results that are superior to any previous set and also markedly reduce the computer time required.

The techniques discussed above were used by Bauschlicher et al [2] and Bauschlicher and Langhoff [3] to identify the ground states of Al_2, and Si_2, even though the separation between the two lowest states for these molecules is less than 300 cm^{-1}. These calculations were made in a two-step process. A full CI calculation was made in a small basis set to confirm the reliability of the approximate treatment, and then the approximate treatment was carried out in an expanded atomic natural orbital basis to give accurate results.

The calculation of reaction rates requires considerably more time than that for the properties of isolated diatomic molecules. For example, it takes about 50 hours of Cray-2 time to calculate the reaction rate for the relatively simple $N + O_2 \rightarrow NO + O$ reaction to an accuracy of about 10%, Jaffe, Pattengill, and Schwenke [11]. The 50 hours breaks down to about 49 hours to generate the potential surface of the N–N–O complex and about 1 hour to perform several thousand trajectory calculations on the surface to give reasonable reaction statistics. Of course, this does not count the large number of person-hours required to make an analytic fit to the potential surface before the trajectory calculations can be made (Walch and Jaffe, [17]). Fitting the potential surface with analytic functions is one of the most difficult parts of the reaction-rate problem and requires considerable skill and ingenuity.

The quality of the spectroscopic results obtainable is demonstrated by the recent publication of the quintet states of N_2 by Partridge et al [15]. Their paper also indicates the way computational research can augment and complement experimental research. A portion of their work on the quintet states is included here to illustrate these points.

The lower electronic states of N_2 are shown in Fig. 12, which was taken from the paper by Partridge et al [15]. Here the energy of the states is shown as a function of the internuclear distance in Bohr radii. Note that the curve for the $X\ ^1\Sigma_g^+$ ground state extends 50,000 cm^{-1} below the bottom of the Figure. The quintet states calculated by Partridge et al are shown with the closely spaced vibrational levels. The $A'\ ^5\Sigma_g^+$ state dissociates to ground state ^4S nitrogen atoms, and the $C''\ ^5\Pi_u$ state dissociates to ^4S and ^2D nitrogen atoms.

The existence of these quintet states has been discussed in the literature for many years. However, the only experimental evidence for the $A'\ ^5\Sigma_g^+$ state is from the predissociation it includes in the $B\ ^3\Pi_g$ and $a\ ^1\Pi_g$ states (Douglas and Herzberg, [7], and Lofthus and Krupenie, [13]) and for the $C''\ ^5\Pi_u$ state is the predissociation it induces in the $C\ ^3\Pi_u$ state (Carroll and Mulliken, [5]). All previous theoretical calculations of these states gave shallow potential wells with only one or two vibrational levels in the A' state and less than half the well depth of the C'' state shown here.

The new potential curves for the quintet states calculated by Partridge et al correctly account for the observed predissociation data and provide much new information about the complex intersystem interactions that occur among the N_2 states. Further, they identify for the first time the states involved in the Hermann Infrared band system.

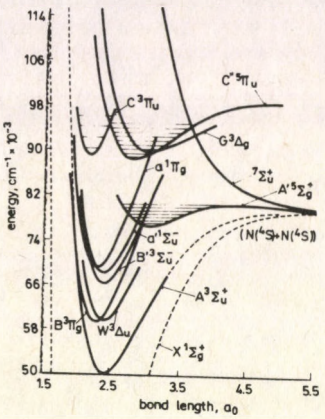

Fig. 12. Potential energy curves for N_2 (Partridge et al. [15])

The Hermann Infrared bands were first observed by Hermann [10] by a low current discharge in N_2 at liquid nitrogen temperature. Carroll and Sayers [4] determined that the bands were formed either by a triplet or a quintet transition. A comparison of the band positions and relative intensities (as calculated by Partridge et al) with the experimental values is shown in Table III. The comparison is remarkable and demonstrates conclusively that the Hermann Infrared system is produced by the $C''\ ^5\Pi_u \rightarrow A'\ ^5\Sigma_g^+$ transition. Their work also shows that this transition does not account for the expected very short lifetime of the C'' state, and thus the main pathway for deexcitation of this state remains unknown.

The identification of the Hermann Infrared system is only one of several puzzles concerning N_2 that this work has helped to understand. Perhaps the most sophisticated explanation given is for the evidence that the $A'\ ^5\Sigma_g^+$ state is a precursor state for populating the $B\ ^3\Pi_g$ state during the recombination of ground-state nitrogen atoms.

The paper by Partridge et al is a superb example of theoretical spectroscopic analysis. It also provides guidance for future experimental work, such as possible absorption measurements on the Hermann Infrared bands which might identify the principal pathway for deexcitation of the $C''\ ^5\Pi_u$ state and more fully explain the combined roles of both the $A'\ ^5\Sigma_g^+$ and $A\ ^3\Sigma_g^+$ states in the recombination of ground state nitrogen atoms.

Table III
Band positions and relative intensities
of the Hermann infrared system taken from Partridge et al. [15]

Band	Band positions (nm)		Relative intensities	
	Theory	Experiment	Theory	Experiment
0-0	806[a]	806	3.5	4.0
0-1	855	855	1.0[b]	1.0
0-2	907	907	0.6	
0-3	961	963	0.3	
0-4	1016	1023	0.1	
1-0	753	752	6.0[b]	6.0
1-1	795	795	0.2	
1-2	840	840	0.7	<0.5
1-3	886	887	1.6	
1-4	933	938	1.4	
2-0	708	706	10.0[b]	10.0
2-1	745	744	8.8	8.0
2-2	783	783	6.6	5.0
2-3	824	824	0.3	<0.5
2-4	864	868	0.7	
3-0	668	667	1.5[b]	1.5
3-1	701	700	10.4	9.0
3-2	736	735	0.6	<0.5
3-3	771	771	4.8	3.0
3-4	806	809	2.5	

[a] The 0-0 bands were shifted into coincidence; this required a shift of 559 cm^{-1} in the theoretical T_e.

[b] These bands were normalized to experiment by adjusting the vibrational populations. This requires that the relative populations of v'=0-3 be 0.073,0.295,1.00, and 0.725, respectively

Concluding remarks

The proposed development of advanced entry vehicles, such as the National Aero-Space Plane and Aero-assisted Orbital Transfer Vehicle, provides new and challenging problems to be studied and understood. Many of these problems are related to the likelihood that large portions of the flow field around such vehicles will be characterized by chemical and thermal nonequilibrium.

Further, the radiative heating will be enhanced significantly by nonequilibrium effects and can be a significant portion of the total heating load. In particular, a detailed study of the radiative transport in the vacuum ultraviolet region between 100 and 200 nm is necessary to assess the impact of radiative transport on the flow-field solution and the vehicle heating. Such a study must be done at high spectral

resolution so that the overlap of atomic and molecular rotational lines is handled correctly. The computational tools necessary for such a study have been developed.

The solution of many of the problems encountered in atmospheric entry have been, and will continue to be, found in the application of spectroscopic techniques and results. The Computational Chemistry Branch at Ames Research Center is helping to build the base of needed spectroscopic knowledge and is making important contributions to the understanding of molecular properties and processes by computational methods.

In closing, we express our thanks to the Hungarian Academy of Sciences for sponsoring this Conference and honoring our colleague, friend, and teacher, Professor Kovács.

References

1. C. W. Bauschlicher Jr. and P. R. Taylor, J. Chem. Phys., *85*, 2779, 1986.
2. C. W. Bauschlicher Jr., H. Partridge, S. R. Langhoff, P. R. Taylor and S. P. Walch, J. Chem. Phys., *86*, 7007, 1987.
3. C. W. Bauschlicher Jr. and S. R. Langhoff, J. Chem. Phys., *87*, 2919, 1987.
4. P. K. Carroll and N. P. Sayers, Proc. Phys. Soc., London, Sect. A, *66*, 1138, 1953.
5. P. K. Carroll and R. S. Mulliken, J. Chem. Phys., *43*, 2170, 1965.
6. R. N. Dixon, Can. J. Phys., *37*, 1171, 1959.
7. A. E. Douglas and G. Herzberg, Can. J. Phys., *29*, 294, 1951.
8. G. Funke, Z. Physik, *96*, 787, 1935.
9. G. Funke, Z. Physik, *101*, 104, 1936
10. R. Hermann, C. R. Acad. Sci. /Paris/, *233*, 738, 1951.
11. R. L. Jaffe, M. D. Pattengill and D. W. Schwenke, Classical Trajectory Studies of Gas Phase Reaction Dynamics and Kinetics Using Ab Initio Potential Energy Surfaces, to be published in Proceedings of the NATO Advanced Research Workshop on Supercomputer Algorithms for reactivity, Dynamics, and Kinetics of Small Molecules, 1988, NATO ASI Series, Reidel, Dordrecht.
12. I. Kovács, Rotational Structure in the Spectra of Diatomic Molecules, Adam Hilger Ltd., London, 1969.
13. A. Lofthus and P. H. Krupenie, J. Phys. Chem. Ref. Data, *6*, 113, 1977.
14. T. Murai and M. Shimauchi, Science of Light, *15*, 48, 1966.
15. H. Partridge, S. R. Langhoff and C. W. Bauschlicher Jr., J. Chem. Phys., *88*, 3174, 1988.
16. L. Veseth, J. Phys. B: Atom. Molec. Phys., *5*, 229, 1972.
17. S. P. Walch and R. L. Jaffe, J. Chem. Phys., *86*, 6946, 1987.
18. E. E. Whiting, J. O. Arnold and G. C. Lyle, A Computer Program for a Line-by-Line Calculation of Spectra from Diatomic Molecules and Atoms Assuming a Voight Line Profile, NASA TND-5088, 1969.
19. E. E. Whiting, Computer Program for Determining Rotational Line Intensity Factors for Diatomic Molecules, NASA TND-7268, 1973.

Acta Physica Hungarica 67 (1-2), pp. 47-66 (1990)

FINE AND HYPERFINE STRUCTURE IN THE $a^3\Pi$ STATE OF CH^+*

T. P. SOFTLEY

University Chemical Laboratory, Cambridge CB2 1EW, UK

(Received 24 September 1988)

Spectroscopic and theoretical studies concerning the $a\ ^3\Pi$ state of CH^+ are reviewed, with particular consideration given to the infrared predissociation spectrum of the ion. This spectrum is primarily due to vibration-rotation transitions of the $a\ ^3\Pi$ state involving $v=5$ to 12 and $J=20$ to 35. Some results of a spectral simulation, making use of a rotationally-adiabatic model, are presented to justify the proposed assignment. The nuclear-hyperfine structure of the observed transitions is studied in detail, with a new calculation of splittings presented. Some semi-quantitative conclusions can be drawn with reference to the variation of the Fermi Contact parameter, b, as a function of internuclear distance.

1. Introduction

The CH^+ ion has been the subject of over one hundred theoretical and spectroscopic studies, since the $A\ ^1\Pi - X\ ^1\Sigma^+$ emission spectrum was first identified by Douglas and Herzberg in 1942 [1]. This considerable volume of work has been stimulated by two important features: (a) The ion has only 6 electrons and is therefore amenable to ab-initio calculations of high accuracy. Comparison between theory and experiment stands as an important test for the calculations. (b) CH^+ is a major intermediate of many molecule-building reaction paths in interstellar space, and therefore spectroscopy is useful for identification of the ion, and can help in the understanding of its kinetic behaviour.

The potential curves for the lowest two singlet states are now quite well characterized by a combination of classical spectroscopic studies [1,2,3], laser-induced fluorescence measurements [4], laser ion-beam photofragment spectroscopy [5,6], and ab-initio calculations [7,8,9]. Rather less is known about the triplet states of the molecule. Although these states may be of lesser importance for understanding the astrophysical behaviour of the ion, they are possibly of more interest theoretically as I intend to show subsequently. In this paper, I shall summarise present knowledge regarding the triplet states of CH^+ concentrating particularly on the infrared predissociation spectrum of the ion recorded by Carrington and Softley at Southampton University, which has also been reported in some detail elsewhere [10]. It will be seen that further theoretical work would be a valuable aid to the complete understanding of the experimental results.

*Presented at the Conference on High Resolution Electronic Spectroscopy of Molecules, Tihany, Hungary, 19-24 September 1988

2. Triplet state studies

a) Non-laser spectroscopy and ab-initio calculations

Figure 1 shows the potential curves for the lowest four triplet states of CH^+ together with the lowest two singlet states. The $a\ ^3\Pi$ and $c\ ^3\Sigma^+$ states converge to the $C^+(^2P) + H(^2S)$ lowest dissociation limit and the potential curves shown are a composite of those calculated by Green et al [7] at short range, and the long range potentials calculated using exchange perturbation theory by Bazet et al [8]. The $b\ ^3\Sigma^-$ and $d\ ^3\Pi$ states converge to the $C(^3P) + H^+$ dissociation limit and the potential curves shown are those calculated by Lévy [11]. It should be noted that the c and d states are essentially repulsive, but have long range minima with calculated well-depth 200 cm^{-1} and 710 cm^{-1} respectively..

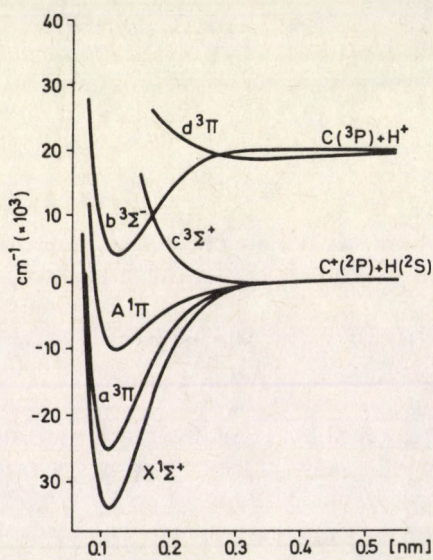

Fig. 1. Potential energy curves for the lowest lying triplet and singlet states of CH^+. $X\ ^1\Sigma^+$ and $A\ ^1\Pi$ from [5], $a\ ^3\Pi$, $b\ ^3\Sigma^-$, $d\ ^3\Pi$ from [11], $c\ ^3\Sigma^+$ from [7,8]

The first spectroscopic observation involving the triplet states was made by Carré in 1968 [12]. Emission bands, attributed to the $b\ ^3\Sigma^- - a\ ^3\Pi$ transition of CH^+ were found to result from the collisional destruction of CH_4 or C_2H_4 using proton beams. Rotational constants were derived for the 1–0 and 0–0 bands and an approximate value of A=23 cm^{-1} was obtained for the spin–orbit constant of the $a\ ^3\Pi$ state. Subsequently Kusunoki and Ottinger [13] observed several vibrational bands of the same electronic transition in the chemiluminescence following the reaction of $C^+(^4P)$ with H_2. No rotational structure was resolved however due to the

low intensity of the emission and the low resolving power of the monochromator used. The knowledge of the triplet states of CH^+ from non-laser spectroscopy can therefore be summarised as in Table I. No classical spectroscopic studies involving the $c\ ^3\Sigma^+$ or $d\ ^3\Pi$ states have been reported, and so overall the triplet states are rather poorly characterised by these few measurements. Neither the dissociation energy D_e, nor the $^1\Sigma^+ - {}^3\Pi$ separation are known experimentally.

Table I

Summary of vibration–rotation constants for the $a\ ^3\Pi$ and $b\ ^3\Sigma^-$ states of CH^+ from non–laser spectroscopy ([12] and [13])

(a) Vibration (Kusunoki and Ottinger)

		ω_e	$\omega_e x_e$
$b\ ^3\Sigma^-$	(v =0–3)	2040 ± 25	50 ± 15
$a\ ^3\Pi$	(v =0–2)	2631	64

(b) Rotation and Spin–Orbit (Carré)

		B_e	α_e	D_e	A
$b\ ^3\Sigma^-$	(v =0–2)	11.705	0.538	0.00135	–
$a\ ^3\Pi$	(v =0,1)	14.048	0.603	0.00140	23

b) Laser ion-beam photofragment studies

More recently laser ion-beam studies in both the visible/UV and the infrared have been performed which are considered to involve the triplet states of the CH^+ molecule. In all these experiments, a fast ion-beam interacts collinearly with a laser beam, and transitions are observed by monitoring the production of photofragment ions as a function of excitation wavelength. The transitions appear as resonances in the photofragmentation cross-section. In the visible/UV region two different types of triplet state transition are observed. Helm et al first reported a number of transitions in the UV range which lead to photofragments with excess energies between 1.6 and 2 eV [5]. A full assignment has not been reported, but it is believed that the lines belong to the (4,3) and (7,5) bands of the $b\ ^3\Sigma^- - a\ ^3\Pi$ transitions. The b state levels are predissociated via a curve crossing with the c state to produce the detected C^+ ions at resonance.

At Nottingham University, Whitham and Sarre have recorded a number of transitions of CH^+ in the wavelength region of 540 nm at high resolution, employing the interaction between a single-mode dye laser and a fast mass-selected ion beam [14,15]. The same transitions had also been observed previously at lower resolution by Helm et al [5]. Sarre and Whitham believe that these transitions originate from high vibrational levels of the $a\ ^3\Pi$ state and/or levels of the $c\ ^3\Sigma^+$ state, going to levels lying in the shallow minimum of the $d\ ^3\Pi$ state. The excitation is then followed by the radiative decay of the molecules back to the dissociation continuum

of either the $a\ ^3\Pi$ or the $c\ ^3\Sigma^+$ states, and hence the production of C^+ ions e.g., $CH^+(a\ ^3\Pi) + h\nu_1 \rightarrow CH^+(d\ ^3\Pi) \longrightarrow CH^+(c\ ^3\Sigma^+) + h\nu_2 \rightarrow C^+ + H$.

Evidence for this mechanism is provided by the measurement of the fragment ion kinetic-energy distribution in the laboratory frame, while the laser is tuned to a specific resonance. The observed distributions when converted to the centre-of-mass frame correspond to a distribution of kinetic energies around a small value, typically 20 meV, characteristic of direct dissociation from a pure continuum state. Calculations for the Franck–Condon factors representing this process suggest that there is a relatively high probability of radiation to the continuum rather than the bound levels of the lower lying states [15]. It is not clear at present however whether such intensity calculations would be strongly influenced by the R-dependence of the transition moment between the relevent states in the fluorescence process, as this transition moment has not been calculated to date. The observed bands have not been fully assigned to rotational and vibrational levels, although the long-wavelength cut-off of the bands is in agreement with the predictions of ab-initio calculations. Some of the lines show a doublet splitting up to 600 MHz, and as I will show later, this is consistent with the expected magnitude of the proton nuclear hyperfine Fermi-contact interaction for the lower states of the proposed transitions.

It is worth noting that the proposed explanation of their spectrum involves highly excited levels of the $a\ ^3\Pi$ state e.g., v=14–19, and it is not easy to relate these measurements to those involving the lowest vibrational levels. The population of these high vibrational levels is a consequence of the method of formation of the ions; i.e., by electron impact on CH_4 followed by ion extraction under collision free conditions. The CH^+ is a relatively minor product of the ion-source and the precise mechanism of formation is not clear.

The other set of spectroscopic results involving triplet levels of CH^+ were obtained by Carrington and Softley [10]. In our experimental arrangement the ions were formed by the same mechanism as in the studies of Sarre et al, but interacted with a tunable infrared laser in the range 870–1090 cm^{-1} rather than a visible laser. We observed 87 transitions in this wavelength range by monitoring the production of photofragment ions (C^+) as a function of wavelength. Full experimental details have been given elsewhere [10]. The indirect detection method employed requires that for a single-photon infrared transition, the upper state must lie energetically above the lowest dissociation limit of the molecule ($C^+(^2P) + H(^2S)$). In our case the C^+ ions arise from the predissociation of the upper states of the transitions. Obviously with only a wavelength range of 870–1090 cm^{-1} available (cf $a\ ^3\Pi$ state dissociation energy $\approx$ 25000 cm^{-1}) the lower states of the observed transitions must also be highly excited.

We have recently concluded that the infrared spectrum is primarily due to vibration–rotation transitions within the $a\ ^3\Pi$ state. The upper states are rotationally-quasibound predissociated levels of this electronic state lying a few hundred cm^{-1} above the lowest dissociation limit

$$CH^+(a\ ^3\Pi, v'', J'') + h\nu \longrightarrow CH^+(a\ ^3\Pi, v', J') \longrightarrow C^+ + H.$$

The vibrational quantum numbers of the observed transitions are believed to range from 5 to 12; much of the energy required to reach the dissociation limit is provided by rotation, with typical rotational quantum numbers J=20–35. It is interesting to note that, assuming all vibrational assignments of the laser studies are correct, there is a complementarity between the various measurements involving the $a\,^3\Pi$ state. i.e., v=0–2 from classical spectroscopy, v=3,5 from UV laser studies, v=5–12 from infrared studies and v=14–19 from visible laser spectroscopy. Almost all vibrational levels are covered in this way.

In addition to measuring the line positions, we have also accurately recorded the line widths of the infrared transitions which are found to lie in the range 10-4000MHz. The varying linewidths are a result of lifetime broadening and to a good approximation the linewidths are inversely proportional to the upper-state predissociation lifetimes. 43 of the observed transitions appear as doublets with splittings in the range 16–672 MHz. These splittings are due to the nuclear hyperfine interaction as in the spectra of Sarre et al. We have also measured the laboratory-frame fragment-ion kinetic energy distributions and find that, as expected, these correspond to single values of the fragment-ion energy in the centre-of-mass frame rather than distributions as in the case of the visible spectrum. The single value is directly related to the energy of the upper states above the dissociation limit. The excess energy values for the 87 transitions vary from 10–1270 cm^{-1}, but with over 70% in the range 200–1200 cm^{-1}. Full details of all the recorded transitions are given in reference [10].

The reasoning behind our identification of the spectrum is quite complex and I will discuss it in some detail in the following Section. Fig. 2 shows a stick spectrum of the observed line positions. Although there might appear to be bandheads observable at 949 and 987 cm^{-1} these are certainly not bandheads in the usual sense. There is no recognisable P,Q or R branch structure in this observed spectrum. The lack of structure arises primarily because, for a given vibrational level, only one or two upper-state rotational levels will be predissociated with lifetimes in the appropriate range for observation in our experiments (in this case the operative range is 10^{-6} – 10^{-10} s).

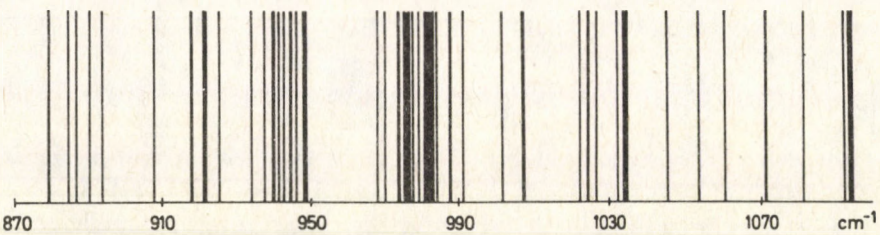

Fig. 2. Stick spectrum showing positions of the observed lines in the infrared predissociation spectrum of CH^+

3. Infrared spectrum

3a) Identification of the infrared predissociation spectrum

The detection of C^+ ions as opposed to H^+ ions implies that the observed electronic states must predissociate to $C^+ + H$ as opposed to $H^+ + C$. This feature in conjunction with energetic considerations points fairly strongly to the involvement in our spectrum of just the lowest electronic states, i.e. those four states correlating with the lowest dissociation limit. Although the $b\ ^3\Sigma^-$ state may also be predissociated by the c state to the lowest dissociation limit, the upper states would have much larger excess energies than those which are experimentally observed. Confining attention to just the four lowest states, it is apparent at the outset that many different types of transition could potentially be contributing to the spectrum. These include allowed electronic transitions

$$X\ ^1\Sigma^+ - A\ ^1\Pi,$$
$$a\ ^3\Pi - C\ ^3\Sigma^+,$$

vibrational transitions

$$X\ ^1\Sigma^+ - X\ ^1\Sigma^+,$$
$$a\ ^3\Pi - a\ ^3\Pi, \qquad \text{etc.},$$

and even spin-forbidden transitions

$$X\ ^1\Sigma^+ - a\ ^3\Pi,$$
$$A\ ^1\Pi - a\ ^3\Pi.$$

In all cases the upper states would be predominantly of the rotationally-quasibound type. There are no a priori reasons for supposing that any one of the possible lower states is preferentially populated in the ion source so none of the above possibilities can be excluded on those grounds.

In order to try to understand the spectrum we have performed a simulation making use of the best available ab-initio and spectroscopic data, including a prediction of the expected fine and hyperfine structure. The key to the simulation was the use of rotationally-adiabatic potentials and this method will form a central theme of the remainder of this paper. This method was first applied to a prediction of the lambda doubling of the $A\ ^1\Pi$ state of CH^+ by Helm et al [16]. In our work we have extended their method to include the interaction between all the states correlating with the lowest dissociation limit. Sarre and his coworkers are also currently using the same method in attempting to fully analyse the visible spectrum [15].

3b) Rotationally-adiabatic potentials for CH^+

The diatomic molecular Hamiltonian may be written in the simple form;

$$H = H_{el} + H_{so} + H_{rot} - \frac{\hbar}{2\mu R^2}\frac{d}{dR}R^2\frac{d}{dR}.$$

The calculation begins with a set of ab-initio potential curves, such as those shown in Fig. 1, which are the R-dependent eigenvalues of H_{el}. In the present case we chose to use just the $X\ ^1\Sigma^+$, $A\ ^1\Pi, a\ ^3\Pi$ and $c\ ^3\Sigma^+$ states which are 1-,2-,6- and 3-fold degenerate, respectively. This total of 12 electronic wavefunctions may be represented by the parity-defined Hund's case (a) basis functions;

$$\begin{aligned}
^1\Sigma^+ &\equiv |0,0,0,J\rangle, && p_+,\\
^1\Pi_\pm &\equiv (1/\sqrt{2})[|1,0,0,J\rangle \pm |-1,0,0,J\rangle], && p_\pm,\\
^3\Sigma^+_0 &\equiv |0,1,0,J\rangle, && p_-,\\
^3\Sigma^+_{1\pm} &\equiv (1/\sqrt{2})[|0,1,1,J\rangle \mp |0,1,-1,J\rangle], && p_\pm,\\
^3\Pi_{0\pm} &\equiv (1/\sqrt{2})[|1,1,-1,J\rangle \mp |-1,1,1,J\rangle], && p_\pm,\\
^3\Pi_{1\pm} &\equiv (1/\sqrt{2})[|1,1,0,J\rangle \mp |-1,1,0,J\rangle], && p_\pm,\\
^3\Pi_{2\pm} &\equiv (1/\sqrt{2})[|1,1,1,J\rangle \mp |-1,1,-1,J\rangle], && p_\pm,
\end{aligned}$$

(using the notation $|\Lambda,S,\Sigma,J\rangle$). It is then assumed that all fine structure splittings of the energy levels of these states are caused by the rotational and spin–orbit interactions within this set only; interactions with higher states are ignored in the first instance. Rather than calculate these splittings in terms of perturbations between energy levels, the perturbations (which are J-dependent) are directly incorporated into the potential curves; for each value of J, a set of 12 potential curves is generated which represents eigenfunctions of the electronic, spin–orbit and rotational parts of the Hamiltonian and is diagonal in these operators for all R. These eigenfunctions will be linear combinations of the basis functions listed above, with coefficients dependent on R. In practice the generation of these "rotationally-adiabatic potential curves" will involve the diagonalisation of two 6×6 matrices (one block for each parity) at say 200 values of R in the range 0.01 to 2nm and then interpolation between these eigenvalues to produce the potential curves.

The matrix elements used to generate the curves are listed explicitly in reference [10,17]. Rotationally-adiabatic potential curves generated for J=3 and for J=25 are shown in Figs 3 and 4. At large R the curves converge to two limits separated by 63.4 cm^{-1} representing the two spin-orbit components of the $C^+(^2P)$ state. No curve crossings can occur between states of the same J with the same parity; thus the $^1\Sigma^+$ state and 3 components of the $^3\Pi$ state converge to the lower limit, while all the other states converge to the upper limit. Of course the description of these states with their Hund's case (a) labels is not strictly correct (as they are really mixtures of such states), but is used here as an indication of the dominant character of the state near to the potential minimum.

Having obtained this set of ≈ 500 potential curves representing J=0 to 40 the

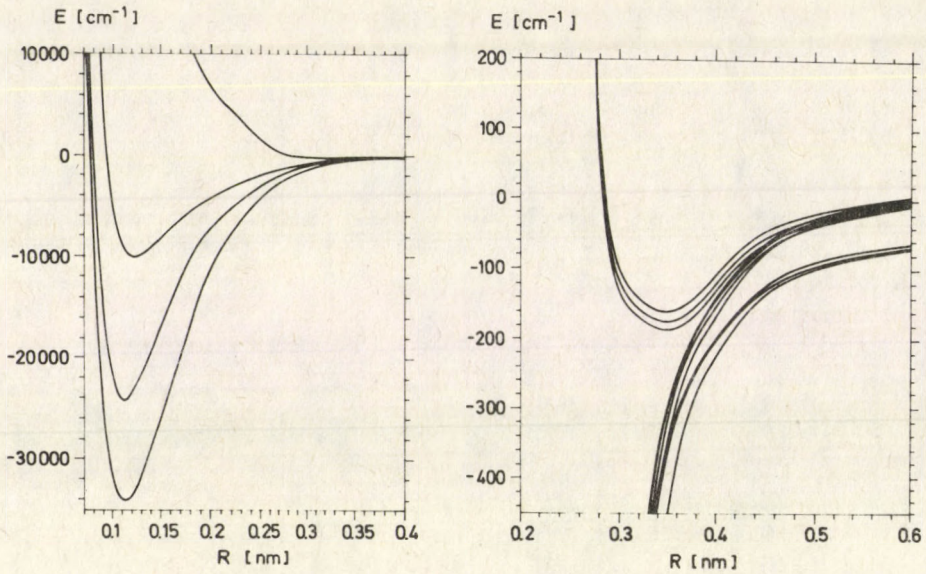

Fig. 3. Rotationally–adiabatic potentials generated from $X\ ^1\Sigma^+$, $A\ ^1\Pi$, $a^3\Pi$, and $c\ ^3\Sigma^+$ for $J = 3$

vibration–rotation levels are then calculated by solving the Radial Schrödinger equation for each potential curve (using the Leroy–Zare–Numerov–Cooley programme [18,19]). The energy levels thus obtained automatically include all fine structure splittings. In principle there is no reason why other interactions should not be included in this method, such as the nuclear hyperfine interactions thus directly calculating hyperfine splittings for each level. However, in the latter case larger matrices would be needed because the hyperfine interaction is off-diagonal in J and such couplings become important at large R. To calculate the hyperfine structure in this particular case we have employed a more simple method as described later.

To simulate the spectrum 5 pieces of information available from the experiments must be reproduced; (a) the observed line frequencies, (b) the excess energies, (c) linewidths, (d) intensities, (e) hyperfine splittings. (a) and (b) are obtained directly from the energy levels as calculated above, while (c) can be calculated as the semi-classical tunnelling rate through the barrier in the rotationally-adiabatic potential [19,20]. Note that we ignore any contributions from non-adiabatic interactions between the rotationally-adiabatic states. The importance of such interactions has been discussed in some detail by Freed and his coworkers in a number of papers [21,22]. The intensities for the transitions are given by a population factor, which is totally unknown in this case and hence is set to unity, and the square of the transition dipole moment between the rotationally-adiabatic states integrated over the vibrational wavefunctions

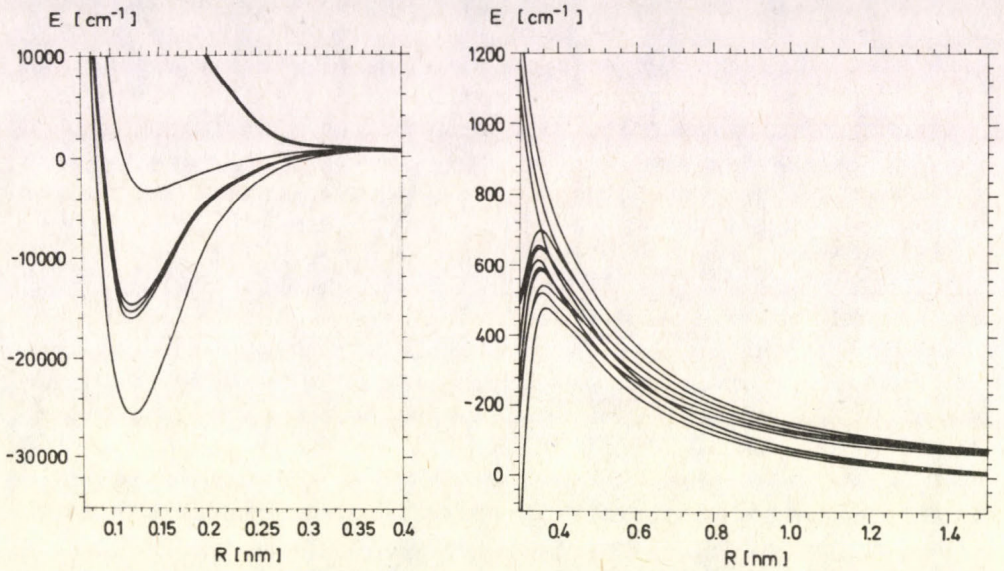

Fig. 4. Rotationally–adiabatic potentials for $J = 25$

$$I \propto |\int \chi_{iJ''}(R)\ \langle i, J''|\mu_Z|f, J'\rangle \chi_{fJ'}(R)\ dR|^2.$$

Here $\chi_{fJ'}$ and $\chi_{iJ''}$ are the vibrational wavefunctions for the final and initial states calculated from the rotationally–adiabatic potentials. $\langle i, J''|\mu_Z|f, J'\rangle$ is an R-dependent transition moment, and because $|i, J''\rangle$ and $|f, J'\rangle$ are linear combinations of the various Hund's case (a) states there will be a contribution to the transition moment from the $^1\Sigma^+ - ^1\Pi$ and $^3\Sigma^+ - ^3\Pi$ transition dipole moments, and also from the permanent dipole moments for each state (i.e. a vibration–rotation contribution to the intensity) suitably weighted by a product of R-dependent coefficients. Further details of the intensity calculation can be found in reference [10].

In order to perform a reliable simulation of the observed spectrum using rotationally–adiabatic potentials there is a requirement for;

(a) Good zero-order potential energy curves for all interacting states.

(b) Good calculations of the variation of spin–orbit coupling matrix elements, Coriolis coupling matrix elements and dipole/transition moments as a function of R.

(c) A large computer with plenty of time available!

Given that quantities such as those listed in (b) are not known for most molecules and would require considerable computational effort, it is worth asking what the particular advantages of this method are. First for the near-dissociation levels of interest, the important region of internuclear distance, R, is at mid- to long-range where the potential curves approach closely and their interaction is strong.

Under these circumstances it is not clear whether the levels are easily predicted by, or fitted to, the usual term formulae. The states may be intermediate between Hund's cases (a),(b), and (c) and be subject to severe perturbations. Second, in order to estimate lifetimes of the upper states for the possible transitions (and hence predict whether a transition is observable, and if so predict its linewidth), a good representation is required for the shape of the rotational barrier for each fine structure state, for each value of J. The shape of the barrier may vary between the various fine-structure components of the $^3\Pi$ state; these effects must be understood in order to correctly predict the spectrum. Third, the use of this method gives a good idea of the variation of the electronic eigenfunction with internuclear distance. In particular this will help in the determination of whether singlet-triplet bands are observable, or indeed whether such labels as "singlet" and "triplet" are at all meaningful, and will also help in the prediction of the nuclear-hyperfine structure.

It is also important to assess the likely accuracy of the calculation. In the case of CH^+ the error in the calculated dissociation energy for the $a\ ^3\Pi$ potential may be of order 1000 cm^{-1} (by comparison with known errors for the $^1\Sigma^+$ state,) giving rise to errors in the predicted vibrational energy levels of comparable magnitude. Although relative errors may be better than this, it would be fortuitous if the calculation correctly predicted which transitions should appear in our relatively narrow window of 220 cm^{-1}. The best that can be hoped for is to predict qualitatively the line density, the approximate vibration/rotation quantum numbers and any characteristic fine-structure patterns. The fine-structure patterns may also only be qualitative at best because they are dependent on the accuracy of spin–orbit and rotational coupling matrix elements over a wide range of R, and also on the separation between zero-order potential curves. In these calculations we have assumed the spin–orbit matrix elements are constant with R (equal to their value at the dissociation limit) and have used values for $\langle {}^3\Sigma^+|L^+|{}^3\Pi\rangle$ taken from calculations at the SCF level by Cooper [23].

The simulated spectrum is obtained by considering all transitions between states obeying the basic selection rules $\Delta J = 0,\pm 1$ and $+ \longleftrightarrow -$ (parity selection rule) whose transition frequencies, linewidths and excess energies fall in the experimentally observed range. The calculated intensities for these transitions vary over 10 orders of magnitude, and so we arbitrarily choose to include only the top 4 orders of magnitude in our simulation. On making this division we find that the predicted spectrum has approximately the same line density as that observed and is primarily composed of 5 types of transition

$$X\ ^1\Sigma^+ - A\ ^1\Pi,$$
$$A\ ^1\Pi - X\ ^1\Sigma^+,$$
$$X\ ^1\Sigma^+ - X\ ^1\Sigma^+,$$
$$A\ ^1\Pi - A\ ^1\Pi,$$
$$a\ ^3\Pi - a\ ^3\Pi.$$

About 75% of the transitions belong to the $a\ ^3\Pi$ vibration–rotation bands, and this is the basis for our assumption regarding the important contribution of these transitions to our spectrum. Consequently, I shall focus attention on this band system only. It is interesting to note that the high intensity of these vibration-rotation transitions, which generally involve $\Delta v = 1$ or $\Delta v = 2$ for this energy range, arise mainly as a result of the strong "monopolar" contribution to the dipole moment arising from the separation of the centre of charge from the centre of mass. At large R the dipole moment increases linearly with R reaching a value of ∞ at $R = \infty$. This property is only possible for states of heteronuclear molecular ions, or ion-pair states of neutral molecules. It may be concluded that transitions between high vibrational levels of molecular ions would commonly have high intensity, provided that there is sufficient population of the lower states of the transitions.

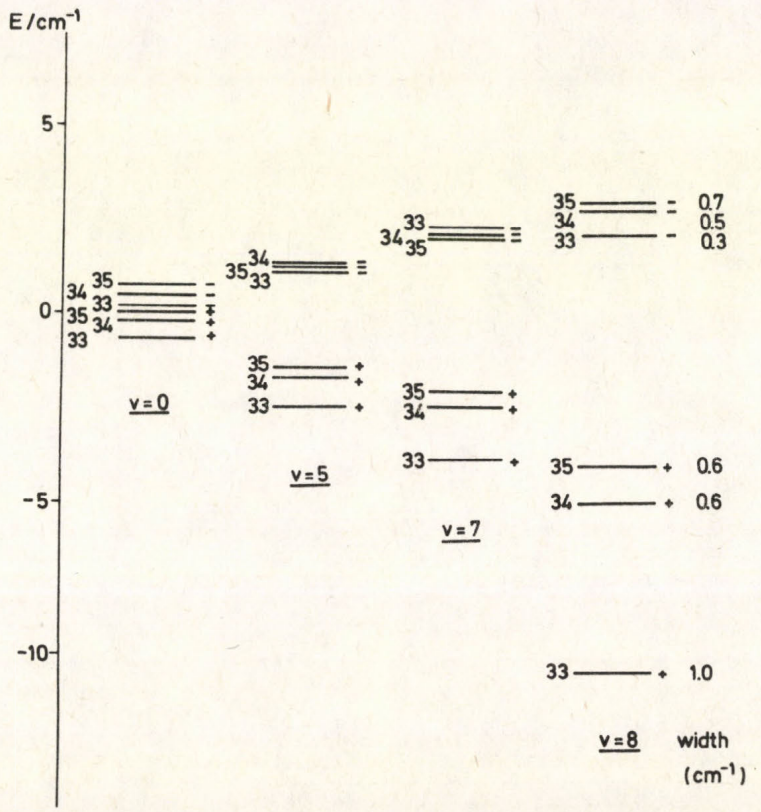

Fig. 5. Fine structure splittings calculated for different vibrational levels with $K = 34$. Individual levels are marked with quantum number J and parity $\pm$. For $v = 8$ calculated widths are given also

It may be recalled that 70% of the experimentally observed transitions have excess energies in the range 200–1200 cm^{-1}; it may be determined from the calculations that this range of excess energies is only possible for $J > 20$. This conclusion

is fairly insensitive to the exact form of the potential energy curves chosen. In fact the magnitude of the excess energies in conjunction with the linewidths allows us to define the possible range of J values for a given transition quite closely. Examination of the rotationally-adiabatic wavefunctions for the $^3\Pi$ states for $J > 20$ shows that, for the important range of internuclear distance, the wavefunctions correspond essentially to Hund's case (b) coupling with very little singlet–triplet mixing. This feature helps to explain the lack of predicted singlet–triplet transitions in the spectrum. For Hund's case (b) the energy levels are described approximately by

$$E(K) = E_v + BK(K+1) - DK^2(K+1)^2 + \ldots,$$

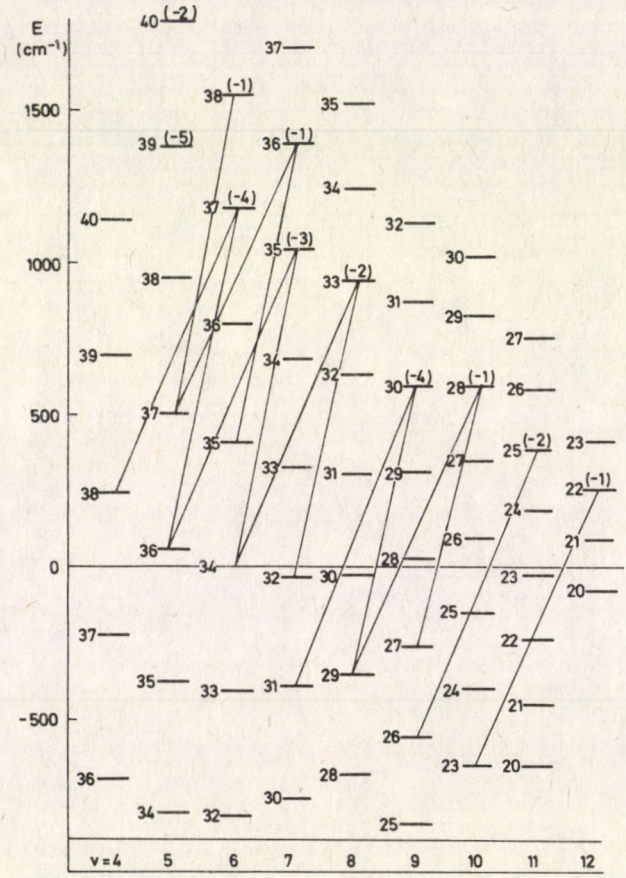

Fig. 6. Calculated energy levels for a $^3\Pi$, K =20–40. Fine structure splittings are not shown. Transitions predicted in the infrared predissociation spectrum are indicated. Lifetimes (order of magnitude, cm^{-1}) are shown for predissociated levels

where K is just an effective quantum number and each level (v, K) is nearly 6-fold degenerate with J taking the values $K-1$, K and $K+1$ for each set of six levels (two

levels of opposite parity for each J). The use of the rotationally-adiabatic potentials then allows the prediction of the magnitude of the splitting of the near-degenerate fine structure states. The calculated fine-structure for several levels v,K is shown in Fig. 5, and as expected the perturbations become most severe as the vibrational quantum number increases. For two of the levels shown the states are rotationally-quasibound and the widths are shown on the figure for the highest level. It is seen that a perturbation of the energy level pattern gives rise to a variation in widths.

Figure 6 shows the calculated energy levels for the $a\ ^3\Pi$ state with mean widths of the quasibound levels marked. The intensity calculations show a predominant $\Delta K = \pm 1$ selection rule, with the $\Delta J = \Delta K$ components having greatest intensity. Weaker transitions with $\Delta K = \pm 1$, $\Delta J = 0$ should also be observable. The $\Delta K = \pm 1$ transitions occurring in the predicted spectrum are marked in Fig. 6, while Fig. 7 shows the individual fine structure transitions for two of these bands. From Fig. 6 it is quite clear that there is no overall P, Q or R branch structure; for any particular vibrational band only one or at most two transitions occur in the spectrum within the observable energy window. Furthermore the relative positions of the observed transitions in different vibrational bands cannot be reliably predicted using the currently available potential curves. This point can be illustrated by repeating the calculations using a different potential curve for the $a\ ^3\Pi$ state. In Table II, a comparison is made between the predicted transitions using (a) the ab-initio potential with dissociation energy 24360 cm^{-1} and (b) a reconstructed potential with the same long range form but a dissociation energy of 26100 cm^{-1}. The true potential probably lies somewhere between these two limits. It can be seen that a different set of transitions are predicted, and there is no real consistent pattern of line positions. We can however say that the vibrational and rotational quantum numbers of transitions appearing in the spectrum can be identified to within ± 1.

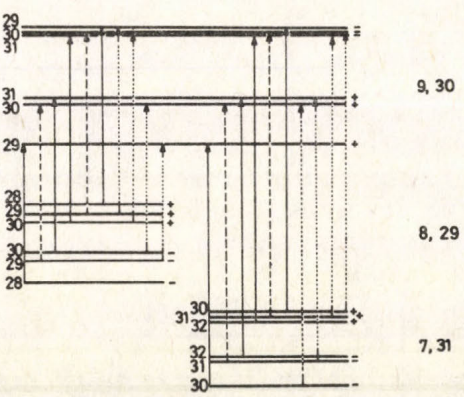

Fig. 7. Predicted fine-structure components for a transition $(a\ ^3\Pi, v', K') - (a\ ^3\Pi, v'', K'')$. Solid lines; $\Delta J = \Delta K, J = K \pm 1$ (intense with medium splittings). Dashed lines; $\Delta J = \Delta K, J = K$ (intense with small splittings). Dotted lines; $\Delta K = \pm 1, \Delta J = 0$ (weak with large splittings)

Table II
Predicted transitions ($a\ ^3\Pi$, v', $K' - a\ ^3\Pi$, v'', K'') from two different $a\ ^3\Pi$ potentials

(v', $K'v''$, K'')	Wavenumber	Excess energy	Width(cm^{-1})
(a) Potential A (D_e = 24360 cm^{-1})			
6,38 – 5,37	1065	1560	10^{-1}
7,36 – 6,35	994	1180	10^{-1}
7,35 – 6,34	1060	1044	10^{-3}
8,33 – 7,32	990	950	10^{-2}
9,30 – 8,29	963	620	10^{-4}
10,28 – 9,27	870	615	10^{-1}
6,37 – 4,38	980	1180	10^{-4}
7,36 – 5,37	895	1390	10^{-1}
7,35 – 5,36	990	1050	10^{-3}
8,33 – 6,34	970	950	10^{-2}
9,30 – 7,31	1020	620	10^{-4}
10,28 – 8,29	957	615	10^{-1}
11,25 – 9,26	961	415	10^{-2}
12,22 – 10,23	926	290	10^{-1}
(b) Potential B (D_e = 26100 cm^{-1})			
8,36 – 7,35	1044	1301	10^{-1}
9,33 – 8,32	985	900	10^{-2}
10,30 – 9,29	914	586	10^{-4}
11,28 – 10,27	1013	586	10^{-1}
8,36 – 6,37	1040	1301	10^{-1}
9,33 – 7,34	1056	900	10^{-2}
10,31 – 8,32	924	839	10^{-1}
10,30 – 8,31	1042	586	10^{-4}
11,28 – 9,29	914	586	10^{-1}
11,27 – 9,28	1013	359	10^{-5}
12,25 – 10,26	890	407	10^{-1}

The most profitable method for assigning specific lines in the spectrum is to identify fine structure patterns, i.e., groups of up to 10 lines showing spacings characteristic of a $\Delta K = \pm 1$ transition for the $a\ ^3\Pi$ state. To assist this type of analysis the hyperfine structure must be considered.

4. Hyperfine structure

The standard hyperfine Hamiltonian may be written in the form of [24]

$$\mathcal{H}_{hfs} = aI_zL_z + bI.S + c/3(I_zS_z - (I.S)) + d/2(S_+I_+ + S_-I_-).$$

At the present time there are no measured or calculated values available for the hyperfine parameters a,b,c,d representing the $a\ ^3\Pi$ state. At large R, the

parameters should approach limiting values of $a, c, d = 0$, and b=710 MHz (half the H(^2S) constant assuming the wavefunction is pure triplet state at $R = \infty$). The $a\ ^3\Pi$ state has the nominal configuration ($1\sigma^2$, $2\sigma^2$ 3σ 1π) and the magnitude of the b parameter will depend primarily on the contribution of the H($1s$) orbital to the 3σ molecular orbital. The $A^2\Delta$ state of neutral CH has essentially the same nominal configuration but with one additional 1π electron. Therefore to a first approximation it might be assumed that the hyperfine constants are the same in the two cases near to the potential minimum. The measured b value for CH is 543 MHz [25], but for CH^+ the parameter should be half this value, b=272 MHz, because we are dealing with a triplet state rather than a doublet state. For the high vibrational levels of interest we assume that b lies somewhere between 272 and 710 MHz, say 400–500 MHz. For a first approximation we also assume that the other hyperfine parameters are relatively small in the range of internuclear distance of interest and ignore terms involving these parameters. Calculating the diagonal matrix element of the hyperfine Hamiltonian for the high K levels of the Hund's case (b) triplet pi state therefore yields the following approximate results for the hyperfine splittings of the various fine structure states [26]

$$\text{for} \quad J = K \pm 1 \qquad \Delta E \approx b,$$

$$\text{for} \quad J = K \qquad \Delta E \approx b/J.$$

Using the selection rule $\Delta F = \Delta J$ the hyperfine splittings for the 10 components of a given transition are given approximately by

$\Delta J = \Delta K, J = K \pm 1$, $\Delta E \approx \Delta b$ (4 strong lines) medium splitting (10–100MHz),
$\Delta J = \Delta K, J = K$, $\Delta E \approx \Delta b/J$ (2 strong lines) small splitting (0–10MHz),
$\Delta J = 0$, $\Delta E \approx b$ (4 weak lines) large splitting (400–600MHz).

In Fig. 8, the predicted fine structure for various transitions in the simulated spectrum is shown, and the approximate hyperfine splitting is indicated. Although there is some diversity of pattern, the spread of lines is characteristically about 5 cm^{-1}, and it can be seen that a line with small splitting is nearly always accompanied by one or two closely spaced lines of medium splitting. The fairly tight grouping of the sets of ten lines offers an explanation of the high density of lines in some parts of the experimental spectrum, especially if more than one such transition is overlayed. In Fig. 9 four sets of lines selected from the observed spectrum are shown, and it is apparent that although there is no direct reproduction of the predictions there are certainly characteristics in common. The sets were chosen such that the measured excess energies and linewidths for the transitions shown are nearly equal within a group. It is notable that for each of these transitions, a corresponding transition with approximately the same linewidth and excess energy is predicted in the simulation to lie within 30 cm^{-1} of the observed positions.

At this stage the situation can be summarised by saying that we are encouraged by the similarities between the ab-initio predictions and the experimental

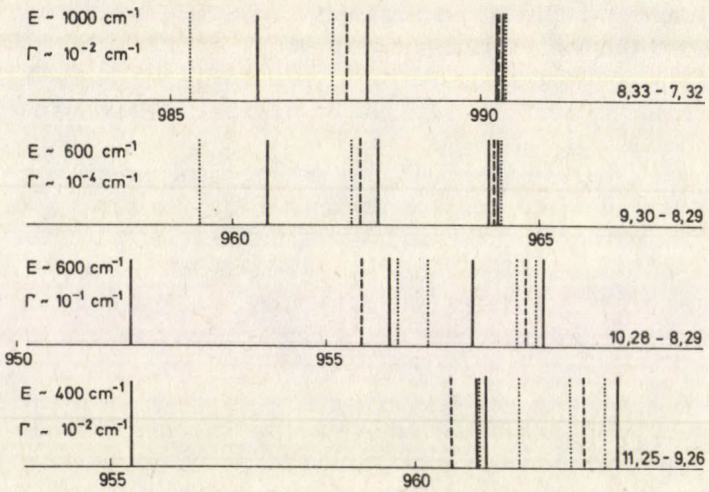

Fig. 8. Predicted line positions for transitions of the type illustrated in Fig. 7. Solid, dotted and dashed lines have the same meaning as in Fig. 7

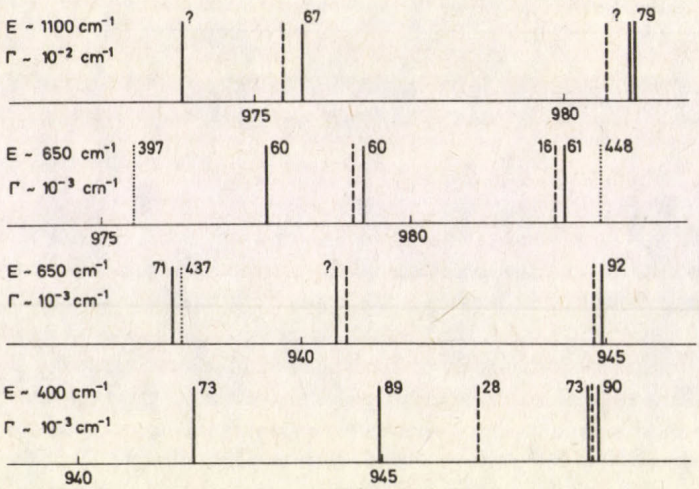

Fig. 9. Selected groups of observed lines from the infrared predissociation spectrum. Doublet splittings are marked for each transition ("?" indicates an incompletely resolved doublet). Dotted, dashed, and solid lines have the same meaning as in Fig. 7 and 8

results. It is not yet possible to adjust the input parameters for the calculation to fit the predictions to the results precisely. Any assignments that can be made

must remain tentative at this stage. Probably the best hope for pinning down the assignment relies on bringing together these results with those of Sarre et al. Work is currently in progress in that direction.

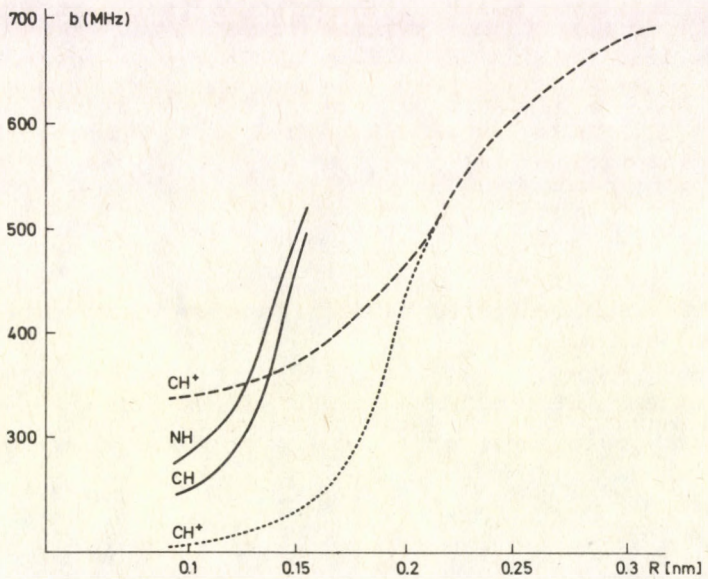

Fig. 10. Variation of the nuclear hyperfine parameter b (MHz) as a function of internuclear distance R. Solid lines show the calculated variation for NH($A\ ^3\Pi$) and CH($A\ ^2\Delta$)[27]. (The magnitude is multiplied by 0.5 for CH). The dashed line shows b (MHz) calculated from the weighting of the ($C^+ + H$) configuration in [11]. The dotted line is the form used in calculation A as described in the text

Finally, the hyperfine structure is considered here in a little more detail. Recently I have embarked on a more sophisticated calculation of the hyperfine splittings with a view to determining whether the typically observed $b \approx 400$–450 MHz and $\Delta b \approx 60$–90 MHz is reasonable for the predicted transitions. The calculation requires an estimate for the variation of the hyperfine parameters with internuclear distance. Kristiansen and Veseth has recently calculated the variation of the hyperfine parameters for a number of first-row hydrides [27], but unfortunately not including CH^+. The calculated variation for the b parameters is shown for CH($A\ ^2\Delta\ [3\sigma 1\pi^3]$) and NH($A\ ^3\Pi\ [3\sigma 1\pi^3]$) in Fig. 10. If it is assumed that there is an equivalence of the 3σ orbital in CH and CH^+ then the curve shown for CH could be used as an estimate for the $a\ ^3\Pi$ state of CH^+. However, the calculations of Lévy et al [11] suggest that in CH^+ there is strong configuration interaction between the $a\ ^3\Pi$ state and the $d\ ^3\Pi$ state. They have calculated the contribution of the configuration ($H + C^+$) as opposed to ($H^+ + C$) or ($H^- + C^{2+}$) as a function of R for the two states. To a first approximation it might be assumed that b for

Table III

Calculated hyperfine splittings for various $a^3\Pi$ - $a^3\Pi$ transitions, using two different functions for $b(R)$ of the $a^3\Pi$ state

$J' \cdot p' - J''p''$	Splitting (MHz)	
	A	B
$(v = 8, K = 33) - (v = 6, K = 34)$		
34+ – 35–	84	35
34– – 35+	51	5
33– – 34+	5	4
33+ – 34–	1	1
32+ – 33–	75	25
32– – 33+	61	10
34+ – 34–	494	609
34– – 34+	465	576
33– – 33+	431	599
33+ – 33–	439	611
$(v = 9, K = 30) - (v = 8, K = 29)$		
31– – 30+	60	29
31+ – 30–	21	13
30+ – 29–	4	3
30– – 29+	1	2
29– – 28+	50	18
29+ – 28–	45	8
30+ – 30–	434	564
30– – 30+	427	572
29– – 29+	485	637
29+ – 29–	520	594
$(v = 10, K = 28) - (v = 8, K = 29)$		
29– – 30+	51	2
29+ – 30–	48	6
28+ – 29–	9	18
28– – 29+	3	5
27– – 28+	46	51
27+ – 28–	33	15
29– – 29+	484	569
29+ – 29–	479	561
28+ – 28–	452	594
28– – 28+	467	614

the $a\ ^3\Pi$ state is directly proportional to the square of the coefficient of the first configuration, which gives the form of the dashed curve shown in Fig. 10. For the calculations described below I have actually used the curve shown in dotted lines in the Figure, which follows the trend shown by NH and CH at short R while following the curve in dashed lines for large R. The a,c,d parameters were assumed to vary with R with the same magnitude as the same parameters calculated for the $X\ ^2\Pi$ state of CH [27].

In the calculation the hyperfine splitting for each level is calculated individually as an electronic matrix element averaged over the vibrational wavefunction. For a given hyperfine state $|n, J, F\rangle$ where $F = J \pm 1/2$

$$E(n, J, F) = E(n, J) + \int \chi_{nJ}(R).\langle n, J, F|\mathcal{H}_{hfs}|n, J, F\rangle \chi_{nJ}(R)\, dR.$$

The diagonal electronic matrix element of the hyperfine operator is calculated for the rotationally adiabatic wavefunction, $|n, J, F\rangle$, and this explicitly considers the mixing of the singlet and triplet states. The matrix element may be written out fully as

$$\langle n, J, F|\mathcal{H}_{hfs}|n, J, F\rangle = \sum_{ij} c_{ni} \cdot c_{nj} \langle i, J, F|\mathcal{H}_{hfs}|j, J, F\rangle,$$

where the c_{ij} are the coefficients of the Hund's case (a) states in the rotationally adiabatic representation, and $|j, J, F\rangle$ is a zero-order wavefunction representing one of Hund's case (a) states. These zero-order matrix elements have been listed by Brown et al [24]. An estimate is needed for the hyperfine interactions for zero-order $^1\Sigma^+$,$^1\Pi$, and $^3\Sigma^+$ states, as the $^3\Pi$ rotationally-adiabatic states contain an admixture of these states which contributes to the final hyperfine splitting. We assume for simplicity that the singlet states have zero hyperfine splitting, while the $^3\Sigma^+$ parameter is 710 MHz, the anticipated limiting value at the dissociation limit. Thus the hyperfine interaction for the $^3\Pi$ state as a function of internuclear distance first increases as a consequence of the increasing value of the parameter b, but when singlet-triplet mixing becomes important (typically R >0.3 nm) the hyperfine interaction actually decreases as the state is losing some of it's triplet character. In reality these effects may be compensated by other interactions, such as hyperfine couplings off-diagonal in J or other non-adiabatic interactions, as the potential curves approach closely. In general the vibrational wavefunctions for the states of interest in our spectrum are such that these long range effects are unimportant.

Table III lists the calculated hyperfine splittings (A) for three sample transitions; for comparison a second calculation (B) was performed in which the $a\ ^3\Pi$ parameter b was set equal to half the value for CH and extrapolated to it's limiting value of 710 MHz at large R. It can be seen that for calculation A, the results are in reasonable agreement with the magnitudes of the observed splittings and with those predicted from the simpler theory. Calculation B is less in agreement; the large splittings are too large while the medium splittings are too small. It would appear that even without a firm assignment some semi-quantitative conclusions can be drawn concerning the variation of the hyperfine parameter b with internuclear distance for the $a\ ^3\Pi$ state. It is hoped that in future a reliable calculation for the variation of hyperfine parameters will become available, so that some of the interesting features emerging from this preliminary calculation can be examined in more detail.

5. Summary

The observation of fine and hyperfine structure in the $a\ ^3\Pi$ state of CH^+ for highly excited vibrational levels is a tough test for ab-initio calculations. The method of rotationally-adiabatic potentials is shown to be useful for making semi-quantitative predictions on the term structure for strongly interacting sets of states. The method is computationally expensive however and it is not easy to vary the input parameters to try and fit the experimental results. I am currently investigating whether the calculated energy levels can be conveniently expressed by means of term formulae with a limited number of parameters. CH^+ is one of a very small set of examples where hyperfine structure has been observed for highly excited levels. These measurements when fully understood should certainly provide a valuable contribution to our understanding of the behaviour of electronic wavefunctions as the dissociation limit is approached.

References

1. A. E. Douglas and G. Herzberg, Can. J. Res., *20*, A71, 1942.
2. A. E. Douglas and J. R. Morton, Astrophys J., *131*, 1, 1960.
3. A. Carrington and D. A. Ramsay, Physica Scripta, *25*, 272, 1982.
4. F. J. Grieman, B. H. Mahan, A. O'Keefe and J. S. Winn, Faraday Discussions Chem. Soc., *71*, 191, 1981.
5. H. Helm, P. C. Cosby, M. M. Graff and J. T. Moseley, Phys. Rev., *A25*, 304, 1982; H. Helm in "Physics of Electronic and Atomic Collisions" ed. J. Eichler, North-Holland, Amsterdam, 1984.
6. P. J. Sarre, J. M. Walmsley and C.J. Whitham, J. Chem. Soc. Faraday Trans, II *82*, 1243, 1986.
7. S. Green, P. S. Bagus, B. Liu, A. D. McLean and M. Yoshamine, Phys Rev., *A5*, 1614, 1972.
8. J. F. Bazet, C. Harel, R. McCarroll and A. Riera, Astron. Astrophys., *43*, 223, 1975.
9. R. Klotz, Private communication, 1984.
10. A. Carrington and T. P. Softley, Chemical Physics, *106*, 315, 1986.
11. B. Lévy, J. Ridard and E. LeCoarer, Chem. Phys., *92*, 295, 1985.
12. M. Carré, Physica, *41*, 63, 1969.
13. I. Kusunoki and Ch. Ottinger, J. Chem. Phys., *73*, 2069, 1980.
14. P. J. Sarre and C. J. Whitham, Mol. Phys., *62*, 1505, 1988.
15. P. J. Sarre and C. J. Whitham, Chem. Phys., *124*, 439, 1988.
16. H. Helm, P. C. Cosby, R. P. Saxon and D. L. Huestis, J. Chem. Phys., *76*, 2516, 1982.
17. In reference[10], p325, Table 2, $^3\Pi_1 - ^3\Sigma_1$ matrix element should read "$2^{1/2}\langle BL^+\rangle_3 + \langle AL^+\rangle_3$". p326 eqn (15) should read, "$\langle ^3\Pi_1|H_{so}|^1\Pi\rangle = -w/3$".
18. J. W. Cooley, Math. Comp., *15*, 303, 1961.
19. Programme supplied by R. J. LeRoy, modified version of the method of R. N. Zare.
20. R. J. LeRoy and W. K. Liu, J. Chem. Phys., *69*, 3622, 1978.
21. S. J. Singer, K. F. Freed and Y. B. Band, J. Chem. Phys., *79*, 6060, 1983.
22. C. J. Williams and K. F. Freed, J. Chem. Phys., *85*, 2699, 1986.
23. D. L. Cooper, Private communication, 1983.
24. J. M. Brown, I. Kopp, C. Malmberg and B. Rydh, Physica Scripta, *17*, 55, 1978.
25. C. R. Brazier and J. M. Brown, Can. J. Phys., *62*, 1563, 1984.
26. M. Mizushima, The Theory of Rotating Diatomic Molecules, Wiley and Sons, New York, 1975.
27. P. Kristiansen and L. Veseth, J. Chem. Phys., *84*, 6336, 1986.

Acta Physica Hungarica 67 (1-2), pp. 67-72 (1990)

HIGH RESOLUTION FOURIER-TRANSFORM SPECTRA OF THE $a\,^1\Delta_{(g)} \rightarrow X\,^3\Sigma^-_{(g)}$, $b\,^1\Sigma^+_{(g)} \rightarrow X\,^3\Sigma^-_{(g)}$ AND $b\,^1\Sigma^+_{(g)} \rightarrow a\,^1\Delta_{(g)}$ SYSTEMS OF O_2, SO, S_2 AND ISOELECTRONIC MOLECULES IN THE NIR REGION*

E. H. FINK, H. KRUSE and K. D. SETZER

Bergische Universität-GH Wuppertal, D-5600 Wuppertal, F. R. G.

and

D. A. RAMSAY and M. VERVLOET

Herzberg Institute of Astrophysics, NRC Canada, Ottawa, Canada

(Received 24 September 1988)

Emission spectra of the $a\,^1\Delta_{(g)} \rightarrow X\,^3\Sigma^-_{(g)}$, $b\,^1\Sigma^+_{(g)} \rightarrow X\,^3\Sigma^-_{(g)}$ and $b\,^1\Sigma^+_{(g)} \rightarrow a\,^1\Delta_{(g)}$ systems of a number of group VI–group VI diatomics have been measured at high resolution with a Fourier-transform spectrometer in the near-infrared region. Analysis of the spectra allows a systematic test of different Hamiltonians for the $X\,^3\Sigma^-_{(g)}(X_1 0^+_{(g)}, X_2 1^\pm_{(g)})$ ground states and of the line strength formulae for the electric quadrupole, magnetic dipole and electric dipole transitions involved.

Introduction

The group VI–group VI diatomics (O_2, SO, S_2, SeO,...,Te_2) have $X\,^3\Sigma^-_{(g)}$ ground states and low-lying $a\,^1\Delta_{(g)}$ and $b\,^1\Sigma^+_{(g)}$ electronically excited states. In the limit of Hund's cases (a) and (b) transitions between these states are forbidden for electric dipole radiation. Hence the excited states are metastable exhibiting radiative lifetimes in the range of $10^{-3} - 10^3$ s. Consequently, high concentrations of the excited radicals can be generated which are of potential interest as reactants or energy carriers in chemical and physical systems. Weak transitions between the states can occur by electric quadrupole or magnetic dipole radiation. In case of the heteronuclear species, electric dipole transitions are possible due to spin–orbit interaction of the states. The spectra appear in the near-infrared region between 0.9 and 3.0 μm, outside the sensitivity range of photomultipliers. Recently highly sensitive solid state detectors (Ge, InGaAs, InSb) have allowed observation of a number of new $a \rightarrow X$ and $b \rightarrow X$ emission systems of group VI–VI dimers from fast-flow chemiluminescence systems [1]. In the present work we report on high

*Presented at the Conference on High Resolution Electronic Spectroscopy of Molecules, Tihany, Hungary, 19-24 September 1988

resolution measurements of these spectra with a BOMEM FT spectrometer which yielded accurate spectroscopic constants of the states involved and allowed thorough tests of the line strength formulae for the transitions and determination of ratios of electric and magnetic transition moments.

Experimental

The radicals were generated by microwave discharges and chemical reactions in fast-flow systems. The ground state species were excited by energy transfer and energy pooling processes using an added flow of $O_2(a\,^1\Delta_g)$ as energy source. Details of the experimental arrangements are given in recent publications [2–6]. The spectra were measured in the Herzberg Institute of Astrophysics in Ottawa with a BOMEM DA3.002 Fourier-transform spectrometer. The maximum spectral resolution was between 0.015 and 0.1 cm^{-1}. The internal precision of the measurements ranged from ± 0.00005 to ± 0.002 cm^{-1} depending on the resolution and the intensity of the lines. Absolute calibration of the wavenumber scale was achieved by using the lines of the 0–0 band of the $a\,^1\Delta_g \rightarrow X\,^3\Sigma_g^-$ system of O_2, which appeared in all spectra, as secondary standards. The O_2 lines are considered to have an absolute wavenumber accuracy of ± 0.005 cm^{-1} [7].

Results and discussion

Energy levels and molecular constants

The following electronic transitions and bands have been measured and analysed:

O_2	$a\,^1\Delta_g$	$\rightarrow$	$X\,^3\Sigma_g^-$	:	0–0,	0–1			
	$b\,^1\Sigma_g^+$	$\rightarrow$	$X\,^3\Sigma_g^-$	:	0–0,	0–1			
	$b\,^1\Sigma_g^+$	$\rightarrow$	$a\,^1\Delta_g$	:	0–0				
SO	$a\,^1\Delta$	$\rightarrow$	$X\,^3\Sigma^-$	:	0–0				
	$b\,^1\Sigma^+$	$\rightarrow$	$X\,^3\Sigma^-$	:	0–0,	0–1,	1–1,	1–2	
S_2	$b\,^1\Sigma_g^+$	$\rightarrow$	$X\,^3\Sigma_g^-$	:	0–0,	0–1,	1–1		
^{80}SeO	$a\,^1\Delta$	$\rightarrow$	$X\,^3\Sigma^-$	:	0–0				
	$b\,^1\Sigma^+$	$\rightarrow$	$X\,^3\Sigma^-$	:	0–0,	0–1,	1–1,	1–2	
^{80}SeS	$b\,^1\Sigma^+$	$\rightarrow$	$X\,^3\Sigma^-$	:	0–0,	0–1,	0–2,	1–0,	1–2
$^{80}Se_2$	$b\,^1\Sigma_g^+$	$\rightarrow$	$X\,^3\Sigma_g^-$	:	0–0,	0–1,	1–1,	1–2,	1–3, 2–3
^{130}TeO	$b\,^1\Sigma^+$	$\rightarrow$	$X\,^3\Sigma^-$	:	0–0,	0–1,	1–1		
^{130}TeS	$b\,^1\Sigma^+$	$\rightarrow$	$X\,^3\Sigma^-$	:	0–0,	0–1,	1–1,	1–2	
$^{130}Te^{80}Se$	$b\,^1\Sigma^+$	$\rightarrow$	$X\,^3\Sigma^-$	:	0–0				

Due to the simple structures of the bands, in all spectra the lines could easily be assigned. The spectroscopic constants of the states involved were derived from

least-squares fits of the unblended lines, each line being weighted according to the square of its intensity since the precision of measurement is inversely proportional to intensity. Case (b) [7] and case (c) [8] Hamiltonians were used to describe the rotational structure in the $X\,^3\Sigma^-_{(g)}$ ground states of the molecules, and were found to give least-squares fits with similar standard deviations even for the heavier species Se_2, TeO and TeS. Table I shows the rotational constants of the $X\,^3\Sigma^-_{(g)}, v{=}0$ ground states when described with the case (b) formalism.

Table I
Rotational constants of the $X^3\Sigma^-(g)$, $v = 0$ ground states of group VI–group VI diatomics (in cm^{-1})

Molecule	B	10^7D	λ	$10^3\lambda_D$	γ	$10^6\gamma_D$
O_2	1.437680	48.33	1.9847	0.00191	−0.00842	−0.0065
SO	0.717932	11.09	5.2790	0.00833	−0.00567	0.0179
S_2	0.294592	1.96	11.7931	0.00105	−0.00716	0.0
^{80}SeO	0.468944	4.966	84.1129	0.0716	−0.00689	0.0
^{80}SeS	0.178527	0.731	98.9833	0.0458	−0.0102	0.0981
$^{80}Se_2$	0.089973	0.197	256.215	0.0	−0.00832	0.0
^{130}TeO	0.355113	3.090	391.2015	0.2000	0.0065	0.0
^{130}TeS	0.132170	0.382	410.1168	0.0900	−0.00052	0.0

For the first time spin–rotation constants γ were derived for the heavier species SeS, Se_2, TeO and TeS. According to Brown et al [9] γ can be written as a sum of second and third order terms,

$$\gamma = \gamma^{(2)} + \gamma^{(3)}, \tag{1}$$

$$\gamma^{(2)} = -4B\Sigma_n \frac{\langle X^3\Sigma^- \,|\, 1/\sqrt{2}(L_x - iL_y) \,|\, {}^3\Pi_n\rangle\langle {}^3\Pi_n \,|\, H_{SO} \,|\, X^3\Sigma^-\rangle}{E({}^3\Pi_n) - E(X^3\Sigma^-)}, \tag{2}$$

$$\gamma^{(3)} = B\frac{|\langle X^3\Sigma_o^- \,|\, H_{SO} \,|\, b^1\Sigma_o^+\rangle|^2}{(E(b^1\Sigma^+) - E(X^3\Sigma^-))} = 2B\lambda^{(2)}/\Delta E(b - X), \tag{3}$$

with

$$\lambda^{(2)} = |\langle X^3\Sigma_o^- \,|\, H_{SO} \,|\, b^1\Sigma_o^+\rangle|^2/2\Delta E(b - X). \tag{4}$$

Since there is an inverse dependence on reduced mass in the mixing of the $^3\Pi$ and $X\,^3\Sigma^-$ states, variation of the values of γ for a series of molecules is better gauged by comparing the values of $\gamma^{(2)}/B$. As is seen from Table II, these data show a systematic trend reflecting the lowering of the $^3\Pi$ state energies and the increase in spin–orbit interaction on going down the series of molecules. The same trend is found in the literature data [10,11] of the spin–rotation constants hitherto known for the $X\,^3\Sigma^-$ states of group V halides (Table II).

Table II
Trends in the values of the spin–rotation constants of the $X\,^3\Sigma^-_{(g)}$ ground states of group VI–VI and group V–VII molecules

Molecule	γ/MHz	$\gamma^{(3)}$/MHz	$\gamma^{(2)}$/MHz	$10^3 \cdot \gamma^{(2)}/B$
O_2	−252.6	13.0	−265.6	−6.2
SO	−170.5	21.7	−192.2	−8.9
S_2	−214.6	26.1	−240.7	−27.3
^{80}SeO	−208.3	248.5	−456.8	−32.5
^{80}SeS	−305.7	135.7	−441.4	−82.5
$^{80}Se_2$	−249.3	173.7	−423.0	−156.8
^{130}TeO	194.9	838.5	−643.6	−60.5
^{130}TeS	−15.9	385.1	−401.0	−101.2
NF	−139.4	4.6	−144.0	−4.0
NCl	−208.6	4.9	−213.5	−11.0
NBr	−749.5	17.9	−767.4	−57.6
	(−20986	15.6	−21001	−1578)
NI	−1292	65.9	−1358	−131.5
PF	44.9	7.5	37.5	2.2
PCl	−91.4	5.3	−96.8	−12.8
PBr	−212.6	11.8	−224.4	−45.4
AsF	626.6	111.6	514.9	46.7

Line strengths and transition moments

The $b\,^1\Sigma^+_g \rightarrow a\,^1\Delta_g$ transition of O_2 is the only electronic transition of diatomic molecules known that is entirely electric quadrupole in nature. The line intensities of the five branches of its 0–0 band were calculated using the formula

$$I_{J'-J} \alpha\, \tilde{\nu}^6 \cdot S_{J'J} \exp(-hcB'J'(J'+1)/kT), \tag{5}$$

where $S_{J,J}$ is the line strength (including the statistical weight factor) as given by Kovács [12], and B' is the rotational constant in the $b\,^1\Sigma^+_g$ state. A least-squares fit yielded a value of 313 ± 10 K for the rotational temperature showing that the rotational distribution in the long-lived $b\,^1\Sigma^+_g$ state is completely relaxed. The standard deviation of the differences between the observed and calculated intensities was 3% of the intensity of the strongest line and corresponded to the noise level in the spectrum.

The relative line intensities of the four branches in the magnetic dipole transitions $b\,^1\Sigma^+_g \rightarrow X\,^3\Sigma^-_g$ of O_2, S_2 and Se_2 could be fitted with similar small standard deviations using the line strengths formulae given by Watson [13]. In case of Se_2, the $^RQ(J)$ branch ending in the F_1 levels of the $X\,^3\Sigma^-_g$ state was not observed. Due to the large spin–spin splitting in this state of 511 cm^{-1} Watson's line strength formulae predict the intensity of this branch to be lower by more than a factor of 1000 than those of the other branches.

Recently, Bellary and Balasubramanian [14] have given improved line strength formulae for the nine branches of $^1\Delta_g \rightarrow {}^3\Sigma_g^-$ magnetic dipole transitions which, besides purely vibronic transitions moments, contain two additional parameters ρ and σ of rovibronic origin. They have analysed our relative line intensities and determined ρ and σ values for the $a\,^1\Delta_g \rightarrow X\,^3\Sigma_g^-$ system of O_2. Work is in progress to use high resolution spectra of the $a\,^1\Delta \rightarrow X\,^3\Sigma^-$ system of SO to further test these line strength formulae.

Due to spin–orbit interaction of the states, the $b\,^1\Sigma^+ \rightarrow X\,^3\Sigma^-$ transitions of the heteronuclear species SO, SeO, SeS, TeO, TeS and TeSe are mostly electric dipole in nature and show five branches, for which line strength formulae have been given by Watson [13]. According to Watson's theory the line intensities are determined by the parallel and perpendicular electric dipole moments for the $b\,^1\Sigma_0^+ \rightarrow X\,^3\Sigma_0^-(\mu_0)$ and $b\,^1\Sigma_0^+ \rightarrow X\,^3\Sigma_{\pm1}^-(\mu_1)$ transitions, as well as by the magnetic dipole moment (M) of the latter. In addition the line strength formulae contain factors c_J and s_J given by the energy separations of the triplet components of the $^3\Sigma^-$ state, which in case of large spin–spin splitting may have major effects on the relative intensities of the branches. From the analysis of the relative line intensities accurate values of the ratios of the transition moments μ_1/μ_0 and M/μ_0 can be obtained. Then, if the radiative lifetime of the $b\,^1\Sigma^+$ state is known, absolute values of μ_1 and μ_0 can be calculated by the equation

$$A_{ul} = 1/\tau_u = 64\pi^4 \tilde{\nu}_{ul}^3 \cdot |R^e|^2/(3c^3h), \tag{6}$$

where in the present case

$$|R^e|^2 = |\mu_0|^2 + 2|\mu_1|^2. \tag{7}$$

In most cases the contribution to $|R^e|^2$ of the magnetic dipole transition moment can be neglected. The ratios as well as the absolute values of the transition moments represent interesting data for comparison with the results of quantummechanical ab-initio calculations.

Table III

Comparison of relative and absolute transition moments of the $b\,^1\Sigma^+ \rightarrow X\,^3\Sigma^-$ transitions with ab-initio data

Molecule	μ_1/μ_0		$\mu_0(ea_0)$		$\tau(b^1\Sigma^+)(ms)$		Ref.
	Exp.	Theor.	Exp.	Theor.	Exp.	Theor.	
SO	−1.06	0.28	±0.0043	0.005	7.0	13.8	1,15
SeO	−0.70	−1.1	±0.0140	0.0056	1.4	4.7	5,16
SeS	−0.059	−0.038	±0.051	0.0223	0.40	2.0	4,17
Molecule	M/μ_0	(μ_B/ea_0)	M (Bohr magnetons)				Ref.
	Exp.	Theor.	Exp.	Theor.			
SeS	±13.9	−132	±071	−0.2949			4,17

In the strong 0–0 band of the $b\,^1\Sigma^+ \rightarrow X\,^3\Sigma^-$ spectrum of ^{80}SeS, for the first time, both electric and magnetic dipole branches have been detected. Analysis of the relative line intensities yielded the ratios of transition moments μ_1/μ_0 as well as M/μ_0. In all cases Watson's line strength formulae allowed accurate fits of the relative line intensities. In Table III the deduced transition moment data are compared with the results of ab-initio calculations. The comparison shows that the calculations obviously can predict the transition moments and the radiative lifetimes of the $b\,^1\Sigma^+_{(g)}$ (and hopefully also of $a\,^1\Delta_{(g)}$) states to factors of 2 and 4, respectively.

Acknowledgements

E. H. F., H. K. and K. D. S. wish to thank the Deutsche Forschungsgemeinschaft for financial support of this work. We acknowledge the valuable technical assistance of M. Barnett, M. Kalb and W. S. Neil.

References

1. M. Bielefeld, G. Elfers, E. H. Fink, H. Kruse, J. Wildt, R. Winter and F. Zabel, J. Photochem., *25*, 419, 1984.
2. E. H. Fink, H. Kruse, D. A. Ramsay and M. Vervloet, Can. J. Phys., *64*, 242, 1986.
3. E. H. Fink, H. Kruse and D. A. Ramsay, J. Mol. Spectrosc., *119*, 377, 1986.
4. E. H. Fink, H. Kruse, D. A. Ramsay and Ding–Chang Wang, Mol. Phys., *60*, 277, 1987.
5. E. H. Fink, K. D. Setzer, D. A. Ramsay and M. Vervloet, J. Mol. Spectrosc., *125*, 66, 1987.
6. E. H. Fink, K. D. Setzer, D. A. Ramsay and M. Vervloet, submitted to J. Mol. Spectrosc., 1988.
7. C. Amiot and J. Verges, Can. J. Phys., *59*, 1391, 1981.
8. L. Veseth, J. Phys. B., *6*, 1473, 1973.
9. J. M. Brown, K. Dumper and C. R. Parent, Mol. Phys., *36*, 1149, 1978.
10. K. P. Huber and G. Herzberg, Molecular Spectra and Molecular Structure, IV. Constants of Diatomic Molecules, Van Nostrand Reinhold, New York, 1979.
11. E. H. Fink et al., unpublished results.
12. I. Kovács, Rotational Structure in the Spectra of Diatomic Molecules, Adam Hilger, London, 1969.
13. J. K. G. Watson, Can. J. Phys., *46*, 1637, 1968.
14. V. P. Bellary and T. K. Balasubramanian, J. Mol. Spectrosc., *126*, 436, 1987.
15. M. Bettendorf, R. Klotz and S. D. Peyerimhoff, Chem. Phys., *110*, 315,1986.
16. T. Matsushita, R. Klotz, C. Marian and S. D. Peyerimhoff, submitted to Mol. Phys.
17. J. R. Alvarez–Collado and R. J. Buenker, Mol. Phys., *64*, 725, 1988.

Acta Physica Hungarica 67 (1-2), pp. 73-89 (1990)

PERTURBATION AND THE EFFECTS ON THE TRANSITION INTENSITY AND THE LINE SHAPE STUDIED ON ALKALI METAL DIATOMIC MOLECULES*

HAJIME KATÔ, MITSUHIKO OTANI and MASAAKI BABA

Department of Chemistry, Faculty of Science, Kobe University
Nada-ku, Kobe 657, Japan

(Received 24 September 1988)

We have studied the molecular structure and the dynamics of alkali metal diatomic molecules. Professor István Kovács's book [1] has been very useful to study the energy levels, the transition intensities, the perturbations, etc. In this article, we report a theoretical study on the energy levels of the alkali metal diatomic molecules, and then a study on perturbation of the $A\ ^1\Sigma_u^+$ and the $b\ ^3\Pi_u$ states, and the effects on the transition intensity and the line splitting.

1. Theory on the energy levels of the alkali metal diatomic molecules

1a) Hamiltonian

The Hamiltonian for a rotating diatomic molecule in the absence of an external field can be written in the form

$$H = H_e + H_v + H_r, \tag{1}$$

where H_e is the electronic part and H_v is the vibrational part. The rotational part H_r is written as [2]

$$\begin{aligned} H_r &= B_v[(J_x - L_x - S_x)^2 + (J_y - L_y - S_y)^2], \\ &= B_v[(J^2 - J_z^2) + (L^2 - L_z^2) + (S^2 - S_z^2) \\ &+ (L_+S_- + L_-S_+) - (J_+L_- + J_-L_+) - (J_+S_- + J_-S_+)], \end{aligned} \tag{2}$$

where B_v is the rotational constant, and the rotational angular momentum is expressed as the total angular momentum ($\mathbf{J}$) minus the electronic orbital and spin angular momenta ($\mathbf{L}$ and $\mathbf{S}$), $J_\pm = J_x \pm iJ_y$, $L_\pm = L_x \pm iL_y$, $S_\pm = S_x \pm iS_y$, and the suffixes x and y denote the components of the molecule-fixed coordinates, and the z axis is along its internuclear axis.

*Presented at the Conference on High Resolution Electronic Spectroscopy of Molecules, Tihany, Hungary, 19-24 September 1988

1b) Basis functions

As a set of basis functions, we use wave functions of simple products, $|\Lambda\rangle\,|S\Sigma\rangle\,|v\rangle\,|J\Omega M\rangle$. The function $|\Lambda\rangle\,|S\Sigma\rangle\,|v\rangle$ is a wave function for a nonrotating molecule, where Λ and Σ represent the projections of the total electronic orbital and total electronic spin angular momenta along the molecular axis, respectively, and v represents the vibrational quantum number. All of these are expressed in molecule-fixed coordinates. The rotational part $|J\Omega M\rangle$ is expressed in laboratory-fixed coordinates, where the quantum numbers J and M specify the total angular momentum and its projection along the laboratory-fixed Z axis, respectively, and $\Omega = \Lambda + \Sigma$.

1c) Matrix elements of angular momentum

We shall always use the representation of the rotation group, the angular momenta, the coupling coefficients and tensors defined by Brink and Satchler [3]. The nonvanishing matrix elements of the components of the spin angular momentum operator **S** and the orbital angular momentum operator **L** are the following:

$$\langle S\Sigma\,|\,\mathbf{S}^2\,|\,S\Sigma\rangle = S(S+1), \qquad \langle S\Sigma\,|\,S_z\,|\,S\Sigma\rangle = \Sigma,$$
$$\langle S\Sigma \pm 1\,|\,S_\pm\,|\,S\Sigma\rangle = [(S \mp \Sigma)(S \pm \Sigma + 1)]^{1/2}, \tag{3}$$
$$\langle L\Lambda\,|\,\mathbf{L}^2\,|\,L\Lambda\rangle = L(L+1), \qquad \langle L\Lambda\,|\,L_z\,|\,L\Lambda\rangle = \Lambda,$$
$$\langle L\Lambda \pm 1\,|\,L_\pm\,|\,L\Lambda\rangle = [(L \mp \Lambda)(L \pm \Lambda + 1)]^{1/2}. \tag{4}$$

The nonvanishing matrix elements of the total angular momentum **J** are similar, but the matrix element of $J_\pm$ is different. We must be careful on this somewhat surprising difference in behaviour of **J** from **L** and **S** [2,4].

$$\langle J\Omega\,|\,\mathbf{J}^2\,|\,J\Omega\rangle = J(J+1), \qquad \langle J\Omega\,|\,J_z\,|\,J\Omega\rangle = \Omega,$$
$$\langle J\Omega \mp 1\,|\,J_\pm\,|\,J\Omega\rangle = [(J \pm \Omega)(J \mp \Omega + 1)]^{1/2}. \tag{5}$$

1d) Electronic states obtainable from the union of two atoms

Possible electronic configurations resulting from the union of two atoms in specified states can be obtained by applying the general rules [5]. If the molecules in equilibrium can be described in terms of Hund's coupling cases (a) and (b), the electronic states described from specified atomic states of the same element are

[A]: $^1\Sigma_g^+$, $^3\Sigma_u^+$ for $^2S + {}^2S$
[B]: $^1\Pi_g$, $^3\Pi_g$, $^1\Pi_u$, $^3\Pi_u$, $^1\Sigma_g^+$, $^3\Sigma_g^+$, $^1\Sigma_u^+$, $^3\Sigma_u^+$ for $^2P + {}^2S$,

and those of different elements are

[A']: $^1\Sigma^+$, $^3\Sigma^+$ for $^2S + {}^2S$,
[B']: $^1\Pi$, $^3\Pi$, $^1\Sigma^+$, $^3\Sigma^+$ for $^2P + {}^2S$.

In a case of alkali metal diatomic molecules of the same element, the electronic wave functions for [A] are approximately expressed in terms of simple molecular orbitals

$$|^1\Sigma_g^+\rangle = |(\sigma_g s)\overline{(\sigma_g s)}| = [|0\rangle|0\,0\rangle],$$
$$|^3\Sigma_u^+\rangle = |(\sigma_g s)(\sigma_u s)| = [|0\rangle|1\,1\rangle], |\overline{(\sigma_g s)}\,\overline{(\sigma_u s)}| = [|0\rangle|1-1\rangle],$$
$$\text{and}\quad (2)^{-1/2}(|(\sigma_g s)\overline{(\sigma_u s)}| + |\overline{(\sigma_g s)}(\sigma_u s)|) = [|0\rangle|1\,0\rangle], \tag{6}$$

where normalization factors for the determinant functions are omitted, orbital (...) denotes a molecular orbital with spin α, orbital $\overline{(...)}$ denotes an orbital with spin β, and the symbols in parentheses [ ] denote $|\Lambda\rangle|S\Sigma\rangle$. The electronic wave functions for [B] are:

$$|^1\Sigma_u^+\rangle = (2)^{-1/2}(|(\sigma_g s)\overline{(\sigma_u p_0)}| - |\overline{(\sigma_g s)}(\sigma_u p_0)|) = [|0\rangle|0\,0\rangle],$$
$$|^1\Pi_u\rangle = (2)^{-1/2}(|(\sigma_g s)\overline{(\pi_u p_\pm)}| - |\overline{(\sigma_g s)}(\pi_u p_\pm)|) = [|\pm 1\rangle|0\,0\rangle],$$
$$|^3\Pi_u\rangle = |(\sigma_g s)(\pi_u p_\pm)| = [|\pm 1\rangle|1\,1\rangle], |\overline{(\sigma_g s)}\,\overline{(\pi_u p_\pm)}| = [|\pm 1\rangle|1\,-1\rangle],$$
$$\text{and}\quad (2)^{-1/2}(|(\sigma_g s)\overline{(\pi_u p_\pm)}| + |\overline{(\sigma_g s)}(\pi_u p_\pm)|) = [|\pm 1\rangle|1\,0\rangle],$$
$$|^1\Sigma_g^+\rangle = (2)^{-1/2}(|(\sigma_g s)\overline{(\sigma_g p_0)}| - |\overline{(\sigma_g s)}(\sigma_g p_0)|) = [|0\rangle|0\,0\rangle],$$
$$|^3\Sigma_g^+\rangle = |(\sigma_g s)(\sigma_g p_0)| = [|0\rangle|1\,1\rangle], |\overline{(\sigma_g s)}\,\overline{(\sigma_g p_0)} = [|0\rangle|1-1\rangle],$$
$$\text{and}\quad (2)^{-1/2}(|(\sigma_g s)\overline{(\sigma_g p_0)}| + |\overline{(\sigma_g s)}(\sigma_g p_0)|) = [|0\rangle|1\,0\rangle],$$
$$|^1\Pi_g\rangle = (2)^{-1/2}(|(\sigma_g s)\overline{(\pi_g p_\pm)}| - |\overline{(\sigma_g s)}(\pi_g p_\pm)|) = [|\pm 1\rangle|0\,0\rangle],$$
$$|^3\Pi_g\rangle = |(\sigma_g s)(\pi_g p_\pm)| = [|\pm 1\rangle|1\,1\rangle], |\overline{(\sigma_g s)}\,\overline{(\pi_g p_\pm)}| = [|\pm 1\rangle|1-1\rangle],$$
$$\text{and}\quad (2)^{-1/2}(|(\sigma_g s)\overline{(\pi_g p_\pm)}| + |\overline{(\sigma_g s)}(\pi_g p_\pm)|) = [|\pm 1\rangle|1\,0\rangle],$$
$$|^3\Sigma_u^+\rangle = |(\sigma_g s)(\sigma_u p_0)| = [|0\rangle|1\,1\rangle], |\overline{(\sigma_g s)}\,\overline{(\sigma_u p_0)}| = [|0\rangle|1-1\rangle],$$
$$\text{and}\quad (2)^{-1/2}(|(\sigma_g s)\overline{(\sigma_u p_0)}| + |\overline{(\sigma_g s)}(\sigma_u p_0)|) = [|0\rangle|10\rangle]. \tag{7}$$

1e) Spin–orbit interaction

The operator of the spin–orbit interaction is represented by $A\mathbf{L}\cdot\mathbf{S}$ or $\sum_i \xi(r_i)\mathbf{l}_i\cdot\mathbf{s}_i$, where $\mathbf{l}_i$ and $\mathbf{s}_i$ are operators representing the electronic orbital and electronic spin angular momenta for the individual electrons. The operator

$$H_{so} = A\mathbf{L}\cdot\mathbf{S} \tag{8}$$

is used to compute spin splittings within a given spin multiplet.

The operator

$$H_{so} = \sum_i \xi(r_i) \mathbf{l}_i \cdot \mathbf{s}_i \tag{9}$$

must be used to compute the interaction between states belonging to different S or L values. Matrix elements of $A\mathbf{L}\cdot\mathbf{S}$ are given by

$$\langle S\Sigma | \langle \Lambda | A\mathbf{L}\cdot\mathbf{S} | \Lambda \rangle | S\Sigma \rangle = A\Lambda\Sigma,$$

and

$$\langle S\Sigma | \langle \Lambda | A\mathbf{L}\cdot\mathbf{S} | \Lambda' \rangle | S'\Sigma' \rangle = 0 \quad \text{if} \quad |\Lambda\rangle |S\Sigma\rangle \neq |\Lambda'\rangle |S'\Sigma'\rangle. \tag{10}$$

The selection rules for matrix elements of H_{so} are [6]

$$\begin{aligned} &\Delta J = 0,\ \Delta\Omega = 0,\ g \not\leftrightarrow u,\ e \not\leftrightarrow f,\ \Sigma^+ \leftrightarrow \Sigma^-, \\ &\Delta S = 0 \text{ and } \Delta\Lambda = \Delta\Sigma = 0 \text{ or } \Delta S = \pm 1 \text{ and } \Delta\Lambda = -\Delta\Sigma = \pm 1. \end{aligned} \tag{11}$$

In the single-configuration limit, if the two interacting states belong to the same configuration, then

$$\Delta\Lambda = \Delta\Sigma = 0, \tag{12}$$

and if the two interacting states differ by at most one spin–orbital, then

$$\Delta\Lambda = -\Delta\Sigma = \pm 1. \tag{13}$$

The spin–orbit Hamiltonian of Eq. (9) can be written as

$$H_{so} = \sum_i \xi(r_i)[(1_{+i}s_{-i} + 1_{-i}s_{+i})/2 + 1_{zi}s_{zi}]. \tag{14}$$

Let us calculate the spin–orbit matrix element for the electronic states expressed by Eq.(7). From the selection rule $g \not\leftrightarrow u$ for the spin–orbit operator, only the states having the same g or u symmetry can interact. By omitting the suffixes g and u, we shall use the following configuration representation for the electronic states

$$|^1\Sigma^+\, 0^+\rangle = |0\rangle |0\,0\rangle = (2)^{-1/2}(|(\sigma s)\overline{(\sigma p_0)}| - |\overline{(\sigma s)}(\sigma p_0)|), \tag{15}$$

$$|^3\Sigma^+ +1\rangle = |0\rangle |1\,1\rangle = |(\sigma s)(\sigma p_0)|, \tag{16}$$

$$|^3\Sigma^+ -1\rangle = |0\rangle |1\,-1\rangle = |\overline{(\sigma s)}\,\overline{(\sigma p_0)}|, \tag{17}$$

$$|^3\Sigma^+\, 0^-\rangle = |0\rangle |1\,0\rangle = (2)^{-1/2}(|(\sigma s)\overline{(\sigma p_0)}| + |\overline{(\sigma s)}(\sigma p_0)|), \tag{18}$$

$$|^1\Pi + 1\rangle = |+1\rangle |0\,0\rangle = (2)^{-1/2}(|(\sigma s)\overline{(\pi p_+)}| - |\overline{(\sigma s)}(\pi p_+)|), \tag{19}$$

$$|^1\Pi - 1\rangle = |-1\rangle |0\,0\rangle = (2)^{-1/2}(|(\sigma s)\overline{(\pi p_-)}| - |\overline{(\sigma s)}(\pi p_-)|), \tag{20}$$

$$|^3\Pi\ +2\rangle = |+1\rangle|1\ 1\rangle = |(\sigma s)(\pi p_+)|, \tag{21}$$

$$|^3\Pi\ 0'\rangle = |+1\rangle|1-1\rangle = |\overline{(\sigma s)}\,\overline{(\pi p_+)}|, \tag{22}$$

$$|^3\Pi\ 0''\rangle = |-1\rangle|1\ 1\rangle = |(\sigma s)(\pi p_-)|, \tag{23}$$

$$|^3\Pi\ -2\rangle = |-1\rangle|1-1\rangle = |\overline{(\sigma s)}\,\overline{(\pi p_-)}|, \tag{24}$$

$$|^3\Pi+\ 1\rangle = |+1\rangle|1\ 0\rangle = (2)^{-1/2}(|(\sigma s)\overline{(\pi p_+)}| + |\overline{(\sigma s)}(\pi p_+)|), \tag{25}$$

$$|^3\Pi-\ 1\rangle = |-1\rangle|1\ 0\rangle = (2)^{-1/2}(|(\sigma s)\overline{(\pi p_-)}| + |\overline{(\sigma s)}(\pi p_-)|). \tag{26}$$

For one electron operators l_+, l_-, s_+, and s_-

$$\begin{aligned} &l_+|p_0\rangle = (2)^{1/2}|p_+\rangle, && l_-|p_+\rangle = (2)^{1/2}|p_0\rangle, \\ &l_+|p_-\rangle = (2)^{1/2}|p_0\rangle, && l_-|p_0\rangle = (2)^{1/2}|p_-\rangle, \\ &s_+|1/2-1/2\rangle = |1/2\ 1/2\rangle, && s_-|1/2\ 1/2\rangle = |1/2-1/2\rangle. \end{aligned} \tag{27}$$

The non-vanishing matrix elements for the electronic wave functions of Eqs (15) – (26) are

$$\begin{aligned} &\langle{}^1\Sigma^+\ 0^+|H_{so}|^3\Pi\ 0'\rangle = \langle{}^3\Pi\ 0'|H_{so}|^1\Sigma^+0^+\rangle = -A, \\ &\langle{}^1\Sigma^+\ 0^+|H_{so}|^3\Pi\ 0''\rangle = \langle{}^3\Pi\ 0''|H_{so}|^1\Sigma^+0^+\rangle = A, \\ &\langle{}^3\Sigma^+\ +1|H_{so}|^1\Pi\ +1\rangle = \langle{}^1\Pi\ +1|H_{so}|^3\Sigma^+ +1\rangle = A, \\ &\langle{}^3\Sigma^+ +1|H_{so}|^3\Pi\ +1\rangle = \langle{}^3\Pi+1|H_{so}|^3\Sigma^+ +1\rangle = A, \\ &\langle{}^3\Sigma^+ -1|H_{so}|^1\Pi\ -1\rangle = \langle{}^1\Pi-1|H_{so}|^3\Sigma^+ -1\rangle = -A, \\ &\langle{}^3\Sigma^+ -1|H_{so}|^3\Pi\ -1\rangle = \langle{}^3\Pi-1|H_{so}|^3\Sigma^+ -1\rangle = A, \\ &\langle{}^3\Sigma^+\ 0^-|H_{so}|^3\Pi\ 0'\rangle = \langle{}^3\Pi\ 0'|H_{so}|^3\Sigma^+0^-\rangle = A, \\ &\langle{}^3\Sigma^+\ 0^-|H_{so}|^3\Pi\ 0''\rangle = \langle{}^3\Pi\ 0''|H_{so}|^3\Sigma^+0^-\rangle = A, \\ &\langle{}^1\Pi\ +1|H_{so}|^3\Pi\ +1\rangle = \langle{}^3\Pi+1|H_{so}|^1\Pi+1\rangle = -B, \\ &\langle{}^1\Pi\ -1|H_{so}|^3\Pi\ -1\rangle = \langle{}^3\Pi-1|H_{so}|^1\Pi-1\rangle = B, \\ &\langle{}^3\Pi\ +2|H_{so}|^3\Pi\ +2\rangle = B, \\ &\langle{}^3\Pi\ 0'|H_{so}|^3\Pi\ 0'\rangle = -B, \\ &\langle{}^3\Pi\ 0''|H_{so}|^3\Pi\ 0''\rangle = -B \end{aligned}$$

and $$\langle{}^3\Pi\ -2|H_{so}|^3\Pi\ -2\rangle = B, \tag{28}$$

where

$$A = \langle(\sigma p_0)|\xi(r)|(\sigma p_0)\rangle/2 \text{ and } B = \langle(\pi p_\pm)|\xi(r)|(\pi p_\pm)\rangle/2. \tag{29}$$

At the limit of $R \to \infty$, $A = B$ and the matrix is

	$^1\Sigma^+$ 0^+	$^3\Sigma^+$ 0^-	$^3\Pi$ $0'$	$^3\Pi$ $0''$	$^3\Sigma^+$ $+1$	$^1\Pi$ $+1$	$^3\Pi$ $+1$	$^3\Sigma^+$ -1	$^1\Pi$ -1	$^3\Pi$ -1	$^3\Pi$ $+2$	$^3\Pi$ -2
$^1\Sigma^+0^+$	0	0	$-A$	A	0	0	0	0	0	0	0	0
$^3\Sigma^+0^-$	0	0	A	A	0	0	0	0	0	0	0	0
$^3\Pi\ 0'$	$-A$	A	$-A$	0	0	0	0	0	0	0	0	0
$^3\Pi\ 0''$	A	A	0	$-A$	0	0	0	0	0	0	0	0
$^3\Sigma^+ + 1$	0	0	0	0	0	A	A	0	0	0	0	0
$^1\Pi + 1$	0	0	0	0	A	0	$-A$	0	0	0	0	0
$^3\Pi + 1$	0	0	0	0	A	$-A$	0	0	0	0	0	0
$^3\Sigma^+ - 1$	0	0	0	0	0	0	0	0	$-A$	A	0	0
$^1\Pi - 1$	0	0	0	0	0	0	0	$-A$	0	A	0	0
$^3\Pi - 1$	0	0	0	0	0	0	0	A	A	0	0	0
$^3\Pi + 2$	0	0	0	0	0	0	0	0	0	0	A	0
$^3\Pi - 2$	0	0	0	0	0	0	0	0	0	0	0	A

(30)

The eigenfunctions for eigenvalue $= A$ are

$$|^3\Pi \pm 2\rangle,$$
$$(2)^{-1/2}(|^3\Sigma^+ \pm 1\rangle + |^3\Pi \pm 1\rangle),$$
$$(6)^{-1/2}(|^3\Sigma^+ \pm 1\rangle - |^3\Pi \pm 1\rangle \pm 2|^1\Pi \pm 1\rangle),$$
$$(6)^{-1/2}(2|^3\Sigma^+\ 0^-\rangle + |^3\Pi\ 0'\rangle + |^3\Pi\ 0''\rangle)$$
and
$$(6)^{-1/2}(2|^1\Sigma^+\ 0^+\rangle - |^3\Pi\ 0'\rangle + |^3\Pi\ 0''\rangle). \quad (31)$$

The eigenfunctions for eigenvalue $= -2A$ are

$$(3)^{-1/2}(|^3\Sigma^+ \pm 1\rangle - |^3\Pi \pm 1\rangle \mp |^1\Pi \pm 1\rangle),$$
$$(3)^{-1/2}(|^3\Sigma^+\ 0^-\rangle - |^3\Pi\ 0'\rangle - |^3\Pi\ 0''\rangle),$$
and
$$(3)^{-1/2}(|^1\Sigma^+\ 0^+\rangle + |^3\Pi\ 0'\rangle - |^3\Pi\ 0''\rangle). \quad (32)$$

1f) Eigenfunction and eigenvalue

The eigenfunction and the eigenvalue can be obtained by solving the secular equation composed of the matrices for $H_e + H_v + H_r + H_{so}$ in terms of the basis set $|\Lambda\rangle|S\Sigma\rangle|v\rangle|J\Omega M\rangle$.

A). $^1\Sigma^+$ *state*

Matrix element for a $^1\Sigma^+$ state, whose basis set function is $|0^+\rangle|00\rangle|v\rangle|J0M\rangle$

$$\langle J0M|\langle v|\langle 00|\langle 0^+|H|0^+\rangle|00\rangle|v\rangle|J0M\rangle = E + B_v[J(J+1) + \langle L_\perp^2\rangle], \quad (33)$$

where E represents the vibrational–electronic energy, and $\langle L_\perp^2\rangle$ is the matrix elements of $(L^2 - L_z^2)$. The eigenfunction for a level of the state $^1\Sigma^+$ is

$$|^1\Sigma^+ vJM\rangle = |0^+\rangle|00\rangle|v\rangle|J0M\rangle. \quad (34)$$

The eigenvalue is

$$E(^1\Sigma^+ vJM) = E + B_v[J(J+1) + \langle L_\perp^2\rangle]. \quad (35)$$

B). $^1\Pi$ *state*

Matrix elements for a $^1\Pi$ state, whose basis set functions are $|1\rangle|00\rangle|v\rangle|J1M\rangle$ and $|-1\rangle|00\rangle|v\rangle|J-1M\rangle$;

$$\begin{aligned}
&\langle J1M|\langle v|\langle 00|\langle 1|H|1\rangle|00\rangle|v\rangle|J1M\rangle = E + B_v[J(J+1) - 1 + \langle L_\perp^2\rangle],\\
&\langle J1M|\langle v|\langle 00|\langle 1|H|-1\rangle|00\rangle|v\rangle|J-1M\rangle = 0,\\
&\langle J-1M|\langle v|\langle 00|\langle -1|H|-1\rangle|00\rangle|v\rangle|J-1M\rangle = E + B_v[J(J+1) - 1 + \langle L_\perp^2\rangle].
\end{aligned} \quad (36)$$

The eigenfunctions for levels of the state $^1\Pi$ are

$$|^1\Pi vJM\rangle = (|1\rangle|00\rangle|v\rangle|J1M\rangle \pm |-1\rangle|00\rangle|v\rangle|J-1M\rangle)/(2^{1/2}. \quad (37)$$

The eigenvalues are

$$E(^1\Pi vJM) = E + B_v[J(J+1) - 1 + \langle L_\perp^2\rangle]. \quad (38)$$

C). $^3\Sigma$ *state*

The symmetric matrix elements for a $^3\Sigma$ state, whose basis set functions are $|0\rangle|11\rangle|v\rangle|J1M\rangle$, $|0\rangle|10\rangle|v\rangle|J0M\rangle$, and $|0\rangle|1-1\rangle|v\rangle|J-1M\rangle$, are given by

$$\begin{aligned}
&\langle J1M|\langle v|\langle 11|\langle 0|H|0\rangle|11\rangle|v\rangle|J1M\rangle = E + B_v[J(J+1) + \langle L_\perp^2\rangle],\\
&\langle J1M|\langle v|\langle 11|\langle 0|H|0\rangle|10\rangle|v\rangle|J0M\rangle = -B_v[2J(J+1)]^{1/2},\\
&\langle J1M|\langle v|\langle 11|\langle 0|H|0\rangle|1-1\rangle|v\rangle|J-1M\rangle = 0,\\
&\langle J0M|\langle v|\langle 10|\langle 0|H|0\rangle|10\rangle|v\rangle|J0M\rangle = E + B_v[J(J+1) + 2 + \langle L_\perp^2\rangle],\\
&\langle J0M|\langle v|\langle 10|\langle 0|H|0\rangle|1-1\rangle|v\rangle|J-1M\rangle = -B_v[2J(J+1)]^{1/2},\\
&\langle J-1M|\langle v|\langle 1-1|\langle 0|H|0\rangle|1-1\rangle|v\rangle|J-1M\rangle = E + B_v[J(J+1) + \langle L_\perp^2\rangle].
\end{aligned} \quad (39)$$

The eigenfunctions for levels of the state $^3\Sigma^+$ are

$$
\begin{aligned}
&|^3\Sigma^+ vN = J+1JM\rangle \\
&= [J/(2J+1)]^{1/2}(|0^+\rangle|11\rangle|v\rangle|J1M\rangle + |0^+\rangle|1-1\rangle|v\rangle|J-1M\rangle)/2^{1/2} \\
&- [(J+1)/(2J+1)]^{1/2}|0^+\rangle|10\rangle|v\rangle|J0M\rangle, \\
&|^3\Sigma^+ vN = JJM\rangle = (|0^+\rangle|11\rangle|v\rangle|J1M\rangle - |0^+\rangle|1-1\rangle|v\rangle|J-1M\rangle)/2^{1/2}, \\
&|^3\Sigma^+ vN = J-1JM\rangle \\
&= [(J+1)/(2J+1)]^{1/2}(|0^+\rangle|11\rangle|v\rangle|J1M\rangle + |0^+\rangle|1-1\rangle|v\rangle|J-1M\rangle)/2^{1/2} \\
&+ [J/(2J+1)]^{1/2}|0^+\rangle|10\rangle|v\rangle|J0M\rangle, \qquad (40)
\end{aligned}
$$

where N is the rotational quantum number. The eigenvalues are

$$E(^3\Sigma^+ vNJM) = E + B_v[N(N+1) + \langle L_\perp^2\rangle]. \qquad (41)$$

D). $^3\Pi$ *state*

The symmetric matrix elements for a $^3\Pi$ state, whose basis set functions are $|1\rangle|1-1\rangle|v\rangle|J0M\rangle = |X1\rangle$, $|1\rangle|10\rangle|v\rangle|J1M\rangle = |X2\rangle$, $|1\rangle|11\rangle|v\rangle|J2M\rangle = |X3\rangle$, $|-1\rangle|11\rangle|v\rangle|J0M\rangle = |X4\rangle$, $|-1\rangle|10\rangle|v\rangle|J-1M\rangle = |X5\rangle$,and $|-1\rangle|1-1\rangle|v\rangle|J-2M\rangle = |X6\rangle$, are given by

$$
\begin{aligned}
\langle X1|H|X1\rangle &= E - A + B_v[J(J+1)+1+\langle L_\perp^2\rangle], \\
\langle X1|H|X2\rangle &= -B_v[2J(J+1)]^{1/2}, \\
\langle X1|H|X3\rangle &= 0, \\
\langle X1|H|X4\rangle &= 0, \\
\langle X1|H|X5\rangle &= 0, \\
\langle X1|H|X6\rangle &= 0, \\
\langle X2|H|X2\rangle &= E + B_v[J(J+1)+1+\langle L_\perp^2\rangle], \\
\langle X2|H|X3\rangle &= -B_v[2(J+2)(J-1)]^{1/2}, \\
\langle X2|H|X4\rangle &= 0, \\
\langle X2|H|X5\rangle &= 0, \\
\langle X2|H|X6\rangle &= 0, \\
\langle X3|H|X3\rangle &= E + A + B_v[J(J+1)-3+\langle L_\perp^2\rangle], \\
\langle X3|H|X4\rangle &= 0, \\
\langle X3|H|X5\rangle &= 0, \\
\langle X3|H|X6\rangle &= 0, \\
\langle X4|H|X4\rangle &= E - A + B_v[J(J+1)+1+\langle L_\perp^2\rangle], \\
\langle X4|H|X5\rangle &= -B_v[2J(J+1)]^{1/2},
\end{aligned}
$$

$$\begin{aligned}
\langle X4|H|X6\rangle &= 0,\\
\langle X5|H|X5\rangle &= E + B_v[J(J+1)+1+\langle L_\perp^2\rangle],\\
\langle X5|H|X6\rangle &= -B_v[2(J+2)(J-1)]^{1/2},\\
\langle X6|H|X6\rangle &= E + A + B_v[J(J+1)-3+\langle L_\perp^2\rangle].
\end{aligned} \tag{42}$$

When $A \gg B_v J$, Hund's case (a) occurs.

The eigenfunctions for levels of the state $^3\Pi$ are

$$\begin{aligned}
|^3\Pi_0 vJM\rangle &= (|1\rangle|1-1\rangle|v\rangle|J0M\rangle \pm |-1\rangle|11\rangle|v\rangle|J0M\rangle)/2^{1/2},\\
|^3\Pi_1 vJM\rangle &= (|1\rangle|10\rangle|v\rangle|J1M\rangle \pm |-1\rangle|10\rangle|v\rangle|J-1M\rangle)/2^{1/2},\\
|^3\Pi_2 vJM\rangle &= (|1\rangle|11\rangle|v\rangle|J2M\rangle \pm |-1\rangle|1-1\rangle|v\rangle|J-2M\rangle)/2^{1/2}.
\end{aligned} \tag{43}$$

The eigenvalues are respectively,

$$\begin{aligned}
E(^3\Pi_0\, vJM) &= E - A + B_v[J(J+1)+1+\langle L_\perp^2\rangle],\\
E(^3\Pi_1\, vJM) &= E + B_v[J(J+1)+1+\langle L_\perp^2\rangle],\\
E(^3\Pi_2\, vJM) &= E + A + B_v[J(J+1)-3+\langle L_\perp^2\rangle].
\end{aligned} \tag{44}$$

When $B_v J \gg A$, Hund's case (b) occurs.

The eigenfunctions for levels of the state $^3\Pi$ are

$$\begin{aligned}
|^3\Pi\, vN = JJM\rangle &= (2)^{-1/2}|^3\Pi_0 vJM\rangle\\
&+ [J(J+1)]^{-1/2}|^3\Pi_1 vJM\rangle\\
&- [(J-1)(J+2)/2J(J+1)]^{1/2}|^3\Pi_2 vJM\rangle,
\end{aligned}$$

$$\begin{aligned}
|^3\Pi\, vN = J-1JM\rangle &= [(J-1)/2(2J+1)]^{1/2}|^3\Pi_0 vJM\rangle\\
&+ [(J-1)(J+1)/J(2J+1)]^{1/2}|^3\Pi_1 vJM\rangle\\
&+ [(J+1)(J+2)/2J(2J+1)]^{1/2}|^3\Pi_2 vJM\rangle,
\end{aligned}$$

$$\begin{aligned}
|^3\Pi\, vN = J+1JM\rangle &= [(J+2)/2(2J+1)]^{1/2}|^3\Pi_0 vJM\rangle\\
&- [J(J+2)/(J+1)(2J+1)]^{1/2}|^3\Pi_1 vJM\rangle\\
&+ [J(J-1)/2(J+1)(2J+1)]^{1/2}|^3\Pi_2 vJM\rangle.
\end{aligned} \tag{45}$$

The eigenvalues are

$$E(^3\Pi\, vNJM) = E + B_v[N(N+1)-1+\langle L_\perp^2\rangle] \tag{46}$$

1g) Transformation between the laboratory-fixed system and the molecule-fixed system, the rotational wave function, and calculation of the electric dipole transition moments

The spherical component of the laboratory-fixed coordinates $\mathbf{R}(X, Y, Z)$ and the molecule-fixed coordinates $\mathbf{r}(x, y, z)$ are defined as

$$\begin{aligned} R_{\pm 1} &= \mp (X \pm iY)/2^{1/2}, \qquad R_0 = Z, \\ r_{\pm 1} &= \mp (x \pm iy)/2^{1/2}, \qquad r_0 = z. \end{aligned} \tag{47}$$

The transformation between the laboratory-fixed system and the molecule-fixed system can be expressed by the rotation matrix D^J_{MN}. The coordinates $\mathbf{R}$ and $\mathbf{r}$ are related by the following equations:

$$\begin{aligned} R_\lambda &= \sum_{t=0,\pm 1} (-)^{\lambda - t} D^1_{-\lambda - t} r_t, \\ r_t &= \sum_{\lambda=0,\pm 1} D^1_{\lambda t} R_\lambda. \end{aligned} \tag{48}$$

The wave function $|J\Omega M\rangle$ of the rotational part is expressed as

$$|J\Omega M\rangle = (-)^{M-\Omega}[(2J+1)/(8\pi^2)]^{1/2} D^J_{-M-\Omega}. \tag{49}$$

The matrix element of the laboratory-fixed R_λ component of an electric dipole moment μ_{R_λ} can be calculated as

$$\begin{aligned} &\langle \Lambda' S' \Sigma' v' J' \Omega' M' | \mu_{R_\lambda} | \Lambda S \Sigma v J \Omega M \rangle \\ &= \sum_{t=0,\pm 1} (-)^{\lambda - t} \langle \Lambda' S' \Sigma' v' | \mu_{r_t} | \Lambda S \Sigma v \rangle \langle J' \Omega' M' | D^1_{-\lambda - t} | J \Omega M \rangle \\ &= \sum_{t=0,\pm 1} (-)^{\lambda - t} \langle \Lambda' S' \Sigma' v' | \mu_{r_t} | \Lambda S \Sigma v \rangle (-)^{M-\Omega} [(2J'+1)(2J+1)]^{1/2} \\ &\times \begin{pmatrix} J & J' & 1 \\ -M & M' & -\lambda \end{pmatrix} \begin{pmatrix} J & J' & 1 \\ -\Omega & \Omega' & -t \end{pmatrix}. \end{aligned} \tag{50}$$

These matrix elements for any types of states are listed in [1].

2. Perturbations of the $A\ ^1\Sigma_u^+$ and $b\ ^3\Pi_u$ states of Na_2

The perturbation between the $A\ ^1\Sigma_u^+$ and $b\ ^3\Pi_u$ states was known from the observation of a magnetic rotation spectrum for the red band $A\ ^1\Sigma_u^+ - X\ ^1\Sigma_g^+$ [7–9]. Through absorption spectroscopy, the $A\ ^1\Sigma_u^+$ state was found to be perturbed

by the $b\ ^3\Pi_u$ state [10], which separates into three Hund's case (a) components $b\ ^3\Pi_{0u}$, $b\ ^3\Pi_{1u}$, and $b\ ^3\Pi_{2u}$. The excitation spectra of the $A\ ^1\Sigma_u^+ - X\ ^1\Sigma_g^+$ and $b\ ^3\Pi_{0u} - X\ ^1\Sigma_g^+$ bands of Na_2 in a supersonic beam were first observed by Engelke et al [11]. Using a collimated supersonic beam, Atkinson et al [12,13] obtained more resolution, and observed transitions to the perturbed $b\ ^3\Pi_{0u}$, $b\ ^3\Pi_{1u}$, and $b\ ^3\Pi_{2u}$ states. Shimizu and Shimizu [14] also observed the transitions $b\ ^3\Pi_{0u} - X\ ^1\Sigma_g^+$ and $b\ ^3\Pi_{1u} - X\ ^1\Sigma_g^+$. The vibrational numbering of the $b\ ^3\Pi_u$ state was established by analysing the rotationally resolved fluorescence spectra resulting from optical–optical double resonance excitation [15]. More recently, the fluorescence spectrum of the $(2)\ ^1\Sigma_g^+ - A\ ^1\Sigma_u^+$ transition induced by collisional transfer following the $B\ ^1\Pi_u - X\ ^1\Sigma_g^+$ excitation was measured at high resolution by Fourier-transform spectroscopy, and the spin–orbit interaction matrix element between the $A\ ^1\Sigma_u^+$ and $b\ ^3\Pi_u$ states as well as the molecular constants were reported [16].

2a) Energy shifts and spin–orbit interaction

We have applied the technique of polarization spectroscopy [17–19] to obtain a Doppler-free high resolution spectrum. We observed the polarization spectrum of Na_2 around 15570 cm^{-1}, where the $A\ ^1\Sigma_u^+$ ($v = 8$) and $b\ ^3\Pi_u$ ($v = 14$) states are strongly perturbed near the band origin. Striking anomalies in the line intensities and shapes as well as the line positions were observed [20]. Some line spectra of the $A\ ^1\Sigma_u^+$ $(v = 8, J - 1) - X\ ^1\Sigma_g^+$ $(v = 0, J)$ transitions are shown in Fig. 1.

The rotational levels of even J values are symmetric and those of odd J values are antisymmetric in a $^1\Sigma_g^+$ state. In a $^1\Sigma_u^+$ state, the odd J levels are symmetric and the even J levels are antisymmetric. The total nuclear spin quantum number of Na_2 ($I_1 = I_2 = 3/2$) can take the values $I = 0$, 1, 2, and 3. The nuclear spin functions are symmetric for $I = 3$ and 1, and antisymmetric for $I = 2$ and 0. Since the total wave function has to be antisymmetric for nuclei of half-integral spin, the nuclear spin states of even I values are possible for the symmetric rotational levels and those of odd I values are possible for the antisymmetric rotational levels. The selection rules for the electronic transition $^1\Sigma^+ - {}^1\Sigma^+$ are $\Delta J = \pm 1$, and no change of the nuclear spin state. The spin-forbidden transition $b\ ^3\Pi_u - X\ ^1\Sigma_g^+$ is made allowed by the spin–orbit interaction between the $A\ ^1\Sigma_u^+$ and $b\ ^3\Pi_u$ states. The two mutually perturbing levels of both states must have the same J value and the same symmetry. Therefore, the levels populated in the $b\ ^3\Pi_u$ state with even J values are antisymmetric and those with odd J values are symmetric.

The term energies of the $A\ ^1\Sigma_u^+$ levels with v=8 and J=0–13 are calculated from the molecular constants reported by Kaminsky [21], and the results are shown in Fig. 2 as the unperturbed term energies (UPT). From the observed line positions in the $A\ ^1\Sigma_u^+ - X\ ^1\Sigma_g^+$ transition and the molecular constants of the $X\ ^1\Sigma_g^+$ state [22], we derived the term energies for the $A\ ^1\Sigma_u^+$ levels with v=8 and J=0–13, and the results are shown in Fig. 2 as the observed term energies (Obs). From the molecular constants of the $X\ ^1\Sigma_g^+$ state [22] and the reported line positions of the

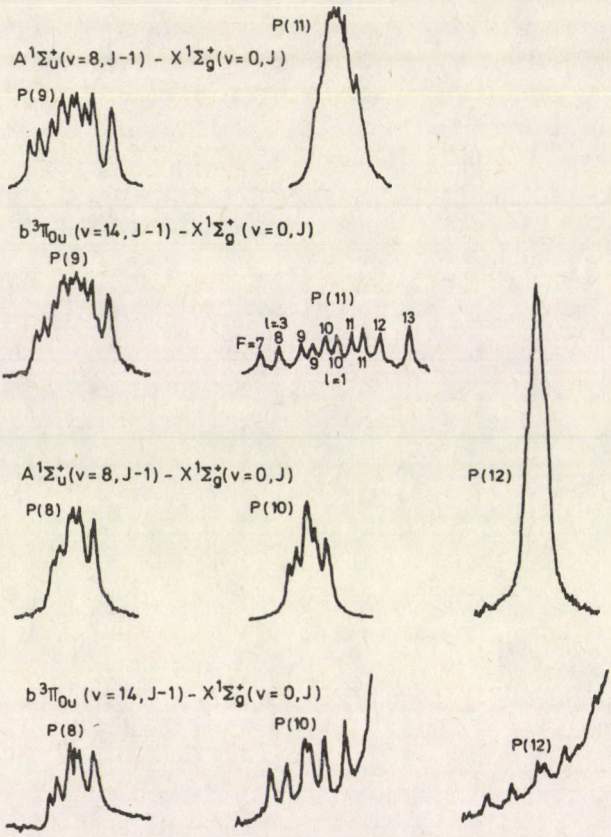

Fig. 1. J dependence of the spectral line shape of perturbed lines of the $A\ ^1\Sigma_u^+(v = 8,\ J - 1) - X\ ^1\Sigma_g^+(v = 0,\ J)$ transitions and the $b\ ^3\Pi_{0u}(v = 14,\ J - 1) - X\ ^1\Sigma_g^+(v = 0,\ J)$ transitions

$b\ ^3\Pi_{0u}$ and $b\ ^3\Pi_{1u}$ states [14], we derived experimental term energies for the $b\ ^3\Pi_{0u}$ and $b\ ^3\Pi_{1u}$ levels with v=14 and J=0–13, and the results are shown in Fig. 2 as the observed term energies (Obs). The term energies of $^3\Pi_{\Omega u}$ ($\Omega = 0, 1, 2$), which are intermediate between Hund's cases (a) and (b), can be calculated by diagonalizing the symmetric energy matrix. The term energies for the $b\ ^3\Pi_u$ levels with v=14 and J=0–13 are calculated by using the molecular constants reported by Effantin et al [16], and the calculated term energies for the $b\ ^3\Pi_{0u}$ and $b\ ^3\Pi_{1u}$ states are shown in Fig. 2 as unperturbed term energies. (UPT).

The unperturbed term energies of J=9 in the $A\ ^1\Sigma_u^+$ and $b\ ^3\Pi_{0u}$ states are close to each other, and this also holds for J=8. From their relative positions (See Fig. 2), the J=9 level of the $A\ ^1\Sigma_u^+$ state is expected to be shifted by the perturbation toward high energy and the J=9 level of the $b\ ^3\Pi_{0u}$ state toward

high energy. Both shifts are estimated to be of almost the same magnitude. The directions of the shifts will be opposite for the J=8 level. The J assignments for strongly perturbed lines of the $A\ ^1\Sigma_u^+\ (v = 8) - X\ ^1\Sigma_g^+\ (v = 0)$ transition were made by using these results. These assignments are confirmed by the hyperfine structure, as shown below.

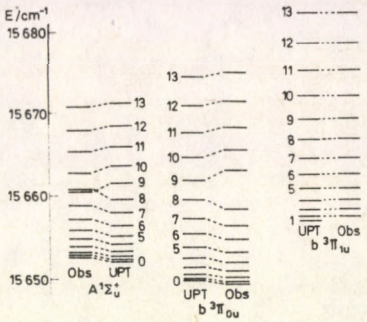

Fig. 2. Term energies of the states $A\ ^1\Sigma_u^+(v = 8)$, $b\ ^3\Pi_{0u}(v = 14)$ and $b\ ^3\Pi_{1u}(v = 14)$

The perturbation between $^3\Pi$ and $^1\Sigma^+$ is caused by the spin-orbit interaction H_{so}, and this occurs between levels of the same J. The perturbed term values can be calculated by solving the 4×4 secular determinant composed of Hund's case (a) states $b\ ^3\Pi_{\Omega u}\ (\Omega = 0, 1, 2)$ and $A\ ^1\Sigma_u^+$. The perturbing coupling constant ξ is determined so that the calculated $A\ ^1\Sigma_u^+ - b\ ^3\Pi_{0u}$ splittings fit the observed splittings. Once the value of ξ=1.272 cm^{-1} is determined, we can calculate the term values of the $b\ ^3\Pi_{0u}$, $b\ ^3\Pi_{1u}$, $b\ ^3\Pi_{2u}$, and $A\ ^1\Sigma_u^+$ states as well as the eigenfunctions. The results are listed in Table I.

2b) Hyperfine structure

We observed the hyperfine structure for strongly perturbed lines of the $A\ ^1\Sigma_u^+ - X\ ^1\Sigma_g^+$ and $b\ ^3\Pi_{0u} - X\ ^1\Sigma_g^+$ transitions (Fig. 1). We could not observe the hyperfine structure for unperturbed lines in the $A\ ^1\Sigma_u^+ - X\ ^1\Sigma_g^+$ band. The hyperfine splitting of the $X\ ^1\Sigma_g^+$ state was reported to be negligibly small [23]. Therefore, the observed hyperfine structure can be attributed to the hyperfine splitting of the $b\ ^3\Pi_u$ state. The observed hyperfine patterns were quantitatively explained [13] by the magnetic dipole term:

$$H_{hfs} = H_{MD}(1) + H_{MD}(2), \tag{51}$$

where $H_{MD}(i)$ is the interaction between the electrons and nucleus i $(i = 1, 2)$. The matrix elements are given by [24]

Table I

Perturbed term energies (PTE) and eigenfunctions of the $A\ ^1\Sigma_u^+$, $b\ ^3\Pi_{0u}$, and $b\ ^3\Pi_{1u}$ state expressed as a linear combination of the Hund's case (a) wave functions: $C_1|^3\Pi_{0u}\rangle + C_2|^3\Pi_{1u}\rangle + C_3|^3\Pi_{2u}\rangle + C_4|^1\Sigma_u^+\rangle$

State	J	PTE $[cm^{-1}]$	Eigenfunctions C_1	C_2	C_3	C_4
$A^1\Sigma_u^+$	0	15652.5587	0.4003	0.0000	0.0000	0.9164
	1	15652.7796	0.4053	−0.0288	0.0000	0.9137
	2	15653.2223	0.4156	−0.0498	0.0019	0.9082
	3	15653.8889	0.4322	−0.0704	0.0042	0.8990
	4	15654.7829	0.4564	−0.0914	0.0072	0.8850
	5	15655.9098	0.4899	−0.1135	0.0109	0.8643
	6	15657.2784	0.5345	−0.1378	0.0153	0.8337
	7	15658.9020	0.5911	−0.1653	0.0206	0.7892
	8	15660.7992	0.6578	−0.1963	0.0270	0.7266
	9	15660.5054	−0.6312	0.1406	−0.0176	0.7626
	10	15662.8571	−0.5390	0.1261	−0.0169	0.8326
	11	15665.3726	−0.4482	0.1079	−0.0153	0.8873
	12	15668.0549	−0.3683	0.0899	−0.0133	0.9253
	13	15670.9133	−0.3031	0.0742	−0.0113	0.9500
$b^3\Pi_{0u}$	0	15649.0912	0.9164	0.0000	0.0000	−0.4003
	1	15649.3553	0.9132	−0.0350	0.0000	−0.4061
	2	15649.8825	0.9064	−0.0600	0.0018	−0.4181
	3	15650.6711	0.8956	−0.0832	0.0038	−0.4371
	4	15651.7179	0.8794	−0.1045	0.0064	−0.4644
	5	15653.0176	0.8562	−0.1231	0.0093	−0.5016
	6	15654.5616	0.8232	−0.1376	0.0123	−0.5507
	7	15656.3372	0.7765	−0.1465	0.0150	−0.6127
	8	15658.3257	0.7126	−0.1478	0.0169	−0.6857
	9	15662.9922	0.7276	−0.2299	0.0344	0.6454
	10	15665.5004	0.7899	−0.2635	0.0426	0.5521
	11	15668.3322	0.8365	−0.2945	0.0510	0.4592
	12	15671.4846	0.8665	−0.3217	0.0595	0.3770
	13	15674.9487	0.8833	−0.3456	0.0679	0.3095
$b^3\Pi_{1u}$	1	15656.7982	0.0437	0.9990	0.0000	0.0121
	2	15657.3671	0.0753	0.9949	−0.0639	0.0203
	3	15658.2204	0.1056	0.9889	−0.1004	0.0272
	4	15659.3580	0.1350	0.9812	−0.1337	0.0328
	5	15660.7796	0.1633	0.9720	−0.1650	0.0372
	6	15662.4852	0.1906	0.9613	−0.1949	0.0403
	7	15664.4748	0.2168	0.9494	−0.2235	0.0423
	8	15666.7483	0.2419	0.9364	−0.2507	0.0433
	9	15669.3056	0.2659	0.9224	−0.2766	0.0437
	10	15672.1469	0.2887	0.9078	−0.3012	0.0434
	11	15675.2720	0.3105	0.8925	−0.3245	0.0427
	12	15678.6809	0.3312	0.8767	−0.3464	0.0416
	13	15682.3737	0.3508	0.8606	−0.3671	0.0404

$$\langle S'\Lambda'\Omega' v' J'(I_1 I_2) I' F' M_F' | H_{MD}(i) | S\Lambda\Omega\, v J(I_1 I_2) I F M_F \rangle$$

$$= \delta_{FF'}\delta_{M_F M_F'}(-1)^{1+I_1+I_2+F+I+I'+J+J'} f_1(iS'\Lambda'\Sigma'\Omega' v' S\Lambda\Sigma\Omega v)$$

$$\times[(2I+1)(2I'+1)(2J+1)(2J'+1)]^{1/2}$$

$$\begin{pmatrix} J' & 1 & J \\ -\Omega' & \Delta\Omega & \Omega \end{pmatrix} \begin{Bmatrix} I_2 & I_1 & I \\ 1 & I' & I_1 \end{Bmatrix} \begin{Bmatrix} F & I' & J' \\ 1 & J & I \end{Bmatrix}, \tag{52}$$

$$f_1(iS'\Lambda'\Sigma'\Omega' v' S\Lambda\Sigma\Omega v)$$

$$= [I_1(I_1+1)(2I_1+1)]^{1/2}[\delta_{\Sigma'\Sigma}\delta_{S'S}(-1)^{-\Omega'} G_{\Lambda'\Lambda}(i)$$

$$+(-1)^{-\Lambda+1+S'} \begin{pmatrix} S' & 1 & S \\ \Sigma' & -\Delta\Sigma & -\Sigma \end{pmatrix} \begin{pmatrix} 1 & 1 & 2 \\ \Delta\Sigma & -\Delta\Sigma - \Delta\Lambda & \Delta\Lambda \end{pmatrix} D_{\Lambda'\Lambda}(i)$$

$$+(-1)^{-\Lambda+1+S'-\Sigma'+\Sigma} \begin{pmatrix} S' & 1 & S \\ \Sigma' & -\Delta\Sigma & -\Sigma \end{pmatrix} K_{\Lambda'\Lambda}(i), \tag{53}$$

where $F = J + I$, $\Delta\Omega = \Omega' - \Omega$, $\Delta\Sigma = \Sigma' - \Sigma$, and $\Delta\Lambda = \Lambda' - \Lambda$. $D_{\Lambda'\Lambda}(i)$ is the reduced matrix element of the interaction between the electron spin and the magnetic dipole moment of nucleus i:

$$D_{\Lambda'\Lambda}(i) = -g_s g_{I_i}\mu_B\mu_N \langle S'\Lambda' v' \| \sum_e (4\pi/5)^{1/2} T^1(s_e) Y^2(\theta_{ie}, \phi_{ie})/r_{ie}^3 \| S\Lambda v\rangle \mu_o/4\pi. \tag{54}$$

$G_{\Lambda'\Lambda}(i)$ is the reduced matrix element of the interaction between the electronic angular momentum and the magnetic dipole moment of nucleus i:

$$G_{\Lambda'\Lambda}(i) = -2g_{I_i}\mu_B\mu_N \langle \Lambda' v' \| \sum_e T^1(l_e)/r_{ie}^3 \| \Lambda v\rangle \mu_o/4\pi. \tag{55}$$

$K_{\Lambda'\Lambda}(i)$ is the reduced matrix element of the Fermi contact interaction:

$$K_{\Lambda'\Lambda}(i) = -(8\pi/3) g_s g_{I_i}\mu_B\mu_N \delta_{\Lambda'\Lambda} \langle S'\Lambda' v' \| \sum_e T^1(s_e)\delta(r_{ie}) \| S\Lambda v\rangle \mu_o/4\pi, \tag{56}$$

where μ_o, μ_B and μ_N are respectively the permeability of a vacuum, the Bohr magneton and the nuclear magneton, r_{ie} is the distance between a nucleus i and an electron e, T^1 and Y^2 are respectively the spherical tensor operators of rank 1 and 2.

The matrix elements of the hyperfine Hamiltonian in Eq. (51) between the three Hund's case (a) states $^3\Pi_\Omega$ ($\Omega = 0,1,$and 2) and the $^1\Sigma^+$ state are symmetric.

When evaluated using Eqs (52) and (53), they become:

$$\begin{aligned}
\langle {}^3\Pi_0|H_{MD}{}^3\Pi_0\rangle &= 0,\\
\langle {}^3\Pi_0|H_{MD}{}^3\Pi_1\rangle &= [Z/24(X)^{1/2}][(10)^{-1/2}D_{11} - (3)^{1/2}K_{11}],\\
\langle {}^3\Pi_0|H_{MD}{}^3\Pi_2\rangle &= 0,\\
\langle {}^3\Pi_0|H_{MD}{}^1\Sigma^+\rangle &= 0,\\
\langle {}^3\Pi_1|H_{MD}{}^3\Pi_1\rangle &= [Z/24(X)^{1/2}]6G_{11}(X)^{-1/2},\\
\langle {}^3\Pi_1|H_{MD}{}^3\Pi_2\rangle &= [Z/24(X)^{1/2}][(10)^{-1/2}D_{11} - (3)^{1/2}K_{11}](1-2/X)^{1/2},\\
\langle {}^3\Pi_1|H_{MD}{}^1\Sigma^+\rangle &= [Z/24(X)^{1/2}](3/5)^{1/2}D_{10},\\
\langle {}^3\Pi_2|H_{MD}{}^3\Pi_2\rangle &= [Z/24(X)^{1/2}][(16/5)^{1/2}D_{11} + 12G_{11} + (24)^{1/2}K_{11}](X)^{-1/2},\\
\langle {}^3\Pi_2|H_{MD}{}^1\Sigma^+\rangle &= 0,\\
\langle {}^1\Sigma^+|H_{MD}{}^1\Sigma^+\rangle &= 0, \qquad (57)
\end{aligned}$$

where $Z = F(F+1) - J(J+1) - I(I+1)$ and $X = J(J+1)$. The selection rules for the present electronic transitions are $\Delta F = \Delta J = \pm 1$ and no change of the nuclear spin. For a given J and I, F takes values of $J+1$, $J+I-1$, ..., $|J-I|$. In the $A\ {}^1\Sigma_u^+$ state and the coupled $b\ {}^3\Pi_u$ state, the hyperfine structure pattern of rotational lines for even J values consists of 7+3 components corresponding to I=3 and 1, while for odd J values it consists of 5+1 components corresponding to I= 2 and 0. From the observed hyperfine structure of $P(9)$ and $P(10)$ (Fig. 1), we can confirm the assignment of J to be correct. All the nonvanishing matrix elements in Eq. (57) are proportional to Z. Hence, the hyperfine splitting increases with J. The term energy of each component can be calculated by solving the 4×4 secular determinant for the Hamiltonian $H + H_{so} + H_{hfs}$. Because the observed hyperfine splittings are much smaller than the separation between the term energies for a given J, the $A\ {}^1\Sigma_u^+ - b\ {}^3\Pi_u$ mixing coefficients in the eigenfunctions for $H + H_{so} + H_{hfs}$ can be approximated with good accuracy by the mixing coefficients for $H + H_{so}$.

2c) Intensity and line splitting

Let us consider the change of intensities. The line intensity of a $P(J)$ line of even J is proportional to [20]

$$(C_4)^4\, J^2(2J^2 + J - 1)^2/36(2J-1)^2(2J+1)^4$$

multiplied by $6(2J-1)$, which is the number of degenerate transitions. The calculated relative intensities of $P(2)$,$P(4)$,$P(6)$,$P(8)$,$P(10)$, $P(12)$,$P(14)$, and $P(16)$ are, respectively 0.3, 0.7, 1.0, 0.9, 1.0, 2.3, 3.5, and 4.5. The observed intensities are 0.4, 0.8, 1.0, 1.0, 0.9, 2.5, 3.1, and 4.1, respectively. The intensities of strongly perturbed lines of the transitions to the $A\ {}^1\Sigma_u^+$ and $b\ {}^3\Pi_{0u}$ states are almost of

the same magnitude (see $P(9)$ lines in Fig. 1). This is consistent with the fact that the mixing coefficients (C_1 and C_4 for $A\ ^1\Sigma_u^+$, C_1 and C_4 for $b\ ^3\Pi_{0u}$) of the $^1\Sigma_u^+$ and $^3\Pi_{0u}$ states are almost equal at $J=8$ of both states $A\ ^1\Sigma_u^+(v = 8)$ and $b\ ^3\Pi_{0u}(v = 14)$. The change of line splitting as a result of the hyperfine interaction is different for transitions to the $A\ ^1\Sigma_u^+$ and $b\ ^3\Pi_{0u}$ states (see Fig. 1). Thus, the intensities give important information on the mixing of the perturbing states.

H. K. and M. B. are grateful to the Ministry of Education (Science and Culture) of Japan for Grant-in-Aid for Scientific Research.

References

1. I. Kovács, Rotational Structure in the Spectra of Diatomic Molecules, Adam Hilger, London, 1969.
2. J. T. Hougen, Natl. Bur. Stand. (U.S.) Monogr.,*115*, 1970.
3. D. M. Brink and G. R. Satchler, Angular Momentum, Oxford University Press, Oxford, 1968.
4. J. H. Van Vleck, Rev. Mod. Phys., *23*, 213, 1951.
5. R. S. Mulliken, Rev. Mod. Phys., *4*, 1, 1932.
6. H. Lefebvre-Brion and R. W. Field, Perturbation in the Spectra of Diatomic Molecules, Academic Press, New York, 1986.
7. R. W. Wood and F. E. Hackett, Astrophys. J., *30*, 339, 1909.
8. W. R. Frederickson and C. R. Stannard, Phys. Rev., *44*, 632, 1933
9. T. Carroll, Phys. Rev., *52*, 822, 1937.
10. P. Kusch and M. M. Hessel, J. Chem. Phys., *63*, 4087, 1975.
11. F. Engelke, H. Hage, and C. D. Caldwell, Chem. Phys., *64*, 221, 1982
12. J. B. Atkinson, J. Becker, and W. Demtröder, Chem. Phys. Lett., *87*, 92, 1982.
13. J. B. Atkinson, J. Becker, and W. Demtröder, Chem. Phys. Lett., *87*, 128, 1982.
14. K. Shimizu and F. Shimizu, J. Chem. Phys., *78*, 1126, 1983.
15. L. Li, S. F. Rice, and R. W. Field, J. Mol. Spectrosc., *105*, 344, 1984.
16. C. Effantin, O. Babaky, K. Hussein, J. d'Incan, and R. F. Barrow, J. Phys., *B18*, 4077, 1985.
17. C. Wieman and T. W. Hänsch, Phys. Rev. Lett., *36*, 1170, 1976.
18. R. E. Teets, F. V. Kowalski, W. T. Hill, N. Carlson, and T. W. Hänsch, SPIE Vol. *113*, Laser Spectroscopy, 80, 1977.
19. W. Demtröder, Laser Spectroscopy, Springer, Berlin, 1982.
20. H. Katô, M. Otani and M. Baba, J. Chem. Phys., *89*, 653, 1988.
21. M. E. Kaminsky, J. Chem. Phys., *66*, 4951, 1977, Erratum, *73*, 3520, 1980.
22. P. Kusch and M. M. Hessel, J. Chem. Phys., *68*, 2591, 1978.
23. S. D. Rosner, R. A. Holt, and T. D. Gaily, Phys. Rev. Lett., *35*, 785, 1975.
24. M. Broyer, J. Vigue, and J. C. Lehmann, J. Phys. (Paris), *39*, 347, 1979.

Acta Physica Hungarica 67 (1–2), pp. 91–105 (1990)

TIME-RESOLVED MOLECULAR CHEMILUMINESCENCE FROM REACTIONS OF Ca(^3P,^1D) ATOMS WITH N_2O*

G. ROBERTS

Department of Physical Chemistry, University of Cambridge
Cambridge, CB2 1EP England

(Received 24 September 1988)

Chemiluminescence from electronically excited CaO generated by reaction of metastable Ca($4s4p(^3P_J)$) and Ca($4s3d(^1D_2)$) atoms with N_2O is investigated in the time-resolved mode under bulk conditions. By monitoring molecular emission from some 41 transitions, the time dependence of chemiluminescence from excited CaO states is compared with that for decay of emission from the atomic precursor states from which they are derived, enabling formation of specific product states to be ascribed to either direct generation from chemical reaction between Ca(^3P) and Ca(^1D) atoms with N_2O or to an energy transfer mechanism involving the metastable atoms and long-lived dark states of CaO. The different routes leading to specific molecular states are found to be in accord with simple energetic considerations and correlation rules governing the conservation of spin and spatial symmetry. Measurements of vibrational temperatures in one particular product state, CaO($A'\,^1\Pi$), indicate some degree of vibrational excitation accompanying these processes. Relative populations in all emitting states of CaO are found to be in agreement with the results of molecular beam experiments.

In addition to the study of electronic chemiluminescence from CaO, effective second-order quenching rate constants are determined for collisional removal of Ca(^3P) and Ca(^1D) atoms via all available physical and chemical pathways. Measurements over a wide range of temperature lead to estimates of activation energies for quenching of both Ca states by N_2O.

1. Introduction

The last ten or more years have witnessed a marked proliferation of both spectroscopic and kinetic investigations of the reactions of alkaline earth metal atoms with O-atom-containing species. Several review articles now exist which provide a critical appraisal of much of this work [1–7]. Interest in these processes stems from the fact that there are usually a number of energetically accessible exit channels available, leading to several electronically excited states of the diatomic metal monoxide product whose formation and decay can be probed either by chemiluminescence or laser fluorescence excitation. Much of this work has therefore been triggered by the possibility of stimulated emission between electronic levels of the metal monoxide reaction products, leading to the proposed development of high-power chemical laser systems operating in the visible and ultraviolet regions [8].

*Presented at the Conference on High Resolution Electronic Spectroscopy of Molecules, Tihany, Hungary, 19-24 September 1988

From a fundamental point of view, it is of paramount importance in attempting to obtain even a rudimentary understanding of the collision dynamics of excited metal atom plus oxidant systems to be able to predict branching ratios for those product electronic states which are energetically accessible and to identify the factors that govern their nascent formation [9]. These reactions thus afford an ideal opportunity to test current theories which attempt to explain their many and varied characteristics, especially the number and type of product states.

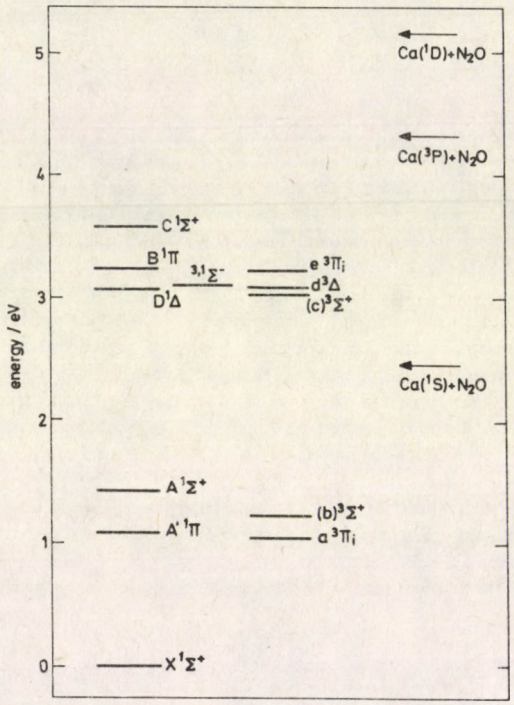

Fig. 1. Energy level diagram showing electronic states of CaO below 3.6 eV and available energies for reactions of $Ca(^1S, ^3P, ^1D)$ atoms with N_2O

Reactions of ground-state and electronically excited Ca atoms are particularly well documented, having been studied extensively under molecular beam conditions [10–17] and in low-pressure flames [18–21]. Several early molecular beam investigations of alkaline earth atom reactions, like their alkali metal counterparts, concentrated on the measurement of differential scattering cross sections and product angular distributions [3,4,11]. It was realized, however, initially by Zare and coworkers [10], that the light-producing efficiency of these processes may be employed as an *in situ* spectroscopic and dynamical probe for reaction products. Many later experiments carried out in similar vain have taken advantage of this fact, and have

been directed primarily to the measurement of electronic energy disposal amongst reaction products [1,12–17], leading to photon yields and chemiluminescence cross section for production of radiating states. Much of the flame work has also been approached from a spectroscopic point of view, leading mainly to product emitter analyses [18,19,22–24].

This paper addresses the task of obtaining direct information in real time on the identity of the exit channels giving rise to a large number of specific product states from the reactions of metastable $Ca(4s4p(^3P_J))$ and $Ca(4s3d(^1D_2))$ atoms with N_2O under bulk conditions. The energetics of these processes is presented pictorially in Figure 1, which displays the available reaction energies for $Ca(4s^2(^1S_0),4s4p(^3P_J),4s3d(^1D_2)) + N_2O$ [7,25]. We have previously determined radiative lifetimes of 0.331 ± 0.008 and 1.71 ± 0.03 ms for $Ca(^3P)$ and $Ca(^1D)$ respectively [26,27].

Our aim of identifying and differentiating between different pathways leading to specific radiating product states is realized by simultaneous characterization of the temporal behaviour of electronically excited CaO states and their atomic precursors $Ca(^3P)$ and $Ca(^1D)$. By making quantitative use of relationships between the parameters describing the time variation of emission from molecular and atomic states, chemical and energy transfer routes leading to different CaO products are distinguished. Measurements of emission intensities further permit estimation of relative populations of radiating states and also vibrational temperatures. Apparent rate constants for quenching of $Ca(^3P)$ and $Ca(^1D)$ atoms by N_2O as a function of temperature are also reported, leading to activation energies for overall collisional removal of both excited atomic states.

2. Electronic spectroscopy of CaO

It is readily apparent that an understanding of the complex state manifold of CaO and the radiative properties of excited states is an essential prerequisite for determination of the mechanisms of chemiluminescence reactions in which these species are formed. The visible and near infra-red spectrum of CaO, a major portion of which comprises the chemiluminescence observed from the $Ca(^3P,^1D) + N_2O$ reactions, is somewhat complex, and indeed has not yet been unambiguously assigned [19,22–24,28,29]. The ordering of electronic states of CaO lying below about 3.6 eV above the $X\,^1\Sigma^+$ ground state [29] is shown in Fig. 1. For the well-known singlet states $A\,^1\Sigma^+$, $B\,^1\Pi$ and $C\,^1\Sigma^+$ term values have been taken from the compilation of Huber and Herzberg [28]. Space limitations preclude a full description of how the energies of all other electronic states of CaO were estimated other than to note that they rely heavily on the spectroscopic investigations of Field and co-workers [22–24,29] and complementary theoretical calculations [30,31]. Details may be found elsewhere [25,27]. The term manifold shown in Fig. 1 is employed in Section 3 to assign chemiluminescence from CaO monitored in this work.

3. Experimental

The experimental arrangement used for studying molecular chemiluminescence from the $Ca(^3P,^1D) + N_2O$ reactions has been given in previous publications [25,32] and so only a brief description is given here. Metastable Ca atoms were prepared from the ground-state vapour by laser excitation in the presence of small varying concentrations of N_2O diluted by $39.9966\times10^2 N/m^2$ of He in a stainless steel reaction cell constituting a quasi-static kinetic system. Optical excitation of $Ca(^3P_J)$ and $Ca(^1D_2)$ atoms was accomplished using a Nd:YAG-pumped pulsed dye laser [25,26,32]. Generation of the $Ca(4s4p(^3P_J))$ state, lying 1.888 eV above the $4s^2(^1S_0)$ ground state [33], was achieved by laser pumping of the intercombination line at $\lambda = 657.3$ nm ($Ca(^3P_1) \leftarrow Ca(^1S_0)$). Following rapid Boltzmann equilibration of the population within the individual spin–orbit states of the triplet manifold [34], the decay of $Ca(^3P_J)$ was monitored in the time-resolved mode by resonance emission spectroscopy. $Ca(4s3d(^1D_2))$ atoms, lying 2.709 eV above the ground state [33], were excited by optical pumping at $\lambda = 457.5$ nm corresponding to the electric-quadrupole-allowed transition $Ca(^1D_2) \leftarrow Ca(^1S_0)$ and also monitored at the resonance wavelength. Atomic and molecular emission signals were optically isolated by means of a small monochromator, employing fixed slits of width 300 μm for increased light-gathering power, and detected photoelectrically [32]. Signal averaging was performed using a Boxcar integrator, the output from which was transferred to a microcomputer for data storage and analysis [26].

Table I

Electronic/vibronic transitions of CaO at wavelengths $\lambda \leq 800$ nm monitored in the time-resolved mode following pulsed dye-laser generation of $Ca(^3P)$ and $Ca(^1D)$ atoms in the presence of N_2O

1. CaO orange arc band system (a)
$CaO(8\sigma^2 3\pi^3 4\pi,\ 8\sigma 3\pi^4 4\pi) \rightarrow CaO(A'^1\Pi,\ a^3\Pi_i,\ (b)^3\Sigma^+) + h\nu;\ \lambda \approx 580 - 635$ nm.

Transition number	Electronic assignment	λ_e/nm	$\lambda_{0,0}$/nm	λ_{obs}/nm
1	$^3\Sigma^- \rightarrow a^3\Pi_i$	602.2		602
2	$d^3\Delta_i \rightarrow a^3\Pi_i$	608.6	608.5	609
3	$D^1\Delta \rightarrow a^3\Pi_i$	611.0	611.1	611
4	$^1\Sigma^- \rightarrow A'^1\Pi$	613.5		614
5	$d^3\Delta_2 \rightarrow A'^1\Pi$	620.2	620.1	620
6	$B^1\Sigma^+ \rightarrow (b)^3\Sigma^+$	$621.5^{+88.2}_{-3.9}$		
7	$D^1\Delta \rightarrow A'^1\Pi$	622.7	622.8	623
8	$e^3\Pi_i \rightarrow (b)^3\Sigma^+$	$623.8^{+88.9}_{-3.9}$		
9	$(c)^3\Sigma^+ \rightarrow a^3\Pi_i$	$628.4^{+20.4}_{-11.6}$		632

2. CaO green arc band system (a)
$CaO(8\sigma^2 10\sigma 3\pi^3,\ 8\sigma 10\sigma 3\pi^4) \rightarrow CaO(A'^1\Pi,\ a^3\Pi_i,\ (b)^3\Sigma^+) + h\nu;\ \lambda \approx 540 - 565$ nm.

10				547
11				550

Table I (continued)

3. $CaO(A'^1\Pi \rightarrow X^1\Sigma^+)$ band system

Transition number	Vibronic assignment v', v''	λ_{calc}/nm	λ_{obs}/nm
12	9,1	796.1	(b)
13	12,3	792.8	793
14	15,5	789.9	790
15	8,0	782.3	782
16	11,2	779.3	779
17	14,4	776.7	777
18	10,1	766.0	766
19	13,3	763.7	764
20	9,0	752.8	753
21	12,2; 15,4	750.9; 749.4	750
22	11,1; 14,3	738.3; 737.0	738
23	10,0; 13,2	725.8; 724.8	725
24	12,1; 15,3	712.8; 712.4	713
25	11,0; 14,2	700.9; 700.7	701
26	13,1	689.2	689
27	15,2; 12,0	678.4; 677.8	678
28	14,1	667.4	667
29	13,0	656.5	657(c)
30	15,1	647.1	647
31	14,0	636.7	637(d)
32	15,0	618.2	618(d)

4. $CaO(A^1\Sigma^+ \rightarrow X^1\Sigma^+)$ band system

Transition number	Δv sequence	λ_{calc}/nm(e)	λ_{obs}/nm
33	−2	769.5 – 772.7	770 – 773
34	−3	731.0 – 733.6	731 – 734
35	−4	695.3 – 698.7	695 – 699
36	−4	695.3(f)	695
37	−5	663.1 – 667.1	663 – 667
38	−6	634.0 – 638.0	634 – 638(d)
39	−7	607.4 – 611.0	607 – 611(d)
40	−8	583.2 – 585.8	583 – 586(d)
41	−9	560.9 – 562.3	561 – 562(g)

(a) Configurations of valence electrons of CaO taken from References [22,23,30]; (b) Not observed, out of range of infra-red detection; (c) Overlaps with $Ca(^3P_1 \rightarrow {}^1S_0)$ atomic intercombination line; (d) Overlaps with CaO orange arc bands. (e) Wavelengths calculated for $v' \leq 10$; (f) Vibronic assignment (see Section 3); (g) Overlaps CaO green arc bands.

Decay traces for $Ca(^3P)$ and $Ca(^1D)$ atoms were recorded as a function of quenching gas pressure over the temperature ranges 725–1100 K and 750–1100 K, respectively. Higher-lying atomic states of Ca, generated by energy pooling collisions between metastable $Ca(^3P)$ and $Ca(^1D)$ atoms [26] were observed at temperatures

greater than about 950 K following excitation of both atomic states in the absence of significant concentrations of quenching gas. An earlier study has indicated that fractional yields of short-lived highly excited atomic states, $[Ca^*]_{t=0}/[Ca(^3P_1)]_{t=0}$ and $[Ca^*]_{t=0}/[Ca(^1D_2)]_{t=0}$, are of the order of 10^{-5}–10^{-7} in 39.9966×10^2 N/m^2 of He at $T = 1100$ K [26]. Energy pooling collisions notwithstanding, decay traces for laser-excited $Ca(^3P)$ and $Ca(^1D)$ atoms were always observed to be kinetically first-order under the conditions of temperature and pressure employed in this work.

Electronic transitions of CaO monitored as a function of time following the $Ca(^3P,^1D) + N_2O$ reactions are displayed in Table I. That the observed molecular chemiluminescence arises from a mechanism involving the metastable $Ca(^3P)$ and $Ca(^1D)$ states with N_2O was confirmed by the failure to observe molecular emission from excited states of CaO when the supply of oxidant gas was extinguished and/or when the laser excitation source was prohibited from probing the reaction zone. The number of molecular transitions that could be readily monitored was found, as expected, to vary with temperature. Those transitions which were recorded at each of the temperatures investigated in this study have been listed elsewhere [25]. It may be noticed that the $\Delta v = -4$ transition of the $A\,^1\Sigma^+ \rightarrow X\,^1\Sigma^+$ band system is listed twice in Table I (Transitions 35 and 36). The reason for this is that following reaction of $Ca(^3P)$ atoms with N_2O, the $\Delta v = -4$ sequence can be ascribed specifically to the $v' = 4 \rightarrow v'' = 0$ transition with the aid of the energetics appropriate to the $E - (E,V)$ transfer processes thought to be established following initial O-atom abstraction by the excited metal atom (see Section 4(b)), whereas for $Ca(^1D) + N_2O$ it cannot.

In assigning individual transitions of the celebrated 'orange arc band', we have been guided by the recent observations of Field and co-workers [22,23], who have extracted deperturbed spectroscopic parameters for the $a^3\Pi_i$, $A'\,^1\Pi$, $d^3\Delta$ and $D^1\Delta$ states from a rotational analysis of some 900 lines of the orange arc band by sub-Doppler intermodulation spectroscopy. Computed wavelengths λ_e for (hypothetical) transitions between the minima of p.e. curves of the upper and lower electronic states as well as calculated wavelengths λ_{00} for transitions between the lowest vibrational levels of the same electronic states are shown in Table I. The assignment of individual electronic transitions to the 'green arc band' system invokes [23] upper electronic states of CaO of valence configurations $8\sigma^2 10\sigma 3\pi^3$ and $8\sigma^2 10\sigma 3\pi^4$ whose term energies have yet to be determined, either experimentally or by *ab initio* computation. For this reason, the assignment of individual electronic transitions to the green arc band system is not given.

The identification of lines within the $A\,^1\Sigma^+ \rightarrow X\,^1\Sigma^+$ and $A'\,^1\Pi \rightarrow X\,^1\Sigma^+$ band system is facilitated by the assigned peak positions for the Δv sequences of the $A\,^1\Sigma^+ \rightarrow X\,^1\Sigma^+$ system taken from [29] and band-head positions of the strongest $A'\,^1\Pi \rightarrow X\,^1\Sigma^+$ vibronic lines reported in [24]. Vibrational assignments were made using the equilibrium vibration constants reported by Field and co-workers [24,29], from which calculated wavelengths λ_{calc} are presented in Table I. Owing to the similar spacing of vibrational energy levels in the $CaO(A\,^1\Sigma^+)$ and $CaO(X\,^1\Sigma^+)$ states coupled with the necessarily limited spectral resolution of about $\pm$ 1 nm for the present experimental arrangement, only Δv sequences of the $A\,^1\Sigma^+ \rightarrow X\,^1\Sigma^+$ band

system were monitored in emission. The very off-diagonal $A\,^1\Sigma^+ \rightarrow X\,^1\Sigma^+$ Franck–Condon array ensures that a range of Δv sequences can be observed within this electronic band system [25]. Individual vibronic transitions within the $A'\,^1\Pi \rightarrow X\,^1\Sigma^+$ band system could be distinguished however, on account of favourable molecular constants [24,29] giving rise to appreciably different spacings between vibrational levels of the two electronic states. Since the $A'\,^1\Pi \rightarrow X\,^1\Sigma^+$ Franck–Condon array is also off-diagonal, a broad range of v'-levels of $CaO(A'\,^1\Pi)$ could be observed during the present experiments. The search for, and assignment of, bands belonging to the $A\,^1\Sigma^+ \rightarrow X\,^1\Sigma^+$ and $A'\,^1\Pi \rightarrow X\,^1\Sigma^+$ band systems in the blue and green regions was terminated at $v' \leq 10$ for $CaO(A\,^1\Sigma^+)$ and $v' \leq 15$ for $CaO(A'\,^1\Pi)$ due to severe spectral congestion of lines at higher frequencies and a lack of reliable spectroscopic information pertaining to high v'-levels of the emitting states. Observed wavelengths λ_{obs}, also listed in Table I, are those wavelengths at which the intensity of molecular chemiluminescence was observed to be a maximum.

4. Results and discussion

(a) Production of radiating CaO states by chemical reaction*

Figures 2(b), 2(c) and 2(d) give examples of time-resolved molecular chemiluminescence from the orange arc bands $(CaO(d^3\Delta) \rightarrow CaO(a^3\Pi_i) + h\nu)$ at $\lambda =$ 608.5 nm, the green arc band at $\lambda \approx 537$ nm and the $A' - X$ band system $(CaO(A'\,^1\Pi\ v' = 15) \rightarrow CaO(X\,^1\Sigma^+ v'' = 0) + h\nu)$ at $\lambda = 618.2$ nm of CaO (Transitions 2, 10 and 32 of Table I) following pulsed laser generation of $Ca(^3P)$ atoms in the presence of N_2O at $T = 1100$ K. Within a 10% statistical error, each of the chemiluminescence decay traces shown in Figs 2(b), 2(c) and 2(d) are characterized by the same pseudo first-order decay coefficient as that for the decay of atomic fluorescence from $Ca(^3P_1)$ shown in Fig. 2(a). Exponential decay traces such as these were observed for emission of electronic chemiluminescence from the upper orange and green arc band states and from the $v' = 13$, 14 and 15 vibrational levels of the $A'\,^1\Pi$ state following optical excitation of $Ca(^3P)$ atoms (Transitions 1–5, 7, 9–11, 14, 17, 19, 21–32). A similar relationship between the time dependence of orange and green arc band chemiluminescence and atomic emission arising from $Ca(^1D)$ atoms following laser generation of this state was also observed.

In those cases where the time dependence of molecular chemiluminescence follows the exponential decay of the metastable precursor atoms, we may postulate that radiating states of CaO arise from direct reaction between the excited atomic states and N_2O via the processes:

$$Ca(^3P) + N_2O \rightarrow CaO^* + N_2; \quad (1)$$

$$Ca(^1D) + N_2O \rightarrow CaO^* + N_2. \quad (2)$$

In view of the short mean radiative lifetimes of the electronically excited product states CaO^* of interest here [14,16,31], $[CaO^*]$ may be placed in stationary state on

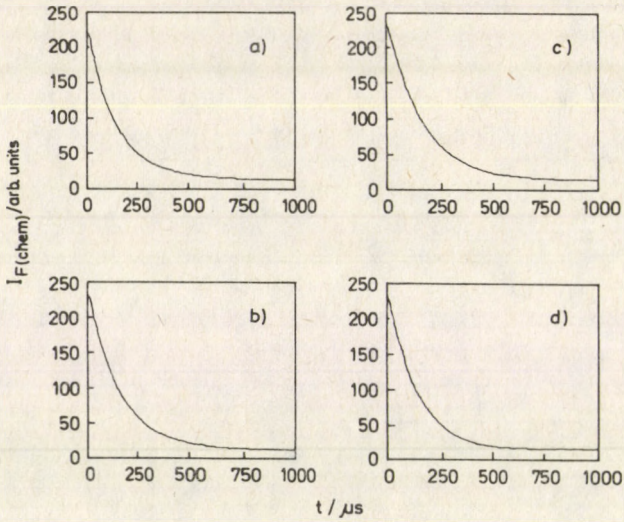

Fig. 2. Exponential time dependence of atomic fluorescence from $Ca(^3P_1)$ and molecular chemiluminescence from CaO*, $I_{F(chem)}$, following laser excitation of $Ca(^3P_1)$ in the presence of N_2O at $T = 1100$ K.

($p_{He} = 39.9966 \times 10^2$ N/m^2; $[N_2O] = 2.0 \times 10^{13}$ molecule cm^{-3}.)
(a) $Ca(^3P_1) \rightarrow Ca(^1S_0) + h\nu$; $\lambda = 657.3$ nm.
(b) $CaO(d^3\Delta) \rightarrow CaO(a^3\Pi_i) + h\nu$; $\lambda = 608.5$ nm (orange arc band).
(c) CaO green arc band; $\lambda = 547$ nm.
(d) $CaO(A'\,^1\Pi\ v' = 15) \rightarrow CaO(X\,^1\Sigma^+\ v'' = 0) + h\nu$; $\lambda = 618.2$ nm.
(Adapted from Reference [25])

account of its rapid removal by spontaneous emission. It may readily be shown that the time dependence of molecular chemiluminescence from CaO* states populated via reaction (1) is given by [25]:

$$I_{chem}(\mathrm{CaO}^*) = \phi_1 \alpha k_1 [\mathrm{N_2O}][\mathrm{Ca}(^3P_J)]_{t=0} \cdot \exp(-k'_P t), \qquad (3)$$

together with an analogous expression for the chemiluminescence emitted from reaction (2). Here ϕ_1 is a time-independent constant which reflects the fraction of molecular chemiluminescence collected by the detection apparatus and arbitrary electronic amplification of the time-resolved signal, α represents the branching ratio for formation of a specific electronically excited product state, k_1 is the rate constant for reaction (1) and k'_P is the first-order decay coefficient for removal of $Ca(^3P)$. Equation (3) thus predicts that first-order decay coefficients for chemiluminescence from these CaO* states should be equal to that describing decay of atomic emission from the metastable Ca states from which they are derived, as found above. The variation of first-order decay coefficients k'_P derived from equation (3) with N_2O concentration yields an estimate of the effective second-order

rate constant, designated $k^{mol}_{N_2O}(T)$, for collisional removal of $Ca(^3P)$ (or $Ca(^1D)$) atoms with N_2O. Values of $k^{mol}_{N_2O}(T)$ should of course be identical to $k^{at}_{N_2O}(T)$, the rate constants determined from atomic decay data (see Section 4(e)). We find this to hold to within a 10–15% uncertainty.

An adiabatic correlation diagram constructed on the basis of C_S symmetry in the collision complex and the weak spin-orbit approximation [25] indicates that whilst production of $CaO(D^1\Delta)$ (one of the upper arc band states) from $Ca(^1D)$ + N_2O reactants is adiabatically allowed, its formation from $Ca(^3P)$ + N_2O is forbidden and must involve one or more surface crossings. Similarly, the low-lying $A'\,^1\Pi$ and $A\,^1\Sigma^+$ product states of CaO correlate adiabatically with $Ca(^1D)$ + N_2O starting materials, though it is only for $Ca(^3P)$ as atomic reactant that we observe direct chemical production of the $v' = 13$–15 vibrational levels of $CaO(A'\,^1\Pi)$. For the Ca + N_2O system, the adiabatic correlation rules do not therefore provide a reliable guide to the types of product oxide states formed.

(b) Production of radiating CaO states by electronic energy transfer*

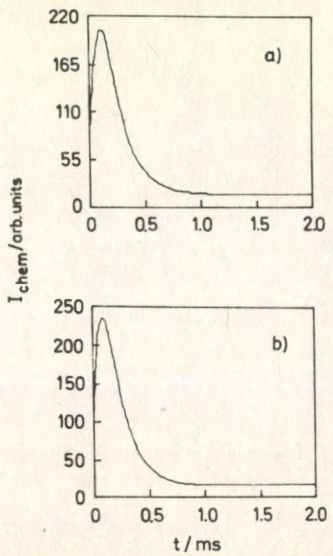

Fig. 3. Bi-exponential time dependence of molecular chemiluminescence from CaO*, I_{chem}, following laser excitation of $Ca(^3P_1)$ in the presence of N_2O at $T = 1100$ K.

($p_{He} = 39.9966\times10^2$ N/m^2; $[N_2O] = 2.0 \times 10^{13}$ molecule cm^{-3}.)
(a) $CaO(A'\,^1\Pi\ v' = 8) \rightarrow CaO(X\,^1\Sigma^+\ v'' = 0) + h\nu$; $\lambda = 782.3$ nm.
(b) $CaO(A'\,\Sigma^+\ v' = 4) \rightarrow CaO(X\,^1\Sigma^+\ v'' = 0) + h\nu$; $\lambda = 695.3$ nm.
(Adapted from reference [25])

Figure 3 gives examples of molecular chemiluminescence signals characterized by a bi-exponential dependence on time. In the case of Fig. 3, typical data are

presented for the specific transitions $CaO(A'\,^1\Pi\ v' = 8) \rightarrow CaO(X\,^1\Sigma^+\ v'' = 0) + h\nu$ at $\lambda = 782.3$ nm and $CaO(A\,^1\Sigma^+\ v' = 4) \rightarrow CaO(X\,^1\Sigma^+\ v'' = 0) + h\nu$ at $\lambda = 695.3$ nm (Transitions 15 and 36) observed following laser generation of $Ca(^3P)$ atoms in the presence of N_2O. Profiles of this form were monitored for a number of molecular transitions following separate reaction of $Ca(^3P)$ and $Ca(^1D)$ atoms with added oxidant: following excitation of $Ca(^3P)$ atoms, vibronic transitions out of vibrational levels $v' = 8$–12 of $CaO(A'\,^1\Pi)$ and vibrational levels $v' = 2$–4 of $CaO(A\,^1\Sigma^+)$ (Transitions 13, 15, 16, 18, 20, 33, 34 and 36) exhibited bi-exponential kinetics; following excitation of $Ca(^1D)$ atoms vibronic transitions out of vibrational levels $v' = 8$–15 of $CaO(A'\,^1\Pi)$ and vibrational sequences $\Delta v = -2$–9 of the $CaO(A\,^1\Sigma^+ \rightarrow X\,^1\Sigma^+)$ band system (Transitions 13–35, and 37–41) displayed an identical time dependence.

Chemiluminescence profile of the type portrayed in Fig. 3 may be seen to be consistent with an electronic energy transfer mechanism involving $Ca(^3P)$ and $Ca(^1D)$ atoms and ground-state $CaO(X^1\Sigma^+)$ produced via reactions (1) and (2). The energetics of such energy transfer processes may conveniently be represented by the equations:

$$Ca(^3P) + CaO(X^1\Sigma^+\, v = 0) \rightarrow Ca(^1S) + CaO(A^1\Sigma^+\, v \leq 4, A'^1\Pi\, v \leq 12), \tag{4}$$

$$Ca(^1D) + CaO(X^1\Sigma^+\, v = 0) \rightarrow Ca(^1S) + CaO(A^1\Sigma^+\, v \leq 15, A'^1\Pi\, v \leq 28), \tag{5}$$

which indicate the accessible vibrational levels of $CaO(A\,^1\Sigma^+)$ and $CaO(A'\,^1\Pi)$. Small quantities of long-lived electronically and/or vibrationally excited states of CaO, particularly $CaO(a^3\Pi_i)$, may also be generated via reactions (1) and (2), but are neglected in this simplified treatment. Restricting the present example to chemical generation of $CaO(X\,^1\Sigma^+)$ via reaction (1) we may obtain the expression [25]:

$$I_{chem}(CaO^*) = (\phi_2\beta\gamma k_1 k_4[Ca(^3P_J)]^2_{t=0}/k'_P) \cdot (\exp(-k'_P t)) - \exp(-2(k'_P t)) \tag{6}$$

for the intensity of chemiluminescence as function of time assuming slow removal of $CaO(X\,^1\Sigma^+)$ at short times and an exponential decay of $Ca(^3P)$. An analogous expression for generation of excited molecular states via process (5) may likewise be derived. Here β is the branching ratio for formation of $CaO(X\,^1\Sigma^+)$ via reaction (1) and γ that for production of a specific emitting state of CaO^* (= $CaO(A\,^1\Sigma^+)$ or $CaO(A'\,^1\Pi)$) via process (4). ϕ_2 is a further time-independent instrumental constant.

The agreement between rate constants obtained from values of k'_P derived from Eq. (6) as a function of N_2O pressure and those determined from atomic emission measurements is usually to within 10–15%. Figure 4 shows examples of second-order rate constants derived from measurements of molecular chemiluminescence arising from direct chemical reaction and $E - (E,V)$ transfer, designated $k^{mol}_{N_2O}(T)$, plotted against rate constants $k^{at}_{N_2O}(T)$ obtained from measurements of

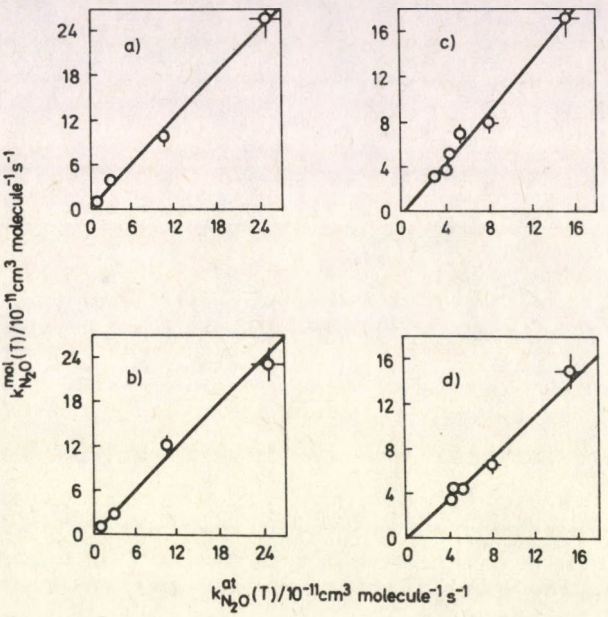

Fig. 4. Plot of effective second-order rate constants for removal of electronically excited CaO*, $k^{mol}_{N_2O}(T)$, against those for loss of metastable atoms, $k^{at}_{N_2O}(T)$, at $T = 950$ K.

(a) $k^{mol}_{N_2O}(T)$ derived from orange arc band versus $k^{at}_{N_2O}(T)$ derived from decay of Ca(^3P)
(b) $k^{mol}_{N_2O}(T)$ derived from CaO($A\,^1\Sigma^+ \rightarrow X\,^1\Sigma^+$) band versus $k^{at}_{N_2O}(T)$ derived from decay of Ca(^3P)
(c) $k^{mol}_{N_2O}(T)$ derived from orange arc band versus $k^{at}_{N_2O}(T)$ derived from decay of Ca(^1D)
(d) $k^{mol}_{N_2O}(T)$ derived from CaO($A\,^1\Sigma^+ \rightarrow X\,^1\Sigma^+$) band versus $k^{at}_{N_2O}(T)$ derived from decay of Ca(^1D)

the decay of atomic emission from Ca(^3P) and Ca(^1D) at $T = 950$ K. The gradients of all graphs of the type shown in Fig. 4 are unity to within a 10–15% statistical uncertainty.

(c) Vibrational temperatures of CaO($A'\,^1\Pi$)

Table I lists a large number of vibronic lines that were monitored in the CaO($A'\,^1\Pi \rightarrow X\,^1\Sigma^+$) system in these experiments, with transitions arising from vibrational levels $v' = 8$–15 of the $A'\,^1\Pi$ state inclusive. These can be employed to estimate the degree of vibrational excitation accompanying direct reaction of Ca(^3P) atoms with N_2O using equation (3) and $E - (E,V)$ energy transfer between both excited atoms and CaO($X\,^1\Sigma^+$) using equation (6) via the effective vibrational temperature T_{vib}. The procedure adopted for determination of T_{vib} of CaO($A'\,^1\Pi$)

Table II

Effective vibrational temperatures T_{vib}/K of CaO($A'\,^1\Pi$) product following reaction of Ca(^3P) and Ca(^1D) atoms with N_2O as a function of ambient reactor temperature T_{amb}/K over which $A'\,^1\Pi \rightarrow X\,^1\Sigma^+$ chemiluminescence could be monitored

T_{amb}/K	Ca(^3P)+N_2O T_{vib}/K	Ca(^1D)+N_2O T_{vib}/K
950± 5	1422^{+351}_{-235}	2183^{+578}_{-377}
1000± 5	1443^{+281}_{-202}	1975^{+431}_{-300}
1050± 5	1412^{+355}_{-237}	1928^{+394}_{-280}
1100± 5	1360^{+255}_{-185}	1892^{+295}_{-225}

product follows that given by Herzberg [35] and relies fundamentally upon the assumption of a Boltzmann population distribution amongst the vibrational quantum states of $A'\,^1\Pi$ state on the timescale of chemiluminescence measurements. Using this method, estimates of T_{vib} are determined from values of the maximum chemiluminescence intensity $I^{v'v''}_{chem}(\max)$ for emission from vibrational levels $v' = 8$–15 of the $A'\,^1\Pi$ state at all ambient reactor temperatures at which the $A'\,^1\Pi \rightarrow X\,^1\Sigma^+$ bands could be observed. For production of CaO($A'\,^1\Pi$ $v' = 8$–12) by $E - (E,V)$ energy transfer following initial oxidation of Ca(^3P), equation (6) indicates that $I^{v'v''}_{chem}(\max)$ is given by:

$$I^{v'v''}_{chem}(\max) = \phi_2\beta\gamma k_1 k_4[N_2O][Ca(^3P_J)]^2_{t=0}/4k'_P, \tag{7}$$

together with an analogous expression for collisional energy transfer involving Ca(^1D) atoms to yield the $v' = 8$–15 vibrational levels. For production of CaO($A'\,^1\Pi$ $v' = 13$–15) by direct reaction of Ca(^3P) atoms with N_2O, Eq. (3) predicts that $I^{v'v''}_{chem}(\max)$ is simply given by:

$$I^{v'v''}_{chem}(\max) = \phi_1\alpha k_1[N_2O][Ca(^3P_J)]_{t=0}. \tag{8}$$

In order to determine effective vibrational temperatures from maximum chemiluminescence intensities, values of $I^{v'v''}_{chem}(\max)$ are corrected for the effect of the fourth power of the transition frequency $\nu^4_{v'v''}$, the appropriate Franck–Condon factor $f_{v'v''}$ and the variation of photomultiplier sensitivity with applied voltage across the tube. According to Herzberg [35], for a given ambient reactor temperature (and hence constant value of $[Ca(^3P_J)]_{t=0}$ or $[Ca(^1D_2)]_{t=0}$) and N_2O concentration, $I^{v'v''}_{chem}(\max)/\phi\nu^4_{v'v''}f_{v'v''}$ for a particular transition is a measure of the maximum population in the specific upper vibrational level v' of CaO($A'\,^1\Pi$) giving rise to that transition. Effective vibrational temperatures T_{vib} may be extracted from a linear plot of $\ln[(I^{v'v''}_{chem}(\max)/\phi\nu^4_{v'v''}f_{v'v''})/\text{arb. units}]$ against $G(v')/\text{cm}^{-1}$

in the normal manner [35]. Vibrational energy levels $G(v')$ were computed assuming Morse potentials for both the $A'\,^1\Pi$ and $X\,^1\Sigma^+$ states [25]. On account of the uncertainty associated with determination of photomultiplier gain as a function of applied voltage, large statistical errors were computed for individual values of $\ln[(I^{v'v''}_{chem}(\max)/\phi\nu^4_{v'v''}f_{v'v''})/\text{arb. units}]$ which swamp any errors incurred by the assumption of Morse potential energy curves for the upper and lower electronic states.

Values of T_{vib} for $CaO(A'\,^1\Pi)$ as a function of ambient reactor temperature T_{amb} are listed in Table II. Whilst the uncertainties associated with these measurements are clearly large, it can be seen that a certain degree of vibrational excitation accompanies $Ca(^1D) + CaO(X\,^1\Sigma^+)E - (E,V)$ energy transfer. This is not so pronounced for $Ca(^3P)$ as the atomic precursor, where the vibrational levels $v' = 13$, 14 and 15 of $CaO(A'\,^1\Pi)$ lie above the exoergicity limit for energy transfer process (4). In this case, the observed values of T_{vib} thus represent an overall average distribution resulting from both direct chemical reaction and indirect $E - (E,V)$ energy transfer to yield $CaO(A'\,^1\Pi)$.

*(d) Electronic state distribution in CaO**

Relative populations in emitting electronic states of CaO may be estimated from values of $I^{v'v''}_{chem}(\max)/\phi\nu^4_{v'v''}f_{v'v''}$ at (i) times $t_{max} = \ln(2)/k'_P$ and $\ln(2)/k'_D$ following $E-(E,V)$ energy transfer using Eq. (7) and (ii) zero time for production of excited molecular states following chemical reaction using Eq. (8). Procedural details may be found elsewhere [25]: here we simply state the main conclusions that may be drawn from over 200 measurements of $I^{v'v''}_{chem}(\max)/\phi\nu^4_{v'v''}f_{v'v''}$ for the orange and green arc bands and the $A\,^1\Sigma^+ \rightarrow X\,^1\Sigma^+$ and $A'\,^1\Pi \rightarrow X\,^1\Sigma^+$ band systems. In the case of product CaO electronic states arising from collisions of $Ca(^3P)$ atoms with either N_2O or $CaO(X\,^1\Sigma^+)$, and allowing for the Boltzmann distribution of vibrational population within $CaO(A'\,^1\Pi)$ described above, the relative populations of all product electronic states monitored here are of comparable magnitude, being in the range $[CaO^*]_{t=0(max)}/[Ca(^3P_1)]_{t=0} \approx 10^{-6} - 10^{-7}$. In the case of those molecular states arising from collisions of $Ca(^1D)$ atoms with either N_2O or $CaO(X\,^1\Sigma^+)$, the relative populations of radiating states giving rise to orange and green arc band chemiluminescence are approximately $10^{-4} - 10^{-5}$, whilst for the lower-lying $A'\,^1\Pi$ and $A\,^1\Sigma^+$ product states, values about $10^{-6} - 10^{-7}$ were determined. These results are in accord with those obtained from single-collision experiments [16,17], and may be broadly rationalized by application of the adiabatic correlation rules for determining symmetry-allowed pathways between defined reactant and product states in that products which require only a limited number of surface crossings appear to be favoured. It may further be shown that the variation of $I^{v'v''}_{chem}(\max)/\phi\nu^4_{v'v''}f_{v'v''}$ with temperature is consistent with vapour pressure data for atomic Ca [25].

(e) Atomic emission measurements

Although not of prime concern in this paper, it is worth mentioning that apparent second-order rate constants for collisional quenching of $Ca(^3P)$ and $Ca(^1D)$ atoms by N_2O may readily be extracted from time-resolved measurements of atomic emission at the resonance wavelengths as a function of quenching gas pressure. Rate constants $k^{at}_{N_2O}(T)$ for both $Ca(^3P)$ and $Ca(^1D)$ are extracted from plots of k'_P or k'_D against $[N_2O]$ at constant p_{He}. We observe a breakdown in simple Arrhenius kinetics for both reactions at temperatures greater than about 900 K, which has been attributed [25] to additional rapid removal of both excited states by molecular O_2 generated by thermal decomposition of N_2O. $k^{at}_{N_2O}(T)$ does not therefore represent a fundamental second-order rate constant for collisional removal of the ^3P or ^1P metastable states by N_2O across the temperature range 725/750 – 1100 K. This effect gives rise to a bi-exponential dependence of $k^{at}_{N_2O}(T)$ on temperature, from which we may extract Arrhenius parameters for the bimolecular quenching processes for temperatures below about 900 K. By curve-fitting to the appropriate functional form we find that $E_{act} = 36.1 \pm 11.6$ kJ mol^{-1} and $A = (3.5\ ^{+8.5}_{-2.5}) \times 10^{-10}$ cm^3 molecule^{-1} s^{-1} for $Ca(^3P) + N_2O$ and $E_{act} = 17.5 \pm 3.7$ kJ mol^{-1} and $A = (3.8\ ^{+2.9}_{-1.7}) \times 10^{-10}$ cm^3 molecule^{-1} s^{-1} for $Ca(^1D) + N_2O$ [25,27].

5. Acknowledgements

The author wishes to thank Dr. D. Husain for his helpful advice and encouragement. This work was supported by S. E. R. C. by way of a generous equipment grant for purchase of a dye-laser system.

References

1. R. N. Zare and P. J. Dagdigian, Science, *185*, 739, 1974.
2. R. W. Field, in Molecular Spectroscopy: Modern Research, ed. K. N. Rao Academic Press, New York, 1976, Vol. 2, p. 261.
3. R. Grice, in Molecular Scattering: Physical and Chemical Applications, Adv. Chem. Phys., ed. K. P. Lawley, J. Wiley & Sons, London, 1975, Vol. XXX, p. 247.
4. M. Menzinger, in Potential Energy Surfaces, Adv. Chem. Phys., ed. K. P. Lawley, J. Wiley & Sons, London, 1980, Vol. XLII, p. 1.
5. W. H. Breckenridge and H. Umemoto, in Dynamics of the Excited State, Adv. Chem. Phys., ed. K. P. Lawley, J. Wiley & Sons, London, 1982 Vol., L., Ch. 5, p. 325; W. H. Breckenridge, in Reactions of Small Transient Species: Kinetics and Energetics, eds. A. Fontijn and M. A. A. Clyne, Academic Press, London, 1983,Ch. 4, p. 157.
6. J. C. Whitehead, in Comprehensive Chemical Kinetics, eds. C. H. Bamford, C. F. H. Tipper, Elsevier, Amsterdam, 1983, Vol. 24, Ch. 5, p. 357.
7. D. Husain and G. Roberts, in Bimolecular Collisions, Advances in Gas-Phase Photochemistry and Kinetics, eds. M. N. R. Ashfold and J. E. Baggott, The Royal Society of Chemistry, London, 1989,Ch. 6, p. 263 .
8. C. R. Jones and H. P. Broida, Laser Focus, 1974, 37.
9. M. H. Alexander and P. J. Dagdigian, Chem. Phys., *33*, 13, 1978.

10. Ch. Ottinger and R. N. Zare, Chem. Phys. Lett., *5*, 243, 1970.
11. R. R. Herm, S-M. Lin and C. A. Mims, J. Phys. Chem., *77*, 2931, 1973.
12. F. Engelke, R. K. Sander and R. N. Zare, J. Chem. Phys., *65*, 1146, 1976.
13. P. J. Dagdigian, Chem. Phys. Lett, *55*, 239, 1978.
14. L. Pasternack and P. J. Dagdigian, J. Chem. Phys., *33*, 1, 1978.
15. J. A. Irvin and P. J. Dagdigian, J. Chem. Phys., *73*, 176, 1980.
16. J. A. Irvin and P. J. Dagdigian, J. Chem. Phys., *74*, 6178, 1981.
17. H. Wang and M. Menzinger, Canad. J. Chem., *61*, 2708, 1983.
18. D. J. Bernard, Chem. Phys. Lett., *35*, 167, 1975; D. J. Bernard, W. D. Slafer and P. H. Lee, Chem. Phys. Lett., *43*, 69, 1976; D. J. Bernard, W. D. Slafer and J. Hecht, J. Chem. Phys., *66*, 1012, 1977; D. J. Eckstrom, J. R. Barker, J. G. Hawley and J. P. Reilly, Appl. Opt., *16*, 2102, 1977; D. J. Bernard, W. D. Slafer, P. J. Love and P. H. Lee, Appl. Opt., *16*, 2108, 1977.
19. G. A. Capelle, C. R. Jones, J. Zorskie and H. P. Broida, J. Chem. Phys., *61*, 4777, 1974.
20. J. van der Hurk, Tj. Hollander and C. Th. J. Alkemade, J. Quant. Spectrosc. Radiat. Transfer, *13*, 273, 1973.
21. O. E. Kashireninov, V. A. Kuznetsov and G. B. Manelis, Zh. Fiz. Khim., *49*, 775, 1975 (Russ. J. Phys Chem., *49*, 454, 1975); Zh. Fiz. Khim., *51*, 958, 1977 (Russ. J. Phys Chem., *51*, 556, 1977); AIAA J., *15*, 1035, 1977; V. A. Kuznetsov, L. F. Repka and O. E. Kashireninov, Zh. Fiz. Khim., *52*, 430, 1978 (Russ. J. Phys Chem., *52*, 237, 1978); O. E. Kashireninov and V. A. Kuznetsov, Dokl. Akad. Nauk. SSSR, *257*, 636, 1981 (Engl. Trans., *257*, 109, 1981).
22. R. F. Marks, R. A. Gottscho and R. W. Field, Scr., *25*, 312, 1982.
23. R. F. Marks, H. S. Schweda, R. A. Gottscho and R. W. Field, J. Chem. Phys., *76*, 4689, 1982, J. Chem. Phys., *77*, 4795, 1982.
24. R. W. Field, G. A. Capelle and C. R. Jones, J. Molec. Spectrosc., *54*, 156, 1975.
25. D. Husain and G. Roberts, Chem. Phys., *109*, 393, 1986.
26. D. Husain and G. Roberts, J. Chem. Soc. Faraday Trans., 2, *82*, 1921, 1986.
27. D. Husain, J. Chem. Soc. Faraday Trans. 2, 85, 85, 1989 .
28. K. P. Huber and G. Herzberg, Molecular Spectra and Molecular Structure IV: Constants of Diatomic Molecules, Van Nostrand Reinhold, New York, 1977, pp. 124 – 125.
29. R. W. Field, J. Chem. Phys., *60*, 2400, 1974.
30. C. W. Bauschlicher Jr. and D. R. Yarkony, J. Chem. Phys., *68*, 3990, 1978, W. B. England, Chem. Phys., *53*, 1, 1980.
31. R. N. Diffenderfer and D. R. Yarkony, J. Chem. Phys., *77*, 5573, 1982, J. Chem. Phys., *78*, 7017, 1984.
32. D. Husain and J. Schifino, J. Chem. Soc. Faraday Trans. 2, *78*, 2083, 1982; J. Chem. Soc. Faraday Trans. 2, *79*, 1265, 1983; J. Chem. Soc. Faraday Trans. 2, *80*, 321, 1984.
33. C. E. Moore, Atomic Energy Levels, Nat Stand. Ref. Data Ser., Nat. Bur. Stand. (U.S.) 35, U.S. Government Printing Office, Washington, D.C.,1971 Vol. I, pp 242 – 245.
34. T. J. McIlrath and J. L. Carlsten, J. Phys. B.: Atom. Molec. Phys., *6*, 697, 1973; H-J. Yuh and P. J. Dagdigian, Phys Rev. A, *28*, 63, 1983; M. H. Alexander, T. Orlikowski and J. E. Straub, Phys. Rev. A, *28*, 73, 1983.
35. G. Herzberg, Molecular Spectra and Molecular Structure I: Spectra of Diatomic Molecules, 2nd edn. Van Nostrand Reinhold, New York, 1950, Ch. 4, pp. 200 – 204.

Acta Physica Hungarica 67 (1-2), pp. 107-122 (1990)

HIGH-RESOLUTION SPECTROSCOPY ON THE $E^2\Sigma^+ \leftarrow A^2\Sigma^+$ TRANSITION OF NO*

G. MEIJER, M. EBBEN and J. J. TER MEULEN

Department of Molecular and Laser Physics
Catholic University Nijmegen
6525 ED Nijmegen, The Netherlands

(Received 24 September 1988)

A double-resonance technique combining a high power pulsed laser with a narrow bandwidth cw laser is presented for the high resolution study of the NO molecule.

1. Introduction

In the last two decades several laser spectroscopic methods have been developed to study highly excited electronic states of atoms and molecules. With the rapid progress of pulsed laser technology intense radiation ranging far into the ultraviolet has become available. Multiphoton processes or double resonance techniques using several pulsed lasers are successfully applied to reach the special electronic states one wants to investigate. The ultimate spectral resolution in these experiments is often determined by the bandwidth of the laser system used, although in many cases other broadening mechanisms, especially lifetime broadening, may be the limiting factor. With a typical bandwidth of pulsed laser systems of 0.01 cm^{-1} or larger, this means the finer structures of the electronic states are not observable.

In combination with molecular beam techniques or other Doppler-width reducing or Doppler-free methods single-mode cw lasers allow a spectral resolution of several MHz. High resolution studies of this kind have been performed in the visible and near UV on both stable molecules and transient species [1]. A disadvantage of cw lasers, however, is the difficulty of reaching the far UV.

In this paper we present a double-resonance technique in which full advantage of specific properties of a pulsed laser and a cw laser is taken; the pulsed laser is used to reach high energy states whereas the cw laser is used for its resolving power. We investigated the NO molecule in a well defined collimated molecular beam. The excitation scheme we used is indicated in Fig. 1. Pulsed laser radiation around 226 nm is used to reach the first electronically excited $A^2\Sigma^+$, $v'=0$ state of NO. Population of single rotational levels, monitored by the laser induced $A \rightarrow X$ fluorescence is possible. From the $A^2\Sigma^+$, $v'=0$ state the NO molecules are excited

*Presented at the Conference on High Resolution Electronic Spectroscopy of Molecules, Tihany, Hungary, 19-24 September 1988

with single frequency 600 nm cw radiation to the $E^2\Sigma^+$, $v'=0$ state. Both electronically excited states are studied under high resolution by detecting the resonant $E \rightarrow A$ fluorescence. The spectral resolution we obtained is mainly determined by the residual Doppler broadening due to the divergence of the molecular beam and is about 17 MHz. This resolution allows the spin rotation splitting constant γ of the $E^2\Sigma^+$, $v'=0$ state to be determined. An effect of a heterogeneous perturbation between the $E^2\Sigma^+$, $v'=0$ and the $B^2\Pi$, $v'=17$ states is observed and analyzed. This perturbation had not been observed in previous [2] Doppler limited spectroscopic studies. Time resolved fluorescence from the excited states gives information on the magnitude of the radiative loss channels out of these states. The time resolved fluorescence from the E-state allows the experimental study of a (more or less) isolated two-level system, with coherent pumping and with radiative losses out of both levels. The time dependence of this fluorescence could be correctly described using the optical Bloch equations.

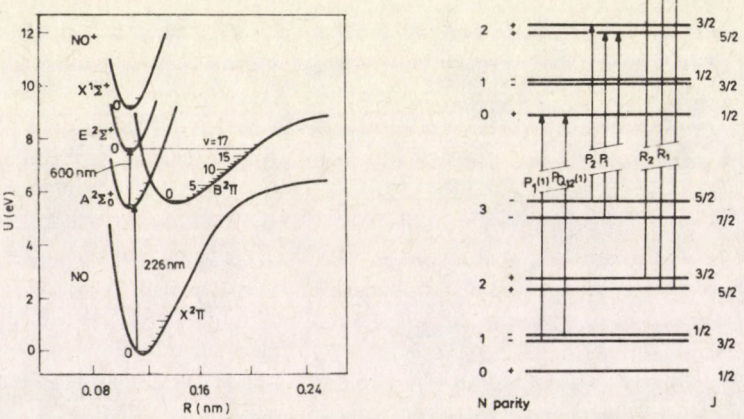

Fig. 1. Selected potential energy curves of NO and schematic representation of the excitation process we used. Pulsed laser radiation around 226 nm is used to induce the $A \leftarrow X$ transition, and in the next step cw laser radiation around 600 nm pumps the excited molecules further up to the E-state. The $B^2\Pi$, $v=17$ state lies at almost the same energy as the $E^2\Sigma^+$, $v=0$ state and a small effect of the perturbation between these states is seen in the $E \leftarrow A$ spectra

Fig. 2. Energy level scheme of both $^2\Sigma^+$ states of NO. The inverted spin splitting, shown enlarged in the Figure, gives F_2 levels that are higher in energy than the F_1 levels. In the left side of the Figure the two possible transitions to the $N=0$ level in the upper $^2\Sigma^+$ state are indicated (see Fig. 4). Except for the lowest rotational levels, pairs of lines from each ρ-doublet are seen. The weaker $\Delta J = 0$ transitions (thinner arrows) are not observed in this case. Two lines belonging to the same pair (e.g. $P_1(N)$ and $P_2(N)$) are separated by the difference in ρ-doubling in the upper and the lower state

2. Description of the apparatus

The pulsed laser system consists of a dye laser operating on Coumarin 47, pumped with an XeF (351 nm) excimer laser. The typical dye laser output of 10 mJ in a 10 ns pulse was frequency doubled in an angle tunable β-BaB_2O_2 (BBO) crystal. With an efficiency of nearly 30 % several mJ of tunable UV radiation were produced at 226 nm. The bandwidth of the UV radiation was about 0.5 cm^{-1}, which is large enough to populate different fine-structure levels of the $A\,^2\Sigma^+$, $v'=0$ state simultaneously. The pulsed laser system operated most times at a repetition rate of 15 Hz.

The cw laser radiation was produced by a ring dye laser (Spectra Physics) operating on Rhodamine 6G and pumped with 5 W of an Ar-ion laser. Relatively low output powers between 0.5 and 60 mW were used for the experiment. The bandwidth of this laser system, determined by high frequency jitter, is less than 0.3 MHz. Single mode laser scans over a spectral range of about 40 GHz could be made.

To ensure high resolution the double resonance experiment was performed on a well-defined nozzle beam of NO molecules in a three chamber vacuum system. In the detection region, about 15 cm upstream of the beam orifice, the background pressure was below 10^{-5} mbar, to ensure collision free conditions. Here the counter-propagating pulsed UV laser beam and the cw red laser beam cross the molecular beam perpendicularly. Both laser beams were unfocused and have a more or less circular intersection with the molecular beam of typically 2.0 mm for the cw laser beam and a somewhat smaller value of 1.0 mm for the pulsed laser beam. The polarization of both lasers was in the same plane, although this turned out to be unimportant even at low laser powers (far from saturation); no effects of anisotropy of the double-resonance fluorescence were observed when the polarization of one laser was rotated with respect to the polarization of the other. The laser induced fluorescence was collected at right angles to both the molecular beam and the laser beams and imaged on the entrance window of a photomultiplier. This PMT has a quantum efficiency of about 25% in the 200–300 nm region whereas the quantum efficiency for radiation of around 600 nm is roughly a factor of three less. The fluorescence signal thus obtained was fed into a boxcar integrator and simultaneously displayed on a digital oscilloscope. With an appropriate setting of the gate of the boxcar the total fluorescence, averaged over 10 or 30 samples, was measured and recorded on a strip chart recorder. Time resolved fluorescence curves were directly plotted from the oscilloscope.

In the double resonance experiment the pulsed laser was usually kept fixed in frequency to populate a certain rotational level N' in the $A\,^2\Sigma^+$, $v'=0$ state. This first step was controlled by looking for the resulting $A \rightarrow X$ fluorescence. Once this laser was set at the correct frequency a cut-off filter transmitting essentially only radiation above 590 nm was inserted in front of the PMT, to block the UV background. The cw laser was then scanned and the resulting resonant $E \rightarrow A$ fluorescence, which is only a fraction of the total emission of the $E\,^2\Sigma^+$, $v' = 0$ state, could be measured against a zero background level. The only radiation background

was due to scattered cw laser light, which was almost completely eliminated by the use of a narrow boxcar gate. The absolute frequency of the cw laser, used to induce a certain rotational transition in the $E \leftarrow A$ band [2], was determined by the simultaneous recording of the well cataloged I_2 absorption spectrum in a cell [3]. Linewidths and splittings between closely spaced lines were measured in terms of the free spectral ranges with an accuracy of several MHz.

Any combination of a pulsed laser and a cw laser causes a loss in duty cycle. It should be explicitly noted, however, that this loss is not as large as the ratio of the duration of a laser pulse to its repetition time. It depends on the experimental set-up as well as on certain properties of the molecular system under study. In the molecular beam machine the NO molecules travel with a speed of about 500 m/s and are irradiated with the pulsed laser over a length of 1 mm. With a repetition rate of 5 Hz this means that a fraction 3.0×10^{-5} of the beam is irradiated. With the high energy per pulse this fraction is excited very efficiently; in NO we nearly saturated the $A \leftarrow X$ step. Another important factor is the bandwidth of the pulsed laser. This bandwidth is very large compared with the residual Doppler width in a molecular beam, so all velocity groups are excited equally well.

For the second step to be successfully applied the lifetime of the intermediate electronic state should not be too short. The lifetime of NO ($A\,^2\Sigma^+$, $v' = 0$) is known to be about 200 ns [4]. During this lifetime the excited state molecules can absorb another photon. As the double resonance signal appears essentially in this period of time, the use of a boxcar with a gatewidth of 500 ns enables us to suppress both the scattered cw radiation and the dark current of the PMT. Due to the narrow bandwidth of the cw laser only a certain velocity group of excited state molecules is selected to be promoted to the next electronic state.

The application of two pulsed lasers is not a good alternative when one desires high spectral resolution. With two pulsed lasers, however, the lifetime of the excited $E\,^2\Sigma^+$, $v' = 0$ state can be determined directly, without the need to deconvolve the time resolved fluorescence curves. For this special purpose we used a second pulsed dye laser, pumped by a Nd:YAG laser and operating on R6G, with 1 mJ in a 6 ns pulse.

3. Spectroscopic investigation of the NO (E←A) bands

3.1 Theory

The rotational, fine and hyperfine structure of NO in both $^2\Sigma^+$ states can be described by the effective Hamiltonian:

$$H = B\mathbf{N}^2 - D\mathbf{N}^4 + \gamma \mathbf{N} \cdot \mathbf{S} + b\mathbf{I} \cdot \mathbf{S} + cI_z S_z, \qquad (1)$$

where $\mathbf{N}$ is the angular momentum vector of the end-over-end rotation of the molecule, $\mathbf{S}$ is the total electronic spin vector and $\mathbf{I}$ is the spin of the nitrogen

nucleus. The values for the rotational constant B as well as for the centrifugal distortion D for both $^2\Sigma^+$ states are taken from the work of Amiot et al [2]. An accurate value for the band origin ν_{00} of the $E\,^2\Sigma^+$, $v = 0 \leftarrow A\,^2\Sigma^+$, $v = 0$ electronic transition was also given in their work. The spin rotation interaction $\gamma\mathbf{N}\cdot\mathbf{S}$ splits each N level by an amount $\gamma(N + 1/2)$ into two J-levels, where $\mathbf{J} = \mathbf{N} + \mathbf{S}$. For the NO ($A\,^2\Sigma^+$, v=0) state the magnitude of this γ constant is well known from a Doppler-free two photon spectroscopic study of the NO ($A \leftarrow X$) transition, using a cw ring dye laser, as $\gamma = -$ (80.35 $\pm$ 0.15) MHz [5]. A negative value for this constant γ means that F_1 levels ($J = N+1/2$) are lower in energy than F_2 levels ($J = N-1/2$). The ρ doubling in the $E\,^2\Sigma^+$, v=0 state was too small to be determined from the Doppler-limited Fourier transform spectra, and was therefore not known until now. We determined a value of $\gamma = -(3.15 \pm 0.20)$ MHz for this splitting which means the E-state also has an inverted fine structure. In Figure 2 the energy level structure for both $^2\Sigma^+$ states is schematically presented.

For electric dipole transitions the $+\leftrightarrow -$ parity selection rule together with the $\Delta J = 0,\pm1$ selection rule restricts the possible rotational transitions to $\Delta N = \pm1$. There are six possible rotational branches, three starting from each fine structure level. The two $\Delta J = 0$ branches are very weak as they must change spin states, and can in practice only be observed for the lowest rotational levels. This means for higher energy levels only two pairs of closely spaced lines will show up in the spectrum. The splitting between the two almost equally strong lines belonging to the same ΔJ pair (between $P_1(N)$ and $P_2(N)$ or between $R_1(N)$ and $R_2(N)$) is equal to the difference in ρ-doubling of the A-state and the E-state, as seen in the Figure.

In both electronically excited states the hyperfine interaction due to the spin I=1 of the nitrogen nucleus, splits each fine structure level into levels characterized by the total quantum number $\mathbf{F} = \mathbf{J} + \mathbf{I}$. In the A-state the hyperfine structure is well known for v=3 [6]. We assume that the hyperfine structure in the $A\,^2\Sigma^+$, v=0 level can be described using similar values for the Frosch and Foley parameters of $b \approx 40$ MHz and $c \approx 2$ MHz. The interaction between the electronic spin and the quadrupole moment of the nitrogen nucleus can be neglected within the present experimental accuracy.

3.2 General results

In Fig. 3 two spectra are shown to demonstrate the double resonance technique. The upper part of the figure shows a part of the normal LIF spectrum of the NO ($A\,^2\Sigma^+$, $v' = 0 \leftarrow X^2\Pi$, v''=0) transition, obtained by scanning the pulsed laser and detecting the total $A \rightarrow X$ fluorescence. The cw laser is switched off here. The different rotational transitions induced are indicated by the quantum number J in the electronic ground state. In the lower part of the figure the double resonance spectrum is shown. Now the cw laser is switched on and kept fixed on the $F' = 3/2 \leftarrow F'' = 5/2$ hyperfine component of the $E\,^2\Sigma^+$, $v = 0 \leftarrow A\,^2\Sigma^+$, v=0 $P_1(1)$ transition. Only the red $E \rightarrow A$ fluorescence is now detected while the pulsed laser

is scanned over the same part of the $A \leftarrow X$ transition. Thus only transitions which reach the labeled $N=1$, $J=3/2$, $F=5/2$ level in the $A\,^2\Sigma^+$, $v'=0$ state are seen. In both spectra the linewidth is determined by the bandwidth of the pulsed laser.

The linewidth was reduced in the measurements where the pulsed laser was kept fixed on a certain transition while the cw laser was scanned. A typical high resolution $E \leftarrow A$ spectrum of this latter type is shown in Fig. 4. The pulsed laser excites the $A \leftarrow X\,Q_1(1)$ and the $^QP_{21}(1)$ rotational transitions simultaneously. Both fine structure levels of the $A\,^2\Sigma^+$, $v'=0$, $N'=1$ state are therefore populated. When the cw laser is scanned both the $P_1(1)$ and the $^PQ_{12}(1)$ transitions of the $E \leftarrow A$ band appear in the double resonance spectrum. The line strength for these two transitions is the same which means the intensity of these lines in the spectrum directly reflects the degree of population of both fine structure levels in the A-state by the pulsed laser. From this it can be concluded that the pulsed laser is not saturating the first step, as the expected intensity ratio of 3:1 is almost observed. The linewidth of 17 MHz is mainly determined by residual Doppler broadening due to the divergence of the molecular beam. As will be shown later the contribution to the linewidth caused by the finite lifetime of both electronically excited states is only of the order of 5 MHz. When allowing a larger molecular beam divergence the linewidth increased to 25 MHz (fwhm) and a SNR of 1000 or better was achieved on the lowest rotational transitions, by averaging over 30 samples (2 sec).

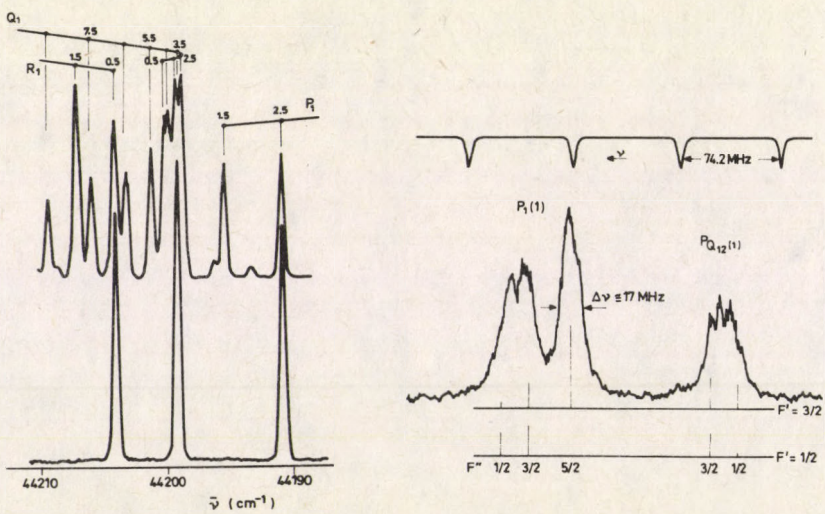

Fig. 3. Upper trace: normal LIF spectrum of the $A \leftarrow X$ transition induced by the pulsed laser. Lower trace: double resonance $E \leftarrow A$ fluorescence with the cw laser fixed on the $E \leftarrow A\,P_1(1)$ transition, whereas the pulsed laser is scanned. Only transitions that reach the labeled hyperfine level in the A-state are seen in double resonance. In both spectra the linewidth is determined by the bandwidth of the pulsed laser. The UV fluorescence (upper trace) is roughly a factor 100 more intense than the red fluorescence (lower trace)

Fig. 4. High resolution spectrum of the $E \leftarrow A\,Q_1(1)$ and $^PQ_{12}(1)$ transitions (see Fig. 2). The pulsed laser is kept fixed in frequency. The hyperfine structure in the $A\,^2\Sigma^+$ state is shown partly resolved. The linewidth of 17 MHz for the single resolved hyperfine component is mainly determined by the residual Doppler broadening due to the divergence of the molecular beam

Table I

Observed splittings (MHz) of rotational transitions in the $E^2\Sigma^+, v = 0 \leftarrow A^2\Sigma^+, v = 0$ band due to spin–rotation interaction in both coupled electronic states. The error given is equal to one standard deviation in the average of at least six measurements

Transitions	Obs. splitting [MHz]
$P_1(5) - P_2(5)$	431.0 ± 3.0
$P_1(9) - P_2(9)$	738.9 ± 3.0
$R_1(8) - R_2(8)$	656.9 ± 3.0
$R_1(9) - R_2(9)$	733.0 ± 3.0
$P_1(12) - P_2(12)$	970.8 ± 3.5
$R_1(11) - R_2(11)$	888.7 ± 6.0
$R_1(12) - R_2(12)$	973.9 ± 3.0
$P_1(14) - P_2(14)$	1132.7 ± 3.0
$R_1(13) - R_2(13)$	1018.0 ± 4.5
$P_1(15) - P_2(15)$	1178.5 ± 3.5
$R_1(14) - R_2(14)$	1142.8 ± 3.5
$R_1(15) - R_2(15)$	1183.8 ± 6.0
$R_1(16) - R_2(16)$	1281.2 ± 6.0

In the $P_1(1)$ transition the hyperfine structure due to the splitting in the $A^2\Sigma^+$ state can be clearly recognized. The vertical bars underneath the experimental curve indicate the positions and intensities of the individual hyperfine components. The horizontal bars contain transitions to either one of the two possible F' levels in the E-state. Their relative position is determined by the splitting between both F' levels. Positioning these bars exactly underneath each other means no hyperfine splitting in the E-state is assumed. From this and similar spectra an upper limit for the Fermi-contact term $b_f = b + c/3$ in the E-state of $b_f \leq 15$ MHz can be given.

3.3 ρ-doubling in $E^2\Sigma^+$, $v'=0$

A quite extensive series of measurements has been performed to determine the magnitude of the spin-rotation splitting in the $E^2\Sigma^+$, $v'=0$ state. This ρ-doubling can be determined from an accurate measurement of the splitting between a $P_1(N)$ and a $P_2(N)$ or between a $R_1(N)$ and a $R_2(N)$ line. To make these measurements possible both fine structure levels for a given quantum number N in the $A^2\Sigma^+$, $v'=0$ state must be populated. We chose to do this by pumping with the pulsed laser in the $A \leftarrow X$ R_1 and ${}^RQ_{21}$ branches. Both branches have equal line strengths and are induced simultaneously within the bandwidth of the laser. With the pulsed laser fixed on a certain $R_1(N)$ line, the cw laser was scanned to determine the splitting between lines from both fine structure levels in the $A^2\Sigma^+$, $v' = 0, N+1$ state. Only measurements up to $N'=17$ in the $E^2\Sigma^+$ state were possible because rotational levels with higher quantum numbers are less well populated in the molecular beam.

In Table I the observed splittings between different rotational transitions are given. Each value is the averaged result from at least 6 laser scans. The error given is one standard deviation. The splittings are measured between the centers of the more or less Gaussian envelopes of the rotational transitions, consisting of several unresolved hyperfine components. The hyperfine transitions with $\Delta F \neq \Delta J$ are weaker by a factor of J^2 than the $\Delta F = \Delta J$ transitions, which means only three hyperfine transitions will contribute for high J. As the position of the different hyperfine levels is not symmetrically distributed around the position of the unsplit fine structure level, this was corrected for. This correction is in most cases far within the experimental error.

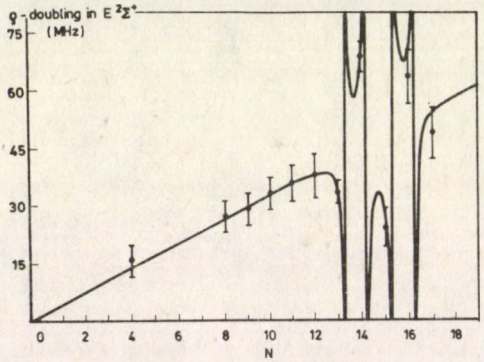

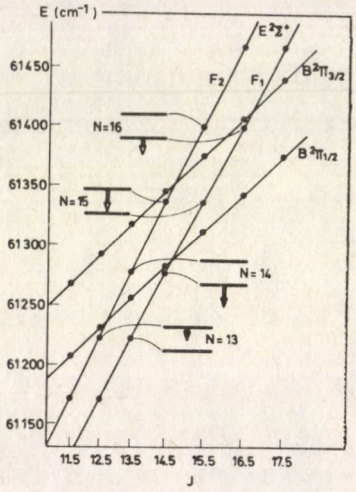

Fig. 5. Magnitude of the observed ρ-doubling in the $E\,^2\Sigma^+$, $v'=0$ state as a function of the rotation quantum number N. The best fit to the experimental points which includes the effect of the perturbation between the $E\,^2\Sigma^+$ state and the $B\,^2\Pi$ state is also given

Fig. 6. Total energy curves of the $E\,^2\Sigma^+$, $v'=0$ and the $B\,^2\Pi$, $v=17$ states. The crossing between $J=12.5$ and $J=16.5$ causes the observed perturbations. In the figure only the effect of the strongest interactions (i.e. interactions with those levels of the same J that are closest) are taken into account to explain quantitatively the deviations from a linear N-dependence as observed in Fig. 5

In Fig. 5 the ρ-doubling in the $E\,^2\Sigma^+$, $v=0$ state is given as a function of the rotational quantum number N. These values are obtained from the data presented in Table I after correcting for the ρ-doubling in the A-state as well as for the minor effect of the hyperfine splitting in the A-state, as discussed above. For low rotational quantum numbers the spin–rotation splitting increases linearly with N, as expected, but in the region $N=13 - N = 17$ the effect of a perturbation is seen. The small size of this perturbation explains why it escaped prior observation, and explicitly demonstrates the high resolution obtainable with the present technique. This perturbation is due to the $v=17$ level of the $B\,^2\Pi$ state which nearly coincides

with the $E\,^2\Sigma^+$, $v'=0$ state in this region, as shown in Fig. 6. Unfortunately, spectroscopic information on the $v=17$ level of the $B\,^2\Pi$ state is scarce; in VUV absorption studies transitions to this vibrational level are hidden under the $B'^2\Delta$, $v'=1 \leftarrow X\,^2\Pi$, $v''=0$ band and, of course, under the $E\,^2\Sigma^+$, $v'=0 \leftarrow X\,^2\Pi$, $v''=0$ band. Only a few rotational transitions of the $B\,^2\Pi_{1/2}$, $v'=17 \leftarrow X\,^2\Pi_{1/2}$, $v''=0$ band up to $N'=11$ in the upper state are given in the literature [7]. Using these transition frequencies and taking the known term values in the electronic ground state [8], we fitted the rotational structure of the $B\,^2\Pi$, $v'=17$ state, and extrapolated to higher rotational levels. Neither centrifugal distortion nor Λ-doubling corrections were included. A value of $A = 58\ \mathrm{cm}^{-1}$ was taken as an interpolation between the (deperturbed) spin-orbit splitting constants of neighbouring vibrational levels [9]. The accuracy of the thus obtained rotational energies of the B-state is estimated to be $\approx 1\ \mathrm{cm}^{-1}$.

It should be noted that the $E\,^2\Sigma^+$ state is a $4s\sigma$ Rydberg state, differing in two electron orbitals from the $\pi^3\pi^2$ $B^2\Pi$ valence state. Therefore, a coupling between these states via one-electron operators is not possible and formally, a perturbation between these states is configurationally forbidden. Only when a configuration interaction and/or two electron operators are taken into account such a perturbation can be explained [10].

In Fig. 6 we have schematically indicated how the magnitude of the ρ-doubling in the E-state is affected in the neighbourhood of a crossing. Although only the strongest interactions are taken into account in this simplified picture, it qualitatively explains the deviations observed in Fig. 5. In a more quantitative description the shift of the energy level E_i due to the interaction with levels of the same symmetry and with the same quantum number J positioned at an energy E_k is proportional to:

$$\sum_k \frac{H_{ik}^2}{E_i - E_k}. \tag{2}$$

This approximation is correct as long as $H_{ik} \ll |E_i - E_k|$, thus when the total shift of the energy levels is small compared with their unperturbed energy distance. In our case this approximation is certainly correct. The matrix element H_{ik} for a $a\,^2\Sigma^+ - {}^2\Pi$ (Hund's case a) interaction is given by Kovács [11] as:

$$\begin{aligned}
\langle {}^2\Sigma^+, J,\ N &= J \pm 1/2|H|{}^2\Pi_{3/2}, J\rangle = -2\eta\sqrt{(J-1/2)(J+3/2)},\\
\langle {}^2\Sigma^+, J,\ N &= J - 1/2|H|{}^2\Pi_{1/2}, J\rangle = \xi - 2\eta(J-1/2),\\
\langle {}^2\Sigma^+, J,\ N &= J + 1/2|H|{}^2\Pi_{1/2}, J\rangle = \xi + 2\eta(J+3/2).
\end{aligned} \tag{3}$$

In a least squares fit program the observed ρ-doubling in the $E\,^2\Sigma^+$ state shown in Fig. 5 is fit to an expression including both the expected $\gamma_E(N+1/2)$ dependence and the interaction with the $B\,^2\Pi$ state. For each J-level in the $B\,^2\Pi$ state the fraction of ${}^2\Pi_{1/2}$ and ${}^2\Pi_{3/2}$ character is calculated, and then the formulas (2) and (3) are used. The parameters that follow from the best fit, which is also given in Fig. 5 are:

$$\gamma_E = -(3.15 \pm 0.20)\text{MHz},$$
$$\eta = (2.08 \pm 0.15) \times 10^{-3}\text{cm}^{-1},$$
$$\xi = (7.9 \pm 4.4) \times 10^{-3}\text{cm}^{-1}.$$

The error is equal to one standard deviation. The physical origin of the two interaction parameters is such that the ratio ξ/η is equal to the ratio of the spin–orbit interaction constant A of the perturbing $^2\Pi$ state to the rotational constant B of the perturbed $E\,^2\Sigma^+$ state. Although the parameter ξ is not accurately determined we find a low value for the A-constant, which is typical for the NO Rydberg states. This Rydberg state must mix with the $B^2\Pi$ non-Rydberg state causing the observed perturbation. Recently de Vivie calculated the magnitude of the spin–orbit interaction between the $E\,^2\Sigma^+$ and the $B\,^2\Pi$ state for different values of the internuclear distance [12]. The small value of about 1.0 cm^{-1} she finds for this interaction must be multiplied with the vibrational overlap before it can be compared with our value of ξ [10]. A typical vibrational overlap of 1 % gives good agreement in sign and order of magnitude with the value of ξ we find.

4. Time evolution of the excited state populations

Time-resolved fluorescence both from the A-state and the E-state show directly the time evolution of the excited state populations. In Fig. 7 the UV fluorescence from the $N=1$ level in the $A\,^2\Sigma^+$, $v=0$ state following pulsed laser excitation on the $A \leftarrow X\,Q_1(1)$ transition is shown. From this curve a radiative lifetime of $\tau = (208 \pm 7)$ns is found for the $N=1$ level, in good agreement with literature values [4]. The relatively slow rise of the UV signal is due to a small retarding effect of the PMT we used of about 12 ns.

In order to determine the radiative lifetime of the E-state we used two pulsed lasers in a similar double resonance experiment. The NO ($A\,^2\Sigma^+$, $v=0$) molecules are now excited to the $E\,^2\Sigma^+$, $v=0$ state using several mJ of red radiation from a Nd-YAG laser pumped pulsed dye laser operating on Rhodamine B. The bandwidth of this laser was 0.5 cm^{-1} and the pulse-length approximately 6 ns. With the pulsed UV laser on the $A \leftarrow X\,Q_1(1)$ transition and the second pulsed laser on the $E \leftarrow A\,P_1(1)$ transition the time resolved $E \rightarrow A$ fluorescence as shown in Fig. 8 was obtained. The red laser was delayed by about 80 ns with respect to the UV laser. In this way a radiative lifetime of $\tau = (41 \pm 2)$ ns is found for the $E\,^2\Sigma^+$, $v=0$, $N=0$ level. Within the experimental error the same lifetime was found for different N values up to $N=10$.

Once the radiative loss rates out of both excited electronic states are known, the time-dependence of the E-state fluorescence in the pulsed-cw experiment can be quantitatively explained. The E-state is continuously coupled to the A-state by the cw laser. This coherent coupling lasts as long as there are molecules in the A-state interacting with the cw laser, typically on a time scale of a few hundred

ns. The coupling of the A-state to the electronic ground state is only present for 10 ns, which justifies the description of the $E - A$ system as an isolated two-level system. In this description we assume that at a given time zero a certain number of molecules are instantaneously pumped out of the ground state into the A-state. At this moment there are no molecules in the E-state yet. The two-level system described here is schematically given in Fig. 9. It is an interesting and uncommon system in that both levels undergo radiative decay. The decay rates γ_1 and γ_2 are the inverse of the lifetimes of the A-state and the E-state respectively, and are set equal to $\gamma_1 = 4.80\times10^6\ s^{-1}$ and $\gamma_2 = 2.44\times10^7\ s^{-1}$.

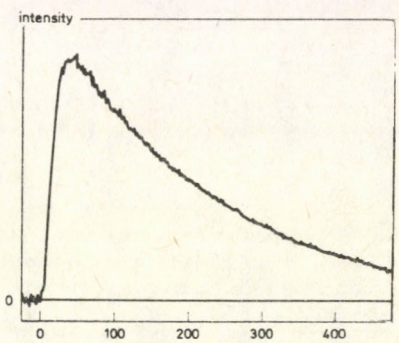

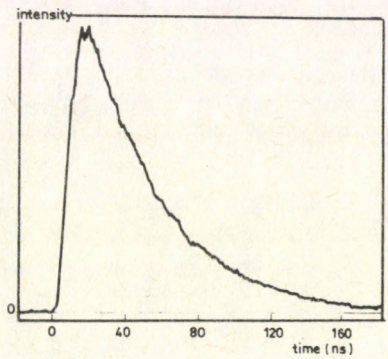

Fig. 7. Time resolved $A \rightarrow X$ fluorescence following pulsed laser excitation on the $A\,^2\Sigma^+$, $v' = 0 \leftarrow X\,^2\Pi$, $v''=0$ $Q_1(1)$ transition. A radiative lifetime of $\tau=(208\pm7)$ ns is found for the $A\,^2\Sigma^+$, $v'=0$, $N=1$ level

Fig. 8. Time resolved $E \rightarrow A$ fluorescence following pulsed laser excitation on the $E\,^2\Sigma^+$, $v = 0 \leftarrow A\,^2\Sigma^+, v = 0 P_1(1)$ transition. A radiative lifetime of $\tau=(41\pm2)$ ns is found for the lowest rovibrational level in the $E\,^2\Sigma^+$ state

The rate of spontaneous fluorescence from the excited level in the E-state back to the pumped level in the A-state is indicated by γ_r. This parameter is not known precisely. All of the time-resolved $E \rightarrow A$ state fluorescence measurements we discuss here are made with the cw laser set at the top of the Doppler-broadened profile of the single resolved $F' = 3/2 \leftarrow F'' = 5/2$ hyperfine component of the $E\,^2\Sigma^+$, $v' = 0, \leftarrow A\,^2\Sigma^+$, $v'' = 0$ $P_1(1)$ transition (see Fig. 4). For this special transition the rate γ_r is almost exactly 50 % of the total $E \rightarrow A$ emission rate, denoted by γ_{21} [13]. It is known from VUV absorption and emission studies that only about 50 % of the radiation absorbed in the $E \leftarrow X$ transition is emitted to the ground state again [14]. On the other hand the lifetime of the E-state we measure is too long to make predissociation very probable. As the $E \rightarrow A$ emission band is thought to be the strongest of the other radiative loss channels out of the E-state [28] an $E \rightarrow A$ fluorescence rate of $\gamma_{21} \approx 1/2\ \gamma_2$ is deduced. The time evolution of such a two-level system can be correctly described using the Bloch equations for the components ρ_{11}, ρ_{22}, $\tilde{\rho}_{12}$, $= \rho_{12}\exp(i\Delta\omega t)$ and $\tilde{\rho}_{21} = \rho_{21}\exp(-i\Delta\omega t)$ of the density matrix $\rho(t)$ as [15]:

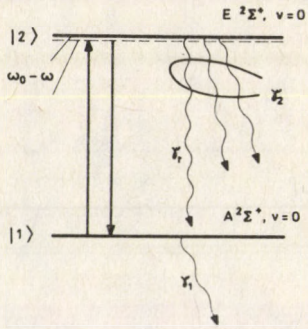

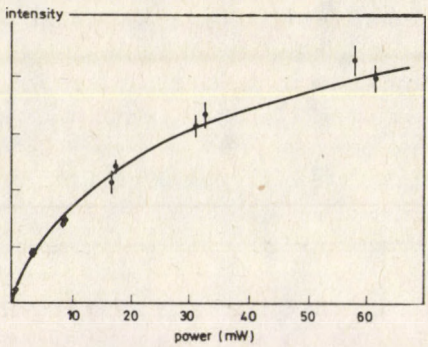

Fig. 9. Schematic representation of the two-level system described in the text. The total radiative loss rate out of the E-state is equal to γ_2 and only a small fraction of this radiation (rate γ_r) radiates back into the initially pumped level in the A-state. The radiative loss rate out of the A-state is γ_1. The solid arrows indicate the coherent (de)excitation with the narrow band cw laser, with a rate V

Fig. 10. Observed time-integrated $E \rightarrow A$ fluorescence intensity as a function of the applied cw laser power. The cw laser is set at the maximum of the Doppler broadened profile of the single resolved $F' = 3/2 \leftarrow F''=5/2$ hyperfine component of the $E \leftarrow A$ $P_1(1)$ transition (see Fig. 4). From the best fit to the experimental points the relation between the excitation rate V and the applied laser power is determined

$$
\begin{aligned}
\dot{\rho}_{11} &= \frac{1}{2}iV(\tilde{\rho}_{12} - \tilde{\rho}_{21}) + \gamma_r\rho_{22} - \gamma_1\rho_{11},\\
\dot{\rho}_{22} &= -\frac{1}{2}iV(\tilde{\rho}_{12} - \tilde{\rho}_{21}) - \gamma_2\rho_{22},\\
\dot{\rho}_{12} &= \frac{1}{2}iV(\rho_{11} - \rho_{22}) - (\frac{1}{2}\gamma_1 + \frac{1}{2}\gamma_2 - i\Delta\omega)\tilde{\rho}_{12},\\
\dot{\rho}_{21} &= -\frac{1}{2}iV(\rho_{11} - \rho_{22}) - (\frac{1}{2}\gamma_1 + \frac{1}{2}\gamma_2 + i\Delta\omega)\tilde{\rho}_{21}. \qquad (4)
\end{aligned}
$$

In these formulas V is the excitation rate, which is proportional to the square-root of the applied cw laser power, and $\Delta\omega = \omega - \omega_0$ is the detuning of the laser frequency ω with respect to the transition frequency ω_0. The bandwidth of the cw laser (0.3 MHz) is much smaller than the natural linewidth of the NO $E \leftarrow A$ transition ($\approx$ 4.7 MHz). Therefore the laser profile is assumed to be infinitely narrow. The above system of four coupled differential equations can be solved analytically if $\gamma_r = 0$ [15]. As pointed out above, in our case $\gamma_r \approx 1/4\ \gamma_2$, of the same order as γ_1, and certainly cannot be neglected. Therefore, we solved the equations (4) numerically, with the initial conditions $\rho_{11}(0) = \rho_{11}(0, \Delta\omega)$, $\rho_{22}(0) = 0$, $\tilde{\rho}_{12}(0) = \tilde{\rho}_{21}(0) = 0$. The component $\rho_{22}(t)$ describes the time evolution of the E-state population, which is the quantity we determined experimentally.

First, the Eqs (4) were used to fit the measured power dependence of the total (time integrated) $E \rightarrow A$ state fluorescence, as shown in Fig. 10. From this fit the

excitation rate V, which is in fact the only unknown parameter in our problem, can be accurately determined, for a given laser power.

For the numerical solution of $\rho_{22}(t)$ from Eq. (4) the finite Doppler-width has to be taken into account. This is done by adding the solutions for $\rho_{22}(t)$ for different values of $\Delta\omega$, i.e., by summing over different velocity groups. The number of molecules in each velocity group ($\rho_{11}(0, \Delta\omega)$) is weighted by a Gaussian envelope with a 25 MHz half-width. A typical time resolved $E \rightarrow A$ fluorescence decay curve is shown in Fig. 11. This curve is an average over about 100 samples, with the cw laser set at the maximum of the line. The simulation following equations (4) is given as curve I in the same Figure. The agreement between theory and experiment is excellent, especially when one considers that no parameters are fitted. Only the vertical scale of the calculated curve was adjusted. The slight deviations between theory and experiment can be explained by the approximations we made. From the theoretical curve we deduce that in the peak, around 65 ns, as much as 17 % of all the molecules initially in the probed hyperfine level of the $A\,^2\Sigma^+$ state have been excited to the $E\,^2\Sigma^+$ state by the cw laser. This seemingly low value is mainly due to the relatively large Doppler-width; the velocity group that is exactly in resonance with the cw laser is for almost 40 % excited.

Burshtein and Storozhev have shown recently [15] that, when $\gamma_r = 0$, the transition process has a typical "dephasing time" τ_{dp} given by $\tau_{dp} = 2/(\gamma_2 - \gamma_1)$. In our case this should mean that phase-relaxation takes place on a time scale of 100 ns. Therefore, especially at short times, the quantum-mechanical description will be necessary. This is shown explicitly in Fig. 11 by curve II which is the solution of the so-called balance or master equation treatment for the system. The master equations are obtained from the Bloch equations by setting $\tilde{\rho}_{21} = \tilde{\rho}_{12} = 0$ [15]. It is clear that the master equations will describe the situation correctly only when phase-relaxation has taken place. The following set of master equations is found:

$$\begin{aligned} \dot{\rho}_{11} &= -(W + \gamma_1)\rho_{11} + (W + \gamma_r)\rho_{22}, \\ \dot{\rho}_{22} &= W\rho_{11} - (W + \gamma_2)\rho_{22}. \end{aligned} \tag{5}$$

The "classical" (non-coherent) excitation rate W is proportional to the applied laser power that is related to the excitation rate V. An advantage of the Eqs (5) is that an exact analytical solution can be given. Starting with the same initial conditions as before we find:

$$\rho_{22}(t) = \frac{W}{(\lambda_+ + \lambda_-)}(e^{\lambda_+ t} - e^{\lambda_- t})\rho_{11}(0, \Delta\omega),$$

with

$$\lambda_\pm = -\left(W + \frac{\gamma_1 + \gamma_2}{2}\right) \pm \sqrt{\left(\frac{\gamma_1 - \gamma_1}{2}\right)^2 + W(W + \gamma_r)}. \tag{6}$$

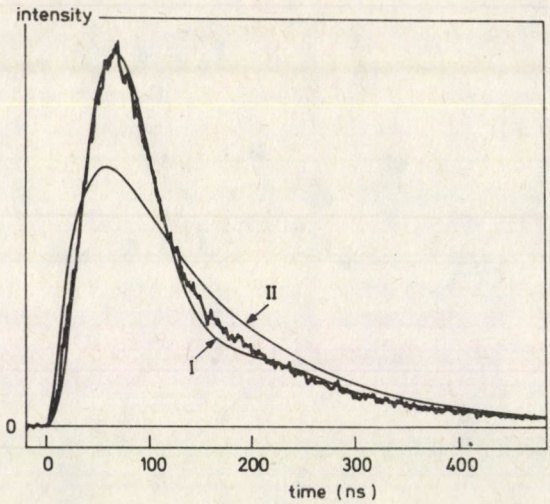

Fig. 11. Time resolved $E \rightarrow A$ fluorescence following excitation with the cw laser on the single resolved $F = 3/2 \leftarrow F=5/2$ hyperfine component of the $E \leftarrow A$ $P_1(1)$ transition. A cw laser power of 58 mW has been used. This simulation following the Bloch equations (curve I) as well as the experimental curve clearly show the effect of an oscillation around the solution following the master equation description (curve II) of the system

The master equation curve (curve II) is scaled relative to the Bloch equation curve (curve I), using the same excitation rate V. Now a maximum excitation of nearly 12 % is obtained. It is clear from Fig. 11 that both the experimental curve and the exact theoretical curve (curve I) show the effect of Rabi oscillations, which cannot be explained with the master equations.

At higher laser powers strong oscillations are predicted. Although the finite Doppler width tends to smear out these oscillations, some additional maxima should be observable under the same experimental conditions, using only a slightly higher laser power. This is shown in Fig. 12, which shows the calculated time dependence of the $E \rightarrow A$ fluorescence when about 4 times higher cw laser power is used.

5. Conclusions

It has been shown experimentally that the combination of a high power pulsed laser with a narrow bandwidth cw laser makes a high resolution study of highly excited electronic states possible. The signal-to-noise ratio on the double resonance signal is shown to be very good. The use of a pulsed molecular beam and a more efficient detection scheme for the excited state population will provide further improvements. This suggests that this method has a very general applicability, also for the study of electronic states of less abundant transient species. From the time-resolved fluorescence curves the lifetimes of the excited states and the corresponding

transition dipole moment can be determined. The observed Rabi oscillations nicely demonstrate the coherence properties of a two-level system with radiative losses.

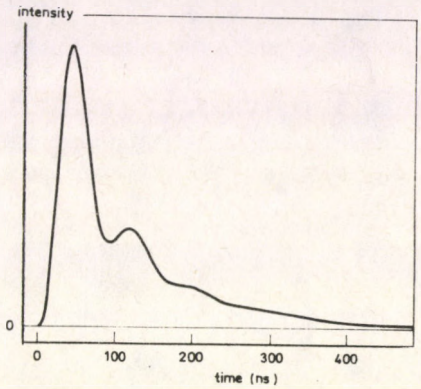

Fig. 12. Calculated time dependent $E \rightarrow A$ fluorescence when 250 mW of cw laser power is used. Only the correct solution, following out of the Bloch equations, is shown

Acknowledgements

We wish to thank dr. S. Stolte, Profs. A. Dymanus and J. Reuss for helpful and stimulating discussions, and Prof. D. H. Parker for a careful reading of the manuscript. The help of dr. Freek Keijzer in the experiment determining the lifetime of the E-state using two pulsed lasers is gratefully acknowledged. This work has been supported by the Stichting voor Fundamenteel Onderzoek der Materie (FOM) and has been made possible by financial support from the Nederlandse Organisatie voor Wetenschappelijk Onderzoek. (NWO).

References

1. See for instance: W. Ubachs, J. J. ter Meulen and A. Dymanus, Can. J. Phys., *62*, 1374, 1984; G. Meijer, W. Ubachs, J.J. ter Meulen and A. Dymanus, Chem. Phys. Lett., *139*, 603, 1987.
2. C. Amiot and J. Verges, Physica Scripta, *26*, 422, 1982.
3. S. Gerstenkorn and P. Luc, Atlas du spectroscopie d'absorption de la molecule d'iode, CNRS, Paris, 1978; Rev. Phys. Appl. *14*, 791, 1979.
4. L. G. Piper and L. M. Cowles, J. Chem. Phys., *85*, 2419, 1986.
5. A. Timmermann and R. Wallenstein, Opt. Comm., *39*, 239, 1981.
6. T. Bergeman and R. N. Zare, J. Chem. Phys., *61*, 4500, 1974.
7. A. Lagerqvist and E. Miescher, Helv. Ph. Acta, *31*, 221, 1958.
8. H. Zacharias, private communication.
9. A. Lagerqvist and E. Miescher, Can. J. Phys., *44*, 1525, 1966.
10. Ch. Jungen and E. Miescher, Can. J. Phys., *46*, 987, 1968.
11. I. Kovács, Rotational Structure in the Spectra of Diatomic Molecules, Adam Hilger Ltd., London, 1969.
12. Regina de Vivie, Ph.D. Thesis, Bonn, 1987.
13. R. W. Nicholls, J. Res. Nat. Bur. Stand., *68*, 535, 1964.
14. J. A. Guest and L. C. Lee, J. Phys. B: At. Mol. Phys., *14*, 3401, 1981.
15. A. I. Burshtein and A. V. Storozhev, Chem Phys., *119*, 1, 1988.

Acta Physica Hungarica 67 (1–2), pp. 123–134 (1990)

A STUDY OF PULSATILE BLOOD FLOW IN A TUBE WITH PULSATING WALLS

J. K. MISRA and R. S. CHAUHAN

Department of Mathematics
I. I. T. Kanpur, India

(Received 15 May 1986)

A mathematical model for pulsatile blood flow in a small diameter tube whose walls pulsate is analysed. Blood is modelled as a two layered fluid by considering core fluid as micro-polar covered by a very thin cell free layer of Newtonian fluid.The effects of various parameters on the flow rate and wall shearing stress are computed and discussed.

Nomenclature

J	micro-inertia coefficient
p	pressure
Q	flow rate
Q_c	flow rate in core-region
Q_p	flow rate in peripheral layer
r	radial co-ordinate
t	time
u_1	radial component of velocity in core-region
u_2	radial component of velocity in peripheral layer
v_1	axial component of velocity in core-region
v_2	axial component of velocity in peripheral layer
w	rotational velocity of cells
z	axial co-ordinate
ρ	density of the fluid
ν	viscosity gradient of rotation
μ_S	viscosity of suspending media (plasma)
μ_R	relative rotational viscosity
ω	frequency
τ	shearing stress

1. Introduction

Pulsatile flow of blood in the cardiovascular system stems from the cyclic nature of the ventricular ejection. The sudden ejection of blood into aorta from the ventricle of the heart produces a wave of increased pressure and slight distention of

vessels which change their diameter. Pulsatile blood flow in a small blood vessel is studied primarily for its effects on flow and pressure relations. The pulsatile character of microcirculation was first examined by Landis [1]. In a number of recent investigations, it is reported that pulsatile flow exists throughout the microcirculation [2–4]. But most of the studies on pulsatile blood flow in the microcirculation are confined to flow through rigid tubes only [5–9]. It is remarkable in all these studies, the presence of cell free plasma layer near the wall which plays a significant role in a small diameter tube, is neglected [10].

In the present paper, we therefore aim to study the pulsatile blood flow in a distensible tube. Here, blood is modelled as a two layered fluid by representing core fluid as micropolar [11]. The problem is solved by using an iterative technique in three steps [12]. First, the steady state fully developed solution through rigid tube is obtained. In the second step, this steady flow is generalized to pulsatile flow in rigid tube and finally, the rigid tube solution is generalized to pulsatile flow in a pulsating tube.

2. Mathematical formulation

We shall consider the axis-symmetric pulsatile blood flow in a tube whose radius varies as [13]

$$R_1 = R_0(1 + \varepsilon_1 \sin \omega_1 t), \quad \varepsilon_1 \ll 1, \tag{2.1}$$

where R_0 is the mean radius of tube and ω_1 is the characteristic frequency of wall oscillations.

The governing equations for the fluid flow in different regions are as follows: for the core-region $(0 \leq r \leq R)$

$$(\mu_S + \mu_R)\left[\frac{1}{r}\frac{\partial}{\partial r}\left(r\frac{\partial v_1}{\partial r}\right) + \frac{\partial^2 v_1}{\partial z^2}\right] + \mu_R \frac{1}{r}\frac{\partial}{\partial r}(r\omega) = \frac{\partial p}{\partial z} + \rho\left(\frac{\partial v_1}{\partial t} + v_1\frac{\partial v_1}{\partial z}\right), \tag{2.2a}$$

$$\nu\frac{\partial}{\partial r}\left[\frac{1}{r}\frac{\partial}{\partial r}(rw)\right] - \mu_R\frac{\partial v_1}{\partial z} - 2\mu_R w + \nu\frac{\partial^2 w}{\partial z^2} = \rho J\left(\frac{\partial w}{\partial t} + v_1\frac{\partial w}{\partial z}\right), \tag{2.2b}$$

$$\frac{1}{r}\frac{\partial}{\partial r}(ru_1) + \frac{\partial v_1}{\partial z} = 0 \tag{2.3}$$

for the peripheral layer $(R \leq r \leq R_1)$

$$\mu_S\left[\frac{1}{r}\frac{\partial}{\partial r}\left(r\frac{\partial v_2}{\partial r}\right) + \frac{\partial^2 v_2}{\partial z^2}\right] = \frac{\partial p}{\partial z} + \rho\left[\frac{\partial v_2}{\partial t} + v_2\frac{\partial v_2}{\partial z}\right] \tag{2.4}$$

$$\frac{1}{r}\frac{\partial}{\partial r}(ru_2) + \frac{\partial v_2}{\partial z} = 0. \tag{2.5}$$

The boundary conditions of the problem are

$$\left.\begin{aligned} &u_1 = 0, \frac{\partial v_1}{\partial r} = 0, w = 0 \text{ at } r = 0, \\ &u_1 = u_2, v_1 = v_2, \tau_1 = \tau_2, \frac{1}{r}\frac{\partial}{\partial r}(rw) = 0 \text{ at } r = R, \\ &u_2 = \frac{dR_1}{dt}, v_2 = 0 \text{ at } r = R_1, \end{aligned}\right\} \tag{2.6}$$

where τ_1 and τ_2 are stresses in the two regions.

3. Method of solution

Step 1: steady flow in rigid tube

For steady flow through a rigid tube, equations (2.2) to (2.6) become: for the core-region:

$$(\mu_S + \mu_R)\left[\frac{1}{r}\frac{\partial}{\partial r}\left(r\frac{\partial v_1}{\partial r}\right)\right] + \mu_R\frac{1}{r}\frac{\partial}{\partial r}(rw) = \frac{\partial p}{\partial z}, \tag{3.1a}$$

$$\nu\frac{\partial}{\partial r}\left[\frac{1}{r}\frac{\partial}{\partial r}(rw)\right] - 2\mu_R w = 0, \tag{3.1b}$$

$$\frac{\partial}{\partial r}(ru_1) = 0, \tag{3.2}$$

for the peripheral layer

$$\mu_S\left[\frac{1}{r}\frac{\partial}{\partial r}\left(\frac{r\partial v_2}{\partial r}\right)\right] = \frac{\partial p}{\partial z}, \tag{3.3}$$

$$\frac{\partial}{\partial r}(ru_2) = 0 \tag{3.4}$$

with conditions

$$\left.\begin{aligned} &u_1 = 0, \frac{\partial v_1}{\partial r} = 0, w = 0 \text{ at } r = 0, \\ &u_1 = u_2, v_1 = v_2, \tau_1 = \tau_2, \frac{1}{r}\frac{\partial}{\partial r}(rw) = 0 \text{ at } r = R, \\ &u_2 = 0, v_2 = 0 \text{ at } r = R_1, \end{aligned}\right\} \tag{3.5}$$

The solutions of these equations are

$$v_1(r) = -\frac{1}{4\mu_S}\frac{\partial p}{\partial z}\left[(R_1^2 - R^2) + \mu_1(R^2 - r^2) - \frac{\mu_1\mu_2}{\lambda^2}\frac{I_0(\lambda R) - I_0(\lambda r)}{I_0(\lambda R)}\right], \quad (3.6)$$

$$v_2(r) = -\frac{1}{4\mu_S}\frac{\partial p}{\partial z}(R_1^2 - r^2), \quad (3.7)$$

where $\mu_1 = \frac{2\mu_S}{2\mu_S+\mu_R}$, $\mu_2 = \frac{2\mu_R}{\mu_S+\mu_R}$, $\lambda^2 = \frac{\mu_2\mu_S}{\mu_1\nu}$ and I_n is modified Bessel function of order n.

Step 2: unsteady pulsatile flow in rigid tube

For pulsatile flow, the pressure gradient will be function of time only since the flow of incompressible fluid in rigid tube exhibits no local pressure gradients. According to Ariman et al [6], the pressure gradient can be expressed as

$$-\frac{\partial p}{\partial z} = p(t) = p_m(1 + \varepsilon_2 \sin\omega_2 t), \quad (3.8)$$

where $\varepsilon_2 = \frac{p_S}{p_m}$, p_m is the constant mean pressure gradient and p_S is the amplitude of sinusoidal pressure gradient.

Since there are no local pressure gradients different from the overall gradient and pressure is the only driving force in the fluid, it follows that the velocity will be a function of r and t only. Hence, the equation of motion for peripheral layer (2.4) after integration becomes

$$v_2(r,t) - \frac{p(t)}{4\mu_S}(R_1^2 - r^2) - \frac{\rho}{\mu_S}\int_r^{R_1}\frac{1}{r_2}\left(\int_R^{r_2} r_1\frac{\partial v_2}{\partial t}dr_1\right)dr_2. \quad (3.9)$$

This is an operator equation where the first term is the classical parabolic velocity profile, and we use it as the initial iterate. Thus the initial value of $v_2(r,t)$ is

$$v_2^0(r,t) = \frac{p(t)}{4\mu_S}(R_1^2 - r^2), \quad (3.10)$$

in the following operator equation

$$v_2^{n+1}(r,t) = \frac{p(t)}{4\mu_S}(R_1^2 - r^2) - \frac{\rho}{\mu_S}\int_r^{R_1}\frac{1}{r_2}\left(\int_R^{r_2} r_1\frac{\partial v_2^n}{\partial t}dr_1\right)dr_2. \quad (3.11)$$

The first iteration yields the following expression

$$v_2^1(r,t) = \frac{p(t)}{4\mu_S}(R_1^2 - r^2) - \frac{\rho p'(t)}{64\mu_S^2}\left[(R_1^2 - r^2)^2 + 2R_1^2(R_1^2 - r^2) + 4R^2(R^2 - 2R_1^2)\ln\frac{R_1}{r}\right], \tag{3.12}$$

where $p'(t) = \frac{dp(t)}{dt}$.

Similarly the operator equation for core-region can be written as

$$v_1(r,t) = \frac{p(t)}{4\mu_S}\left[(R_1^2 - R^2) + \mu_1(R^2 - r^2) - \frac{\mu_1\mu_2}{\lambda^2}\frac{I_0(\lambda R) - I_0(\lambda r)}{I_0(\lambda R)}\right] - \frac{\rho}{\mu_S + \mu_R}\int_r^R \frac{1}{r_4}\left(\int_0^{r_4} r_3 \frac{\partial v_1}{\partial t} dr_3\right) dr_4. \tag{3.13}$$

The first iterate of this operator equation yields the following expression for core region velocity profile

$$v_1^1(r,t) = \frac{p(t)}{4\mu_S}\left[(R_1^2 - R^2) + \mu_1(R^2 - r^2) - \frac{\mu_1\mu_2}{\lambda^2}\cdot\frac{I_0(\lambda R) - I_0(\lambda r)}{I_0(\lambda R)}\right] - \frac{\rho p'(t)}{64\mu_S}\left[\frac{1}{\mu_S + \mu_R}\left\{\mu_1(R^2 - r^2)^2 + \left(4R_1^2 + (2\mu_1 - 4)R^2 - 4\frac{\mu_1\mu_2}{\lambda^2}\right)\right.\right.$$
$$\times (R^2 - r^2) + \frac{16\mu_1\mu_2}{\lambda^4}\cdot\frac{I_0(\lambda R) - I_0(\lambda r)}{I_0(\lambda R)}\Big\} - \frac{1}{\mu_S}\Big\{(R_1^2 - R^2)(3R_1^2 - R^2)$$
$$\left.\left. + 4R^2(R^2 - 2R_1^2)\ln\frac{R_1}{R}\Big\}\right]. \tag{3.14}$$

Step 3: pulsatile flow in pulsating tube

When the tube walls are pulsating, local pressure gradients develop and consequently the pressure gradient will be a function of both z and t. Hence,

$$-\frac{\partial p}{\partial z} = F(z,t) = zp(t). \tag{3.15}$$

But the spatial gradient of pressure is the driving force in the fluid. If it changes from point to point, the velocity certainly must change. Hence, for a pulsating tube the velocity is no longer the same in each cross section and it will vary with z also.

The operator equation for peripherial layer fluid, in this case, will take the

following form

$$v_2(r,z,t) = \frac{zp(t)}{4\mu_S}(R_1^2 - r^2) - \frac{\rho}{\mu_S}\int_r^{R_1}\frac{1}{r_2}\left(\int_R^{r_2} r_1 \frac{\partial v_2}{\partial t}dr_1\right)dr_2$$
$$- \frac{\rho}{\mu_S}\int_r^{R_1}\frac{1}{r_2}\left(\int_R^{r_2} r_1 v_2 \frac{\partial v_2}{\partial z}dr_1\right)dr_2$$
$$+ \int_r^{R_1}\frac{1}{r_2}\left(\int_R^{r_1} r_1 \frac{\partial^2 v_2}{\partial z^2}dr_1\right)dr_2. \tag{3.16}$$

We iterate the operator on the right, which contains now z as well as t derivatives. It should be noted that pulsatile flow in a pulsating tube is treated as a modification of pulsatile flow in a rigid tube rather than as a modification of stationary flow in a rigid tube. So the initial iterate for the present case will be a corresponding solution for pulsatile flow in a rigid tube (obtained in Step 2) with the pressure gradient $p(t)$ replaced by $F(z,t)$.

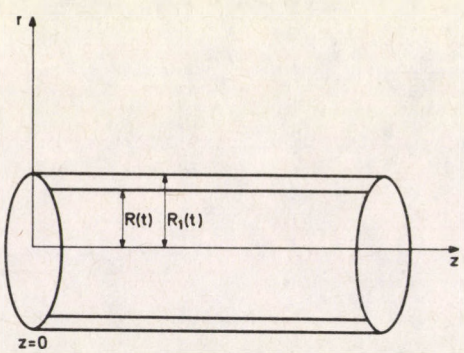

Fig. 1. Flow geometry

Assuming the amplitude of wall motion small, one correction of rigid tube flow velocities might be sufficient. Thus the velocity profile in the peripheral layer region is

$$v_2^1(r,z,t) = zv_2^1(r,t) + z\Big[A_2(1-\alpha_1^2) + A_3(1-\alpha_1^4) + A_4(1-\alpha_1^6)$$
$$+ \frac{2K_7 - K_8}{16}(1-\alpha_1^8) - \frac{K_7}{100}(1-\alpha_1^{10}) + A_6 + A_5 \ln\frac{1}{\alpha}$$

$$+\frac{A_1\alpha_1^2}{4}\left\{4K_8(\alpha_1^2-4)+\frac{K_7A_1}{8}+\frac{K_7(\alpha_1^4-9\alpha_1^2)}{18}\right\}$$
$$\times\ln\frac{1}{\alpha_1}+\frac{A_1\alpha_1^2}{8}\left\{4K_8(\alpha_1^2-8)+3K_7\ln\frac{1}{\alpha}+\frac{A_1K_7}{8}\left(\ln^2\frac{1}{\alpha_1}+1\right)\right\}\Bigg], \tag{3.17}$$

where $\alpha=\frac{r}{R}, \alpha_1=\frac{r}{R_1}$ and other parameters involved are given in the Appendix.

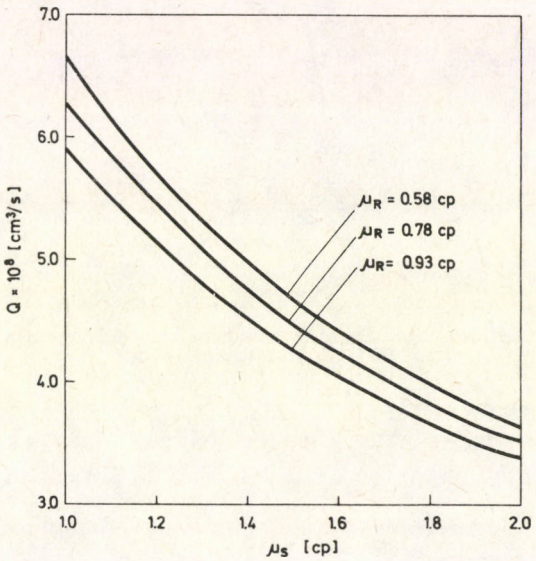

Fig. 2. Variation of the flow rate with peripheral layer viscosity μ_S for different values of μ_R

Similarly the expression for velocity profile in the core-region is

$$v_1^1(r,z,t)=zv_1^1(r,t)-\frac{\rho z}{\mu_S+\mu_R}\Bigg[X_1(1-\alpha^2)+X_2(1-\alpha^4)+X_3(1-\alpha^6)$$
$$+\frac{R^8}{8}\left\{\frac{\mu_1K_{10}}{4}-K_3^2\mu_1(R_1^2+(\mu_1-1)R^2)\right\}(1-\alpha^8)$$
$$+\frac{K_3^2\mu_1^2R^{10}}{100}(1-\alpha^{10})+X_4\{I_0(\lambda R)-I_0(\lambda r)\}+X_5\{RI_1(\lambda R)-rI_1(\lambda r)\}$$
$$+X_6\{R^2I_2(\lambda R)-r^2I_2(\lambda r)\}+\frac{12K_3K_4\mu_1}{\lambda^3}\{R^3I_3(\lambda R)-r^3I_3(\lambda r)\}$$
$$-\frac{K_4^2}{4}\{R^2I_1^2(\lambda R)-r^2I_1^2(\lambda r)-R^2I_0(\lambda R)I_2(\lambda R)+r^2I_0(\lambda r)I_2(\lambda r)\}$$
$$-\frac{2K_3K_4\mu_1}{\lambda^2}\{R^4I_2(\lambda R)-r^4I_2(\lambda r)\}\Bigg]-z\left[K_6B_1+4K_8(B_2-B_3)+K_7B_4\right]. \tag{3.18}$$

The flow rate is

$$Q = Q_c + Q_p, \tag{3.19}$$

where

$$Q_c = 2\pi \int_0^R r v_1^1(r, z, t) dr$$

and

$$Q_p = 2\pi \int_R^{R_1} r v_2^1(r, z, t) dr.$$

The wall shearing stress is

$$\tau_w = -\mu_S \left. \frac{\partial v_2^1(r, z, t)}{\partial r} \right|_{r=R_1}. \tag{3.20}$$

4. Results and discussion

Using the parameter values $\mu_S = 1.2$cp, $\mu_R = 0.98$cp, $\nu = 12 \times 10^{-8}$gm cm/s, $\varepsilon_1 = 0.1, \varepsilon_2 = 0.1, z = 0.1$cm, $R_0 = 40\mu$m, $\beta = 0.95$, the flow rate Q and wall shearing stress τ_w have been computed and the results are presented in Figs 2-4.

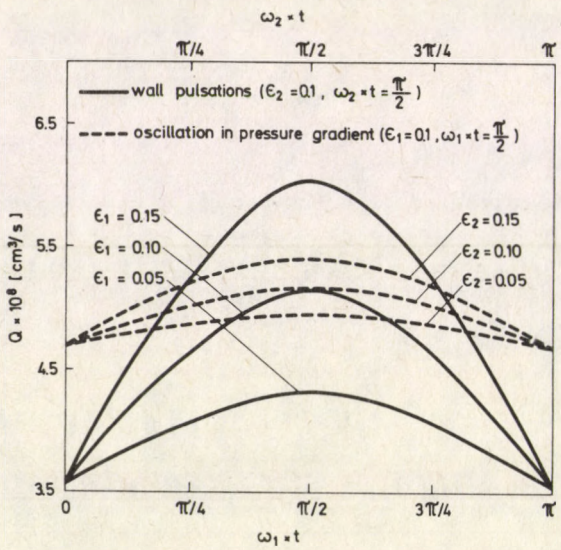

Fig. 3. Variation of the flow rate with phase angles for different values of ε_1 and ε_2

Fig. 2 shows that the flow rate decreases tremendously as we increase the peripheral layer viscosity. It is also observed that an increase in the rotational viscosity decreases the flow rate considerably.

Fig. 3 shows the effect of wall pulsation and oscillation in pressure gradient on the flow rate. It is noted that the effect of wall pulsations is more significant as compared to corresponding oscillations in pressure gradient. It is also observed that the flow rate increases for the phase angles lying between 0 to $\pi/2$ and decreases symmetrically for the phase angles between $\pi/2$ to π. The effect of phase angle becomes more important as we increase the parameter ε_1.

Fig. 4 shows the effect of wall pulsation on wall shearing stress. It is seen that the wall shearing stress increases when the phase angle lies between 0 to $\pi/2$ and decreases symmetrically for a phase angle lying between $\pi/2$ to π. The effect of ε_1 on wall shearing stress is similar as on the flow rate.

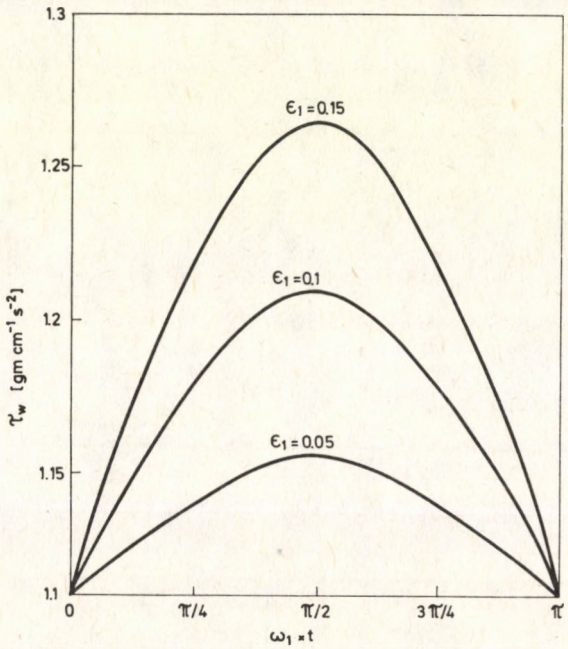

Fig. 4. Variation of the wall shearing stress with phase angle for different values of ε_1

Acknowledgement

Authors are thankful to Prof. P. Singh for his constructive suggestions.

Appendix

$$\beta = \frac{R}{R_1},$$

$$A_1 = \beta^2(\beta^2 - 2),$$

$$A_2 = -9K_6 - \frac{K_7}{128}(A_1^2 + 48A_1 - 288) + 3K_8,$$

$$A_3 = \frac{9}{2}K_6 + \frac{K_7}{16}(A_1 + 24) - \frac{7K_8}{4},$$

$$A_4 = -K_6 - \frac{K_7}{216}(A_1 + 123) + \frac{5K_8}{9},$$

$$A_5 = U_1K_6 - K_7\left\{-U_3 + \frac{A_1U_4}{72} - \frac{\beta^2A_1^2}{32}\ln\frac{1}{\beta}\left(\ln\frac{1}{\beta} + 1\right) - \frac{A_1^2}{64}\beta^2\right\} + 4K_8U_2 + A_1K_8\beta^2\left\{\beta^2 - 4 + 4(\beta^2 - 2)\ln\frac{1}{\beta}\right\},$$

$$A_6 = \frac{A_1}{8}\left(28K_8 - 3K_7\ln\beta - \frac{A_3K_7}{8}\right),$$

$$B_1 = \frac{11}{2} - \frac{\beta^2}{2}(18 - 9\beta^2 + 2\beta^4) - U_1\ln\frac{1}{\beta},$$

$$B_2 = -0.4357638 - U_2\ln\frac{1}{\beta} + \beta^2\left(\frac{3}{4} - \frac{7}{16}\beta^2 + \frac{5}{36}\beta^4 - \frac{\beta^6}{64}\right),$$

$$B_3 = \frac{A_1}{8}\left\{8\beta^2(\beta^2 - 2)\ln^2\frac{1}{\beta} + 4\beta^2(\beta^2 - 4)\ln\frac{1}{\beta} + \beta^2(\beta^2 - 8) + 7\right\},$$

$$B_4 = -3.2538889 + \beta^2\left(\frac{9}{4} + \frac{3}{2}\beta^2 - \frac{11}{18}\beta^4 + \frac{1}{8}\beta^6 - \frac{\beta^8}{100}\right) - \left[U_3 - \frac{A_1}{72}\{U_4 - \beta^4(\beta^2 - 9) - 27\}\right]\ln\frac{1}{\beta} + \frac{A_1}{512}\{137 - \beta^2(162 - 27\beta^2 + 2\beta^4)\} + \frac{A_1^2}{32}\left\{\frac{3}{4} - \frac{\beta^2}{4} - \beta^2\left(\ln\frac{1}{\beta} + 1\right)\ln^2\frac{1}{\beta} - \frac{\beta^2}{2}\ln\frac{1}{\beta} - \frac{\beta^2}{2}\left(\ln\frac{1}{\beta} + 1\right)^2\right\},$$

$$B_5 = K_5\left\{(1 - \beta^2)(3 - \beta^2) + 4A_1\ln\frac{1}{\beta}\right\},$$

$$K_1 = \frac{p(t)}{4\mu_S},$$

$$K_2 = \frac{\mu_1\mu_2}{\lambda^2 I_0(\lambda R)},$$

$$K_3 = \frac{\rho p'(t)}{64\mu_S(\mu_S + \mu_R)},$$

$$K_4 = \frac{K_2}{\lambda^2}(16K_3 + K_1\lambda^2),$$

$$K_5 = \frac{\rho R_1^4 p'(t)}{64\mu_S^2},$$

$$K_6 = \frac{\rho R_1^6 K_1^2}{36\mu_S},$$

$$K_7 = \frac{\rho^3 R_1^{10} p'^2(t)}{16\mu_S^5},$$

$$K_8 = \frac{\rho R_1^4 K_1 K_5}{2\mu_S},$$

$$K_9 = \frac{4\mu_1\mu_2}{\lambda^4}(4 - \lambda^2 R^2),$$

$$K_{10} = K_3\mu_1\left(K_1 + \frac{4K_3\mu_2}{\lambda^2}\right),$$

$$N_1 = \frac{K_1\mu_1}{4}\{K_1(\mu_1 + 2(1-\beta^2)R_1^2) - 2B_8\} + 2K_3^2 R_1^2(1-\beta^2)K_9,$$

$$N_2 = \frac{K_1 K_2}{\lambda}[K_1(\mu_1 R^2 + (1-\beta^2)R_1^2) - B_8 - K_1 K_2 I_0(\lambda R)],$$

$$N_3 = \frac{2K_2}{\lambda^6}\Big[\mu_1(\lambda^4 K_1^2 + 8K_3^2\mu_2) + 4K_3\lambda^2\{K_1(4\mu_1 - \lambda^2\mu_1 R^2$$

$$- (1-\beta^2)\lambda^2 R_1^2 + \mu_1\mu_2) - 16(K_3(1-\beta^2)R_1^2 + \mu_1 R^2)\}\Big],$$

$$N_4 = -\frac{2K_3 K_4}{\lambda}\{K_9 + R^2(4(1-\beta^2)R_1^2 + 3\mu_1 R^2)\},$$

$$N_5 = \frac{\mu_1 K_9 K_3^2}{3},$$

$$N_6 = \frac{2K_3}{\lambda^2}[\mu_1\mu_2 K_1 - \lambda^2(B_5 + K_1\mu_1 R^2 + K_1(1-\beta^2)R_1^2)],$$

$$U_1 = 6\beta^2(\beta^4 - 3\beta^2 + 3),$$

$$U_2 = \frac{\beta^2}{24}(3\beta^6 - 20\beta^4 + 42\beta^2 - 36),$$

$$U_3 = \frac{\beta^2}{30}(3\beta^8 - 30\beta^6 + 110\beta^4 - 180\beta^2 + 135),$$

$$U_4 = -\beta^2\left(\beta^4 - 9\beta^2 + 27 + 6(\beta^2 - 3)^2 \ln\frac{1}{\beta}\right),$$

$$X_1 = \frac{R^2}{4}\Big[N_6 K_9 + K_1^2\left\{(1-\beta^2)^2 R_1^4 - \frac{\mu_1^2\mu_2^2}{\lambda^4}\right\} + B_5^2 + K_3^2 K_9^2$$

$$- 2\{(1-\beta^2)R_1^2 B_5 K_1 + \lambda N_2 I_0(\lambda R)\} + 4R^2(N_1 + N_6(1-\beta^2)R_1^2)$$

$$+ 3R^4(N_6\mu_1 + 6N_5) + 8K_3^2(1-\beta^2)R_1^2\left(\frac{2}{\beta^2} + 3\mu_1\right)R^6\Big] + \frac{9K_3^2\mu_1^2 R^{10}}{4},$$

$$X_2 = \frac{R^4}{16}\left[4N_6\left\{\frac{\mu_1\mu_2}{\lambda^2} - (1-\beta^2)R_1^2\right\} - 4N_1 + 2K_9K_{10}\right.$$
$$+ \frac{2K_1^2\mu_1^2\mu_2}{\lambda^2} + 4R^2\{2(1-\beta^2)R_1^2K_{10} - 6N_5 - N_6\mu_1\}$$
$$\left. + \{6\mu_1K_{10} - 8K_3^2(1-\beta^2)R_1^2(4\beta^{-2} + 7\mu_1)\}R^4\right] - \frac{3}{2}K_3^2\mu_1^2R^{10},$$

$$X_3 = \frac{R^6}{36}\left[6N_5 - 8(1-\beta^2)R_1^2K_{10} + N_6\mu_1 + \frac{4\mu_1\mu_2}{\lambda^2}(K_{10}K_1K_3\mu_1)\right.$$
$$\left. + 16\left\{K_3^2(1-\beta^2)R_1^2(\beta^{-2} + 2\mu_1) - \frac{\mu_1K_{10}}{2}\right\}R^2\right] + \frac{11}{18}K_3^2\mu_1^2R^{10},$$

$$X_4 = \lambda^{-6}[(N_4 + 2N_2)\lambda^5 - 4N_3\lambda^4 - 16N_6K_2\lambda^2 - 128K_3K_4\mu_1],$$

$$X_5 = 2\lambda^{-5}(N_3\lambda^4 + 32K_3K_4\mu_1),$$

$$X_6 = -\lambda^{-4}(16K_3K_4\mu_1 + N_3\lambda^4).$$

References

1. E. M. Landis, Am. J. Physiol., *75*, 548, 1926.
2. M. B. Rappaport, E. H. Bloch and J. W. Irvin, J. Appl. Physiol., *14*, 651, 1959.
3. P. A. Gaethagens, Puffüers Arch. ges. Physiol., *316*, 14, 1970.
4. M. Intaglietta, D. R. Richardson and W. R. Tompkins, Am. J. Physiol., *221*, 922, 1971.
5. J. Aroesty and J. F. Gross, Microvasc. Res., *4*, 1, 1972.
6. T. Ariman, M. A. Turk and N.D. Sylvester, J. App. Mech., *41*, 1, 1974.
7. N. Iida and T. Murata, Biorheology, *17*, 377, 1980.
8. P. D. S. Verma, D. V. Singh and K. Singh, Wear, *71*, 333, 1981.
9. S. Parvathamma and R. Devanathan, Bull. Math. Biol., *45*, 721, 1983.
10. J. H. Barbee and G. R. Cokelet, Microvasc. Res., *3*, 17, 1971.
11. P. N. Tandon, J. K. Misra and R. L. Verma, Math. Biosci., *62(1)*, 7, 1982.
12. H. M. Leiberstein, Mathematical Physiology, Am. Elsevier Publishing Company, Inc. New York, 1973.
13. T. W. Secomb, J. Fluid Mech., *88(2)*, 273, 1978.

Acta Physica Hungarica 67 (1–2), pp. 135–141 (1990)

IMPARTING INHOMOGENEITY TO BIANCHI TYPE II, VIII AND IX SPACE–TIMES WITH ELECTROMAGNETIC FIELD

L. K. PATEL, SHARDA S. KOPPAR* and N. R. PANDYA

Department of Mathematics, Gujarat University
Ahmedabad, 380 009 India

(Received 5 December 1986)

A unified treatment of Bianchi type II, VIII and IX space–times is given. A general scheme of imparting inhomogeneity to such space–time is developed. Exact solutions of Einstein–Maxwell field equations with Bianchi II, VIII and IX symmetrics are derived. The solutions describe the gravitational fields of a mass particle embedded in Bianchi type II, VIII and IX universes with electromagnetic fields. The details of the solutions are also discussed.

1. Introduction

Batakis and Cohen [1] have discussed an anisotropic Bianchi type IX cosmological model. The source of this model is a mixture of source-free electromagnetic fields and a scalar field. Vaidya and Patel [2] have discussed gravitational fields with space-times of Bianchi type IX. The source of their solutions is a mixture of rotating perfect fluid, a source-free electromagnetic field and a pure radiation field. Lorenz [3] has derived some exact Bianchi type VIII and type IX cosmological models with matter and electromagnetic fields. Damiao Soares and Assad [4] have presented a class of cosmological solutions of Einstein's equations, with matter and electromagnetic field, which are anisotropic and spatially homogeneous of Bianchi types VIII and IX. Banerjee, Duttachoudhury and Sanyal [5] have discussed a Bianchi type II cosmological model with viscous fluid. There is a large literature concerning specific Bianchi spaces-times which contain fluids with specified equations of state. A partial list of such space-times is given by Bayin and Krisch [6]. For the sake of brevity we shall not repeat this list here.

Assad and Damiao Soares [7] have given a unified treatment of Bianchi type II, VIII and IX space-times. Taking (ψ, α, β) as the local co-ordinates on the homogeneity sections $t =$ constant, they have expressed the metric in the form

$$ds^2 = dt^2 - A^2(d\psi + 4m^2\, d\beta)^2 -$$

$$-B^2K^2\,(d\alpha^2 + \sin^2\alpha\, d\beta^2), \tag{1}$$

*Present address: Department of Mathematics, Ohio State University, Columbus, OH 43210, USA

where A and B are functions of time t and m and K are functions of α satisfying

$$\frac{4m}{K^2 \sin \alpha} \frac{dm}{d\alpha} = \lambda_1, \tag{2}$$

$$\frac{d^2K}{d\alpha^2} - \frac{1}{K}\left(\frac{dK}{d\alpha}\right)^2 + \cot \alpha \frac{dK}{d\alpha} - K = \lambda K^3. \tag{3}$$

Here λ_1 and λ are constants, λ being proportional to the curvature of the two dimensional surface with the metric $d\Sigma^2 = K^2(\alpha)[d\alpha^2 + \sin^2 \alpha \, d\beta^2]$. They have shown that the metric (1) with $\lambda_1 \neq 0$

(i) represents a Bianchi type II space-time if $\lambda = 0$ and $K = \text{cosec } \alpha$,
(ii) represents a Bianchi type VIII space-time if $\lambda_1 = 0$, $K = \tan \alpha$ and
(iii) represents a Bianchi type IX space-time if $\lambda = -1$ and $K = 1$.

The object of the present investigation is to impart inhomogeneity to the homogeneous space-time described by the line-element (1). For this purpose we first transform the metric (1) into a more convenient form. Let us apply the transformation

$$d\psi = \frac{1}{A^2} dx - du \quad , \quad dt = \frac{1}{A} dx. \tag{4}$$

From (1), we obtain

$$ds^2 = 2 \, (du - 4m^2 d\beta) \, dx - A^2 \, (du - 4m^2 \, d\beta)^2 -$$

$$-B^2K^2 \, (d\alpha^2 + \sin^2 \alpha \, d\beta^2), \tag{5}$$

where A and B are now treated as functions of x.

2. The metric and the Ricci tensor

We introduce inhomogeneity in (5) by adding a term $-H(\alpha, u, x)(du - 4m^2 d\beta)^2$. Consequently, we consider the metric in the form

$$ds^2 = 2 \, (du - 4m^2 \, d\beta) dx - 2L \, (du - 4m^2 \, d\beta)^2 -$$

$$-B^2K^2 \, (d\alpha^2 + \sin^2 \alpha \, d\beta^2), \tag{6}$$

where

$$2L = A^2 + H(\alpha, u, x). \tag{7}$$

Introducing the basic 1-forms

$$\begin{aligned} \theta^{(1)} &= du - 4m^2 \, d\beta, & \theta^{(2)} &= BK \, d\alpha, \\ \theta^{(3)} &= BK \sin \alpha \, d\beta, & \theta^{(4)} &= dx - L\theta^{(1)} \end{aligned} \tag{8}$$

the metric (6) takes the form

$$ds^2 = 2\,\theta^{(1)}\theta^{(4)} - \left(\theta^{(2)}\right)^2 - \left(\theta^{(3)}\right)^2 = g_{ab}\theta^{(a)}\theta^{(b)}. \tag{9}$$

The metric (6) is a particular case of the Kerr–NUT metric discussed by Vaidya, Patel and Bhatt [8]. Using their results and the tetrad (8) one can easily compute the tetrad components $R_{(ab)}$ of Ricci tensor for the metric (6). The surviving $R_{(ab)}$ are listed below for ready reference.

$$\begin{aligned}
R_{(44)} &= 2\left(\frac{B_{xx}}{B} - \frac{\lambda_1^2}{B^4}\right),\\
R_{(14)} &= L_{xx} + 2\left(L\,\frac{B_{xx}}{B} + L_x\,\frac{B_x}{B} + \frac{L\lambda_1^2}{B^4}\right),\\
R_{(12)} &= -\frac{4m^2}{BK\,\sin\alpha}\left(L_{xy}^{-2}\,\frac{\lambda_1}{B^2}\,L_u\right),\\
R_{(13)} &= \frac{4m^2}{BK\,\sin\alpha}\left(L_{xu} + \frac{2\lambda_1}{B^2}\,Ly\right),\\
R_{(22)} &= R_{(33)} = \frac{\lambda}{B^2} + 4L\,\frac{\lambda_1^2}{B^4} - 2L_x\,\frac{B_x}{B} - 2L\left(\frac{B_{xx}}{B} - \frac{B_x^2}{B^2}\right),\\
R_{(11)} &= L^2 R_{(44)} + \frac{16\,m^4}{B^2K^2\,\sin^2\alpha}\left(L_{uu} + L_{yy}\right) - 2\,\frac{\lambda_1}{B^2}\,L_y + 2\,L_u\,\frac{B_x}{B},
\end{aligned} \tag{10}$$

where the variable y is defined by

$$dy = -\frac{4m^2}{\sin\alpha}\,d\alpha$$

and a suffix denotes partial differentiation e.g. $B_x = \dfrac{\partial B}{\partial x}$, $L_{yx} = \dfrac{\partial^2 L}{\partial y \partial x}$, etc. Throughout the paper bracketed indices indicate tetrad components with respect to the tetrad (8).

3. The source fields and the field equations

The material content of the universe is modelled by a mixture of perfect fluid, the source-free electromagnetic field and pure radiation field. Therefore, the Einstein–Maxwell field equations for such distributions take the form

$$R_{ik} - \frac{1}{2}\,g_{ik}R + \Lambda g_{ik} = -8\pi\left[(p+\rho)v_i v_k - p g_{ik} + E_{ik} + \sigma\xi_i\xi_k\right], \tag{11}$$

where

$$v_i v^i = 1, \qquad \xi_i\xi^i = 0, \qquad v^i\xi_i = 1. \tag{12}$$

In (11), E_{ik} is the electromagnetic energy momentum tensor, $\sigma\xi_i\xi_k$ is the tensor arising from the flowing null radiation and Λ is the cosmological constant. Let us choose the electromagnetic 4–potential A_i as

$$A_i = (\phi, 0, -4m^2\phi, 0), \tag{13}$$

where ϕ is a function of x and the co-ordinates are named as $x^1 = u$, $x^2 = \alpha$, $x^3 = \beta$, and $x^4 = x$. Using (13) one can find the electromagnetic field tensor $F_{ik} = A_{i;k} - A_{k;i}$. Using these F_{ik}, the metric (6) and the formula $E_{ik} = -g^{lm}F_{il}F_{km} + \frac{1}{4}g_{ik}F_{lm}F^{lm}$, one can determine E_{ik}. With the aid of the formulae $E_{(ab)} = e^i_{(a)}e^k_{(b)}E_{ik}$, $e^i_{(a)}\theta^{(a)} = dx^i$ we can obtain the tetrad components $E_{(ab)}$. All these are straightforward calculations. The non-vanishing $E_{(ab)}$ are found to be

$$E_{(14)} = E_{(22)} = E_{(33)} = \frac{1}{2}\left(\phi_x^2 + \frac{4\,\lambda_1^2\phi^2}{B^4}\right). \tag{14}$$

The Maxwell equations $F^{ik}_{\ ;k} = 0$ are satisfied if $\phi(x)$ is chosen to satisfy

$$B^4\phi_x^2 + 4\,\lambda_1^2\phi^2 = \text{constant} = b^2. \tag{15}$$

It is easy to see that the field equations (11) can be expressed in the tetrad form as

$$R_{(ab)} = -8\pi\left[(p+\rho)v_{(a)}v_{(b)} - \frac{1}{2}(\rho - p)\,g_{(ab)}\right] +$$

$$+\Lambda g_{(ab)} - 8\pi E_{(ab)} - 8\pi\sigma\xi_{(a)}\xi_{(b)}. \tag{16}$$

For the metric (6) with the tetrad (8) we take

$$v_a = (\frac{1}{2z}, 0, 0, z), \qquad \xi_a = (\frac{1}{z}, 0, 0, 0). \tag{17}$$

It is painless to verify that v_i and ξ_i given by (17) satisfy the conditions (12). Using the results (14), (15) and (17) in (16) we obtain the following relations:

$$8\pi p = \Lambda - R_{(14)} - 8\pi E_{(14)}, \tag{18}$$

$$8\pi\rho = -\Lambda - \left[R_{(14)} + 8\pi E_{(14)} + 2R_{(22)} + 16\pi E_{(22)}\right], \tag{19}$$

$$2z^2 = \frac{R_{(44)}}{R_{(14)} + 8\pi E_{(14)} + R_{(22)} + 8\pi E_{(22)}}, \tag{20}$$

$$8\pi\sigma = \frac{R_{(11)}\cdot R_{(44)}}{8\pi(p+\rho)} - 2\pi(p+\rho), \tag{21}$$

$$R_{(12)} = R_{(13)} = 0, \tag{22}$$

where $R_{(ab)}$ are given by (10).

4. Solution of the field equations

The two differential equations (22) can be explicitly expressed as

$$-H_{xy} + \frac{2\lambda_1}{B^2} H_u = 0, \qquad H_{xu} + \frac{2\lambda_1}{B^2} H_y = 0.$$

If we define the co-ordinate r by $r = u - \int \frac{dx}{B^2}$, it is easy to integrate the above two equations. The solution can be expressed as $H = F(r)e^{-2\lambda_1 y}$, where $F(r)$ satisfies $\frac{d^2F}{dr^2} + 4\lambda_1^2 F = 0$. Consequently we get

$$2L = A^2 + F(r)e^{-2\lambda_1 y}, \qquad \frac{d^2F}{dr^2} + 4\lambda_1^2 F = 0. \tag{23}$$

The pressure p, the density ρ, z^2 and the radiation density σ can be obtained from (18), (19), (20) and (21). They are given by

$$8\pi p = \Lambda - \left[AA_{xx} + A_x^2 + 2A\frac{A_x B_x}{B} + A^2\left(\frac{B_{xx}}{B} + \frac{\lambda_1^2}{B^4}\right) + \right.$$
$$\left. + \frac{4\pi b^2}{B^4} + Fe^{-2\lambda_1 y}\left(\frac{B_{xx}}{B} - \frac{\lambda_1^2}{B^4}\right)\right], \tag{24}$$

$$8\pi(p+\rho) = -2\left[\frac{\lambda}{B^2} + \frac{8\pi b^2}{B^4} + AA_{xx} + A_x^2 + A^2\left(\frac{3\lambda_1^2}{B^4} - \frac{B_x^2}{B^2}\right) + \right.$$
$$\left. + Fe^{-2\lambda_1 y}\left(\frac{\lambda_1^2}{B^4} - \frac{B_x^2}{B^2}\right) + \frac{dF}{dr}e^{-2\lambda_1 y}\frac{B_x}{B}\right], \tag{25}$$

$$z^2 = -\frac{\left(\frac{B_{xx}}{B} - \frac{\lambda_1^2}{B^4}\right)}{4\pi(p+\rho)}, \tag{26}$$

$$8\pi\sigma = -2\pi(p+\rho) + \frac{1}{8\pi(p+\rho)}\left[\left(A^2 + Fe^{-2\lambda_1 y}\right)^2\left(\frac{B_{xx}}{B} - \frac{\lambda_1^2}{B^4}\right)^2 + \right.$$
$$\left. + 2\left(\frac{B_{xx}}{B} - \frac{\lambda_1^2}{B^4}\right)\left(\frac{2\lambda_1^2}{B^2}F + \frac{dF}{dr}\frac{B_x}{B}\right)e^{-2\lambda_1 y}\right]. \tag{27}$$

It should be noted that the metric potentials A and B remain undetermined.

The velocity field v_i can be determined from

$$v_i = e_i^{(a)v}(a), \qquad e_i^{(a)}\, dx^i = \theta^{(a)}.$$

It is given by

$$v_i = (Y, 0, -4m^2Y, z), \tag{28}$$

where Y is given by

$$Y = \frac{1}{2z} - Lz. \tag{29}$$

The angular velocity vector Ω^i of the flow vector v_i is given by

$$\Omega^i = \frac{\epsilon^{ijkl}}{\sqrt{-g}} w_{jkl}$$

where ϵ^{ijkl} is the Levy–Civita symbol and

$$w_{jkl} = \frac{1}{3!}\left[v_j(v_{k,l} - v_{l,k}) + v_k(v_{l,j} - v_{j,l}) + v_l(v_{j,k} - v_{k,j})\right].$$

The magnitude Ω of the angular velocity vector Ω^i is given by $\Omega^2 = -g_{ik}\Omega^i\Omega^k$. It is found that

$$\Omega^2 = \frac{16m^4}{\sin^2\alpha\, B^2K^2}\left[(Yz_u - zY_u)^2 + (zY_y - Yz_y)^2\right] +$$

$$+8Y^2z\frac{\lambda_1^2}{B^4}(Lz - 1). \tag{30}$$

We know that in the homogeneous case (i.e., $F = 0$) we have solutions with $\sigma = 0$. From the above results it can be readily seen that $F = 0$, $\sigma = 0$ imply

$$2LR_{(44)} + 8\pi(p + \rho) = 0 \qquad \text{and} \qquad 2Lz^2 = 1. \tag{31}$$

Using (31) we have $Y = 0$ and consequently $\Omega = 0$. Also we get the following relation between the functions A and B

$$\frac{B_{xx}}{B} + \frac{B_x^2}{B^2} - 4\frac{\lambda_1^2}{B^4} - \frac{\lambda}{A^2B^2} - \frac{8\pi b^2}{B^4A^2} - \frac{A_{xx}}{A} - \frac{A_x^2}{A^2} = 0. \tag{32}$$

If A and B are related by (32), then we have

$$8\pi p = \Lambda - A^2\left(\frac{2B_{xx}}{B} + \frac{B_x^2}{B^2} + 2\frac{A_xB_x}{AB} - \frac{4\pi b^2}{A^2B^4} - \frac{\lambda}{A^2B^2} - \frac{3\lambda_1^2}{B^4}\right) -$$

$$- Fe^{-2\lambda_1 y}\left(\frac{B_{xx}}{B} - \frac{\lambda_1^2}{B^4}\right), \tag{33}$$

$$8\pi(p + \rho) = -2A^2\left(\frac{B_{xx}}{B} - \frac{\lambda_1^2}{B^4}\right) - 2Fe^{-2\lambda_1 y}\left(\frac{\lambda_1^2}{B^4} - \frac{B_x^2}{B^2}\right) -$$

$$- 2\frac{dF}{dr}\frac{B_x}{B}e^{-2\lambda_1 y}, \tag{34}$$

$$z^2 = \frac{\dfrac{B_{xx}}{B} - \dfrac{\lambda_1^2}{B^4}}{A^2\left(\dfrac{B_{xx}}{B} - \dfrac{\lambda_1^2}{B^4}\right) + Fe^{-2\lambda_1 y}\left(\dfrac{\lambda_1^2}{B^4} - \dfrac{B_x^2}{B^2}\right) - \dfrac{dF}{dr}\dfrac{B_x}{B}e^{-2\lambda_1 y}}. \tag{35}$$

The radiation density σ is given by (27) where $8\pi(p+\rho)$ is given by (34). Thus if the metric (5) is a solution of the field equations

$$R_{ik} - \frac{1}{2} g_{ih} R + \Lambda g_{ih} = -8\pi [(p+\rho) v_i v_h - p g_{ih}] - 8\pi E_{ik}$$

(i.e., if A and B are related by (32)), then the metric

$$ds^2 = 2(du - 4m^2 d\beta)\, dx - B^2 K^2 (d\alpha^2 + \sin^2\alpha\, d\beta^2) - \\ - \{A^2 + F_{(x)} e^{-2\lambda_1 y}\} (du - 4m^2 d\beta)^2 \tag{36}$$

is a solution of the field equations (11). The functions m and K satisfy (2) and (3), and F satisfies $\dfrac{d^z F}{dr^z} + 4\lambda_1^2 F = 0$.

5. Concluding remarks

If we choose A_i as

$$A_i = (0, 0, -4m^z \ell, 0), \qquad \ell = \text{constant}, \tag{37}$$

then we get purely magnetic field. In this the electromagnetic field is not source-free. The Maxwell equations $F^{ik}_{\ \ ;k} = 4\pi J^i$ imply that $J^i = (-\dfrac{4\lambda_1^2 \ell}{B^u}, 0, 0, 0)$. In this case we have the non-zero $E_{(ab)}$ as

$$E_{(14)} = E_{(22)} = E_{(33)} = \frac{1}{2}\left(\frac{4\ell^2\lambda_1^2}{B^4}\right). \tag{38}$$

Comparing the above result with (14) we get $b^2 = 4\lambda_1^2\ell^2$, thus replacing b^2 by $4\lambda_1^2\ell^2$ in Section 4 we can prove that the metric (36) is a solution of the field equations (11) where the electromagnetic energy tensor is given by (38).

We have seen that imparting inhomogeneity on the metric (5) gives rise to a pure radiation field and the rotation of the stream lines of the perfect fluid.

If the electromagnetic field is switched off (i.e. $b = 0$ or $\ell = 0$), we obtain an inhomogeneous Bianchi type II, VIII or IX cosmological model filled with rotating perfect fluid and pure radiation field.

References

1. N. Batakis and J. M. Cohen, Ann. Phys. (N. Y.), *73*, 578, 1972.
2. P. C. Vaidya and L. K. Patel, Pramana (J. Phys.), *27*, 63, 1986.
3. D. Lorenz, Phys. Rev., *D22*, 1848, 1980.
4. I. Damiao Soares and M. J. D. Assad, Phys. Lett., *66A*, 359, 1978.
5. A. Banerjee, S. B. Duttachoudhury and A. K. Sanyal, Gen. Rel. Grav., *18*, 461, 1986.
6. S. S. Bayin and J. P. Krisch, J. Math. Phys., *27*, 262, 1986.
7. M. J. D. Assad and I. Damiao Soares, Phys. Rev., *D28*, 1858, 1983.
8. P. C. Vaidya, L. K. Patel and P. V. Bhatt, Gen. Rel. Grav., *7*, 701, 1976.

Acta Physica Hungarica 67 (1-2), pp. 143-162 (1990)

AXIALLY SYMMETRIC EINSTEIN–MAXWELL AND SCALAR FIELDS WITH SELF GRAVITATING STIFF FLUID

G. MOHANTY*

P.G. Department of Mathematics, Khallikote College
Berhampur 760001, India

and

U. K. PANIGRAHI

Department of Mathematics and Science, Engineering School
Berhampur 760010, India

(Received 11 March 1987)

The problem of charged perfect fluid and massive scalar field is investigated in the spacetime described by a general axially symmetric Jordan–Ehlers metric with two degrees of freedom. It is shown that the meson restmass $\bar{M}$ and the cosmological constant vanish, the electromagnetic field becomes source free and the perfect fluid degenerates to become a stiff perfect fluid ($P = \rho$). A class of exact solutions has been obtained removing one of the metric potentials. A method is also suggested to generate the most general solution. The physical behaviour and region of validity of the solutions are studied analytically.

1. Introduction

A non-static axially symmetric spacetime with two degrees of freedom is usually considered as a model of gravitational radiation. This spacetime has been studied for various purposes by many authors, viz., J. Ehlers [1, 2], Jordan et al [3], Kompaneets [4], Stachel [5, 6], Singh and Jadav [7] and Letelier [8]. However, the problem of linearly coupled fields in this spacetime is seldom taken up in the literature.

Therefore, in this paper we consider the general charged perfect fluid and massive scalar field in the presence of a cosmological constant λ in the field equations. We have taken λ to be positive for an expanding universe. Finally, it turns out that the mass parameter of scalar field $\bar{M}$ and the cosmological constant λ vanish. Further, the electromagnetic field becomes source free and the perfect fluid reduces to a stiff perfect fluid. In order to avoid complications due to the non-linear character of the field equations, we have dropped a degree of freedom imposing some restrictions on the electromagnetic field and found a class of exact solutions in Section 3. A method for generating a most general solution is given in Section 4. The physical nature and region of validity of the solutions and duality, nullity and uniformity of the electromagnetic fields are studied analytically in Section 5. The general character of the solution is revealed in the conclusion in Section 6.

*Present address: School of Mathematical Sciences, Sambalpur University, Jyoti Vihar, Burla–768019, India

2. Field equations

The relativistic cosmological field equations for the spacetime containing charged perfect fluid and mesonic fields are

$$G_{ij} = R_{ij} - \frac{1}{2}g_{ij}R + \lambda g_{ij} = -K(T_{ij} + E_{ij} + E'_{ij}), \tag{2.1}$$

where

$$T_{ij} = \frac{1}{4\pi}\left[V_{,i}V_{,j} - \frac{1}{2}g_{ij}(V_{,s}V^{,s} - \bar{M}^2V^2)\right], \tag{2.1a}$$

$$E_{ij} = \frac{1}{4\pi}\left[-F_{is}F^{s}_{j.} + \frac{1}{4}g_{ij}F_{ab}F^{ab}\right], \tag{2.1b}$$

$$E'_{ij} = \frac{1}{4\pi}[(P+\rho)U_iU_j - Pg_{ij}], \qquad (g^{ij}U_iU_j = 1) \tag{2.1c}$$

are respectively stress tensors of the massive scalar field, electromagnetic field and perfect fluid distributions. Units are so chosen that the velocity of light is unity and ρ, P and U_i are respectively the proper mass density, pressure and four-velocity vector of the distributions. In addition to these, the electromagnetic field tensor F_{ij} and massive scalar field V satisfy the following equations:

$$F_{ij} = \psi_{i,j} - \psi_{j,i}, \tag{2.2}$$

$$F^{ij}{}_{;j} = -4\pi\sigma U^i, \tag{2.3}$$

and

$$g^{ij}V_{;ij} + \bar{M}^2V = 0, \tag{2.4}$$

where ψ_i is the electromagnetic four-potential. Here the comma and the semicolon denote partial and covariant differentiations, respectively.

We now consider the spacetime described by the axially symmetric Jordan–Ehlers metric [1, 2, 3,]

$$ds^2 = e^{2A-2B}(dt^2 - dr^2) - r^2e^{-2B}d\theta^2 - e^{2B}(Cd\theta + dz)^2, \tag{2.5}$$

where $A = A(r,t)$, $B = B(r,t)$ and $C = C(r,t)$, and r, θ, z and t correspond to the coordinates x^1, x^2, x^3 and x^4 respectively. Due to the symmetry of the spacetime imposed by the metric (2.5), the field variables are independent of the coordinates θ and z. The coordinates are chosen to be comoving so that

$$U_1 = U_2 = U_3 = 0 \quad \text{and} \quad U_4 = (g^{44})^{-\frac{1}{2}}. \tag{2.6}$$

The consistency of two of the field equations (2.1),

$$G_{11} = -K(T_{11} + E_{11} + E'_{11}) \quad \text{and} \quad G_{44} = -K(T_{44} + E_{44} + E'_{44})$$

demands that (see Appendix)

$$\bar{M} = 0, \quad \lambda = 0, \quad P = \rho, \quad F_{14} = 0 \quad \text{and} \quad F_{23} = 0. \tag{2.7}$$

We get from (2.3) and (2.7) that

$$\sigma = 0, \quad \text{since} \quad U_4 \neq 0. \tag{2.8}$$

Now it may be shown that all the surviving components of F_{ij} can be obtained from ψ_2 and ψ_3 of the electromagnetic four potential ψ_i. For the sake of simplicity we take

$$\psi_2 = M \quad \text{and} \quad \psi_3 = N.$$

Using (2.5) to (2.8), the field equations (2.1) to (2.4) finally take the form:

$$A_1 = r(A_{11} - A_{44} + 2B_1^2) + \frac{e^{4B}}{2r} C_4^2 + \\ + \frac{K}{4\pi r}\left[e^{2B}(M_4 - CN_4)^2 + r^2 e^{-2B} N_1^2 + r^2 V_1^2\right], \tag{2.9}$$

$$A_4 = \frac{C_1 C_4}{2r} e^{4B} + 2rB_1 B_4 + \frac{K}{4\pi r}\left[e^{2B} M_1 M_4 + (C^2 e^{2B} + r^2 e^{-2B}) N_1 N_4 - \right. \\ \left. - Ce^{2B}(M_1 N_4 + N_1 M_4) + r^2 V_1 V_4\right], \tag{2.10}$$

$$\nabla_1 B - \frac{1}{2r^2} e^{4B}(C_1^2 - C_4^2) = \frac{K}{8\pi r^2}\left[(M_1^2 - M_4^2)e^{2B} - 2C(M_1 N_1 - M_4 N_4)e^{2B} + \right. \\ \left. + (C^2 e^{2B} - r^2 e^{-2B})(N_1^2 - N_4^2)\right], \tag{2.11}$$

$$\nabla_2 C + 4(B_1 C_1 - B_4 C_4) = \frac{K}{2\pi}\left[M_4 N_4 - M_1 N_1 + C(N_1^2 - N_4^2)\right] e^{-2B}, \tag{2.12}$$

$$P(=\rho) = \frac{2\pi}{K} e^{-2A+2B}\left[A_{11} - A_{44} + \frac{A_1}{r} - 2B_4^2 - \frac{e^{4B}}{2r^2} C_1^2 - \right. \\ \left. - \frac{K}{4\pi}\left\{\frac{e^{2B}}{r^2}(M_1 - CN_1)^2 + e^{-2B} N_4^2 + V_4^2\right\}\right], \tag{2.13}$$

$$\nabla_2 M + 2(M_1 B_1 - M_4 B_4) = C \nabla_2 N + C_1 N_1 - C_4 N_4 + \\ + 2C(N_1 B_1 - N_4 B_4), \tag{2.14}$$

$$\nabla_1 N + 2(N_4 B_4 - N_1 B_1) = \frac{e^{4B}}{r^2}\left[C_1 M_1 - C_4 M_4 - \right. \\ \left. - C(C_1 N_1 - C_4 N_4)\right] \tag{2.15}$$

and

$$\nabla_1 V = 0, \tag{2.16}$$

where

$$\nabla_1 \equiv \frac{\partial^2}{\partial r^2} - \frac{\partial^2}{\partial t^2} + \frac{1}{r}\frac{\partial}{\partial r}$$

and

$$\nabla_2 \equiv \frac{\partial^2}{\partial r^2} - \frac{\partial^2}{\partial t^2} - \frac{1}{r}\frac{\partial}{\partial r}. \tag{2.17}$$

For the sake of brevity the comma is dropped and the suffixes 1 and 4 represent partial differentiations with respect to r and t, respectively.

In this paper, our interest is to solve the overdetermined set of nonlinear field equations (2.9) to (2.16) to determine the unknowns A, B, C, M, N, V and $P(=\rho)$. The question of overdeterminacy has been settled in each case by the satisfaction of all the field equations by actual substitution of the solutions in the field equations.

3. Solutions

It is difficult to find an exact solution in general due to the nonlinearity of the field equations. Therefore, we impose certain restrictions on the electromagnetic fields when $C = 0$. Equation (2.12) is identically satisfied in the following cases:

(i) $C = 0,\ M_1 = M_4 = N_1 = 0,$
(ii) $C = 0,\ M_1 = M_4 = N_4 = 0,$
(iii) $C = 0,\ N_1 = N_4 = M_1 = 0,$
(iv) $C = 0,\ N_1 = N_4 = M_4 = 0,$
(v) $C = 0,\ M_4 = 0 = N_1,$
(vi) $C = 0,\ M_1 = 0 = N_4$ and
(vii) $C = 0,\ M_1 \neq 0 \neq M_4$ and $N_1 \neq 0 \neq N_4$.

Case (i) $M_1 = M_4 = N_1 = 0 = C$

This case implies that N is a function of time only and the equation (2.14) is satisfied identically. Then from (2.15), we obtain

$$B = \frac{1}{2}[\ln N_4 - L(r)], \tag{3.1}$$

where L is an arbitrary function of r only. With the help of (3.1), equation (2.11) yields

$$\frac{d^2 L}{dr^2} + \frac{1}{r}\frac{dL}{dr} + \frac{d^2}{dt^2}\ln N_4 = -\frac{K}{4\pi} N_4 e^{L(r)}. \tag{3.2}$$

Since N is a function of time only and L is a function of r only, the equation (3.2) will hold if and only if either N_4 or L is a constant.

Subcase (i) a.

We first assume N_4 to be a constant, say f.

Then

$$N = ft + d. \tag{3.3}$$

With this value N, the equation (3.2) yields a solution

$$L = -\ln\left[\frac{2u}{q^2}r^2\cosh^2\left(\frac{q}{2}\ln r + s\right)\right]. \tag{3.4}$$

Hereafter, the lower case Latin letters except r, t and z represent arbitrary constants and $u = \frac{kf}{4\pi}$.

With the help of (3.1), (3.3) and (3.4), we get

$$B = \frac{1}{2}\ln\left[\frac{2uf}{-q^2}r^2\cosh^2\left(\frac{q}{2}\ln r + s\right)\right]. \tag{3.5}$$

Solving (2.16) by the method of separation of variables, we get

$$V = \frac{a_1}{2}\left(t^2 + \frac{r^2}{2}\right) + a_2 t + a_3\ln r + a_4, \tag{3.6}$$

where the a's with different suffixes represent arbitrary constants. Substituting (3.3), (3.5) and (3.6) in (2.10), we get

$$A = \frac{u}{f}\left(\frac{a_1}{2}r^2 + a_3\right)\left(\frac{a_1 t^2}{2} + a_2 t\right) + S(r), \tag{3.7}$$

where S is an arbitrary function of r only. Using (3.3), (3.5), (3.6) and (3.7) in (2.9), we get

$$r^2 S_{11} - rS_1 = \frac{u}{f}\left(\frac{a_1^2 r^4}{4} - a_3^2\right) - 2 - \frac{q^2}{2}\tanh^2\left(\frac{q}{2}\ln r + s\right) -$$

$$-2q\tanh\left(\frac{q}{2}\ln r + s\right).$$

As it is difficult to solve the above differential equation for a general value of q, we therefore solve it for certain specific values of q, say, $q = 2$. Thus, we get the solution as

$$A = a_6 + a_5 r^2 + \frac{ua_1^2 r^4}{32f} + \ln\left[r^{\left(\frac{ua_1^2}{2f}+2\right)}\cosh^2(\ln r + s)\right] +$$

$$+\frac{u}{f}\left(\frac{a_1 r^2}{2}+a_3\right)\left(\frac{a_1 t^2}{2}+a_2 t\right). \tag{3.8}$$

The pressure of the distribution can be obtained from (2.13) as

$$P(=\rho)=\frac{f^2}{4}\left[4a_5-\frac{u}{f}(a_1a_3+a_2^2)\right]r^{-\left(2+\frac{ua_3^2}{f}\right)}\cdot$$
$$\cdot\operatorname{sech}^2(\ln r+s)\cdot\exp\left[-2\left\{a_6+a_5r^2+\frac{u}{32f}a_1^2r^4+\right.\right.$$
$$\left.\left.+\frac{u}{f}\left(\frac{a_1r^2}{2}+a_3\right)\left(\frac{a_1t^2}{2}+a_2t\right)\right\}\right]. \tag{3.9}$$

In this subcase the solution of the field equations is given by (3.3), (3.5), (3.6), (3.8) and (3.9) when $q=2$.

Subcase (i) b.

In the alternative case when L is a constant, say

$$L=\ln f, \tag{3.10}$$

the general solution of (3.2) is

$$N=b-\frac{q}{u}\tanh\left(-\frac{q}{2}t+s\right). \tag{3.11}$$

Thus, we get from (3.1)

$$B=\frac{1}{2}\ln\left[\frac{q^2}{2uf}\operatorname{sech}^2\left(-\frac{q}{2}t+s\right)\right]. \tag{3.12}$$

As before considering the solution (2.16),

$$V=\frac{a_1}{2}\left(t^2+\frac{r^2}{2}\right)+a_2t+a_3\ln r+a_4, \tag{3.13}$$

we calculate A and $P(=\rho)$ from (2.9), (2.10) and (2.13) as

$$A=a_6+a_5r^2+\frac{u}{f}\left[\frac{a_1^2r^4}{32}+\frac{a_3^2}{2}\ln r+\left(\frac{a_1r^2}{2}+a_3\right)\left(\frac{a_1t^2}{2}+a_2t\right)\right] \tag{3.14}$$

and

$$P(=\rho)=\frac{q^2}{4u^2}\left[4a_5-\frac{u}{f}(a_1a_3+a_2^2)-\frac{q^2}{2}\right]\cdot r^{-\frac{ua_3^2}{f}}\cdot$$
$$\cdot\operatorname{sech}^2\left(-\frac{q}{2}t+s\right)\cdot\exp\left[-2\left\{a_6+a_5r^2+\frac{ua_1^2}{32f}r^4+\right.\right.$$
$$\left.\left.+\frac{u}{f}\left(\frac{a_1r^2}{2}+a_3\right)\left(\frac{a_1t^2}{2}+a_2t\right)\right\}\right]. \tag{3.15}$$

Thus, (3.11) to (3.15) constitute the solution of the field equations in this subcase.

Case (ii) $M_1 = M_4 = N_4 = 0 = C$

This case implies that N is a function of r only. Proceeding as before, we get the following two sets of solutions:

Subcase (ii) a.

$$N = b - \frac{q}{u}\tanh(-\frac{q}{2}\ln r + s),$$

$$B = \frac{1}{2}\ln\left[\frac{q^2}{2uf}\operatorname{sech}^2(-\frac{q}{2}\ln r + s)\right],$$

$$V = \frac{a_1}{2}(t^2 + \frac{r^2}{2}) + a_2 t + a_3 \ln r + a_4,$$

$$A = a_6 + a_5 r^2 + \frac{u a_1^2 r^4}{32 f} + (\frac{q^2}{4} + \frac{u}{2f}a_3^2)\ln r + \\ + \frac{u}{f}(\frac{a_1 r^2}{2} + a_3)(\frac{a_1 t^2}{2} + a_2 t)$$

and

$$P(=\rho) = \frac{q^2}{u^2}\left[a_5 - \frac{u}{4f}(a_1 a_3 + a_2^2)\right]\cdot r^{-(\frac{q^2}{2}+\frac{u a_3^2}{f})}\cdot$$

$$\cdot\operatorname{sech}^2(-\frac{q}{2}\ln r + s)\cdot\exp\left[-2\left\{a_6 + a_5 r^2 + \frac{u a_1^2}{32 f}r^4 + \right.\right. \\ \left.\left. + \frac{u}{f}(\frac{a_1 r^2}{2} + a_3)\cdot(\frac{a_1 t^2}{2} + a_2 t)\right\}\right]. \qquad (3.16)$$

Subcase (ii) b.

$$N = \frac{f r^2}{2} + d,$$

$$B = \frac{1}{2}\ln\left[\frac{2uf}{q^2}r^2\cdot\cosh^2(\frac{qt}{2} + s)\right],$$

$$V = \frac{a_1}{2}(t^2 + \frac{r^2}{2}) + a_2 t + a_3 \ln r + a_4,$$

$$A = a_6 + a_5 r^2 + \frac{u a_1^2}{32 f}r^4 + \ln\left[r^{(1+\frac{u a_3^2}{2f})}\cosh^2(\frac{qt}{2} + s)\right] + \\ + \frac{u}{f}(\frac{a_1}{2}r^2 + a_3)(\frac{a_1 t^2}{2} + a_2 t)$$

and

$$P(=\rho) = \frac{f^2}{q^2}\left[4a_5 - \frac{q^2}{2} - \frac{u}{f}(a_1 a_3 + a_2^2)\right]r^{\frac{-u a_3^2}{f}}\cdot$$

$$\cdot\operatorname{sech}^2\left(\frac{qt}{2}+s\right)\cdot\exp\left[-2\left\{a_6+a_5r^2+\frac{ua_1^2}{32f}r^4+\right.\right.$$

$$\left.\left.+\frac{u}{f}\left(\frac{a_1}{2}r^2+a_3\right)\left(\frac{a_1t^2}{2}+a_2t\right)\right\}\right]. \tag{3.17}$$

Case (iii) $N_1 = N_4 = M_1 = 0$

In this case M depends on the time only. As in case (i), here we get the following two sets of solutions:

Subcase (iii) a.

$$M = b - \frac{q}{u}\tanh\left(-\frac{qt}{2}+s\right),$$

$$B = \frac{1}{2}\ln\left[\frac{2uf}{q^2}r^2\cosh^2\left(-\frac{qt}{2}+s\right)\right],$$

$$V = \frac{a_1}{2}\left(t^2+\frac{r^2}{2}\right)+a_2t+a_3\ln r+a_4,$$

$$A = a_6+a_5r^2+\frac{ua_1^2r^4}{32f}+\ln\left[r^{\left(1+\frac{ua_3^2}{2f}\right)}\cosh^2\left(-\frac{qt}{2}+s\right)\right]+$$

$$+\frac{u}{f}\left(\frac{a_1r^2}{2}+a_3\right)\left(\frac{a_1t^2}{2}+a_2t\right)$$

and

$$P(=\rho) = \frac{f^2}{q^2}\left[4a_5-\frac{q^2}{2}-\frac{u}{f}(a_1a_3+a_2^2)\right]\cdot r^{\frac{-ua_3^2}{f}}\cdot$$

$$\cdot\operatorname{sech}^2\left(-\frac{qt}{2}+s\right)\cdot\exp\left[-2\left\{a_6+a_5r^2+\frac{ua_1^2r^4}{32f}+\right.\right.$$

$$\left.\left.+\frac{u}{f}\left(\frac{a_1r^2}{2}+a_3\right)\left(\frac{a_1t^2}{2}+a_2t\right)\right\}\right]. \tag{3.18}$$

Subcase (iii) b.

$$M = ft+d,$$

$$B = \frac{1}{2}\ln\left[\frac{q^2}{2uf}\operatorname{sech}^2\left(-\frac{q}{2}\ln r+s\right)\right],$$

$$V = \frac{a_1}{2}\left(t^2+\frac{r^2}{2}\right)+a_2t+a_3\ln r+a_4,$$

$$A = a_6+a_5r^2+\frac{ua_1^2r^4}{32f}+\left(\frac{ua_3^2}{2f}+\frac{q^2}{4}\right)\ln r+$$

$$+\frac{u}{f}\left(\frac{a_1}{2}r^2+a_3\right)\left(\frac{a_1t^2}{2}+a_2t\right)$$

and

$$P(=\rho) = \frac{q^2}{4u^2}\left[4a_5 - \frac{u}{f}(a_1a_3 + a_2^2)\right] \cdot \operatorname{sech}^2(-\frac{q}{2}\ln r + s) \cdot$$
$$\cdot r^{-(\frac{ua_3^2}{f}+\frac{q^2}{2})} \cdot \exp\left[-2\left\{a_6 + a_5r^2 + \frac{ua_1^2}{32f}r^4 + \right.\right.$$
$$\left.\left. + \frac{u}{f}(\frac{a_1}{2}r^2 + a_3)(\frac{a_1t^2}{2} + a_2t)\right\}\right]. \tag{3.19}$$

Case (iv) $N_1 = N_4 = M_4 = 0$

In this case M depends on r only. The following two sets of solutions are obtained.

Subcase (iv) a.

$$M = b + \frac{2}{u}\tanh(\ln r + s),$$
$$B = \frac{1}{2}\ln\left[\frac{uf}{2}r^2\cosh^2(\ln r + s)\right],$$
$$V = \frac{a_1}{2}(t^2 + \frac{r^2}{2}) + a_2t + a_3\ln r + a_4,$$
$$A = a_6 + a_5r^2 + \frac{ua_1^2}{32f}r^4 + \ln\left[r^{(2+\frac{ua_3^2}{2f})} \cdot \cosh^2(\ln r + s)\right] +$$
$$+ \frac{u}{f}(\frac{a_1}{2}r^2 + a_3)(\frac{a_1t^2}{2} + a_2t)$$

and

$$P(=\rho) = \left[f^2a_5 - \frac{uf}{4}(a_1a_3 + a_2^2)\right]\operatorname{sech}^2(\ln r + s) \cdot r^{-(2+\frac{ua_3^2}{f})} \cdot$$
$$\cdot \exp\left[-2\left\{a_6 + a_5r^2 + \frac{ua_1^2}{32f}r^4 + \frac{u}{f}(\frac{a_1}{2}r^2 + a_3)(\frac{a_1t^2}{2} + a_2t)\right\}\right]. \tag{3.20}$$

Subcase (iv) b.

$$M = \frac{fr^2}{2} + d,$$
$$B = \frac{1}{2}\ln\left[\frac{q^2}{2uf}\operatorname{sech}^2(-\frac{q}{2t} + s)\right],$$
$$V = \frac{a_1}{2}(t^2 + \frac{r^2}{2}) + a_2t + a_3\ln r + a_4,$$
$$A = a_6 + a_5r^2 + \frac{u}{f}\left[\frac{a_1^2}{32}r^4 + \frac{a_3^2}{2}\ln r + (\frac{a_1}{2}r^2 + a_3)\cdot(\frac{a_1t^2}{2} + a_2t)\right]$$

and

$$P(=\rho) = \frac{q^2}{4u^2}\left[4a_5 - \frac{q^2}{2} - \frac{u}{f}(a_1a_3 + a_2^2)\right]\operatorname{sech}^2\left(-\frac{q}{2}t + s\right)\cdot$$
$$\cdot r^{\frac{-ua_3^2}{f}} \cdot \exp\left[-2\left\{a_6 + a_5r^2 + \frac{ua_1^2}{32f}r^4 + \right.\right.$$
$$\left.\left. + \frac{u}{f}\left(\frac{a_1}{2}r^2 + a_3\right)\left(\frac{a_1t^2}{2} + a_2t\right)\right\}\right]. \tag{3.21}$$

Case (v) $M_4 = 0 = N_1$

Following the case (i), we get the following two sets of solutions:

Subcase (v) a.

$$M = \frac{fr^2}{2} + d, \quad N = b - \frac{q}{2u}\tanh\left(-\frac{q}{2}t + s\right),$$
$$B = \frac{1}{2}\ln\left[\frac{q^2}{4uf}\operatorname{sech}^2\left(-\frac{q}{2}t + s\right)\right],$$
$$V = \frac{a_1}{2}\left(t^2 + \frac{r^2}{2}\right) + a_2t + a_3\ln r + a_4,$$
$$A = a_6 + a_5r^2 + \frac{u}{f}\left[\frac{a_1^2}{32}r^4 + \frac{a_3^2}{2}\ln r + \left(\frac{a_1}{2}r^2 + a_3\right)\cdot\left(\frac{a_1t^2}{2} + a_2t\right)\right]$$

and

$$P(=\rho) = \frac{q^2}{8u^2}\left[4a_5 - \frac{q^2}{2} - \frac{u}{f}(a_1a_3 + a_2^2)\right]\operatorname{sech}^2\left(-\frac{q}{2}t + s\right)\cdot$$
$$\cdot r^{-\frac{ua_3^2}{2f}} \cdot \exp\left[-2\left\{a_6 + a_5r^2 + \frac{ua_1^2}{32f}r^4 + \right.\right.$$
$$\left.\left. + \frac{u}{f}\left(\frac{a_1}{2}r^2 + a_3\right)\left(\frac{a_1t^2}{2} + a_2t\right)\right\}\right]. \tag{3.22}$$

Subcase (v) b.

$$M = ft + d, \quad N = b + \frac{1}{u}\tanh(\ln r + s),$$
$$B = \frac{1}{2}\ln\left[ufr^2\cosh^2(\ln r + s)\right],$$
$$V = \frac{a_1}{2}\left(t^2 + \frac{r^2}{2}\right) + a_2t + a_3\ln r + a_4,$$
$$A = a_6 + a_5r^2 + \frac{ua_1^2}{32f}r^4 + \ln\left[r^{\left(2+\frac{ua_3^2}{2f}\right)}\cdot\cosh^2(\ln r + s)\right] +$$
$$+ \frac{u}{f}\left(\frac{a_1}{2}r^2 + a_3\right)\left(\frac{a_1t^2}{2} + a_2t\right)$$

and

$$P(=\rho)=\frac{f^2}{2}\left[4a_5-\frac{u}{f}(a_1a_3+a_2^2)\right]\operatorname{sech}^2(\ln r+s)\cdot$$
$$\cdot r^{-(2+\frac{ua_3^2}{f})}\cdot\exp\left[-2\left\{a_6+a_5r^2+\frac{ua_1^2}{32f}r^4+\right.\right.$$
$$\left.\left.+\frac{u}{f}\left(\frac{a_1}{2}r^2+a_3\right)\left(\frac{a_1t^2}{2}+a_2t\right)\right\}\right]. \tag{3.23}$$

Case (vi) $M_1=0=N_4$

As before, in this case, we get the following two sets of solutions:

Subcase (vi) a.

$$N=\frac{fr^2}{2}+d,\quad M=b-\frac{q}{2u}\tanh\left(-\frac{q}{2}t+s\right),$$
$$B=\frac{1}{2}\ln\left[\frac{4uf}{-q^2}r^2\cosh^2\left(-\frac{q}{2}t+s\right)\right],$$
$$V=\frac{a_1}{2}\left(t^2+\frac{r^2}{2}\right)+a_2t+a_3\ln r+a_4,$$
$$A=a_6+a_5r^2+\frac{ua_1^2}{32f}r^4+\ln\left[r^{(1+\frac{ua_3^2}{2f})}\cosh^2\left(-\frac{q}{2}t+s\right)\right]+$$
$$+\frac{u}{f}\left(\frac{a_1}{2}r^2+a_3\right)\left(\frac{a_1t^2}{2}+a_2t\right),$$

and

$$P(=\rho)=\frac{2f^2}{q^2}\left[4a_5-\frac{q^2}{2}-\frac{u}{f}(a_1a_3+a_2^2)\right]\operatorname{sech}^2\left(-\frac{q}{2}t+s\right)\cdot$$
$$\cdot r^{\frac{-ua_3^2}{f}}\cdot\exp\left[-2\left\{a_6+a_5r^2+\frac{ua_1^2}{32f}r^4+\right.\right.$$
$$\left.\left.+\frac{u}{f}\left(\frac{a_1}{2}r^2+a_3\right)\left(\frac{a_1t^2}{2}+a_2t\right)\right\}\right]. \tag{3.24}$$

Subcase (vi) b.

$$M=ft+d,\quad N=b-\frac{q}{2u}\tanh\left(-\frac{q}{2}\ln r+s\right),$$
$$B=\frac{1}{2}\ln\left[\frac{q^2}{4uf}\operatorname{sech}^2\left(-\frac{q}{2}\ln r+s\right)\right],$$
$$V=\frac{a_1}{2}\left(t^2+\frac{r^2}{2}\right)+a_2t+a_3\ln r+a_4,$$
$$A=a_6+a_5r^2\frac{ua_1^2}{32f}r^4+\left(\frac{q^2}{4}+\frac{ua_3^2}{2f}\right)\ln r+$$
$$+\frac{u}{f}\left(\frac{a_1}{2}r^2+a_3\right)\left(\frac{a_1t^2}{2}+a_2t\right)$$

and

$$P(=\rho) = \frac{q^2}{8u^2}\left[4a_5 - \frac{u}{f}(a_1a_3 + a_2^2)\right]\operatorname{sech}^2(-\frac{q}{2}\ln r + s)\cdot$$

$$\cdot r^{-(\frac{q^2}{2}+\frac{ua_3^2}{f})}\cdot\exp\left[-2\left\{a_6 + a_5r^2 + \frac{ua_1^2}{32f}r^4 + \right.\right.$$

$$\left.\left. + \frac{u}{f}(\frac{a_1}{2}r^2 + a_3)(\frac{a_1t^2}{2} + a_2t)\right\}\right]. \tag{3.25}$$

Case (vii) $C = 0, \quad M_1 \neq 0 \neq M_4$ *and* $N_1 \neq 0 \neq N_4$

If we assume in this case $M = N$ then the equation (2.12) reduces to

$$M_1^2 - M_4^2 = 0 \tag{3.26}$$

which implies that $M(= N)$ can be an arbitrary function of $(r \pm t)$. Thus, we first consider

$$M(= N) = M(r - t). \tag{3.27}$$

In view of (3.27), Eqs (2.14) and (2.15) lead to a single equation, i.e.,

$$B_1 + B_4 = \frac{1}{2r} \tag{3.28}$$

and (2.11) reduces to

$$\nabla_1 B = 0. \tag{3.29}$$

A common solution of (3.28) and (3.29) is

$$B = \frac{1}{2}\ln(\frac{r}{m}). \tag{3.30}$$

Here we also consider the solution of (2.16) as

$$V = \frac{a_1}{2}(t^2 + \frac{r^2}{2}) + a_2t + a_3\ln r + a_4. \tag{3.31}$$

Substituting the value of $M(= N)$, B and V from (3.27), (3.30) and (3.31) in (2.10) and after integration, we get

$$A = S(r) - \frac{u}{f}\cdot\frac{1+m^2}{m}\int M'^2\,dt + \frac{u}{f}(\frac{a_1}{2}r^2 + a_3)\cdot(\frac{a_1t^2}{2} + a_2t), \tag{3.32}$$

where $S(r)$ is an arbitrary function of r only and prime denotes differentiation w.r.t. the argument. As it is difficult to solve the equation (3.32) for arbitrary values of M, we consider the particular functional value of $M(= N)$ as

$$M = N = (r - t)^n, \tag{3.33}$$

where $n(\neq 0, \frac{1}{2})$ is any real number. It is evident that $n = 0$ corresponds only to matter fields where as $n = \frac{1}{2}$ corresponds to only an electromagnetic field. Solving Eq. (2.9) with the help of (3.30), (3.31), (3.32) and (3.33), we have

$$\begin{aligned} A = a_6 + a_5 r^2 + \frac{u a_1^2}{32 f} r^4 + \left(\frac{u a_3^2}{2f} + \frac{1}{4}\right) \ln r + \\ + \frac{u}{f}\left[\left(\frac{a_1}{2} r^2 + a_3\right)\left(\frac{a_1 t^2}{2} + a_2 t\right) + \frac{1 + m^2}{m} \cdot n^2 \frac{(r-t)^{2n-1}}{2n-1}\right], \end{aligned} \tag{3.34}$$

and

$$\begin{aligned} P(= \rho) = \frac{f}{2um}\left[4a_5 - \frac{u}{f}(a_1 a_3 + a_2^2)\right] \cdot r^{\left(\frac{1}{2} - \frac{u a_3^2}{f}\right)} \cdot \\ \cdot \exp\left[-2\left\{a_6 + a_5 r^2 + \frac{u a_1^2}{32 f} r^4 + \frac{u}{f}\left(\frac{a_1}{2} r^2 + a_3\right)\left(\frac{a_1 t^2}{2} + a_2 t\right) + \right.\right. \\ \left.\left. + \frac{1 + m^2}{m} \cdot n^2 \cdot \frac{(r-t)^{2n-1}}{2n-1}\right\}\right]. \end{aligned} \tag{3.35}$$

4. A method for general solution

As mentioned earlier the field equations except equation (2.16) are highly nonlinear. Moreover, the equation (2.16) is an equation in V alone whose integral can be obtained using Hankel [9] and Fourier [10] transforms as

$$V(r,t) = \int_0^\infty V(\eta, 0)\left[\int_0^\infty \mathrm{Cos}\xi t\, J_0(\eta\xi)\, J_0(r\xi)\xi\, d\xi\right]\eta d\eta, \tag{4.1a}$$

where

$$V_t(r, 0) = 0$$

and

$$V(r,t) = \int_0^\pi F(t + r\cos u)\, du + \int_0^\infty E(t + r\cosh u)\, du, \tag{4.1b}$$

where F and E are two arbitrary functions of their respective arguments. The latter solution exists when the integral exists and the differentiation is allowed under the integral sign. It may be mentioned here that the particular solution $V(r,t) = \ln r$

[11] of Eq. (2.16) can be shown to be a particular case of (4.1b) by a limiting process as follows:

$$\ln r = \lim_{n\to\infty} V_n(r,t), \tag{4.2}$$

where

$$V_n(r,t) = \frac{1}{\pi}\int_0^{\pi} \ln\frac{n}{2}\,du - \int_0^{\infty} \exp\{-n(t+r\cosh u)\}\,du. \tag{4.3}$$

However, all the solutions obtained in Section 3 may not be particular cases of (4.1b). The field equations (2.9), (2.10) and (2.16) enable us to redefine the metric potential A for linearly coupled source-free electromagnetic and massless scalar fields as

$$\overset{e-v}{A} = \overset{e}{A} + \overset{v}{A}, \tag{4.4}$$

where

$$\overset{v}{A} = \frac{K}{8\pi}\int r\left[(V_1^2+V_4^2)dr + 2V_1V_4\,dt\right] \tag{4.5}$$

and $\overset{e-v}{A}$ corresponds to the coupled source-free electromagnetic fields and massless scalar fields. The pressure cum energy density for this problem can be obtained from Eq. (2.13) using $\overset{e-v}{A}$ from (4.4). However, it is not possible to find out the explicit solution of the field equations with these values of V unless the exact functional forms of $V(r,0)$, E and F are known.

5. Physical behaviour of the solutions

(1) Energy conditions

(a) The stress energy density of scalar fields

$$T_{44} = \frac{1}{8\pi}(V_1^2+V_4^2)$$

is non negative and on t-constant hypersurface $T_{44} \to$ finite or ∞ as $r \to$ either 0 or ∞ and on r-constant hypersurface $T_{44} \to$ finite as $t \to 0$ and $T_{44} \to \infty$ as $t \to \infty$, for all solutions.

(b) The energy density associated with electromagnetic field

$$E_{44} = \frac{1}{8\pi}\left[\frac{e^{2B}}{r^2}\left\{(M_1-CN_1)^2+(M_4-CN_4)^2+e^{-2B}(N_1^2+N_4^2)\right\}\right]$$

is also non negative for all solutions.

(c) The pressure $P(=\rho)$ of the matter field is given by the field equation (2.13) on a t =constant hypersurface, we have $P \to \infty$ as $r \to 0$ and $P \to 0$ as $r \to \infty$ for all solutions except the case vii of Section 3. For this case on the t-constant hypersurface, we have as $r \to 0$, $P \to 0$ or finite or ∞ according as $\frac{Ka_3^2}{2\pi} \lesseqgtr 1$ and as $r \to \infty$, $P \to 0$.

In the range $0 < r < \infty$ the matter density is physically realistic subject to some restrictions on the arbitrary constants involved in the solutions. On r-constant hypersurface $= r_1$, we have $P \to$ finite as $t \to 0$ for all solutions and the pressure obtained in the cases i(a), ii(a), iii(b), iv(a), v(b) and vi(b) behave as follows:

(1) $P \to 0$ as $t \to \infty$ for the following cases
  (i) a_1 and a_3 are of the same sign,
  (ii) $a_3 > 0$ and $a_1 < -\frac{2a_3}{r_1^2}$,
  (iii) $a_3 < 0$ and $a_1 > -\frac{2a_3}{r_1^2}$.

(2) $P \to \infty$ as $t \to \infty$ for the following cases
  (i) $a_3 < 0$ and $0 < a_1 < -\frac{2a_3}{r_1^2}$,
  (ii) $a_3 > 0$ and $-\frac{2a_3}{r_1^2} < a_1 < 0$.

(3) If $a_1 = -\frac{2a_3}{r_1^2}$ then P being independent of t is finite for all t.

(4) The case $a_1 = 0$ leads to that of Mohanty [12].

For the rest of the solutions obtained in Section 3, on r-constant hypersurface, we get $P \to 0$ as $t \to \pm\infty$ when the arbitrary constants a_1, a_2 and a_3 are of the same sign.

(d) For the present case we have

$$T^{ab}U_aU_b = P + \frac{1}{2}e^{2B-2A}\left[\frac{e^{2B}}{r^2}(M_1^2 + M_4^2) + \right.$$
$$\left. + e^{-2B}(N_1^2 + N_4^2) + V_1^2 + V_4^2\right]$$

and

$$(T_{ab} - \frac{1}{2}g_{ab}T)U^aU^b = 2P + \frac{1}{2}e^{2B-2A}\left[\frac{e^{2B}}{r^2}(M_1^2 + M_4^2) + \right.$$
$$\left. + e^{-2B}(N_1^2 + N_4^2) + 2V_4^2\right].$$

Here both expressions being the sum of exponential and squared quantities are non-negative and they satisfy the Hawking and Penrose [13] energy conditions.

(2) Curvature scalar

The behaviour of curvature scalar is similar to that of scalar pressure P in each case.

(3) Behaviour of four velocity vector

The only surviving component of the four velocity vector is U_4 which for the solutions of the cases i(a), ii(a), iii(b), iv(a), v(b) and vi(b) behaves as follows:

On a t-constant hypersurface, we get the following three cases:

Case (i) $Ka_3^2 = 2\pi$

$$U_4 \to 0 \text{ as } r \to 0 \text{ when } |q| \neq 1, 0$$

$$\text{and } U_4 \to \text{ finite as } r \to 0 \text{ when } |q| = 1.$$

Case (ii) $Ka_3^2 > 2\pi$

$$U_4 \to 0 \text{ as } r \to 0 \text{ for all } q \neq 0.$$

Case (iii) $Ka_3^2 < 2\pi, \qquad q \neq 0$

as $r \to 0$, $U_4 \to 0$ or finite or ∞ according as $||q| - 1| \gtreqless \sqrt{1 - \frac{Ka_3^2}{2\pi}}$.

However, for all cases (except $q = 0$), we have $U_4 \to -\infty$ as $r \to \infty$. On r-constant hypersurface, we have $U_4 \to$ finite as $t \to 0$ and the limit of U_4 is similar to that of P as $t \to \pm\infty$ as shown earlier. For the rest of the solutions (except solution of case (vii)), t-constant hypersurface we get $U_4 \to 0$ as $r \to 0$ and $U_4 \to \infty$ as $r \to \infty$ and limit of U_4 as $t \to \infty$ on r-constant hypersurface depends on the arbitrary constants appearing in the solutions. The solution of case (vii) behaves as follows:

On t-constant hypersurface, we get as $r \to 0$, $U_4 \to 0$ or finite or ∞ according as $\frac{Ka_3^2}{2\pi} \gtreqless 1$ and as $r \to \infty$, $U_4 \to \infty$.

On r-constant hypersurface, we have $U_4 \to$finite as $t \to 0$ and the limit of U_4 as $t \to \pm\infty$ depends on a_1, a_2, a_3 and n.

U_4 tends either to zero or infinity indicating the presence of a singularity matching with that studied earlier in the case of the scalar pressure.

(4) Behaviour of the solutions in pseudo-Cartesian coordinates

Here we introduce pseudo-Cartesian coordinates in place of cylindrical polar coordinates with the help of the transformations $x = r\cos\theta$, $y = r\sin\theta$, $z = z$ and $t = t$ in order to avoid the coordinate singularity. In the transformed coordinates, it is found that the behaviour of $|g_{ij}|$ is exactly similar to that of U_4. Moreover, the cases where $|g_{ij}|$ tends to finite quantity the individual components are studied analytically [14]. It is observed that axis of symmetry, spatial infinity and temporal infinity are singularities for all solutions obtained in Section 3. This study supports the analysis already done in the earlier cases.

(5) Types of singularity

The P-symbol as defined by Liang [15] may be written in the present case as $\vec{P} = \left[\frac{A-B}{A-B}, \frac{-B}{A-B}, \frac{B}{A-B}\right]$.

For all solutions obtained in Section 3, it is evident that $\sum_i P_i = 1$ and $\sum_i P_i^2 \neq 1$. Thus, these singularities are called semi-Kasner type of singularities.

(6) Electromagnetic fields

(a) Duality: The set of solutions of the cases (i) and (ii) can be obtained from the solutions of the cases (iii) and (iv) and vice-versa by using the dual theorem [16]. Thus, these two sets of solution are dual to each other. The solutions found under the cases (v) and (vi) are self dual whereas the solution under the case (vii) is not self dual. We mean self dual in the sense that the solution is unchanged under the application of the dual theorem [16].

(b) Nullity: The only solution obtained under the case (vii) represents non-null electromagnetic field [17] whereas the rest of the solutions correspond to null-electromagnetic field which classically represents propagation of electromagnetic radiation with fundamental velocity.

(c) Uniformity: All the solutions obtained in Section 3 represent non-uniform electromagnetic fields i.e., $F_{ij;k} \neq 0$.

(7) W.M.P. class of solutions

The class of solutions generated by a relation between one of the metric potentials and one of the electromagnetic potentials is due to Weyl [18], Majumdar [19] and Papapetrou [20] and is known as W.M.P. Class. The class of solutions obtained in Section 3 includes both W.M.P. type and non-W.M.P. type of solutions [21].

(8) Line mass representation

None of the solutions represents the field due to line mass [22]. This is due to the presence of stiff fluid and zeromass scalar fields.

(9) Gravitational radiation

Pirani [23] has shown that the gravitational radiation exists if $r \equiv B_{14} + 5B_1B_4 + A_1B_4 - 3B_1A_4 \neq 0$. Each solution of Section 3 corresponds to a radiating field since $r \neq 0$. We may mention, however, in this case that the stiff fluid is present in contrast to the analysis of Pirani [23] which is based on empty spacetime.

6. Conclusion

It may be mentioned here that

1) the solutions of Mohanty [12] can be obtained from the corresponding solutions derived in Section 3 by putting $a_1 = 0$, $a_2 = a$, $a_3 = k$ and $a_4 = e$;
2) the solutions of Mohanty et al [24] can also be derived from the solutions obtained in Section 3 by putting $a_1 = a_2 = a_3 = a_4 = 0$;
3) the solutions of Rao et al [11] can also be obtained from the corresponding solutions in Section 3 if we remove the contribution of the stiff perfect fluid and consider $a_1 = a_2 = a_4 = 0$ and $a_3 = k$ with proper identification of the constants involved and
4) the solutions of Misra and Radhakrishna [25] can also be derived from the corresponding solutions of Section 3 removing the contributions of stiff perfect fluid and massless scalar fields with proper adjustment of arbitrary constants.

References

1. J. Ehlers, Z. Physik *143*, 139, 1955.
2. J. Ehlers, Dissertation, Hamburg, 1957.
3. P. Jordan, J. Ehlers and W. Kundt, Akad. Wiss. Mainz. Abh. Math. Nat. Kl. Jahg. No. 2, 1960.
4. A. Kompaneets, Soviet Phys. JETP, *34*, 659, 1958.
5. J. Stachel, Bull. Ann. Phys. Soc., *6*, 305, 1961.
6. J. Stachel, J. Math. Phys., *29*, 61, 1966.
7. T. Singh and B. S. Yadav, Acta Phys. Hung., *45*, 107, 1978.
8. P. S. Letelier, J. Math. Phys., *20*, 2079, 1979.
9. L. A. Pipes and L. R. Harvill, Applied Mathematics for Engineers and Physicists, Third Ed., 545, 1970.
10. P. Letelier and R. Tabensky, J. Math. Phys., *16*, 8, 1975.
11. J. R. Rao, A. R. Roy and R. N. Tiwari, Ann. Phys. (N. Y.), *69*, 473, 1972.
12. G. Mohanty, Ph. D. Thesis submitted to I. I. Kharagpur, India, Feb. 1981.
13. S. W. Hawking and R. Penrose, Proc. Roy. Soc., *A 314*, 529, 1970.
14. W. B. Bonnor, J. Math. Mach., *6*, 203, 1957.
15. E. P. T. Liang, J. M. P., *13*, 386, 1972.
16. W. B. Bonnor, Proc. Phys. Soc., *67*, 225, 1954.
17. J. L. Synge, Relativity: The Special Theory, North Holland Publishing Company, Amsterdam, 322, 1958.
18. H. Weyl, Ann. der Phys. 4th Series, *54*, 117, 1917.
19. S. D. Majumdar, Phys. Rev., *72*, 390, 1947.
20. A. Papapetrou, Proc. Roy. Irish. Acad. A, *51*, 191, 1947.
21. G. Mohanty, J. R. Rao and R. N. Tiwari, Proc. IAGRG–X, 111, 1979.
22. T. Levi–Cività, Anti. Acad. Naz. Lincei, *28*, (1), 101, 1919.
23. F. A. E. Pirani, Phys. Rev., *105*, 1089, 1957.
24. G. Mohanty, R. N. Tiwari and J. R. Rao, Int. J. Theor. Phys., *21*, 105, 1982.
25. M. Misra and L. Radhakrishna, Proc. Nat. Inst. Sci. India, Part A *28*, 632, 1962.

Appendix

The field equations (2.1) for the metric (2.5) take the following form:

$$G_{11} \equiv \frac{1}{4r^2}(C_1^2 + C_4^2)e^{4B} + B_1^2 + B_4^2 - \frac{A_1}{r} - \lambda e^{2A-2B} =$$
$$= -\frac{K}{8\pi}(V_1^2 + V_4^2 + g_{11}\bar{M}^2V^2) - \frac{K}{8\pi}\left[-g^{22}F_{12}^2 - g^{33}F_{13}^2 - g^{44}F_{14}^2 + \right.$$
$$\left. + g_{11}(g^{22}g^{33} - g^{23}g^{23})F_{23}^2 - g^{22}F_{24}^2 - g^{33}F_{34}^2 - 2g^{23}(F_{12}F_{13} + F_{24}F_{34})\right] -$$
$$- \frac{K}{4\pi}\left[(P+\rho)U_1^2 - Pg_{11}\right], \tag{A.1}$$

$$G_{22} \equiv \frac{3C^4}{4r^2}(C_4^2 - C_1^2)e^{8B-2A} + \left[\frac{1}{4}(C_1^2 - C_4^2) + 4C(B_1C_1 - B_4C_4) + C \bigtriangledown_2 C + \right.$$
$$\left. + C^2(2 \bigtriangledown_1 B - B_1^2 + B_4^2 - A_{11} + A_{44})\right] e^{4B-2A} + r^2(B_4^2 - B_1^2 + A_{44} - A_{11}) -$$
$$- \lambda(C^2e^{2B} + r^2e^{-2B}) = \frac{K}{8\pi}g_{22}\left[g^{11}(V_1^2 - V_4^2) + \bar{M}^2V^2\right] -$$
$$- \frac{K}{8\pi}\left[g^{11}\left\{(g_{22}g^{22} - 2)F_{12}^2 + g_{22}(g^{33}F_{13}^2 + g^{44}F_{14}^2)\right\} + \right.$$
$$\left. + \left\{g_{22}(g^{22}g^{33} - g^{23}g^{23}) - 2g^{33}\right\}F_{23}^2 + g^{44}(g_{22}g^{22} - 2)F_{24}^2 + \right.$$
$$\left. + g_{22}\left\{g^{33}g^{44}F_{34}^2 + 2g^{23}(g^{11}F_{12}F_{13} + g^{44}F_{24}F_{34})\right\}\right] -$$
$$- \frac{K}{4\pi}\left[(P+\rho)U_2^2 - Pg_{22}\right], \tag{A.2}$$

$$G_{33} \equiv \frac{3}{4r^2}(C_4^2 - C_1^2)e^{8B-2A} + (2 \bigtriangledown_1 B - B_1^2 + B_4^2 - A_{11} + A_{44}) \cdot$$
$$\cdot e^{4B-2A} - \lambda e^{2B} = \frac{K}{8\pi}g_{33}\left[g_{11}(V_1^2 - V_4^2) + \bar{M}^2V^2\right] -$$
$$- \frac{K}{8\pi}\left[g^{11}\left\{g^{22}g_{33}F_{12}^2 + (g_{33}g^{33} - 2)F_{13}^2 + g_{33}g^{44}F_{14}^2\right\} + \right.$$
$$\left. + \left\{g_{33}(g^{22}g^{33} - g^{23}g^{23}) - 2g^{22}\right\}F_{23}^2 + g^{22}g_{33}g^{44}F_{24}^2 + \right.$$
$$\left. + g^{44}(g_{33}g^{33} - 2)F_{34}^2 + 2g^{23}g_{33}(g^{11}F_{12}F_{13} + g^{44}F_{23}F_{34})\right] -$$
$$- \frac{K}{4\pi}\left[(P+\rho)U_3^2 - Pg_{33}\right], \tag{A.3}$$

$$G_{44} \equiv \frac{1}{4r^2}(C_1^2 + C_4^2)e^{4B} + B_1^2 + B_4^2 - \frac{A_1}{r} + \lambda e^{2A-2B} =$$
$$= -\frac{K}{8\pi}(V_1^2 + V_4^2 - g_{11}\bar{M}^2V^2) - \frac{K}{8\pi}\left[-g^{22}F_{12}^2 - g^{33}F_{13}^2 - \right.$$
$$\left. - g^{11}F_{14}^2 + g_{44}(g^{22}g^{33} - g^{23}g^{23})F_{23}^2 - g^{22}F_{24}^2 - g^{33}F_{34}^2 - \right.$$
$$\left. - 2g^{23}(F_{12}F_{13} + F_{24}F_{34})\right] - \frac{K}{4\pi}\left[(P+\rho)U_4^2 - Pg_{44}\right], \tag{A.4}$$

$$G_{14} \equiv \frac{C_1 C_4}{2r^2} e^{4B} + 2B_1 B_4 - \frac{A_4}{r} = -\frac{K}{4\pi} V_1 V_4 - \frac{K}{4\pi} [g^{22} F_{12} F_{24} + \\ + g^{33} F_{13} F_{34} + g^{23} (F_{12} F_{34} + F_{13} F_{24})] - \frac{K}{4\pi} (P + \rho) U_1 U_4, \qquad \text{(A.5)}$$

$$G_{23} \equiv \frac{3C}{4r^2} (C_4^2 - C_1^2) e^{8B-2A} + \left[\frac{1}{2} \nabla_2 C + 2(B_1 C_1 - B_4 C_4) + \right. \\ \left. + C(2 \nabla_1 B - B_1^2 + B_4^2 - A_{11} + A_{44})\right] e^{4B-2A} - \lambda C e^{2B} = \\ = \frac{K}{8\pi} g_{23} [g^{11} (V_1^2 - V_4^2) + \bar{M}^2 V^2] - \frac{K}{8\pi} [g^{11} g_{23} (g^{22} F_{12}^2 + \\ + g^{33} F_{13}^2 + g^{44} F_{14}^2) + \{g_{23} (g^{22} g^{33} - g^{23} g^{23}) - 2g^{23}\} F_{23}^2 + \\ + g_{23} g^{44} (g^{12} F_{24}^2 + g^{33} F_{34}^2) + 2g^{11} (g_{23} g^{23} - 1) F_{12} F_{13} + \\ + 2g^{44} (g_{23} g^{23} - 1) F_{24} F34] - \frac{K}{4\pi} [(P + \rho) U_2 U_3 . - P g_{23}]. \qquad \text{(A.6)}$$

In a comoving coordinate system (2.6), Eqs (A.1) and (A.4) yield

$$2\lambda g_{11} + \frac{K}{4\pi} [g^{11} F_{14}^2 + g_{11} (g^{22} g^{33} - g^{23} g^{23}) F_{23}^2 + \\ + (\rho - P) g_{11} + g_{11} \bar{M}^2 V^2] = 0. \qquad \text{(A.7)}$$

For the metric (2.5), Eq. (A.7) leads to

$$2\lambda + \frac{K}{4\pi} \left[e^{4B-4A} F_{14}^2 + \frac{1}{r^2} F_{23}^2 + (\rho - P) + \bar{M}^2 V^2\right] = 0. \qquad \text{(A.8)}$$

For an expanding universe $\lambda \geq 0$ and with a known physical distribution $\rho \geq P$, the above equation implies the only possibility that is given in (2.7). Since $\bar{M}$, P, ρ and σ are invariants, the results obtained in (2.7) and (2.8) viz., $\bar{M} = 0$, $P = \rho$ and $\sigma = 0$ for a comoving coordinate system will also hold for any other coordinate system. Thus the spacetime (2.5) does not sustain a charged perfect fluid with massive scalar fields even though this is not true in general for axially symmetric spacetimes. This may happen due to the implicitly cylindrical nature of the geometry (2.5). However, the same results i.e. (2.7) and (2.8) can also be derived separately choosing each field explicitly in Einstein's field equations. The equation of state is usually considered as an additional physical condition either with underdetermined physical situations or with the study of relativistic hydrodynamical conditions. In our problem the stiff nature of the perfect fluid is an inherent property of the spacetime considered.

Acta Physica Hungarica 67 (1–2), pp. 163–170 (1990)

THEORETICAL ANALYSIS OF THE EFFECTIVE ELECTRON MASS IN *n*-CHANNEL INVERSION LAYERS ON TERNARY SEMICONDUCTORS

N. CHATTOPADHYAY, K. P. GHATAK* and M. MONDAL**

Department of Physics

University College of Science and Technology, Calcutta-700009, India

(Received in revised form 14 May 1987)

An attempt is made to investigate theoretically the effective electron mass in *n*-channel inversion layers on ternary semiconductors on the basis of three band Kane model which has been stated in the literature to be the most valid model for the same semiconductor. It is found, taking *n*-channel inversion layers on $Hg_{1-x}Cd_xTe$ as an example, that for the low electric field limit the effective electron mass at the Fermi level depends both on the electric subband index and the Fermi energy due to the combined influence of the spin-orbit splitting parameter and the band non-parabolicity, respectively, whereas the same mass for high electric field limit depends on the electric subband index due to the spin-orbit splitting only. Besides, the Fermi level masses differ widely for relatively low values of the surface electric field in the low electric field limit and they decrease with increasing subband index for both limits. The well-known results for inversion layers on two-band Kane model are also obtained from the expressions derived.

Introduction

The effective mass of the carriers in semiconductors, which is strongly connected with the mobility, is known to be one of the most important device parameters [1]. In semiconductors with parabolic E-$\vec{k}$ dispersion relation the effective mass is independent of the energy whereas for non-parabolic bands it is not so. It must be mentioned that, among the various definitions of the electron effective mass [2], it is the momentum effective mass that should be regarded as the basic quantity. This is due to the fact that it is the momentum effective mass that appears in the description of the transport phenomena and all other properties of the electron gas in a band with arbitrary band non-parabolicity [3]. It can also be shown that it is this effective mass which enters in various types of transport coefficients and plays the most dominant role in explaining the experimental results of the different types of scattering mechanisms [4–5]. The carrier degeneracy in semiconductors influences the effective mass when it is energy dependent. Under degenerate conditions,

*Address for correspondence: Dr. K. P. Ghatak, Department of Electronics and Telecommunication Engineering, Faculty of Engineering and Technology, University of Jadavpur, Calcutta–700032 India.

**Department of Physics, Palpara College, Post-Palpara, District Midnapare, West-Bengal, India.

only the electrons at the Fermi surface of n-type semiconductors participate in the conduction process and hence the electron effective mass (hereafter referred to as EMM) corresponding to the Fermi energy would be of interest in electron transport under such conditions. The Fermi energy is again determined by the E-$\vec{k}$ dispersion relation and the carrier concentration and, therefore, these two parameters would mainly determine the dependence of the EMM in degenerate semiconductor on the degree of degeneracy.

In recent years various E-$\vec{k}$ relations for semiconductors under various physical conditions have been proposed, which have created the interest for studying the EMM in such semiconductors having varying band structures [6–15]. Besides, it is well-known that the electric quantization of the 2D electron gas in inversion layers on semiconductors drastically changes the basic E-$\vec{k}$ dispersion relation [16]. The various transport properties under such conditions have been studied for different types of energy bands [16]. It appears from the literature that the EMM in inversion layers on ternary semiconductors has been theoretically investigated on the basis of the two-band Kane model [22] since these semiconductors are increasingly used for the fabrication of infrared photo detectors and also since they have peculiar physical features [2]. The conduction band in ternary semiconductors is strongly non-parabolic where $E/Eg \simeq 1$ instead of being much less than unity as is often assumed in the literature (E is the electron energy as measured from the edge of the conduction band and Eg is the bandgap). It would be of much interest to study theoretically the EMM in inversion layers on ternary semiconductors for the more interesting case which occurs from the consideration of three-band Kane model [17,18], since the above model has been stated to be the most valid model for ternary semiconductors [19]. In what follows, we shall investigate the surface electric field dependence of the EMM by deriving the appropriate electron statistics, taking n-channel inversion layers on $Hg_{1-x}Cd_xTe$ as an example.

Theoretical background

The E-$\vec{k}$ dispersion relation of the conduction electrons in bulk specimens of Kane-type semiconductors in the absence of any quantization can be expressed [18], following Kane [17], as

$$\frac{\hbar^2 K^2}{2m_0^*} = r(E), \quad r(E) \equiv \frac{E(E+Eg)(E+Eg+\Delta)[(Eg+\frac{2}{3}\Delta)]}{Eg(Eg+\Delta)(E+Eg+\frac{2}{3}\Delta)}, \tag{1}$$

where $K^2 \equiv [k_x^2 + k_y^2 + k_z^2]$, $\hbar \equiv h/2\pi$, h is the Planck's constant, m_0^* is the effective electron mass at the edge of the conduction band and Δ is the spin-orbit splitting of the valence band. Thus, using Eq. (1) and following the method of Paasch et al [20], the corresponding 2D electron energy spectra can, respectively, be expressed under weak and strong electric field limits, as:

$$r(\epsilon) = (\hbar^2 k_s^2/2m_0^*) + \left[\hbar e F_s \Psi(\epsilon)/\sqrt{2m_0^*}\right]^{2/3} S_n \tag{2}$$

and

$$r(\epsilon) = (\hbar^2 k_s^2/2m_0^*) + \frac{4}{3}\left(\hbar e F_s/\sqrt{2m_0^* Eg}\right)\sqrt{L(\epsilon)}\; S_n^{3/2}, \tag{3}$$

where $k_s^2 \equiv k_x^2 + k_y^2$, $F_s \equiv \left(\frac{eN_s}{\epsilon_{sc}}\right)$ is the surface electric field applied perpendicular to the surface, e is the electron charge, N_s is the surface electron concentration, ϵ_{sc} is the semiconductor permittivity, $\psi(\epsilon) \equiv L(\epsilon)\Big[1+2\alpha\epsilon+\epsilon(1+\alpha\epsilon)\{(\epsilon+Eg+\Delta)^{-1} - -(\epsilon+Eg+\frac{2\Delta}{3})^{-1}\}\Big]$, $L(\epsilon) \equiv r(\epsilon)\,[\epsilon(1+\alpha\epsilon)]^{-1}$, ϵ is the energy measured from the edge of the conduction band at the surface, $\alpha \equiv 1/Eg$, S_n values are the zeros of the Airy function $\{A_i(-S_n) = 0\}$ [21] and $n(\equiv 0, 1, 2, \ldots)$ is the electronic subband index.

Using Eqs (2) and (3), the effective electron mass at the Fermi level can respectively be written under weak and strong electric field limits, as:

$$m_{n\omega}^*(E_{F\omega}) = m_0^*\left[D(\epsilon) - B(\epsilon)a_n\{\Psi(\epsilon)\}^{-1/3}\right]\Big|_{\epsilon=E_{F\omega}} \tag{4}$$

and

$$m_{ns}^*(E_{Fs}) = m_0^*\left[D(\epsilon) - b_n\{L(\epsilon)\}^{-1/2)}\delta(\epsilon)\right]\Big|_{\epsilon=E_{Fs}}, \tag{5}$$

where

$$D(\epsilon) \equiv \gamma(\epsilon)\left[\epsilon^{-1} + (\epsilon+Eg)^{-1} + (\epsilon+Eg+\Delta)^{-1} - (\epsilon+Eg+\frac{2}{3}\Delta)^{-1}\right],$$

$$B(\epsilon) \equiv \Psi(\epsilon)\delta(\epsilon)\,[L(\epsilon)]^{-1} + L(\epsilon)\Big[2\alpha + (1+2\alpha\epsilon)\{(\epsilon+Eg+\Delta)^{-1} - -(\epsilon+Eg+\frac{2}{3}\Delta)^{-1}\} - \epsilon(1+\alpha\epsilon)\{(\epsilon+Eg+\Delta)^{-2} - (\epsilon+Eg+\frac{2}{3}\Delta)^{-2}\}\Big],$$

$$\delta(\epsilon) \equiv [\epsilon(1+\alpha\epsilon)]^{-1}\,[B(\epsilon) - L(\epsilon)(1+2\alpha\epsilon)],$$

$$a_n \equiv \frac{2}{3}\left[\hbar e F_s/\sqrt{2m_0^*}\right]^{2/3} S_n, \qquad b_n \equiv \frac{2}{3}\left(eF_s\hbar/\sqrt{2m_0^* Eg}\right) S_n^{3/2},$$

$E_{F\omega}$ is the Fermi energy as measured from the edge of the conduction band at the surface in the low electric field limit and E_{Fs} is the Fermi energy corresponding to high electric field limit. It appears then that for evaluating $m_{n\omega}^*(E_{F\omega})$ and $m_{ns}^*(E_{Fs})$ corresponding to a given electric subband, one has to obtain the electron statistics, for both low and high electric field limits, which in turn is determined by the corresponding density-of-states function. Using Eqs (2) and (3) the density-of-state function can, respectively, be expressed under weak and strong electric field limits, as:

$$\rho_\omega(\epsilon) = \frac{m_0^*}{\pi\hbar^2}\sum_{n=0}^{n_{max}}\left[D(\epsilon) - B(\epsilon)a_n\{\Psi(\epsilon)\}^{-1/3}\right]H(\epsilon-\epsilon_{n\omega}), \tag{6}$$

$$\rho_s(\epsilon) = \frac{m_0^*}{\pi\hbar^2}\sum_{n=0}^{n_{max}}\left[D(\epsilon) - b_n\delta(\epsilon)\{L(\epsilon)\}^{-1/2}\right]H(\epsilon-\epsilon_{n\omega}), \tag{7}$$

where H is the Heaviside step function, $\epsilon_{n\omega}$ can be determined from the equation

$$r(\epsilon_{n\omega}) - S_n \left[\hbar e F_s \Psi(\epsilon_{n\omega})/\sqrt{2m_0^*}\right]^{2/3} = 0 \tag{8}$$

and ϵ_{ns} can be determined from the equation

$$r(\epsilon_{ns}) - \frac{4}{3}\frac{\hbar e F_s \sqrt{L(\epsilon_{ns})}}{\sqrt{2m_0^* E g}} S_n^{3/2} = 0. \tag{9}$$

Using Eqs (6) and (7) the surface electron concentration in low and high electric field limits can respectively be expressed as

$$N_{s\omega} = \frac{m_0^*}{\pi\hbar^2} \sum_{n=0}^{n_{max}} \left[X(n, E_{F\omega}) + Y(n, E_{F\omega})\right], \tag{10}$$

$$N_{ss} = \frac{m_0^*}{\pi\hbar^2} \sum_{n=0}^{n_{max}} \left[U(n, E_{Fs}) + V(n, E_{Fs})\right], \tag{11}$$

where the symbols are defined in the Appendix 1.1.

Incidentally, for large values of n, $S_n \to \left[\frac{3\pi}{8}(4n+3)\right]^{2/3}$ [22]. Thus, under the conditions $\Delta \to \infty$ and $S_n \to \left[\frac{3\pi}{8}(4n+3)\right]^{2/3}$, the Eqs (2) and (3) assume the forms

$$\epsilon(1+\alpha\epsilon) = \frac{\hbar^2 k_s^2}{2m_0^*} + \left[\frac{3}{2}\frac{\hbar e F_s \pi}{\sqrt{2m_0^*}}(1+2\alpha\epsilon)\right]^{2/3} \left(n+\frac{3}{4}\right)^{2/3} \tag{12}$$

and

$$\epsilon(1+\alpha\epsilon) = \frac{\hbar^2 k_s^2}{2m_0^*} + \left[\frac{2\pi\hbar e F_s}{\sqrt{2m_0^* E g}}\left(n+\frac{3}{4}\right)\right]. \tag{13}$$

Equations (12) and (13) were derived for the first time by Antcliffe et al for the two-band Kane model [22]. It is thus expected that, under these substitutions, the results derived in this paper should convert to simpler forms reported in the literature for the two-band Kane model. Using the above substitutions the Eqs (4) and (5) assume the following well-known forms [22]:

$$m_{n\omega}^*(E_{F\omega}) = m_0^* \left[1 + 2\alpha E_{F\omega} - \frac{4\alpha}{3}(1+2\alpha E_{F\omega})^{-1/3} \left\{\frac{3}{2}\frac{\hbar e F_s \pi}{\sqrt{2m_0^*}}\left(n+\frac{3}{4}\right)\right\}^{2/3}\right] \tag{14}$$

and

$$m_{ns}^*(E_{Fs}) = m_0^*(1+2\alpha E_{Fs}), \tag{15}$$

where the notations are defined in Appendix 1.2. The Eqs (14) and (15) were derived for the first time by Antcliffe et al [22]. Finally, it may be noted that

under the conditions $\Delta \to \infty$ and $S_n \to \left[\frac{3\pi}{8}(4n+3)\right]^{2/3}$, the Eqs (10) and (11) get simplified into

$$N_{s\omega} = \frac{m_0^* k_B T}{\pi\hbar^2} \sum_{n=0}^{n_{max}} \left[\left(1 + \frac{2}{3}\alpha\epsilon_{n\omega}\right) F_0(\eta_\omega) + 2\alpha k_B T F_1(\eta_\omega)\right] \tag{16}$$

and

$$N_{ss} = \frac{m_0^* k_B T}{\pi\hbar^2} \sum_{n=0}^{n_{max}} \left[(1 + 2\alpha\epsilon_{ns})\, F_0(\eta_s) + 2\alpha k_B T F_1(\eta_s)\right], \tag{17}$$

where the notations are defined in Appendix 1.2. The Eqs (16) and (17) were derived for the first time by Chakravarti et al [23].

Results and discussion

Using Eqs (4) and (10) together with the parameters [14, 2]

$$Eg(x) = \left[-0.303 + 1.73x + 5.6 \times 10^{-4}(1-2x)T + 0.25x^4\right] \text{eV},$$
$$m_0^*(x) = Eg(x)\left[0.1m_0^*\right], \qquad \Delta = 0.9 \text{ eV},$$

and

$$\epsilon_{sc}(x) = \left[20.262 - 14.812x + 5.279x^2\right] \epsilon_0$$

we have plotted $m_{n\omega}^*(E_{F\omega})/m_0$ for the first three electric subbands in n-channel inversion layers on $Hg_{1-x}Cd_xTe$ to $x = 0.23$ at 4.2 K as functions of the surface electric field limit by using Eqs (5) and (11), as function of the surface electric field as shown in Fig.1 in which the same dependence is also plotted by using the two-band Kane model for the purpose of comparison. Using the same parameters as used in obtaining Fig. 1, we have also plotted the EMM at the Fermi level for the first three electric subbands under strong electric field limit by using Eqs (5) and (11), as functions of the surface electric field as shown in Fig. 2, in which the simplified cases for the two-band Kane model have further been shown. From these Figures and the above discussion the following features follow:

(i) The EMM at the Fermi level in n-channel inversion layers on ternary semiconductors depends on both the electric subband index and Fermi energy due to the combined influence of the spin-orbit splitting parameter and the band non-parabolicity, respectively, for the low electric field limit;

(ii) the spin-orbit splitting parameter enhances the numerical values of the EMM's for both limits;

(iii) the EMM's at the Fermi level for high electric field limits depend on the electric subband index due to the influence of spin orbit splitting parameter only. For the two-band Kane model the EMM is independent of the electric subband index only for high electric field limit;

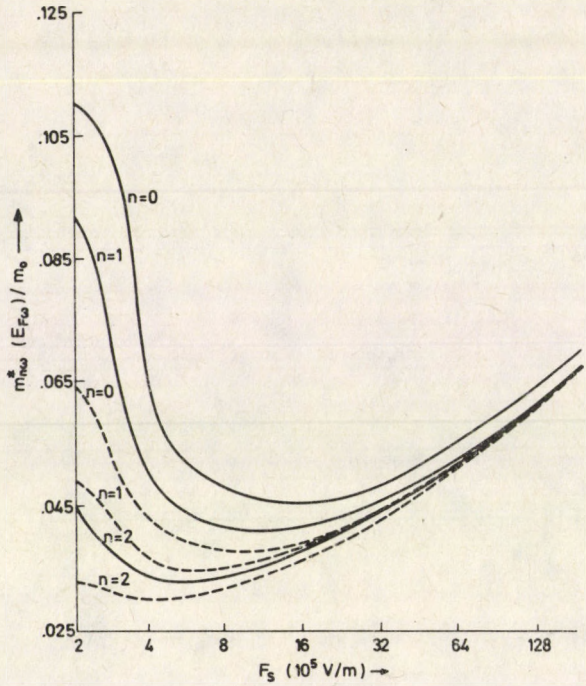

Fig. 1. Plot of the normalized effective electron masses under weak electric field limit as a function of F_s corresponding to $n = 0, 1$ and 2 in n-channel inversion layers on $Hg_{1-x}Cd_xTe$ for $x = 0.23$. The dashed plots corresponds to the two-band Kane model

(iv) the EMM's differ widely from each other for relatively small values of the surface electric field, especially under weak electric field, and they converge to a single value for relatively higher values of surface field for both limits and

(v) the EMM's decrease with increasing electric subband index for both limits.

It may be noted that for the purpose of simplicity, the effect of electron–electron interactions, the hot-electron effects and the formation of band tails have not been considered in the theoretical formulation. Besides, though the experimental verification of the basic content of this paper is not yet available to the best of our knowledge, the importance of the EMM in semiconductor physics has already been discussed. Furthermore, though the theoretical formulation is valid for the three-band Kane model but the numerical computations are valid for $x > 0.17$ since for $x < 0.17$ the bandgap becomes negative in $Hg_{1-x}Cd_xTe$ leading to semimetallic state [2]. Finally, it may be stated that, though in a more rigorous treatment the above modifications should be considered along with a self-consistent procedure, the simplified triangular potential well approximation exhibits the basic qualitative features of the EMM in n-channel inversion layers on ternary semiconductors and

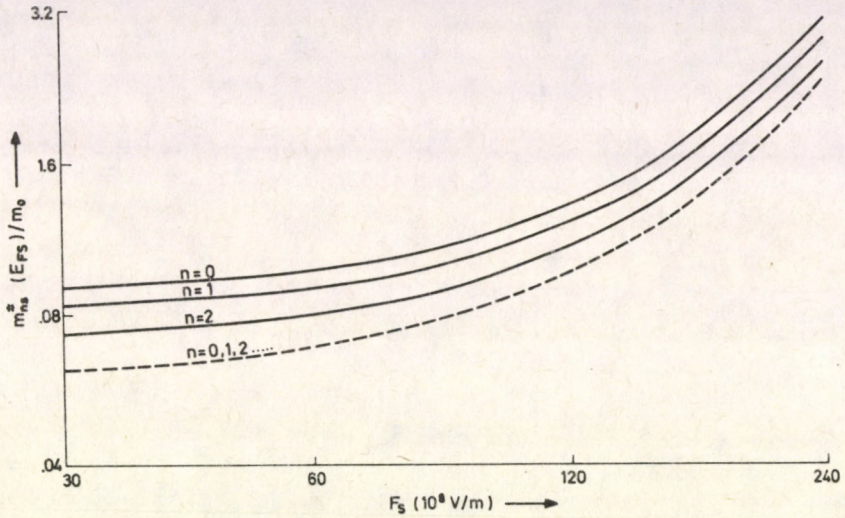

Fig. 2. Plot of the normalized effective electron masses under strong electric field limit as a function of F_s corresponding to $n = 0, 1$ and 2 in n-channel inversion layers on $Hg_{1-x}Cd_xTe$ for $x = 0.23$. The dotted plot corresponds to the two-band Kane model

the contributions of the index-dependent mass on the oscillatory mobility would be important.

Appendix

1.1. The functions $X(n,\epsilon)$, $Y(n,\epsilon)$, $U(n,\epsilon)$ and $V(n,\epsilon)$ are defined as follows:

$$X(n,\epsilon) = \left[r(\epsilon) - S_n\left\{\hbar e F_s \Psi(\epsilon)/\sqrt{2m_0^*}\right\}^{2/3}\right], \tag{1.1}$$

$$Y(n,\epsilon) = \sum_{r=1}^{s} 2\,(k_B T)^{2r}\left(1 - 2^{1-2r}\right)\zeta(2r)\frac{d^{2r}}{d\epsilon^{2r}}\left[X(n,\epsilon)\right], \tag{1.2}$$

$$U(n,\epsilon) = \left[r(\epsilon) - \frac{4}{3}\frac{eF_s\hbar\sqrt{L(\epsilon)}}{\sqrt{2m_0^* E g}}S_n^{3/2}\right] \tag{1.3}$$

and

$$V(n,\epsilon) = \sum_{r=1}^{s} 2\,(k_B T)^{2r}\left(1 - 2^{1-2r}\right)\zeta(2r)\frac{d^{2r}}{d\epsilon^{2r}}\left[U(n,\epsilon)\right], \tag{1.4}$$

where k_B is the Boltzmann constant, T is the temperature, r is the set of real positive integers and $\zeta(2r)$ is the zeta function of order $2r$ [21].

2.1. The functions $\epsilon_{n\omega}$, ϵ_{ns}, $F_j(\eta_{\omega,s})$ and $\eta_{\omega,s}$ are defined as follows:

$$\epsilon_{n\omega}(1+\alpha\epsilon_{n\omega}) - \left(\frac{3}{2}\frac{\hbar e F_s \pi}{\sqrt{2m_0^*}}\right)^{2/3}(1+2\alpha\epsilon_{n\omega})^{2/3}\left(n+\frac{3}{4}\right)^{2/3} = 0, \quad (2.1)$$

$$\epsilon_{ns}(1+\alpha\epsilon_{ns}) - \left[2\pi\hbar e F_s/\sqrt{2m_0^* Eg}\right]\left(n+\frac{3}{4}\right) = 0, \quad (2.2)$$

$$F_j(\eta_{n,s}) = \left(\sqrt{j+1}\right)^{-1}\int_0^\infty t^j\left[1+\exp(t-\eta_{\omega,s})\right]^{-1}dt, \quad (2.3)$$

$$\eta_{\omega,s} = (k_B T)^{-1}\left[E_{F\omega,s} - \epsilon_{n\omega,s}\right], \quad (2.4)$$

t is the dummy variable and j is the set of real numbers.

References

1. S. Adachi, J. Appl. Phys., *58*, 11, 1985.
2. R. Dornhaus and G. Nimtz , Springer Tracts in Mod. Phys., *78*. p. 1, Springer, Heidelberg, New York, 1976.
3. W. Zawadzki, in Handbook of Semiconductor Physics, *1*, p. 719, North-Holland Publishing Company, Amsterdam, 1982.
4. I. M. Tsidilkovskii, Cand. Thesis, Leningrad University, USSR, 1955.
5. F. G. Bass and I. M. Tsidilkovskii, Izv. Acad. Nauk. Azerb. SSR, *3*, No. 10, 1956.
6. V. K. Arora and H. Jeafarian, Phys. Rev., *13B*, 4457, 1976.
7. W. Zawadzki, Adv. Phys., *23*, 435, 1974.
8. M. I. Belovolov, N. B. Brandt, V. S. Vavilov and I. Ponomarev, Zh. eksper. teor. Fiz. *73*, 721, 1977.
9. I. M. Tsidilkovskii, Band Structure of Semiconductors, Pergamon Press, Oxford, 1982.
10. A. N. Chakravarti, K. P. Ghatak, K. K. Ghosh, S. Ghosh and A. Dhar, Z. Phys., *B17*, 149, 1982.
11. P. R. Wallace, Phys. Stat. Sol. (b), *92*, 49, 1979.
12. R. Rossler, Solid State Commun., *49*, 943, 1984.
13. F. L. Madarsaz, F. Szmulowicz and J. R. MeBath, J. Appl. Phys., *58*, 361, 1985.
14. M. Mondal and K. P. Ghatak, Phys. Stat. Sol. (b), *129*, 745, 1985.
15. H. Hazama, T. Sugimasa, T. Imachi and C. Hamaguchi, Jour. Phys. Soc. Japan, *55*, 1282, 1985.
16. T. Ando, A. H. Fowler and F. Stern, Rev. Mod. Phys., *54*, 437, 1982. and the references cited therein.
17. E. O. Kane, J. Phys. Chem. Solids, *1*, 249, 1957.
18. V. A. Villkotskii, D. S. Domanevskii, R. D. Kakanokov and V. V. Krasovskii, Sov. Phys. Semicond., *13*, 553, 1979.
19. C. Fan, J. F. Dame, M. De. Curalho, J. Calas, M. Averous and B. A. Lombos, Phys. Stat. Sol. (b), *125*, 831, 1984.
20. G. Paasch, T. Fiedler, M. Kolar and I. Bratos, Phys. Stat. Sol. (b), *118*, 641, 1983.
21. M. Abramovitz and I. A. Stegun, Handbook of Mathematical Functions, Washington D. C., 1964.
22. G. A. Antcliffe, R. T. Bate and R. A. Reynolds, Proc. Int. Conf. Phys. Semi-metals and Narrow-gap Semiconductors, Pergamon Press, Oxford, p.499, 1971.
23. A. N. Chakravarti, A. K. Chowdhury, K. P. Ghatak, A. Dhar and D. R. Choudhury, Czech. J. Phys., *B31*, 905, 1981.

Acta Physica Hungarica 67 (1-2), pp. 171–175 (1990)

SPECTROSCOPIC INVESTIGATION OF PRASEODYMIUM (III) CHLORIDE COMPLEXES OF SOME DICARBOXYLIC ACIDS

A. SURESH KUMAR and S. BUDDHUDU

Spectroscopic Laboratories, Department of Physics
Sri Venkateswara University, Tirupati - 517 502 India

(Received 4 June 1987)

The energy levels such as $^3P_{2,1,0}$, $^1D_2$, $^3F_{4,3}$ with $^3H_4$ as the ground term for $PrCl_3$ mixed in malic, α-ketoglutamic and tartaric acids have been determined. The environmental effects of coordination on the energy level structure and band intensities have been investigated by evaluating the necessary spectral characteristic parameters. The parameters thus obtained have been used for theoretically predicting the lifetimes of the fluorescent levels of the metal ion in three organic acids.

Introduction

During the last two years a few papers have been published on the electronic spectra of rare-earths in mineral acids [1, 2] and in laser liquids [3–6]. The infrared spectra of rare earth metals in organic complexes have been reported in the literature [7–10]. The present paper reports the energy levels, band intensities and radiative lifetimes of certain fluorescent levels of Pr(III) complexed with malic, α-ketoglutamic and tartaric acids.

Experimental studies

The organic acid complexes have been prepared by adding 0.1 M of $PrCl_3$ into liquid matrices of malic, α-ketoglutamic and tartaric (each in 5 ml quantity). These three acid complexes have been used in recording the UV-VIS spectra on Perkin-Elmer 551 and NIR spectra on Carl-Zeiss 61 spectrophotometers. The refractive indices of the complexes are measured on a Warszawa 3275 refractometer.

Results and discussion

The recorded spectral profiles of these Pr(III) complexes have revealed six energy levels that are assigned to the appropriate electronic transitions.

The theoretical evaluation of energies of the levels has been carried out by performing a least-square fit method as was made in the literature [11, 12]. The

experimental and calculated energies of the bands such as $^3P_{2,1,0}$; $^1D_2$; $^3F_{4,3}$ of Pr(III) in three organic acids are presented in Table I.

Table I

Experimental and calculated energies of $PrCl_3$ in organic complexes

Levels from $^3H_4$	Malic acid		α-ketoglutamic acid		tartaric acid	
	E_{expt} cm^{-1}	E_{calc} cm^{-1}	E_{expt} cm^{-1}	E_{calc} cm^{-1}	E_{expt} cm^{-1}	E_{calc} cm^{-1}
$^3P_2$	22618	22567	22516	22484	22721	22731
$^3P_1$	21449	21407	21316	21314	21546	21557
$^3P_0$	20741	20741	20698	20692	20915	20924
$^1D_2$	16973	16973	16916	16898	16973	16975
$^3F_4$	6800	6807	6750	6728	6850	6832
$^3F_3$	6150	6140	6150	6182	6200	6219
R. M. S. deviation	±27		±21		±12	

Table II

Values of Slater–Condon (F_2, F_4, F_6), Racah (E^1, E^2, E^3), configurational interaction (α, β), spin-orbit (ξ_{4f}), Judd–Ofelt (T_2, T_4, T_6), intensity ($\Omega_2, \Omega_4, \Omega_6$) parameters and refractive indices (n) for $PrCl_3$: organic acids

Parameters		Pr^{3+}		
		Malic acid	α-ketoglutamic acid	tartaric acid
F_2	[cm^{-1}]	320.75	314.88	321.75
F_4	[cm^{-1}]	54.67	50.05	54.67
F_6	[cm^{-1}]	5.32	4.94	5.24
E^1	[cm^{-1}]	5081.32	4832.56	5071.31
E^2	[cm^{-1}]	21.55	22.15	21.60
E^3	[cm^{-1}]	482.55	475.05	486.64
ξ_{4f}	[cm^{-1}]	765.21	746.96	760.21
α	[cm^{-1}]	111.32	22.17	12.08
β	[cm^{-1}]	−667.20	−600.15	−733.94
n		1.3460	1.3455	1.3660
T_2	[10^{-9}]	−11.87486	−8.67810	6.67958
T_4	[10^{-9}]	1.96166	1.03697	0.80086
T_6	[10^{-9}]	6.12216	4.44171	5.55092
Ω_2	[10^{-20}]	−82.13	−60.04	45.58
Ω_4	[10^{-20}]	13.57	7.17	5.46
Ω_6	[10^{-20}]	42.34	30.73	37.88
$^3P_1$	(T_R in μs)	43.55	70.29	20.37
$^3P_0$	(T_R in μs)	172.09	298.58	108.39
$^1D_2$	(T_R in μs)	528.28	314.94	137.64

The evaluated spectroscopic parameters of Slater–Condon (F_k), Racah (E^k), configurational interaction (α, β) and spin-orbit (ξ_{4f}) for Pr(III) complexes are

given in Table II. By following the mathematical expressions [13] relating to the determination of spectral intensities (both experimental and theoretical) of the bands, the values of band intensities for $^3P_{2,1,0}$ and $^1D_2$ of Pr(III) complexes have been calculated and presented in Table I. The band intensities of $^3F_{4,3}$ are weak which could not be measured. While calculating the theoretical intensity values from the experimental data a set of three phenomenological parameters T_λ (Judd–Ofelt), which characterize the band intensities, have been calculated and tabulated in Table II along with the energy-level structure parameters of the ion studied.

Table I reveals a good fitting between the experimental and calculated values of energies and band intensities, as the rms deviations appear to be reasonably low. Among the three Judd–Ofelt parameters only T_2 takes a negative sign in two hosts namely malic and α-ketoglutamic acids. It is due to the mixing of $4f - 5d$ orbitals in the electronic configurations ($4f^2$) of the ion. Previously Tandon et al [14] and Lakshman et al [15] have also reported such negative T_2 parameter values in various other hosts. From the Judd–Ofelt (T_λ) and the refractive indices (n), the intensity parameters (Ω_λ) have also been calculated and given in Table II following the procedures of Krishnamurthy et al [16]. According to Choppin et al [17], the band intensities remain varying with the coordination environment. The effectiveness of the hosts on the bands can be understood through these three Judd–Ofelt parameters. They have also pointed out that T_2 and T_6 parameters will significantly monitor the band intensities compared to the T_4 parameter. Such an observation can be noticed in the present work also by looking at the data presented in Tables I and II.

Table III

Measured and computed intensities for observed bands of $PrCl_3$: organic acids

	Pr^{3+}					
	Malic acid		α-ketoglutamic acid		tartaric acid	
Levels from $^3H_4$	f_{expt} [$\times 10^6$]	f_{calc} [$\times 10^6$]	f_{expt} [$\times 10^6$]	f_{calc} [$\times 10^6$]	f_{expt} [$\times 10^6$]	f_{calc} [$\times 10^6$]
$^3P_2$	20.50	20.51	14.38	14.49	17.88	17.88
$^3P_1$	7.18	7.18	5.01	3.76	4.91	2.94
$^3P_0$	1.01	7.01	2.50	3.70	9.91	2.88
$^1D_2$	5.31	5.31	3.73	3.73	5.39	5.39
R. M. S. deviation	±3.00		±0.87		±3.65	

As reported by Carnall et al [13], we have also made an attempt for calculating the values of lifetimes of fluorescent levels of Pr(III) complexes with the Judd–Ofelt intensity parameters. The necessary equations required for the evaluation of lifetimes of the levels are obtained by following Carnall et al [13]. The values of lifetimes thus received for the fluorescent levels such as $^3P_{1,0}$ and $^1D_2$ of Pr(III) complexes are given in Table III. Among these three levels, $^1D_2$ has the maximum T_R value and the least for $^3P_1$. From Table III it is noted that the T_R value for $^1D_2$ is found to be 12.4, which is 7 times greater than $^3P_1$ in malic, α-ketoglutamic

and tartaric acids, respectively. The lifetimes of the fluorescent levels are found to be in the following order

$$^1D_2 > {}^3P_0 > {}^3P_1.$$

This kind of trend has been noticed for Pr(III) ion in all the three acids. Looking at the numerical data of the lifetimes of fluorescent levels, it is noted that the lifetimes in three hosts are as follows

$$\begin{aligned} T_R(\mu s): \quad & |^3P_1\rangle : \alpha - \text{ketoglutamic} > \text{malic} > \text{tartaric} \\ & |^3P_0\rangle : \alpha - \text{ketoglutamic} > \text{malic} > \text{tartaric} \\ & |^1D_2\rangle : \text{malic} > \alpha - \text{ketoglutamic} > \text{tartaric} \end{aligned}$$

Similar observations have earlier been made for Pr^{3+} in organic complexes [18, 19].

Conclusion

About six energy levels have been measured from the recorded spectra of Pr(III) organic acid complexes of the present study. Since the rms deviations are reasonbly low between ± 12 and ± 27, a good energy level fitting between the experimental and calculated energies has been possible. The important results thus obtained are presented in Table I.

With regard to the band intensities only four bands could be correlated with the theoretical spectral intensities as shown in Table II.

The energy level parameters:

$$\begin{aligned} F_2, \quad F_4, \quad F_6 \quad & \text{(Slater–Condon)} \\ \alpha, \quad \beta \quad & \text{(configurational interaction)} \\ \xi_{4f} \quad & \text{(spin–orbit)} \end{aligned}$$

and the intensity parameters

$$\begin{aligned} T_2, \quad T_4, \quad T_6 \quad & \text{(Judd–Ofelt)} \\ \Omega_2, \quad \Omega_4, \quad \Omega_6 \quad & \text{(intensities)} \end{aligned}$$

are completed from the observed bands of Pr(III) and these values are presented in Table II. Through the absorption measurements, the lifetimes of the fluorescent levels $^3P_{1'}$, $^3P_0$ and $^1D_2$ of Pr(III) acid complexes have also been computed and the data are presented in Table II. The importance of the environments in predicting the lifetimes of excited electronic states of the ion studied has been understood. The influence of both on the spectral intensities has been found to be noteworthy by looking at the data shown in Table III.

Acknowledgement

The authors express their grateful thanks to Prof. S. V. J. Lakshman for his kind help and cooperation in the present work.

References

1. C. Krishna Murthy and S. Buddhudu, Ind. J. Physics, *60B*, 1, 1968.
2. V. R. Babu, S. V. J. Lakshman and S. Buddhudu, Bull. Pure and Appl. Sciences, *4D*, 33, 1985.
3. A. Heller, J. Molec. Spectrosc., *28*, 101, 1968.
4. S. V. J. Lakshman and L. R. Moorthy, J. Quart. Spec. Radiat. Transt., *29*, 439, 1983.
5. Y. C. Ratnakaram and S. Buddhudu, Material letters,*3 (9, 10)*, 389, 1985.
6. V. R. Babu, S. V. J. Lakshman and S. Buddhudu, J. Quart. Spec. Radiat., *33*, 657, 1985.
7. C. Krishna Murthy, L. R. Moorthy and S. Buddhudu, Mat. Sci. and Engg., *72*, L-31, 1985.
8. A. Suresh Kumar and S. Buddhudu, Ind. J. Pure and Appl. Phys., *24*, 90, 1986.
9. L. B. Zenner, E. Castro and E. Silva, J. Less Com. Metals, *94*, 309, 1983.
10. G. Vicentini and L. R. F. Cargalho, Lanthanide Actinides Res., *1*, 49, 1985.
    A. D. Sherry, A. Singh and C. F. G. C. Geraldes, J. Less Com. Metals, *112*, 255, 1985.
11. W. T. Carnall, J. P. Hessler and F. J. Wagner, J. Chem. Phys., *82*, 2152, 1979.
12. W. T. Carnall, H. M. Crosswhite and H. Crosswhite, Energy level structure and transition probabilities of trivalent lanthanides in LaF_3, Argonne National Laboratory, Argonne, USA, 1978.
13. W. T. Carnall, H. M. Crosswhite and H. Crosswhite, J. Chem. Phys., *64*, 3582, 1976.
14. S. P. Tandon, S. S. L. S. Sura and R. C. Mathur, J. Phys. C., *8*, 2323, 1975.
15. S. V. J. Lakshman and S. Buddhudu, J. Phys. and Chem. Solids, *43*, 849, 1982.
16. C. Krishnamurthy, M. Phil. Dissertation, S. V. University, Tirupati, 1985.
17. G. R. Choppin, R. L. Fellow and D. E. Henrie, Coord. Chem. Rev., *18*, 199, 1976.
18. A. S. Kumar and S. Buddhudu, Phys. Chem. Liq., *18*, 321, 1988.
19. A. S. Kumar and S. Buddhudu, J. Quant. Spec. Rad. Trans., *40*, 79, 1988.

Acta Physica Hungarica 67 (1–2), pp. 177–182 (1990)

PRECISE LATTICE CONSTANTS DETERMINATION OF ORTHORHOMBIC CRYSTALS FROM X-RAY POWDER DIFFRACTOMETRIC DATA

N. A. RAZIK, G. EL-BARAKATI and M. A. MOMEN

Physics Department, Faculty of Science, King Abdulaziz University
Jeddah, Saudi Arabia

(Received in revised form 4 June 1987)

An analytical method was formulated which can be used for the best estimates of the orthorhombic lattice constants from powder X-ray diffractometric measurements. The uncertainties in the values of these constants can be also estimated. Both random and systematic errors are minimized and no internal standard is required.

The method was applied to X-ray powder diffractometric data from sodium nitrite and was considered as highly reliable. With a simple BASIC computer program, the parameters and their uncertainties can be computed with unambiguous indexing.

1. Introduction

An analytical method has been produced for precise determination of lattice constants of cubic crystals [1] and of hexagonal, rhombohedral and tetragonal crystals [2]. The method was applied to X-ray powder diffractometric data from Si [1], from Al_2O_3 and calcium formate [2] and from T and α-phases in an Al-Zn-Mg alloy [3] and was found to be reliable for the best estimates of the lattice constants for these materials. In this paper, the method is extended to orthorhombic crystals.

2. Best estimates of lattice constants

When a diffractometer is used, the result of the combined action of the systematic errors is [1] an amount of error $(A \cos^2\theta_i \sin\theta_i)$ in the observed $\sin^2\theta_i$ value, where A is the drift constant. For the orthorhombic system, this error can be added to the Bragg equation in its quadratic form as

$$\sin^2\theta_i = \frac{\lambda^2}{4a_0^2} h_i^2 + \frac{\lambda^2}{4b_0^2} k_i^2 + \frac{\lambda^2}{4c_0^2} \ell_i^2 + A \cos^2\theta_i \sin\theta_i, \tag{1}$$

where a_0, b_0 and c_0 are the true values of lattice constants. Equation (1) can be written as

$$\frac{\sin^2\theta_i}{\delta_i} = A + B_1 \frac{h_i^2}{\delta_i} + B_2 \frac{k_i^2}{\delta_i} + B_3 \frac{\ell_i^2}{\delta_i} \tag{2}$$

or

$$y_i = A + B_1 x_{1i} + B_2 x_{2i} + B_3 x_{3i}, \tag{3}$$

where

$$B_1 = \frac{\lambda^2}{4\, a_0^2}, \qquad B_2 = \frac{\lambda^2}{4\, b_0^2}, \qquad B_3 = \frac{\lambda^2}{4\, c_0^2},$$

$$\delta_i = \cos^2 \theta_i \cdot \sin \theta_i, \quad x_{1i} = \frac{h_i^2}{\delta_i}, \quad x_{2i} = \frac{k_i^2}{\delta_i} \quad \text{and} \quad x_{3i} = \frac{\ell_i^2}{\delta_i} \tag{4}$$

Equation (3) represents a multiple linear regression model [4, 5] with three regression coefficients. The method of least squares can be used to estimate the regression coefficients. The best estimates of B_1, B_2 and B_3 are those which minimize $\sum_{i=1}^{N} \{y_i - A - \sum_{j=1}^{3} B_j x_{ji}\}^2$, with respect to A, B_1, B_2 and B_3, where N is the number of observations. The least squares normal equations are obtained in [4, 5] as:

$$\sum_i y_i = AN + B_1 \sum_i x_{1i} + B_2 \sum_i x_{2i} + B_3 \sum_i x_{3i}, \tag{5}$$

$$\sum_i x_{1i} y_i = A \sum_i x_{1i} + B_1 \sum_i x_{1i}^2 + B_2 \sum_i x_{1i} x_{2i} + B_3 \sum_i x_{1i} x_{3i}, \tag{6}$$

$$\sum_i x_{2i} y_i = A \sum_i x_{2i} + B_1 \sum_i x_{1i} x_{2i} + B_2 \sum_i x_{2i}^2 + B_3 \sum_i x_{2i} x_{3i}, \tag{7}$$

$$\sum_i x_{3i} y_i = A \sum_i x_{3i} + B_1 \sum_i x_{1i} x_{3i} + B_2 \sum_i x_{2i} x_{3i} + B_3 \sum_i x_{3i}^2. \tag{8}$$

The solution to the above normal equations will yield the least squares estimates of the coefficients. However, it is more convenient to deal with multiple regression models if they are expressed in matrix notation. Applying matrix algebra, it can be shown that the least squares estimates of A, B_1, B_2 and B_3 can be expressed as

$$A = \frac{1}{S}\left(S_1 \sum_i y_i - S_2 \sum_i x_{1i} y_i + S_3 \sum_i x_{2i} y_i - S_4 \sum_i x_{3i} y_i\right), \tag{9}$$

$$B_1 = \frac{1}{S}\left(-S_2 \sum_i y_i + S_5 \sum_i x_{1i} y_i - S_8 \sum_i x_{2i} y_i + S_7 \sum_i x_{3i} y_i\right), \tag{10}$$

$$B_2 = \frac{1}{S}\left(S_3 \sum_i y_i - S_6 \sum_i x_{1i} y_i + S_9 \sum_i x_{2i} y_i - S_{10} \sum_i x_{3i} y_i\right), \tag{11}$$

$$B_3 = \frac{1}{S}\left(-S_4 \sum_i y_i + S_7 \sum_i x_{1i} y_i - S_{10} \sum_i x_{2i} y_i + S_{11} \sum_i x_{3i} y_i\right), \tag{12}$$

where

$$S_1 = f_4 f_5 f_6 - f_4 f_9^2 - f_6 f_7^2 + 2 f_7 f_8 f_9 - f_8^2 f_5, \tag{13}$$

$$S_2 = f_1 f_5 f_6 - f_1 f_9^2 - f_2 f_6 f_7 + f_2 f_8 f_9 + f_3 f_7 f_9 - f_3 f_5 f_8, \tag{14}$$

$$S_3 = f_1 f_6 f_7 - f_1 f_8 f_9 - f_2 f_4 f_6 + f_2 f_8^2 + f_3 f_4 f_9 - f_3 f_7 f_8, \tag{15}$$

$$S_4 = f_1 f_7 f_9 - f_1 f_5 f_8 - f_2 f_4 f_9 + f_2 f_7 f_8 + f_3 f_4 f_5 - f_3 f_7^2, \tag{16}$$

$$S = S_1 N - S_2 f_1 + S_3 f_2 - S_4 f_3, \tag{17}$$

$$S_5 = N f_5 f_6 - N f_9^2 - f_2^2 f_6 + 2 f_2 f_3 f_9 - f_3^2 f_5, \tag{18}$$

$$S_6 = N f_6 f_7 - N f_8 f_9 - f_1 f_2 f_6 + f_2 f_3 f_8 + f_1 f_3 f_9 - f_3^2 f_7, \tag{19}$$

$$S_7 = N f_7 f_9 - N f_5 f_8 - f_1 f_2 f_9 + f_2^2 f_8 + f_1 f_3 f_5 - f_2 f_3 f_7, \tag{20}$$

$$S_8 = N f_6 f_7 - N f_8 f_9 - f_1 f_2 f_6 + f_1 f_3 f_9 + f_2 f_3 f_8 - f_3^2 f_7, \tag{21}$$

$$S_9 = N f_4 f_6 - N f_8^2 - f_1^2 f_6 + 2 f_1 f_3 f_8 - f_3^2 f_4, \tag{22}$$

$$S_{10} = N f_4 f_9 - N f_7 f_8 - f_1^2 f_9 + f_1 f_2 f_8 + f_1 f_3 f_7 - f_2 f_3 f_4, \tag{23}$$

$$S_{11} = N f_4 f_5 - N f_7^2 - f_1^2 f_5 + 2 f_1 f_2 f_7 - f_2^2 f_4, \tag{24}$$

$$f_1 = \sum_i x_{1i}, \qquad f_2 = \sum_i x_{2i}, \qquad f_3 = \sum_i x_{3i},$$

$$f_4 = \sum_i x_{1i}^2, \qquad f_5 = \sum_i x_{2i}^2, \qquad f_6 = \sum_i x_{3i}^2,$$

$$f_7 = \sum_i x_{1i} x_{2i}, \qquad f_8 = \sum_i x_{1i} x_{3i} \qquad \text{and} \qquad f_9 = \sum_i x_{2i} x_{3i}.$$

Therefore, to find the best estimates of the orthorhombic lattice constants, a_0, b_0 and c_0, we calculate the sum $S_1, S_2, \ldots, S, \ldots, S_{11}$ using (13)–(24), substitute their values into (10)–(12) and estimate the coefficients B_1, B_2 and B_3. The values of a_0, b_0 and c_0 can then be obtained with the aid of the relations $B_1 = \lambda^2/4a_0^2$, $B_2 = \lambda^2/4b_0^2$ and $B_3 = \lambda^2/4c_0^2$, respectively.

3. Uncertainties

The uncertainties in B_1, B_2 and B_3 can be obtained using the following relationships:

$$\sigma_{B_1}^2 = \frac{S_5}{S(N-4)} \sum_i \epsilon_i^2, \tag{25}$$

$$\sigma_{B_2}^2 = \frac{S_9}{S(N-4)} \sum_i \epsilon_i^2, \tag{26}$$

$$\sigma_{B_3}^2 = \frac{S_{11}}{S(N-4)} \sum_i \epsilon_i^2, \tag{27}$$

where

$$\epsilon_i = y_i - (A + B_1 x_{1i} + B_2 x_{2i} + B_3 x_{3i}). \tag{28}$$

It can be shown that the uncertainties in a_0, b_0 and c_0 are related to the uncertainties in B_1, B_2 and B_3, repectively, by the following relationships:

$$\sigma_{a_0}^2 = \sigma_{B_1}^2 \frac{\lambda^2}{16\, B_1^3}, \tag{29}$$

$$\sigma_{b_0}^2 = \sigma_{B_2}^2 \frac{\lambda^2}{16\, B_2^3}, \tag{30}$$

$$\sigma_{c_0}^2 = \sigma_{B_3}^2 \frac{\lambda^2}{16\, B_3^3}. \tag{31}$$

Thus, to estimate the uncertainties in the orthorhombic lattice constants, we calculate first the uncertainties in B_1, B_2 and B_3 using (9) and (25)–(28), substitute into (29)–(31) and find σ_{a_0}, σ_{b_0} and σ_{c_0}.

4. Experimental

An X-ray diffraction pattern was obtained from sodium nitrite ($NaNO_2$) at 298 K, which has an orthorhombic crystal structure, using Philips PW 1710 automated powder diffractometer with filtered Cu Kα radiation, wavelength 0.1541838 nm [6]. Each diffraction peak was detected by fitting a parabola on five points around the top and the 2θ-angle was given to three decimal places.

5. Results

To determine the best estimates of the lattice parameters a BASIC computer program was specially written. The program incorporates a continuous reindexing of the diffraction peaks for many times, based upon minimizing the difference $\Delta \sin^2\theta$ $(= \sin^2\theta_{\text{obs}} - \sin^2\theta_{\text{calc}})$, until no changes in the values of the lattice constants are obtained. The best estimates of the lattice constants of sodium nitrite, which were obtained by this procedure using our experimental data are:

$$a_0 = 0.35624 \pm 0.00013 \text{ nm},$$
$$b_0 = 0.55751 \pm 0.00023 \text{ nm},$$
$$c_0 = 0.53917 \pm 0.00014 \text{ nm}.$$

6. Discussion

Table I lists the observed and calculated lattice spacings, $\Delta \sin^2 \theta$ and Miller

Table I

Observed and calculated crystallographic data for $NaNO_2$

d_{obs} (nm)	d_{calc} (nm)	$\Delta \sin^2 \theta (\times 10^4)$	(hkl)
0.3850	0.3876	+5.2	011
0.2977	0.2974	−1.2	101
0.2789	0.2788	−0.8	020
0.2692	0.2696	+2.1	002
0.2034	0.2034	−0.1	121
0.2005	0.2006	+2.3	112
0.1937	0.1938	+0.9	022
0.1785	0.1783	−4.0	200
0.1709	0.1711	+3.4	013
0.1649	0.1648	−1.9	130
0.1504	0.1502	−6.0	220
0.1406	0.1406	−1.2	132
0.1391	0.1391	−1.4	123
0.1349	0.1348	−3.5	004
0.1312	0.1312	−0.6	222
0.1292	0.1292	+1.9	033
0.1262	0.1262	−2.1	141
0.1237	0.1238	+9.6	042
0.1213	0.1213	+1.2	024
0.1163	0.1163	−0.4	310
0.1071	0.1072	+4.1	321
0.1053	0.1052	−6.1	143
0.1046	0.1046	+4.8	233
0.1033	0.1032	−5.2	105
0.1018	0.1017	−6.1	242
0.1003	0.1003	−0.1	224
0.0968	0.0968	−1.1	125

indices for this material. The standard cell dimensions for sodium nitrite [7] at 299 K were given as

$$a_0 = 0.3570 \text{ nm},$$

$$b_0 = 0.5578 \text{ nm},$$

$$c_0 = 0.5390 \text{ nm}.$$

It may be seen that the present method of analysis can be considered as highly reliable. However, this method would yield only the best estimates or optimum values of lattice constants which can be obtained from an experimental set of data, and not necessarily the accurate or true values. If higher precision is required, certain refinements of experimental techniques should be carried out first. These include: accurate alignment and calibration of the diffractometer for more precise determination of the 2θ-values and the use of a good flat specimen held at a constant temperature.

Most correction methods [8, 9] were devoted mainly to the accuracy obtained from camera powder data. The present procedure considers the accuracy of diffractometric data and minimizes both random and systematic errors. The method is advantageous over other correction methods [10, 11] since: (i) it does not imply the use of an internal standard [10] to correct for systematic errors, (ii) a plot of $\Delta \sin^2 \theta$ versus θ to detect the degree of systematic errors and randomness [11] is not required and is subjective, and (iii) with a simple BASIC computer program, the parameters and their uncertainties can be computed with unambiguous indexing.

References

1. N. A. Razik, Appl. Phys., *A36*, 187, 1985.
2. N. A. Razik, Phys. Stat. Sol. (a), *90*, k125, 1985.
3. N. A. Razik, J. Mater. Sci. Lett., *4*, 1225, 1985.
4. D. C. Montgomery and E. A. Peck, Introduction to Linear Regression Analysis, Wiley, New York, 1982, p. 109.
5. N. R. Draper and H. Smith, Applied Regression Analysis, Wiley, New York, 1981, p. 193.
6. International Tables for X-Ray Crystallography, Kynoch Press, Birmingham, England, Vol. 4, 1974.
7. Powder Diffraction File, National Bureau of Standards, USA, Circular No. 539, Vol. 4, p. 62.
8. J. I. Langford and A. J. C. Wilson, J. Appl. Cryst., *6*, 197, 1973.
9. A. J. C. Wilson, Accuracy in Powder Diffraction, U.S. Natl. Bur. Stand. Spec. Publ., *567*, 1980, p. 325.
10. J. I. Langford, J. Appl. Cryst., *6*, 190, 1973.
11. M. Heaton and K. T. Miller, Acta Cryst., *13*, 828, 1960.

Acta Physica Hungarica 67 (1-2), pp. 183-191 (1990)

ATOMIC PROPERTIES THROUGH THOMAS–FERMI–DIRAC–WEIZSÄCKER THEORY

MARIO D. GLOSSMAN and EDUARDO A. CASTRO*

Research Institute for Theoretical and Applied Physical Chemistry
*Department for Theoretical Chemistry, La Plata, Republic of Argentina***

(Received 11 September 1987)

By using an approximate trial density and the consideration of an energy density functional which includes gradient corrections, total ground-state energies, its different components and some physical properties are calculated for atoms of low atomic number Z. The results are compared with Hartree–Fock values and with available experimental data.

Introduction

The main aim of density functional theory [1,2] is to use the density as the fundamental variable instead of the many-particle wavefunction and then to explore the ground-state properties of a system of interacting electrons. The fact that the ground-state properties of a system of interacting electrons are functionals of the electron density provides the basic framework of such formalism.

According to Hohenberg–Kohn theorems [1], both the ground state density ρ and the energy E can be variationally determined by minimizing the energy functional $E(\rho)$ with respect to a trial density subject to the normalization condition $\int \rho d\sigma = N$, or by means of the use of the stationary condition

$$\delta(E(\rho) - \mu \int \rho d\sigma) = 0,$$

where μ is a Lagrange multiplier that has been interpreted as chemical potential. The exact form of the functional $E(\rho)$ is unknown. The design of such functional would lead to a single differential equation useful for an ab initio calculation of the electron density. So, it would be highly desirable to obtain good approximate forms of the functional $(E\rho)$ and then solving the Euler equation for ρ, to obtain E.

It has been shown [3–5] that, for atoms, energy density functionals including gradient terms can give energy values that have excellent agreement with the experimental ones when Hartree–Fock charge densities are used [6]. But it would

*To whom all correspondence should be addressed

**Address: Instituto de Investigaciones Fisicoquímicas Teóricas y Aplicadas (INIFTA) - División Química Teórica - Casilla de Correo 16 Sucursal 4 -1900 - La Plata - República Argentina

be very important to minimize the energy functional in a variational way without making use of any other method.

Of course, the differential equations to be solved are non-linear and a variation of them represents a very complicated task. Although accurate numerical solutions of the variational equations are available for atoms and ions [7], analytical approximations for the ground-state density are of interest.

Then, a more direct approach is the use of trial density functions depending on some parameters which are determined by minimizing the total energy with respect to them.

The fundamental purpose of this paper is to work with an accurate analytical solution of the Thomas–Fermi–Dirac–Weizsäcker equation for atoms in order to obtain good values for the total energy and its different components for atoms of low atomic number Z, and to calculate some of their physical properties.

Theory

The ground-state energy functional $E(\rho)$ of an atom with atomic number Z can be written as (8)

$$E(\rho) = \int v(r)\rho(r)d\sigma + F(\rho), \tag{1}$$

where $F(\rho)$ is a universal functional that includes the contribution from kinetic energy and electron–electron interaction energy. It is possible to separate the Coulomb self-energy part from $F(\rho)$

$$F(\rho) = 1/2 \int\int \frac{\rho(r)\rho(r')}{|r-r'|} d\sigma d\sigma' + G(\rho) \tag{2}$$

and $G(\rho)$ can be decomposed as

$$G(\rho) = T(\rho) + E_{xc}(\rho), \tag{3}$$

where $T(\rho)$ and $E_{xc}(\rho)$ are the kinetic energy and the exchange-correlation energy functionals, respectively.

In this way, the total energy functional will be

$$E(\rho) = \int v(r)\rho(r)d\sigma + 1/2 \int\int \frac{\rho(r)\rho(r')}{|r-r'|} d\sigma d\sigma' + T(\rho) + E_{xc}(\rho). \tag{4}$$

As the exact form of $T(\rho)$ and $E_{xc}(\rho)$ is not known, it is necessary to resort to the approximate form of these functionals. In this work we are going to neglect the correlation energy part of $E_{xc}(\rho)$ and write

$$E_x(\rho) = K_0(\rho) + K_2(\rho), \tag{5}$$

where $K_0(\rho)$ is the homogeneous electron gas approximation of Dirac for exchange energy [9a,9b]

$$K_0(\rho) = -\frac{3}{4}\left(\frac{3}{\pi}\right)^{1/3} \int \rho^{4/3}(r)\, d\sigma,$$

and $K_2(\rho)$ is the exchange-inhomogeneity correction term [10,11]

$$K_2(\rho) = C_x \int \frac{|\nabla\rho|^2}{\rho^{4/3}} d\sigma, \tag{6}$$

with C_x a constant whose value is -4.64×10^{-3}.

In general, the kinetic energy functional can be expressed as an infinite gradient expansion as follows (12)

$$T(\rho) = T_0(\rho) + T_2(\rho) + T_4(\rho) + \ldots \tag{7}$$

In this work, we are going to consider only the first two terms in the expansion, namely, the so called Thomas–Fermi term [13]

$$T_0(\rho) = \frac{3}{10}(3\pi^2)^{2/3} \int \rho^{5/3} d\sigma \tag{8}$$

and the second, that is one ninth of the inhomogeneity correction term suggested by Weizsäcker [14]

$$T_2(\rho) = \frac{1}{72} \int \frac{|\nabla\rho|^2}{\rho} d\sigma. \tag{9}$$

In order to minimize the energy functional $E(\rho)$ we are going to choose a trial density function represented by a superposition of decreasing exponential functions [15]. In this way we write

$$\rho(r) = \left[\sum_i^4 \alpha_i e^{-\beta i n}\right]^3, \tag{10}$$

where α_i, β_i are variational parameters that may be determined by a variation of the energy functional with respect to these parameters.

The introduction of the approximate trial density ρ from (10) in the energy functional $E(\rho)$ leads to the following analytical expressions for the different components of energy:

$$T_0 = \frac{12}{5}\pi(3\pi^2)^{2/3} \sum_i^4 \frac{\alpha_i\alpha_j\alpha_k\alpha_l\alpha_m}{(\beta_i+\beta_j+\beta_k+\beta_l+\beta_m)^3}, \tag{11}$$

$$T_2 = \pi \sum_i^4 \frac{\alpha_i\alpha_j\alpha_k\beta_j\beta_k}{(\beta_i+\beta_j+\beta_k)^3}, \tag{12}$$

$$K_0 = 6\pi(3/\pi)^{1/3} \sum_i^4 \frac{\alpha_i\alpha_j\alpha_k\alpha_l}{(\beta_i+\beta_j+\beta_k+\beta_l)^3}, \tag{13}$$

$$K_2 = 72\pi C_x \sum_i^4 \frac{\alpha_i\alpha_j\beta_i\beta_j}{(\beta_i+\beta_j)^3}, \tag{14}$$

$$V_{ne} = -4\pi Z \sum_i^4 \frac{\alpha_i\alpha_j\alpha_k}{(\beta_i+\beta_j+\beta_k)^2}, \tag{15}$$

and

$$J = 16\pi^2 \sum_i^4 \alpha_i\alpha_j\alpha_k\alpha_l\alpha_m\alpha_n$$

$$\frac{[(\beta_i+\beta_j+\beta_k+\beta_l+\beta_m+\beta_n)^2+(\beta_i+\beta_j+\beta_k)(\beta_l+\beta_m+\beta_n)]}{[(\beta_i+\beta_j+\beta_k)^2(\beta_l+\beta_m+\beta_n)^2\times(\beta_i+\beta_j+\beta_k+\beta_l+\beta_m+\beta_n)^3]}. \tag{16}$$

The ground-state energy is determined by minimizing $E(\rho)$ subject to the condition (normalization) expressed by

$$\sum_i^4 \frac{\alpha_i\alpha_j\alpha_k}{(\beta_i+\beta_j+\beta_k)^3} = \frac{N}{8\pi}. \tag{17}$$

Several atomic properties, such as the diamagnetic susceptibility (16), the polarizability (17) and the cross-section for coherent X-ray scattering, can each be related to a certain expectation value of the type $\langle r^n\rangle$.

Thus, the diamagnetic susceptibility of an atom is given by the well-known formula (18)

$$\chi \equiv S = -\frac{Ne^2}{6mc^2}\langle r^2\rangle, \tag{18}$$

where N is the Avogadro's number, m the electron-mass, e the electron charge, c the speed of light, and

$$\langle r^2\rangle = 4\pi \int_0^\infty r^4\rho dr. \tag{19}$$

In the present model, the diamagnetic susceptibility of an atom is given (in units of 10^{-6} cm^3/mole) by

$$S = -238.8575 \sum_i^4 \frac{\alpha_i\alpha_j\alpha_k}{(\beta_i+\beta_j+\beta_k)^5}. \tag{20}$$

The atomic polarizability is given by (18)

$$\alpha = \frac{4}{9Za_0}\langle r^2\rangle^2 \tag{21}$$

and it is possible to relate this quantity with the diamagnetic susceptibility through (17)

$$\alpha = \frac{16m^2c^4}{N^2e^4a_0}\,\frac{S^2}{Z}. \tag{22}$$

Although the formulas of these properties have been derived on the basis of quantum-mechanical considerations, the calculation of them is an interesting way to check the accuracy of the optimized density function.

Results and discussion

We have applied the model to the calculation of total energy, diamagnetic susceptibilities and polarizabilities of atoms of low atomic number Z.

Table I

Optimized density parameters α_i and β_i for the trial density function

Z	α_1	α_2	α_3	α_4
8	5.10857	1.67104	0.59401	0.00052
9	5.34972	1.94432	0.57802	0.00050
10	5.43145	2.10325	0.63521	0.00048
11	5.91451	2.21448	0.66957	0.00047
12	6.32278	2.22253	0.69611	0.00046
13	7.67259	2.02289	0.71444	0.00045
14	9.80929	1.28731	0.92823	0.00042
15	9.87723	1.74658	0.70877	0.00040
16	10.56805	1.81933	0.66223	0.00037
17	11.05978	1.66683	0.89479	0.00035
18	11.12978	2.27303	0.48697	0.00032
	β_1	β_2	β_3	β_4
8	8.95324	2.35906	0.39002	0.08099
9	9.32852	2.33106	0.37263	0.08954
10	9.41795	2.27854	0.42356	0.09988
11	9.87188	2.28512	0.44046	0.10104
12	9.83453	2.27154	0.44512	0.10221
13	10.78348	2.00083	0.47261	0.10340
14	11.59864	1.34775	0.66715	0.10527
15	11.57611	1.55104	0.50422	0.10754
16	11.93070	1.51320	0.46386	0.10914
17	12.35952	1.30267	0.74625	0.11057
18	12.59123	1.20082	0.85333	0.11579

Table II

Total kinetic energy T and its components T_0 and T_2

Z	T_0		T_2		T	
	a	*b*	*a*	*b*	*a*	*b*
8	71.8	67.1	6.7	6.4	78.4	73.5
9	91.4	90.1	7.7	8.1	99.2	98.2
10	119.3	117.8	8.8	10.1	128.1	127.8
11	150.3	148.8	10.5	12.3	160.7	161.1
12	182.3	184.0	12.0	14.7	194.3	198.7
13	224.6	223.4	15.2	17.4	239.8	240.8
14	267.2	267.2	19.8	20.3	287.1	287.5
15	317.7	315.5	21.7	23.5	339.4	339.0
16	360.0	368.6	24.4	26.8	384.5	395.4
17	419.0	426.7	26.9	30.4	445.9	457.1
18	484.8	489.9	28.9	34.3	513.7	524.2

a) Present results

b) Results obtained by using Hartree–Fock densities - Ref.[22]

In Table I we give the values of α_i, β_i parameters obtained by minimization of the energy functional. By considering that not only the total energy but also its various components are important, it is interesting to present the latter and to compare them with those results obtained by making use of Hartree–Fock densities [5,20–23], as has been told before. Thus, in Table II we give the total kinetic energy T and its components T_0 and T_2 for the atoms studied here together with the values obtained through Hartree–Fock densities. The same is done in Tables III and IV for the case of the exchange-interaction terms K_0 and K_2, the electron–electron repulsion energy V_{ee} and the electron–nuclear attraction V_{ne}.

Table III

Total exchange energy K, its components K_0 and K_2 and electron–nuclear interaction energy V_{ne}

Z	$-K_0$	$-K_2$	$-K(a)$	$-K_{HF}$	$-V_{ne}(a)$	$-V_{ne}(HF)$
8	7.1	1.0	8.1	7.7	181.8	178.1
9	8.6	1.2	9.7	9.7	236.0	238.7
10	10.7	1.3	12.0	12.1	308.5	308.0
11	12.6	1.4	14.0	14.0	387.7	389.7
12	14.5	1.5	16.0	16.0	471.9	462.0
13	16.4	1.7	18.1	18.0	576.8	578.4
14	18.0	2.0	20.0	20.1	683.9	689.5
15	20.3	2.1	22.3	22.3	805.3	812.3
16	21.9	2.2	24.1	24.7	919.6	916.9
17	25.3	2.4	27.7	27.3	1079.5	1068.3
18	28.7	2.5	31.2	30.2	1251.0	1255.1

a) Present results

HF) Hartree–Fock values

Table IV

Kinetic energies T, exchange energies K, electron–nuclear interaction energies V_{ne} and electron–electron interaction energies V_{ee}

Z	T	$-K$	$-V_{ne}$	V_{ee}	$-E(a)$	$-E_{HF}$
8	78.4	8.1	181.8	33.4	78.0	79.8
9	99.2	9.7	236.0	43.9	102.6	99.4
10	128.1	12.0	308.5	61.8	130.6	128.5
11	160.7	14.0	387.7	77.9	163.2	161.9
12	194.3	16.0	471.8	94.3	199.3	199.6
13	239.8	18.1	576.8	112.1	243.0	241.9
14	287.1	20.0	683.9	127.3	289.5	288.9
15	339.4	22.3	805.3	148.7	339.5	340.7
16	384.5	24.1	919.6	165.0	394.2	397.5
17	445.9	27.7	1079.5	205.5	455.8	459.5
18	513.7	31.2	1251.0	247.4	521.1	526.8

a) Present results
HF) Hartree–Fock values of total energy

We can see that the total energy values are very close to the Hartree–Fock ones. The difference ranges, in all cases, from 1 to 2%. The same conclusion is valid when we consider the various energy components. Although the differences between the calculated total kinetic energies $T_0 + T_2$ and the Hartree–Fock values is very low, it is probable that the consideration of another term in the gradient expansions will permit us to obtain better results. On the other hand, for the case of the total exchange energy, that is $K_0 + K_2$, our results are practically the same as those obtained through Hartree–Fock densities.

Table V

Diamagnetic susceptibilities (in units of 10^{-6} cm^3/mole)

Z	$-S(a)$	$-S(b)$
8	8.85	24.99
9	8.11	29.09
10	7.47	21.62
11	21.52	21.23
12	23.46	22.62
13	26.52	20.20
14	25.56	14.87
15	23.99	19.79
16	23.11	23.89
17	21.86	14.22
18	20.63	11.80

a) Hartree–Fock values - Ref. [24]
b) Present results

In Table V we report the diamagnetic susceptibilities for the atoms under consideration and in Table VI we give the corresponding atomic polarizabilities. As the latter are related to the former through Eq. (22), both present similar discrepancies with the results obtained by means of Hartree–Fock densities [24]. In this manner, the errors are large and it is probably due to the fact that the trial density used in this work cannot reproduce the Hartree–Fock ones in detail, but only in a general way. Nevertheless, the results show certain oscillations or monotonicity with the atomic number Z that cannot be obtained when gradient corrections are not considered.

In the light of the above results, we can conclude that a variational procedure like the considered one used in this work, including gradient corrections in the energy functional, combined with the trial density function proposed in this paper, is a useful way of calculating atomic total energies, its components, charge densities and some physical properties that are independent of the details of the density, and open the question about the possibility of obtaining good expectation values of quantities which are not directly associated with the energy density functional.

Table VI

Atomic polarizabilities (in units of 10^{-24} cm^3)

Z	$\alpha(a)$	$\alpha(b)$
8	0.73	8.22
9	0.53	9.90
10	0.39	4.92
11	18.67	4.32
12	14.13	4.49
13	10.97	3.31
14	6.81	1.66
15	4.42	2.75
16	3.44	3.76
17	2.61	1.25
18	1.98	0.81

a) Hartree–Fock values - Ref. [24]
b) Present results

Acknowledgement

INIFTA is a research institute jointly established by the Universidad Nacional de La Plata, the Consejo Nacional de Investigaciones Científicas y Técnicas and the Comisión de Investigaciones Científicas de la Provincia de Buenos Aires.

References

1. P. Hohenberg and W. Kohn, Phys. Rev., B *136*, 864, 1964.
2. R. G. Parr, Ann. Rev. Phys. Chem., *34*, 63, 1983.
3. Y. S. Kim and R. G. Gordon, J. Chem. Phys., *60*, 1842, 1974.
4. C. C. Shih and R. D. Present, Bull. Am. Phys. Soc., *21*, 381, 1976.
5. W. P. Wang, R. G. Parr, D. R. Murphy and G. A. Henderson, Chem. Phys. Lett., *43*, 409, 1976.
6. S. K. Ghosh and B. M. Deb, Phys. Rep., *92*, 1, 1982.
7. W. Stich, E. K. U. Gross, P. Malzacher and R. M. Dreizler, Z. Phys. A. Atoms and Nuclei, *309*, 5, 1982
8. W. Kohn and L. J. Sham, Phys. Rev. A *140*, 1133, 1965.
9. a) P. A. M. Dirac, Proc. Camb. Philos. Soc., *26*, 376, 1930.
   b) N. H. March, Self-Consistent Fields in Atoms, Pergamon, Oxford, 1975.
10. F. Herman, J. P. Van Dyke and I. B. Ortenburger, Phys. Rev. Lett., *22*, 807, 1969.
11. W. P. Wang and R. G. Parr, Phys. Rev., A *16*, 891, 1977.
12. C. H. Hodges, Can. J. Phys., *51*, 1428, 1973
13. N. H. March, Adv. Phys., *6*, 1, 1957.
14. C. F. von Weizsäcker, Z. Phys., *96*, 431, 1935.
15. W. P. Wang and R. G. Parr, Phys. Rev., A *16*, 409, 1976.
16. J. H. van Vleck, Phys. Rev., *31*, 587, 1928.
17. J. G. Kirkwood, Z. Phys., *33*, 57, 1932.
18. P. Gombás, Die Statistische Theorie des Atoms, Springer, Vienna, 1949.
19. P. Csavinszky, J. Chem. Phys., *52*, 304, 1970.
20. M. Berrondo and A. Flores-Riveros, J. Chem. Phys., *72*, 6299, 1980
21. C. Shih, J. Chem. Phys., *72*, 1404, 1980.
22. D. R. Murphy and W. P. Wang, J. Chem. Phys., *72*, 429, 1980.
23. P. Politzer, J. Chem. Phys., *72*, 3027, 1980.
24. S. Fraga, J. Karwowski and K. M. S. Saxena, Handbook of Atomic Data, Elsevier, Amsterdam, 1976.

Acta Physica Hungarica 67 (1-2), pp. 193-202 (1990)

STOPPING POWER FOR HEAVY IONS IN SOLIDS

M. M. ABDEL-HADY, A. M. SALEM and M. MORSY

Physics Department, Faculty of Science, Ain Shams University
Cairo, Egypt

(Received in revised form 25 November 1987)

Monte Carlo calculations have been performed to simulate both electronic and nuclear stopping power for different projectile $Z_1 = (2 \rightarrow 95)$ moving in several elemental stoppers (Cu, Au, Ag, Fe, Ni). The calculations have been carried out for different values of energies up to 30 MeV. The percentages of nuclear stopping power were obtained at various energies. By comparing the simulated electronic stopping power with published experimental data, adjustable factor $f_e(Z_1, Z_2)$ was established for particular values of projectile energies to correct data from (LSS) theory.

Introduction

The importance of investigations on the stopping powers of heavy ions in matter refers to their widely used applications in nuclear and atomic physics. In some experiments aiming at the determination of nuclear data, the accuracy of the results obtained depends drastically on the actual value of stopping powers, used during evaluation, (e.g. in the measurement lifetimes from Doppler broadened gamma-ray lineshapes, or the measurement of cross-sections using thick targets).

LSS [1] theory is widely used to describe the slowing process of ions moving in a stopper, where the ion loses its energy due to both inelastic and elastic collisions. The first process is due to interactions with atomic electrons which continuously decelerate the ions but do not affect its direction of motion, while elastic collisions are due to interactions of ions with atomic nuclei. This interaction results in discrete scattering events associated with deviations in the direction of motion of the ion. The basic characteristics of the slowing process are strongly determined by the potential function adopted for the description of Coulomb interactions between slowing ions and stopping atoms. The Thomas–Fermi potential is normally used in calculating the scattering function. On the other hand, the energy loss due to inelastic collisions with the electron shells of the stopper atoms could be treated in different ranges of energies using different models [2,3,4,5].

Lindhard and coworkers introduced the correction factors f_e and f_n to compensate for several approximations introduced by them in the mathematical treatment for electronic and nuclear stopping powers, respectively. The correction factors have been used by many authors, e.g. by Blaugrund [6] in his formalism of multiple scattering theory, by Kregar et al [7] in their discontinuous stopping model and

by Schane et al [8], who displayed a complete description of optimization for both electronic and nuclear stoppings of Ca penetrating in carbon, for some initial energies. The latter authors determined f_e and f_n values from a comparison between γ-ray experimental lineshapes and Monte Carlo calculations by χ^2 fitting. Abdel-Hady et al [9,10] used the same method in their Monte Carlo calculations of γ-ray lineshape of 6.2 MeV excited state of N^{14} nucleus produced as an excited recoil in $C^{13}(p,\gamma)N^{14}$ reaction. They concluded that f_e is slightly fluctuating around unity. On the other hand, f_n is usually less than 1. They deduced correction factors dependent on the atomic numbers of both recoil and stopper atoms (Z_1,Z_2) as well as on the energy of the recoil. Recently, Keinonen et al [11] have investigated the velocity dependence of electronic stopping powers in low velocity region and Ziegler et al [12] have studied the dependence of energy loss on the atomic numbers of both target and projectile.

The aim of the present work is to test the validity of the LSS stopping theory by comparing simulated electronic stopping powers with the experimental results for different projectiles moving in different stoppers. From such comparison, the correction factor f_e could be formulated in the polynomial form of $f_e(Z_1,Z_2)$ to improve the application performances of the LSS theory.

Experimental data were taken from the literature. The Chalk River group [13] published the electronic stopping powers for projectiles with atomic number $Z_1 = 8 \rightarrow 20$, penetrating through five different stoppers (Cu, Au, Ag, Fe, Ni) with a projectile energy $E = 0.5$ MeV/a.m.u. Also, Brown and Moak [14], Ramavataram [15], Both and Garant [16] have measured the electronic stopping powers for ions of $Z_1 = 2 \rightarrow 95$, penetrating through stoppers Au, Ag and Ni for particular values by energy $E = 0.25$ and 1.0 MeV/a.m.u.

Theoretical basis for the Monte Carlo method

(LSS) theory describes the slowing process of heavy ions. It uses Thomas–Fermi potential to derive the general expressions for the stopping power of ions being slowed down in an elemental material. The specific energy loss (dE/dX) for an ion or an excited recoil nucleus is a consequence of collision processes. The electronic stopping power is given in the (LSS) theory, after several approximations, by a simple formula,

$$(d\varepsilon/d\rho)_e = f_e K \varepsilon^p, \tag{1}$$

where

$$\varepsilon = E[aM_2/Z_1Z_2\, e^2(M_1 + M_2)], \tag{1.a}$$

$$\rho = X \cdot 4\pi a^2 N[M_1M_2/(M_1 + M_2)^2] \tag{1.b}$$

are dimensionless variables for the energy E and the range X, a is the screening length given by

$$a = 0.8853a_0(Z_1^{2/3} + Z_2^{2/3})^{-\frac{1}{2}}, \tag{1.c}$$

with $a_0 = (\hbar^2/me^2)$, $\hbar$ is Planck's constant, e and m are the electronic charge and mass, respectively. Constant K depends on the atomic and mass numbers of both recoil ion and stopper and is given by

$$K = Z_1^{1/6}[0.0793\ Z_1^{1/2}\ Z_2^{1/2}(M_1+M_2)^{3/2}]/[(Z_1^{2/3}+Z_2^{2/3})^{3/4}\cdot M_1^{3/2}\cdot M_2^{1/2}], \quad (1.d)$$

where Z_1, Z_2 and M_1, M_2 are the atomic and mass numbers for both recoil and target, respectively, $p \simeq 0.5$, f_e is an adjustable correction factor near unity, N is the number of atoms per unit volume of target.

The nuclear stopping powers were derived according to the scattering theory of Lindhard. On the basis of several approximations, it gives the conclusion that the scattering angle Θ in the centre of mass system depends on the energy and energy transfer in the collision process. The scattering angle and differential cross-section can be calculated in terms of an arbitrary variable x given by:

$$x = \varepsilon \sin(\Theta/2) \quad (2)$$

and

$$d\sigma = f_n \pi a^2 [F(x)/x^2]dx, \quad (3)$$

while the corresponding nuclear stopping power is given by:

$$(d\varepsilon/d\rho)_n = (f_n/\varepsilon)\int_0^{\varepsilon} F(x)dx, \quad (4)$$

where a is the screening length depending on the impact parameter. f_n is an adjustable factor close to unity, $F(x)$ is a universal scattering function derived by Lindhard [4] using the potential

$$V(r) = Z_1 Z_2 e^2 U(r/a)/r, \quad (5)$$

where $U(r/a)$ is a screening function which can be derived using the so called magic formula of Lindhard [4].

The Monte Carlo method is a statistical technique used to calculate the frequency distribution of given statistical phenomena. Its basic feature is the randomisation of all variables during the current histories of calculations, e.g., the initial energy and direction of recoil, the scattering angles (polar, asimuthal). The description is published in details in [10]. In the stopping power calculations by Monte Carlo method, a projectile enters a stopper of a given thickness with a given energy and direction. Using (LSS) theory [Eqs (1), (4)], both electronic and nuclear stopping powers have to be aggregated on the current version of history, repeating for a large number of histories, (e.g. 10 000), and calculating the average of $(dE/dX)_e$ and $(dE/dX)_n$. On the path of current histories, the random variables are taken from suitable distributions satisfying the physical meaning of interest.

Computations

The computations have been made by writing a program for Monte Carlo calculations based on the LSS Theory. The present program is a major modification to the technique used by Currie [17] and produces both electronic and nuclear stopping powers as functions of recoil energy for certain projectiles moving in a particular elemental stopper. The modifications were done to improve the statistics of results and to minimize the consumption in calculation time. The modifications are described in details by Abdel-Hady et al [9,10,18].

The process has been simulated by the Monte Carlo Method for 10000 histories with $f_e = f_n = 1$. The initial energy of each history is considered to be the same in the forward direction of the beam. The stopping powers are calculated for projectiles of atomic numbers $Z_1 = 2 \rightarrow 95$ penetrating through targets Cu, Au, Fe and Ni. The energy of a projectile is taken as variable up to 30 MeV. Least square fitting procedures have been followed to compare the available experimental and calculated electronic stopping for projectile energies 0.25, 0.5, 1 MeV/a.m.u. Dividing the experimental formula by the theoretical one, the correction factor f_e could be obtained and formulated using χ^2 fitting as polynomial of second order

$$f_e(Z_1, Z_2) = A(Z_2) + B(Z_2) \cdot Z_1 + C(Z_2) \cdot Z_1^2. \tag{6}$$

Polynomial interpolation procedures have been applied to formulate the functions $A(Z_2)$, $B(Z_2)$, $C(Z_2)$.

The applied formula is

$$P(Z) = \sum_{i=1}^{n} R_i(Z_i) \prod_{\substack{i=1 \\ j \neq i}}^{n} \left(\frac{Z - Z_i}{Z_j - Z_i} \right), \tag{7}$$

where n is the number of points (R_i, Z_i).

The above formula is used three times to derive A, B and C, for each available value of projectile energy.

Results and conclusions

The predicted electronic stopping powers simulated by the Monte Carlo method for a Ca projectile moving in various stoppers (Ni, Ag, Cu, Fe), as the function of projectile energy up to 30 MeV are presented in Fig. 1, while the nuclear stopping powers are displayed in Fig. 2. The correction factors (f_e, f_n) are considered to be unity in these calculations. The results presented in Fig. 3 are the percentage of nuclear stopping power as the function of projectile energy. A sample of curves is chosen for Ca moving in stoppers Ni and Ag. The solid curves in Figs 4, 5, 6 are the simulated electronic stopping powers as functions of projectile atomic number up to 95, with f_e=1. The experimental results of various authors are also

shown in the Figures. The dotted curves are the results of applying the correction factor $f_e(Z_1, Z_2)$. The Figures are typical relations corresponding to the values of projectile energies E =0.25, 0.5, and 1.0 MeV/a.m.u., respectively. The curves in Fig. 7 present the predicted correction factor f_e as a function of projectile atomic number up to $Z_1 = 60$, at fixed projectile energy $E = 1$ MeV/a.m.u. Three curves are displayed for three stoppers (Ag, Au and Ni).

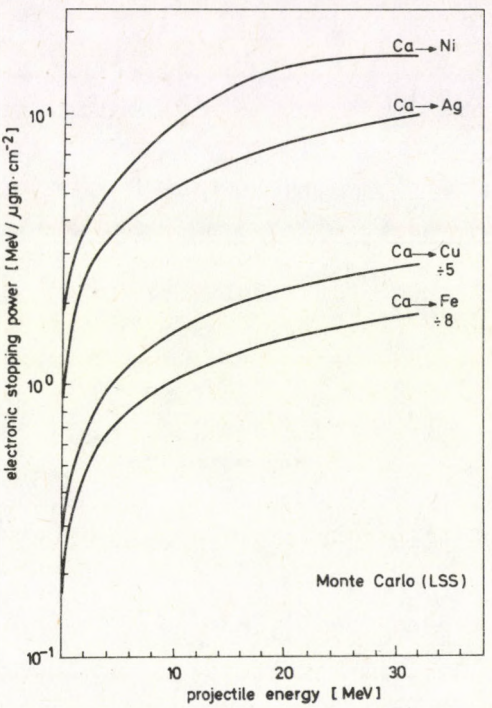

Fig. 1. Monte Carlo electronic stopping power as a function of projectile energy

The results obtained for the function A, B, C are as follows:
a) For projectile energy $E = 0.25$ MeV/a.m.u.

$$A(Z_2) = -2.802 \times 10^{-4} \cdot Z_2^2 + 0.0375 \cdot Z_2 + 0.2803,$$
$$B(Z_2) = -0.061 \times 10^{-4} \cdot Z_2^2 + 0.037 \times 10^{-3} \cdot Z_2 - 0.0129$$

and

$$C(Z_2) = 0.7505 \times 10^{-7} \cdot Z_2^2 - 0.6057 \times 10^{-5} \cdot Z_2 + 0.166 \times 10^{-3}. \quad (8)$$

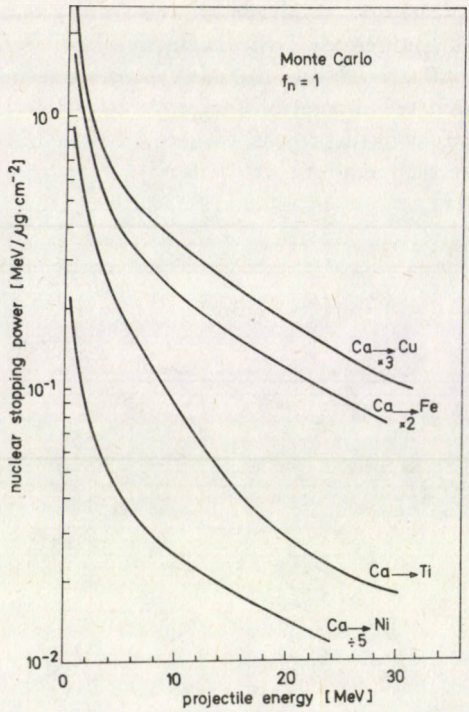

Fig. 2. Monte Carlo nuclear stopping power as a function of projectile energy

b) For projectile energy $E = 0.5$ MeV/a.m.u.

$$A(Z_2) = -2.875 \times 10^{-3} \cdot Z_2^4 + 0.05241 \cdot Z_2^3 - 3.334 \cdot Z_2^2 + 88.67 \cdot Z_2 - 842.1,$$

$$B(Z_2) = 0.404 \times 10^{-4} \cdot Z_2^4 - 0.7374 \times 10^{-2} \cdot Z_2^3 + 0.4698 \cdot Z_2^2 - 12.52 \cdot Z_2 + 119.2$$

and

$$C(Z_2) = -0.185 \times 10^{-5} \cdot Z_2^4 + 0.3366 \times 10^{-3} \cdot Z_2^3 - 0.02136 \times Z_2^2 + 0.5661 \cdot Z_2 - 5.358. \quad (9)$$

c) For projectile energy $E = 1.0$ MeV/a.m.u.

$$A(Z_2) = -0.0779 \times 10^{-3} \cdot Z_2^2 + 0.01944 \cdot Z_2 - 0.4955,$$

$$B(Z_2) = 0.08 \times 10^{-4} \cdot Z_2^2 - 0.18 \times 10^{-2} \cdot Z_2 + 0.1217$$

and

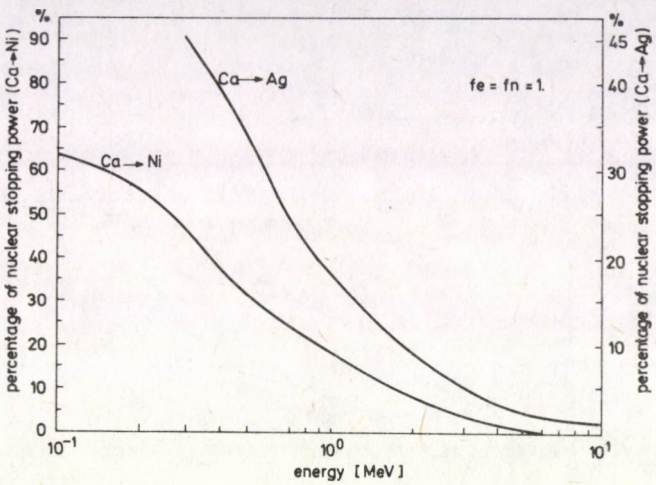

Fig. 3. Percentage of nuclear stopping power as a function of projectile energy

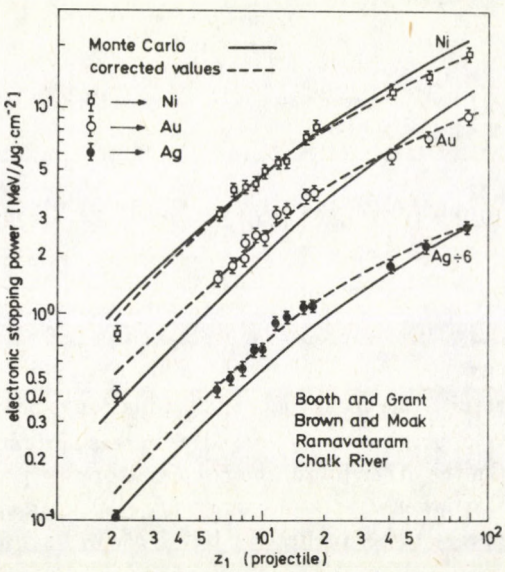

Fig. 4. Electronic stopping power as a function of atomic number of projectile for fixed energy $E = 0.25$ MeV/nucleon

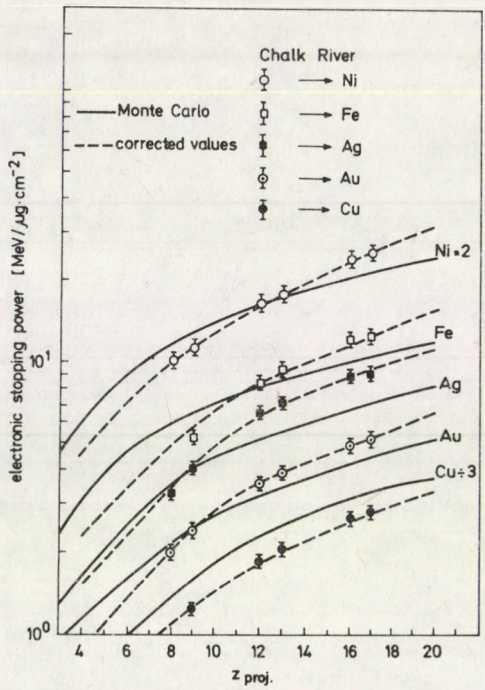

Fig. 5. Z_{proj} dependence of electronic stopping power at fixed energy $E = 0.5$ MeV/nucleon

$$C(Z_2) = -0.04912 \times 10^{-5} \cdot Z_2^2 + 0.072 \times 10^{-3} \cdot Z_2 - 0.2727 \times 10^{-2}. \tag{10}$$

The factor $f_e(Z_1, Z_2)$ can be used to correct in the LSS theory according to the actual particle energy.

From the above results, the following conclusions could be drawn:

i) The electronic stopping power is a rapidly increasing function of projectile energy up to 20 MeV. On the other hand, the nuclear stopping process is dominant with a percentage ≥ 65 at lower values of energy ($E \leq 0.1$ MeV) and rapidly decreases with projectile energy to be uneffective $E > 3$ MeV, where it becomes about 3%.

ii) From a comparison with published experiments, the calculated electronic stopping power given by the LSS theory is not accurate enough, and should be corrected according to the expected range of energy.

iii) The correction factor $f_e(Z_1, Z_2)$ is drastically varying with atomic numbers of both projectile and stopper, and the validity of LSS theory is questionable in particular for lighter projectiles.

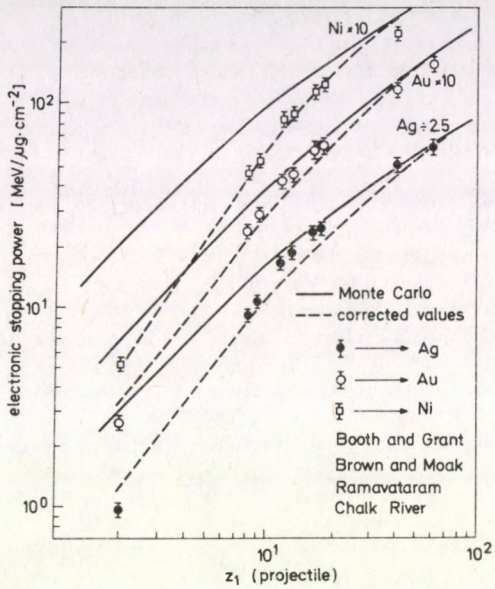

Fig. 6. Electronic stopping power as a function of projectile atomic number for fixed energy $E = 1$ MeV/nucleon

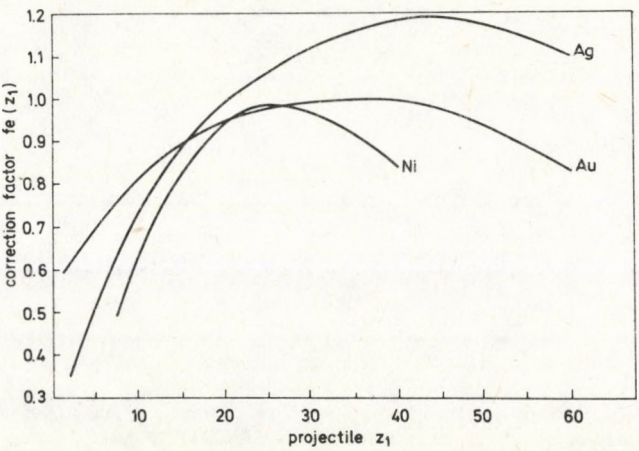

Fig. 7. Correction factor as a function of projectile atomic number for different stopper $E = 1$ MeV/amu

Acknowledgements

The authors are grateful to Prof. Dr. A. Goned for useful discussions. Thanks are due to Prof. Dr. E. Koltay for valuable advice.

References

1. J. Lindhard, M. Scharff and H. E. Schiott, K. Dan. Vidensk. Selsk., Mat. Phys. Medd., *33*, No. 14, 1963.
2. N. Bohr, Mat. Fys. Medd. Dan. Vid. Selsk., *18*, 8, 1948.
3. O. B. Firsov, Interaction Energy of Atoms for Small Nuclear Separations, Sov. Phys. JETP, *5*, 1192, 1957.
4. J. Lindhard, Vebeke Nielson and M. Scharff, Mat. Fys. Med., *36*, 10, 1968.
5. Hans E. Schiott, Mat. Fys. Medd., *35*, 9, 1966.
6. A. E. Blaugrund, Nuc. Phys., *88*, 501, 1966.
7. M. Kregar, P. Kump, M. Pavsic and M. Vakselj, NIM, *109*, 1973.
8. K. C. Schane, H. Laumer and G. G. Seaman, J. of Applied Phys., *47*, 6, 1976.
9. M. M. Abdel-Hady, A. Z. Kiss, E. Koltay, B. Nyakó and M. Hautala, Acta Phys. Hung., *58*, 11, 1985.
10. M. M. Abdel-Hady, A. Z. Kiss, E. Koltay, B. Nyakó, Gy. Szabó, Atomki Közlemények, *25*, 207, 1983.
11. J. Keinonen, A. Kuronen, M. Hautala, V. Karttunen, R. Lappalainen, Phys. Lett., *A 123*, 307, 1987.
12. J. F. Ziegler, J. P. Biersack and U. Littmark, (Vol. 1 Pergamon, New York, 1985).
13. D. Ward, J. S. Froster, H. R. Andrew, I. V. Michel, G. C. Ball, W. G. Davies and G. J. Costa, Berkeley Super HILAC User Meeting, Berkeley, December 15-17, 1975.
14. M. D. Brown and C. D. Moak, Phys. Rev., *B6*, 90, 1972.
15. D. I. Porat and K. Ramavataram, Proc. Roy. Soc., *A252*, 394, 1959; Proc. Phys. Soc., *77*, 97, 1961 and *78*, 1135, 1961.
16. D. W. Booth and I. S. Garant, Nucl. Phys., *63*, 481, 1965.
17. W. M. Currie, NIM *73*, 173, 1969.
18. M. M. Abdel-Hady, Ph. D. Thesis, Institute of Nuclear Research of the Hungarian Academy of Sciences, 1983.

Acta Physica Hungarica 67 (1–2), pp. 203–209 (1990)

MAGNETO-THERMOSOLUTAL CONVECTION IN A VISCOELASTIC FLUID IN POROUS MEDIUM

R. C. SHARMA and Y. D. SHARMA

Department of Mathematics, Himachal Pradesh University
Shimla-171 005 India

(Received 5 January 1988)

The thermosolutal convection in a layer of electrically conducting Oldroyd fluid heated and soluted from below in porous medium is considered to include the effect of a uniform vertical magnetic field. The magnetic field and stable solute gradient are found to have stabilizing effects whereas the medium permeability is shown to have a destabilizing effect. For stationary convection, the Oldroyd fluid behaves like a Newtonian fluid. The sufficient conditions for the nonexistence of overstability are obtained.

1. Introduction

A detailed account of thermal convection in a Newtonian fluid, under varying assumptions of hydrodynamics and hydromagnetics, has been given by Chandrasekhar [2]. Veronis [8] has investigated the thermohaline convection in a layer of fluid heated from below and subjected to a stable salinity gradient. Sharma [5] has studied the stability of a layer of electrically conducting Oldroyd fluid (i. e. fluid obeying Oldroyd's constitutive equation) heated from below in the presence of a uniform magnetic field. Eltayeb [3] has considered the convective instability in a rapidly rotating viscoelastic (Oldroydian) fluid. Sharma [6] has also studied the thermal instability of a layer of Oldroyd fluid acted on by a uniform rotation and found that the rotation has stabilizing as well as destabilizing effect under certain conditions in contrast to a Maxwell viscoelastic fluid where rotation has a destabilizing effect (Bhatia and Steiner [1]). Experimental demonstration by Toms and Strawbridge [7] has revealed that a dilute solution of methyl methacrylate in n-butyl acetate agrees well with the theoretical model of Oldroyd fluid. The stability of flow of a single component fluid through a porous medium taking into account the Darcy resistance has been studied by Lapwood [4] and Wooding [9].

The present paper deals with the thermosolutal instability of a layer of electrically conducting viscoelastic (Oldroydian) fluid in porous medium in the presence of a uniform vertical magnetic field. The analysis would be relevant to the stability of some polymer solutions like a dilute solution of methyl methacrylate in n-butyl acetate.

2. Perturbation equations

Consider an infinite horizontal layer of an electrically conducting viscoelastic (Oldroyd) fluid of depth d in porous medium, heated and solute concentrated uniformly from below and acted on by a uniform vertical magnetic field $\mathbf{H}\ (0,0,H)$ and gravity force $\mathbf{g}\ (0,0,-g)$. The Oldroyd fluid is described by the constitutive relations

$$\begin{aligned} T_{ij} &= -p\delta_{ij} + \tau_{ij}, \\ \left(1+\lambda\frac{\partial}{\partial t}\right)\tau_{ij} &= 2\mu\left(1+\lambda_0\frac{\partial}{\partial t}\right)e_{ij}, \\ e_{ij} &= \frac{1}{2}\left(\frac{\partial v_i}{\partial x_j}+\frac{\partial v_j}{\partial x_i}\right), \end{aligned} \tag{1}$$

where T_{ij}, τ_{ij}, e_{ij}, p, v_i, x_i, μ, λ and $\lambda_0\ (<\lambda)$ denote respectively the stress tensor, shear stress tensor, rate-of-strain tensor, scalar pressure, velocity, position vector, viscosity, stress relaxation time and strain retardation time. These fluids have been shown to explain the rheological behaviour of some polymer solutions at small rates of shear and rate-of-strain by Toms and Strawbridge [7].

When a fluid permeates a porous material, the actual path of an individual particle of fluid cannot be followed analytically. The gross effect, as the fluid slowly percolates through the pores of the rock, must be represented by a macroscopic law which is the usual Darcy's law. As a consequence of this, the resistance term $(\mu/k_1)\mathbf{q}$ where μ is the viscosity of the fluid, k_1 the permeability of the medium (which has the dimension of length squared), and $\mathbf{q}$ the filter velocity of the fluid, will replace the usual viscous term in the equations of fluid motion. Let $\delta\rho$, δp, $\mathbf{q}\ (u,v,w)$, $\mathbf{h}\ (h_x,h_y,h_z)$, θ and γ denote respectively the perturbations in density ρ, pressure p, filter velocity (zero initially), magnetic field $\mathbf{H}$, temperature T and solute concentration C. Then the linearized thermosolutal hydromagnetic perturbation equations through porous medium, following Boussinesq approximation, are

$$\frac{1}{\epsilon}\left(1+\lambda\frac{\partial}{\partial t}\right)\frac{\partial\mathbf{q}}{\partial t} = \left(1+\lambda\frac{\partial}{\partial t}\right)\left[-\frac{1}{\rho_0}\nabla\delta p + \frac{\mu_e}{4\pi\rho_0}(\nabla x\mathbf{h})x\mathbf{H} + \frac{\mathbf{g}\delta\rho}{\rho_0}\right] - \frac{\nu}{k_1}\left(1+\lambda_0\frac{\partial}{\partial t}\right)\mathbf{q}, \tag{2}$$

$$\nabla\cdot\mathbf{q} = 0, \tag{3}$$

$$E\frac{\partial\theta}{\partial t} = \beta\omega + \kappa\nabla^2\theta, \tag{4}$$

$$E\frac{\partial\gamma}{\partial t} = \beta'\omega + \kappa'\nabla^2\gamma, \tag{5}$$

$$\nabla\cdot\mathbf{h} = 0, \tag{6}$$

$$\epsilon\frac{\partial\mathbf{h}}{\partial t} = (\mathbf{H}\cdot\nabla)\mathbf{q} + \epsilon\eta\nabla^2\mathbf{h}. \tag{7}$$

Here μ_e, η, ϵ, μ, ν $(= \mu/\rho_0)$, κ, κ', β $(= |dT/dz|)$ and β' $(= |dC/dz|)$ stand for the medium permeability, the electrical resistivity, the medium porosity, the viscosity, the kinematic viscosity, the thermal diffusivity, the solute diffusivity, uniform temperature gradient and uniform solute concentration gradient respectively. The equation of state

$$\rho = \rho_0[1 - \alpha(T - T_0) + \alpha'(C - C_0)], \tag{8}$$

contains a thermal coefficient of expansion α and an analogous solvent coefficient α'. The suffix zero refers to values at the reference level $z = 0$. The layer of fluid of thickness d is heated and solute concentrated from below so that the temperatures and solute concentrations at the bottom surface $z = 0$ are T_0 and C_0 and at the upper surface $z = d$ are T_1 and C_1, respectively, z-axis being taken as vertical. The change in density $\delta\rho$, caused by the perturbations θ and γ in temperature and concentration, is given by

$$\delta\rho = -\rho_0(\alpha\theta - \alpha'\gamma). \tag{9}$$

Equations (2)–(7), using (9) , give

$$\left(1 + \lambda\frac{\partial}{\partial t}\right)\left[\frac{1}{\epsilon}\frac{\partial}{\partial t}\nabla^2 w - g\left(\frac{\partial^2}{\partial x^2} + \frac{\partial^2}{\partial y^2}\right)(\alpha\theta - \alpha'\gamma) - \frac{\mu_e H}{4\pi\rho_0}\nabla^2\frac{\partial h_z}{\partial z}\right] =$$

$$= -\frac{\nu}{k_1}\left(1 + \lambda_0\frac{\partial}{\partial t}\right)\nabla^2\omega, \tag{10}$$

$$\left(E\frac{\partial}{\partial t} - \kappa\nabla^2\right)\theta = \beta\omega, \tag{11}$$

$$\left(E\frac{\partial}{\partial t} - \kappa'\nabla^2\right)\gamma = \beta'\omega, \tag{12}$$

$$\epsilon\left(\frac{\partial}{\partial t} - \eta\nabla^2\right)h_z = H\frac{\partial\omega}{\partial z}. \tag{13}$$

Here $E = \epsilon + (1 - \epsilon)\rho_s c_s/\rho c$, where ρ, c and ρ_s, c_s stand for density and specific heat of fluid and solid matrix, respectively.

3. Dispersion relation

Here we analyze the disturbances into normal modes, assume that the perturbations ω, θ, γ and h_z have the forms

$$[\omega, \theta, \gamma, h_z] = [W(z), \Theta(z), \Gamma(z), K(z)]\exp(ik_x x + ik_y y + nt), \tag{14}$$

where k_x, k_y are wave numbers along the x and y directions respectively, $k = (k_x^2 + k_y^2)^{1/2}$ is the resultant wave number and n is the growth number which is, in general, a complex constant.

Assuming that x, y, z stand for the coordinates in the new unit of length d and letting $a = kd$, $\sigma = nd^2/\nu$, $p_1 = \nu/\kappa$, $p_2 = \nu/\eta$, $q = \nu/\kappa'$, $F = \lambda\nu/d^2$, $F_0 = \lambda_0\nu/d^2$, $P_l = k_1/d^2$ and $D = d/dz$, Eqs (10)–(13), using expression (14), in nondimensional form become

$$\left[(1+F\sigma)\frac{\sigma}{\epsilon}+\frac{1}{P_l}(1+F_0\sigma)\right](D^2-a^2)W+(1+F\sigma)\frac{gd^2a^2}{\nu}(\alpha\Theta-\alpha'\Gamma)-$$
$$-\frac{\mu_e H d}{4\pi\rho_0\nu}(1+F\sigma)(D^2-a^2)DK=0, \tag{15}$$

$$(D^2-a^2-Ep_1\sigma)\Theta=-\left(\frac{\beta d^2}{\kappa}\right)W, \tag{16}$$

$$(D^2-a^2-Eq\sigma)\Gamma=-\left(\frac{\beta' d^2}{\kappa'}\right)W, \tag{17}$$

$$(D^2-a^2-p_2\sigma)K=-\left(\frac{Hd}{\epsilon\eta}\right)DW. \tag{18}$$

Operating Eq. (15) by $(D^2-a^2-Ep_1\sigma)(D^2-a^2-Eq\sigma)(D^2-a^2-p_2\sigma)$ and using (16)–(18), thus eliminating Θ, Γ and K, we obtain

$$\left[(1+F\sigma)\frac{\sigma}{\epsilon}+\frac{1}{P_l}(1+F_0\sigma)\right](D^2-a^2-Ep_1\sigma)(D^2-a^2-Eq\sigma)\cdot$$
$$\cdot(D^2-a^2-p_2\sigma)(D^2-a^2)W-$$
$$-Ra^2(1+F\sigma)(D^2-a^2-Eq\sigma)(D^2-a^2-p_2\sigma)W+ \tag{19}$$
$$+Sa^2(1+F\sigma)(D^2-a^2-Ep_1\sigma)(D^2-a^2-p_2\sigma)W+$$
$$+Q(1+F\sigma)(D^2-a^2-Ep_1\sigma)(D^2-a^2-Eq\sigma)(D^2-a^2)D^2W=0,$$

where $R = g\alpha\beta d^4/\nu\kappa$ is the Rayleigh number, $S = g\alpha'\beta' d^4/\nu\kappa'$ is the analogous solute Rayleigh number and $Q = \mu_e H^2 d^2/4\pi\rho_0\nu\eta\epsilon$ is the modified Chandrasekhar number.

Here we assume that the temperatures and concentrations at the boundaries are kept fixed, the fluid layer is confined between two free boundaries and the adjoining medium is electrically nonconducting. The case of two free boundaries, though little artificial to consider, provides exact solution without obscuring any of the essential features of the problem. The boundary conditions appropriate for the problem become

$$W = D^2W = \Theta = \Gamma = DK = 0 \quad \text{at} \quad z = 0 \text{ and } 1. \tag{20}$$

Using the above boundary conditions, it can be shown that all the even order derivatives of W must vanish for $z = 0$ and 1 and hence the proper solution of Eq. (19) characterizing the lowest mode is

$$W = W_0 \sin \pi z, \tag{21}$$

where W_0 is a constant.

Substituting (21) in Eq. (19) and letting $x = a^2/\pi^2$, $R_1 = R/\pi^4$, $S_1 = S/\pi^4$, $Q_1 = Q/\pi^2$, $i\sigma_1 = \sigma/\pi^2$ and $P = \pi^2 P_l$, we obtain the dispersion relation

$$R_1 = \frac{(1+x)(1+x+iEp_1\sigma_1)}{x(1+i\pi^2 F\sigma_1)}\left[\frac{i\sigma_1}{\epsilon}(1+i\pi^2 F\sigma_1) + \frac{1}{P}(1+i\pi^2 F_0\sigma_1)\right] + \\ + S_1\frac{(1+x+iEp_1\sigma_1)}{(1+x+iEq\sigma_1)} + Q_1\left(\frac{1+x}{x}\right)\frac{(1+x+iEp_1\sigma_1)}{(1+x+ip_2\sigma_1)}. \tag{22}$$

4. The stationary convection

For the stationary convection $\sigma = 0$ and Eq. (22) reduces to

$$R_1 = \frac{(1+x)^2}{xP} + S_1 + Q_1\frac{(1+x)}{x}. \tag{23}$$

We thus find that for the stationary convection, the stress relaxation time parameter F and the strain retardation time parameter F_0 vanish with σ and the Oldroyd fluid behaves like an ordinary Newtonian fluid.

To study the effects of magnetic field, stable solute gradient and medium permeability, we examine the natures of dR_1/dQ_1, dR_1/dS_1 and dR_1/dP analytically. It follows from Eq. (23) that

$$\frac{dR_1}{dQ_1} = \frac{(1+x)}{x}, \tag{24}$$

$$\frac{dR_1}{dS_1} = +1, \tag{25}$$

and

$$\frac{dR_1}{dP} = -\frac{(1+x)^2}{xP^2}. \tag{26}$$

Thus for stationary convection, the magnetic field and stable solute gradient are found to have stabilizing effects whereas the medium permeability has a destabilizing effect.

The critical value of R_1, denoted by R_{1c} for the onset of instability, given by $dR_1/dx = 0$, is attained at the value of x given by

$$x = \sqrt{1+PQ_1}. \tag{27}$$

Thus x is independent of S_1 but depends on P and Q_1. Substituting this value of x in (23) gives the critical Rayleigh number

$$R_{1C} = \frac{1}{P}\left[1+\sqrt{1+PQ_1}\right]^2 + S_1. \tag{28}$$

When $Q_1 = 0$ and $S_1 = 0$ (corresponding to hydrodynamic and absence of solute gradient case), this reduces to Lapwood's [4] value

$$R_c = \frac{4\pi^2}{P_l}. \tag{29}$$

From (28) and (29), it is re-affirmed that the critical Rayleigh number increases with the increase in Q_1 (magnetic field parameter) and S_1 (stable solute gradient parameter) implying thereby the stabilizing effects of magnetic field and stable solute gradient.

5. The overstable case

Here we consider the possibility of whether instability may occur as an overstability. Since for overstability we wish to determine the critical Rayleigh number for the onset of instability via a state of pure oscillations, it suffices to find conditions for which (22) will admit of solutions with σ_1 real. First we consider the effects of magnetic field and stable solute gradient for the overstable case. Equation (22) yields

$$\frac{dR_1}{dQ_1} = \left(\frac{1+x}{x}\right) \frac{[(1+x)^2 + Ep_1p_2\sigma_1^2 + i\sigma_1(1+x)(Ep_1 - p_2)]}{\{(1+x)^2 + p_2^2\sigma_1^2\}}. \tag{30}$$

Equating imaginary parts of Eq. (30) yields $Ep_1 = p_2$. Substituting $Ep_1 = p_2$ in the equation obtained by equating the real parts of (30), we obtain

$$\frac{dR_1}{dQ_1} = \frac{1+x}{x}, \tag{31}$$

which is always positive. Similarly it can be shown that $dR_1/dS_1 = +1$. The stable solute gradient and magnetic field thus have stabilizing effects on the magneto-thermosolutal convection in an Oldroyd fluid in porous medium.

Separating the real and imaginary parts of Eq. (22) and eliminating R_1 between them, we obtain

$$A_3c_1^3 + A_2c_1^2 + A_1c_1 + A_0 = 0, \tag{32}$$

where we have put $1 + x = b$, $\sigma_1^2 = c_1$ and

$$A_3 = E^2Fp_2^2q\pi^4b\left(\frac{bF}{\epsilon} + \frac{EF_0p_1}{P}\right), \tag{33}$$

$$A_0 = b^5\left(\frac{b}{\epsilon} + \frac{Ep_1}{P}\right) + \frac{b^6\pi^2}{P}(F_0 - F) + S_1(b-1)b^3E(p_1 - q) + Q_1b^4(Ep_1 - p_2). \tag{34}$$

Since σ_1 is real for overstability, the three values of $c_1 (= \sigma_1^2)$ are positive. Equation (32) is cubic in c_1 and the product of the roots is $(-A_0/A_3)$ and if this is to be positive then $A_0 < 0$ since from (33), $A_3 > 0$.

Equation (34) shows that this is clearly impossible, i. e. A_0 is always positive if

$$F_0 > F, \quad p_1 > q \quad \text{and} \quad Ep_1 > p_2, \tag{35}$$

which implies that

$$\lambda < \lambda_0, \quad \kappa < \kappa' \quad \text{and} \quad \kappa < [\epsilon + (1-\epsilon)\rho_s c_s/\rho c]\,\eta. \tag{36}$$

Thus if $\kappa < \kappa'$, $\kappa < \eta[\epsilon + (1-\epsilon)\rho_s c_s/\rho c]$ and $\lambda < \lambda_0$ are satisfied, overstability is impossible and the principle of exchange of stabilities holds good. $\kappa < \kappa'$, $\kappa < \eta[\epsilon + (1-\epsilon)\rho_s c_s/\rho c]$ and $\lambda < \lambda_0$ are, therefore, the sufficient conditions for the nonexistence of overstability, the violation of which does not necessarily imply occurrence of overstability.

In the absence of solute gradient and for the Newtonian fluid, the sufficient condition for nonexistence of overstability reduces to $\kappa < \eta[\epsilon + (1-\epsilon)\rho_s c_s/\rho_c]$ which for non-porous medium ($\epsilon = 1$) further reduces to $\kappa < \eta$ (Chandrasekhar [2]), but the introduction of solute gradient introduces an additional sufficient condition $\kappa < \kappa'$ and the viscoelasticity further introduces the sufficient condition $\lambda < \lambda_0$ for the nonexistence of overstability.

Acknowledgement

This research was supported by the University Grants Commission, New Delhi through a research project awarded to the first author (R. C. S.).

References

1. P. K. Bhatia and J. M. Steiner, Z. A. M. M., *52*, 321, 1972.
2. S. Chandrasekhar, Hydrodynamic and Hydromagnetic Stability, Dover Publication, New York, 1981.
3. I. A. Eltayeb, Z. A. M. M., *55*, 599, 1975.
4. E. R. Lapwood, Proc. Camb. Phil. Soc., *44*, 508, 1948.
5. R. C. Sharma, Acta Phys. Hung., *38*, 293, 1975.
6. R. C. Sharma, Acta Phys. Hung., *40*, 11, 1976.
7. B. A. Toms and D. J. Strawbridge, Trans. Faraday Soc., *49*, 1225, 1953.
8. G. Veronis, J. Marine Res., *23*, 1, 1965.
9. R. A. Wooding, J. Fluid Mech., *9*, 183, 1960.

Acta Physica Hungarica 67 (1–2), pp. 211–216 (1990)

CONTRIBUTION TO THE LATTICE THERMAL CONDUCTIVITY DUE TO THE THREE PHONON NORMAL PROCESSES IN THE PRESENCE OF CORE DISLOCATIONS IN THE FRAME OF THE CALLAWAY INTEGRAL

A. H. AWAD

Department of Physics, College of Education, University of Basrah
Basrah, Iraq

(Received 23 February 1988)

The contribution of the correction term due to the three phonon normal processes has been studied for a sample having core dislocation in the frame of Callaway integral by obtaining an analytical expression for it. To test the applicability of the expression obtained, the contribution of the correction term toward total phonon conductivity has been calculated in the temperature range of 0.2–5 K owing to which a negligible contribution has been found.

1. Introduction

The expression of the lattice thermal conductivity proposed by Callaway [1] was based on the two mode conduction of phonon. The first one gives the lattice thermal conducitivity of an insulator due to the combined scattering relaxation rate, while the second term has a complicated form known as the correction term due to the three phonon normal processes. It was found that the contribution of the correction term (ΔK) is usually small enough compared to the total lattice thermal conductivity [2, 5].

Recently, the lattice thermal conductivity due to the correction term has been studied by several workers [6–8] using the Callaway expression of the correction term in which no distinction is made between transverse and longitudinal phonons. These studies are confined to samples having boundary, point defect and phonon–phonon scattering processes only.

The aim of the present work is to derive an analytical expression for ΔK in the frame of the Callaway integral at very low temperatures in the presence of core dislocations. The contribution of the correction term (ΔK) to the lattice thermal conductivity was calculated also in the frame of Callaway integral for the different values of P which is the ratio of the three phonon normal and umklapp processes scattering strengths.

2. Theory

The generalized Callaway expression of the lattice thermal conductivity is

$$K = c_0 \cdot \int_0^{\theta/T} (\tau_N^{-1} + \tau_R^{-1})^{-1} x^4 e^x (e^x - 1)^{-2} dx + \Delta K, \tag{1}$$

where

$$\Delta K = c_0 T_2^2 / T_3, \tag{2}$$

$$T_2 = \int_0^{\theta/T} \tau_N^{-1} (\tau_N^{-1} + \tau_R^{-1})^{-1} x^4 e^x (e^x - 1)^{-2} dx, \tag{3}$$

$$T_3 = \int_0^{\theta/T} \tau_R^{-1} \tau_N^{-1} (\tau_N^{-1} + \tau_R^{-1})^{-1} x^4 e^x (e^x - 1)^{-2} dx, \tag{4}$$

$$c_0 = (K_B/2\pi^2 v)(K_B T/\hbar)^3, \quad x = \hbar w/K_B T,$$

where K_B is the Boltzmann constant, $\hbar$ is the Planck constant divided by 2π, θ is the Debye temperature of the specimen under study, v is the average phonon velocity, $\tau^{-1} = B_1 w^2 T^3$ is the three phonon normal process scattering relaxation rate, $\tau_R^{-1} = \tau_B^{-1} + Aw^4 + B_2 w^2 T^3 + aw^3$ is the combined scattering relaxation rate of umklapp processes, τ_B^{-1} is the boundary scattering [9], Aw^4 is the point defect scattering relaxation rate [10], $B_2 w^2 T^3$ is the three phonon umklapp process scattering relaxation rate and aw^3 is the core dislocation relaxation rate [10]. A, a, B_1, B_2 are scattering strengths of point defect, core dislocation and three phonon normal and umklapp processes, respectively. The τ_N^{-1} and τ_R^{-1} can be expressed as

$$\tau_N^{-1} = B_1 w^2 T^3 = b_1 x^2, \tag{5}$$

$$\tau_{pt}^{-1} = Aw^4 = Dx^4, \tag{6}$$

$$\tau_U^{-1} = B_2 w^2 T^3 = b_2 x^2, \tag{7}$$

$$\tau_{cd}^{-1} = aw^3 = cx^3, \tag{8}$$

$$E = b_1 + b_2. \tag{9}$$

It is necessary to mention here that through the numerical analysis of above integral for τ_R^{-1}, it is found that at low temperatures, either τ_{cd}^{-1} dominates over τ_B^{-1} or τ_{cd}^{-1} is dominated by τ_B^{-1}. Therefore, the analytical expressions are obtained under two different approximations, i. e. $\tau_{cd}^{-1} \gg \tau_B^{-1}$ and $\tau_B^{-1} \gg \tau_{cd}^{-1}$.

(A) If $\tau_{cd}^{-1} \gg \tau_B^{-1}$:

In the above approximations, the integrals T_2 and T_3 can be reexpressed as follows

$$T_2 = \frac{b_1}{c} \int_0^{\theta/T} \left(1 - \frac{\tau_B^{-1}}{c} x^{-3} - \frac{D}{c} x - \frac{E}{c} x^{-1}\right) x^3 e^x (e^x - 1) dx, \tag{10}$$

which reduces to

$$T_2 = \frac{b_1 I_3}{c}\left(1 - \frac{\tau_B^{-1}}{c}F_3^0 - \frac{D}{c}F_3^4 - \frac{E}{c}F_3^2\right), \tag{11}$$

where

$$F_n^m = I_m/I_n, \qquad I_r = \int_0^{\theta/T} x^r e^x (e^x - 1)^{-2} dx.$$

m, n and r are integers. Similarly

$$T_3 = b_1 I_6\Big(1 - \frac{PA_3}{1+P}F_6^5 - \frac{(2+P)}{(1+P)}A_2A_3 - A_1^2F_6^0 - 2A_1A_2F_6^4 - A_2^2F_6^8 - \\ - A_1A_3\frac{(2+P)}{(1+P)}F_6^2 - \frac{A_3^2}{1+P}\Big). \tag{12}$$

At low temperatures, the contribution of τ_U^{-1} is very small compared to τ_R^{-1} and it can be ignored in this case, Eq. (2) reduces to

$$K = \frac{c_0 E I_3 F_6^3}{c^2}(1 - 2A_1F_3^0 - 2A_2F_3^4 - 2A_3F_3^2 - A_3F_6^5), \tag{13}$$

where

$$A_1 = \frac{\tau_B^{-1}}{c}, \quad A_2 = \frac{D}{c}, \quad A_3 = \frac{E}{c} \quad \text{and} \quad P = \frac{b_1}{b_2}.$$

(B) If $\tau_B^{-1} \gg \tau_{cd}^{-1}$:
For this case, the integrals T_2 and T_3 can be expressed as

$$T_2 = b_1\tau_B I_6(1 - c\tau_B F_6^9 - D\tau_B F_6^{10} - E\tau_B F_6^8), \tag{14}$$

$$T_3 = b_1 I_6\big(1 - b_1\tau_B F_6^8 - c^2\tau_B^2 F_6^{12} - 2Dc\tau_B^2 F_6^{10} - (E+b_2)c\tau_B^2 F_6^{11} - \\ - D^2\tau_B^2 F_6^{12} - (E+b_2)D\tau_B^2\big). \tag{15}$$

Using these equations ΔK can be approximated as

$$\Delta K = c_0 b_1 \tau_B^2 I_6\Big(1 - 2c\tau_B F_6^9 - 2D\tau_B F_6^{10} - E\tau_B F_6^8\frac{(2+P)}{(1+P)} - \\ - \frac{2PE}{(1+P)}\tau_B^2 F_6^8(cF_6^9 - DF_6^{10}) - \frac{2E^2P}{(1+P)}\tau_B^2 F_6^8 F_6^8 + \\ + c^2\tau_B^2 F_6^{12} + 2Dc\tau_B^2 F_6^{10} + \frac{(2+P)}{(1+P)}Ec\tau_B^2 F_6^{11} + D^2\tau_B^2 F_6^{12} + \\ + \frac{(2+P)}{(1+P)}ED\tau_B^2\Big). \tag{16}$$

Table I*

Contribution of the correction term ΔK to the total phonon conductivity in the temperature range of 0.2–5 K for different values of P (10^{-3} to 10^{3}), K and ΔK are expressed in Watt/deg/cm

TK	K^*	ΔK									
		10^{-3}	10^{-2}	10^{-1}	1	10	10^{2}	10^{3}
0.2	$4.08\ 10^{-4}$	$3.02\ 10^{-16}$	$2.99\ 10^{-15}$	$2.81\ 10^{-14}$	$1.51\ 10^{-13}$	$2.75\ 10^{-13}$	$2.99\ 10^{-13}$	$3.02\ 10^{-13}$
0.4	$3.26\ 10^{-3}$	$7.92\ 10^{-14}$	$7.85\ 10^{-13}$	$7.21\ 10^{-12}$	$3.96\ 10^{-11}$	$7.21\ 10^{-11}$	$7.85\ 10^{-11}$	$7.92\ 10^{-11}$
0.6	$1.10\ 10^{-2}$	$2.03\ 10^{-12}$	$2.01\ 10^{-11}$	$1.85\ 10^{-10}$	$1.01\ 10^{-9}$	$1.84\ 10^{-9}$	$2.01\ 10^{-9}$	$2.03\ 10^{-9}$
0.8	$2.61\ 10^{-2}$	$2.03\ 10^{-11}$	$2.01\ 10^{-10}$	$1.84\ 10^{-9}$	$1.01\ 10^{-8}$	$1.84\ 10^{-8}$	$2.01\ 10^{-8}$	$2.03\ 10^{-8}$
1.0	$5.09\ 10^{-2}$	$1.21\ 10^{-10}$	$1.20\ 10^{-9}$	$1.01\ 10^{-8}$	$1.01\ 10^{-7}$	$1.10\ 10^{-7}$	$2.20\ 10^{-7}$	$1.21\ 10^{-7}$
2.0	$4.07\ 10^{-1}$	$3.09\ 10^{-8}$	$3.06\ 10^{-7}$	$2.81\ 10^{-6}$	$6.06\ 10^{-6}$	$2.80\ 10^{-5}$	$3.06\ 10^{-5}$	$3.09\ 10^{-5}$
3.0	1.37	$7.82\ 10^{-7}$	$7.75\ 10^{-6}$	$7.12\ 10^{-5}$	$1.54\ 10^{-4}$	$7.12\ 10^{-4}$	$7.75\ 10^{-4}$	$7.82\ 10^{-4}$
4.0	3.20	$8.27\ 10^{-6}$	$8.20\ 10^{-5}$	$7.53\ 10^{-4}$	$4.14\ 10^{-3}$	$7.53\ 10^{-3}$	$8.20\ 10^{-3}$	$8.27\ 10^{-3}$
5.0	6.14	$4.55\ 10^{-5}$	$4.51\ 10^{-4}$	$4.14\ 10^{-3}$	$2.28\ 10^{-2}$	$4.14\ 10^{-2}$	$4.51\ 10^{-2}$	$4.55\ 10^{-2}$

*From the earlier report of Dubey [11]

Neglecting τ_U^{-1} as well as the term of lower values, Eq. (16) becomes

$$\Delta K = c_0 b_1 \tau_B^2 I_6 \left(1 - 2c\tau_B F_6^9 - 2D\tau_B F_6^{10} - b_1 \tau_B F_6^8\right). \tag{17}$$

Due to the very low value of temperature and the large value of θ, one can evaluate integral I's with the help of the Riemann zeta function, and one gets an expression for ΔK

$$\Delta K = 720 \rightarrow c_0 b_1 \tau_B^2 (1 - 1008 c\tau_B - 10080 D\tau_B - 56 b_1 \tau_B).$$

In the absence of dislocations, the expression for ΔK stated in Eq. (17) becomes

$$\Delta K = c_0 b_1 \tau_B^2 I_6 (1 - 2D\tau_B F_6^{10} - b_1 \tau_B F_6^8), \tag{18}$$

which is the same as obtained by Dubey [4] for a pure sample.

3. Results and discussion

Using the above expression, ΔK is calculated in the temperature range of 0.2–5 K for a sample having core dislocations for different values of P (10^3 to 10^{-3}) as shown in Table I. The values of constants τ_B^{-1}, A and a are taken from the earlier report of Dubey [11], but an approximate value of E has been calculated as $E = 1.0 \times 10^{-23}$s. deg^{-3}. To test the applicability of the analytical expressions, the value of ΔK has been calculated in the temperature range of 0.2–5 K.

From Table I, it is clear that the contribution of ΔK to the total phonon conductivity is very small in comparison with K, thus we can neglect its contribution, which is similar to the earlier finding of [2–5]. With the help of Table II, the values of ΔK obtained in the frame of the analytical expression are very close to those obtained using numerical integrations.

Table II

Phonon conductivity correction term ΔK in the frame of Callaway integral, $(\Delta K)_{\text{anal.}}$ is the value of ΔK obtained in the frame of analytical expression, $(\Delta K)_{\text{num. int.}}$ is the value of ΔK based on numerical integration

T K	$(\Delta K)_{\text{anal.}}$	$(\Delta K)_{\text{num. int.}}$	Percentage difference*
0.2	$2.819\ 10^{-14}$	$2.819\ 10^{-14}$	0
0.4	$7.217\ 10^{-12}$	$7.218\ 10^{-12}$	$1.385\ 10^{-2}$
0.6	$1.849\ 10^{-10}$	$1.850\ 10^{-10}$	$5.405\ 10^{-2}$
0.8	$1.847\ 10^{-9}$	$1.849\ 10^{-9}$	0.108
1.0	$1.099\ 10^{-8}$	$1.102\ 10^{-8}$	0.272
2.0	$2.786\ 10^{-6}$	$2.816\ 10^{-6}$	1.065
3.0	$6.910\ 10^{-5}$	$7.125\ 10^{-5}$	3.017
4.0	$6.389\ 10^{-4}$	$7.532\ 10^{-4}$	15.175
5.0	$3.237\ 10^{-3}$	$4.148\ 10^{-3}$	21.962

*Percentage difference $= \frac{(\Delta K)_{\text{num. int.}} - (\Delta K)_{\text{anal.}}}{(\Delta K)_{\text{num. int.}}} \cdot 100.$

With the help of Eq. (17), it can be concluded that for $\tau_B^{-1} \gg \tau_{cd}^{-1}$, $\Delta K \propto b_1 \tau_B^2$, which indicates that ΔK mainly depends on τ_B^{-1} and $\tau_{3Ph,N}^{-1}$. The present results are in good accord with the findings of previous works [4, 12]. At the same time, with the help of Eq. (13), it is clear that for $\tau_{cd}^{-1} \gg \tau_B^{-1}$, $\Delta K \propto B_1/c^2$, which shows that ΔK is mainly governed by $\tau_{3Ph,N}^{-1}$ and τ_{cd}^{-1}.

Acknowledgement

The author wishes to express his thanks to Dr. K. S. Magdy, Dr. C. A. Emshary and J. S. Saif for their interest in the present work.

References

1. J. Callaway, Phys. Rev., *113*, 1046, 1959.
2. K. S. Dubey, Sol. Stat. Comms., *23*, 963, 1977.
3. K. S. Dubey, Phys. Stat. Sol., (b) *79*, K119, 1977.
4. K. S. Dubey, Phys. Stat. Sol., (b) *81*, K83, 1977.
5. Y. P. Joshi, M. D. Tiwari and G. S. Verma, Physica, *47*, 213, 1970.
6. B. K. Agrawal and G. S. Verma, Phys. Rev., *128*, 603, 1962.
7. J. Callaway and C. V. Baeyer, Phys. Rev., *120*, 1149, 1960.
8. R. M. Samuel, R. H. Misho and K. S. Dubey, Current Sciences, *46*, 220, 1977.
9. H. B. G. Casimir, Physica, *5*, 495, 1938.
10. P. G. Klemens, Sol. Stat. Phys., *1*, 7, 1958.
11. K. S. Dubey, Current Science, *49*, 508, 1980.
12. A. F. Saleh, R. H. Misho and K. S. Dubey, Acta Phys. Hung., *47*, 325, 1979.

Acta Physica Hungarica 67 (1–2), pp. 217–222 (1990)

PHONON DRAG THERMOELECTRIC POWER OF Sb AT LOW TEMPERATURE

J. S. SAIF

Department of Physics, College of Education, University of Basrah
Basrah, Iraq

(Received 24 March 1988)

The phonon drag thermoelectric power of Sb in the temperature range of 0.4–5 K is studied. An approximate expression for the charge carriers-phonon scattering relaxation has been used. The study shows that the interacting phonons should have a certain wave vector. It is found that the electron contribution is higher than the contribution of holes. The study shows that only one characteristic temperature gives good agreement with the experimental value.

Introduction

The thermoelectric power (TEP) is an important conduction phenomenon, and it gives information about the scattering processes in the crystal. At low temperatures, the high value of the TEP was explained by suggesting an extra contribution due to the phonon drag [1,2].

In the presence of a temperature gradient, the thermal–vibrations of the lattice are not isotropic, and the scattering of the charge carriers by phonons is such as to push the charge carriers more often to the cold end of the sample.

From the earlier studies, it is clear that the electron (or hole)–phonon scattering relaxation rate is an important factor in determining the phonon drag thermoelectric power (PDTEP) of the crystals at low temperatures.

The band structure of Sb indicates concentrations of electrons and holes in the order of 10^{17} cm^{-3}, which suggests that the electrons and holes are the most important scatterers of phonons. This makes it interesting to analyse the phonon drag thermoelectric power of Sb at low temperatures and to see the role of the scattering mechanisms.

The aim of the present work is to study the PDTEP of a metal at low temperatures by calculating the PDTEP of Sb in the temperature range of 0.4–5 K. The effect of the characteristic temperature θ, which has an important role in the electron (or hole)–phonon scattering relaxation rate, has also been studied by calculating the PDTEP of Sb for different values of θ.

Scattering relaxation rates and the PDTEP integrals

In metals, as well as in doped semiconductors, the most important scatterers of phonons are the charge carriers, crystal boundaries, point defects and phonons.

According to an earlier report [3], it is well established that the expressions for the scattering relaxation rates are:

$$\tau_B^{-1} = v/l, \tag{1}$$

$$\tau_{pt}^{-1} = A\omega^4, \tag{2}$$

$$\tau_N^{-1} = B_N \omega^2 T^3, \tag{3}$$

where τ_B^{-1}, τ_{pt}^{-1}, τ_N^{-1} are the scattering relaxation rates due to boundary, point defects and phonons, v the average phonon velocity, l is the Casimir length of the sample, ω is the phonon frequency, T is the temperature, B_N and A are the scattering strengths for the normal phonon–phonon and the point defects, respectively.

The electron (or hole)–phonon scattering relaxation rate can be expressed in terms of Ziman [4] expression. At low temperatures, this expression can be approximated as :

$$\tau_e^{-1} = m_e^2 E_e^2 \omega/(2\pi\rho\hbar^3 v), \tag{4}$$

$$\tau_h^{-1} = m_h^2 E_h^2 \omega/(2\pi\rho\hbar^3 v), \tag{5}$$

It has been found [4] that because of the conservation of energy and momentum, not all phonons can interact with the charge carriers. An electron with wave vector $\overline{K}_e$ can only interact with phonons of wave vector $\overline{q} < 2\overline{K}_e$. Such phonons are known as non–peripheral phonons, other phonons cannot interact with electrons and are known as peripheral phonons. The same is also true for the holes. Hence, Eqs.(4) and (5) will be :

$$\tau_e^{-1} = m_e^2 E_e^2 \omega/(2\pi\rho\hbar^3 v) \quad \text{for} \quad \omega < \omega_e, \tag{6}$$

$$= 0 \quad \text{for} \quad \omega > \omega_e, \tag{7}$$

$$\tau_h^{-1} = m_h^2 E_h^2 \omega/(2\pi\rho\hbar^3 v) \quad \text{for} \quad \omega < \omega_h, \tag{8}$$

$$= 0 \quad \text{for} \quad \omega > \omega_h, \tag{9}$$

where m_e and m_h are the effective masses of electrons and holes, respectively, E_e and E_h are the deformation potentials of electrons and holes, respectively, ρ is the density of the sample, $\hbar$ is the Dirac constant, ω_e and ω_h are the phonon frequencies corresponding to the wave vectors $2K_e$ and $2K_h$, respectively.

Using the above facts, the PDTEP of a metal is :

$$P = P_e + P_h + P_D, \tag{10}$$

where P_e and P_h are the contributions due to electrons and holes, respectively, P_D is the contribution due to the rest scattering mechanisms. It should be noted that

the P_D has been neglected in the actual calculations because its contribution is zero to the PDTEP. These contributions can be expressed as :

$$P_e = (\eta/\theta_e)^3 \int_0^{\theta_h/T} (\tau_1^{-1})^{-1}(\tau_e^{-1} + \tau_h^{-1})F(x)\,dx,$$

$$P_h = (\eta/\theta_h)^3 \int_{\theta_h/T}^{\theta_e/T} (\tau_2^{-1})^{-1}\tau_h^{-1}F(x)\,dx, \tag{11}$$

$$P_D = (\eta/\theta_D)^3 \int_{\theta_e/T}^{\theta_D/T} (\tau_3)^{-1}F(x)\,dx,$$

where $\tau_1^{-1} = \tau_B^{-1} + \tau_N^{-1} + \tau_{pt}^{-1} + \tau_e^{-1} + \tau_h^{-1}$, $\tau_2^{-1} = \tau_1^{-1} - \tau_e^{-1}$, $\tau_3^{-1} = \tau_2^{-1} - \tau_h^{-1}$, $\eta = (3K_B/e)^{1/3}T$, $F(x) = x^4e^x(e^x - 1)^{-2}$, θ_e and θ_h are the characteristic temperatures (separates the non–peripheral phonons from the peripheral phonons) for the electrons and holes, respectively, K_B is the Boltzmann constant, e is the electronic charge, $x = \hbar\omega/K_BT$ is a dimensionless parameter and θ_D is the Debye temperature.

Phonon drag thermoelectric power of Sb

The values of constants are taken from Bhatia and Horton's report [5], whereas the carrier concentration n_e and n_h are taken from the report of Rao et al [6]. The effective masses m_e and m_h are taken from the report of Blewer et al [7] and all these constants are reported in Table I. τ_B^{-1} has been calculated with the help of the sample dimension reported by Long et al [8]. The deformation potentials E_e and E_h have been estimated at 0.4 K, while the point–defects scattering strength A and the three phonon scattering strength B_N has been estimated at 1 and 3 K, respectively.

Table I
The constants used in the calculations of the PDTEP of Sb in the temperature range of 0.4–5 K

$m_e = 0.28\,m$	m is the rest mass of the electron
$m_h = 0.14\,m$	$\theta_e = 24.96$ K
$\tau_B^{-1} = 7.0 \times 10^5\ s^{-1}$	$\theta_h = 19.24$ K
$A = 1.02 \times 10^{-45}\ s^3$	$v = 2.2 \times 10^5$ m/s
$B = 4.0 \times 10^{-21}\ sK^{-3}$	$\theta_D = 210$ K
$n_e = 4.15 \times 10^{19}\ cm^{-3}$	$n_h = 3.80 \times 10^{19}\ cm^{-3}$

Using these constants, the PDTEP of Sb has been calculated in the temperature range of 0.4–5 K with the help of the numerical integration of Eq.(11). The

results are reported in Fig.1. The PDTEP of Sb due to the electronic contribution in Eq.(11) has also been illustrated in this Figure for comparison. From this Figure, one can see that the PDTEP increases with the temperature in the entire range of investigation. This increase is due to the increase of phonon energy leading to an increase in the amplitude of the lattice waves travelling along the direction of motion of the charge carriers. A similar variation was reported for doped semiconductors [3]. The second curve in this Figure shows that the electronic contribution is less than the total value of P_T, but still its value is higher than that of the hole contribution due to the fact that the electronic concentration is higher than the hole concentration in such sample.

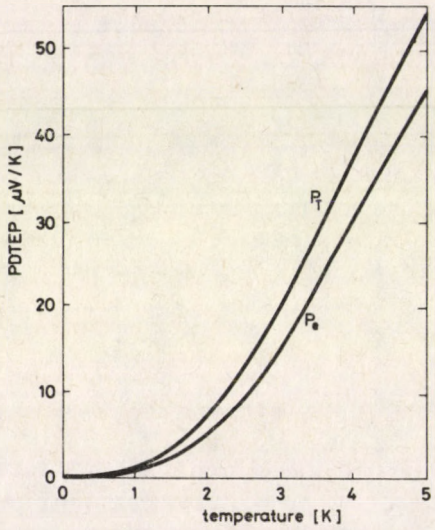

Fig. 1. The variation of the PDTEP with the temperature of Sb in the temperature range of 0.4–5 K. Curves P_T and P_e correspond to the total and the electronic PDTEP.

The effect of the characteristic temperature

As stated earlier, the characteristic temperature θ which distinguishes peripheral phonons from non-peripheral phonons has an important role in the value of the PDTEP.

The numerical analysis of the PDTEP integrals stated in Eq.(11) shows that P_h is much smaller than P_e, thus for simplicity one can assume the same value for θ_e and θ_h.

Figure 2 shows the PDTEP of Sb in the same temperature range for different values of θ_e in the range of 16–32 K. It is clear that the value of the PDTEP at very

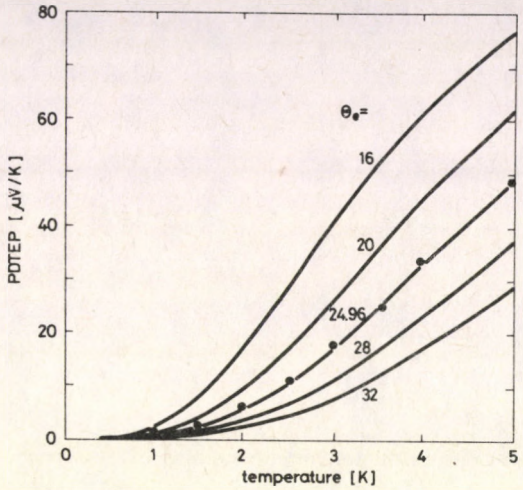

Fig. 2. The variation of the PDTEP of Sb with the temperature in the range of 0.4–5 K, for different values of θ_e in the range of 16–32 K. Values near the curves correspond to the value of θ_e. Circles represent the experimental data.

low temperatures (say below 1 K) are in good agreement with the experimental data of Sb for any value of θ_e, which is due to the high electron concentration causing an extra electron–phonon scattering. Also, one can see that for the lower values of θ_e the calculated values of the PDTEP are larger than the experimental values, whereas for higher values of θ_e the calculated values are smaller than the experimental values. Thus only one particular value of θ_e can give good agreement with the experimental data of the PDTEP of a metal.

Figure 3 shows the PDTEP of Sb in the same temperature range by using θ_D instead of θ_e. It is clear that the value of the PDTEP in this case is less than the experimental data because of the dominating nature of the other scattering mechanisms in Sb. The energy transported along the direction of the charge carriers will be less, and the value of the PDTEP stated in Eq.(11) will be less due to the factor $(\eta/\theta_D)^3$, (for more details see [4].)

Conclusions

Separating between peripheral and non-peripheral phonons and simplifying the Ziman expression for the scattering of phonons by the charge carriers, the phonon drag thermoelectric power of Sb has been calculated in the temperature range of 0.4–5 K. It is reported that the calculated values increase with temperature in the entire range of the study. The values are in good agreement with the experimental values. It is also reported that the hole contribution is less than the

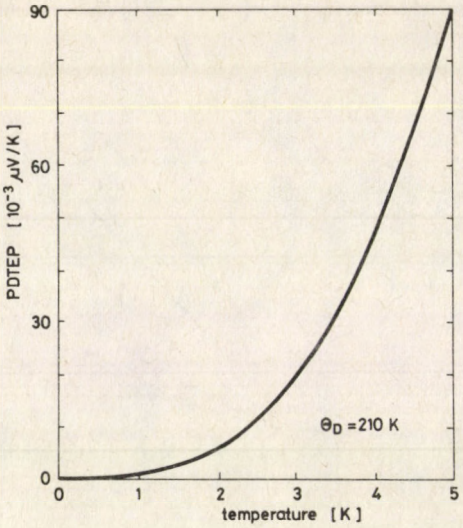

Fig. 3. The variation of the PDTEP with the temperature in the temperature range of 0.4–5 K by Debye temperature $\theta_D = 210$K.

electron contribution. It is found that only one particular value of the characteristic temperature can give good agreement with the experimental values.

Acknowledgements

The author wishes to thank Dr. K.S. Majdy for his interest in the present work. He is also thankful to Dr. K.S. Dubey for his help during the work.

References

1. H.P.R. Frederikse, Phys. Rev., *91*, 491, 1953.
2. C. Herring, Phys. Rev., *96*, 1163, 1954.
3. K.S. Dubey, Phys. Stat. Sol.(b), *100*, 671, 1980.
4. J.M. Ziman, Electrons and Phonons, Oxford University Press, London, 1960.
5. A.B. Bhata and G.K. Horton, Phys. Rev., *104*, 43, 1956.
6. G.N. Rao, N.H. Zebouni, C.G. Grenier and J.M. Reynold, Phys. Rev., *133*, A141, 1963.
7. R.S. Blewer, N.H. Zebouni and C.G. Grenier, Phys. Rev., *174*, 700, 1968.
8. J.R. Long, C.G. Grenier and J.M. Reynold, Phys. Letters, *16*, 214, 1965.

Acta Physica Hungarica 67 (1-2), pp. 223-228 (1990)

ELECTRICAL CONDUCTIVITY, THERMOELECTRIC POWER AND THERMAL CONDUCTIVITY OF $CuTlTe_2$ IN THE SOLID AND LIQUID STATES

N. ABDEL MOHSEN, S. N. ELSAYED and A. H. ABOU EL-ELA

Physics Department, Faculty of Sciences
Al Azhar University, Nasr City
Cairo, Egypt

(Received 5 April 1988)

The electrical conductivity, thermoelectric power and thermal conductivity of $CuTlTe_2$ in the solid and liquid states were measured over a wide range of temperature. The experimental data were analyzed in terms of a model developed for the density of states and electrical transport in solid amorphous semiconductors. Positive thermoelectric power suggests a large predominance of holes in electrical transport.

The mechanism of electronic conduction in amorphous materials is of considerable interest. Various models were suggested [1-3] and it has been demonstrated that some semiconductors retain their predominantly covalent semiconducting properties in the amorphous and liquid states, whereas others acquire metallic properties above the melting point.

The aim of the present contribution is to study the electrical conductivity, thermoelectric power and thermal conductivity of $CuTlTe_2$ in a wide range of temperature in the solid and liquid states. $CuTlTe_2$ has chalcopyrite structure [4,5] and its melting point is 375 °C. Ternary chalcopyrite semiconductors have attracted recently a great deal of attention because of their possible applications in electrooptical devices.

Experimental details

$CuTlTe_2$ samples were prepared by melting the proper amounts of highly pure component elements (99.999%). The material was sealed in evacuated quartz tubes at 10^{-3} Pa and heated at 1000 °C for 12h with frequent rocking to ensure homogenization of the melt. Then the tubes were quenched in ice to obtain the samples in the amorphous state. The solid material is then heated in an inert atmosphere until it melts and then transferred to the measuring cell.

Measurements of the electrical conductivity and thermoelectric power were carried out in the measuring cell which was fitted with graphite electrodes, heaters and thermocouples for accurate measurements of temperature up to 0.2 °C. A highly

stabilized power supply, a sensitive voltmeter, and a sensitive galvanometer capable of measuring currents as low as 10^{-9} A were used [10].

Measurements of thermal conductivity were carried out using the concentric cylinder method, where the material in the liquid state was poured into the cylindrical gap between two concentric graphite cylinders kept in nitrogen atmosphere. The system was fitted with a heater and sensitive thermocouples for accurate measurements of temperature, and the thermal conductivity was calculated using the formula:

$$K = \frac{QLn(d_2/d_1)}{2\pi L(t_1 - t_2)},$$

where d_1 and d_2 are the diameters of the inner and outer cylinders, t_1 and t_2 are the temperature on both sides of the sample, L is the length of the cylinders, and Q is the quantity of heat generated. Measurements were carried out in a wide range of temperature up to 375 °C above the melting point, and were repeated for more than three runs. The results were reproducible.

Results and discussion

Figures 1 and 2 show the temperature dependence of the electrical conductivity and thermoelectric power. In the solid state the activation energy is 0.12 eV. The low value of the activation energy suggests that $CuTlTe_2$ remains extrinsic p-type semiconductor. Positive values of thermoelectric power indicate a large predominance of holes in electrical transport.

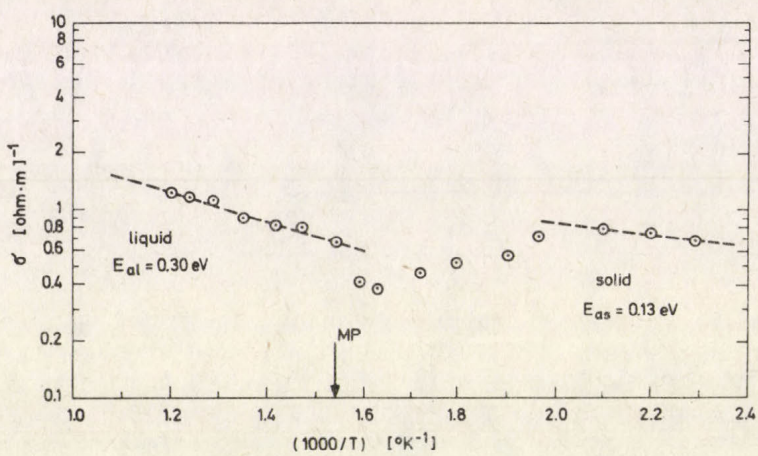

Fig. 1. Temperature dependence of the electric conductivity of $CuTlTe_2$ in solid and liquid states

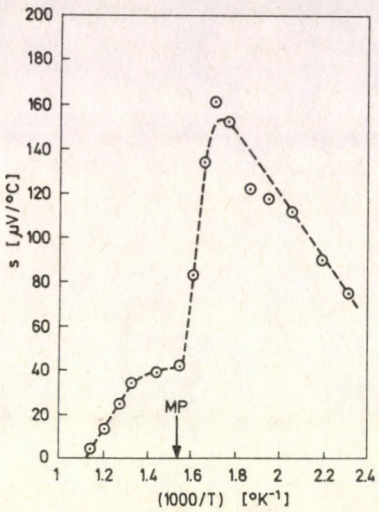

Fig. 2. Temperature dependence of the thermoelectric power of $CuTlTe_2$ in solid and liquid states

At the melting point a sudden decrease in the electrical conductivity and thermoelectric power is observed which may be attributed to changes in the short range order on melting and the subsequent decrease in carrier mobility.

In the liquid state the electrical conductivity is increased and the activation energy is 0.20 eV. The thermoelectric power is decreased as the temperature rises which may be attributed to changes in the short range order and the energy band structure due to weakening the intermolecular forces. The measured transport data in liquid state can be interpreted in terms of the model developed by Mott [6,7]. According to this model the main difference between amorphous and crystalline state is that the electronic states at the band edges are tailed in the forbidden gap and become localized. To explain the positive sign of the thermoelectric power usually observed, it is supposed that the range of localized states in the conduction band is wider than in the valence band. Moreover, two conduction processes may occur:

a) conduction due to holes excited in extended states at E_v;
b) conduction due to holes excited in localized states near the band edges with an activated mobility.

The present results show that conduction due to defect states occurs with an activation energy of 0.20 eV. Mott [8] and Cutler [7] have shown that when the activation energy for the hole mobility is small compared with the energy gap the electrical conductivity is given by

$$\sigma = \sigma_0 \exp\left(\frac{E_f - E_v}{kT}\right). \tag{1}$$

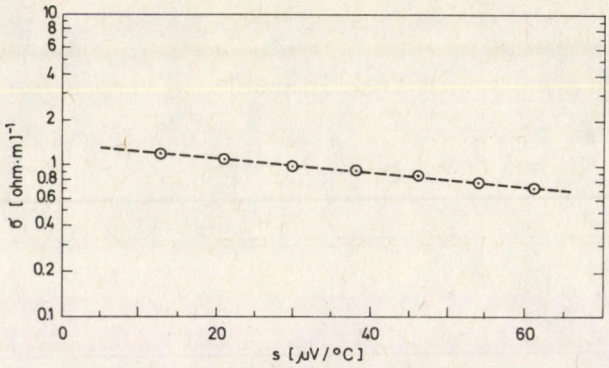

Fig. 3. The electric conductivity versus thermoelectric power for liquid $CuTlTe_2$

The value of σ_0 varies with the conduction process and can be calculated from the intercept of $\lg\sigma$ curve at $\frac{1}{T} = 0$ which is equal to $10(\Omega m)^{-1}$. Moreover, $(E_f - E_v)$ depends on the temperature and is given by [8].

$$E_f - E_v = E(0) - \gamma T. \tag{2}$$

When $E_\sigma = E_s$ the temperature coefficient γ may be calculated directly from the thermoelectric power which is given by

$$S = \frac{K}{e}\left(\frac{E_f - E_v}{kT} + A\right), \tag{3}$$

$$S = \frac{K}{e}\left(\frac{E(0)}{kT} - \frac{\gamma}{k} + A\right),$$

where kTA is the average energy of the transported hole s measured with respect to E_v, A depends on the nature of the scattering process, e is the electron charge and k is Boltzmann's constant.

The kinetic term A is of the order of unity for conduction in extended states [7,9] when the density of states and the mobility are temperature independent. The value of the coefficient γ is found to be 3×10^{-4} eV/k which gives the temperature dependence of the energy gap for liquid $CuTlTe_2$. γ can be determined from the intercept of thermoelectric power curve on the $\frac{1}{T}$ =zero axis.

Mott [13] had attributed the linear decrease of the gap with increasing temperature to the fact that the difference between the distance from one atom to nearest and next–nearest neighbour decreases.

From Eqs (1) and (3) one obtains the relation between σ and S

$$\sigma = \sigma_0 \exp(-e\frac{S}{K} + A). \tag{4}$$

Figure 3 shows a plot of the electrical conductivity (logarithmic scale) versus the thermoelectric power in liquid state. The value of intercept on the S = zero axis yields σ_0. The low value of σ_0 in the liquid state indicates that holes in localized states near the band edges are responsible for conduction. As the energy gap contracts with increasing temperature the tails of the conduction and valence bands become more pronounced.

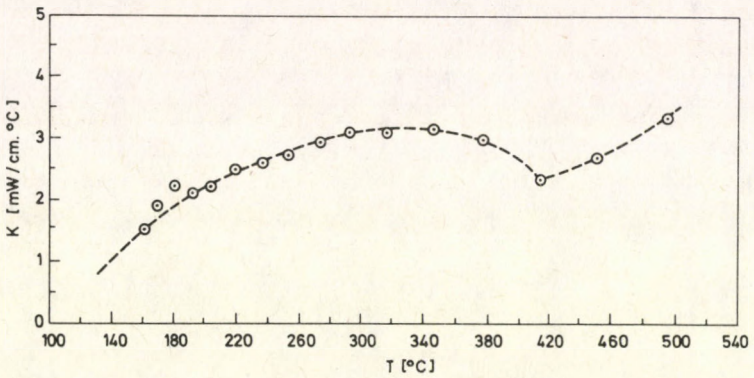

Fig. 4. Temperature dependence of the thermal conductivity of $CuTlTe_2$ in solid and liquid states

The temperature dependence of the thermal conductivity of $CuTlTe_2$ is shown in Fig.4. In the solid state the increase of thermal conductivity with temperature may be due to the increase of heat capacity and the phonon mean free path. Moreover, the additional increase of thermal conductivity before melting may be attributed to the transition from the amorphous to a highly elastic state characterized by an increase of the mobility of molecules and the distance between them, which is followed by the stimulation of rotational oscillations of molecules. These rotational oscillations will spread along and between the molecules, transferring thermal energy and so the value of K will increase.

The decrease of the thermal conductivity on melting can be attributed to the decrease of the density and subsequent increase of the distance between the molecules, which leads to a weakening of the bonds between the molecules and an increase in the disordered arrangement. The mean free path and heat capacity decrease and the thermal conductivity decreases correspondingly.

In the liquid state in spite of the weakening of the bonds between the molecules, the thermal conductivity continues to increase with temperature with a faster rate which indicates that an additional mechanism contributes to the thermal conduction process. In solid semiconductors the thermal conductivity can be adequately explained by transport due to phonons and free electrons. In liquid semiconductors, however, it is necessary to invoke an additional process involving photon transport [11]. It is usually convenient to analyse the thermal conductivity of liquid semicon-

ductors in terms of four contributions [11].

$$K = K_a + K_e + K_m + K_r,$$

where K_a is the contribution of atomic motion, K_e is the electron contribution, K_m is the bipolar contribution and K_r is the photon component of thermal conductivity. The quantity K_a states a lower limit to K and is given by the expression

$$K_a = CD,$$

where C is the heat capacity for unit volume and D is the thermal diffusivity. Most of the thermal motion of a liquid near its melting point is vibrational in character so that the equipartition law gives a value of $3k/(4\pi a^3/3)$ for C, where a is the atomic radius and k is Boltzmann's constant. At high temperature vibrational energy diffuses with a mean distance $\simeq 2a$ so that $D \simeq 4a^2 r$, where r is the vibration frequency. Putting this together gives for K_a

$$K_a = \frac{9}{\pi} \frac{K\upsilon}{a}. \tag{5}$$

According to Eq.(5), the value of K_a is about 5.9 m watt. deg^{-1}. cm^{-1}, and its small value can be attributed to the fact that a and υ for heavier elements do not vary much about the value 0.2 nm and $\upsilon \simeq 3 \times 10^{12}\ \mathrm{s}^{-1}$, respectively.

For liquid semiconductors the theory for K_e and K_m is complicated, however, calculation for metallic materials [12] shows that the contribution of K_e and K_m to thermal conduction is relatively small.

References

1. N.F. Mott, Phil. Mag., *13*, 989, 1969; *24*, 1, 1971.
2. N.F. Mott, Adv. Phys., *16*, 49, 1971.
3. M. Cutler, C.E. Mallon, J. Appl. Phys., *36*, 201, 1965.
4. V.P. Zhuze, V.M. Sergeeva and E.L. Shtrum, Sov. phys.-Tech. phys., *3*, 1925, 1958.
5. J.L. Shay and J.M. Wernick, Ternary Chalcopyrite Semiconductors, Pergamon Press, Oxford, 1975.
6. M.M. Cohen, H. Fritzsche and S.R. Ovshinsky, Phys. Rev. Lett., *22*, 1065, 1969.
7. M. Cutler and N.F. Mott, Phys. Rev., *181*, 1336, 1969.
8. N.F. Mott, Phil. Mag., *22*, 7, 1970.
9. N.F. Mott and E.A. Davis, Electronic Processes in Non-crystalline Materials, 2nd. ed., University Press, Oxford, 1979.
10. A.H. Abou El Ela and N. Abdel Mohsen, J. Appl. Phys., A *29*, 39, 1982.
11. V.I. Fedorov and L.S. Stilbans, High Temperature, *11*, 206, 1967.
12. M. Cutler, Liquid Semiconductors, Academic Press, New York, 1977.
13. N.F. Mott and E.A. Davis, Electronic Processes in Non-crystalline Materials, 2nd. ed., University Press, Oxford, 1979.

Acta Physica Hungarica 67 (1–2), pp. 229–233 (1990)

AN ANALOGUE OF DE-SITTER UNIVERSE

R. R. PATTANAIK

Department of Physics, Biswasray Science College
Pattapur 761013, Orissa, India

and

G. MOHANTY*

P. G. Department of Mathematics, Khallikote College
Berhampur 760001, Orissa, India

(Received 7 April 1988)

It is shown that the perfect fluid distribution without cosmological constant is quite analogous to homogeneous de-Sitter type universe with equation of state $p + \rho = 0$. Some physical and geometrical properties of the model are also studied.

1. Introduction

Einstein [1] exercised the option of including the cosmological constant term in the field equations in constructing his universe. A few years later due to empirically observed unphysical results obtained by Hubble and others, he abandoned the introduction of the cosmological constant. In view of the fact we propose a relativistic cosmological model in this paper without cosmological constant where we consider the spacetime described by a metric of the type

$$ds^2 = a^2 \left\{ m(dx)^2 + \frac{n^2}{2}(dy)^2 + m(dz)^2 - (dt + ndy)^2 \right\}, \tag{1}$$

where a =constant, $m = m(x)$ and $n = n(t)$.

We derive the field equations and their consequences with solution in Section 2. It is shown that the general perfect fluid distribution degenerates to a homogeneous perfect fluid with equation of state $p + \rho = 0$. In Section 3 and Section 4 we study some of the geometrical and physical properties of the problem, respectively. We mention the concluding remarks in Section 4.

*Present address: School of Mathematical Sciences, Sambalpur University, Burla–768019, Orissa, India

2. Field equations and their consequences with solution

The relativistic field equations for perfect fluid distribution may be given by

$$G_{ij} \equiv R_{ij} - \frac{1}{2}Rg_{ij} = -8\pi[(p+\rho)V_iV_j + pg_{ij}] \tag{2}$$

and

$$V_iV^i = -1, \tag{3}$$

where p, ρ and V_i are internal pressure, rest mass density and four velocity vector of the distribution, respectively. The units are so chosen that the velocity of light $c = 1$ and the gravitational constant $G = 1$.

The explicit forms of the field equations (2) and (3) for the metric (1) are

$$G_{11} \equiv \frac{\ddot{n}}{n}m = 8\pi[(p+\rho)V_1^2 + pa^2m], \tag{4}$$

$$G_{22} \equiv \frac{m''}{4m^2}n^2 - \frac{m'^2}{4m^3}n^2 = -8\pi\left[(p+\rho)V_2^2 - p\frac{a^2}{2}n^2\right], \tag{5}$$

$$G_{33} \equiv \frac{\ddot{n}}{n}m = 8\pi[(p+\rho)V_3^2 + pa^2m], \tag{6}$$

$$G_{44} \equiv \frac{m''}{2m^2} - \frac{m'^2}{2m^3} = -8\pi[(p+\rho)V_4^2 - pa^2], \tag{7}$$

$$G_{24} = G_{42} \equiv \frac{m''}{2m^2}n - \frac{m'^2}{2m^3}n = -8\pi[(p+\rho)V_2V_4 - pa^2n], \tag{8}$$

$$G_{12} \equiv (p+\rho)V_1V_2 = 0, \tag{9}$$

$$G_{13} \equiv (p+\rho)V_1V_3 = 0, \tag{10}$$

$$G_{14} \equiv (p+\rho)V_1V_4 = 0, \tag{11}$$

$$G_{23} \equiv (p+\rho)V_2V_3 = 0, \tag{12}$$

$$G_{34} \equiv (p+\rho)V_3V_4 = 0 \tag{13}$$

and

$$\frac{1}{2a^2m}(V_1^2 + V_3^2) + \left(\frac{V_2}{an} - \frac{V_4}{a}\right)^2 = \frac{1}{2}\left\{\left(\frac{V_4}{a}^2\right) - 1\right\}. \tag{14}$$

Hereafter the prime and dot represent differentiation with respect to x and t, respectively. Since $V_4 \neq 0$ for a perfect fluid distribution, Eqs (11) and (13) give

$$V_1 = 0 = V_3. \tag{15}$$

Thus Eqs (9), (10) and (12) are identically satisfied. Now comparing Eqs (7) and (8), we get

$$V_2 = V_4 n. \tag{16}$$

Equations (14) and (16) yield

$$V_4 = a \quad \text{and} \quad V_2 = an. \tag{17}$$

With the help of Eq. (17), Eqs (7) and (8) lead to a single equation i. e.:

$$\frac{m''}{2m^2} - \frac{m'^2}{2m^3} + 8\pi\rho a^2 = 0. \tag{18}$$

Further the use of Eqs (17) and (18) in Eq. (5), we get

$$p + \rho = 0. \tag{19}$$

Then equations (4) and (6) reduce to

$$\ddot{n} + 8\pi\rho a^2 n = 0, \tag{20}$$

which yields a general solution

$$n = k_1 \cos at\sqrt{8\pi\rho} + k_2 \sin at\sqrt{8\pi\rho}. \tag{21}$$

Hereafter k_n's denote arbitrary constants.

Equation (18) is equivalent to

$$Y'' + k_3 e^Y = 0, \tag{22}$$

where $k_3 = 16\pi\rho a^2$ and $Y = \ln m$. One can easily get the solution of Eq. (22) as

$$m = \frac{k_4}{2k_3} \operatorname{Sec} h^2 \left(\frac{\sqrt{k_4}}{2} x + k_5 \right). \tag{23}$$

3. Geometrical properties

(i) Space of constant curvature

The solution obtained in Eqs (21) and (23) implies that the spacetime (1) does not describe a space of constant curvature since the Weyl tensor $W_{hijk} \neq 0$ and also $R_{hijk} = K(g_{hj}g_{ik} - g_{hk}g_{ij})$ for all $h, i, j, k = 1, 2, 3, 4$, where the Riemannian curvature K is not a unique constant.

(ii) Einstein space

It can also be shown that the spacetime (1) is an Einstein space since $R_{ij} = \frac{R}{4} g_{ij}$, for $i, j = 1, 2, 3, 4$.

4. Physical properties

(i) Motion of test particle

The motion of the test particle is given by the geodesic equations

$$\frac{d^2X^i}{ds^2} + \Gamma^i_{jk}\frac{dX^j}{ds}\frac{dX^k}{ds} = 0, \tag{24}$$

where s is a parameter along the path of the particle. The x and z components of the geodesic equations (24) are

$$\frac{d^2x}{ds^2} + \frac{1}{2}\frac{m'}{m}\left(\frac{dx}{ds}\right)^2 - \frac{1}{2}\frac{m'}{m}\left(\frac{dz}{ds}\right)^2 = 0 \tag{25}$$

and

$$\frac{d^2z}{ds^2} + \frac{1}{2}\frac{m'}{m}\frac{dx}{ds}\cdot\frac{dz}{ds} = 0, \tag{26}$$

respectively. Now one can easily obtain from the results already obtained in Eq. (15) that $\frac{dx}{ds} = 0 = \frac{dz}{ds}$. Thus the test particle has zero velocity in x and z directions as well. Subsequently one gets from equations (25) and (26) that

$$\frac{d^2x}{ds^2} = \frac{d^2z}{ds^2} = 0. \tag{27}$$

It concludes from Eq. (27) that if the particle is at rest in both x and z directions then the particle remains at rest for ever in the same directions.

(ii) Doppler effect

For the velocity of light in y direction, we have $ds = 0$, $dx = 0$ and $dz = 0$. Therefore, the velocity of light emitted by a star towards the origin from $(0, y, 0)$ in y direction is given by

$$\frac{n^2}{2}dy^2 = dt^2 + n^2dy^2 + 2n\,dy\,dt, \tag{28}$$

which yields

$$\frac{dy}{dt} = \frac{-2 \pm \sqrt{2}}{n}. \tag{29}$$

We suppose that t_1 and t_2 are the times of emission of light from the star situated at $(0, y, 0)$ and reception at the origin respectively. Thus for two waves emitted with interval dt between them, we have

$$\int_0^y dy = (-2 \pm \sqrt{2}) \int_{t_1}^{t_2} \frac{dt}{n}. \tag{30}$$

Using (21) in (30), one can easily get

$$e^{y/M} = \tan \frac{z}{2}\Big|_{t_1}^{t_2} \approx \frac{z}{2}\Big|_{t_1}^{t_2}, \tag{31}$$

where $M = \frac{-2\pm\sqrt{2}}{k_6 k_7}$, $z = (k_6 t + \theta)$, $k_6 = a\sqrt{8\pi\rho}$,

$$k_7 = k_1^2 + k_2^2 \quad \text{and} \quad \theta = \tan^{-1} \frac{k_2}{k_1}.$$

The Doppler shift is given by

$$\frac{\delta t_2 - \delta t_1}{\delta t_1} = \frac{\lambda + \delta\lambda}{\lambda} = \frac{2}{M} e^{y/M} \frac{dy}{dt} > 0.$$

Since $M < 0$ and the velocity is negative at the time of emission, the shift is in the direction of larger wavelength.

5. Discussion

The model presented in the paper refers to a homogeneous model with equation of state $p + \rho = 0$, which is quite analogous to that of de-Sitter in isotropic co-ordinates. However, the model does not allow matter because $p + \rho = 0$ and $p \geq 0$. Even then there is motion. It may be mentioned here that this model revives the so-called inflationary model to describe the earliest phases of the "Big Bang" even though it is without the cosmological constant.

This inflation of the universe due to the increase of negative pressure energy is compensated by increasing production of particles with positive energy. The model thus predicts a density equal to the critical density at all epochs accounting for the equality between the kinetic and gravitational energies. It is to be mentioned here that a closed universe has zero total energy, the negative gravitational potential energy neutralising the energy of matter and radiation.

It has also been verified earlier [2] that this spacetime does not admit incoherent matter and stiff matter distributions.

References

1. A. Einstein, Pruss. Akad. der Wiss. Sitzber., Part-1, 142, 1917.
2. G. Mohanty and R. R. Pattanaik, J. Aust. Math. Soc. Ser. B, 1988 (communicated).

Acta Physica Hungarica 67 (1–2), pp. 235–240 (1990)

THE ABELIAN DYON AND A MASSLESS SCALAR FIELD IN THE BI-METRIC THEORY OF GRAVITATION

C. WOLF

Department of Physics
North Adams State College
North Adams, MA. 01247, USA

(Received 21 April 1988)

The gravitational field in the linearized approximation (far field) is found for the composite system of an Abelian dyon and a massless scalar field in the bi-metric theory of gravitation.

1. Introduction

Dyons were originally proposed as particles carrying both electric and magnetic charges that emerged from the solution of the gauge–Higgs system [1], [2]. The idea of a dyon or monopole is not unique to any one gauge group but emerges when a gauge group G is broken to $H \times U(1)$, $G \to H \times U(1)$ with unbroken $U(1)$ factor. The physical interest in dyons arises because of the observation on the part of Callan that a dyon or monopole would catalyze proton decay with strong interaction rates because of the conversion mechanism provided by the dyon field by converting two u quarks to a positron and $\bar{d}$ anti-quark, effectively giving rise to proton decay as $P \to e^+ + \pi^0$ [3]. In a previous note we have studied the gravitational field of the Abelian dyon in the linearized approximation in the bi-metric theory and have identified the two masses and the electric and magnetic charge in this theory with the constants in the solution [4]. In this note we generalize this result to the case when a massless scalar field of scalar charge C is added to the system. It is generally believed that event horizons are absent in the bi-metric theory and there has been conflicting evidence for their presence for a system of massless scalar field in general relativity. Agnese and La Camera proved that the presence of a static scalar field could shrink the topology of event horizon to a point [5], while recently Goldwirth and Piran [6] have shown that the collapse of a scalar field in general relativity always leads to a singularity engulfed by an event horizon. These studies are significant because scalar fields emerge not only in variable G theories [7] but also in the low energy effective Lagrangian of super-gravity theory (graviscalar) [8] and their effect on the topology of space time is all important. In this note we do not discuss the near field but study only the far field of a dyon and scalar field in the bimetric theory. Such a solution would represent the effect of an electrically and magnetically charged system in the presence of any scalar field from unknown origin (variable G, super-gravity source) far from the origin. This far field expansion for the metric is found in terms of the two masses identified in the bi-metric theory, the electric and magnetic charge and the scalar charge C.

2. The Abelian dyon coupled to a massless scalar field in the bi-metric theory

To begin we write for the isotropic metric in the bi-metric theory

$$(ds)^2 = e^{2\phi}(dx^4)^2 - e^{2X}(dr)^2 - e^{2X}r^2\left(d\theta^2 + \sin^2\theta(d\overline{\phi})^2\right),$$
$$x^4 = ct, \quad x^1 = r, \quad x^2 = \theta, \quad x^3 = \overline{\phi}, \tag{2.1}$$

also with $F_{14} = E(r)$, $F_{23} = r^2\sin\theta B_r$. For the matter Lagrangian we have where $F_{\mu\nu} = E.M.$ field tensor, $\phi =$ scalar field,

$$L = -\frac{1}{16\pi}F_{\mu\nu}F^{\mu\nu}\sqrt{-g} + \frac{\partial\mu\phi\partial^\mu\phi}{2}\sqrt{-g} \tag{2.2}$$

with field equation

$$\frac{\partial}{\partial x\nu}\left(\sqrt{-g}F^{\mu\nu}\right) = 0, \tag{2.3}$$

$$\Box\phi = 0, \tag{2.4}$$

giving

$$F_{14} = E(r) = \frac{e}{r^2}e^{\phi+\chi-2X}, \quad F_{23} = r^2\sin\theta B_r = \overline{g}\sin\theta, \tag{2.5}$$

following from $\frac{\partial}{\partial x^\nu}(\varepsilon^{\mu\nu\alpha\beta}F_{\alpha\beta}) = 0$ outside the dyon core. Here e and $\overline{g}$ are electric and magnetic charge, respectively. Also

$$\phi_r = \frac{C}{r^2}e^{-\phi+\chi-2X} \quad (C = \text{scalar charge}). \tag{2.6}$$

For the energy momentum components we have [4]

$$T_{\mu\nu} = \frac{2}{\sqrt{-g}}\frac{\partial L}{\partial g^{\mu\nu}} = -\frac{1}{4\pi}F_{\mu\alpha}F^{\alpha}_{\nu} + \frac{1}{16\pi}g_{\mu\nu}F_{\alpha\beta}F^{\alpha\beta} + \partial_\mu\phi\partial_\nu\phi - \frac{1}{2}g_{\mu\nu}(\partial^\alpha\phi\partial_\alpha\phi)$$

or using Eq. (2.5), Eq. (2.6) we have

$$T^1_1 = \frac{1}{8\pi}\left[\frac{e^2}{r^4} + \frac{\overline{g}^2}{r^4}\right]e^{-4X} - \frac{C^2}{2r^4}e^{-2\phi-4X},$$

$$T^2_2 = T^3_3 = -\frac{1}{8\pi}\left[\frac{e^2}{r^4} + \frac{\overline{g}^2}{r^4}\right]e^{-4X} + \frac{C^2}{2r^4}e^{-2\phi-4X},$$

$$T^4_4 = \frac{1}{8\pi}\left[\frac{e^2}{r^4} + \frac{\overline{g}^2}{r^4}\right]e^{-4X} + \frac{C^2}{2r^4}e^{-2\phi-4X}.$$

The field equations for the bi-metric theory are

$$N_{\mu\nu} - \frac{1}{2} N g_{\mu\nu} = -\frac{8\pi G(k)}{C_L^4} T_{\mu\nu}, \quad C_L = \text{speed of light}, \left(\text{with } k = \left(\frac{g}{\gamma} \right)^{1/2} \right)$$

($\gamma_{\mu\nu}$ =background metric), γ =determinant $\gamma_{\mu\nu}$, g =determinant $g_{\mu\nu}$), or

$$N_{\mu\nu} = -\frac{8\pi G(k)}{C_L^4} \left(T_{\mu\nu} - \frac{1}{2} T g_{\mu\nu} \right), \tag{2.7}$$

or

$$N_{\nu}^{\mu} = -\frac{8\pi G(k)}{C_L^4} \left(T_{\nu}^{\mu} - \frac{1}{2} T \delta_{\nu}^{\mu} \right), \tag{2.8}$$

with

$$N_4^4 = -\phi'' - \frac{2}{r}\phi', \tag{2.9}$$

$$N_1^1 = -\chi'' - \frac{2}{r}\chi' - \frac{2}{r^2} \sinh Z, \tag{2.10}$$

$$N_2^2 = N_3^3 = -X'' - \frac{2}{r} X' + \frac{1}{r^2} \sinh Z, \tag{2.11}$$

here $Z = 2X - 2\chi$.

Equation (2.8) becomes with $C_L = 1$

$$-\phi'' - \frac{2}{r}\phi' = -8\pi G e^{\phi+\chi+2X} \left(\frac{1}{8\pi} \left(\frac{e^2}{r^4} + \frac{\overline{g}^2}{r^4} \right) \right) e^{-4X}, \tag{2.12}$$

$$-\chi'' \frac{2}{r}\chi' - \frac{2}{r^2} \sinh Z =$$

$$= -8\pi G(e^{\phi+\chi+2X}) \left[\frac{1}{8\pi} \left(\frac{e^2}{r^4} + \frac{\overline{g}^2}{r^4} \right) e^{-4X} - \frac{C^2}{r^4} e^{-2\phi-4X} \right], \tag{2.13}$$

$$-X'' - \frac{2}{r} X' + \frac{1}{r^2} \sinh Z = -8\pi G e^{\phi+\chi+2X} \left[-\frac{1}{8\pi} \left(\frac{e^2}{r^4} + \frac{\overline{g}^2}{r^4} \right) e^{-4X} \right]. \tag{2.14}$$

We next define

$$\begin{aligned} \phi + \chi - 2X &= W, \\ 2X - 2\chi &= Z, \\ \phi + \chi + 2X &= \overline{X}. \end{aligned} \tag{2.15}$$

We have upon adding the appropriate combinations of Eq. (2.12), Eq. (2.13) and Eq. (2:14) using the definitions in Eq. (2.15)

$$W'' + \frac{2}{r}W' + \frac{4}{r^2}\sinh Z = 4G\left(\frac{e^2}{r^4} + \frac{\overline{g}^2}{r^4}\right)e^W - \frac{8\pi G}{r^4}C^2 e^{-\frac{W}{2}-Z-\frac{\overline{X}}{2}}, \tag{2.16}$$

$$Z'' + \frac{2}{r}Z' - \frac{6}{r^2}\sinh Z = -4G\left(\frac{e^2}{r^4} + \frac{\overline{g}^2}{r^4}\right)e^W + \frac{16\pi GC^2}{r^4}e^{-\frac{W}{2}-Z-\frac{\overline{X}}{2}}, \tag{2.17}$$

$$\overline{X}'' + \frac{2}{r}\overline{X}' = -\frac{8\pi G}{r^4}C^2 e^{-\frac{W}{2}-Z-\frac{\overline{X}}{2}}. \tag{2.18}$$

If we linearize Eqs (2.16), (2.17) and (2.18) in the gravitational potentials we have

$$W'' + \frac{2}{r}W' + \frac{4}{r^2}Z = 4G\left(\frac{e^2}{r^4} + \frac{\overline{g}^2}{r^4}\right)(1+W) - \frac{8\pi G}{r^4}C^2\left(1 - \frac{W}{2} - Z - \frac{\overline{X}}{2}\right), \tag{2.19}$$

$$Z'' + \frac{2}{r}Z' - \frac{6}{r^2}Z = -4G\left(\frac{e^2}{r^4} + \frac{\overline{g}^2}{r^4}\right)(1+W) + \frac{16\pi GC^2}{r^4}\left(1 - \frac{W}{2} - Z - \frac{\overline{X}}{2}\right), \tag{2.20}$$

$$\overline{X}'' + \frac{2}{r}\overline{X}' = -\frac{8\pi GC^2}{r^4}\left(1 - \frac{W}{2} - Z - \frac{\overline{X}}{2}\right). \tag{2.21}$$

We next expand the functions W, Z, $\overline{X}$ in inverse power for large r, or

$$W = \sum_{i=1}^{\infty}\frac{A_i}{r^i}, \quad Z = \sum_{i=1}^{\infty}\frac{B_i}{r^i}, \quad \overline{X} = \sum_{i=1}^{\infty}\frac{C_i}{r^i}. \tag{2.22}$$

This gives for the first two inverse powers in Eqs (2.19), (2.20) and (2.21)

$$\begin{aligned} 2A_1 - 2A_1 + 4B_1 &= 0, \\ 2B_1 - 2B_1 - 6B_1 &= 0, \\ 2C_1 - 2C_1 &= 0, \quad \text{to order } \frac{1}{r^3} \end{aligned} \tag{2.23}$$

and

$$\begin{aligned} 6A_2 - 4A_2 + 4B_2 &= 4Ge^2 + 4G\overline{g}^2 - 8\pi GC^2, \\ 6B_2 - 4B_2 - 6B_2 &= -4Ge^2 - 4G\overline{g}^2 + 16\pi GC^2, \\ 6C_2 - 4C_2 &= -8\pi GC^2, \quad \text{to order } \frac{1}{r^4}. \end{aligned} \tag{2.24}$$

Solving Eqs (2.23) and (2.24) we have

$$\begin{aligned} A_1 &= \text{arb} = A_1 \quad \text{and} \quad & B_2 &= Ge^2 + G\overline{g}^2 - 4\pi GC^2, \\ C_1 &= \text{arb} = C_1, & C_2 &= -4\pi GC^2, \\ B_1 &= 0, & A_2 &= 4\pi GC^2, \end{aligned} \tag{2.25}$$

or

$$W = \frac{A_1}{r} + \frac{4\pi GC^2}{r2},$$
$$Z = \frac{Ge^2 + G\bar{g}^2}{r2} - \frac{4\pi GC^2}{r2},$$
$$\overline{X} = \frac{C_1}{r} - \frac{4\pi GC^2}{r2}. \tag{2.26}$$

If we now solve Eq. (2.15) for ϕ, χ, X in terms of W, Z, $\overline{X}$ we have

$$\phi = \frac{3A_1 + C_1}{4r} + \frac{Ge^2 + G\bar{g}^2}{2r^2},$$
$$\chi = \frac{C_1 - A_1}{4r} - \left(\frac{Ge^2 + G\bar{g}^2}{2r^2}\right),$$
$$X = \frac{C_1 - A_1}{4r} - \frac{2\pi GC^2}{r^2}. \tag{2.27}$$

The line element is from Eq. (2.1)

$$(ds)^2 = e^{\left(\frac{3A_1+C_1}{2r}\right)+\frac{Ge^2+G\bar{g}^2}{r^2}}(dx)^2,$$
$$- e^{\left(\frac{C_1-A_1}{2r}\right)-\frac{Ge^2+G\bar{g}^2}{r^2}}(dr)^2,$$
$$- e^{\left(\frac{C_1-A_1}{2r}\right)}e^{-\frac{4\pi GC^2}{r^2}} r^2\left(d\theta^2 + \sin^2\theta(d\phi)^2\right). \tag{2.28}$$

We now identify

$$\frac{3A_1 + C_1}{2} = -2Gm,$$
$$\frac{C_1 - A_1}{2} = 2Gm', \tag{2.29}$$

where m, m' are the x^4 and x^1 component masses in the bi-metric theory. Eq. (2.28) finally becomes

$$(ds)^2 = e^{\frac{-2Gm}{r}+\frac{Ge^2+G\bar{g}^2}{r^2}}(dx^4)^2$$
$$- e^{\frac{2Gm'}{r}-\left(\frac{Ge^2+G\bar{g}^2}{r^2}\right)}(dr)^2$$
$$- e^{\frac{2Gm'}{r}-\frac{4\pi GC^2}{r^2}} r^2\left(d\theta^2 + \sin^2\theta(d\phi)^2\right). \tag{2.30}$$

We see in Eq. (2.30) that the scalar charge only appears in the $\theta\phi$ component of the metric and any radial motion in such a metric would be insensitive to the scalar charge and be effected by the electric and magnetic charge only. We also note that

the difference of the metric in Eq. (2.30) and that in the result from [4] is only in the term $\frac{4\pi GC^2}{r^2}$ in the θ, ϕ components of the metric. This term effectively diminishes the length of arc for a complete revolution in the plane $\theta = \frac{\pi}{2}$ by $e^{\frac{-2\pi GC^2}{r^2}}$ since

$$(ds)_\phi^2 = e^{\frac{2Gm'}{r} - \frac{4\pi GC^2}{r^2}} r^2 (d\phi)^2,$$
$$L_\phi = 2\pi r e^{\frac{Gm'}{r} - \frac{2\pi GC^2}{r^2}}. \tag{2.31}$$

This is the effect produced both in general relativity as pointed out in [5] and in the bi-metric theory as is shown in Eq. (2.31). However, this discussion is derived for the far field and a more precise discussion would entail solving the field equations more exactly for small r. Before closing we emphasize that scalar fields enter into gravitational physics through variable G theories and super-gravity theories and their implications on both black hole solutions in G. R. as well as spherically symmetric solutions in the bi-metric theory (a theory void of a principle of cosmic censorship) are both relevant and interesting in many astrophysical situations.

Acknowledgements

I should like to thank the Physics Department at Williams College for the use of their facilities as well as Dr. Tisenger at North Adams State College for her support of this work.

References

1. K. M. Prasad and C. M. Sommerfield, Phys. Rev. Lett., *35*, 760, 1975.
2. B. Julia and A. Zee, Phys. Rev., *D11*, 2227, 1975.
3. C. G. Callan, Jr., Phys. Rev., *D26*, 2058, 1982.
4. C. Wolf (to appear in Acta Physica Slovaca).
5. A. G. Agnese and M. La Camera, Phys. Rev., *D31*, 1280, 1985.
6. D. S. Goldwirth and T. Piran, Phys. Rev., *D36*, 3575, 1987.
7. C. H. Brans and R. Dicke, Phys. Rev., *124*, 925, 1961.
8. M. M. Nieto, T. Goldman and R. J. Hughes, Phys. Rev., *D36*, 3684, 1987.

Acta Physica Hungarica 67 (1–2), pp. 241–243 (1990)

BOOK REVIEWS

M. GÖCKELER and T. SCHÜCKER: *Differential Geometry, Gauge Theories and Gravity*

Cambridge University Press, Cambridge, New York, 1987, pp. 230

This excellent Volume published in the series of Cambridge Monographs on Mathematical Physics is based on lecture notes of a course given at Heidelberg University. It provides a concise introduction to those concepts and theorems of differential geometry which are of fundamental importance in modern field theory. In Chapters 1, 2, 3, 6 the authors deal with differential forms, metric structures. Manifolds, Lie groups, fibre bundles, spinors are treated in turn in Chapters 7, 8, 9, 11. Physical applications are presented in Chapters 4 (Yang–Mills theories), 5 (Einstein-Cartan theory), 10 (monopoles, instantons), 12 (gauge anomalies), 13 (anomalies from Feynman graphs).

The concepts presented in the book are inevitably important in the research of the past few years, in connection with anomalies and theories of superstrings. We recommend the book to graduate students and physicists working in the field.

G. Pócsik

R. J. RIVERS: *Path Integral Methods in Quantum Field Theory*

Cambridge University Press, Cambridge, New York, 1987, pp. 339

This new volume of the Cambridge Monograph series on Mathematical Physics presents a self-contained introduction to the functional integral methods in quantum field theory. Sometimes called the Feynman path integral method, the approach has a large number of applications in quantum electrodynamics, gauge theories, finite temperature field theory etc.

The discussion begins with some mathematical preliminaries pertinent to the structure of quantum field theory, Green function methods and to regularization. The next five sections acquaint the reader with the scalar functional integral and its series expansion, with the Lorentzian theory and the trouble with i, topological complications and stochastic quantization. Yet another section is devoted to fermionic path integrals and the cancellation of ultraviolet divergences in the supersymmetric theory. The very highlights are discussed in the final sections. To mention only some of the outstanding problems: Taylor–Slavnov and BRS identities, the background-field method, gauging away the Goldstone modes, the Coleman–Weinberg mechanism, instantons and the large-N limit. What a treat!

All required of the reader is a "rudimentary understanding of Feynman diagrams in relativistic quantum field theory, and the need for renormalization". In fact, the discussion stays on the graduate level. Mathematical intricacies are never indulged beyond the immediate relevance, though the treatment appears correct. As the author frequently points out, for example, the Lorentzian theory lacks a serious foundation. Snags like this do not appear to be a big price for the ease with which functional integrals lend themselves to applications.

The book is likely to become a fond piece of the field theorist's library.

Z. Perjés

Sir ARTHUR EDDINGTON: *Space, Time and Gravitation; An Outline of the General Relativity Theory*

Cambridge Science Classic Series, Cambridge University Press, Cambridge, New York, 1987

This is a new edition of a famous book first published in 1920, only 4 years after the birth of the full theory of General Relativity. In that time, obviously, introductory books were needed in order to present the new theory for

physicists and astronomers who were not familiar with its proper mathematical machinery; and this meant practically the whole scientific community. Namely the formalism of the new physical theory " ... had already been worked out as a branch of pure mathematics by Riemann, Christoffel Ricci, Levi-Civita who, it may be presumed, never dreamt of this physical application" (Eddington's own words) and not as a branch of physics.

One can imagine that Eddington's task was enormous; in any case he became successful. While obviously the primary goal for reissuing the book was historical, even today this book could be used by physicists working far from General Relativity for obtaining some insight into the philosophy of relativity theory. Namely, as Sir Hermann Bondi emphasizes in the Foreword written in 1986, there is only one statement in the book which has been proven incorrect in the last 67 years: the Fitzgerald (or, more continentally Lorentz) contraction cannot be seen by the external observer.

Of course, by subtler ways the reader can detect that the book is 2/3 century old: e.g. it does not contain any Quantum Mechanics, only vague remarks about quantisation, because Quantum Mechanics had not yet been elaborated when the author finished this book. Pondering over this fact one can better realize, how immense a success this book was with respect to its original goal. The reader can even contemplate what had greater part in this success: the genius of the author (one of the greatest astrophysicists of the history of science and in the same time an inspired science writer), or the outstanding quality of General Relativity even in statu nascendi (indeed, there has been no need to correct it up to now). However, it would be improper to emphasize anyone of these alternative explanations against the other, since Eddington was one of the earliest scientists accepting, adopting and developing General Relativity.

Reading this excellent book we are being comforted with the thinking process of a great brain and also with some not quite definite but very deep ideas concerning fundamental problems on physics (moreover, of all natural sciences); and none of the problems left open in the book has been completely solved up to now. In some points today the answer is hoped in directions different from that suggested by the author, but even then the old ideas are still inspiring.

By tracing back farther the present trends into the past we can make better established predictions for the future. A better understood history of physics may help even in finding the long desired "Quantum Gravity", whatsoever it will be. This book is an excellent possibility to keep direct contact with the history of physics.

B. Lukács

Particle Physics

Edited by: N. G. Cooper and G. B. West

Cambridge University Press, Cambridge, New York, 1988, pp. 200

The volume contains the most recent information on the subject and can be divided into three parts: The first one, about 130 pages, deals with theoretical questions of particle physics; the second, about 50 pages, with problems of experimental particle physics; and finally this is followed by 16 pages devoted to a round-table discussion dealing with the history and future of particle physics. Each chapter is written by a different author.

In large part the book treats the theory of particle physics, reflected not only by the lengthy introductory part but also by its style and level which demands a fair amount of mathematical knowledge. The book could hardly be recommended for readers less familiar with mathematics. This theoretical part expands on e.g. scaling and standard models, on a unified theory of interactions and on supersymmetry. The following experimental part deals practically with the possibility of experimentally verifying the standard model and gives an outline of present and future high energy accelerators, including the new American dream, the SSC.

The book claims to be enjoyable reading for both specialists and laymen. In my opinion it primarily is geared towards particle physicists with the aim of making them acquainted with certain concepts of theoretical particle physics. It can be a useful reference book for interested students of physics and possibly for physicists engaged in a discipline other than particle physics.

The book does not wish to treat the entire field of particle physics, which would in fact assume a much more extensive volume and

would be even more difficult to digest. It only reports on some - arbitrarily selected - results of the past two decades and this in rough outlines.

The book is useful and enjoyable reading for qualified particle physicists and can also serve as a manual for experimental particle physicists willing to invest a fair amount of additional in-depth study in the field.

Dezső Kiss

W. J. WITTEMAN: *The CO_2 Laser*

Springer Series in Optical Sciences, Springer-Verlag, Berlin, Heidelberg, New York, 1987, pp. 309, 135 figs

The field of quantum electronics is continuously growing since the discovery of the first laser in 1960. This is also denoted by the increasing number of books dealing with lasers and various applications. The CO_2 laser is one of the basic laser systems widely used today in many applications of which scientific research, material processing, medical use and laser fusion experiments are some of the most important. Thus it is useful to have a review dealing specifically with questions of this laser. The book is an excellent summary of the scientific aspects of laser problems and some special techniques used in this type of laser.

The book begins with a short summary on applications and the author then outlines basic questions of stable and unstable resonators, which are used in various types of CO_2 lasers. This is followed by two chapters, one of them dealing with the rotational-vibrational structure of the CO_2 molecule and the other describing processes leading to population inversion. The next parts deal with various excitation methods, lasers working in continuous discharges, lasers operating using fast gas flow systems and pulsed laser systems are discussed. The latter is a detailed chapter and includes also description of various technical problems. Two chapters deal with methods used for the synchronization of modes of transversally excited atmospheric pressure CO_2 lasers, these are the so-called mode locking techniques. The methods described are amplitude modulation and frequency modulation mode locking, respectively, which are followed by a chapter on passive mode locking. The last chapter of the book is devoted to short pulse amplification questions.

The structure of the book follows a double line, one line is the description of basic phenomena related to problems of laser physics, these are of general value and are valid not only specifically for the CO_2 laser, but for many other laser systems too. The other line is the description of CO_2 laser phenomena based on this background of laser physics. In many places engineering questions are dealt with, the scientific background being emphasized for understanding the phenomena. The author gives reference to another book dealing with gas dynamic lasers, inclusion of a short description of this topic for understanding basic principles and seeing practical realization would have been useful. The parts of the book dealing with mode locking techniques are very interesting from the pure scientific point of view, but since these are not connected with any application, the significance of these techniques is not easily acknowledged by readers who are less experienced in the field of lasers.

The book is well written, its style is easy to follow, all problems are well presented. The book can be recommended to research scientists, engineers and graduate students, who are interested in the relevant basic physics related to operation principles and special techniques of the CO_2 laser.

M. Jánossy

NOTES TO CONTRIBUTORS

I. PAPERS will be considered for publication in Acta Physica Hungarica only if they have not previously been published or submitted for publication elsewhere. They may be written in English, French, German or Russian.

Papers should be submitted to

Prof. I. Kovács, Editor
Department of Atomic Physics, Technical University
1521 Budapest, Budafoki út 8, Hungary

Papers may be either articles with abstracts or short communications. Both should be as concise as possible, articles in general not exceeding 25 typed pages, short communications 8 typed pages.

II. MANUSCRIPTS

1. Papers should be submitted in three copies.
2. The text of papers must be of high stylistic standard, requiring minor corrections only.
3. Manuscripts should be typed in double spacing on good quality paper, with generous margins.
4. The name of the author(s) and of the institutes where the work was carried out should appear on the first page of the manuscript.
5. Particular care should be taken with mathematical expressions. The following should be clearly distinguished, e.g. by underlining in different colours: special founts (italics, script, bold type, Greek, Gothic, etc.); capital and small letters; subscripts and superscripts, e.g. x^2, x_3; small *l* and l; zero and capital O; in expressions written by hand: *e* and *l*, *n* and *u*, *v* and v, etc.

A List of Symbols on a separate sheet should be attached to each paper.

6. References should be numbered serially and listed at the end of the paper in the following form: J. Ise and W. D. Fretter, Phys. Rev., *76,* 933, 1949.

For books, please give the initials and family name of the author(s), title, name of publisher, place and year of publication, e.g.: J. C. Slater, Quantum Theory of Atomic Structures, I. McGraw-Hill Book Company, Inc., New York, 1960.

References should be given in the text in the following forms: Heisenberg [5] or [5].

7. Captions to illustrations should be listed on a separate sheet, not inserted in the text.
8. In papers submitted to Acta Physica all measures should be expressed in SI units.

III. ILLUSTRATIONS AND TABLES

1. Each paper should be accompanied by three sets of illustrations, one of which must be ready for the blockmaker. The other sets attached to the copies of the manuscript may be rough drawings in pencil or photocopies.
2. Illustrations must not be inserted in the text.
3. All illustrations should be identified in blue pencil by the author's name, abbreviated title of the paper and figure number.
4. Tables should be typed on separate pages and have captions describing their content. Clear wording of column heads is advisable. Tables should be numbered in Roman numerals (I, II, III, etc.).

IV. RETURN OF MATERIAL

Owing to high postage costs, the Editorial Office cannot undertake to return *all* material not accepted for any reason for publication. Of papers to be revised (for not being in conformity with the above Notes or other reasons) only *one* copy will be returned. Material rejected for lack of space or on account of the Referees' opinion will not be returned to authors outside Europe.

Periodicals of the Hungarian Academy of Sciences are obtainable at the following addresses:

AUSTRALIA
C.B.D. LIBRARY AND SUBSCRIPTION SERVICE
Box 4886, G.P.O., *Sydney N.S.W. 2001*
COSMOS BOOKSHOP, 145 Ackland Street
St. Kilda (Melbourne), Victoria 3182

AUSTRIA
GLOBUS, Höchstädtplatz 3, *1206 Wien XX*

BELGIUM
OFFICE INTERNATIONAL DES PERIODIQUES
Avenue Louise, 485, *1050 Bruxelles*
E. STORY-SCIENTIA P.V.B.A.
P. van Duyseplein 8, *9000 Gent*

BULGARIA
HEMUS, Bulvar Ruszki 6, *Sofia*

CANADA
PANNONIA BOOKS, P.O. Box 1017
Postal Station "B", *Toronto, Ont. M5T 2T8*

CHINA
CNPICOR, Periodical Department, P.O. Box 50
Peking

CZECHOSLOVAKIA
MAD'ARSKA KULTURA, Národni třida 22
115 66 Praha
PNS DOVOZ TISKU, Vinohradská 46, *Praha 2*
PNS DOVOZ TLAČE, *Bratislava 2*

DENMARK
EJNAR MUNKSGAARD, 35, Nørre Søgade
1370 Copenhagen K

FEDERAL REPUBLIC OF GERMANY
KUNST UND WISSEN ERICH BIEBER
Postfach 46, *7000 Stuttgart 1*

FINLAND
AKATEEMINEN KIRJAKAUPPA, P.O. Box 128
00101 Helsinki 10

FRANCE
DAWSON-FRANCE S.A., B.P. 40, *91121 Palaiseau*
OFFICE INTERNATIONAL DE DOCUMENTATION ET LIBRAIRIE, 48 rue Gay-Lussac
75240 Paris, Cedex 05

GERMAN DEMOCRATIC REPUBLIC
HAUS DER UNGARISCHEN KULTUR
Karl Liebknecht-Straße 9, *DDR-102 Berlin*

GREAT BRITAIN
BLACKWELL'S PERIODICALS DIVISION
Hythe Bridge Street, *Oxford OX1 2ET*
BUMPUS, HALDANE AND MAXWELL LTD.
Cowper Works, *Olney, Bucks MK46 4BN*
COLLET'S HOLDINGS LTD., Denington Estate,
Wellingborough, Northants NN8 2QT
WM DAWSON AND SONS LTD., Cannon House
Folkstone, Kent CT19 5EE
H. K. LEWIS AND CO., 136 Gower Street
London WC1E 6BS

GREECE
KOSTARAKIS BROTHERS INTERNATIONAL BOOKSELLERS, 2 Hippokratous Street, *Athens-143*

HOLLAND
FAXON EUROPE, P.O. Box 167
1000 AD Amsterdam
MARTINUS NIJHOFF B. V.
Lange Voorhout 9–11, *Den Haag*
SWETS SUBSCRIPTION SERVICE
P.O. Box 830, 2160 Sz Lisse

INDIA
ALLIED PUBLISHING PVT. LTD.
750 Mount Road, *Madras 600002*
CENTRAL NEWS AGENCY PVT. LTD.
Connaught Circus, *New Delhi 110001*
INTERNATIONAL BOOK HOUSE PVT. LTD.
Madame Cama Road, *Bombay 400039*

ITALY
D. E. A., Via Lima 28, *00198 Roma*
INTERSCIENTIA, Via Mazzé 28, *10149 Torino*
LIBRERIA COMMISSIONARIA SANSONI
Via Lamarmora 45, *50121 Firenze*
SANTO VANASIA, Via M. Macchi 58
20124 Milano

JAPAN
KINOKUNIYA COMPANY LTD.
Journal Department, P.O. Box 55
Chitose, *Tokyo 156*
MARUZEN COMPANY LTD., Book Department
P.O. Box 5050 Tokyo International, *Tokyo 100-31*
NAUKA LTD., Import Department
2-30-19 Minami Ikebukuro, Toshima-ku, *Tokyo 171*

KOREA
CHULPANMUL, *Phenjan*

NORWAY
TANUM-TIDSKRIFT-SENTRALEN A.S.
Karl Johansgata 43, *1000 Oslo*

POLAND
WĘGIERSKI INSTYTUT KULTURY
Marszalkowska 80, *00-517 Warszawa*
CKP I W, ul. Towarowa 28, *00-958 Warszawa*

ROUMANIA
D. E. P., *Bucuresti*
ILEXIM, Calea Grivitei 64–66, *Bucuresti*

SOVIET UNION
SOYUZPECHAT — IMPORT, *Moscow*
and the post offices in each town
MEZHDUNARODNAYA KNIGA, *Moscow G-200*

SPAIN
DIAZ DE SANTOS Lagasca 95, *Madrid 6*

SWEDEN
ESSELTE TIDSKRIFTSCENTRALEN
Box 62, *101 20 Stockholm*

SWITZERLAND
KARGER LIBRI AG, Petersgraben 31, *4011 Basel*

USA
EBSCO SUBSCRIPTION SERVICES
P.O. Box 1943, *Birmingham, Alabama 35201*
F. W. FAXON COMPANY, INC.
15 Southwest Park, *Westwood Mass. 02090*
MAJOR SCIENTIFIC SUBSCRIPTIONS
1851 Diplomat, P.O. Box 819074,
Pallas, Tx. 75381-9074
READ-MORE PUBLICATIONS, INC.
140 Cedar Street, *New York, N. Y. 10006*

YUGOSLAVIA
JUGOSLOVENSKA KNJIGA, Terazije 27, *Beograd*
FORUM, Vojvode Mišića 1, *21000 Novi Sad*

Index: 26.022

Acta Physica Hungarica

VOLUME 67 · NUMBERS 3–4, 1990

Akadémiai Kiadó, Budapest

ACTA PHYS. HUNG. APAHAQ 67 (3-4) 245-415 (1990) HU ISSN 0231-4428

ACTA PHYSICA HUNGARICA

A JOURNAL OF THE HUNGARIAN ACADEMY OF SCIENCES

EDITED BY
I. KOVÁCS

Acta Physica publishes original papers on subjects in physics. Papers are accepted in English, French, German and Russian.

Acta Physica is published in two yearly volumes (4 issues each) by

AKADÉMIAI KIADÓ
Publishing House of the Hungarian Academy of Sciences
H-1117 Budapest, Prielle Kornélia u. 19–35

Subscription information

Orders should be addressed to

KULTURA Foreign Trading Company
1389 Budapest P.O. Box 149
or to its representatives abroad.

Acta Physica Hungarica is abstracted/indexed in Chemical Abstracts, Mathematical Reviews, Science Abstracts, Physics Briefs, Risk Abstracts

CONTENTS

GENERAL PHYSICS

ELEMENTARY PARTICLES AND FIELDS

NUCLEAR PHYSICS

ATOMIC AND MOLECULAR PHYSICS

Manuscript received by Akadémiai Kiadó:
26 April 1989
Manuscript received by TYPOTEX GT
for TEX typesetting: 22 August 1989

Date of publication: 6 September 1990

PRINTED IN HUNGARY

Akadémiai Kiadó és Nyomda Vállalat, Budapest

Acta Physica Hungarica 67 (3–4), pp. 245–257 (1990)

EMISSION OF SOFT PIONS IN MESON–NUCLEON INTERACTIONS

K. KRISHNA MURTHY and PRATHIBHA NUTHAKKI

Centre for Theoretical Physics, Andhra University
Visakhapatnam-530 003, India
and
Department of Physics, Andhra University
Visakhapatnam-530 003, India

(Received 16 July 1987)

The formalism of current algebra and partially conserved axial-vector current (PCAC) hypothesis is applied to study the Kp and πp interaction processes involving hyperons and one or two soft pions. The differential cross-sections for the processes are normalized to the differential cross-sections for the corresponding processes without the soft pions. Theoretical predictions for the ratio of cross-sections at various laboratory meson momenta are compared with the existing experimental data. Angular distributions are also given for different incoming meson momenta

1. Introduction

In the study of hadrons, current algebra combined with the hypothesis of partially conserved axial-vector current (PCAC) has been highly successful. The genesis of current algebra was mainly in the study of weak interactions, with the vector and axial-vector weak currents of hadrons being identified as physically observable quantities manifesting the broken chiral SU(2)×SU(2) symmetry. The symmetry is expressed in terms of the equal time commutators of the associated charges and currents. The breaking of the symmetry is reflected in the partial conservation of axial-vector current. The hypothesis of PCAC was first introduced to provide a sound foundation to the Goldberger–Treiman relation. The conclusion is that the axial-vector current $A_\mu(x)$ is not conserved since neither the pion decay constant f_π nor square of the pion mass m_π^2 is equal to zero. With $f_\pi \neq 0$ and m_π being very small, one interprets PCAC as the statement about the approximate chiral symmetry of strong interactions. The hypothesis tells us that the actual world is not very different from the limit in which the pion is massless. The usefulness of PCAC is in that it allows the derivation of scattering amplitudes containing pions from matrix elements of currents.

The current algebra–PCAC formalism has been successful in explaining the experimental results for various strong interaction processes involving soft pions [1–5]. Like $\bar{p}p$ annihilations and $\pi - N$ interactions, the scattering of kaons by nucleons is experimentally well studied. Also the scattering of kaons by nucleons at low

energies occurs in S-state. With the current algebra formalism being particularly successful in the S-state the $K^- p$ interactions are well suited for a theoretical study by using the current algebra–PCAC method. The many possible reactions available in Kp interactions also enable us to relate one reaction amplitude to another. This sort of relationship is a general feature of current algebra. Therefore we consider the processes

$$K^- p \to \Sigma \pi + n \pi^0,$$

where the n-pions are considered to be soft. To simplify the theoretical manipulations we limit ourselves to one or two soft pions and take them to be in the neutral mode. This way we eliminate the gradient coupling as pointed out by Weinberg [6]. In Section 2 we derive the matrix element for the two soft pion emissions in a reaction of the type $i \to f$ and give the differential cross-section for the process $K^- p \to \Sigma \pi$ with two additional soft pions present. In Section 3 we derive the differential cross-section for the same process with an extra soft pion. We need to normalize these expressions to the differential cross-section, for the process without soft pions, given in Section 4. Subscribing to van Hove's point of view we give all our theoretical expressions in the most differential form possible.

To make a comparison with the existing experimental data, we integrate the expressions over the relevant kinematic variables. Finally the expressions derived in Section 2–4 are used in predicting the cross-sections for $\pi N \to \Sigma K + n \pi^0$ normalized to the cross-section of the corresponding process without soft pions. In Section 5 we present the ratio of cross-sections for the various processes considered at different centre of mass energies and compare them with the experimental results.

2. The soft pion reaction amplitude and differential cross-section

We begin by considering the reaction

$$i \to f + \pi^\alpha(k_1) + \pi^\beta(k_2), \tag{1}$$

for multiparticle hadronic states i and f, where pions of momenta k_1 and k_2 and isospins α and β are emitted.

The matrix element for the emission of two pions in the above reaction is given by Lehmann, Symanzik and Zimmerman's reduction formula to be proportional to

$$\int d^4x\, d^4y\, \exp(-ik_1x)\, \exp(-ik_2y) < f\, |T\left[\phi_\pi^\alpha(x), \phi_\pi^\beta(y)\right]|\, i >, \tag{2}$$

where $\phi_\pi^\alpha(x)$ is the interpolating field operator for the pion. According to PCAC

$$\partial_\mu A_\mu^\alpha = (C_\pi/\sqrt{2})\phi_\pi^\alpha, \tag{3}$$

where $C_\pi = \sqrt{2} G_A M_N \mu^2 / g_r(0)$; M_N and μ are the nucleon and pion masses, respectively. G_A is the renormalized axial-vector coupling constant ($\simeq 1.186$) and $g_r(0)$ is the rationalized, renormalized pion–nucleon coupling constant ($g_r^2(0)/4\pi \simeq 14.6$). PCAC given in (3) enable us to rewrite (2) in terms of the divergence of the axial-vector current A_μ. Bringing the derivatives out of the time ordered products gives rise to commutators like

$$\delta(x_0 - y_0)\ \left[A_0^\alpha(x),\ \partial_\mu A_\mu^\beta(y)\right] = \delta_{\alpha\beta}\sigma(x)\ \delta(x-y). \tag{4}$$

These are dropped since they are of the same order as the PCAC correction terms. Integrating the resulting expression by parts and again using PCAC to replace $\partial_\mu A_\mu$ with pion field operator, we have

$$k_1^\mu k_2^\nu R_{\mu\nu}^{\alpha\beta} = \frac{i}{2} \frac{C_\pi^2}{(\mu^2 + k_1^2)(\mu^2 + k_2^2)}\ R_{2\pi}^{\alpha\beta} + i\ \varepsilon_{\alpha\beta\gamma}(k_2 - k_1)^\lambda R_\lambda^\gamma, \tag{5}$$

where we have used the relations

$$\delta(x_0 - y_0)\ [A_0^\alpha(x),\ A_\mu^\beta(y)] = i\ \delta(x-y)\varepsilon_{\alpha\beta\gamma} V_\mu^\gamma(x), \tag{6}$$

and

$$R_{\mu\nu}^{\alpha\beta} = i \int d^4x\ d^4y\ \exp(-ik_1 x)\ \exp(-ik_2 y) < f\ |T\left[A_\mu^\alpha(x),\ A_\mu^\beta(y)\right]|i> . \tag{7}$$

$$R_{2\pi}^{\alpha\beta} = -\int d^4x\ d^4y\ \exp(-ik_1 x)\ \exp(-ik_2 y)\cdot$$

$$\cdot(\mu^2 - \Box_x)(\mu^2 - \Box_y) < f\ |T\left[\phi_\pi^\alpha(x), \phi_\pi^\beta(y)\right]|i> \tag{8}$$

is the matrix element for the emission of two pions of momenta k_1 and k_2 and isospins α and β in the process $i \to f$.

$$R_\lambda^\gamma = \int d^4x\ \exp(-i(k_1 + k_2)) < f|V_\lambda^\gamma(x)|\ i> \tag{9}$$

is the matrix element for the emission of an isovector photon in the process $i \to f$. This term is present for $\pi^+\pi^-$ emission and leads to an expression that depends on which pion is soft, a consequence of simultaneously taking both pions off the mass shell [7]. For pions in neutral mode $\varepsilon_{\alpha\beta\gamma}$ vanishes and therefore is no contribution from this term. The expression (5) can now be written as

$$k_1^\mu k_2^\nu M_{\mu\nu}^{\alpha\beta} = \frac{i}{2} \frac{C_\pi^2}{(\mu^2 + k_1^2)(\mu^2 + k_2^2)}\ M_{2\pi}^{\alpha\beta} + \frac{i}{2}\ \varepsilon_{\alpha\beta\gamma}(k_2 - k_1)^\lambda M_\lambda^\gamma, \tag{10}$$

We now set $k_1 = \xi K_1$ and $k_2 = \xi K_2$ so that $\xi \to 0$ corresponds to the soft pion limit. For a process like $i \to f + n_\pi$, where i and f are different hadronic states, the

matrix elements are of zeroth order in ξ [8]. The left-hand side vanishes as $\xi \to 0$ unless it has pole terms that go as k^{-2}. M_λ^7 term when necessary can be evaluated using the low energy theorem for photon emission due to Low [9].

In the neutral soft-pion limit the expression (10) becomes

$$k_1^\mu k_2^\nu M_{\mu\nu}^{33} = \frac{i}{2}\frac{C_\pi^2}{\mu^4} M_{2\pi}^{33}. \tag{11}$$

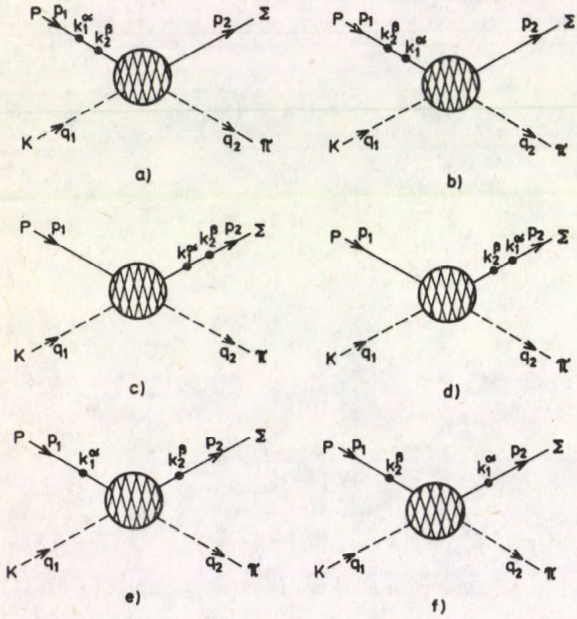

Fig. 1. Diagrams of order k^{-2} contributing to $M_{\mu\nu}^{33}$

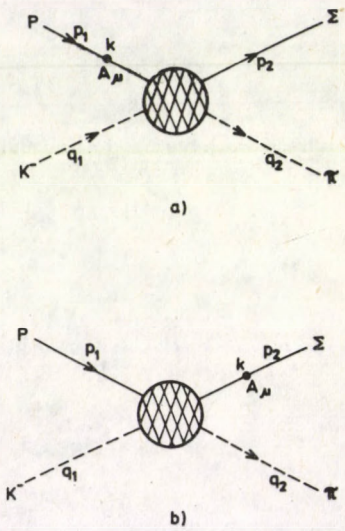

Fig. 2. Diagrams of order k^{-1} contributing to M^{π^0}

The diagrams that give rise to pole terms of order k^{-2} are given in Fig. 1 [10]. The central interaction in the diagrams is

$$m = A + B\,Q, \tag{12}$$

where $Q = q_1 + q_2$, the sum of the kaon and final hard pion momenta. A and B are functions of K^2 and $Q \cdot K$ with $K = p_1 + p_2$, the sum of the proton and hyperon momenta. Retaining only zeroth order terms in pion momenta k_1 and k_2 and in order to facilitate computation dropping terms proportional to A [11] gives us the

matrix element

$$M_{2\pi}^{33} = \frac{-2iBG_A^2\mu^4}{C_\pi^2}\,\bar{u}(p_2)\cdot$$
$$\cdot\left\{\frac{1}{(a+b)a}[-M_N^2Qk_2k_1 + i\,M_N bQk_1 - i\,M_N aQk_2 - abQ] + \right.$$
$$+\frac{1}{(a+b)b}[-M_N^2Qk_1k_2 + i\,M_N aQk_2 - i\,M_N bQk_1 - abQ] +$$
$$+\frac{1}{(c+d)c}[-M_H^2k_1k_2Q + i\,M_H dk_1Q - i\,M_H ck_2Q - cdQ] +$$
$$+\frac{1}{(c+d)d}[-M_H^2k_2Qk_1 + i\,M_H ck_2Q - i\,M_H dk_1Q - cdQ] +$$
$$+\frac{1}{ad}[-M_N M_H k_2Qk_1 - i\,M_H ak_2Q - i\,M_N dQk_1 - adQ] +$$
$$\left.+\frac{1}{bc}[-M_N M_H k_1Qk_2 - i\,M_H bk_1Q - i\,M_N cQk_2 - bcQ]\right\}u(p_1), \tag{13}$$

where $a = p_1 \cdot k_1$, $b = p_1 \cdot k_2$, $c = p_2 \cdot k_1$ and $d = p_2 \cdot k_2$. M_H is the mass of the hyperon. The differential cross-section for the reaction $Kp \to \Sigma\pi + 2\pi^0$ is given by the expression

$$(d\sigma)^{2\pi^0} = \frac{M_N M_H}{2[(p_1\cdot q_1)^2 - m_K^2 M_N^2]^{1/2}}\,\frac{<|M_{2\pi}^{33}|>}{(2\pi)^8}\,dm_{\Sigma\pi}^2\,dm_{\pi\pi}^2\times$$
$$\times\, d(\cos\theta_p)\,d(\cos\theta_K)\,d(\cos\theta_\pi)\,d\phi_1\,d\phi_2\,d\phi_3\times$$
$$\times\frac{1}{8\,M_{Kp}^2}[(M_{Kp}^2 + m_{\pi\pi}^2 - m_{\Sigma\pi}^2)^2 - 4\,m_{\pi\pi}^2 M_{Kp}^2]^{1/2}\times$$
$$\times\frac{1}{4\,m_{\Sigma\pi}^2}[(m_{\Sigma\pi}^2 + m_\Sigma^2 - m_\pi^2)^2 - 4\,m_\Sigma^2 m_{\Sigma\pi}^2]^{1/2}\times$$
$$\times\frac{1}{8\,m_{\pi\pi}}\,(m_{\pi\pi}^2 - 4\,\mu^2)^{1/2}, \tag{14}$$

where we have considered $Kp(p_1 + q_1 = R)$ system decaying into $\Sigma\pi(p_2 + q_2 = R_1)$ and $2\pi(k_1 + k_2 = R_2)$ and integrated over four of the twelve variables trivially. The remaining variables are chosen to be $m_{\Sigma\pi}^2 = -R_1^2$, $m_{\pi\pi}^2 = -R_2^2$, θ_p (the angle between R_2 and p_1), θ_K (the angle between p_2 and R_1), θ_π (the angle between R_2 and k_2), ϕ_1 (the azimuthal angle between R and R_2 in the R_1 rest frame), ϕ_2 (the azimuthal angle between R and R_1 in the R_2 rest frame), ϕ_3 (the azimuthal angle between R_2 and R_1 in the R rest frame). To simplify trace calculations in finding $<|M_{2\pi}^{33}|^2>$ we take the limit $k_1 = k_2 = (\sigma, i\,\mu)$. The variables $<|M_{2\pi}^{33}|^2>$ have to be expressed in terms of $m_{\Sigma\pi}^2$, $m_{\pi\pi}^2$ and various angles. The relevant equations are given in AUPH Report [12].

3. Single soft pion amplitude and differential cross-section

With only one soft pion being emitted there is no time ordered product of pion field operators in the expression given in (2). In the neutral soft-pion mode, one now has

$$i\,k_\mu \,<f|A_\mu^3|\,i>=\frac{M_N G_A \mu^2}{g_r(\mu^2+k^2)}\,<f|(\mu^2-\Box^2)^2\phi_\pi^3|\,i>\,. \tag{15}$$

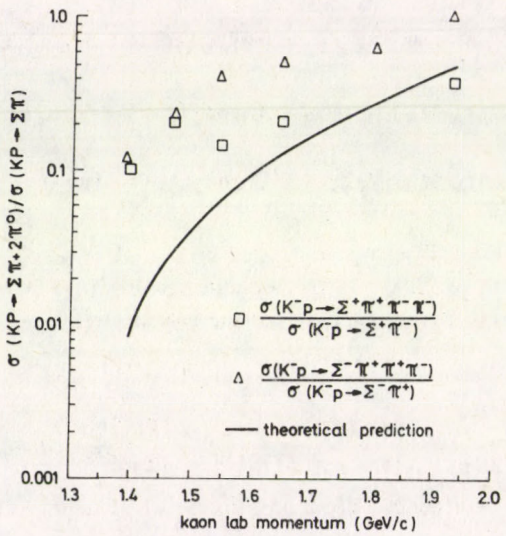

Fig. 3. Comparison of theoretical predictions of $\sigma(Kp \to \Sigma\pi + 2\pi^0)/\sigma(Kp + \Sigma\pi)$ with experiment at various laboratory kaon momenta

Again setting $k = \xi K$, $\xi \to 0$ corresponds to soft pion limit. The left-hand side has pole terms that go as k^{-1} when the axial-vector current A_μ^3 is attached to non-terminating external baryon line. Parity forbids insertion of A_μ^3 into pseudoscalar meson lines. Only two diagrams shown in Fig. 2 contribute. The central interaction in the diagrams is given in (12). We retain only the zeroth order terms in pion momenta [13] and as in the previous section we omit the terms proportional to A. We then have

$$<|M^{\pi^0}|^2> = \frac{g_r^2 B^2}{2M_N^3 M_H}\left[\frac{1}{(p_1\cdot k)^2}(-M_N^3\, M_H\, Q.Q\; k.k - 4M_N^2\, p_1.k\; Q.p_2\; Q.k + \right.$$
$$\left. + 2M_N^2\; Q.p_1\; k.k\; Q.p_2 + 2M_N^2 Q.Q\; k.p_1\; k.p_2 - M_N^2\; Q.Q\; k.k\; p_1.p_2 +\right.$$

$$+\frac{1}{(p_2\cdot k)^2}(-M_H^3\ M_N\ Q.Q\ k.k - 4M_H^2\ Q.k_1\ Q.p_1\ k.p_2+$$
$$+2M_H^2\ k.p_1\ Q.Q\ k.p_2 + 2M_H^2\ k.k\ Q.p_1\ Q.p_2 - M_H^2\ k.k\ Q.Q\ p_1.p_2)+$$
$$+\frac{1}{p_1.k\ p_2.k}(-4M_H^2\ M_N^2\ Q.k\ Q.k + 2M_N^2 M_H^2\ k.k\ Q.Q-$$
$$-4M_N\ M_H\ Q.k\ Q.k\ p_1.p_2 + 4M_N\ M_H\ Q.p_1\ Q.k\ k.p_2+$$
$$+4M_N\ M_H Q.k\ p_1.k\ Q.p_2 - 4M_N\ M_H\ Q.p_1\ k.k\ Q.p_2-$$
$$-4M_N\ M_H\ Q.Q\ k.p_1\ k.p_2 + 2M_N\ M_H\ Q.Q\ k.k\ p_1.p_2)]. \tag{16}$$

The differential cross-section for the reaction $Kp \to \Sigma\pi\pi^0$ is given by the expression

$$(d\sigma)^{\pi^0} = \frac{M_N M_H \pi}{[(p_1\cdot q_1)^2 - m_K^2 M_N^2]^{1/2}} \frac{<|M^{\pi^0}|^2>}{8(2\pi)^5}\, dm_{\Sigma\pi}^2 \times$$
$$\times\, d(\cos\theta_{p_2})\, d(\cos\theta_\pi)\, d\phi \times$$
$$\times \frac{1}{2\, m_{\Sigma\pi}^2}[(m_{\Sigma\pi}^2 + m_\pi^2 - m_\Sigma^2)^2 - 4\, m_\pi^2 m_{\Sigma\pi}^2]^{1/2} \times$$
$$\times \frac{1}{2M_{Kp}^2}[(M_{Kp}^2 + m_{\Sigma\pi}^2 - m_\pi^2)^2 - 4\, M_{Kp}^2 m_{\Sigma\pi}^2]^{1/2}, \tag{17}$$

where $m_{\Sigma\pi}^2 = -R_1^2$ is the invariant mass of the final system. θ_π is the angle between the pion and the proton in the $R(= p_1 + q_1)$ rest frame. θ_{p_2} is the angle between the final particle Σ and the pion in the R_1 rest frame. ϕ is the relative azimuthal angle between the $p_1 q_1$ plane and the R_1 decay plane.

4. Differential scattering cross-section for $K^- p \to \Sigma\pi$

The differential cross-sections of (14) and (17) have to be normalized to the corresponding process $K^- p \to \Sigma\pi$, where soft pions are absent. The relevant expression is

$$d\sigma = \frac{M_N\ M_H}{[(p_1 q_1)^2 - m_K^2 M_N^2]^{1/2}} \frac{<|M|^2>}{16\pi M_{Kp}^2} d(\cos\theta_{p_2}) \times$$
$$\times[(M_{Kp}^2 + m_\Sigma^2 - m_\pi^2)^2 - 4M_{Kp}^2 m_\Sigma^2]^{1/2}, \tag{18}$$

where

$$<|M|^2> = \frac{-B^2}{2M_N M_H}[M_N M_H\ Q^2 - 2\ Q.p_1\ Q.p_2 + Q^2\ p_1.p_2].$$

5. Discussion and comparison of results

We note that the central interaction m given in (12) does not change when the incoming kaon and outgoing pion are interchanged. The matrix elements derived in

Table I

Calculated ratios of cross-sections for various centre of mass energies

Lab meson momentum [GeV/c]	Centre of mass energies [GeV]	$\frac{\sigma(Kp\to\Sigma\pi+2\pi^0)}{\sigma(Kp\to\Sigma\pi)}$	$\frac{\sigma(Kp\to\Sigma\pi\pi^0)}{\sigma(Kp\to\Sigma\pi)}$	$\frac{\sigma(\pi p\to\Sigma K+2\pi^0)}{\sigma(\pi p\to\Sigma K)}$	$\frac{\sigma(\pi p\to\Sigma K\pi^0)}{\sigma(\pi p\to\Sigma K)}$
0.74	1.674		0.0024		
0.917	1.757		0.0055		
1.201	1.889		0.0135		
1.345	1.954		0.0191		
1.396	1.977	0.0081			
1.47	2.01	0.0319			
1.5	2.023		0.0272		
1.5	1.931				0.0054
1.546	2.043	0.0673			
1.653	2.09	0.1381			
1.69	2.02				0.0161
1.694	2.107		0.0416		
1.8	2.152	0.286	0.0548		
1.85	2.093				0.0299
1.934	2.208	0.4783			
1.95	2.137				0.0394
2.031	2.248		0.0839		
2.15	2.223				0.0622
2.24	2.331		0.1061		
2.25	2.265				0.0749
2.35	2.306				0.0884
2.494	2.364			0.0723	
2.7	2.444			0.1887	
2.86	2.505			0.3375	
3.01	2.56			0.5372	
3.21	2.632			0.9157	
3.71	2.805			2.6411	
3.89	2.864			3.607	

Sections 2 and 3 are also valid since there can be no insertion of axial-vector currents in the pseudoscalar meson lines. Therefore as in the case of $\bar{p}p$ annihilation [5] we use the expressions given in (14) and (17) with suitable changes in mass terms to compute the cross-sections for $\pi p \to \Sigma K$ with one or two additional soft pions. Again the cross-sections have to be normalized to the one without soft pions.

The expressions given in (14) and (16) are valid only for low energies near the threshold since the pions produced have to be soft. However, for comparison with experimental data, we generalize the expressions to hold at higher centre of mass energies as well. The theoretical predictions obtained after numerical integration for various lab incoming meson momenta are given in Table I. The results are compared with the experimental data of [14–21] in Figs 3, 4, 5 and 6. Angular distributions for the reactions are given in Figs 7 and 8.

For $\pi p \to \Sigma K + \pi\pi$ the theoretical predictions are remarkably close to the experimental results. For the $Kp \to \Sigma\pi + \pi\pi$ the theoretical values agree to a reasonable extent with experiment. For the single soft pion emission processes

the theoretical results are lower by an order of magnitude even at small centre of mass energies. This sort of difference has been reported in the earlier soft pion

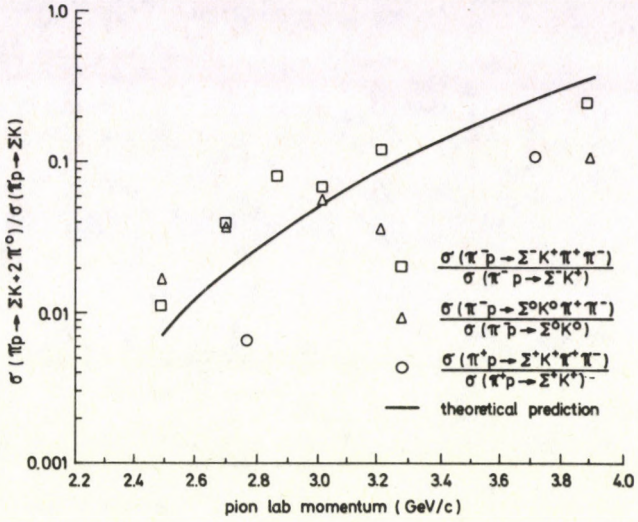

Fig. 4. Comparison of theoretical predictions of $\sigma(\pi p \to \Sigma K + 2\pi^0)/\sigma(\pi p + \Sigma K)$ with experiment at various laboratory pion momenta

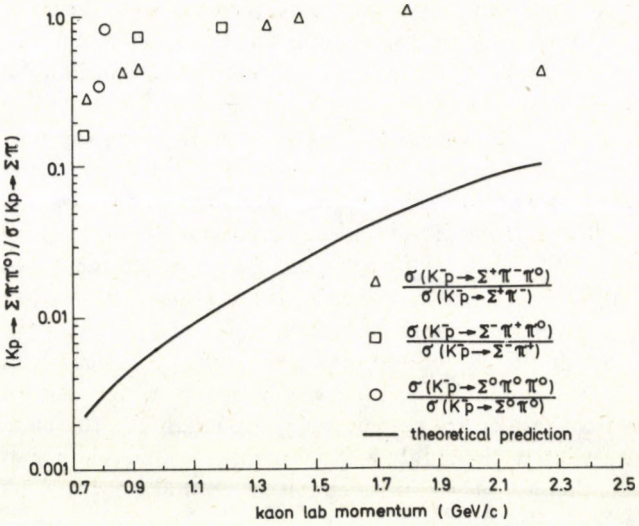

Fig. 5. Comparison of theoretical predictions of $\sigma(Kp \to \Sigma\pi\pi^0)/\sigma(Kp + \Sigma\pi)$ with experiment at various laboratory kaon momenta

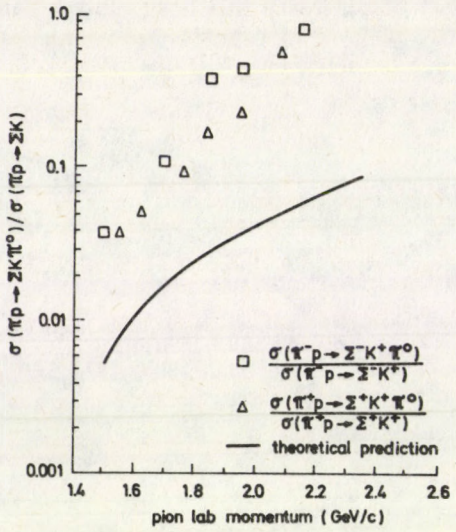

Fig. 6. Comparison of theoretical predictions of $\sigma(\pi p \to \Sigma K \pi^0)/\sigma(\pi p + \Sigma K)$ with experiment at various laboratory pion momenta

calculations [2, 3, 22]. It is worth noting that it is the combination of current algebra and PCAC that gives impressive results. This is perhaps due to the replacement of the commutator between two axial-vector currents with the isospin operator. In the calculations presented here, the A term has been neglected mainly to facilitate computation [11]. Although the size of A relative to B is not known, with the ratios of cross-sections being computed, the effect of neglecting A terms relative to B is expected to be small. This seems to be true especially for the two soft pion cases studied here and elsewhere [11]. We have applied the formalism of current algebra PCAC in a straightforward way and did not take into account the possible resonance effects which partly account for the discrepancies in theoretical and experimental results. During the process of integration the three momenta of soft pions are not kept at a minimum, thereby necessitating a considerable extrapolation based on the PCAC assumption. Also no attempt is made at selecting experimental data relevant to soft pions. The expressions given in the most differential form, therefore, are better suited for comparison with experimental results. In spite of this, the theoretical results are encouraging, especially for the two soft pion cases. It may be noted that in the single soft pion case, no current algebra assumptions are involved and therefore the results enable us to make a direct test of PCAC.

Acknowledgements

We are grateful to the Computer Centre personnel at Andhra University for their help. This work is supported by the Council of Scientific and Industrial Research, New Delhi.

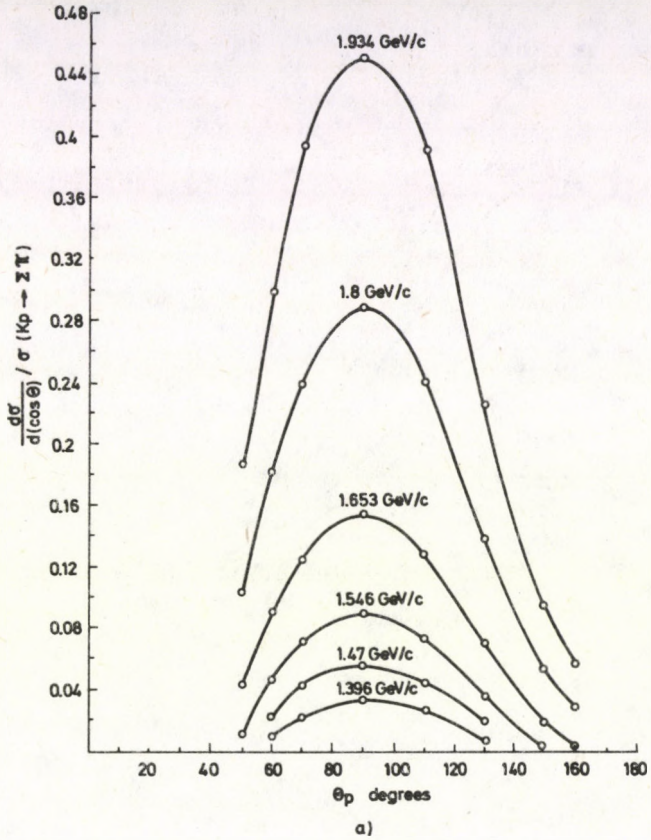

Fig. 7. (a) Variation of differential cross-section for the reaction $Kp \to \Sigma\pi + 2\pi^0$ with θ_p the angle between the incoming proton and the (soft) dipion system

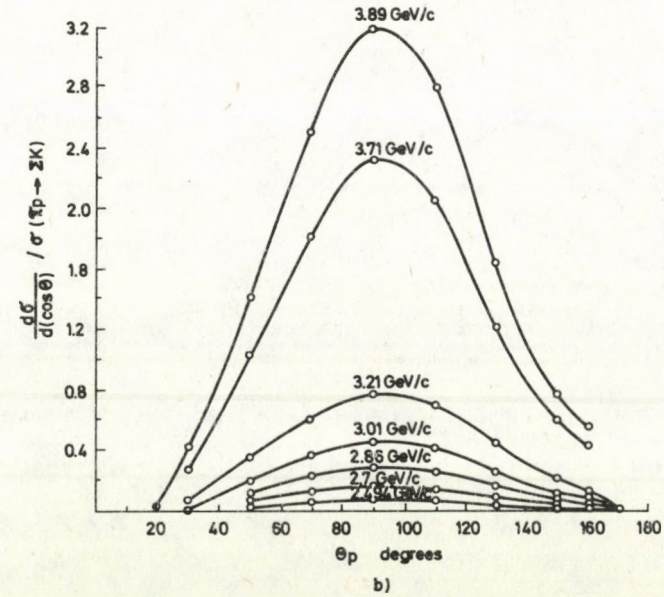

Fig. 7. (b) Variation of differential cross-section for the reaction $\pi p \to \Sigma K + 2\pi^0$ with θ_p the angle between the incoming proton and the (soft) dipion system

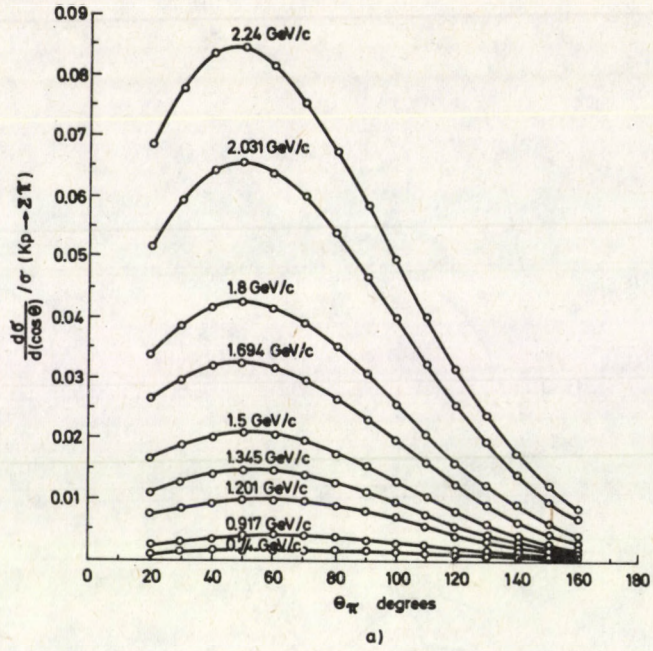

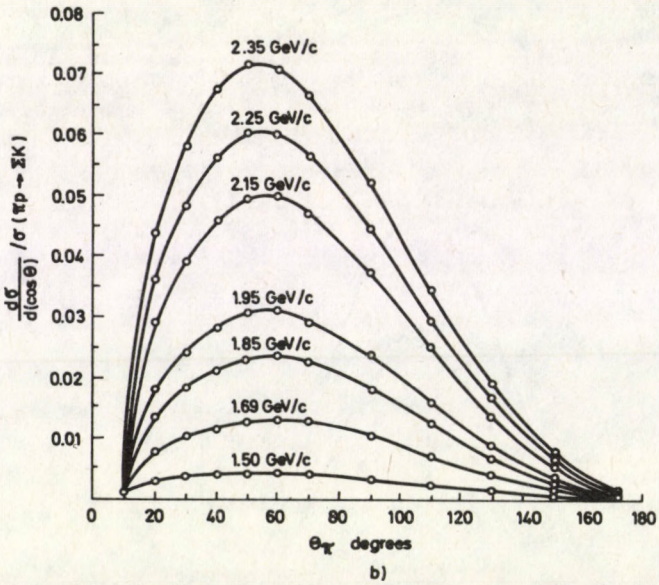

Fig. 8. (a) Variation of differential cross-section for the reaction $Kp \to \Sigma\pi\pi^0$ with θ_π the angle between the incoming proton and the (soft) pion
(b) Variation of differential cross-section for the reaction $\pi p \to \Sigma K\pi^0$ with θ_π the angle between the incoming proton and the (soft) pion

References

1. R. A. Uritam, Phys. Rev., *D6*, 3233, 1972.
2. P. Nuthakki and R. A. Uritam, Phys. Rev., *D8*, 3196, 1973.
3. G. K. Greenhut and G. W. Intemann, Phys. Rev., *D14*, 764, 1976.
4. R. Purushottamudu and P. Nuthakki, Z. Phys., *C14*, 257, 1982.
5. P. Nuthakki and R. Purushottamudu, Phys. Rev. *D27*, 650, 1983.
6. S. Weinberg, Phys. Rev. Lett., *16*, 879, 1966.
7. S. Weinberg, Phys. Rev. Lett., *18*, 188, 1967.
8. R. F. Dashen and M. Weinstein, Phys. Rev., *183*, 261, 1969.
9. P. E. Low, Phys. Rev., *110*, 974, 1958.
10. S. L. Adler, Phys. Rev., *B139*, 1638, 1965.
11. K. K. Murthy, M. L. P. Rao and P. Nuthakki, Pranama-J. Phys., *26*, 399, 1986.
12. K. K. Murthy, and P. Nuthakki, Two-pion emission in kaon-baryon interactions, Andhra University Report, No. PHEP-01/86, 1986.
13. S. L. Adler and R. F. Dashen, Current Algebra and Application to Particle Physics, p. 120, Benjamin, New York, Amsterdam, 1968.
14. Compilation of cross-sections II: K^+ and K^- induced reactions, CERN-HERA 83-02, 1983.
15. Compilation of cross-sections I: π^+ and π^- induced reactions, CERN-HERA 83-01, 1983.
16. A. De Bellefon et al., Nuovo Cimento, *A41*, 451,1977.
17. R. Armenteros et al., Nucl. Phys., *B21*, 15, 1970.
18. J. Griselin et al., Nucl. Phys., *B93*, 189, 1975.
19. W. R. Butler, D. G. Coyne, G. Goldhaber, J. MacNaughton and G. H. Trilling, Phys. Rev., *D7*, 3177, 1973.
20. Orin I. Dahl, Lyndon M. Hardy, Richard I. Hess, Janos Kirz and Donald H. Miller, Phys. Rev., *163*, 1377, 1967.
21. P. Hanson, G. E. Kalmus and J. Louie, Phys. Rev., *D4*, 1296, 1971.
22. E. Shrauner, Phys. Rev., *131*, 1847, 1963.

Acta Physica Hungarica 67 (3–4), pp. 259–262 (1990)

PLANE SYMMETRIC HIGHER DIMENSIONAL SPACE–TIMES

VIDYA GAIKWAD and T. M. KARADE

Department of Mathematics, Nagpur University
Nagpur, India

(Received 24 July 1987)

In this paper the general form of plane symmetric line element and the plane symmetric geometric quantities in five dimensions have been discussed.

1. Introduction

Noting the importance, plane symmetric (PS) space-times (ST) have been studied by many authors (Taub [1], Peres [2], Nordtvedt and Pagels [3], Takeno [4], etc). According to Takeno [4] a four-dimensional Riemannian space of signature -2 is plane symmetric if it admits the three parameter group of transformations composed of

$$R_1 = z\partial_y - y\partial_z, \qquad R_2 = \partial_y, \qquad R_3 = \partial_z, \tag{1}$$

as a subgroup of motions. Here the coordinates are x, y, z, t and t corresponds to time.

In this paper we have obtained the most general line element for five dimensional plane symmetric space-times. Consequently the nature of the infinitesimal generators which transform any PSST to another one and PS geometric quantities are studied.

2. The Killing equation

We define a space-time

$$ds^2 = g_{ij}\, dx^i\, dx^j, \quad i,\, j = 1, \ldots, 5 \tag{2}$$

to be PS if it admits the three parameter group of transformations given in (1) with infinitesimal generators K^h as

$$\overset{1}{K}{}^{(i)} = (0, z, -y, 0, 0), \quad \overset{2}{K}{}^{(i)} = (0, 1, 0, 0, 0), \quad \overset{3}{K}{}^{(i)} = (0, 0, 1, 0, 0). \tag{3}$$

The space-time (2) admits isometry if and only if an infinitesimal generator K^h satisfies the Killing equation

$$K_{i;j} + K_{j;i} = 0, \tag{4}$$

where ; stands for the covariant differentiation. Considering (4) with (3) the straightforward but lengthy calculations yield

$$g_{13} = g_{12} = g_{23} = g_{34} = g_{35} = g_{24} = g_{25} = 0$$

Therefore the nonvanishing components of g_{ij} are g_{11}, $g_{22} = g_{33}$, g_{14}, g_{15}, g_{44}, g_{45}, g_{55} and they are functions of x, t and u.

Letting $g_{11} = -a$, $g_{22} = -b$, $g_{44} = c$, $g_{14} = h$, $g_{15} = e$, $g_{45} = f$, $g_{55} = g$, the most general line element (2) of PSST assumes the form

$$ds^2 = -a\,dx^2 - b\,(dy^2 + dz^2) + c\,dt^2 + g\,du^2 +$$

$$+2h\,dx\,dt + 2e\,dx\,du + 2f\,dt\,du, \tag{5}$$

where a, b, c, e, f, g and h are functions of x, t and u.

Considering the transformation of coordinates

$$(x, t, u) \to (X, T, U),$$

the line element (5) is transformed into another PSST

$$ds^2 = -A\,dX^2 - B\,(dY^2 + dZ^2) + C\,dT^2 + G\,dU^2 +$$

$$+2H\,dX\,dT + 2E\,dX\,dU + 2F\,dT\,dU,$$

where

$$\begin{aligned}
-A &= -a(x_X)^2 + c(t_X)^2 + 2h(x_X)(t_X) + g(u_X)^2 + 2e(x_X)(u_X) + 2f(t_X)(u_X),\\
B &= b,\\
C &= -a(x_T)^2 + c(t_T)^2 + 2h(x_T)(t_T) + g(u_T)^2 + 2e(x_T)(u_T) + 2f(u_T)(t_T),\\
H &= -a(x_X)(x_T) + c(t_X)(t_T) + h((x_T)(t_X) + (x_X)(t_T)) + g(u_X)(u_T) +\\
&\quad + f((t_X)(u_T) + (t_T)(u_X)) + e((x_X)(u_T) + (x_T)(u_X)),\\
E &= -a(x_X)(x_U) + c(t_X)(t_U) + h((x_U)(t_X) + (t_U)(x_X)) + g(u_X)(u_U) +\\
&\quad + e((x_X)(u_U) + (x_U)(u_X)) + f((t_X)(u_U) + (t_U)(u_X)),\\
F &= -a(x_U)(x_T) + c(t_T)(t_U) + h((x_U)(t_T) + (x_T)(t_U)) + g(u_U)(u_T) +\\
&\quad + e((x_T)(u_U) + (x_U)(u_T)) + f((t_T)(u_U) + (u_T)(t_U)),\\
G &= -a(x_U)^2 + c(t_U)^2 + 2h(x_U)(t_U) + g(u_U)^2 + 2e(x_U)(u_U) + 2f(u_U)(t_U),
\end{aligned}$$

where $x_X = \partial x/\partial X$, etc.

Now the condition that X' transforms any PS metric to another PS one is the condition that the group R admits the infinitesimal transformation

$$X' : X^i = x^i + K^i\epsilon. \tag{6}$$

This can be written as

$$(R_a, X') = q_a^b R_b, \qquad a, b = 1, 2, 3. \tag{7}$$

where q_a^b are constants.

Employing (1), (6) and (7), we get

$$\begin{aligned}
&\overset{1}{K} = \overset{1}{K}(x, t, u),\\
&\overset{2}{K} = zy\, q_2^1 - y^2\, q_3^1 - z\, q_2^3 + y\, q_3^3 - y\, q_1^1 + q_1^3,\\
&\overset{3}{K} = z^2\, q_2^1 - z\, q_1^1 - q_1^2 + z\, q_2^2 - yz\, q_3^1 - yq_3^2,\\
&\overset{4}{K} = \overset{4}{K}(x, t, u),\\
&\overset{5}{K} = \overset{5}{K}(x, t, u).
\end{aligned} \tag{8}$$

3. Plane symmetric quantities

We define that a geometric quantity G is PS in the space-time (5) if its Lie derivative is zero i.e., $L_K G = 0$, where K is given by (3).

The various PS quantities in five dimensional PSST are as follows:

(a) PS scalar $P = P(x, t, u)$.

(b) PS scalar density p of weight w : $p = p(x, t, u)$

(c) PS vector v^i: $v^i = (f_1, 0, 0, f_2, f_3)$,
where f's are functions of x, t, u.
The form of PS covariant vector w_i is same as that of v^i.

(d) PS tensors of the second order
Let K_{ij} be a symmetric tensor of second order. If it is PS, then the number of independent components of K_{ij} reduces to seven only and are given by

$$\begin{aligned}
&K_{11} = g_1, \quad K_{22} = K_{33} = g_2, \quad K_{44} = g_3, \quad K_{14} = g_4,\\
&K_{15} = g_5, \quad K_{45} = g_6, \quad K_{55} = g_7,
\end{aligned} \tag{9}$$

where g's are arbitrary functions of x, t and u.

The general form of an antisymmetric PS tensor f_{ij} is given by

$$f_{14} = h_1, \quad f_{15} = h_2, \quad f_{45} = h_3, \quad f_{23} = h_4, \quad \text{other} \quad f_{ij} = 0, \tag{10}$$

where h's are functions of x, t, u.

(e) For the PS tensor H_{ijk} satisfying $H_{ijk} = -H_{jik}$, we have

$$H_{12k} = (0, a_1, a_2, 0, 0), \qquad H_{13k} = (0, -a_2, a_1, 0, 0),$$
$$H_{14k} = (a_3, 0, 0, a_4, a_5), \qquad H_{15k} = (a_6, 0, 0, a_7, a_8),$$
$$H_{23k} = (a_9, 0, 0, a_{10}, a_{11}), \qquad H_{24k} = (0, a_{12}, a_{13}, 0, 0),$$
$$H_{25k} = (0, a_{14}, a_{15}, 0, 0), \qquad H_{34k} = (0, -a_{13}, a_{12}, 0, 0),$$
$$H_{35k} = (0, a_{15}, a_{14}, a_{16}, 0), \qquad H_{45k} = (a_{17}, 0, 0, a_{18}, a_{19}),$$

where a's are arbitrary functions of x, t and u.

(f) The PS tensor F_{ijkl} of the fourth order has twenty two independent components:

$$(1212) = (1313), \quad (1414), \quad (1224) = (1334), \quad (1225) = (1335),$$
$$(1415), \quad (1445), \quad (1515), \quad (1545), \quad (2323), \quad (2424) = (3434) \qquad (11)$$
$$(2525) = (3535), \quad (4545), \quad (2425) = (3435)$$

$$(1235) = -(1325), \quad (1423), \quad (2434) = -(3424),$$
$$(2435) = -(3425), \quad (1541), \quad (1312) = -(1213), \quad (2345), \qquad (12)$$
$$(2535) = -(3525), \quad (1234) = -(1324),$$

where $(ijkl) = F_{ijkl}$ and these components are functions of x, t and u.

If we replace the above 4th order tensor by Riemannian curvature tensor, then all the components in (12) vanish and its independent components are thirteen only as in (11).

It is interesting that all the results of Takeno [4] can be obtained from our investigation by assigning appropriate values to the functions concerned.

References

1. A. Taub, Phys. Rev., *103*, 454, 1956.
2. A. Peres, Phys. Rev., *118*, 1105, 1960.
3. T. Nordtvedt and H. Pagels, Ann. Phys., *17*, 426, 1962.
4. H. Takeno, Sci. Rep Res. Inst. Theor. Phys., Hiroshima University, 1961, Tensor, N. s., *32*, 77, 1978.

Acta Physica Hungarica 67 (3–4), pp. 263–273 (1990)

SIMULATION OF SPATIAL DISTRIBUTIONS OF IMPLANTED IONS IN AMORPHOUS ELEMENTS

M. M. ABDEL-HADY

Physics Department, Faculty of Science
Ain Shams University, Cairo, Egypt

(Received in revised form 14 April 1988)

A Monte Carlo simulation code has been designed to study the spatial distributions of heavy ions in an amorphous element. The LSS formalism has been applied in terms of Thomas–Fermi potential. The code has been used to study the penetration of $_{11}Na^{23}$ in $_{79}Au^{191}$, $_{47}Ag^{108}$ and $_{32}Ge^{67}$, while $_{36}Kr^{84}$ has been studied in $_{79}Au^{197}$, $_{47}Ag^{108}$. The selected range of incident energy is (5–600) keV. The results demonstrate good agreement with experimental data.

Introduction

The importance of investigations on the spatial distribution of heavy ions during penetration through an amorphous stopper refers to its widely used applications in nuclear and atomic physics. It is one of the primary sources of information on atomic collision process. The range studies were important in the stopping theory of Bohr [1]. In recent years, it is due to the use of ion implantation by the semiconductor industry, as well as the choice of a particular energy source to study the radiation damage.

The LSS [2, 3, 4, 5] theory introduces a comprehensive description for the slowing down process of heavy ions in solids where the diffused ions lose their energy due to both elastic and inelastic interactions. The latter is due to collisions with atomic electrons of the stopper which, continuously decelerating the ions, does not affect the direction of motion, while the first is due to the cascade interactions of ions with the Coulomb potential of stopper nuclei. The influence of such interactions are discrete, accompanied by the reorientation of ion motion.

During the last few years, several articles related to this field have been published. Biersack [6] has derived analytically the mean of projected range of implanted ions as a function of its energy. Posselt [7] has applied the TRIM computer simulation scheme to investigate the influence of the energy transport to stopper atoms on the energy loss and damage profiles and Vizkelethy et al [8, 9] have developed the SEISM simulation code to compute the three-dimensional distribution of implanted ions by adopting Molière screening potential with Firsov [3] screening length.

The aim of the present work is to design a Monte Carlo Simulation Code to study the spatial distributions of heavy ions in amorphous elemental solids. So, the differential penetration function, lateral range distributions, collision probability function and mean free path could be simulated.

Theoretical basis

The theoretical formalism adopted to describe the slowing down process is the Lindhard, Scharff and Schiott [2, 3, 4, 5]. They have used a screened Thomas–Fermi type of potential to derive general expressions for both electronic and nuclear stopping powers in terms of universal dimensionless variables ε, ρ. They have derived the following expressions:

$$\varepsilon = EaM_2/[Z_1 Z_2 e^2 (M_1 + M_2)], \tag{1}$$

$$\rho = R \cdot 4\pi a^2 N M_1 M_2/(M_1 + M_2)^2, \tag{2}$$

where a is the screening length given by:

$$a = 0.8853(\hbar^2/me^2)(Z_1^{2/3} + Z_2^{2/3})^{-\frac{1}{2}}. \tag{3}$$

Subscripts 1 and 2 refer to incident ion and target atoms, respectively. N, e, m are the number density of atoms, electronic charge and electron mass, and E, R are the real energy and range.

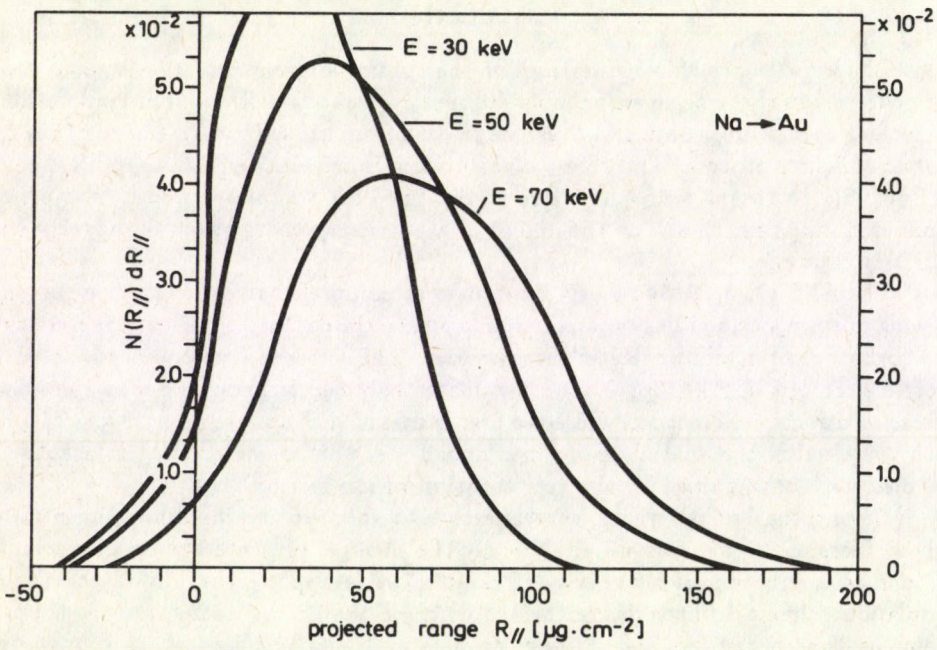

Fig. 1. Penetration probability function of Na→Au for incident energy 30, 50, 70 keV

The electronic stopping power is described by

$$\left(\frac{d\varepsilon}{d\rho}\right)_e = f_e K \varepsilon^{0.5}, \tag{4}$$

where f_e is an adjustable correction factor introduced by Lindhard et al [10] = 1.3 as proposed by Andersen et al [11]. K is a constant, which depends on both projectile and target parameters [5]. The differential scattering cross-section for elastic energy loss is given by:

$$d\sigma = \pi a^2 \left[F(x)x^2\right] dx, \tag{5}$$

where

$$x = \varepsilon \sin\left(\frac{\theta}{2}\right). \tag{6}$$

θ is the polar scattering angle in the CMS, $F(x)$ is a universal scattering fuction calculated in terms of the screened Thomas–Fermi potential and formulated by Winterbon et al [12] using the magic formula of Lindhard et al [4].

The formula of the scattering function given by them is

$$F(x) = Qx^{1/3}\left(1 + (2Qx^{4/3})^{2/3}\right)^{-3/2}, \tag{7}$$

where $Q = 1.309$.

The nuclear stopping power is

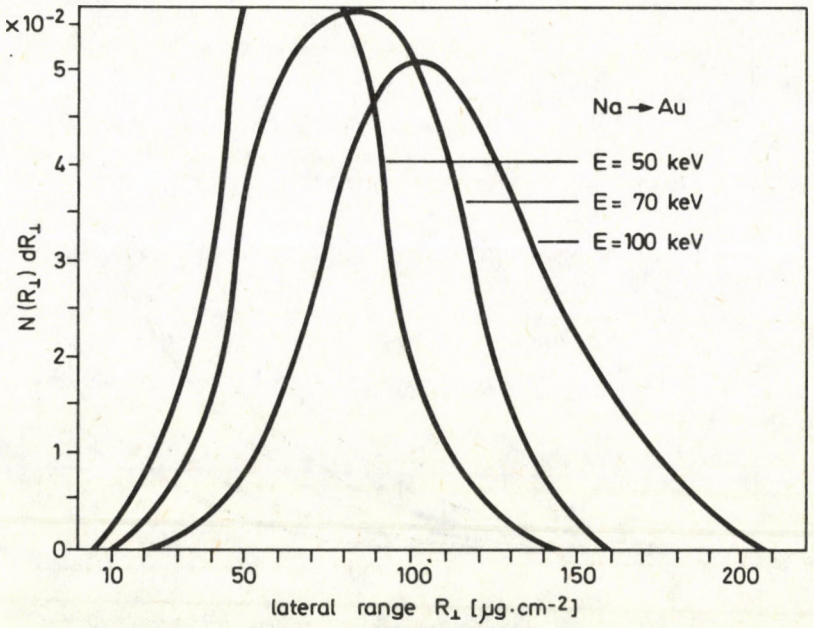

Fig. 2. Lateral range distribution of Na→Au

$$\left(\frac{d\varepsilon}{d\rho}\right)_n = (f_n/\varepsilon)\int_0^{\varepsilon} F(x)dx, \tag{8}$$

f_n is another adjustable correction factor =1.

To avoid singularity in Eq. (8), the lower limit of integration has been approximated to 0.001 with no significant error.

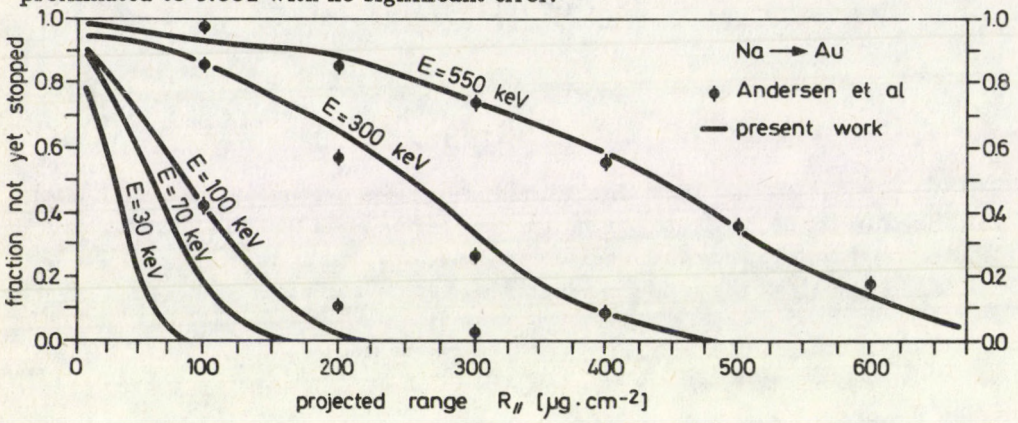

Fig. 3. Fraction not yet stopped of Na→Au for different incident energy

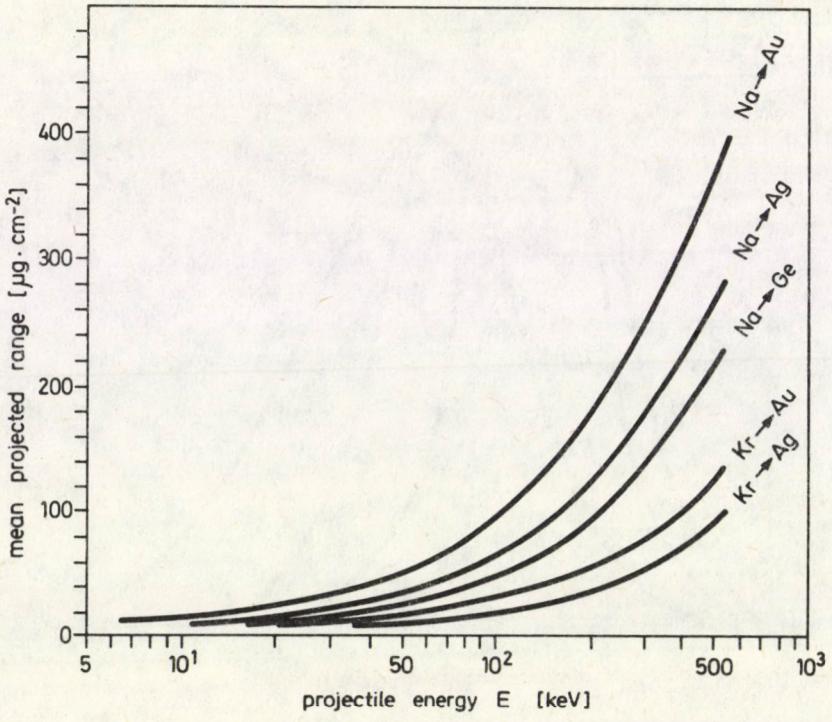

Fig. 4. Mean projected range as a function of projectile energy

Description of the code

An incident projectile with initial energy E penetrates through an amorphous elemental target of infinite thickness undergoing elastic and inelastic interactions described by LSS formalism. Along the projectile trajectory several variables are considered as stochastics:

1. Initial depth of the first interaction is taken as uniform random variable given by $x = P \cdot T/4$, where T is the thickness of the stopper, P is a random value between (0–1).
2. The distance travelled by the ion between two successive collisions is sampled randomly from exponential function

$$D(d) = \frac{1}{\lambda} \exp(-d/\lambda), \tag{9}$$

where $\lambda = 1/N\sigma_t$, $d = -\lambda \log P$, σ_t is the total cross-section of collisions, and N is the number of atoms per unit volume of stopper element.

3. The polar scattering angle after collision is selected randomly from the angular distribution $U(\varepsilon, \theta)$ of the projectile after each collision since it is given by:

$$U(\varepsilon, \theta)d\theta = \frac{d\sigma}{\sigma_t}, \tag{10}$$

where $d\sigma$ is the differential cross-section given by Eq. (5) and σ_t is the total cross-section given by $\int d\sigma$. The scattering angle θ' in CMS could be sampled for a given projectile energy ε as:

$$P = \int_0^{x'} U(\varepsilon, \theta)d\theta. \tag{11}$$

P is a uniform random value (0–1) and $\theta' = 2\sin^{-1}(x'/\varepsilon)$. The integration in Eq. (11) has been solved numerically by the successive approximation method.

4. The azimuthal angle of ions after each scattering is considered to be random, and it is selected from a uniform distribution given by

$$\Phi = 2\pi(P - 0.5). \tag{12}$$

Each scattering reorientation of ion with respect to the beam direction has been followed using Euler angles and the rotation matrix as given by Goldstein mechanics. The electronic and nuclear stopping powers are considered as independent of each other and the cascades of history terminate at an ion energy 10^{-4} E.

Computation procedures

A specific energy beam of heavy ions is incident on a block of elemental amorphous target suffering continuous inelastic interactions with atomic electrons of the stopper, moreover, elastic discrete interactions of ions with atomic nuclei influencing reorientation of ions, the rates of energy loss due to both types of interactions are given by Eqs (4, 8), respectively. The first scattering of ions which occurs in depth is random uniformly $(0, T/4)$, where T is the thickness of the stopper which is relatively infinite $(= 10.000\ \mathrm{ug \cdot cm^{-2}})$.

After each scattering both rates of energy loss are calculated and subtracted from the instantaneous energy of the ion. At the same time, the scattering angles (polar, azimuthal) are calculated randomly, and reorientation follows to keep the angles in the beam frame. The distance travelled by the ion between each two successive scatterings is calculated randomly and its projected and lateral components are accumulated as well as the number of collisions to the end of history when the ion energy becomes relatively zero. When a large number of histories is applied, the projected, the lateral ranges and collision probability distributions as well as their means and mean free path can be calculated.

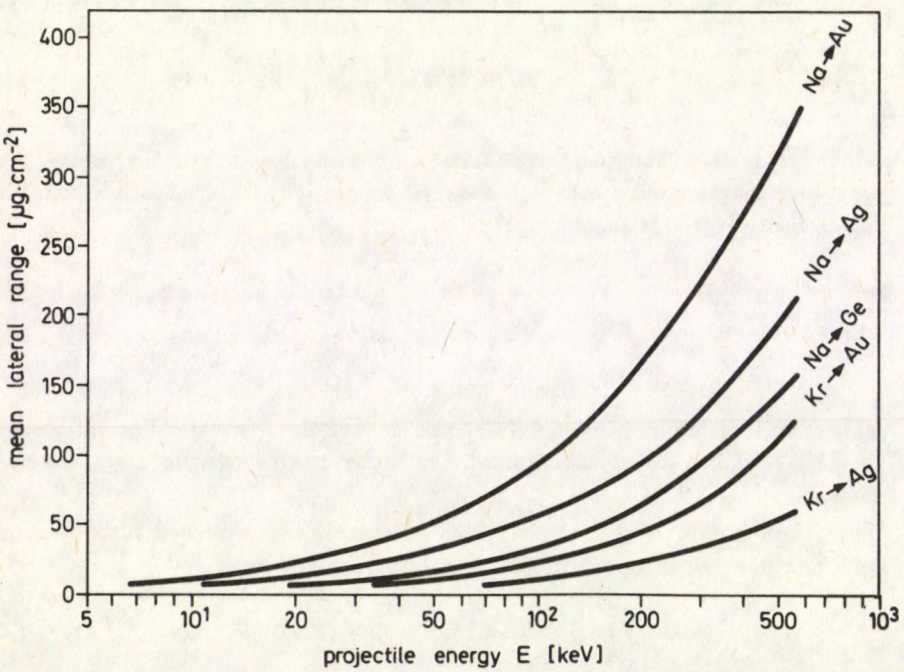

Fig. 5. Mean lateral range as a function of projectile energy

To investigate the features of the penetration profile of projected range distribution, several statistical parameters have been calculated:

1. The range skewness is a measure of the degree of symmetry of range profile about its mean. It would be either positive if the profile skewed to right or negative if it skewed to left. The profile would be quite symmetric with skewness zero. The range skewness is given by:

$$S = \langle(\Delta R_{||})^3\rangle / \langle(\Delta R_{||})^2\rangle^{3/2}. \tag{13}$$

2. The range curtosis is a measure of the degree of peakedness or flatness of the range profile near its center, and it is given by

$$G = \langle(\Delta R_{||})^4\rangle / \langle(\Delta R_{||})^2\rangle^2. \tag{14}$$

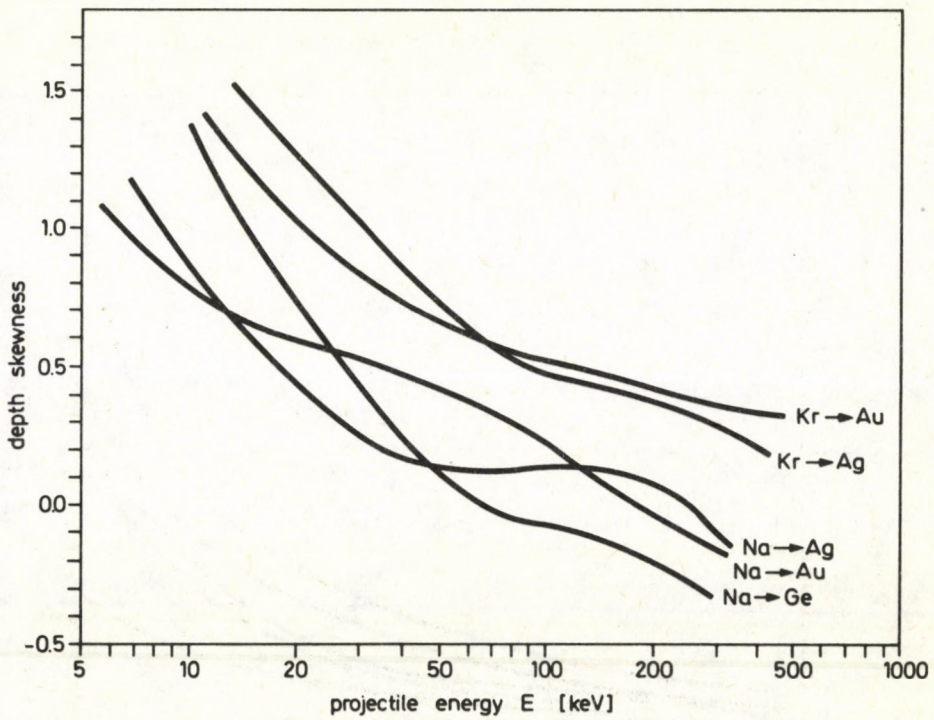

Fig. 6. Depth skewness as a function of projectile energy

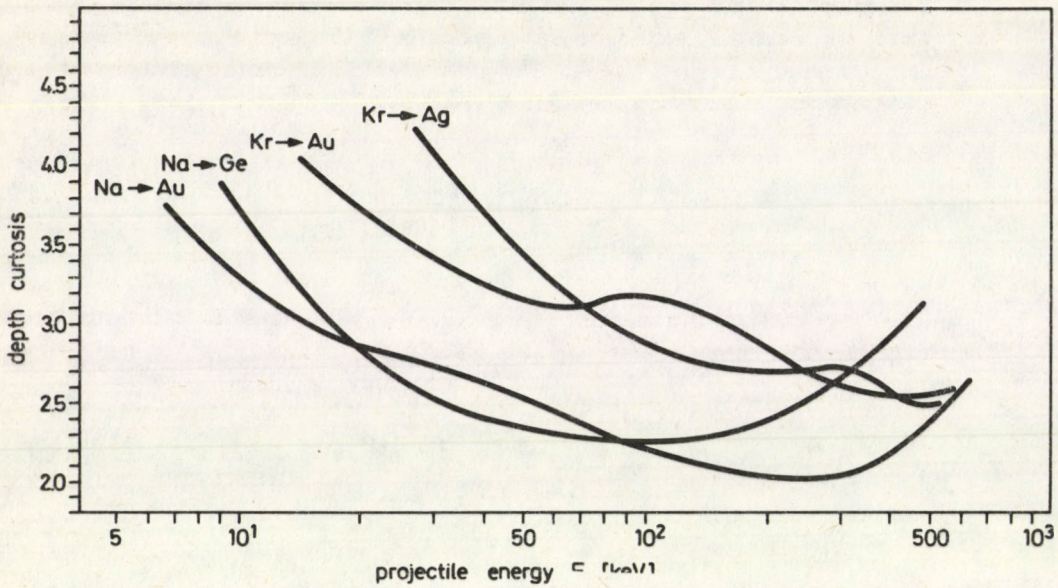

Fig. 7. Depth curtosis as a function of projectile energy

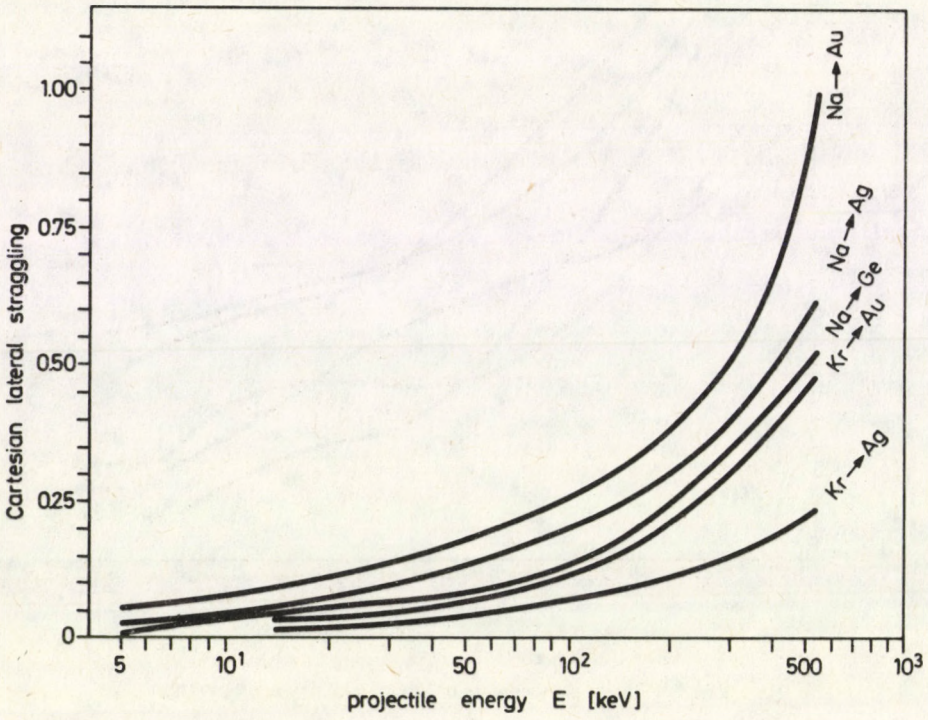

Fig. 8. Cartesian lateral straggling as a function of projectile energy

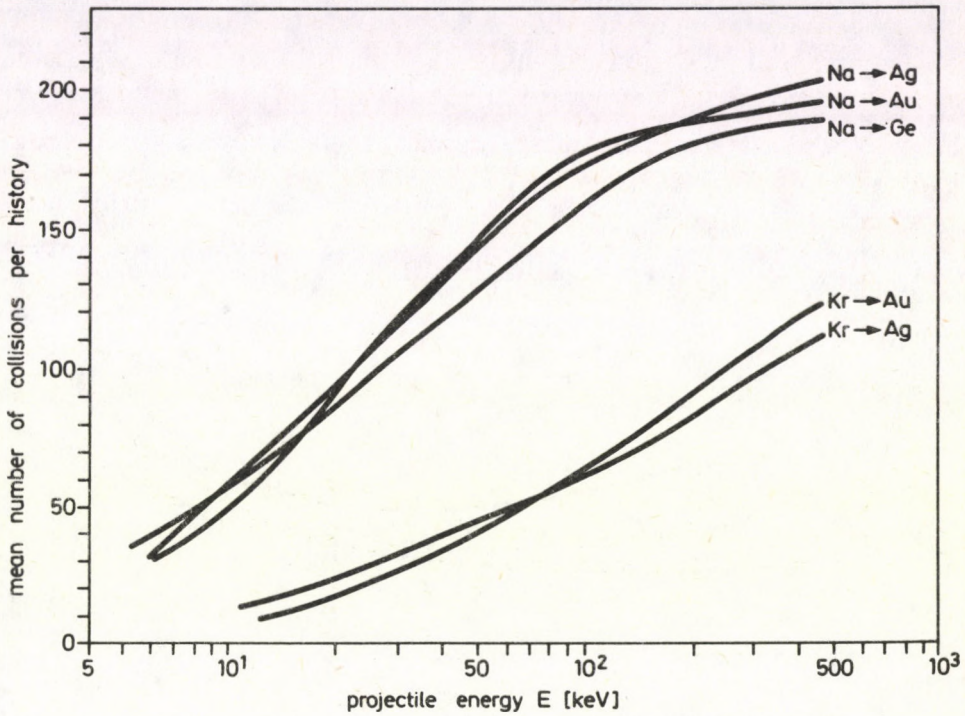

Fig. 9. Mean number of collisions as a function of projectile energy

3. The Cartesian lateral straggling specifies the amount that an implanted beam spreads under a mask during implantation and is expressed as

$$C = \left(\langle(\Delta R_{\perp})^2\rangle/2\right)^{\frac{1}{2}} . \tag{15}$$

Results and conclusions

The designed simulation code has been applied using the Eclipse MV/6000 computer located at Ain Shams University. Several investigations have been carried out to check the statistical validity of the available random generator results. The statistical dependence of program results on the number of histories could be adopted with no significant error, keeping in mind that the time of computation should be minimum, the adopted number of histories is 5.000.

The incident energies of ions have been considered in the present computations in the range (5–600) keV. The computations have been carried out to study the

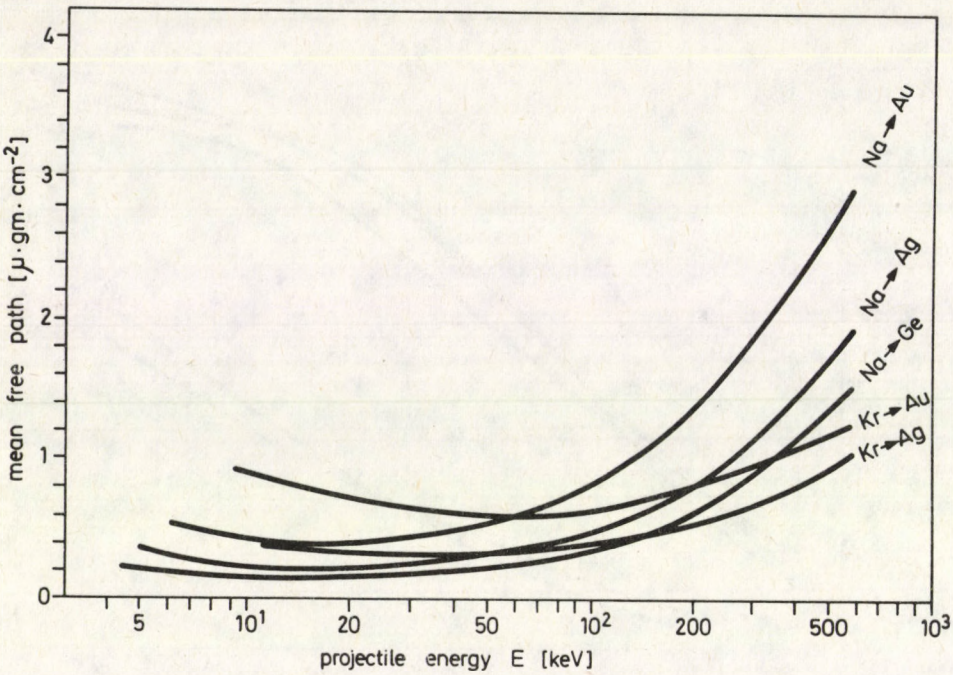

Fig. 10. Mean free path of projectiles range as a function of projectile energy

diffusion of ions of $_{11}Na^{23}$ and $_{36}Kr^{84}$ through each target of $_{79}Au^{197}$, $_{47}Ag^{108}$ and $_{32}Ge^{67}$, then the projected and lateral penetration probabilities have been simulated, and the fraction not yet stopped at depth $R_{||}$ could be calculated by integration:

$$I(R_{||}) = \int_{R_{||}}^{\infty} N(R_{||}) dR_{||} \tag{16}$$

and the mean penetrations, mean number of collisions per history, mean free path, range skewness, curtosis and Cartesian lateral straggling have been computed.

Fig. 1 represents a comparison among three penetration profiles of Na projectile with different values of incident energy (30, 50, 70 keV). The negative parts represent the backscattered fraction of ions, and the peaks are displaced to the left with decreasing energy. The skewness is seen to be positive in the three curves while the curtosis is increasing with decreasing energy. Fig. 2 includes the lateral range profiles for incident energy (50, 70, 100 keV), while Fig. 3 includes a relation between the fraction not yet stopped of Na beam to the projected depth $R_{||}$ of Au for different values of incident energy (E = 30, 70, 100, 300, 550 keV). The

comparison of the present results with those measured by Andersen et al [11] for incident energies of $E = 100, 300, 550$ keV demonstrates good satisfactory agreement. Figs 4 and 5 include relations between both mean projected and mean lateral range distributions for a beam of both Na and Kr penetrating in each of (Au, Ag), in addition to Ge for Na projectile. The Figures indicate approximate linear relations with incident energy. Figs 6, 7 and 8 show the depth skewness, depth curtosis, and Cartesian lateral straggling, respectively. Fig. 8 demonstrates that the spreading of implanted ions is increasing with projectile energy. Fig. 9. represents the relation between the mean number of collisions per history which increases slightly with incident energy. Fig. 10 includes the relation of the mean free path against incident projectile energy, which is slightly increasing for relatively higher energies.

Then, the analysis of the present work demonstrates the potentialities of the Monte Carlo Simulation Method to study the information about the spatial distributions of implanted ions in terms of LSS theory based on Thomas–Fermi potential.

Acknowledgements

The author is grateful to Prof. Dr. A. Goned for useful discussions. Thanks are due to the Referee of the paper for kind comments and valuable advice.

References

1. N. Bohr, Mat. Fys. Medd. Dan. Vid. Selsk, *18*, 8, 1948.
2. J. Lindhard, M. Scharff and H. E. Schiott, K. Dan. Vidensk. Selsk. Mat. Fys. Medd., *33*, No. 14, 1963.
3. O. B. Firsov, Sov. Phys. JETP, *5*, 1192, 1957.
4. J. Lindhard, Vebeke Nielson and M. Scharff, Mat. Fys. Medd., *36*, 10, 1968.
5. M. M. Abdel-Hady, A. Z. Kiss, E. Koltay, B. Nyakó and M. Hautala, Acta Phys. Hung., *58*, 11, 1985.
6. J. P. Biersack, Nuclear Instr. and Meth., *182/183*, 199, 1981.
7. M. Posselt, Phys. Stat. Sol. (a), *94*, 403, 1986.
8. Gy. Vizkelethy, Simulation of Energetic Ions in Solids by Monte Carlo Method, KFKI, 107, 1985.
9. Gy. Vizkelethy, M. Fried, G. Mezey, F. Paszti and J. Gyulai, Phys. Stat. Sol. (a), *94*, 413, 1986.
10. W. M. Currie, Nuclear Instr. and Meth., *73*, 173, 1969.
11. T. Andersen and G. Sørensen, Can. J. Phys., *46*, 483, 1968.
12. K. B. Winterbon, P. Sigmund and J. B. Sanders, Mat. Fys. Medd. Dan. Vid. Selsk., *37*, No. 14, 1970.

Acta Physica Hungarica 67 (3–4), pp. 275–287 (1990)

РАСШИРЕННАЯ ТЕОРИЯ ОТНОСИТЕЛЬНОСТИ И МНОГОМЕРНОЕ (КОМПЛЕКСНОЕ) ПРЕДСТАВЛЕНИЕ РАСШИРЕННЫХ МНОГООБРАЗИЙ

В. С. ГУРИН и А. П. ТРОФИМЕНКО

Астрономическая секция Минского отделения
Всесоюзного астрономо–геодезического общества
абон. ящик № 7, Минск-12
220012, СССР

(Поступило 26. мая 1988)

Рассматривается проблема комплексного пространства-времени в общей теории относительности. Показывается, каким образом возникает представление о комплексном пространстве-времени в расширенной теории относительности при анализе суб- и суперлюминальных явлений как и при исследовании пространственно-временных многообразий с горизонтами событий.

1. Введение

Последнее десятилетие развития теорий фундаментальных взаимодействий, в том числе включая гравитационное, показало большую привлекательность введения представлений о пространстве-времени с числом измерений больше четырех. Большинство работ в этом направлении относятся к развитию идеи Калуцы и Клейна о компактифицированных на очень малые масштабы дополнительных измерениях. Особое место в многомерных теориях, хотя и не самое значительное по числу публикаций, занимают варианты теорий с комплексным пространством-временем, когда не возникает необходимости компактифицировать высшие размерности.

Идея комплексного пространства-времени (ПВ) в теории относительности не нова. Мнимое время было введено еще в работах Пуанкаре и Минковского для представления метрики специальной теории относительности (СТО) в евклидовой форме. Эйнштейн и Штраус [1] в качестве варианта единой теории предлагали эрмитову теорию относительности с комплексной метрикой. Некоторое развитие получил такой подход в последнее время также в работах Тредера [2]. В настоящее время использование комплексного ПВ оказалось довольно плодотворным для разработки евклидовой квантовой теории гравитационного поля [3]. Следует также отметить процедуру комплексификации в точных решения общей теории относительности (ОТО), разрабатываемая рядом авторов для получения вращательных метрик из статических [4, 5]. Довольно интенсивное развитие получил также подход формального введения комплексных многообразий в ОТО [6–11]

и использование комплексных пространственно-временных переменных в теории твисторов Пенроуза [12]. Появились также интересные разработки, прямо называемые авторами комплексной ОТО [13, 14].

Несколько иначе, чем в вышеотмеченных направлениях, встает вопрос о комплексных переменных ПВ при едином рассмотрении сверхсветовых (тахионов) и досветовых (брадионов) объектов [15, 16] в рамках расширенной теории относительности (РТО) [17], основанной на положении о полной симметрии между тахионами и брадионами (принцип дуальности [18]) при инверсии знака интервала ПВ при переходе от сублюминального описания к суперлюминальному. Суперлюминальные преобразования Лоренца в РТО приводят к появлению мнимых величин для наблюдателей, находящихся по другую сторону от светового барьера относительно рассматриваемого физического явления [19]. То же самое имеет место и для наблюдателей, находящихся за горизонтом событий в расширенном пространственно-временном многообразии (ПВМ) при наличии сильных гравитационных полей [20, 21].

Принципиальным отличием комплексных переменных в такой теории от вышеупомянутых состоит в том, что они носят метрический характер и обладают ясным физическим смыслом. В подходящей системе отсчета (суперлюминальной) они могут быть измерены способом, которых обычно, следуя Эйнштейну, рассматривается в теории относительности: с помощью "линеек" и "часов". Мнимый характер координат, формально выражающийся множителем i, означает их физическую ненаблюдаемость, следующую из невозможности обмена световыми сигналами между тахионами и брадионами.

В завершение краткого обзора отметим использование комплексных координат в расширенных ПВМ в ОТО, занимающих важное место в концепции "отонных миров" [20] для интерпретации ряда астрофизических феноменов (гамма-всплески, "скрытая масса", начальные неоднородности, гигантские пустоты в распределении галактик и их скоплений, квазары) как вспышек белых и серых дыр. В цикле работ Храпко [22] из математических соображений было введено 8-мерное комплексное ПВ для простейших гравитационных полей. Определенные физические и методологические основания для этого были предложены авторами на основании рассмотрения координат ПВ под горизонтом событий черной дыры как мнимых [20, 21]. Наиболее адекватным образом обосновать комплексное расширение теории относительности (как общей так и специальной), что будет произведено в настоящей работе, возможно с помощью суперлюминальных преобразований при едином рассмотрении тахионов и брадионов в ПВМ [21].

В последние годы вслед за вышеотмеченными публикациями, посвященными анализу 8-мерной теории относительности в комплексном ПВ на основе единого в таком плоском многообразии без гравитационного поля представления суб- и суперлюминальных явлений эта проблема стала разрабатываться некоторыми авторами довольно интенсивно [23]. Следует отметить также работы [24, 25], в которых предлагается комплексное обобще-

ние электродинамики.

В этой связи в настоящей работе предпринята попытка систематического подхода к введению комплексного представления расширенных ПВМ и комплексного ПВ в РТО.

2. Расширенная теория относительности и ее предельные случаи

Строгое построение теории относительности Эйнштейна производится, как известно, исходя из двух постулатов. 1) Постулат о свойствах ПВ: изотропности пространства и однородности пространства и времени; 2) Постулат о ковариантности физических законов в различных инерциальных системах отсчета (принцип относительности).

Постулат о фундаментальной инвариантной скорости распространения сигналов (физических взаимодействий) не является принципиально необходимым, а может быть выведен на основе первых двух, как показано во многих работах [26, 27], (см. также ссылки в работах [17]). Однако чаще всего в учебниках по СТО он рассматривается как третий постулат для простоты изложения. Существенным моментом при этом является тот факт, что исходные положения теории относительности не включают утверждения о максимальности фундаментальной инвариантной скорости. Если ее величина и имеет особенный (предельный) характер среди других значений скоростей движения, то это вызвано тем, что связь между событиями и системами отсчета в теории устанавливается посредством обмена фундаментальными сигналами. Но любой предел, тем более если он не бесконечен по величине, имеет две стороны [17]. В РТО сверхсветовые скорости рассматриваются на равных правах с досветовыми, восстанавливая таким образом, часто нарушаемую симметрию теории относительно возможных значений скоростей движения.

В РТО вводится также третий постулат (для этого имеются веские основания, см. [17, 28] о несуществовании объектов, перемещающихся назад во времени, что получается обычно при тривиальном распространении СТО в суперлюминальную область, и необходимости их реинтерпретации как антиобъектов.

Итак, описание объектов, находящихся за световым барьером, в РТО производится путем введения обобщенных преобразований Лоренца, составляющих обобщеную группу в рамках вышеуказаннных постулатов [17]:

$$G = \{+\Lambda_<\} \cup \{-\Lambda_<\} \cup \{+i\Lambda_>\} \cup \{-i\Lambda_>\}. \tag{2.1}$$

Здесь $\{\pm\Lambda_<\}$ — собственные ортохронные и неортохронные преобразования, $\{\pm\Lambda_>\}$ — соответствующие суперлюминальные преобразования Лоренца. Довольно важным в такой обобщенной СТО является принцип дуальности, говорящий о симметрии тахионного и брадионного миров: тахион в

суперлюминальной системе отсчета является брадионом, брадион в этой системе — тахионом, т. е. понятия тахион и брадион относительны и зависят от выбора системы отсчета [18].

Как показано во многих работах по РТО (см. ссылки в [17]), (2.1) есть расширение обычной группы Лоренца включением CPT-инверсии и операции замены скорости на дуальную: $V^2/C^2 \to C^2/V^2$ с одновременным умножением на i [29]. Набор преобразований (2.1) соответствует переходу между исходной системой отсчета и системой, полученной из нее при движении с произвольной скоростью $V \gtrless C$ и, посредством двух последовательных преобразований — к CPT-инвертированной системе, соответствующей антиобъектам. Таким образом, РТО разделяет все физические объекты на четыре класса: брадионы, тахионы, антибрадионы и антитахионы в соответствии с релятивистским соотношением между массой и энергией

$$\pm\left(E^2 - p^2c^2\right) = m^2c^4, \tag{2.2}$$

где m — масса покоя, $m \geq 0$, а знак $(+)$ соответствует брадионам, знак $(-)$ — тахионам.

С точки зрения многомерной трактовки РТО [30–33] теория, включающая непротиворечивое описание суб- и суперлюминальных объектов, может быть построена в комплексном (глобально 8-мерном) ПВМ, где действительный сектор соответствует сублюминальным объектам, а мнимый — суперлюминальным, т. е. объектам либо за световым барьером либо за горизонтом событий (см. ниже).

Можно заключить, что понятие скорости, объединяющей по определению пространственное и временное изменения для некоторого объекта, является фундаментальным, и величина скорости объекта по отношению к фундаментальной: суб- или суперлюминальной — определяет принадлежность его к определенному классу.

В этой связи представляет несомненный интерес рассмотрение вариантов теорий (относительности) с качественно различными значениями фундаментальной скорости. Под качественным различием при этом понимается анализ таких ее значений, которые несводимы друг к другу умножением на конечное действительное число, т. е. $c = 0$, $c = \infty$ и $c = const$ (можно отметить также и $c = i\,const$, но ее интерпретация непонятна). Нижеприведенная таблица 1 отражает эти варианты теорий и взаимосвязь между ними. Очевидно, что теория с $c = \infty$ — это не что иное как обычная классическая кинематика (классическая теория относительности — КТО). Теории с $c = const$ составляют РТО: сублюминальную СТО и ее суперлюминальное обобщение.

Наименее известной среди указанных трех теорий является теория с $c = 0$ (упоминания о ней см. в [34]). Ее физическое истолкование было дано С. И. Санько. Ближайшее рассмотрение показывает, что это предельный вариант суперлюминальной теории, когда скорости всех объектов стремятся к бесконечности, т. е. все возможные объекты такой теории суть трансцендентные тахионы. В такой теории имеет место абсолютное отсутствие

двухсторонней причинной связи между любыми точками, даже бесконечно близкими. Ее можно назвать нулевой теорией относительности — НТО. В ее обсуждении ограничимся законом сложения скоростей. Из табл. 1 видно, что переход к $V \to 0$ означает переход к $V \gg c$, следовательно, в обычном релятивистском законе сложения скоростей

$$V = (V_1 + V_2)\left(1 + V_1 V_2/c^2\right)^{-1}$$

Таблица 1

КТО		РТО		НТО	
$c = \infty$		$c = \text{const}$		$c = 0$	
$V < \infty = c$		$V < c$	$V > c$	$V > 0 = c$	
$V \leq \infty$	$V \ll \infty$	$V \ll c$ $V \leq c$	$V \geq c$ $V \gg c$	$V \gg 0$	$V \geq 0$

согласно идеологии РТО нужно перейти к дуальным скоростям: $V(c \to c)V'$, т. е.

$$1/V' = (V_1 + V_2) / (V_1 V_2 + c^2),$$

откуда можно получить

$$V = (V_1 V_2 + c^2)(V_1 + V_2)^{-1}. \tag{2.3}$$

Переходя для НТО к пределу $c \to 0$, получим выражение для закона сложения скоростей

$$V = V_1 V_2/(V_1 + V_2). \tag{2.4}$$

Из этой формулы видно, что закон сложения в НТО довольно необычен. Так, сумма скоростей всегда меньше каждой из слагаемых, если скорости имеют противоположные знаки, то суммарная оказывается бесконечной.

3. Комплексные величины при суперлюминальных преобразованиях

Сохранение принципа относительности для инерциальных систем отсчета при обобщении преобразований Лоренца на сверхсветовые объекты, требует изменения времениподобного интервала на пространственноподобный, и наоборот [17]. Поэтому, если мы обозначим через x, y, z обычные декартовы координаты, а t — время, то между координатами в суб- и суперлюминальной системах отсчета будет иметь место соотношение (здесь и далее, кроме отдельных случаев, мы будем использовать геометризованные единицы, в которых $c = 1$ и G, гравитационная постоянная, $= 1$):

$$dx^2 + dy^2 + dz^2 - dt^2 = -(dx')^2 - (dy')^2 - (dz')^2 + (dt')^2. \tag{3.1}$$

Если ограничиться бустом вдоль оси x, то они удовлетворяются при следующих преобразованиях [17]

$$t' = \pm i(t - Vx)(1-V^2)^{-\frac{1}{2}}, \quad x' = \pm i(x - Vt)(1-V^2)^{-\frac{1}{2}}, \quad y' = \pm iy, \quad z' = \pm iz, \tag{3.2}$$

где V — относительная скорость движения систем (x', t') и (x, t). Мнимые переменные появляются здесь с необходимостью. Более того, как показано в работе Горини, [35], не существует обобщений преобразований Лоренца к суперлюминальным скоростям с действительными переменными, удовлетворяющих условиям: сохранения инерциальности движения, сохранения пространственной изотропии, образования группы и инвариантности интервала (с точностью до знака).

Таким образом, для совместного равноправного рассмотрения суб- и суперлюминальных явлений необходимо аналитически продолжить переменные ПВ на комплексные значения. Это, очевидно, эквивалентно повышению размерности ПВ, так как из принципа причинности следует независимость явлений брадионного мира от тахионного и наоборот, что формально выражается в независимости мнимой и действительной частей координат.

Полезно для дальнейшего рассмотреть также суперлюминальный буст в предельном случае при $V \to \infty$, называемый обычно трансцендентным преобразованием. При этом происходит полное превращение действительных координат в мнимые, что и соответствует физическому смыслу такого предельного случая:

$$x' = \pm ix, \quad y' = \pm iy, \quad z' = \pm iz, \quad t' = \pm it. \tag{3.3}$$

Из условия (3.1) следует [30], что $t' = x$ и $x' = t$, поэтому (3.3) можно представить следующим образом

$$t' = \pm x, \quad x' = \pm t, \quad y' = \pm iy, \quad z' = \pm iz. \tag{3.4}$$

Тогда становится понятным значение выражения "пространство и время меняются местами", которое часто используется для интерпретации свойств тахионов и внутренних областей черных дыр (см. ниже). Смысл его в том, что пространственные и временные координаты становятся чисто мнимыми или, другими словами, ортогональными исходными [20, 30].

Итак, единое рассмотрение многообразия событий при $V \gg c$ приводит к необходимости комплексного ПВ уже в плоском случае с координатами $(x_{Re}, y_{Re}, z_{Re}, t_{Re}, x_{Im}, y_{Im}, z_{Im}, t_{Im})$ в декартовой системе, или (X, Y, Z, T), где [21]

$$X = x_{Re} + ix_{Im}, \quad Y = y_{Re} + iy_{Im}, \quad Z = z_{Re} + iz_{Im}, \quad T = t_{Re} + it_{Im}. \tag{3.5}$$

Переходя к обобщению на случай риманова ПВ метрику можно записать

$$ds^2 = g_{\mu\vartheta} dx_{Re} dx_{Re} - g_{ik} dx^i_{Im} dx^k_{Im}, \tag{3.6}$$

где греческие индексы соответствуют действительным частям координат: $(\mu, \partial) = (1, 2, 3, 4)$, а латинские — мнимым: $(i, k) = (5, 6, 7, 8)$. Разбивка метрики (3.6) на две части не случайна: первое слагаемое описывает многообразие событий, наблюдаемое некоторым локальным наблюдателем для области ПВ, ограниченной световым барьером либо горизонтом, т. е. в той же части светового конуса; второе слагаемое соответствует событиям в суперлюминальной области. Следует сказать, что такое представление соответствует также 6-мерной интерпретации тахион-брадионного ПВМ, разрабатываемого рядом авторов (см. ниже и ссылки в [21]) при введении 3-мерного времени. Как показано в работе Макарроне и Реками [30], такое 6-мерное ПВ можно рассматривать как промежуточный шаг в многомерной интерпретации суперлюминальных явлений, и оно не является альтернативой к комплексному представлению.

4. Место теории 3-мерного времени в комплексном ПВ

Одной из попыток согласованного описания суперлюминальных преобразований в РТО и интерпретации их физического смысла является введение ПВ с тремя пространственными и тремя временными осями: $M_6 = M_{3+3}$, когда любое событие записывается как

$$E = (x, y, z, t_x, t_y, t_z). \tag{4.1}$$

Впервые данный подход был предложен Демерсом [36], а в приложении к РТО —Миньяни и Реками [37]. В последствии вопрос довольно интенсивно и подчас противоречиво обсуждался многими авторами.

При таком подходе квадратичная форма интервала определяется:

$$ds^2 = dx^2 + dy^2 + dz^2 - dt_x^2 - dt_y^2 - dt_z^2. \tag{4.2}$$

Для согласования с обычной 4-мерной теорией допускается, что индивидуально наблюдаемы лишь пространственные компоненты, а наблюдаемой временной координатой является только модуль

$$t = (t_x^2 + t_y^2 + t_z^2)^{\frac{1}{2}}.$$

Изменение знака и сохранение величины интервала (4.2) при переходе от суб- к суперлюминальной системе (или наоборот) определяет вид преобразования [36, 37]:

$$x' = \pm(V^2 - 1)^{-\frac{1}{2}}(x - Vt_x), \quad t'_x = \pm(V^2 - 1)^{-\frac{1}{2}}(t - Vx), \qquad V > 1$$

$$y' = \pm t_y, \quad z' = \pm t_z, \quad t'_y = \pm y, \quad t'_z = \pm x, \tag{4.3a}$$

$$x' = (1 - V^2)^{-\frac{1}{2}}(x - Vt_x), \quad t'_x = (1 - V^2)^{-\frac{1}{2}}(t - Vx), \qquad V < 1$$

$$y' = y, \quad z' = z, \quad t'_y = t_y, \quad t'_z = t_z. \tag{4.3б}$$

Видно, что в сублюминальном случае компоненты t_y и t_z никак не преобразуются, следовательно они необходимы только лишь при описании суперлюминальных объектов. Однако, поскольку для любого наблюдателя существует только 4 координаты (x, y, z, t), то 6-мерное ПВ с 3-мерным временем представляется только лишь вспомогательным для интерпретации суперлюминальных преобразований: физические законы для тахионов в их собственной системе и других системах, движущихся относительно собственной с $V < 1$ (принцип дуальности), выражаются чисто действительными величинами. M_6 выступает как вспомогательное для охвата как суб- так и суперлюминальных явлений. В нем мнимая единица заменяется вращением на 90^o в трехмерном времени, что аналогично ее роли в теории с комплексными координатами, где она устанавливает различие тахионных и брадионных координат, а в пространстве с метрикой Минковского заключает различие пространства и времени. Таким образом трехмерность времени, вводимая симметрично трехмерности пространства не выражает реальную размерность физического ПВ, его введение дает возможность симметрично представить преобразования между суб- и суперлюминальными системами. Так, для трансцендентного преобразования будем иметь

$$x \to t_x, \quad y \to t_y, \quad z \to t_z, \quad t_x \to x, \quad t_y \to y, \quad t_z \to z. \tag{4.4}$$

В работе [38] предложен более обобщенный подход — комплексификация самого 3-мерного времени

$$t_x = t_{x_{Re}} + it_{x_{Im}}, \quad t_y = t_{y_{Re}} + it_{y_{Im}}, \, t_z = t_{z_{Re}} + it_{z_{Im}}, \tag{4.5}$$

тогда

$$t = t_x\mathbf{x}/|\mathbf{x}| + t_y\mathbf{y}/|\mathbf{y}| + t_z\mathbf{z}/|\mathbf{z}|. \tag{4.6}$$

В таком случае при суперлюминальном трансцендентном бусте вдоль оси x будем иметь следующие преобразования

$$\begin{aligned}
x'_{Re} + ix'_{Im} &= t_{x_{Re}} + it_{x_{Im}}, \\
y'_{Re} + iy'_{Im} &= y_{Im} - iy_{Re}, \\
z'_{Re} + iz'_{Im} &= z_{Im} - iz_{Re}, \\
t'_{x_{Re}} + it'_{x_{Im}} &= x_{Re} + ix_{Im}, \\
t'_{y_{Re}} + it'_{y_{Im}} &= t_{y_{Im}} - it_{y_{Re}}, \\
t'_{z_{Re}} + it'_{z_{Im}} &= t_{z_{Im}} - it_{z_{Re}}.
\end{aligned} \tag{4.7}$$

Пусть сублюминальной будет нештрихованная система. Хотя мы написали в обеих системах пока координаты в комплексной форме, но нет никаких оснований считать их таковыми в сублюминальном случае, в то же время мнимые переменные, как указывалось, в суперлюминальном случае являются необходимыми. Поэтому в соотношениях (4.7) справа необходимо

оставить только действительные части, имеющие физический смысл. Осуществив указанные сокращения, получим

$$ix'_{Im} = t_{x_{Re}},\ \ iy'_{Im} = -iy_{Re},\ \ iz'_{Im} = -iz_{Re},\ \ t'_{x_{Re}} = x_{Re},\ \ it'_{Im_{xy}} = -it_{yz_{Re}}. \tag{4.8}$$

Компоненты времени в этих формулах (t_x, t_y, t_z) опять играют ту же вспомогательную роль, а физическая размерность ПВ равна не 12, а 8, т. е. ПВ 4-мерно и комплексно.

5. Суперлюминальные преобразования в комплексном ПВ

Суб- и суперлюминальные преобразования общего вида должны удовлетворять знакопеременности и инвариантности величины интервала. В нашем комплексном ПВ это требование запишется в виде

$$\begin{aligned} dx_{Re}^2 + dx_{Im}^2 + dy_{Re}^2 + dy_{Im}^2 + dz_{Re}^2 + dz_{Im}^2 - dt_{Re}^2 - dt_{Im}^2 = \\ = -dx'_{Re}{}^2 - dx'_{Im}{}^2 - dy'_{Re}{}^2 - dy'_{Im}{}^2 - dz'_{Re}{}^2 - dz'_{Im}{}^2 + dt'_{Re}{}^2 + dt'_{Im}{}^2, \end{aligned} \tag{5.1}$$

где ds^2 задается формулой (3.6). Тогда легко можно показать, что имеют место следующие соотношения для преобразований при бусте вдоль оси x с относительной скоростью $V \gtrless 1$.

$$\begin{aligned} &x'_{Re} = (1-V^2)^{-\frac{1}{2}}(x_{Re} - Vt_{Re}),\quad t'_{Re} = (1-V^2)^{-\frac{1}{2}}(t_{Re} - Vx_{Re}),\\ &x'_{Im} = (1-V^2)^{-\frac{1}{2}}(x_{Im} - Vt_{Im}),\quad t'_{Im} = (1-V^2)^{-\frac{1}{2}}(t_{Im} - Vx_{Im}),\\ &y'_{Re} = y_{Re},\ \ z'_{Re} = z_{Re},\ \ y'_{Im} = y_{Im},\ \ z'_{Im} = z_{Im},\qquad V < 1 \end{aligned} \tag{5.2}$$

$$\begin{aligned} &x'_{Re} = (V^2-1)^{-\frac{1}{2}}(t_{Re} - Vx_{Re}),\quad t'_{Re} = (V^2-1)^{-\frac{1}{2}}(x_{Re} - Vt_{Re}),\\ &x'_{Im} = (V^2-1)^{-\frac{1}{2}}(t_{Im} - Vx_{Im}),\quad t'_{Im} = (V^2-1)^{-\frac{1}{2}}(x_{Im} - vt_{Im}),\\ &y'_{Re} = \pm iy_{Im},\ \ y'_{Im} = \pm iy_{Re},\ \ z'_{Re} = \pm iz_{Im},\ \ z'_{Im} = \pm iz_{Re},\quad V > 1. \end{aligned} \tag{5.2b}$$

Данный набор преобразований показывает, что в сублюминальном случае нет связи между действительными и мнимыми частями координат, в то время как в суперлюминальной они преобразуются друг через друга. Это является формальным выражением того факта, что в отсутствие тахионов (и гравитационных полей с горизонтами) мы имеем обычный 4-мерный мир для всех наблюдателей, а в суперлюминальной области и только в ней появляются мнимые координаты, так что полное ПВ является комплексным. Если при этом вспомнить принцип дуальности в РТО и в его обобщенном смысле [21], то можно констатировать, что как для суперлюминального так и для сублюминального миров, взятых отдельно, существует только

набор четырех действительных координат, подчиняющихся соответствующим преобразованиям (5.2). Все эти координаты наблюдаемы в том смысле, что можно проводить их измерения с помощью "линеек" и "часов". С точки зрения такой "наблюдаемой физики" совершенно безразлично будем ли мы в сублюминальном или в суперлюминальном мире, по одну сторону горизонта или по другую. Важно, чтобы только рассматривалась область, ограниченная либо горизонтом, либо световым барьером. Очевидно, что такое рассмотрение будет неполным, устраняющим априорно суперлюминальные явления. Расширение ведет нас за горизонт событий, либо за световой барьер, и мы вынуждены применять соотношения типа (5.2), что приводит к комплексификации ПВМ. Но, несмотря на появление восьми координат, их непосредственное наблюдение сразу всех в смысле возможности проведения обычных измерений неосуществимо для конкретного локального наблюдателя. Весь набор координат может проявиться только лишь для двух или более наблюдателей: один в суб-, другой — в суперлюминальной области. Таким образом, мы заключаем, что ПВМ глобально 8-мерно и обладает комплексной структурой, локально же оно остается 4-мерным.

6. Форма суперлюминальных объектов в комплексном ПВ

В настоящем разделе мы рассмотрим, каким образом проявляются суперлюминальные объекты конечного размера для различных наблюдателей, продолжив исследования Барута, Макарроне и Реками [39], в свете комплексного представления ПВМ.

Допустим, что рассматриваемый объект имеет форму эллипсоида в собственной системе отсчета. Уравнение эллипсоида в декартовых координатах запишется в виде:

$$x^2/x_0^2 + y^2/y_0^2 + z^2/z_0^2 = 1. \tag{6.1}$$

Такое тело занимает объем:

$$0 \leq x^2/x_0^2 + y^2/y_0^2 + z^2/z_0^2 \leq 1, \tag{6.2}$$

где x_0, y_0 и z_0 — полуоси эллипсоида вдоль соответствующих направлений. В комплексном ПВ будем иметь

$$0 \leq \frac{x_{Re}^2 + x_{Im}^2}{x_0^2} + \frac{y_{Re}^2 + y_{Im}^2}{y_0^2} + \frac{z_{Re}^2 + z_{Im}^2}{z_0^2} \leq 1. \tag{6.3}$$

Из этой формулы следует, что тело как бы разделяется на два — в действительном и мнимом подпространствах, и в общем случае эти две части никак не связаны.

Проанализируем теперь, как изменятся эти соотношения, если эллипсоид начнет двигаться с релятивистской скоростью прямолинейно и равномерно. Осуществим преобразования Лоренца (пока сублюминальные) для движения вдоль оси x:

$$0 \leq \frac{(x_{Re} - Vt_{Re})^2}{x_0^2(1-V^2)} + \frac{(x_{Im} - Vt_{Im})^2}{x_0^2(1-V^2)} + \frac{y_{Re}^2}{y_0^2} + \frac{y_{Im}^2}{y_0^2} + \frac{z_{Re}^2}{z_0^2} + \frac{z_{Im}^2}{z_0^2} \leq 1. \qquad (6.4)$$

Как для действительной так и для мнимой частей эллипсоида получаем сокращение вдоль осей x_{Re} и x_{Im}, соответственно, что является хорошо известным фактом в СТО для действительного подпространства. Теперь наличие двух несвязанных частей эллипсоида означает, что в тахионных и брадионных мирах взятых отдельно, можно наблюдать деформированное тело. Эллипсоидальная форма исходного объекта, которая имеет место в покое в брадионном мире, соответствует движению с бесконечной скоростью в тахионном мире. Деформация тела в тахионном мире заметным образом происходит при замедлении до околосветовых скоростей ($V \geq 1$).

Рассмотрим теперь тот же самый объект, движущийся равномерно и прямолинейно с суперлюминальной скоростью относительно брадионного мира (либо с сублюминальной относительно тахионного). В обоих случаях необходимо совершить суперлюминальные преобразования. Согласно соотношениям (5.2) для объема, занимаемого телом, будем иметь

$$-1 \leq -\frac{(x_{Re} - Vt_{Re})^2}{(V^2-1)x_0^2} - \frac{(x_{Im} - Vt_{Im})^2}{(V^2-1)x_0^2} + \frac{y_{Re}^2}{y_0^2} + \frac{y_{Im}^2}{y_0^2} + \frac{z_{Re}^2}{z_0^2} + \frac{z_{Im}^2}{z_0^2} \leq 0. \qquad (6.5)$$

Опять получаем две структуры тела, каждая из которых представляет собой область между двойным конусом (световым) и двуполостным гиперболоидом, который асимптотически приближается к конусу. Ясно, что относительно как брадионного так и тахионного миров структуры располагаются по разные стороны светового конуса, который в данном случае является горизонтом. Таким образом, для мира, где эллипсоид находился в покое или двигался медленнее света, тело становится ненаблюдаемым. Однако, рассматривая выполнение преобразования (5.2), можно заключить, что тело переходит их действительной части ПВ в мнимую, поэтому, переходя от эллипсоида в одном мире к структуре, заключенной между конусом и гиперболоидом в другом, мы переходим из действительной части ПВ с координатами x_{Re}, y_{Re}, z_{Re}, t_{Re} к мнимой, где x_{Im}, y'_{Im}, z_{Im}, t_{Im}.

При трансцендентных преобразованиях, полученных из (5.2) при $V \to \infty$, непосредственно примененных к эллипсоиду, мы будем наблюдать его превращение в указанную структуру с гиперболоидом, имеющим полуоси исходного эллипсоида; но так как теперь координаты стали мнимые, то структура ненаблюдаема непосредственно из исходного мира. Если вспомнить наше представление действительной и мнимой частей полного комплексного ПВ как некоторых гиперповерхностей в общем случае искривленных при наличии гравитационного поля, то возможность наблюдения

структуры тела после суперлюминального преобразования сводится к пересечению гиперповерхностей.

Следует при этом отметить, что анализ формы тела с точки зрения различных систем отсчета, разделенных световым барьером, применим не только в плоском ПВ. Как известно, в случае многих гравитационных полей (Шварцшильда, Де Ситтера, Керра-Ньюмена и др., см. [40]) при помощи подходящих преобразований координат метрику можно привести к конформно плоскому виду. Поэтому, осуществляя необходимые преобразования, можно повторить вышепроведенный анализ и прийти к выводу, что в гравитационном поле при переходе через горизонты форма тела меняется таким образом, что из эллипсоида будет получаться структура, находящаяся между световым конусом и двуполостным гиперболоидом. Она расположена в мнимой системе координат и ненаблюдаема по другую сторону горизонта для брадионов.

Обратимся теперь к обсуждению предельного случая светового барьера, то есть рассмотрим форму эллипсоида либо при ускорении его относительно брадионного наблюдателя до скорости света, либо при замедлении относительно тахионного наблюдателя также до скорости света. В таком случае соотношение (6.2) дает ($V \to 1$):

$$0 \le (x - Vt)x_0^{-2}(1 - V^2)^{-1} \le 1 \;\Rightarrow\; x = t. \tag{6.6}$$

Очевидно, что тело сжимается, превращаясь в точку в начале системы координат; оно как бы исчезает как протяженный объект при достижении телом светового барьера с точки зрения некоторого покоющегося (суперлюминального) наблюдателя. Перейдя к ускоренным координатам Риндлера

$$t = e^{\xi}\, sh\, \eta, \quad x = e^{\xi}\, ch\, \eta. \tag{6.7}$$

Можно видеть, что в координатах (ξ, η) тело не преобразуется в какую-либо особенную структуру при $\tilde{V} = d\eta/d\xi = 1$, так как

$$0 \le \frac{e^{\xi}(ch\,\eta - V\,sh\,\eta)}{x_0^2(1-V^2)} + \frac{y^2}{y_0^2} + \frac{z^2}{z_0^2} \le 1, \quad V = \frac{1 + \tilde{V}\,th\,\eta}{th\,\eta + \tilde{V}}. \tag{6.8}$$

Таким образом, в собственной системе ускоряющегося вместе с телом наблюдателя тело остается видимым и далее двигается с $V > c$.

Авторы выражают благодарность Проф. Идлису Г. М., Терлецкому Я. П. за обсуждение проблем, затронутых в работе, Проф. Реками Е. и Павшичу М. за высылку оттисков своих работ, а также членам астрономической секции Минского отделения ВАГО за дискуссии.

Литература

1. A. Einstein, E. Straus, Ann. Math., *47*, 731, 1946; *46*, 578, 1945.
2. H.-J. Treder, Ann. Phys. (DDR), *B40*, 81, 1983.
3. S. W. Hawking, in: General Relativity: An Einstein Centenary Survey, Cambridge University Press, Cambridge, 1979, p. 746.
4. E. T. Newman, J. Math. Phys., *14*, 744, 1973.
5. M. M. Schiffer, R. J. Adler, J. Mark, J. Math. Phys., *14*, 52, 1973.
6. J. Mozrzyzmski, Bull. Acad. Polon. Sci.: Math., Astron., Phys., *11*, 593, 599, 1963.
7. A. Krasinski, J. Plebanski, Rep. Math. Phys., *17*, 217, 1980.
8. General Relativity and Gravitation, ed. A. Held, New York–London 1980, pp. 207, 241.
9. A. Das, J. Math. Phys., *7*, 45, 52, 61, 1966.
10. G. H. Derrick, Int. J. Theor. Phys., *23*, 359, 1984.
11. E. G. Kalnins, W. Miller, Jr. and G. J. Reid, Proc. Roy. Soc. (London) *A394*, 183, 1984.
12. R. Penrose, in: Quantum Gravity: An Oxford Symposium, Clarendon Press, Oxford, 1975, Ch. 6.
13. C. B. G. McIntosh and M. S. Hickman, GRG, *17*, 111, 1985.
14. G. S. Hall, M. S. Hickman and C. B. G. McIntosh, GRG, *17*, 475, 1985.
15. M. Pavsic, Lett. Nuovo Cim., *30*, 111, 1981; J. Phys., *A14*, 3217, 1981.
16. H. C. Corben, Nuovo Cim. *A29*, 415, 1975.
17. E. Recami and R. Mignani, Riv. Nuovo Cim., *4*, 209, 1974; *9*, 1, 1986.
18. E. Recami and R. Mignani, Lett. Nouvo Cim. *4*, 144, 1972.
19. E. Recami and G. D. Maccarrone, Lett. Nuovo Cim., *28*, 151, 1980.
20. А. П. Трофименко, Принцип развития в астрофизике. Депонировано в ИНИОН АН СССР, № 2027, 1978; Генезис и современные проблемы астрофизики отонов. Депонировано в ИНИОН АН СССР, № 16810, 1984; Вселенная: творение и развитие, Белорусь, Минск, 1987.
21. V. S. Gurin, Fizika (SFRJ), *16*, 87, 1984; Pramana, *24*, 817, 1985; Acta Phys. Polon., *B17*, 3, 1986.
22. Р. И. Храпко, Доклады АН СССР, *176*, 566 1967; ЖЭТФ, *50*, 1636, 1966.
23. H. C. Chandola and B. S. Rajput, Lett. Nuovo Cim., *40*, 277, 1984; J. Math. Phys., *26*, 208, 1985; Ind. J. Pure and Appl. Phys., *21*, 651, 1984; *22*, 1, 1984; *23*, 589, 1985.
24. D. Weingarten, Ann. Phys. (USA), *76*, 510, 1973.
25. С. А. Меркулов, Известия вузов, физика, *27*, 123, 1984.
26. Я. П. Терлецкий, Парадоксы теории относительности, Наука, Москва, 1966.
27. M. Di Jorio, Nuovo Cim., *B22*, 70, 1974.
28. R. Mignani and E. Recami, Phys. Lett., *B65*, 148, 1976.
29. E. Recami and W. A. Rodrigues, Found. Phys., *12*, 709, 1982; in: Progr. in Particle and Nuclear Phys., V. 15, 1985, Pergamon Press, Oxford, p. 499.
30. G. D. Maccarrone, M. Pavsic and E. Recami, Nuovo Cim., *B73*, 91, 1983.
31. M. T. Teli and V. K. Sutar, Lett. Nuovo Cim. *22*, 503, 1978.
32. V. S. Gurin and A. P. Trofimenko, Fizika (SFRJ), *17*, 101, 1985; Rev. Roum. Phys., *31*, 535, 1986; Acta Phys. Hung., *59*, 371, 1986.
33. А. П. Трофименко, В. С. Гурин, Систематика отонов. Депонировано в ИНИОН АН СССР, № 21353, 1985.
34. L. H. Kauffman, Int. J. Theor. Phys., *24*, 223, 1985.
35. V. Gorini, Comm. Math. Phys., *21*, 150, 1971.
36. P. Demers, Can. J. Phys., *53*, 1643, 1975.
37. R. Mignani and E. Recami, Lett. Nuovo Cim., *16*, 449, 1976.
38. C. Ramon and E. A. Rauscher, Found. Phys., *10*, 661, 1980.
39. A. O. Barut, G. D. Maccarrone and E. Recami, Nuovo Cim., *A71*, 509, 1982.
40. S. Chandrasekhar, The Mathematical Theory of Black Holes, Oxford University Press, 1983.

Acta Physica Hungarica 67 (3–4), pp. 289–296 (1990)

COMPENSATION RULE FOR PHTHALOCYANINES

MARIA ZABKOWSKA-WACŁAWEK

Department of Engineering, Pedagogical University
45–052 Opole, Poland

(Received 5 July 1988)

The electrical conductivity results for pure and doped phthalocyanines are collected (265 points). For all the data one compensation line is obtained using coordinates $(B, \log A)$ derived from Mott's equation. This fact is considered as one of the arguments for hopping conduction mechanism operating in the materials.

Introduction

Each year thousands of papers are concerned with the investigation of electrical properties of organic materials. In many cases their electric conductivity, σ, is measured and discussed on the basis of the band theory equation:

$$\sigma = \sigma_0 \exp\left(-\frac{E_t}{kT}\right), \tag{1}$$

where σ_0 is the preexponential factor, E_t the activation energy for conduction, k the Boltzmann constant and T temperature.

Many authors, for example [1–4] observed the dependence between σ_0 and E_t for the material subjected to various experimental conditions or for materials with similar molecular structure:

$$\log \sigma_0 = \beta E_t + \gamma, \tag{2}$$

where β and γ are constants for a series of substances.

The Equation (2) is called the Meyer–Neldel rule or the compensation rule for conduction.

Considering the compensation rule the equation for the temperature dependence of the conductivity may be written as follows:

$$\sigma = \sigma_0' \exp\left(\frac{E_t}{kT_0}\right) \exp\left(-\frac{E_t}{kT}\right), \tag{3}$$

where σ_0' and T_0 are constants characteristic of the material studied, T_0 is called the characteristic temperature. The aim of this paper is to present 265 pairs of data $(E_t, \log \sigma_0)$ obtained for phthalocyanines and discuss a compensation rule for them.

Sample preparation and measurements

Different phthalocyanines were used for the investigation: copper, cobalt, lead and chloroferric phthalocyanines as well as cobalt-octamethoxyphthalocyanine and cobalt-1,2-naphthalocyanine.

Most of them were synthetised and purified in Prof. R. Dabrowski's laboratory (Warsaw). Copper phthalocyanine single crystals purified three times by sublimation were prepared in Dr. J. Wright's laboratory (Canterbury). Apart from pure phthalocyanine samples the mixtures containing copper or cobalt phthalocyanine and graphite or carbon blacks (type: HAF, P 1250, SAO, FEF, Sapex 20, SRF, PM 15, MT and acetylene carbon black) were prepared (the preparation procedure was described earlier e. g. by Kulesza [5]).

Samples were prepared as compressed pellets and thin films. Pellets were discs with a diameter of 8 or 10 mm or cuboids of (2×8) mm^2 and having a thickness not higher than 2 mm compacted from polycrystalline material under the pressure of $3 \cdot 10^8$–$8 \cdot 10^8$ Pa.

Thin film samples were prepared in a vacuum $\sim 10^{-4}$ Pa by evaporation as surface cells or sandwiches. The thickness of the phthalocyanine film was 0.10 to 4.3 μm. Nearly all the samples were heated prior to measuring at 420 K in vacuum for 20 h in order to have stable electrical properties.

To measure the electric conductivity the conventional dc method [2, 5, 6] was used. Some samples were placed in the atmosphere of different vapours and gases as described in [2]. Some points $(E_t, \log \sigma_0)$ were obtained from the temperature dependence of ac conduction [7].

Compensation rule in $(E_t, \log \sigma_0)$ coordinates

The existence of the compensation rule was strongly criticized by some authors, who pointed out that sometimes the compensation effect observed was only mathematical artifact (see for example [8, 9]).

Hundreds of results passed successfully the tests probing if the compensation rule is really obeyed. This was also the case for our samples. But usually for the samples treated in different experimental conditions separate compensation rules were discovered (Fig. 1).

So in Fig. 1 we can see 8 compensation lines. Three of them obtained for the mixtures of copper and cobalt phthalocyanines with carbon, two for samples doped with iodine (for lead [11] and cobalt phthalocyanines).

Wacławek [2] published the compensation effect for low-conducting phthalocyanine. He found two compensation rule lines (No 5, 6 in Fig. 1) having the correlation coefficients $r = 0.957$ and 0.987, respectively. No reason has been found to explain two compensation rules for the phthalocyanines studied. That is why a single straight line was drawn (No 7) through all points. It has the value of r merely equal to 0.872.

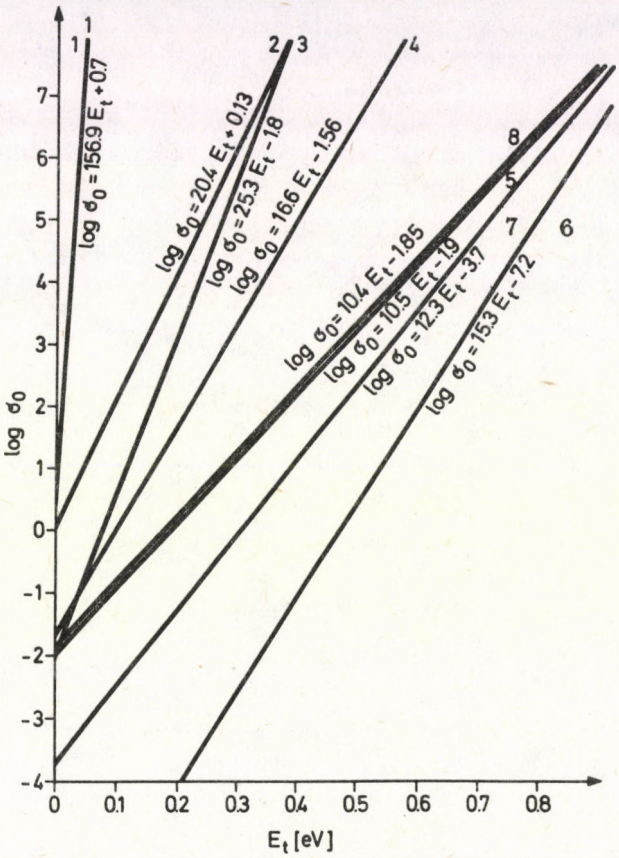

Fig. 1. The compensation effects for phthalocyanines ($[\sigma_0] = \mathrm{Sm}^{-1}$):
1) copper phthalocyanine doped with carbon black,
2) cobalt phthalocyanine doped with carbon,
3) cobalt phthalocyanine doped with iodine,
4) lead phthalocyanine doped with iodine [11],
5–7) low-conductive samples [2],
8) copper phthalocyanine doped with acetylene carbon black [10]

Considering Fig. 1 as well as Fig. 2 published in [2] (many published $(E_t, \log\ \sigma_0)$ data were collected) one could ask: what is the meaning of the compensation effects observed for phthalocyanines.

The parameters T_0 and σ_0' calculated on the basis of Eq. (2) vary in large area: $T_0 \in (32.1;\ 485)$ K and $\sigma_0' \in (6.03 \cdot 10^{-8};\ 5,0)\ \mathrm{Sm}^{-1}$ and experimental points covered nearly all the plane in Fig. 1. So one could answer that for the phthalocyanine

family a compensation rule does not exist in the coordinates $(E_t, \log \sigma_0)$.

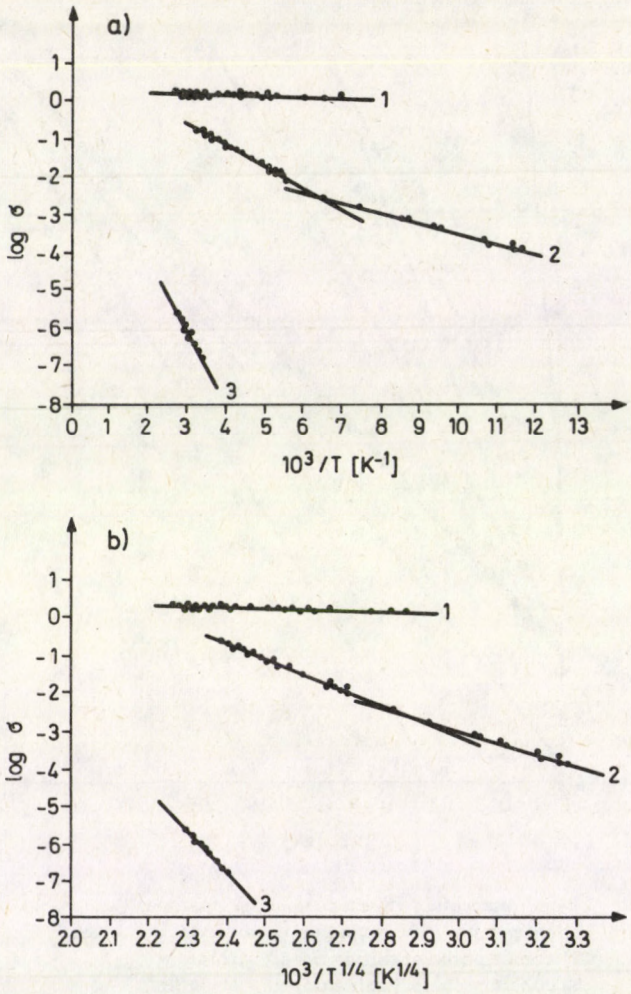

Fig. 2. The dependence of the electrical conductivity σ, ($[\sigma] = \mathrm{Sm}^{-1}$) on temperature plotted in accordance to a) Eq. (1) and b) Eq. (4) for: 1) the mixture: 90% wt copper phthalocyanine + 10% wt acetylene carbon black, 2) cobalt phthalocyanine saturated with iodine sample placed in nitrogen atmosphere and 3) chloroferric phthalocyanine in vacuum after evacuation of γ-picoline vapours

Compensation rule in $(B, \log A)$ coordinates

Anithkumar observed [12] two compensation rule lines for acetanilide, benzoic acid and their derivatives (16 points) (as it was the case with the results presented in [2]).

For the σ data, he used Mott's equation:

$$\sigma = A \exp\left(-\frac{B}{T^{1/4}}\right), \tag{4}$$

where A, B are constants, and in the coordinates $(T^{1/4}; \log \sigma)$ he obtained linear dependences. Moreover, all the points $(B, \log A)$ lay close to a single least squares fit straight line — its correlation coefficient is as high as 0.990 whereas for two compensation rules in coordinates $(E_t, \log \sigma_0)$ it is only 0.975 and 0.967.

For electric conductivity data collected for phthalocyanines in this laboratory the Eq. (4) was also used and in the coordinates $(T^{1/4}, \log \sigma)$ straight lines were obtained (Fig. 2). In most cases the correlation coefficients for least squares lines formed using Eq. (1) or (4) were similar; usually of the order of 0.960 to 0.990 sometimes higher for the first one, sometimes for the second.

For the samples presented in [2] but elaborated using Eq. (4) in $(B, \log A)$ coordinates a single compensation rule line was obtained, as it was in the case of Anithkumar's results. The correlation coefficient was 0.991. It seems that for all low-conducting samples (202 points) one compensation rule line exists (see Fig. 3). It is interesting to note that here some ac and photoconductivity data are also included. Then the equation is:

$$\log A = 0.09530\, B - 4.59 \tag{5}$$

and the correlation coefficient is equal to 0.990. Highly-conducting samples form the second compensation rule lying in close proximity to the first one:

$$\log A = 0.0850\, B + 0.61 \tag{6}$$

and its $r = 0.974$. For all experimental data (265 points) the compensation rule equation is as follows:

$$\log A = 0.08648\, B - 1.28 \tag{7}$$

and its $r = 0.988$. It is interesting to note that Anithkumar [12] obtained the compensation rule equation for his samples:

$$\log A = 0.091\, B - 3.0, \tag{8}$$

having the correlation coefficient $r = 0.990$ and lying in close proximity to the line described by (7).

The existence of the relationship between A and B is difficult to explain at the moment — both constants are coupled to each other since both of them contain the same parameters $N(E_F)$ (the density of states at the Fermi energy) and α (the decay constant of the wave function of the localized states). So one could suspect that for the samples bounded by the compensation rule a relationship between $N(E_F)$ and

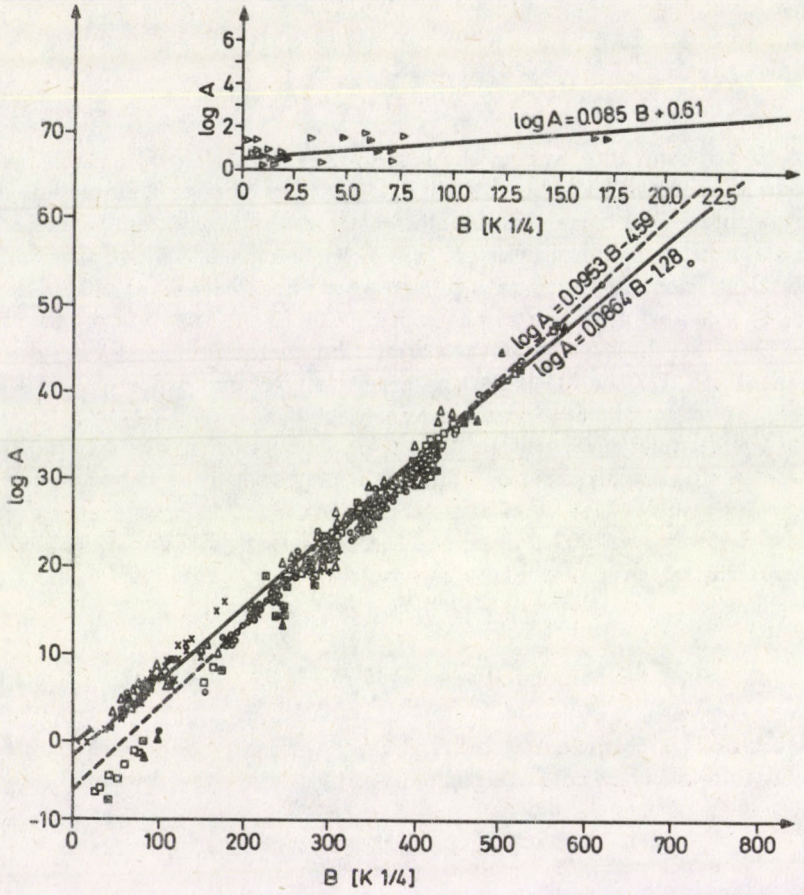

Fig. 9. Compensation rule in $(B, \log A)$ coordinates ($[A] = \mathrm{Sm}^{-1}$) △, o – copper and cobalt phthalocyanines and their derivatives (pellets), □, +, – lead and chloroferric phthalocyanines (pellets), ◬, ⊖, ⊡ – thin film samples ◭, ×, ⊗ – materials doped with iodine. |——| – highly-conducting samples, also shown in the insert, where pellets of the mixtures are included: ▷ – copper phthalocyanine with carbon black, ▶ – cobalt phthalocyanine with carbon

α exists. However, it is evident that the electric conductivity of the samples could be described with 3 factors.

Combining Eq. (4) and of the form of (5–7) we obtain:

$$\sigma = A' \exp\left(\frac{B}{B_0^{1/4}}\right) \exp\left(-\frac{B}{T^{1/4}}\right), \tag{9}$$

where: A', B_0 are factors characterizing materials bounded by the compensation

rule. It has a similar form as (3). For phthalocyanines studied $A' = 0.052$ Sm^{-1} and $B_0 = 636$ K.

Conclusions

Classical variable range hopping operates at low temperatures [17]. However, the hopping conduction for organic materials even at high temperatures has been postulated by many authors e. g. [12–14].

For some phthalocyanine samples (they were included above in compensation rule dependences) Zabkowska [15] has postulated charge carrier transport by hopping on the basis of Seebeck effect results.

The hopping conduction has also been suggested as stemming from our ac results [7].

The Hall measurements made for highly-conducting mixtures also confirmed this hypothesis [18]. However, here the $T^{-1/4}$ law could be also explained by the fluctuation-induced tunneling mechanism.

It seems that the only exception are some lead phthalocyanine samples doped with iodine [11]. Here the band model probably could be applied (the values and temperature dependences of charge carrier mobilities estimated on the basis of electric conductivity and Seebeck effect measurements as well as ac data are consistent with its predictions). However, the estimated mobilities are on the "boundary" of using the band model (0.7 cm^2/Vs). Such data could also be interpreted on the basis of the hopping theory.

In classical variable range hopping theory the constants A and B are coupled to each other since both of them contain the same parameters $N(E_F)$ and α, which does not lead to a linear dependence between B and log A. So the compensation rule could be only explained if a relationship between $N(E_F)$ and α exists for the samples studied or if the constants A and B have another meaning.

It seems that the existence of the compensation rule in coordinates $(B, \log A)$ could be used as one of the arguments for the explanation of charge carrier transport in phthalocyanines by the hopping mechanism, or by an other mechanism operating according to the $T^{-1/4}$ law.

The work is partly supported by Technical University of Wrocław under the contract C.P.B.P. 01.02.V.10.

References

1. H. Meier, Organic Semiconductors, Dark – and Photoconductivity of Organic Solids, Verlag Chemie, Weinheim, 1974.
2. W. Wacławek and M. Zabkowska, Phys. Stat. Sol., (a) *60*, K 17, 1980.
3. M. V. Kurik and J. A. Shabchin, Fiz. Tverd. Tela, *27*, 2665, 1985.

4. D. Sarkar, K. M. Jain and T. N. Misra, Bull. Chem. Soc. Jpn., *59*, 1561, 1986.
5. M. Kulesza, M. Zabkowska and W. Wacławek, Mol. Cryst. Liq. Cryst., *118*, 371, 1985.
6. W. Wacławek and M. Zabkowska, J. Phys., E *14*, 618, 1981.
7. W. Wacławek, M. Kulesza and M. Zabkowska, Materials Science, *7*, 385, 1981.
8. J. R. N. Evans, J. M. Thomas and T. J. Lewis, Bioenergetics, *3*, 245, 1972.
9. R. R. Krug, W. G. Hunter and R. A. Grieger, J. Phys. Chem., *80*, 2341, 1976.
10. R. Piasecki, M. Zabkowska-Wacławek and W. Wacławek, Phys. Stat. Sol. (a), *108*, 331, 1988.
11. W. Wacławek and M. Zabkowska-Wacławek, Thin Solid Films, *146*, 1, 1987.
12. C. S. Anithkumar and N. Umakantha, Phil. Mag. B, *44*, 615, 1981.
13. R. Colson, P. Nagels and R. Speeckaert, in Amorphous and Liquid Semiconductors, ed. W. E. Spear, CICL Edinburgh, 1977, p. 775.
14. G. J. Ashwell, G. H. Cross, I. M. Sandy, W. Wacławek and M. Zabkowska, Z. Naturforsch., *40a*, 731, 1985.
15. M. Zabkowska, Ph. D. Thesis, Warsaw Polytechnical University, Warsaw, 1978.
16. M. Zabkowska, M. Kulesza and W. Wacławek, Materials Science, *10*, 303, 1984.
17. N. F. Mott and G. A. Davis, Electronic Processes in Noncrystalline Materials, Clarendon Press, Oxford, 1979.
18. M. Zabkowska-Wacławek and M. Otto, to be published.

Acta Physica Hungarica 67 (3–4), pp. 297–304 (1990)

A ROTATING BIANCHI TYPE II VISCOUS FLUID COSMOLOGICAL MODEL WITH HEAT FLUX

SHARDA S. KOPPAR* and L. K. PATEL

Department of Mathematics, Gujarat University
Ahmedabad 380009, Gujarat State
India

(Received 8 September 1988)

We present exact solutions of a rotating Bianchi type II cosmological model with viscous fluid and heat flux. Some properties of the model are discussed and some particular cases are also derived.

1. Introduction

Many investigators have taken keen interest in the problem of finding cosmological solutions of Einstein field equations with heat flow. Some remarkably simple solutions of Einstein-field equations with heat flow are discussed by Novello and Reboucas [1], Ray [2], Reboucas and de Lima [3] and Reboucas [4]. Some rotating Bianchi type VIII time-dependent cosmologies with heat flow are studied in detail by Bradley and Sviestins [5]. Adopting the same method Sviestins [6] has given a brief discussion of some Bianchi type IX cosmological models filled with perfect fluid which is not thermalized. Reboucas and Tiomno [7] have discussed some inhomogeneous Gödel type universes. The source of the geometries of their solutions is a perfect fluid with heat flow plus a scalar field. Patel and Pandya [8] have given some perfect-fluid cosmological models with non-zero heat flux.

In recent years viscosity has played an important role in explaining many physical features of homogeneous cosmological models. Therefore anisotropic viscous-fluid cosmological models have been widely studied. Banerjee, Duttachaudhuri and Sanyal [9] have discussed in detail a Bianchi type II cosmological model with viscous fluid. They have a list of papers dealing with different aspects of viscous-fluid cosmological models.

It will be interesting to study the situation in which the heat flow and the viscosity both are present. The principal aim of the present investigation is to obtain a rotating Bianchi type II viscous-fluid cosmological model with non-zero heat flow.

*Present address: Department of Mathematics, 231 West Eighteenth Avenue, The Ohio State University, Columbus, Ohio 43210, USA.

2. The metric and the field equations

Let us consider a rotating Bianchi type II spacetime whose geometry is described by the line-element

$$\begin{aligned} ds^2 =&[dt + \alpha A(dr + 4m^2 d\phi)]^2 - A^2(dr + 4m^2 d\phi)^2 \\ &- [\operatorname{cosec}^2\theta d\theta^2 + d\phi^2], \end{aligned} \tag{1}$$

where α is a constant, A is a function of time t and m is a function of θ satisfying the differential equation

$$4m \sin\theta \frac{dm}{d\theta} = \lambda_1. \tag{2}$$

Here λ_1 is a constant. For the computation of Ricci tensor for the metric (1), we shall use the technique of differential forms. This technique is standard now and we shall not go into the details.

Let us introduce the following basic 1-forms in the 4-dimensional Riemannian manifold defined by the metric (1) along with (2):

$$\begin{aligned} \theta^1 &= A[dr + 4m^2 d\phi], \\ \theta^2 &= \operatorname{cosec}\theta d\theta, \\ \theta^3 &= d\phi, \\ \theta^4 &= dt + \alpha\theta^1. \end{aligned} \tag{3}$$

The metric (1) can be expressed as

$$\begin{aligned} ds^2 &= (\theta^4)^2 - (\theta^1)^2 - (\theta^2)^2 - (\theta^3)^2 \\ &= g_{(ab)}\theta^a\theta^b. \end{aligned} \tag{4}$$

Here and in what follows, bracketed indices denote tetrad components with respect to the tetrad (3). Using Cartan's equations of structure one can easily obtain the tetrad components $R_{(ab)}$ of Ricci tensor for the metric (1).

The explicit expressions for non-zero $R_{(ab)}$ are

$$\begin{aligned} R_{(14)} &= 2\alpha A^2\lambda_1^2, \\ R_{(44)} &= (1-\alpha^2)\frac{\ddot{A}}{A} - 2\alpha^2 A^2\lambda_1^2, \\ R_{(11)} &= (\alpha^2 - 1)\frac{\ddot{A}}{A} - 2A^2\lambda_1^2, \\ R_{(22)} &= R_{(33)} = 2\lambda_1^2(1-\alpha^2)A^2. \end{aligned} \tag{5}$$

An overhead dot implies differentiation with respect to time t.

The energy momentum tensor for a viscous fluid with heat flow vector q_i is

$$T_{ik} = (\bar{p} + \rho)v_i v_k - \bar{p}g_{ik} - \eta\mu_{ik} + (q_i v_k + q_k v_i), \tag{6}$$

where

$$g^{ik}v_i v_k = 1, \qquad g^{ik}q_i v_k = 0, \tag{7}$$

$$\mu_{ik} = v_{i;k} + v_{k;i} - (v_i f_k + v_k f_i), \tag{8}$$

$$f_i = v^a v_{i;a} \tag{9}$$

and

$$\bar{p} = p - \left(\zeta - \frac{2}{3}\eta\right) v^i_{;i}. \tag{10}$$

Here the semicolon denotes the covariant differentiation and ζ and η stand for bulk and shear viscosity coefficients, respectively.

We shall use the co-moving coordinates and take the heat-flow in the direction of θ^1. Therefore the tetrad components $v_{(a)}$ and $q_{(a)}$ of v_i and q_i are

$$v_{(a)} = (\,0,\ 0,\ 0,\ 1\,), \qquad q_{(a)} = (\,q,\ 0,\ 0,\ 0\,), \tag{11}$$

where q is a function of t to be determined from the field equations. The components v^i can be obtained from $v^i = e^i_{(a)}v^{(a)}$, $e^i_{(a)}\theta^a = dx^i$.

It is given by

$$v^i = (\,0,\ 0,0,\ 1\,), \tag{12}$$

where $x^1 = r$, $x^2 = \theta$, $x^3 = \phi$ and $x^4 = t$. The acceleration vector f_i can be determined as

$$f_i = (\,\alpha\dot{A},\ 0,\ 4m^2\alpha\dot{A},\ 0\,). \tag{13}$$

Using (12) and (13) one can quickly compute μ_{ik}. The non-zero μ_{ik} are given by

$$\mu_{11} = -2A\dot{A}, \qquad \mu_{13} = -8m^2A\dot{A}, \qquad \mu_{33} = -32m^4A\dot{A}. \tag{14}$$

Therefore the tetrad components $\mu_{(ab)} = e^i_{(a)}e^k_{(b)}\mu_{ik}$ can be determined easily. The only surviving $\mu_{(ab)}$ is $\mu_{(11)}$ and is given by

$$\mu_{(11)} = -\frac{2\dot{A}}{A}. \tag{15}$$

We shall use the field equations $R_{ik} - \frac{1}{2}Rg_{ik} + \Lambda g_{ik} = -8\pi T_{ik}$, where T_{ik} are given by (6). It is easy to put these field equations in the tetrad form as

$$\begin{aligned} R_{(ab)} = &-8\pi\left[(\bar{p} + \rho)v_{(a)}v_{(b)} - \frac{1}{2}(\rho - \bar{p} - 2\eta\theta^*)g_{(ab)}\right] \\ &-8\pi\left[q_{(a)}v_{(b)} + q_{(b)}v_{(a)} - \eta\mu_{(ab)}\right] + \Lambda g_{(ab)}, \end{aligned} \tag{16}$$

where $\theta^* = v^i_{;i}$ is the scalar of expansion.

One can compute θ^*, the shear σ and the rotation Ω of the flow vector v^i given by (12). They are determined as

$$\theta^* = \sqrt{3}\sigma = \frac{\dot{A}}{A}, \qquad \Omega = \alpha A \lambda. \tag{17}$$

The results (5), (11), (15), (16) and (17) lead us to the relations

$$8\pi\eta\mu_{(11)} = R_{(11)} - R_{(22)}, \tag{18}$$

$$8\pi q = -R_{(14)}, \tag{19}$$

$$8\pi\bar{p} = \Lambda - \frac{1}{2}\left[R_{(44)} - R_{(11)}\right], \tag{20}$$

$$8\pi\rho = -\Lambda - \frac{1}{2}\left[R_{(11)} + R_{(44)} + 2R_{(22)}\right] \tag{21}$$

3. A solution of the field equations

In the previous Section we have seen that we have a system of four equations (18), (19) (20) and (21) for four unknown parameters η, q the effective pressure $\bar{p}$ and the density ρ. Therefore the metric potential A remains undetermined. In order to obtain an exact solution we have to make one additional appropriate assumption. Let us make a simplifying assumption that A varies as some power of t, i.e. let

$$A = A_0 t^{-a}, \tag{22}$$

where A_0 and a are constants and $a \geq 0$. Obviously, such a solution has a singularity at the beginning $t = 0$. Here one thing should be noted that the coefficient ζ of bulk viscosity is not occurring explicitly in our discussion. Therefore, for simplicity, we assume that $\zeta = 0$.

For the solution (22) the values of the parameters q, η, $\bar{p}$ and ρ are given by

$$8\pi q = -2\alpha\lambda_1^2 A_0^2 t^{-2a}, \tag{23}$$

$$16\pi\eta = \frac{(\alpha^2-1)(a+1)}{t} + \frac{2\lambda_1^2(\alpha^2-2)A_0^2}{at^{2a-1}}, \tag{24}$$

$$8\pi\bar{p} = \Lambda + (\alpha^2-1)\left[\frac{a(a+1)}{t^2} + \frac{\lambda_1^2 A_0^2}{t^{2a}}\right], \tag{25}$$

$$8\pi\rho = -\Lambda + \frac{(3\alpha^2-1)A_0^2\lambda_1^2}{t^{2a}}. \tag{26}$$

If $\Lambda = 0$ and $\alpha^2 \geq 2$, the physical requirements $p \geq 0$ and $\rho > 0$ are satisfied. In this case $\eta > 0$.

We now give a brief discussion of the Raychaudhuri [10] equation,

$$\theta^*_{;i}v^i + \frac{1}{3}\theta^{*2} - f^i_{;i} + 2(\sigma^2 - \Omega^2) = R_{ik}v^iv^k. \tag{27}$$

Now clearly assuming $\Lambda = 0$, $R_{ik}v^iv^k = -4\pi(\rho+3\bar{p}+2\eta\theta^*)$. Therefore the Hawking–Penrose [11] energy conditions are satisfied if $R_{ik}v^iv^k \leq 0$ i.e. $\rho + 3\bar{p} + 2\eta\theta^* \geq 0$. From the above discussion it is easy to see that these conditions are satisfied when $\alpha^2 \geq 2$.

From the results (23), (24), (25) and (26) it is clear that, when $a = 1$, η varies inversely as t and $\bar{p}$, ρ and q vary inversely as t^2.

If we allow a to become negative then taking $a = -1$ and $\alpha^2 = 2$ it is easy to verify that the coefficient η of shear viscosity vanishes, consequently we get a non-static perfect fluid cosmological model with non-zero heat flux. The parameters $\bar{p}$, ρ and q for this solution are given by

$$\begin{aligned} 8\pi\bar{p} &= \Lambda + A_0^2\lambda_1^2t^2, \\ 8\pi\rho &= -\Lambda + 5A_0^2\lambda_1^2t^2, \\ 8\pi q &= \mp 2\sqrt{2}A_0^2\lambda_1^2t^2. \end{aligned} \tag{28}$$

When $\Lambda = 0$, the above parameters $\bar{p}$, ρ, q vary directly as t^2. The geometry of this perfect fluid model with heat flux is given by the line element

$$\begin{aligned} ds^2 = &\left[dt \pm \sqrt{2}A_0t(dr + 4m^2d\phi)\right]^2 \\ &- A_0^2t^2(dr + 4m^2d\phi)^2 - (\operatorname{cosec}^2\theta d\theta^2 + d\phi^2), \end{aligned} \tag{29}$$

where $m(\theta)$ satisfies the differential equation (2).

In the case $a = 1$, $\Lambda = 0$ the equation of state for our solution (22) is given by

$$\frac{\bar{p}}{\rho} = \frac{(\alpha^2 - 1)[2 + \lambda_1^2A_0^2]}{(3\alpha^2 - 1)A_0^2\lambda_1^2}. \tag{30}$$

The kinematic quantities θ^*, σ, Ω and f_i for the solution (22) are given by

$$\begin{aligned} \theta^* &= \sqrt{3}\sigma = -\frac{a}{t}, \qquad \Omega = \frac{\alpha A_0\lambda_1}{t^a}, \\ f_i &= \left(-\frac{\alpha a A_0}{t^{a+1}},\ 0,\ \frac{-4m^2\alpha a A_0}{t^{a+1}},\ 0\right). \end{aligned} \tag{31}$$

As θ^* is negative, our model is contracting. As $f_i \neq 0$, the stream lines of the viscous fluid filling the universe are not geodetic. The model described by the solution (22) has non-zero shear and rotation. The model is filled with a viscous fluid which is not thermalized.

When $a = 0$, we get a stationary rotating perfect-fluid cosmological model with $\alpha^2 = 2$ and non-zero heat flow. In this case p, ρ and q are given by

$$8\pi p = \Lambda + A_0^2\lambda_1^2,$$
$$8\pi\rho = -\Lambda + 5A_0^2\lambda_1^2,$$
$$8\pi q = \mp 2\sqrt{2}\lambda_1^2 A_0^2.$$

The physical requirements $\rho > p \geq 0$ imply the inequality

$$-A_0^2\lambda_1^2 < \Lambda < 5A_0^2\lambda_1^2.$$

For the sake of brevity we shall not give other details of this stationary perfect fluid model with heat flow.

4. Concluding remarks

The metric potential A can be chosen in many ways. We shall briefly describe three such choices of A.

Case (i). Let us assume that

$$\frac{8\pi\rho + \Lambda}{\theta^{*2}} = \text{constant} = \ell^2. \tag{32}$$

Using (21) in (32) we obtain

$$\dot{A}^2 = \frac{(3\alpha^2 - 1)\lambda_1^2 A^4}{\ell^2}, \tag{33}$$

where we have assumed that $3\alpha^2 - 1 > 0$. The parameters η, ρ, q and $\bar{p}$ are given by

$$8\pi\eta = \frac{A\lambda_1\ell}{(3\alpha^2 - 1)^{1/2}}\left[(2 - \alpha^2) - \frac{(\alpha^2 - 1)(3\alpha^2 - 1)}{\ell^2}\right],$$

$$8\pi\rho = -\Lambda + (3\alpha^2 - 1)\lambda_1^2 A^2,$$

$$8\pi q = -2\alpha\lambda_1^2 A^2,$$

$$8\pi\bar{p} = \Lambda - (1 - \alpha^2)A^2\lambda_1^2\left[\frac{2(3\alpha^2 - 1)}{\ell^2} + 1\right].$$

If $\Lambda = 0$, then $\rho > 0$ and $\bar{p} \geq 0$ imply $\alpha^2 > 1$. Here it should be noted that the equation (33) can be solved in terms of elliptic functions. We shall not go into the details here.

Case (ii). Let us assume that $\eta = 0$. With the help of (18), $\eta = 0$ gives

$$\dot{A}^2 = \beta - \frac{\lambda_1^2(\alpha^2 - 2)A^4}{(\alpha^2 - 1)}, \tag{34}$$

where β is a constant of integration. In this case we get a perfect-fluid model with heat flow. The fluid parameters p, ρ and q are found to be

$$8\pi p = \Lambda + A^2\lambda_1^2(3 - \alpha^2),$$
$$8\pi q = -2\alpha\lambda_1^2 A^2,$$
$$8\pi\rho = -\Lambda + A^2\lambda_1^2(3\alpha^2 - 1).$$

If $\Lambda = 0$, then $p \geq 0$ and $\rho > 0$ imply $\frac{1}{3} < \alpha^2 < 3$. Here also the equation (34) can be solved in terms of elliptic functions. For brevity, we shall not give the details here. Putting $\alpha^2 = 2$ here, we get the nonstatic perfect fluid model with heat flow, discussed in the previous Section.

Case (iii). Let us assume that η is proportional to θ. Put

$$\eta = k\theta. \tag{35}$$

The results (17), (18) and (35) lead us to

$$(\alpha^2 - 1)\frac{\ddot{A}}{A} + 16\pi k\frac{\dot{A}^2}{A^2} - 2\lambda_1^2(2 - \alpha^2)A^2 = 0. \tag{36}$$

Assuming $k = \dfrac{1 - \alpha^2}{16\pi}$, the equation (36) can be solved to have the solution $A = A_0 \cos b\bar{t}$, where $b^2 = \dfrac{2\lambda_1^2(2 - \alpha^2)}{(1 - \alpha^2)}$ and $\bar{t}$ is defined dy $d\bar{t} = Adt$. Here we have assumed that either $0 < \alpha^2 < 1$ or $\alpha^2 > 2$. The values of η, q, $\bar{p}$ and ρ are given by

$$8\pi\eta = -\frac{(1 - \alpha^2)}{2} A_0 b \sin b\bar{t},$$
$$8\pi q = -2\alpha A_0^2\lambda_1^2 \cos^2 b\bar{t},$$
$$8\pi\bar{p} = \Lambda + b^2 A_0^2(\alpha^2 - 1)\left[\frac{(1 - \alpha^2)}{2(2 - \alpha^2)} \cos^2 b\bar{t} - \cos 2b\bar{t}\right],$$
$$8\pi\rho = -\Lambda + \frac{A_0^2 b^2(1 - \alpha^2)(3\alpha^2 - 1)}{2(2 - \alpha^2)} \cos^2 b\bar{t}.$$

The details of the above case are also omitted.

The problem of deriving many new Bianchi type II, VIII and IX viscous fluid cosmological models with heat flux is at present under investigation. The results of this investigation will be discussed elsewhere.

References

1. M. Novello and M. J. Reboucas, Astrophys. J., *225*, 719, 1978.
2. D. Ray, J. Math. Phys., *21*, 2797, 1980.
3. M. J. Reboucas and J. A. S. de Lima, J. Math. Phys., *22*, 2699, 1981.
4. M. J. Reboucas, Nuovo Cimento, *67B*, 120, 1982.
5. J. M. Bradley and E. Sviestins, Gen. Relativ. Grav., *16*, 1119, 1984.
6. E. Sviestins, Gen. Relativ. Grav., *17*, 521, 1985.
7. M. J. Reboucas and J. Tiomno, Nuovo Cimento, *90B*, 204, 1985.
8. L. K. Patel and B. M. Pandya, Mathematics Today, *5*, 11, 1987.
9. A. Banerjee, S. R. Duttachaudhuri and A. K. Sanyal, Gen. Relativ. Grav., *18*, 461, 1986.
10. A. K. Raychaudhuri, Phys. Rev., *98*, 1723, 1985.
11. S. Hawking and R. Penrose, Proc. R. Soc., London Ser. A *314*, 529, 1970.

Acta Physica Hungarica 67 (3–4), pp. 305–310 (1990)

EFFECT OF γ-IRRADIATION AND CURRENT DENSITY ON THE ELECTROLUMINESCENCE SPECTRA OF GaP:N

M. MOUNIR

Department of Physics, Faculty of Science, Sana'a University
Sana'a, YAR

(Received in revised form 13 December 1988)

Electroluminescence diodes were grown on single crystal GaP substrates, by liquid phase epitaxy. At low current density, the electroluminescence spectra were no longer green but shifted closer to yellow. The donor–acceptor pair Zn–Te, LO phonon and the exciton line A were dominated at higher AC current density.

The irradiation of GaP:N with γ-rays results in strong quenching of recombination radiation, which reduces the quantum efficiency of the luminescence line spectra at 77 and 300K. No new line spectra are generated by γ-irradiation with doses 10^4 –10^6 Gy.

Introduction

The radiative recombination process via nitrogen isoelectronic trap level in GaP is well studied [1–3]. The electroluminescence studies are important for the fabrication of efficient light emitting diodes (LED's). There is a continued interest in the study of this important sample Ga–N, which is the most useful of all visible semiconductor light sources. Luminescence spectra of excitons bound to single N atoms and to NN_i pairs in nitrogen doped GaP are well known [3–4].

Irradiation of semiconductors with γ-rays changes their luminescence because such irradiation produces point defects such as vacancies, interstitial atoms, vacancy–impurity complexes. Irradiation alters also the recombination mechanisms of deep luminescence centres [5]. The changes in the recombination mechanism of deep luminescence centres may also be observed not only by γ-irradiation but also as a result of deformation, annealing and ion implantation.

The aim of this work is to study the effect of γ-irradiation and current density on the electroluminescence spectra of GaP:N.

Experimental method

Light emitting diodes were grown on single crystal GaP substrates by the method of two layer liquid phase epitaxy in a single process, in the same way as in ref. [1]. The *n*- and *p*-type regions were doped with nitrogen from NH_3 vapour. The concentration of nitrogen in alloy varied between 3×10^{18} and 3×10^{19} cm^{-3}. The *p*-type region was doped with Zn from the vapour using a separate source with

a controlled temperature and the Te donor impurity in the epitaxial n-type region was accidental, with concentrations in the range $(0.8 - 1.0) \times 10^{17}$ cm^{-3}. Light was extracted through the p-region. Electroluminescence spectra were studied using pulsed and DC current injection at 300–77K. LED's were driven in the AC mode by a pulse generator, as the current increased, the voltage pulse width and frequency were decreased to minimize the heating effect.

In the present work the diodes were exposed to γ-irradiation from a ^{60}Co-source with doses 10^4, 10^5 and 10^6 Gy, then they were subjected to systematic studies of luminescence.

Results and discussion

Figure 1 shows a wide electroluminescence band spectrum of double epitaxial GaP:N at 300K. The high emission peak (2.21 eV) depends on the concentration of

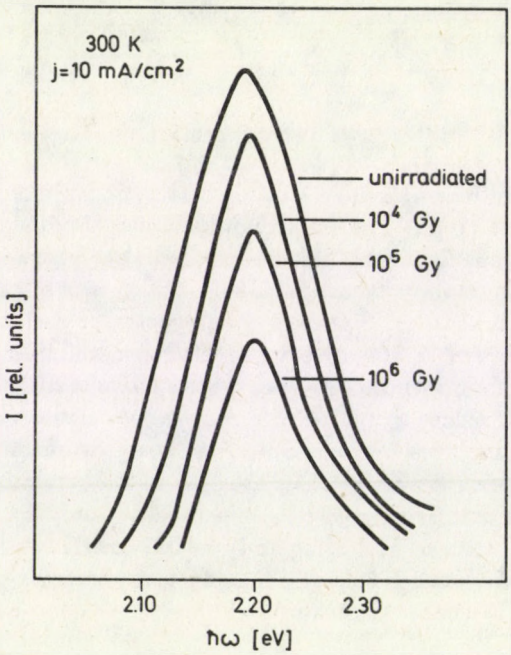

Fig. 1. The electroluminescence spectra of GaP:N at 300K
a) Unirradiated
b) γ-irradiated with doses 10^4 Gy
c) γ-irradiated with doses 10^5 Gy
d) γ-irradiated with doses 10^6 Gy

nitrogen and also on the selective internal absorption of the diode. In the presence of high nitrogen content, the emission of the diode is no longer green but is closer to yellow.

The efficiency of this diode is 0.4 at 10 mA/cm^2. This value is the highest reported under pulsed and DC modes for double epitaxial layer. This efficiency depends on the presence of non-radiative centres, vacancies and defects at p–n junction interface.

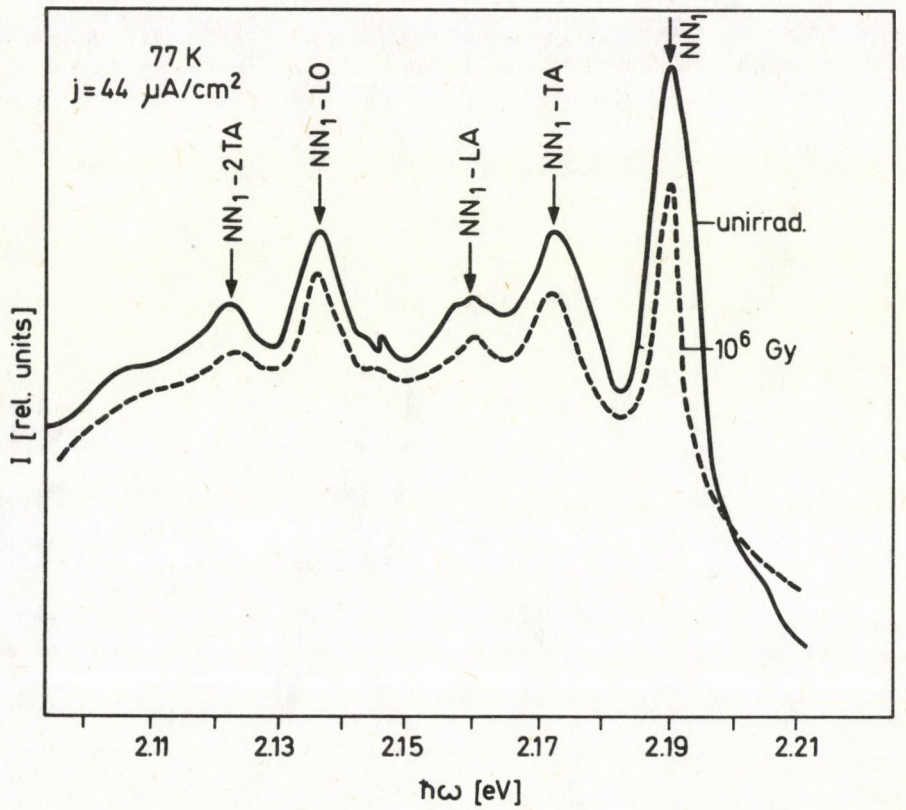

Fig. 2. The electroluminescence spectra of GaP:N at 77K and DC current density 44 μA/cm^2
a) Unirradiated
b) γ-irradiated with doses 10^6 Gy

Prior to irradiation, light emitting diodes were annealed in air for 15 minutes at 50°C. The effect of γ-irradiation at 300K on electroluminescence was shown in Fig. 1, the magnitude of the broad band is reduced without any change in the peak of the band.

Figure 2 shows the electroluminescence spectra at 77K and DC current density ($J = 44\ \mu A/cm^2$), the luminescence dominated by NN_1 exciton line and the phonon replica TA, LA and LO with energies 13, 17 and 49 meV, respectively. The efficiency of the diodes at 77K and DC current density 44 A/cm^2 was 0.1.

Figure 2 shows that the γ-ray doses $> 10^6$ Gy are capable of reducing the internal quantum efficiency η of the luminescence of GaP:N.

The luminescence intensity I is defined by the following equation

$$I = g\eta L, \tag{1}$$

where L is the excitation intensity, η is the internal quantum efficiency and g is the fraction of carriers recombining via luminescence centres. The changes in g are due to the appearance of radiation defects (Ga, P and N vacancies, interstitial atoms,

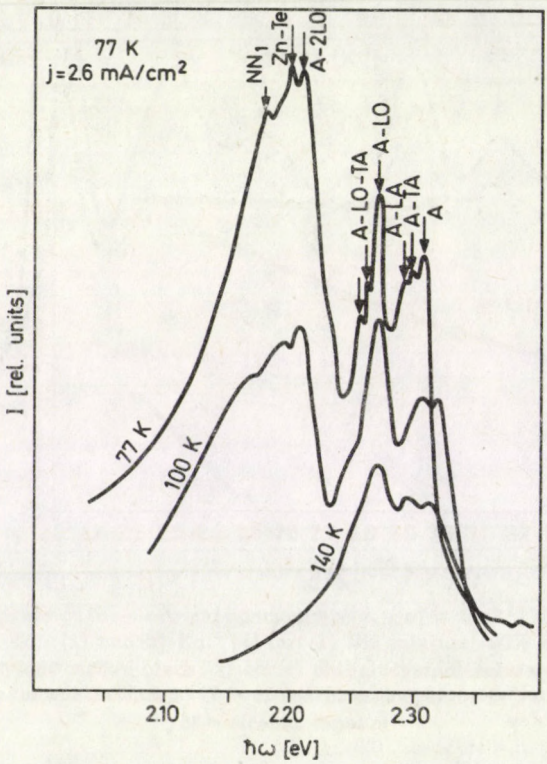

Fig. 3. The electroluminescence spectra of GaP:N at DC current density 2.6 mA/cm^2 and different temperatures: a) 77K b) 100K c) 140K

vacancy complex, etc.) representing radiative and nonradiative recombination centres. The change in η is due to a change in the rate of nonradiative Auger transitions

in the luminescence centres. The internal quantum efficiency is defined by the following equation:

$$\eta = \frac{C_{n1}}{C_{n1} + C_{n2}}, \tag{2}$$

where C_{n1} is the coefficient of radiative centres, C_{n2} is the coefficient of nonradiative centres. This means that the decrease of η is accompanied with an increase in C_{n2} (nonradiative centres). The value of C_{n2} is strongly dependent on the distance between luminescence centres and a defect [6]. The γ-irradiation in semiconductors does not alter the value of n_0, so the luminescence decay time decreases with increasing the doses of γ rays according to the following equation [7]:

$$\tau = \frac{1}{(C_{n1} + C_{n2})n_0} = \frac{\eta}{C_{n1}n_0}. \tag{3}$$

Figure 3 shows the luminescence spectra at different temperatures and current density is 26 mA/cm^2. The luminescence spectra exhibited the familiar recombination lines due to excitons bounded to single nitrogen atoms and to pairs A, NN_1, their phonon replicas and donor–acceptor pair Zn–Te. Figures 2 and 3 shows that the donor-acceptor pair Zn–Te and no phonon exciton line A were dominated at higher current density.

At higher temperature the exciton line NN_1 and Zn–Te were unresolved and the luminescence spectra were shifted toward higher energy.

Conclusions

At higher temperature, high concentration of N and presence of current density, the electroluminescence spectra were no longer green but shifted closer to yellow.

The magnitude of electroluminescence spectra at 300K and 77K were reduced without any change in the peaks and no new line spectra were detectable by irradiation with γ rays.

Formation of radiation defects results in strong quenching of recombination radiation, which reduces the quantum efficiency of the luminescence sources.

The donor–acceptor pair Zn–Te and no phonon line A were dominated at higher AC current density.

Acknowledgements

The author is grateful to A. E. Yunovich for suppling the diodes and to the "Middle East Center for Radio Isotopes" for irradiating the samples.

References

1. M. Mounir, I. K. Lazareva and A. E. Yunovich, Egypt. J. Phys., *12*, 57, 1981.
2. N. R. Nurtdinov and M. Mounir, Sov. Phys. Semicon., *15*, 1210, 1981.
3. M. Mounir and N. R. Nurtdinov, Egypt. J. Sol., *5*, 48, 1984.
4. M. Mounir, N. R. Nurtdinov, R. S. Stegmann and A. E. Yunovich, Sov. Phys. Semicon., *15*, 711, 1981.
5. F. P. Korshunov, G. V. Gatalskii, "Radiation Effects in Semiconductor Devices", (in Russian) Nauka i Tekhnika, Minsk, 1978.
6. E. I. Tolpygo, K. B. Tolpygo and M. K. Sheinkman, Sov. Phys. Semicon., *8*, 326, 1974.
7. V. I. Vovnenko, K. D. Glinchuk and A. V. Prokhorovich, Fiz. Takh. Poluprovodnikov, *11*, 2095, 1977.

Acta Physica Hungarica 67 (3–4), pp. 311–320 (1990)

CONSTRAINTS ON THE STRUCTURE OF RELATIVISTIC CLASSICAL FIELDS

E. COMAY

Raymond and Beverly Sackler Faculty
of Exact Sciences
School of Physics and Astronomy, Tel Aviv University
Tel Aviv 69978, Israel

(Received 15 December 1988)

The equations of motion of relativistic classical linear fields are discussed. It is proved that if some additional postulates are satisfied then the laws of systems of this kind of classical fields are completely analogous to those of classical electrodynamics. Implications on other classical field theories are discussed.

1. Introduction

Classical electrodynamics started as an empirical science where specific laws have followed the accumulation of experimental data. Later, the theoretical work formulated the equations of motion of electromagnetic systems, namely, Maxwell's equations and the Lorentz law of force. The progress of the theoretical side continued and classical electrodynamics has been embedded in special relativity.

This article takes the reverse order of the historical course of events. The validity of special relativity and of some additional postulates is assumed. On this basis it is proved that a relativistic classical linear field theory that satisfies the additional postulates takes the form of classical electrodynamics. Another aspect of this conclusion says that any other relativistic classical field theory must be incompatible with at least one of the additional postulates. Thus, the additional postulates provide constraints on the structure of other relativistic classical fields.

Basic elements of theories discussed here are charges and fields. The precise meaning of these notions is defined in the third Section where the particles equations of motion are derived. These equations of motion together with those of the fields define uniquely the specific theory discussed. As stated above, it is proved in this work that if some additional postulates are adopted, then the classical theory derived agrees formally with classical electrodynamics, namely, the particles equation of motion takes the form of Lorentz law of force and the fields equations of motion take the form of Maxwell equations. These conclusions entail an agreement of the classical theory derived with any specific property of classical electrodynamics. It follows that the derivation of the equations of motion is sufficient for the purpose of the present paper.

Articles discussing interrelations between special relativity and classical electrodynamics have already been published in the literature [1–3]. The present work is different mainly because it makes an extensive use of the linearity requirement. This constraint is not used by most of the previous works which apply other postulates instead. It turns out that linearity is an efficient tool used in the deductive process presented in this paper.

A system of units where the speed of light $c = 1$ is used throughout this article. Greek indices run from 0 to 3 and Latin ones run from 1 to 3. The metric $g^{\mu\nu}$ is diagonal and its elements are $(1, -1, -1, -1)$. $,\nu$ designates the partial differentiation with respect to x^ν. $\mathbf{i}$, $\mathbf{j}$ and $\mathbf{k}$ denote unit vectors of the three dimensional space in the x, y and z-directions, respectively.

The postulates utilized in this work are presented in the second Section. The equations of motion of particles are derived in the third Section. The homogeneous field equations are inferred in the fourth Section. In the fifth Section, the inhomogeneous field equations are deduced. Concluding remarks are the contents of the last Section.

2. Presentation of the postulates

The following postulates are used in the deduction of the results of this article.

(a) It is assumed that special relativity holds.
(b) Particles are classical points, each of which is attributed with two scalar quantities: a self mass m and a charge e [4].
(c) The equations of motion are linear in the fields and in the particles variables.
(d) In an empty space the fields are regular functions of space-time. These functions can be differentiated as many times as required.
(e) Space is homogeneous and isotropic.
(f) The equations of motion conserve parity.
(g) The nonmechanical part of the energy-momentum tensor depends on fields alone.

Later, these postulates are referred to by means of the shorthand notation (a), (b), etc. Special relativity is satisfied when expressions are written in a tensorial form.

3. The particles' equations of motion

A classical particle interacts with the rest of the system when its energy-momentum varies in time. The covariant expression of this process is $dP^\mu/d\tau$ where P^μ denotes the particle's energy-momentum 4-vector and τ is the invariant time. The form of this covariant quantity is discussed in this Section.

The 4-momentum of a particle at rest is $P^\mu = (m, 0, 0, 0)$. Using this expression, one finds

$$2P_\mu \frac{d}{d\tau} P^\mu = \frac{d}{d\tau} P_\mu P^\mu = \frac{d}{d\tau} m^2 = 0. \tag{1}$$

This result proves that $dP^\mu/d\tau$ is orthogonal to P^μ. Using (c) and (1), one finds that $dP^\mu/d\tau$ must depend linearly on P^μ. Therefore, it can be tentatively written as follows

$$\frac{d}{d\tau}P^\mu = G_S^{\mu\nu}P_\nu + G_A^{\mu\nu}P_\nu, \tag{2}$$

where $G_S^{\mu\nu}$ and $G_A^{\mu\nu}$ denote a symmetric and antisymmetric tensor, respectively. The linearity of (2) entails the independence of $G_S^{\mu\nu}$ and $G_A^{\mu\nu}$ of the particle's 4-momentum. The last term of (2) satisfies the orthogonality requirement (1). Therefore, when (2) is substituted into (1), the last term can be dropped and the following expression is obtained

$$G_S^{\mu\nu}P_\mu P_\nu = 0. \tag{3}$$

As stated above, $G_S^{\mu\nu}$ is independent of P^α. Moreover, (3) holds for any value of P^μ. It follows that $G_S^{\mu\nu}$ must vanish identically. Substituting this result into (2), one finds the required expression

$$\frac{d}{d\tau}P^\mu = G_A^{\mu\nu}P_\nu. \tag{4}$$

This expression holds separately for every particle of the system. One may use two scalar quantities of the i'th particle, $m_{(i)}$ and $e_{(i)}$, and define its 4-current

$$J_{(i)}{}^\mu \equiv \frac{e_{(i)}}{m_{(i)}}P^\mu = e_{(i)}V_{(i)}{}^\mu, \tag{5}$$

where $V_{(i)}{}^\mu$ denotes the 4-velocity of the i'th particle. The application of this expression yields the normal form of (4)

$$\frac{d}{d\tau}P_{(i)}{}^\mu = F^{\mu\nu}J_{(i)\nu}, \tag{6}$$

where $F^{\mu\nu}$ is proportional to $G_A^{\mu\nu}$.

Special relativity proves that energy-momentum cannot travel faster than light. Hence, $dP_{(i)}{}^\mu/d\tau$ must depend on the quantities defined at the location $x_{(i)}{}^\alpha$ of the i'th particle. It follows that $F^{\mu\nu}$, which is written in (6), is a function of $x_{(i)}{}^\alpha$. Later, the antisymmetric tensor $F^{\mu\nu}$ is called the fields tensor.

It is shown in this Section that the equations of motion of particles, (6), take the form of the Lorentz law of force. This expression manifests the well known relation between charges and fields as used in classical electrodynamics.

4. The homogeneous fields equations

The tensorial form of the fields is found in the previous Section where it participates in the particles equations of motion. The rest of this work is devoted

to the deduction of the fields equations of motion. This goal is achieved when simple systems of one or two particles are examined.

Consider the fields tensor of a system of a single particle Q which is motionless at the origin. This system is time-independent. Lorentz transformations that leave the system invariant are considered in the following lines. It is well known that under these transformations, the quantities F^{0i} transform like a polar vector (in the three dimensional space) and the quantities F^{jk} transform like an axial vector. The notation of electrodynamics is borrowed for these vectors and $F^{\mu\nu}$ is written in the following form

$$F^{\mu\nu} = \begin{bmatrix} 0 & -E_x & -E_y & -E_z \\ E_x & 0 & -B_z & B_y \\ E_y & B_z & 0 & -B_x \\ E_z & -B_y & B_x & 0 \end{bmatrix}. \tag{7}$$

It should be emphasized that the quantities $\mathbf{E}$ and $\mathbf{B}$ in (7) are just notations and no equations of motion are imposed on them. On the contrary, by means of the postulates presented in the second Section, the fields equations of motion are deduced.

Consider the vector field $\mathbf{E}$ of Q at $\mathbf{r}_1 = (1,0,0)$. The system is invariant under a rotation around the x-axis. Hence, $\mathbf{E}$ is a radial vector. The same result is obtained also for the axial vector $\mathbf{B}$. It is proved in the following lines that an axial vector of this kind vanishes identically.

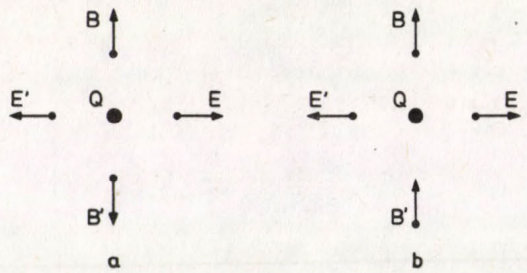

Fig. 1. (a) Given a charge Q at the origin, a radial polar vector $\mathbf{E}(\mathbf{r}_1)$ at $\mathbf{r}_1 = (1,0,0)$ and a radial axial vector $\mathbf{B}(\mathbf{r}_2)$ at $\mathbf{r}_2 = (0,1,0)$. The vectors $\mathbf{E}'(\mathbf{r}'_1)$ and $\mathbf{B}'(\mathbf{r}'_2)$ are obtained from a rotation by π around the z-axis

(b) Given the original vectors $\mathbf{E}$ and $\mathbf{B}$ of (a) and the results $\mathbf{E}'$ and $\mathbf{B}'$ obtained from a parity transformation

Next, consider a rotation by π around the z-axis that transforms $\mathbf{r}_1$ into $\mathbf{r}'_1 = (-1,0,0)$ and $\mathbf{r}_2 = (0,1,0)$ into $\mathbf{r}'_2 = (0,-1,0)$ (see Fig. 1a). This rotation leaves the system invariant and, due to (e), the vectors $\mathbf{E}$ at $\mathbf{r}_1$ and $\mathbf{B}$ at $\mathbf{r}_2$ are transformed continuously to their final values at $\mathbf{r}'_1$ and $\mathbf{r}'_2$, respectively, as depicted in Fig. 1a.

These quantities are compared with the results of a parity transformation. The origin, where the charge is located, is invariant under this transformation. Using (e) and (f), one finds the results depicted in Fig. 1b. In the two transformations, the vectors $\mathbf{r}_1$ and $\mathbf{r}_2$ transform to $\mathbf{r}'_1$ and $\mathbf{r}'_2$, respectively. Similarly, the polar vector $\mathbf{E}(\mathbf{r}_1)$ goes to $\mathbf{E}'(\mathbf{r}'_1)$ and takes precisely the same value in the two cases. On the other hand, the values of the axial vector $\mathbf{B}'(\mathbf{r}_2)$ takes opposite signs in the two kinds of transformations discussed above. This result can happen only if the axial vector part of the fields tensor of a motionless particle vanishes identically.

Another conclusion of the invariance under rotations is that the size of the polar vector field of a motionless particle at the origin depends just on the radial coordinate r. All these results can be written as follows

$$\mathbf{E}(\mathbf{r}) = \psi(r)\mathbf{r}, \tag{8}$$

$$\mathbf{B}(\mathbf{r}) = 0. \tag{9}$$

The form of (8) indicates that, for a motionless charge, one can define a scalar function $\phi(r)$ in the three dimensional space which depends on the radial coordinate r. This function satisfies

$$\mathbf{E}(\mathbf{r}) = -\text{grad}\ \phi(r). \tag{10}$$

This result can be put in a covariant form when an auxiliary 4-vector A_μ is defined in the particle's rest frame

$$A_\mu = (\phi, 0, 0, 0). \tag{11}$$

An antisymmetric fields tensor is defined by means of (11)

$$F_{\mu\nu} = A_{\nu,\mu} - A_{\mu,\nu}. \tag{12}$$

It is clear that, in the particle's rest frame, the substitution of (8) and (9) into (7) yields a result that agrees with the one obtained from the substitution of (10) and (11) into (12). Hence, the two tensors agree in all frames and the tensor (12) is unique.

The expression (12) of the fields tensor renders the required equations of motion. Performing an appropriate differentiation, one finds

$$F_{\mu\nu,\lambda} + F_{\nu\lambda,\mu} + F_{\lambda\mu,\nu} = 0. \tag{13}$$

These are the homogeneous fields equations. They are formally identical to the homogeneous pair of Maxwell equations.

5. The inhomogeneous fields equations

It is proved in this Section that the postulates (a)–(g) yield another set of field equations. For this purpose, let us consider a system of two particles (see

Fig 2). The mass of these particles is finite and their charge is infinitesimal. Hence, using (6), one finds that particles of this kind exchange (at an infinitesimal rate) energy-momentum while each of them stays in its original inertial frame.

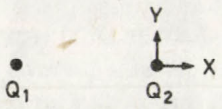

Fig. 2. Two infinitesimally charged particles at rest. $Q_{(1)}$ is at $(-s,0,0)$ and $Q_{(2)}$ is at the origin

The linearity (c) of the system indicates that the overall field tensor can be separated into a sum of tensors, each of which is associated with one of the particles and every tensor included in this sum satisfies the equations of motion. In the case of Fig. 2, the fields related to $Q_{(1)}$ exert force on $Q_{(2)}$ and vice-versa. Hence, each of the particles gains momentum at a certain rate. The particles are static and the fields do not vary in time. It follows that the sum of the rates of the momenta gained by the two particles vanishes. Using (6), one finds that the following relation expresses these results

$$\frac{dP_{(1)}{}^{\mu}}{d\tau} + \frac{dP_{(2)}{}^{\mu}}{d\tau} = F_{(2)}{}^{\mu\nu} J_{(1)\nu} + F_{(1)}{}^{\mu\nu} J_{(2)\nu} = 0, \tag{14}$$

where the subscripts in parentheses denote quantities associated with the corresponding particle.

The definition (5) of $J_{(i)}{}^{\mu}$ shows that it is proportional to $Q_{(i)}$. This property together with (8) and (14) prove that $F_{(i)}{}^{\mu\nu}$ must be proportional to $Q_{(i)}$. This relation is in accordance with the linearity (c) of the system.

Special relativity shows that energy-momentum cannot travel faster than light. Hence, the position of energy-momentum is a continuous function of time. This result, together with the variation of the particles' momentum, are compatible if a momentum current exists in the medium between the two particles. It is well known that the momentum current consists of the i,j entries of the energy-momentum tensor [5, 6]. According to (g), this quantity is a function of the fields. The dependence (6) of the momentum transferred to the particles, is linear in the fields. Considering (14), one finds that we are interested in that part of the energy-momentum tensor which is a bilinear function of $F_{(1)}{}^{\mu\nu}$ and $F_{(2)}{}^{\mu\nu}$. (In other words, we look for the interaction part of the energy-momentum tensor and not for the part that depends on fields of a single particle.) Moreover, the two particles play a symmetric role in the theory. All these requirements are satisfied if the required tensor is a bilinear symmetric function of the fields.

The previous analysis shows that the energy-momentum tensor of the fields can be written tentatively in the following form

$$\begin{aligned} T^{\mu\nu} =& a\left(F_{(1)}{}^{\mu\alpha}F_{(2)}{}^{\beta\nu} + F_{(2)}{}^{\mu\alpha}F_{(1)}{}^{\beta\nu}\right) g_{\alpha\beta} + bF_{(1)\alpha\beta}F_{(2)}{}^{\alpha\beta}g^{\mu\nu} + \\ &+ d\epsilon_{\alpha\beta\gamma\delta}\left(F_{(1)}{}^{\mu\alpha}F_{(2)}{}^{\beta\nu} + F_{(2)}{}^{\mu\alpha}F_{(1)}{}^{\beta\nu}\right) g^{\gamma\delta} + \\ &+ h\epsilon_{\alpha\beta\gamma\delta}F_{(1)}{}^{\alpha\beta}F_{(2)}{}^{\gamma\delta}g^{\mu\nu}, \end{aligned} \tag{15}$$

where $\epsilon_{\alpha\beta\gamma\delta}$ denotes the completely antisymmetric unit tensor of the fourth rank and a, b, d and h are yet undetermined coefficients. The third term of (15) vanishes identically because it contains a contraction of the completely antisymmetric tensor $\epsilon_{\alpha\beta\gamma\delta}$ with the symmetric tensor $g^{\gamma\delta}$. Consider the parity of the fields. Remembering that, in the three dimensional space, **E** is a vector and **B** is an axial vector, one finds after a straightforward calculation that the last term of (15) and the first two ones have opposite parities. Therefore, due to (f), the required tensor is a sum of the first two terms or it consists of just the last one. However, in the rest frame of the two particles (8) and (9) hold. As a result, the last term, whose components are bilinear in **E** and **B**, vanishes identically and can also be omitted from the expression. This discussion proves that the required energy-momentum tensor takes the form

$$T^{\mu\nu} = a\left(F_{(1)}{}^{\mu\alpha}F_{(2)}{}^{\beta\nu} + F_{(2)}{}^{\mu\alpha}F_{(1)}{}^{\beta\nu}\right)g_{\alpha\beta} + bF_{(1)\alpha\beta}F_{(2)}{}^{\alpha\beta}g^{\mu\nu}. \tag{16}$$

Using (8) and (9) for the two motionless particles considered here and the linear dependence of the fields on the charges, one can write the fields tensors of the two particles in the following forms

$$F_{(1)}{}^{\mu\nu} = Q_{(1)}f(|\mathbf{r}+s\mathbf{i}|)\begin{bmatrix} 0 & -x-s & -y & -z \\ x+s & 0 & 0 & 0 \\ y & 0 & 0 & 0 \\ z & 0 & 0 & 0 \end{bmatrix}, \tag{17}$$

$$F_{(2)}{}^{\mu\nu} = Q_{(2)}f(r)\begin{bmatrix} 0 & -x & -y & -z \\ x & 0 & 0 & 0 \\ y & 0 & 0 & 0 \\ z & 0 & 0 & 0 \end{bmatrix}. \tag{18}$$

T^{1j} are the components of the momentum flux in the x-direction. Applying (16), (17) and (18), one finds the following expression for this 3-vector

$$\begin{aligned} T^{1j} =& Q_{(1)}Q_{(2)}f(|\mathbf{r}+s\mathbf{i}|)f(r) \\ & \left[2a(x^2+sx)+2b(r^2+sx),\ a(2xy+ys),\ a(2xz+zs)\right]. \end{aligned} \tag{19}$$

The static situation and the conservation of momentum entail the divergenceless of (19) at every point which is free of charge. Therefore

$$\begin{aligned} \frac{1}{Q_{(1)}Q_{(2)}}T^{1j}{}_{,j} =& f(|\mathbf{r}+s\mathbf{i}|)f(r)\left[4a(2x+s)+2b(2x+s)\right]+ \\ & + r^{-1}f(|\mathbf{r}+s\mathbf{i}|)f'(r)\left[a[2xr^2+s(r^2+x^2)]+2bx(r^2+sx)\right]+ \\ & + |\mathbf{r}+s\mathbf{i}|^{-1}f'(|\mathbf{r}+s\mathbf{i}|)f(r) \\ & \left[a\{2x(s+x)^2+(y^2+z^2)(s+2x)\}+2b(r^2+sx)(s+x)\right]= \\ =& 0. \end{aligned} \tag{20}$$

This expression can be evaluated in the vincinity of the origin where $r \ll s$. It follows that terms containing higher powers of x, y and z can be ignored. Therefore, (20) reduces to

$$f(s)f(r)s(4a+2b)+r^{-1}f(s)f'(r)s[x^2(a+2b)+ar^2]=0. \tag{21}$$

This equation can be divided into two parts, one of which consists of terms depending on r alone and the other one contains terms depending on r and on x. It is evident that each of these parts must vanish. The terms depending on x vanish if the following relation holds

$$b=-\frac{1}{2}a. \tag{22}$$

The substitution of this relation into (21) entails

$$3f(r)+rf'(r)=0. \tag{23}$$

Hence,

$$f(r)=c/r^3, \tag{24}$$

where c denotes a yet undetermined constant.

Using (18) and (24), one finds the following expression for the polar field

$$\mathbf{E}_{(2)}(\mathbf{r})=Q_{(2)}c\mathbf{r}/r^3. \tag{25}$$

The values of the constants a and c are derived from the following requirement: the integration of the momentum current (19) over the surface of a tiny sphere around the origin should balance the rate (6) of momentum transferred to $Q_{(2)}$. These mathematical operations are well known from classical electrodynamics. Using appropriate units, one finds the following values: $c=1$ and $a=1/4\pi$. Hence, in the rest frame of a charge $Q_{(2)}$ which is located at the origin, the fields tensor associated with this charge takes the following form

$$F_{(2)}{}^{\mu\nu}=\frac{Q_{(2)}}{r^3}\begin{bmatrix}0 & -x & -y & -z\\ x & 0 & 0 & 0\\ y & 0 & 0 & 0\\ z & 0 & 0 & 0\end{bmatrix}. \tag{26}$$

The last results hold in the vicinity of the origin. Therefore, the general form of $f(r)$ can be written as follows

$$f(r)=\frac{g(r)}{r^3}, \tag{27}$$

where

$$\lim_{r\to 0} g(r)=1. \tag{28}$$

Substituting (27) into (20) and examining terms of the next power of x, y and z, one finds after a straightforward calculation that (20) holds if

$$g'(r) = 0. \tag{29}$$

This equation, together with (28), prove that $g(r) \equiv 1$ and the inverse square law (26) holds throughout the entire space.

The fields tensor (26) satisfies the following equations

$$F_{(2)}{}^{\mu i}{}_{,i} = -4\pi Q_{(2)}\delta^{\mu}{}_{0} = -4\pi J^{\mu}. \tag{30}$$

As stated above, (30) holds in the particle's rest frame. This equation can be put in a covariant form

$$F^{\mu\nu}{}_{,\nu} = -4\pi J^{\mu}. \tag{31}$$

Indeed, it can be easily seen that (31) reduces to (30) in the static case.

These field equations take the form of the inhomogeneous pair of Maxwell equations. Another result of the analysis carried out above is that the substitution of the constant $a = 1/4\pi$ and $b = -1/8\pi$ into (16) proves that the energy-momentum tensor written above agrees with the interaction part of the well known energy-momentum tensor of electromagnetic fields.

6. Concluding remarks

The compatibility of classical electrodynamics with special relativity is well known. It is proved in this work that the postulates presented in the second Section are sufficient conditions for the conformity of a classical field theory with the structure of classical electrodynamics. However, no claim is made here concerning the uniqueness of these postulates or that they are a minimal set that yields the results derived above.

The derivation of the two sets of fields equations relies on different postulates. The homogeneous fields equations stem from the symmetries of a one particle system. On the other hand, the inhomogeneous fields equations emerge from the dynamical properties of a two particle system. It is well known that the homogeneous Maxwell equation (13) can be put in a form which is very similar to (31) $F^{*\mu\nu}{}_{,\nu} = 0$ where $F^{*\mu\nu} = \frac{1}{2}\epsilon^{\mu\nu\alpha\beta}g_{\alpha\gamma}g_{\beta\delta}F^{\gamma\delta}$. The analysis carried out above shows that, in spite of their similar form, the homogeneous equations and the inhomogeneous ones have different physical foundations.

This work shows also that any other classical field theory must violate at least one of the postulates (a)–(g). Thus, for example, general relativity is a nonlinear theory; the Proca fields [7] are associated with an energy-momentum tensor which is a function of the field and of the potential as well; Yang–Mills fields (except $U(1)$ whose form is identical to classical electrodynamics) use more than one kind of charge and their equations of motion are nonlinear.

The previous examples of other field theories illuminate one more aspect of the analysis carried out in the present work. It is stated above that the postulates (a)–(g) are not unique and that classical electrodynamics can be derived from different sets of postulates. The examples of other field theories which do not satisfy one specific postulate of (a)–(g) (henceforth called (i)), indicate that (i) is essential in the following sense. Consider a different set of postulates from which classical electrodynamics emerges uniquely. In view of the other field theories, one finds that (i) is (at least implicitly) included in the different set. This result holds if the order of argument can be reversed. Thus, for example, one can reverse the analysis carried out in Section 5 and derive (g) from the Coulomb law. Evidently, either (g) or the Coulomb law exclude Proca fields.

The significance of using additional postulates, beside special relativity, in a derivation of classical electrodynamics is discussed in the literature [8, 9]. The analysis carried out in the present work is a realization of this point. It shows the explicit role of every postulate formulated in the second Section.

The foregoing discussion depends upon pure theoretical arguments. However, there is another property required for the establishment of a physical theory, namely the fit to experiment. It is this criterion which makes the distinction between physics and mathematics. It enables one to select well established classical field theories while other formulations remain merely as hypothetical candidates.

References

1. D. H. Frisch and L. Wilets, Am. J. Phys., *24*, 574, 1956.
2. J. R. Tessman, Am. J. Phys., *34*, 1048, 1966.
3. D. H. Kobe, Am. J. Phys., *54*, 631, 1986 and references therein.
4. L. D. Landau and E. M. Lifshitz, The Classical Theory of Fields, Pergamon, Oxford, 1975, pp. 43–44.
5. J. D. Jackson, Classical Electrodynamics, John Wiley, New York, 1975, p. 605.
6. See ref. [4], pp. 77–80.
7. See ref. [5], pp. 598–599.
8. R. P. Feynman, R. B. Leighton and M. Sands, The Feynman Lectures on Physics, Addison-Wesley, Reading, Mass., 1964, Vol. 2, p. 26–2.
9. See ref. [5], pp. 578–581.

Acta Physica Hungarica 67 (3–4), pp. 321–340 (1990)

PHENOMENOLOGICAL THERMODYNAMICS OF IRREVERSIBLE PROCESSES WITHIN LAGRANGE FORMALISM*

K. -H. ANTHONY

Paderborn University
Theoretical Physics
D-4790 Paderborn, W-Germany

(Received 20 December 1988)

Lagrange formalism allows for phenomenological thermodynamics of irreversible processes. This statement is exemplified for heat transport, diffusion and chemical reactions. Traditional formulations of thermodynamics can be included into Lagrange formalism. However, Lagrange formalism goes beyond the scope of traditional thermodynamics. By means of this most general field theoretical approach a unified phenomenological theory of material behaviour including thermodynamics, mechanics and electromagnetism might be obtained. In this paper the skeleton of the theory concerning thermodynamics is briefly reported.

1. Introduction

Phenomenological thermodynamics of irreversible processes (TIP) can be included into Lagrange formalism (LF). Along this line a methodical unification of thermodynamics and various other theories of matter such as continuum mechanics, defect mechanics and electromagnetism may be obtained giving thus rise to a complete and unified phenomenological theory of material behaviour. So far the phenomena of heat transport, diffusion and chemical reactions are described by means of LF [1, 2, 3]. Generalizing the concept of chemical reactions to the dynamics of point-like defects in ordered materials the theory may be applied to the dynamics of disordered materials, too [3]. As an example I refer to lattice vacancies, interstitial atoms, electronically excited atoms and their reactions, creation, annihilation and migration. LF, describing quite generally an unrestricted dynamics, allows for thermodynamical processes outside of local equilibrium [4]. In this respect it goes beyond the scope of traditional theories of TIP which operate more or less in the neighbourhood of local equilibrium depending on the particular constitutive relations [5–8]. However, as a first step the physically very successful traditional theories of TIP have to be incorporated into LF. Starting from this basement, LF may then be generalized for those processes which run outside of local equilibrium.

In LF [9–12] all information concerning the processes of a system is comprised into only one scalar function

*This paper is cordially dedicated to Academician I. Gyarmati on the occasion of his 60-th birthday.

$$\ell = \ell(\psi, \partial\psi), \tag{1}$$

which is called the Lagrange-density function or the *Lagrangian* of the system. Thus the whole theory starts from the smallest possible entity. ψ represents the total set

$$P = \{\psi_i(x,t), \quad i = 1, \ldots, f\} \tag{2}$$

of *fundamental field variables* of the system and ∂ the set of all differential operators with respect to time t and space coordinates $x = (x^1, x^2, x^3)$:

$$\partial = \{\partial_t = \frac{\partial}{\partial t}, \quad \partial_\alpha = \frac{\partial}{\partial x^\alpha}, \quad \alpha = 1,2,3\}. \tag{3}$$

P defines the processes of the system. The Lagrangian depending on the variables ψ and its first order derivatives only results in a first order LF which is sufficient for my actual intentions. Being not explicitly dependent on the space and time coordinates x and t, the Lagrangian (1) is associated with *closed systems* only, i.e. the systems suffer no physical fields from outside. The Lagrangian is the kernel of the *action integral*

$$J_1 = \int_{t_1}^{t_2} \int_V \ell(\psi, \partial\psi)\, d^3x\, dt, \tag{4}$$

which is associated with processes of the system taking place in the spatial region V (= constant for simplicity) during the fixed time interval $[t_1, t_2]$. Among all admissible processes the real processes are distinguished as solutions of *Hamilton's Variational Principle*:

$J_1 =$ extremum (5)
by *free* and independent variation of all fields $\psi_i(x,t)$ in V with fixed values at the beginning and the end of the process:

$$\delta\psi_i(x, t_{1,2}) = 0. \tag{6}$$

Variations at the boundary ∂V are included depending on the particular physics at the boundary.

It should be mentioned that TIP here really starts from Hamilton's Principle in its original sense. This contrasts with the situation in traditional theories of TIP where a lot of variational principles have been established [13–15]. Sometimes these are even called Hamilton's Principles. But they altogether are only quasi-variational principles in so far as the variations suffer from constraints in some way.

Once the Lagrangian is given all characteristics of the system are developed on the ground of Hamilton's Principle and using the well-established methods of LF. For instance *all balance* and *all constitutive equations* which both are associated

with *universal invariance requirements* for the Lagrangian are derived by means of Noether's theorem [16]. This gives specially rise to the *First Law of Thermodynamics*. As a remarkable fact the concept of *entropy* and the *Second Law of Thermodynamics* is also a natural outcome of LF. It is associated with gauge invariance of the Lagrangian according to *complex-valued fundamental field variables in TIP*. The entropy concept is closely related with a *dynamical stability theory* in the sense of Ljapunov's direct method [17, 18], which itself can be established within LF [19]. Finally it is another remarkable fact, that a most general *Principle of Least Entropy Production* can be established in LF. This Principle includes a traditional principle [5, 20] which in the literature is given for the restricted case of the stationary, linear and scalar processes only (linear heat transport and diffusion).

In addition to its fundamental significance LF may be of great importance for numerically solving of complicated initial and boundary value problems in TIP: Hamilton's Principle may be solved by means of Ritz's direct method.

The purpose of this communication is to give an idea of LF as applied to TIP. So I restrict myself to the skeleton of the theory and a few exemplifications. For details and for an extensive presentation of the motivation I refer to other publications [1–4, 12, 19].

2. Basic ideas

TIP as described by LF is based on a set of *complex-valued field variables*:

- The *field of thermal excitation* $\psi(x,t)$ defines together with its complex conjugate $\psi^*(x,t)$ the *absolute temperature* $T(x,t)$:

$$\psi^*(x,t)\cdot\psi(x,t) = T(x,t) \geq 0. \tag{7}$$

  ψ gets a qualitative interpretation by the following statement: Whereever and whenever there is no thermal excitation ($\psi = 0$) the material is found at the absolute zero temperature ($T = 0$) and vice versa. By definition the absolute temperature is positive definite as it should be. A finite temperature $T > 0$ is associated with thermal excitation ($\psi \neq 0$).
- Concerning diffusion I introduce a *matter field* $\Phi(x,t)$ which by

$$\Phi^*(x,t)\cdot\Phi(x,t) = n(x,t) \geq 0 \tag{8}$$

  defines the *mass* or *particle density* $n(x,t)$. Because of its positive definiteness the "vacuum" $n = 0$ is associated with the absence of diffusing material: $\Phi = 0$.
- In the case of a multicomponent system of N diffusing and chemically reacting constituents $S_1, \ldots, S_N$ a *multicomponent matter field*

$$\boldsymbol{\Phi}(x,t) = \{\Phi_1(x,t), \ldots, \Phi_N(x,t)\} \tag{9}$$

is introduced which by

$$\begin{aligned}\Phi^*(x,t)\cdot\Phi(x,t) &= \Phi_1^*(x,t)\cdot\Phi_1(x,t)+\cdots+\Phi_N^*(x,t)\cdot\Phi_N(x,t)= \\ &= n_1(x,t)+\cdots+n_N(x,t)=n(x,t)\geq 0\end{aligned} \tag{10}$$

defines the *total mass density* n by summing-up of the *partial mass densities* n_k.

As compared with traditional TIP the introduction of complex-valued fields means a doubling of the set of real valued, fundamental field variables. The usual variables T and n_k are supplemented by the *phase function* $\varphi(x,t)$ of the thermal excitation field and by the phase functions $\varphi_k(x,t)$ of the matter fields giving thus rise to the concepts of a *thermal excitation wave*

$$\psi(x,t)=\sqrt{T(x,t)}\,\mathrm{e}^{\mathrm{i}\varphi(x,t)} \tag{11}$$

and of *matter waves*

$$\Phi_k(x,t)=\sqrt{n_k(x,t)}\,\mathrm{e}^{\mathrm{i}\varphi_k(x,t)},\qquad k=1,\ldots,N. \tag{12}$$

These waves are physically associated with the *irreversible processes heat transport, diffusion and chemical reactions*. The doubling of the set of variables is necessary for the existence of a Lagrangian in TIP: LF fails in traditional TIP because of the non-selfadjointness of its fundamental field equations [21, 22].

The physical interpretation of the phase functions φ and φ_k gets apparent at a higher stage of the theory: These degrees of freedom are associated with *deviations of the processes from local equilibrium.*

The Lagrangian for the combined process "heat transport, diffusion and chemical reactions" depends on the excitation field $\Psi(x,t)$, on all matter fields $\Phi_k(x,t)$ and on its respective complex conjugates $\Psi^*(x,t)$ and $\Phi_k^*(x,t)$. Equally well it can be defined as a function of the real-valued fields $T(x,t)$, $n_k(x,t)$, $\varphi(x,t)$ and $\varphi_k(x,t)$:

$$\ell=\ell(\Psi,\Psi^*,\Phi_k,\Phi_k^*,\partial\Psi,\partial\Psi^*,\partial\Phi_k,\partial\Phi_k^*,\quad k=1,\ldots,N) \tag{13}$$

$$=\ell(T,n_k,\varphi,\varphi_k,\partial T,\partial n_k,\partial\varphi,\partial\varphi_k,\quad k=1,\ldots,N). \tag{14}$$

Each of these representations has its own merit. The variation in Hamilton's Principle applies to all fields Ψ, Φ_k and Ψ^*, Φ_k^* independently or to T, n_k, φ, φ_k in the respective cases (13) or (14).

The analytical form of the Lagrangian has to fulfil several constraints:

1. ℓ is real-valued.
2. The physical dimension of ℓ has to be "energy density".
3. ℓ fulfils various universal invariance requirements (see Chs 5, 6).
4. ℓ is not invariant with respect to time-reversal.
5. For chemical reactions the microscopically motivated chemical *Principle of Multiple Proportions* has to be taken into account by suitably coupling of the fields Ψ and Φ_k, $k=1,\ldots,N$.
6. The traditional theories of TIP must be incorporated into ℓ.

These constraints are motivated in the following way:

ad 1 and 2: J_1 from Eq. (4) has to be the physical quantity "action". I am dealing with Hamilton's Principle in its original sense.

ad 1, 2, 3: TIP will be methodically unified with those partial material theories which already are incorporated in LF.

ad 4: Thermodynamical processes are irreversible.

ad 5: A phenomenological macroscopic theory has to take care of the microscopic structure of the processes, e.g. of the atomic structure in the case of chemical reactions.

ad 6: Successful traditional theories of TIP serve as a basis for further extensions of the Lagrangian beyond the scope of traditional theories. By the way a unification of traditional TIP by means of LF already has its own worth.

3. Examples for the Lagrangian

The following examples will be taken for illustration of the subsequent considerations. They will be quoted as "examples I and II".

I. Pure heat transport in a rigid body [1, 2]

The thermal excitation field $\Psi(x,t)$ is the only fundamental variable. The Lagrangian

$$\begin{aligned}\ell = &- c\overset{\downarrow}{\Psi}\overset{\downarrow}{\Psi}^* - \\ &- \frac{c}{\omega}\left[\frac{1}{2i}(\overset{\downarrow}{\Psi}^*\partial_t\overset{\downarrow}{\Psi} - \Psi\partial_t\Psi^*) + \frac{1}{2}\,\frac{\ln\dfrac{\Psi\Psi^*}{T_0}}{\dfrac{\Psi\Psi^*}{T_0}}\partial_t(\Psi\Psi^*)\right] + \\ &+ \sum_{\alpha,\beta=1}^{3}\frac{\lambda^{\overset{\downarrow}{\alpha}\overset{\downarrow}{\beta}}}{\omega}\left[\frac{1}{2i}\{(\Psi^*\partial_\alpha\Psi)(\Psi^*\partial_\beta\Psi) - (\Psi\partial_\alpha\Psi^*)(\Psi\partial_\beta\Psi^*)\} + \right. \\ &\left. + \frac{T_0}{2(\Psi\Psi^*)^2}\partial_\alpha(\Psi\Psi^*)\partial_\beta(\Psi\Psi^*)\right]\end{aligned} \tag{15}$$

being of the form (13) reproduces the traditional linear theory of heat transport [5, 6] which will get apparent subsequently. c and $\boldsymbol{\lambda} = (\lambda^{\alpha\beta})$ are the specific heat and the tensor of heat conductivity coefficients, respectively. Here they are assumed to be constant. T_0 is a reference temperature and ω a frequency which is introduced for dimensional reasons. The physical meaning of ω is not yet clarified. In the case

of pure heat transport it is irrelevant. However, I suppose that it can be associated with the material background which is assumed to be rigid in our examples, i.e. the quantity ω will get essential in the case of deformable bodies.

The ansatz (15) fulfils the requirements 1.–6. of Ch. 2. The three different arrows mark the following properties:

$\Rightarrow$: irreversibility,

$\rightarrow$: gauge invariance of ℓ, (substitute Ψ by $\Psi e^{i\varepsilon}$).

$\rightarrow$: the tensor λ is symmetric (*Onsagers reciprocity relation*).

The alternative representation (14) of the Lagrangian reads

$$\ell = -\frac{1}{\omega}\left[cT\partial_t(\varphi - \varphi_0(t,T)) + (-\lambda\cdot\nabla T)\cdot\nabla(\varphi - \varphi_0(t,T)) + \partial_t G(T)\right] \tag{16}$$

with the abbreviations

$$\varphi_0(t,T) = -\omega t + \frac{T_0}{2T}, \tag{17}$$

$$G(T) = \frac{T_0}{2T}\int\limits_{\frac{T}{T_0}}^{1}\frac{p(\xi T)}{\xi^2}\,d\xi. \tag{18}$$

$p(T)$ is the hydrostatic pressure of local equilibrium which in our examples must be regarded as a rigid body reaction of the rigid material background (see Eq. (26)). Due to gauge invariance the phase function $\varphi(x,t)$ does not enter explicitly into (16) but by its derivatives only.

II. Heat transport + diffusion + chemical reaction in a rigid body [3]

In the representation (14) these combined processes are described by the Lagrangian

$$\begin{aligned}\ell = -\frac{1}{\omega}\Big\{&u(T,n_k)\;\partial_t\left[\varphi - \varphi_0(t,T)\right] + \sum_{i=1}^{N} n_i\partial_t\left[\mu_i(T,n_k)\alpha_i\right]\\ &+ \mathbf{J}(T,n_k,\nabla T,\nabla n_k)\cdot\nabla\left[\varphi - \varphi_0(\ldots)\right] + \sum_{i=1}^{N}\mathbf{J}_i(T,n_k,\nabla T,\nabla n_k)\cdot\nabla\left[\mu_i(\ldots)\alpha_i\right] +\\ &+ R(T,n_k,\alpha_k) + \partial_t G(T,n_k)\Big\}\end{aligned} \tag{19}$$

with the abbreviations

$$\varphi_0(t,T) = -\omega t + \frac{T_0}{2T}, \tag{20}$$

$$\varphi_{i0}(t,T,n_i) = -\omega t + \gamma\,\frac{n_i}{2T}, \tag{21}$$

(γ is a dimensional constant),

$$\alpha_i = (\varphi_i - \varphi) - (\varphi_{i0}(t, T, n_i) - \varphi_0(t, T)), \tag{22}$$

$$G(T, n_k) = \frac{T_0}{2T} \int_{\frac{T_0}{T}}^{1} \frac{p(\xi T, \xi n_k)}{\xi^2}\, d\xi. \tag{23}$$

The following interpretations of the state quantities entering into (19) will get apparent later on:

$u(T, n_k)$: density of *internal energy*,

$\mu_i(T, n_k)$: *chemical potential* of constituent S_i,

$\mathbf{J}(T, n_k, \nabla T, \nabla n_k)$: *energy flux* density,

$\mathbf{J}_i(T, n_k, \nabla T, \nabla n_k)$: *diffusion flux* density of constituent S_i,

$R(T, n_k, \alpha_k)$: *reaction potential* with the property

$$R(T, n_k, \alpha_k) = 0 \text{ for all } \alpha_k = 0. \tag{24}$$

As compared with (16) the Lagrangian (19) now depends explicitly on the phase functions φ and φ_i. This happens, however, in such a way as to preserve the gauge invariance with respect to commonly gauging of all functions Ψ and Φ_k. (substitute Ψ and Φ_k by $\Psi e^{i\varepsilon}$ and $\Phi_k e^{i\varepsilon}$ or φ and φ_k by $\varphi + \varepsilon$ and $\varphi_k + \varepsilon$. See definition (22).)

In the case of pure heat transport the Lagrangian (19) reduces to the form (16) with a generalized ansatz for the energy density and for the energy flux: In (16) substitute cT by $u(T)$ and $(-\lambda \cdot \nabla T)$ by $\mathbf{J}(T, \nabla T)$. It should be noticed that the definitions (17) and (18) are preserved in going from example I to example II (see (20, 23)) except for the fact that now the hydrostatic pressure depends on T and n_k.

By means of the Lagrangians (16) and (19) traditional TIP fits into LF. (16) reproduces completely Fourier's linear theory of heat transport whereas (19) defines a generalized theory of the combined processes "heat transport, diffusion and chemical reactions". (16) and (19) are exclusively associated with that restricted class of processes which fulfil the traditional *Principle of Local Equilibrium* (PLE) [5, 6], i.e. the processes are running locally through equilibrium states, only. This statement gets apparent subsequently. The PLE is firstly based on the ad hoc generalization

$$\partial_t u = T\partial_t s - \underbrace{p\partial_t v}_{0 \;\curvearrowleft\; \text{rigid body}} + \sum_i \mu_i \partial_t c_i \tag{25}$$

of Gibbs' Fundamental Form of thermostatics (s: entropy density, v: specific volume, c_i: mass fraction n_i/n). Secondly PLE is based on the use of the state functions of thermostatics. Along this line the pressure p entering into (16) and (19) via (18) and (23) is taken from the wellknown formula of thermostatics

$$u = Ts - p + \sum_i \mu_i n_i. \tag{26}$$

4. Fundamental field equations

Hamilton's Principle (4–6) is associated with the set of *Euler–Lagrange equations*

$$\partial_t \frac{\partial \ell}{\partial(\partial_t \Psi_i)} + \nabla \cdot \frac{\partial \ell}{\partial(\nabla \Psi_i)} - \frac{\partial \ell}{\partial \Psi_i} = 0, \qquad i = 1, \ldots, f, \tag{27}$$

in the bulk V and with the set of *boundary conditions*

$$\mathbf{n} \cdot \frac{\partial \ell}{\partial(\nabla \Psi_i)} = 0, \qquad i = 1, \ldots, f, \tag{28}$$

at the surface ∂V of the *isolated system*. The isolated system is characterized by free variations of the fields $\Psi_i(x,t)$ at the boundary. $\mathbf{n}$ is the normal unit vector at ∂V.

Example I:

Applying (27, 28) to the Lagrangian (16) one finds the following equations due to the variations $\delta\varphi$ and δT:

Field equations in V:

$$\delta\varphi: \qquad c\partial_t T - \lambda \Delta T = 0, \tag{29}$$

$$\delta T: \qquad c\partial_t(\varphi - \varphi_0(t,T)) + \lambda\Delta(\varphi - \varphi_0(t,T)) = 0. \tag{30}$$

Boundary conditions on ∂V for the isolated system:

$$\delta\varphi: \qquad \mathbf{n} \cdot \frac{\partial \ell}{\partial(\nabla\varphi)} \equiv -\frac{1}{\omega}\,\mathbf{n} \cdot (-\lambda \nabla T) = 0, \tag{31}$$

$$\delta T: \qquad \mathbf{n} \cdot \frac{\partial \ell}{\partial(\nabla T)} \equiv -\frac{1}{\omega}\,\mathbf{n} \cdot \left[-\lambda\nabla(\varphi - \varphi_0) + (-\lambda \nabla T)\frac{T_0}{2T^2}\right] = 0. \tag{32}$$

Obviously (29) is *Fourier's equation of heat conduction*. Taking this equation by itself, it would be *non-selfadjoint*. Thus, it cannot be gained from a Lagrangian [21, 22]. However, by the second field equation (30) Fourier's equation (29) is supplemented in such a way as to produce a selfadjoint set of field equations (29, 30) for which a Lagrangian exists. (Originally (30) contains several other terms which, however, drop out by means of (29)). The boundary condition (31) is obviously associated with the thermally isolated system: There is no heat flux $\mathbf{J} = -\lambda\nabla T$ across the boundary.

The set of equations (29–32) is solved in the following way:

$$(29,\ 31): \quad T = T(x,t), \quad \text{solution of Fourier's heat conduction problem,} \tag{33}$$

$$(30,\ 32): \quad \varphi = \varphi_0(t,T) = -\omega t + \frac{T_0}{2T(x,t)}\Big/_{\text{insert (33)}}. \tag{34}$$

Thus heat transport following the PLE is associated in LP with an *excitation wave*

$$\Psi(x,t) = \sqrt{T(x,t)}\,e^{i\left(-\omega t + \frac{T_0}{2T(x,t)}\right)} \tag{35}$$

running down the slope of Fourier's temperature profile.

The singularity $T = 0$ occurring several times in the theory and especially in the solution (34) is physically interpreted by the *Third Law of Thermodynamics*: It is impossible to get to the absolute zero-point by any means.

Of course Eq. (29) is the conservation law of internal energy, i.e. the *First Law of Thermodynamics* for the special process "heat conduction". This coincidence between a field equation and a physically most relevant balance equation is accidental. It is due to the special choice of fundamental field variables in (16). The field equations associated with the variables Ψ and Ψ^* and due to the form (15) of the Lagrangian look rather complicated and do not reveal energy conservation immediately.

Example II:

The same procedure as before results in the following set of equations:
Field equations in V:

$$\delta\varphi: \quad \partial_t u_{(Q)} + \nabla\cdot\mathbf{J}_{(Q)} = \xi_{(Q)}, \tag{36}$$

$$\delta\varphi_i: \quad \partial_t(n_i\mu_i) + \nabla\cdot(\mu_i\mathbf{J}_i) = \xi_i, \quad i = 1,\ldots,N, \tag{37}$$

$$\left.\begin{matrix}\delta T:\\ \\ \delta n_i:\end{matrix}\right\} \quad \begin{matrix}\text{partial differential equation,}\\ \text{homogeneous with respect to the terms } (\varphi-\varphi_0),\\ [(\varphi_k-\varphi)-(\varphi_{k0}-\varphi_0)] \text{ and its } 1^{\text{st}} \text{ and } 2^{\text{nd}} \text{ derivatives.}\end{matrix} \tag{38, 39}$$

Boundary conditions on ∂V for the isolated system:

$$\delta\varphi: \quad \mathbf{n}\frac{\partial\ell}{\partial(\nabla\varphi)} \equiv -\frac{1}{\omega}\,\mathbf{n}\cdot\mathbf{J}_{(Q)} = 0 \tag{40}$$

$$\delta\varphi_i: \quad \mathbf{n}\frac{\partial\ell}{\partial(\nabla\varphi_i)} \equiv -\frac{1}{\omega}\,\mu_i\,\mathbf{n}\cdot\mathbf{J}_i = 0, \quad i = 1,\ldots,N, \tag{41}$$

$$\delta T: \quad \mathbf{n}\frac{\partial\ell}{\partial(\nabla T)} \equiv \ldots \quad = 0, \tag{42}$$

$$\delta n_i: \quad \mathbf{n}\frac{\partial\ell}{\partial(\nabla n_i)} \equiv \ldots \quad = 0, \quad i = 1,\ldots,N. \tag{43}$$

The definitions and the physical meanings of the abbreviations used in (36–43) are

as follows:

$$u_{(Q)} = u - \sum_{i=1}^{N} n_i \mu_i \quad : \quad \text{thermal part of internal energy,} \tag{44}$$

u : total *internal energy,*

$n_i \mu_i$: chemical parts of internal energy,

$$\mathbf{J}_{(Q)} = \mathbf{J} - \sum_{i=1}^{N} \mu_i \mathbf{J}_i \quad : \quad \textit{heat flux,} \tag{45}$$

$\mathbf{J}$: total energy flux,

$\mathbf{J}_i$: partial *diffusion (mass) flux,*

$\mu_i \mathbf{J}_i$: partial chemical energy flux,

$$\xi_i = \frac{\partial R(\ldots, \alpha_k)}{\partial \alpha_i} + n_i \partial_t \mu_i + \mathbf{J}_i \cdot \nabla \mu_i, \tag{46}$$

$$\xi_{(Q)} = -\sum_{i=1}^{N} \xi_i, \tag{47}$$

ξ_i, $\xi_{(Q)}$: production rates of partial internal energies associated with chemical (material) and thermal degrees of freedom, respectively.

Obviously the field equations (36) and (37) describe *balances of the thermal and chemical parts of the internal energy,* respectively. According to

$$\xi_{(Q)} + \sum_{i=1}^{N} \xi_i = 0 \tag{48}$$

(see (47)) there is an energy transfer between thermal and chemical degrees of freedom Ψ and Φ_i, $i = 1, \ldots, N$. Adding (36) and (37) and using (44, 45, 48) one finds conservation of the total internal energy:

$$\partial_t u + \nabla \cdot \mathbf{J} = 0. \tag{49}$$

This is again the *First Law of Thermodynamics.*

Again the boundary conditions (40, 41) define an isolated system: There is no heat or mass transport across the boundary.

An alternative form of the field equations (37) reads

$$\partial_t n_i + \nabla \cdot \mathbf{J}_i = \sigma_i, \qquad i = 1, \ldots, N. \tag{50}$$

These are obviously *partial mass balance equations* with the *partial mass production rates*

$$\sigma_i = \frac{1}{\mu_i} \frac{\partial R(T, n_k, \alpha_k)}{\partial \alpha_i} \tag{51}$$

of constituents S_i. The term R in the Lagrangian (19) is a *reaction potential* by means of which the progress of a chemical reaction is ruled. At this point the atomistic structure must be taken into account: Let

$$\nu_1 S_1 + \cdots + \nu_m S_m \rightleftarrows \nu_{m+1} S_{m+1} + \cdots + \nu_N S_N \tag{52}$$

be a chemical reaction equation and let me subsequently take the stoichiometric coefficients ν_i with positive or negative sign according to their position on the right or left hand side of Eq. (52). Let finally M_i be the molar mass of constituents S_i. Then the phenomenological *Principle of Multiple Proportions*

$$\sigma_1 : \sigma_2 : \ldots : \sigma_N = \nu_1 : \nu_2 : \ldots : \nu_N \tag{53}$$

is solved by

$$\sigma_i = \nu_i \, g\,(T, n_k, \alpha_k), \qquad i = 1, \ldots, N, \tag{54}$$

where g is a state function with the physical meaning of *reaction velocity*. (According to (54) σ_i is measured in molar units.) Together with (54) the gross mass balance

$$\sum_{i=1}^{N} M_i \nu_i = 0 \tag{55}$$

of the chemical reaction leads to

$$\sum_{i=1}^{N} M_i \sigma_i = 0 \tag{56}$$

and thus to a constraint

$$\sum_{i=1}^{N} \frac{M_i}{\mu_i} \frac{\partial R(T, n_k, \alpha_k)}{\partial \alpha_i} = 0 \tag{57}$$

for the reaction potential. Within LF Eq. (57) takes account of the atomic structure of matter. (56) describes the mass transfer between the material degrees of freedom Φ_i, $i = 1, \ldots, N$.

For illustration let me refer to the usual *linear theory of chemical reactions* [5, 6] which is based on the linear constitutive relation

$$g = L \cdot X \tag{58}$$

for the reaction velocity. X is the driving force:

$$X = -\frac{A}{T}, \qquad \text{affinity} \quad A = \sum_{j=1}^{N} \mu_j \nu_j, \tag{59}$$

L is a material parameter. Then the associated reaction potential is given by

$$R = -L \frac{1}{T} \sum_{k=1}^{N} \mu_k \nu_k \alpha_k \cdot \sum_{j=1}^{N} \mu_j \nu_j. \tag{60}$$

(57) is fulfilled and (51) leads to the desired constitutive relation

$$\sigma_i = -L \frac{1}{T} \nu_i \sum_{j=1}^{N} \mu_j \nu_j = \nu_i \cdot \left(-L \frac{A}{T} \right). \tag{61}$$

Again the solutions of Eqs (38, 39, 42, 43) are based on the solutions $T(x,t)$ and $n_k(x,t)$ of Eqs (36, 37 or 50, 40, 41):

$$\varphi(x,t) = \varphi_0(t, T(x,t)) = -\omega t + \frac{T_0}{2T(x,t)}, \tag{62}$$

$$\varphi_i(x,t) = \varphi_{i0}(t, T(x,t), n_i(x,t)) = -\omega t + \gamma \frac{n_i(x,t)}{2T(x,t)}. \tag{63}$$

According to (11, 12) these solutions give rise to coupled thermal excitation and matter waves associated with the combined local equilibrium process "heat transport, diffusion and chemical reaction".

5. Invariance transformations — Observables and balance equations of the first kind — Constitutive equations

The transformations $T_{\varepsilon_1,\ldots,\varepsilon_n}$ of a universal, continuous, n-parameter *invariance group*

$$(\bar{x}, \bar{t}, \bar{\Psi}) = T_{\varepsilon_1,\varepsilon_2,\ldots,\varepsilon_N}(x,t,\Psi) \tag{64}$$

transform each real process $P = \{\Psi_i(x,t), \quad i = 1,\ldots,f\}$ into another real process $P = \{\bar{\Psi}_i(\bar{x},\bar{t}), \quad i = 1,\ldots,f\}$. Both processes which are referred to the same reference frame solve Hamilton's Principle (4-6) simultaneously. This gives rise to an *invariance criterion* for the Lagrangian which must be fulfilled identically with respect to the coordinates x,t, to the field variables Ψ and the group parameters ε:

$$\ell(\bar{x},\bar{t},\bar{\Psi},\bar{\partial}\bar{\Psi})\big|_{\text{insert (64)}} \equiv \ell(x,t,\Psi,\partial\Psi) + \partial_t F(x,t,\Psi,\varepsilon). \tag{65}$$

The function F has to be determined explicitly. From this criterion one finds *Noether's theorem* [16] which for the purpose of TIP is formulated as follows:

Each group parameter ε_κ of a continuous invariance group defines an *observable of the first kind* by means of an associated *balance equation* which is fulfilled by the real processes:

$$\varepsilon_\kappa \rightsquigarrow \text{ observable } \kappa \rightsquigarrow \partial_t a_\kappa + \nabla \cdot \mathbf{J}_\kappa = 0. \tag{66}$$

The density a_κ and the flux density $\mathbf{J}_\kappa$ are uniquely defined from the Lagrangian and from the function F entering into (65). One finds the *constitutive equations*

$$a_\kappa = a_\kappa(x, t, \Psi, \partial\Psi), \tag{67}$$

$$\mathbf{J}_\kappa = \mathbf{J}_\kappa(x, t, \Psi, \partial\Psi), \tag{68}$$

associated with the observable κ.

For the explicit form of (67, 68) I refer to the literature [12, 19, 16]. Here only the most important invariance groups will be reported:

1. *Homogeneity of time* with respect to all physical processes belong to the universal invariance group

$$\bar{t} = t + \varepsilon, \qquad \bar{x} = x, \qquad \bar{\Psi}_i = \Psi_i, \qquad i = 1, \ldots, f, \tag{69}$$

$$-\infty < \varepsilon < \infty.$$

It is associated once and for all with the observable *energy* and (66) as applied to TIP becomes the *First Law of Thermodynamics*:

$$\partial_t u + \nabla \cdot \mathbf{J} = 0. \tag{70}$$

The constitutive equations are defined as

energy density:
$$u = \sum_{i=1}^{f} \frac{\partial \ell}{\partial(\partial_t \Psi_i)} \partial_t \Psi_i - \ell, \tag{71}$$

energy flux density:
$$\mathbf{J} = \sum_{i=1}^{f} \frac{\partial \ell}{\partial(\nabla \Psi_i)} \partial_t \Psi_i. \tag{72}$$

Example I:

For the time-translational group (69) the Lagrangian (15, 16) fulfils the invariance criterion (65) with $F = 0$. Using solution (34) one finds

$$u = c \cdot T \qquad \text{and} \qquad \mathbf{J} = -\lambda \cdot \nabla T \tag{73}$$

as it should be.

Example II:

The same statements hold for the Lagrangian (19). Together with the solution (62, 63) one finds

$$u = u(T, n_k) \qquad \text{and} \qquad \mathbf{J} = \mathbf{J}(T, n_k, \nabla T, \nabla n_k) \tag{74}$$

which justifies the interpretations already given on the occasion of the ansatz (19).

2. *Common gauge transformations* of complex-valued field variables define another important one-parameter invariance group:

$$\begin{aligned} \bar{t} &= t, & \bar{x} &= x, \\ \overline{\Psi}_k &= \Psi_k e^{i\varepsilon}, & \overline{\Psi}_k^* &= \Psi_k^* e^{-i\varepsilon}, \end{aligned} \tag{75}$$

$$-\infty < \varepsilon < \infty.$$

The associated balance equation is proportional to the energy balance in the case of Examples I and II. Thus (75) brings no new information within the concept of first kind observables. However, (75) gets quite essential with respect to the entropy concept.

6. Perturbation equations — Entropy — Variational Principle of Second Order and General Principle of Least Entropy Production

Let me consider a one-parameter class $\Psi(x, t, \varepsilon)$ of real processes which for $\varepsilon = 0$ reduces to the reference process

$$\Psi(x, t, \varepsilon = 0) = \Psi(x, t). \tag{76}$$

The difference

$$\Theta(x, t, \varepsilon) = \Psi(x, t, \varepsilon) - \Psi(x, t) \tag{77}$$

is called a *perturbation* of the reference process associated with the perturbation parameter ε. ε is physically interpreted as the variation of an initial-value parameter. Of course all processes $\Psi(x, t, \varepsilon)$ are ruled by the Euler–Lagrange equations (27):

$$\mathcal{E}_i(\Psi, \partial\Psi, \partial\partial\Psi) \equiv \partial_t \frac{\partial \ell}{\partial(\partial_t \Psi_i)} + \nabla \cdot \frac{\partial \ell}{\partial(\nabla \Psi_i)} - \frac{\partial \ell}{\partial \Psi_i} = 0, \qquad i = 1, \ldots, f. \tag{78}$$

The *main linear part of the perturbation* is defined by a Taylor expansion

$$\Psi(x,t,\varepsilon) = \Psi(x,t) + \varepsilon\eta(x,t) + \dots \tag{79}$$

with

$$\eta(x,t) = \left\{\eta_i(x,t) = \frac{\partial\Psi_i(x,t,\varepsilon)}{\partial\varepsilon}\Big|_{\varepsilon=0}, \qquad i = 1,\dots,f\right\}. \tag{80}$$

The set of functions $\eta(x,t)$ can be taken as an approximate representation of the exact perturbation (77). Subsequently $\eta(x,t)$ will be called a *perturbation of the reference process* $\Psi(x,t)$.

The perturbation $\eta(x,t)$ of a given reference process $\Psi(x,t)$ is ruled by *Jacobi's equations (=variational* or *perturbation equations)*:

$$J_i(\Psi,\partial\Psi,\partial\partial\Psi_i;\eta,\partial\eta,\partial\partial\eta) \equiv \partial_t\,\frac{\partial\Omega}{\partial(\partial_t\eta_i)} + \nabla\cdot\frac{\partial\Omega}{\partial(\nabla\eta_i)} - \frac{\partial\Omega}{\partial\eta_i} = 0, \tag{81}$$

$$i = 1,\dots,f.$$

These are the variational equations of the Euler–Lagrange equations (78). They are based on the kernel Ω which is defined from the Lagrangian:

$$2\Omega(\Psi,\partial\Psi;\eta,\partial\eta) = \sum_{i,j=1}^{f}\left[\frac{\partial^2\ell}{\partial\Psi_i\partial\Psi_j}\,\eta_i\eta_j + 2\sum_{\alpha=0}^{3}\frac{\partial^2\ell}{\partial\Psi_i\partial(\partial_\alpha\Psi_j)}\,\eta_i\partial_\alpha\eta_j\right.$$
$$\left.\sum_{\alpha,\beta=0}^{3}\frac{\partial^2\ell}{\partial(\partial_\alpha\Psi_i)\partial(\partial_\beta\Psi_j)}\,\partial_\alpha\eta_i\partial_\beta\eta_j\right], \tag{82}$$

$$\alpha = 0 \rightsquigarrow t, \qquad \alpha = 1,2,3 \rightsquigarrow x^1,x^2,x^3.$$

(81) must be supplemented by *boundary conditions* which are defined as variational equations of the boundary conditions for the reference process $\Psi(x,t)$. In the case of an isolated system one gets from (28)

$$\mathbf{n}\cdot\frac{\partial\Omega}{\partial(\nabla\eta_i)} = 0, \qquad i = 1,\dots,f. \tag{83}$$

(81, 83) are the *basic equations for a dynamical stability theory of an isolated system.* Via the kernel Ω they are again completely determined by the Lagrangian.

Obviously Jacobi's equations (81) and the boundary conditions (83) can be regarded as the Euler–Lagrange equations of another variational principle of an isolated system. It is called *Variational Principle of the Second Order*:

$$J_2 = \int_{t_1}^{t_2} \int_V \Omega(\Psi, \partial\Psi; \eta, \partial\eta)\, d^3x\, dt, \tag{84}$$

$$J_2 = \text{extremum} \tag{85}$$

by free variations of all perturbation fields $\eta_i(x,t)$

for fixed values at $t_{1,2}$

$$\delta\eta_i(x, t_{1,2}) = 0 \tag{86}$$

and for the given reference process $\Psi(x,t) = \{\Psi_i(x,t)\}$.

For an isolated system free variations $\delta\eta_i(x,t)$ at the boundary ∂V are included.

I emphasize that the variations apply to the functions η_i only, i. e. the principle operates in perturbation space. (84–86) can be regarded as a Hamilton's Principle for the perturbation $\eta(x,t)$; the given fields $\Psi_i(x,t)$ of the reference process play formally the part of control parameters. Eqs (81, 83) can be replaced by the second order variational principle. Thus a dynamical stability theory can also be based on this principle.

Of course the *universal invariance transformations* (64) apply as well to the principle (84–86) giving thus rise to another application of Noether's theorem. Along this line I get the *entropy concept* in TIP and quite generally a *stability theory in the sense of Ljapunov's direct method* [19].

The entropy concept can be based on Noether's theorem on the ground of scaling transformations associated with the parameter ε of the gauge group (75) (see [3]). However, there is a much easier procedure which works as follows:

The kernel $\Omega(\Psi, \partial\Psi; \eta, \partial\eta)$ is homogeneous of 2^{nd} degree with respect to the functions η and $\partial\eta$. By means of Euler's formula this leads to

$$2\Omega = \sum_{i=1}^{f} \left[\eta_i \frac{\partial\Omega}{\partial\eta_i} + \partial_t\eta_i \frac{\partial\Omega}{\partial(\partial_t\eta_i)} + \nabla\eta_i \cdot \frac{\partial\Omega}{\partial(\nabla\eta_i)} \right]. \tag{87}$$

Substituting Jacobi's equations (81) in the first term one gets an *inhomogeneous balance equation*

$$\partial_t\pi + \nabla \cdot \mathbf{J}_\pi = \sigma_\pi \tag{88}$$

in perturbation space which is fulfilled by each perturbation $\eta(x,t)$ of a given reference process $\Psi(x,t)$. The constitutive relations in (88) are given by

$$\pi(\Psi, \partial\Psi; \eta, \partial\eta) = \sum_{i=1}^{f} \frac{\partial\Omega(\Psi, \partial\Psi; \eta, \partial\eta)}{\partial(\partial_t\eta_i)}\, \eta_i, \tag{89}$$

$$\mathbf{J}_\pi(\ldots\ldots) = \sum_{i=1}^{f} \frac{\partial\Omega(\ldots\ldots)}{\partial(\nabla\eta_i)}\, \eta_i, \tag{90}$$

$$\sigma_\pi(\ldots\ldots) = 2\Omega(\ldots\ldots). \tag{91}$$

In the case of complex-valued field variables this concept applies especially to the one-parameter class of real processes

$$\Psi_k(x,t,\varepsilon) = \Psi_k(x,t)\, e^{i\varepsilon}, \qquad k = 1,\ldots,f \tag{92}$$

(see (76, 77)) which obviously is nothing else than the gauging group (75): The reference process $\Psi(x,t)$ is perturbed by a common phase shift ε of all fields Ψ_k. The perturbation (80) associated with (92) is given by

$$\eta_k = i\,\Psi_k(x,t), \qquad \eta_k^* = -i\,\Psi_k^*(x,t). \tag{93}$$

Inserting these expressions into (88–91) one gets an *inhomogeneous balance equation* which operates only *in state space* and which is fulfilled by the reference process $\Psi(x,t)$! In the case of TIP it is called *Second Law of Thermodynamics* (1st part):

$$\partial_t s + \nabla\cdot\mathbf{J}_s = \sigma_s. \tag{94}$$

The associated *constitutive equations* are completely defined from the Lagrangian via the kernel Ω:

$$\left.\begin{aligned}
&\textit{entropy} \text{ density}: && S = \sum_k \frac{\partial\Omega(\ldots)}{\partial(\partial_t\eta_k)}\,\eta_k && (95)\\
&\textit{entropy flux} \text{ density}: && \mathbf{J}_s = \sum_k \frac{\partial\Omega(\ldots)}{\partial(\nabla\eta_k)}\,\eta_k && (96)\\
&\textit{entropy production rate} \text{ density}: && \sigma_s = 2\Omega(\ldots) && (97)\\
&&& \eta_k = i\,\Psi_k(x,t) &\\
&&& \eta_k^* = -i\,\Psi_k^*(x,t) &
\end{aligned}\right|$$

I emphasize that in (95–97) the kernel Ω has to be evaluated with respect to the complex-valued fundamental field variables Ψ_i! This is due to the fact that Ω, being defined by means of ordinary derivatives, is not invariant with respect to a change of the fundamental field variables in state space. However, the entropy concept is regarded as an invariant concept, i. e. one should define Ω by means of "covariant derivatives in state space" rather than by ordinary derivatives as is done by definition (82). To avoid these mathematical complications the complex-valued variables $\Psi_i(x,t)$ are preferred with respect to the entropy concept. (The variables $\Psi_i(x,t)$ are in a way the "rectilinear coordinates" in function space.)

Concerning the *2nd part*

$$\sigma_s \geq 0 \tag{98}$$

of the Second Law this is a natural outcome of dynamical stability theory which also can be done within LF [19].

Inserting the perturbation (93) into the Second Order Variational Principle (84–86) I get a most general *Principle of Least Entropy Production*:

$$\begin{aligned} \mathcal{P} &= \int_{t_1}^{t_2} \int_V 2\Omega(\Psi, \partial\Psi; i\overset{\downarrow}{\Psi}, i\,\partial\overset{\downarrow}{\Psi})\, d^3x\, dt = \\ &= \int_{t_1}^{t_2} \int_V \sigma_s(\Psi, \partial\Psi)\, d^3x\, dt = \\ &= \text{minimum} \\ &\quad \text{by free variations of the fields } \Psi_k(x,t) \text{ at the sites} \\ &\quad \text{marked by "}\downarrow\text{" and subjected to the constraints (6)} \end{aligned} \tag{99}$$

Because of this strange variation, Eq. (99) defines but a *quasi-variational principle* which, however, operates completely in state space. The factor 2 in (99) is conventional because of (97). Obviously $\mathcal{P}$ is the *the total entropy production* of the system in the time interval $[t_1, t_2]$. In general it can only be claimed that the integral $\mathcal{P}$ gets an extremum. However, the minimum is due to the physical constraint (98) which is associated with dynamical stability of the processes. Prigogine's principle of least entropy production [5, 20] which applies but to special processes is implied in the general principle (99).

Example I

Applying the entropy concept (94–97) to the Lagrangian (15) and taking account of the solution (34) one finds the following constitutive equations which are well-known in Fourier's theory of heat transport [5, 6]:

$$s = c\, \ln \frac{T}{T_0}, \tag{100}$$

$$\mathbf{J}_s = \frac{-\underline{\lambda} \cdot \nabla T}{T} = \frac{\mathbf{J}_{(Q)}}{T}, \tag{101}$$

$$\sigma_s = \frac{\nabla T \cdot \underline{\lambda} \cdot \nabla T}{T^2} = \mathbf{J}_{(Q)} \cdot \nabla \left(\frac{1}{T}\right). \tag{102}$$

Example II

The same procedure as applied to (19, 62, 63) results in

$$s = \frac{1}{T}\left(u + p - \sum_{i=1}^{N} n_i \mu_i\right), \tag{103}$$

$$\mathbf{J}_s = \frac{\mathbf{J} - \sum_{i=1}^{N} \mu_i \mathbf{J}_i}{T} = \frac{\mathbf{J}_{(Q)}}{T}, \tag{104}$$

$$\sigma_s = \mathbf{J} \cdot \nabla \left(\frac{1}{T}\right) + \sum_{i=1}^{N} \mathbf{J}_i \cdot \nabla \left(-\frac{\mu_i}{T}\right) + \sum_{i=1}^{N} \sigma_i \left(-\frac{\mu_i}{T}\right) = \tag{105}$$

$$= \mathbf{J}_{(Q)} \cdot \nabla \left(\frac{1}{T}\right) + \sum_{i=1}^{N} \mathbf{J}_i \cdot \frac{\nabla(-\mu_i)}{T} + \sum_{i=1}^{N} \sigma_i \cdot \left(-\frac{\mu_i}{T}\right). \tag{106}$$

Again these relations are known from traditional TIP [5, 6]. (103) coincides with (26) and is part of the PLE. Also the relation (105, 106) is a direct consequence of the PLE.

7. Final remarks

The Lagrangians (15, 16) and (19) completely reproduce traditional TIP as far as examples I and II are concerned. An essential point is the use of the particular solutions (34) and (62, 63) for the phase functions. Being aware of the fact that traditional TIP is associated with the PLE one is led to the following statements:

The particular solutions (34, 62, 63) are associated with the restricted class of those irreversible processes which locally run through equilibrium states, only. The Lagrangians (15, 16) and (19) are *truncated forms of more general Lagrangians* which describe the most general dynamics of the respective systems. By the truncation the dynamics is physically restricted in the sense of the PLE. From these points of view the forms (16) and (19) can be regarded as the first terms of Taylor series of the (yet unknown) complete Lagrangians. Expansions are done with respect to deviations $\varphi - \varphi_0(t, T)$ and $\varphi_i - \varphi_{i0}(t, T, n_i)$ from the local equilibrium. Along this line the Lagrangians can be extended to higher terms of the Taylor expansions giving rise to generalizations of traditional TIP beyond the scope of the PLE. In this way the paradoxa of infinite speeds of heat and diffusion propagation can be cancelled from TIP in quite a natural way [4]. However, generalizing the truncated Lagrangians, the basic structures are preserved for ever. These are

- the existence of a Lagrangian in TIP,
- the complex-valued variables in TIP,
- the universal invariance requirements,
- the universal definitions of observables, balance and constitutive equations,
- the entropy concept in TIP,
- the stability concepts.

References

1. K. -H. Anthony, in Continuum Models of Discrete Systems 4, eds.: O. Brulin and R. T. K. Hsieh, North Holland Publishing Company, Amsterdam, 1981, p. 481.

2. K. -H. Anthony, in Disequilibrium and Self-Organisation, ed.: W. Kilmister, Reidel Publishing Company, Dordrecht, 1986, p. 75.
3. K. -H. Anthony, Archives of Mechanics (Warsaw), *41*, issue 4, 1989.
4. K. -H. Anthony and H. Knoppe, in Kinetic Theory and Extended Thermodynamics, eds.: I. Müller and T. Ruggeri, pitagora editrice bologna, Bologna, 1987, p. 15.
5. S. R. De Groot and P. Mazur, Non-Equilibrium Thermodynamics, North Holland Publishing Company, Amsterdam, 1969.
6. J. Meixner und H. G. Reik, Thermodynamik der irreversiblen Prozesse, in: Handbuch der Physik, Vol. III/2, ed.: S. Flügge, Springer-Verlag, Berlin, 1959.
7. I. Müller, Thermodynamik, Bertelsmann Universitätsverlag, Düsseldorf, 1973.
8. P. Glansdorff and I. Prigogine, Thermodynamic Theory of Structure, Stability and Fluctuations, John Wiley and Sons, London, 1971.
9. E. M. Corson, Introduction to Tensors, Spinors and Relativistic Wave-Equations, Blackie and Son, London, 1953.
10. E. Schmutzer, Relativistische Physik, Teubner Verlagsgesellschaft, Leipzig, 1968.
11. E. Fick, Einführung in die Grundlagen der Quantentheorie, Akademische Verlagsgesellschaft, Leipzig, 1968.
12. K. -H. Anthony, in Continuum Models of Discrete Systems 3, eds.: E. Kröner and K. -H. Anthony, University of Waterloo Press, Waterloo, Ontario, 1980, p. 761.
13. I. Gyarmati, Non-Equilibrium Thermodynamics, Field Theory and Variational Principles, Springer-Verlag, Berlin, 1970.
14. G. Lebon, Variational Principles in Thermodynamics, in Recent Developments in Thermodynamics of Solids, eds.: G. Lebon and P. Perzyna, Springer-Verlag, Wien, 1980.
15. M. A. Biot, Variational Principles in Heat Transfer, At the Clarendon Press, Oxford, 1970.
16. E. Schmutzer, Symmetrien und Erhaltungssätze der Physik, Akademie-Verlag, Berlin, 1972.
17. V. I. Zubov, Methods of A. M. Ljapunov and their Applications, Noordhoff, Groningen, 1964.
18. W. Hahn, Theorie und Anwendungen der direkten Methode von Ljapunov, Springer-Verlag, Berlin, 1959.
19. K. -H. Anthony, in Trends in Applications of Mathematics to Mechanics, eds.: J. F. Besseling and W. Eckhaus, Springer-Verlag, Heidelberg, 1988, p. 297.
20. I. Prigogine, Études thermodynamiques des phénomènes irréversibles, Desoer, Liège, 1947.
21. R. M. Santilli, Foundations of Theoretical Mechanics I, Springer-Verlag, New York, 1978.
22. R. M. Santilli, I Annals of Physics, *103*, 345, 1977; II Annals of Physics, *103*, 409, 1977; III Annals of Physics, *105*, 227, 1977.

Acta Physica Hungarica 67 (3–4), pp. 341–350 (1990)

ON THE STOCHASTIC DESCRIPTION OF NON-ISOTHERMAL CHEMICAL PROCESSES*

P. P. SZCZĘSNY, M. FRANKOWICZ and A. CHŁOBOWSKI

K. Gumiński Department of Theoretical Chemistry
Faculty of Chemistry, Jagellonian University
30–060 Cracow, Poland

(Received 20 December 1988)

Stochastic treatment of an exothermal chemical reaction with Newtonian heat exchange based on the birth and death master equation is proposed. The basic assumption is the discrete mechanism of energy transfer. The analysis of heat exchange process is performed. For the Semenov model the influence of the system size and of the magnitude of elementary energy transfer on the stationary value of temperatures is studied. Also, a simple model of thermokinetic oscillations is considered. It is shown that internal fluctuations may destroy limit cycle.

1. Introduction

The chemical reaction is a discrete process. The usual kinetic description in terms of continuous variables does not take into account inherent fluctuations, which in some situations can deeply influence the evolution. The stochastic theory of isothermal reactions is already well developed by means of discrete master equations [1]. However, the problem of stochastic description of systems with changing temperature is much more complicated. The only exception is the adiabatic thermal explosion, which was recently studied by several authors [2–4]. In other cases it becomes necessary to model the process of energy transfer between the system and the external reservoirs. To this aim exact mechanism must be known, which is true only for very special cases (e. g. Knudsen flow [5]). Recently, we proposed a simplified description of non-isothermal chemical processes with heat exchange, based on a multi-step master equation [6] and applied it to the Semenov model. In the present work we discuss the stationary probability distribution of the Semenov model and also analyze the Frank–Kamenetskii model; it is the simplest model of thermokinetic oscillations.

2. Stochastic description of energy transfer

Let us model an inhomogeneous nonreacting system as an ensemble of coupled cells and let $\mathcal{E}_k$ denote the internal energy in k-th cell. The state of the system is

*Dedicated to Prof. I. Gyarmati on his 60th birthday

then described by the multivariate probability distribution $P(\{\mathcal{E}\};t)$ changing in time because of the energy transfer between cells. The multivariate master equation describing this change has the form [7]

$$\begin{aligned}\partial P(\{\mathcal{E}_k\};t)/\partial t = \\ = \sum_{k,j} \int d\varepsilon \, [W_k(\mathcal{E}_k + \varepsilon, \mathcal{E}_j - \varepsilon \rightarrow \mathcal{E}_k, \mathcal{E}_j) \, P(\ldots, \mathcal{E}_k + \varepsilon, \mathcal{E}_j - \varepsilon, \ldots; t) - \\ - W_k(\mathcal{E}_k, \mathcal{E}_j \rightarrow \mathcal{E}_k - \varepsilon, \mathcal{E}_j + \varepsilon, \ldots; t) P(\ldots, \mathcal{E}_k, \mathcal{E}_j, \ldots; t)] ,\end{aligned} \tag{1}$$

where W_k are correspoding transition rates and j denote the cells being in thermal contact with the k-th cell (e. g. in the case of a linear chain we have $j = k \pm 1$). The main problem in the master equation description is to choose properly the transition rates W_k. It can be done explicitly only in simple models, in which the microscopic mechanism of energy transfer is known, e. g. in the Knudsen gas [5]. In the case of the Newtonian heat exchange, it is not the case (the exact temperature dependence of the heat transfer coefficient is in general not known). However, one can then apply Fokker–Planck or Langevin equation formalism, deriving these equations from Eq. (1); the noise term in these equations turns out to be state-dependent [8].

Recently,we proposed a simplified stochastic approach based on the discretization of the energy transfer [6]. We treat energy transfer as a discrete one-step Markov process with the elementary energy change q. The temperature change corresponding to the elementary heat transfer process is given by

$$\Delta T_E = q/\rho C V, \tag{2}$$

where C is the specific heat capacity, ρ the mass density and V is the system volume. If ΔT_E is small enough, the total temperature of the system can be assumed to be a discrete variable

$$T = m \, \Delta T_E, \tag{3}$$

m is a natural number.

The macroscopic Newton's law has the form

$$\begin{aligned} dT/dt &= -\alpha(T - T_e), \\ \alpha &= \chi S/\rho C V. \end{aligned} \tag{4}$$

χ is the Newtonian heat transfer coefficient, S the surface area of the reactor and T_E the temperature of the reservoir. As the rate of elementary energy transfer from the system to reservoir is proportional to the temperature of the system, and in opposite direction – only to the reservoir temperature, the transition probabilities will be

$$\begin{aligned} W(n \rightarrow n+1) &= \alpha n_e, \\ W(n \rightarrow n-1) &= \alpha n, \end{aligned} \tag{5}$$

where $n_e = T_e \rho CV/q$, and the master equation (1) will assume the form

$$\begin{aligned} \partial P(m,t)/\partial t = \alpha n_e\{P(m-1),t) - P(m,t)\} + \\ + \alpha\{(m+1)P(m+1,t) - mP(m,t)\}. \end{aligned} \tag{6}$$

This equation can be solved analytically by means of the generating function method [1]. With initial condition

$$P(n,0) = \delta_{n,N}$$

the time dependent solution of (6) is

$$P(n,t) = \exp\left[-n_e(1-\mathrm{e}^{-\alpha t})\right] \sum_{r=0}^{n} \frac{N! n_e^{n-r}(1-\mathrm{e}^{-\alpha t})^{N+n-2r}\mathrm{e}^{-\alpha r t}}{(N-r)!\, r!\, (n-r)!}. \tag{7}$$

The time evolution of the mean $< n(t) >$ is given by

$$< n(t) >= n_e(1-\mathrm{e}^{-\alpha t}) + N\mathrm{e}^{-\alpha t} \tag{8}$$

and for the variance $< \delta^2 n(t) >$

$$< \delta^2 n(t) >= \left[(n\mathrm{e}^{-\alpha t} + n_e)(1-\mathrm{e}^{-\alpha t})\right]^{1/2}. \tag{9}$$

The stationary probability distribution is a Poisson distribution centered at n_e

$$P_s(n) = \mathrm{e}^{-n_e} {n_e}^n/n! \tag{10}$$

In the next Section we will apply the above formalism to two simple cases of chemical non-isothermal systems.

3. The system with chemical reactions

(a) The Semenov model

Let us now consider the simplest model of an exothermal reaction with heat exchange (the Semenov model [9]): a closed reactor in thermal contact with a reservoir, with exothermal reaction and Newtonian cooling. The Arrhenius temperature dependence of the reaction rate is assumed. The evolution equation for the temperature T has the form

$$dT/dt = (QA/\rho CV)c_0\mathrm{e}^{-E/RT} - \alpha(T - T_e). \tag{11}$$

c_0 is the concentration of the reactant (reactant consumption is neglected), Q is the reaction heat, A is the preexponential factor, E the activation energy. The parameter characterizing the behaviour of the system is the Semenov number

$$\psi = \mathrm{e}^{-E/RT_e} EQAc_0/RT_e\chi S, \tag{12}$$

which describes the ratio of the self-heating due to the exothermal chemical reaction to heat losses by the Newtonian cooling. For $\psi < \psi_c$ (subcritical regime) the temperature tends to a unique stationary value, while for $\psi > \psi_c$ (supercritical regime) the system has two stationary (low temperature and high temperature) solutions; the latter is called the explosive one.

Stochastic properties of the Semenov model in the supercritical regime ($\psi > \psi_c$) were analyzed by solving numerically the Fokker–Planck equation for the probability distribution $P(T,t)$ and by stochastic simulations based on the Langevin equation [10, 11]. It has been found that in the vicinity of ψ_c the distribution of explosion times becomes broader and its maximum differs significantly from the deterministic explosion time. Usually, the fluctuations accelerated the ignition process.

Let us now pass to the discrete description proposed in Section 2. As the energy change caused by an elementary act of exothermal chemical reaction is usually much larger than the elementary energy transfer, the corresponding temperature change can be approximated as

$$\Delta T_R = Q/\rho CV = wq/\rho CV. \tag{13}$$

The transition probability related to the chemical reaction is

$$W(n \to n+w) = AVc_0\mathrm{e}^{-E\rho CV/Rqn}. \tag{14}$$

The stochastic version of the model (11) is then described by the following two-step master equation:

$$\begin{aligned} \partial P(n,t)/\partial t = {} & W(n-w \to n)P(n-w,t) + W(n-1 \to n)P(n-1,t) + \\ & + W(n+1 \to n)P(n+1,t) - \\ & - [W(n \to n+w) + W(n \to n-1) + \\ & + W(n \to n+1)]P(n,t), \end{aligned} \tag{15}$$

with transition probabilities given by (5) and (14).

From Eq. (16) one gets the recursive formula for the stationary probability

$$\begin{aligned} P_s(n+1) = {} & (n+1)^{-1}\left\{\left[(AVc_0/\alpha)\mathrm{e}^{-E\rho CV/Rqn} + n + n_e\right] P_s(n) - \right. \\ & \left. - n_e P_s(n-1) - AVc_0/\alpha)\mathrm{e}^{-E\rho CV/Rq(n-w)} P_s(n-w)\right\}. \end{aligned} \tag{16}$$

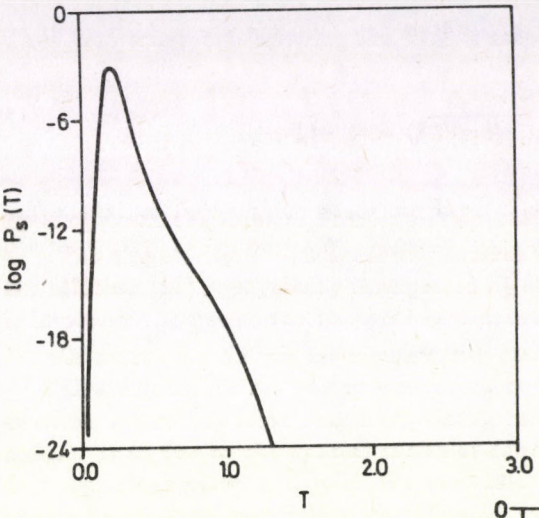

Fig. 1a

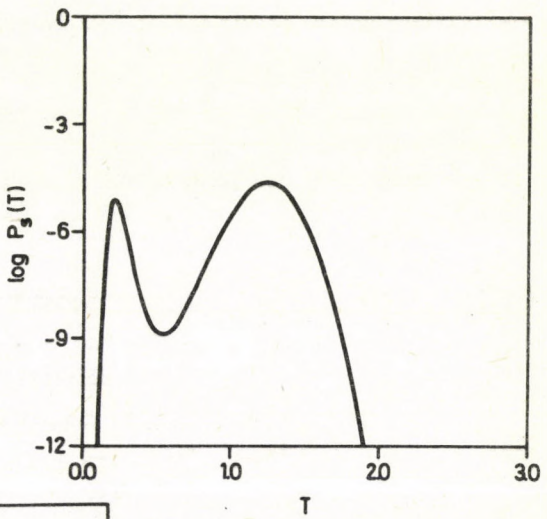

Fig. 1b

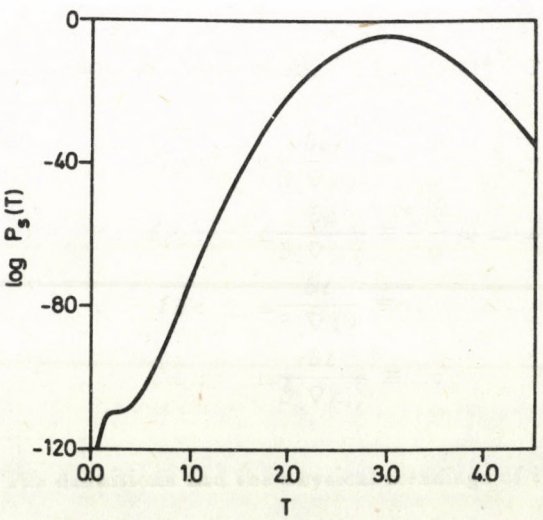

Fig. 1c

Formula (16) can be cast into the form

$$P_s(n+1) = (n+1)^{-1} \cdot \left[n_e P_s(n) + \sum_{k=0}^{w} \left((AV c_0/\alpha) e^{-E\rho CV/Rq(n-w+k)} \right) P_s(n-w+k) \right], \tag{17}$$

which is more convenient for computational purposes. Depending on the values of parameters (reaction heat, heat transfer coefficient, volume, the magnitude of elementary energy transfer q) the stationary probability can be uni- or bimodal (cf. Fig 1a–c).

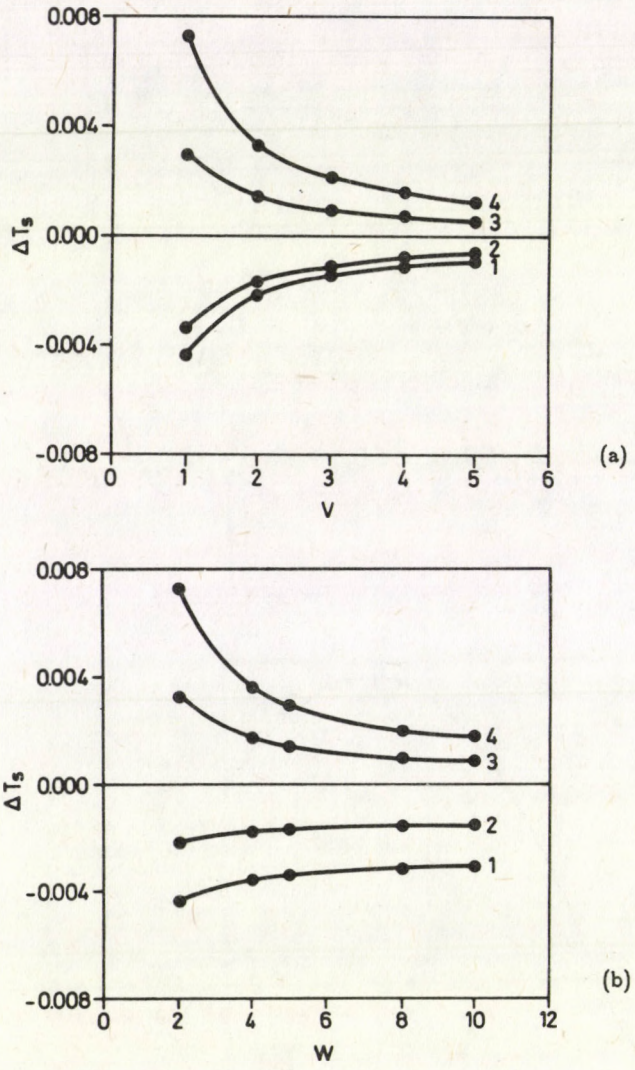

Fig. 2

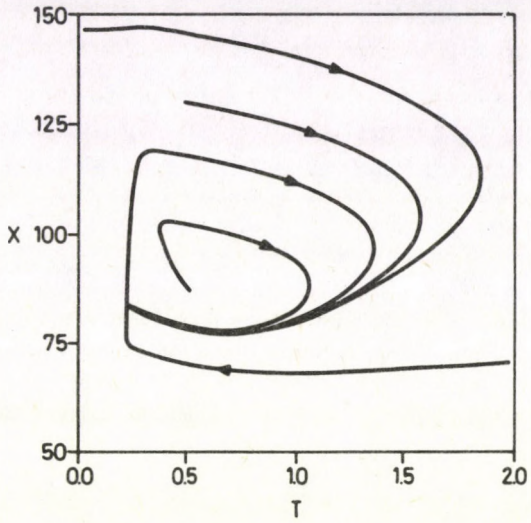

Fig. 3

The formula (17) was also used to study the dependence of stationary temperature on system size and the magnitude of elementary energy transfer for various values of heat transfer α.

Fig. 2a shows the dependence of $\Delta T_s = \langle T_s^{\text{stoch}} \rangle - T_s^{\text{determ}}$ on the system size (measured by an extensive parameter V). Fig. 2b gives the dependence of ΔT_s on the value of W. One can see that the increase of V and W leads to the decrease of ΔT_s. However, if V tends to infinity, ΔT_s tends to zero (fluctuations become negligible), while for finite V ΔT_s tends to a finite value when w increases (fluctuations related to the heat transfer become relatively small, but those related to chemical reaction are still significant, if the system size is finite).

(b) The Frank–Kamenetskii model

The simplest model of thermokinetic oscillations was proposed by Frank-Kamenetskii [9] and Sal'nikov [12]. It consists of the chain of reactions

$$\xrightarrow{k_0} A \xrightarrow{k_1} X \xrightarrow{k_2} B + Q, \tag{18}$$

the latter one being exothermic. The Arrhenius temperature dependence of k_i is assumed. In the sequel we will consider the case when the concentration of A (denoted by a) is kept constant; the reaction scheme will then reduce to two stages, $A \to X$ and $X \to B$. The deterministic evolution of the system is described by the rate equations for the concentration and the temperature

$$dx/dt = k_1 a - k_2 x = Aae^{-E_1/RT} - A_2 xe^{-E_2/RT},$$
$$dT/dt = (QA_2 x/\rho CV)e^{-E_2/RT} - \alpha(T - T_e). \tag{19}$$

As the second stage is exothermic, it will rapidly accelerate up to the exhaustion of the reagent X. Then the temperature rise will stop. Reaction 1 which does not depend strongly on temperature, will proceed, so after some time the concentration of X will be sufficiently large to start again the rapid stage 2. The process will thus repeat periodically (see Fig. 3). More details about deterministic description of thermokinetic oscillations and experimental data can be found in [13]. The stochastic evolution is described by the master equation for the 2-variable probability distribution $P(X, n)$; X is the particle number and n is discretized temperature (as in the previous Sections). This master equation has the form

$$\begin{aligned}\partial P(X,n,t)/\partial t = {} & W(X+1 \to X, n-w \to w)P(X+1, n-w, t) + \\ & + W(X-1 \to X)P(X-1, n, t) + \\ & + W(n+1 \to n)P(X, n+1, t) + W(X, n-1 \to n)P(X, n-1, t) - \\ & - [W(X \to X+1) + W(X \to X-1, n \to n+w) + \\ & + W(n \to n-1) + W(n \to n+1)]\, P(X, n, t).\end{aligned} \tag{20}$$

The transition probabilities $W(n \to n \pm 1)$ are given by (5), the other ones are

$$\begin{aligned} W(X \to X-1, n \to n+w) &= A_2 Xe^{-E_2/RT}, \\ W(X \to X+1) &= A_1 aVe^{-E_1/RT}. \end{aligned} \tag{21}$$

We performed a series of simulations for different system volumes applying Gillespie's algorithm [14]. The results are shown in Figs 4a–c. In Fig 4a (the largest volume) one can see the "probability crater" along the limit cycle. If the system size decreases, the internal fluctuations become more important and the crater gradually disappears (Figs 4b–c); we get unimodal probability distribution. The destruction of limit cycle by fluctuations was already observed in the case of additive external noise for the Van der Pol oscillator and the Sel'kov model [15].

4. Conclusions

We proposed a simplified stochastic model of exothermal chemical reactions with Newtonian heat exchange. The discretization of the energy transfer leads to a two-step master equation. We investigated the stationary solution of this equation for the Semenov model, discussing how the stochastic effects depend on the system size, magnitude of energy transfer and exothermicity of reaction. We performed also stochastic simulations for the model of thermokinetic oscillations, observing a noise-induced phase transition (disappearance of the limit cycle for smaller system sizes).

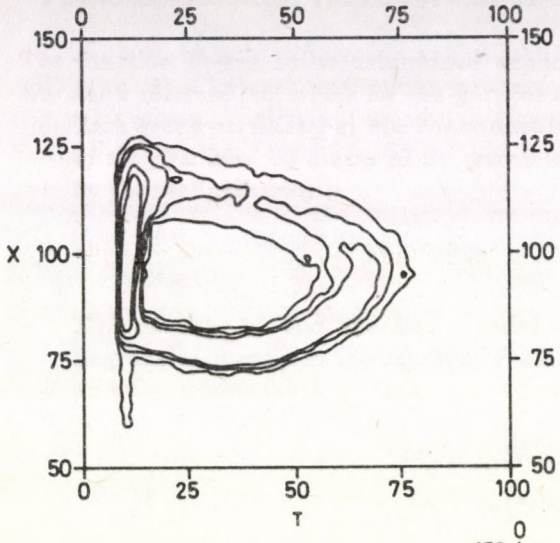

Fig. 4a

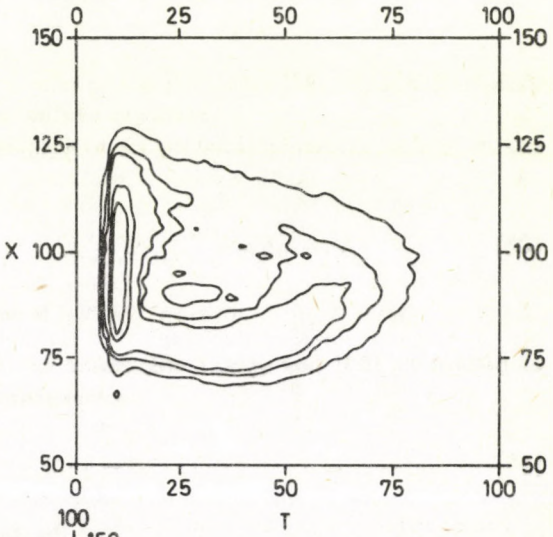

Fig. 4b

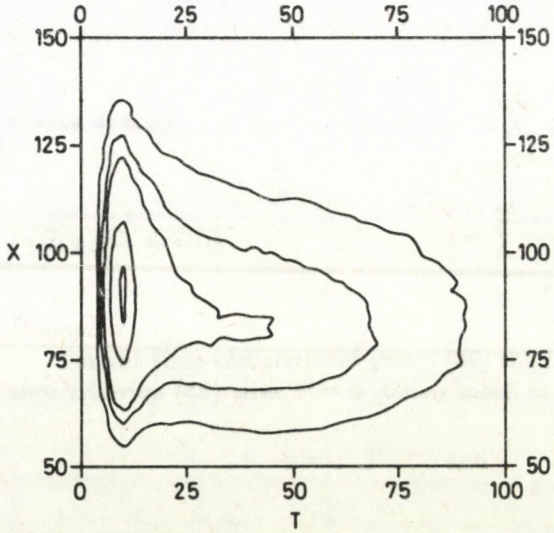

Fig. 4c

The model can be easily generalized to describe compartmental systems. Other possibility of generalization is to take q as a distributed variable (passage from "Einstein-like" to "Debye-like" reservoir). Recent progress in molecular dynamics simulations on nonisothermal chemical systems [16, 17] shall help in finding most appropriate forms of transition probabilities to be used in discrete master equations. The master equations can be then used more extensively to analyze chemical processes with heat transfer. As stochastic simulations are less time-consuming than molecular dynamics, they may be a useful tool to study nonisothermal systems on the mesoscopic level, especially to get qualitative information about non-equilibrium phase transitions.

Acknowledgement

The work was partly supported by Project CPBR 3.20.

References

1. C. W. Gardiner, Handbook of Stochastic Methods, Springer, Berlin, 1983.
2. F. Baras, G. Nicolis, M. Malek-Mansour and J. W. Turner, J. Stat. Phys., *32*, 1, 1983.
3. J. Górecki and J. Popielawski, J. Stat. Phys., *44*, 941, 1986.
4. F. de Pascuale and A. Mecozzi, Phys. Rev. A, *31*, 2454, 1985.
5. G. Nicolis, F. Baras and M. Malek Mansour, in Nonlinear Phenomena in Chemical Dynamics, edited by A. Pacault and C. Vidal, Springer, Berlin, 1981.
6. P. P. Szczęsny, M. Frankowicz and A. Chłobowski, React. Kinet. Catal. Lett., *38*, 363, 1988.
7. G. Nicolis and M. Malek Mansour, Phys. Rev. A, *29*, 2845, 1984.
8. G. Nicolis, F. Baras and M. Malek Mansour, in Nonequilibrium Dynamics of Chemical Systems, edited by A. Pacault and C. Vidal, Springer, Berlin, 1984.
9. D. A. Frank-Kamenetskii, Diffusion and Heat Transfer in Chemical Kinetics, Plenum Press, New York, 1969.
10. G. Nicolis and F. Baras, J. Stat. Phys., *48*, 1071, 1987.
11. M. Frankowicz, Acta Phys. Pol., *A74*, 3, 1988.
12. L. K. Salnikov, Zh. Fiz. Khim., *23*, 258, 1949.
13. J. Griffiths, in Oscillations and Traveling Waves in Chemical Systems, edited by R. J. Field and M. Burger, Wiley, New York, 1985.
14. D. T. Gillespie, J. Phys. Chem., *81*, 2340, 1977.
15. H. Malchow and L. Schimansky-Geier, Noise and Diffusion in Bistable Nonequilibrium Systems, Teubner Verlag, Leipzig, 1985.
16. D. P. Chao and S. Yip, Combust. Flame, *58*, 239, 1984.
17. J. Górecki and J. Gryko, J. Stat. Phys., *46*, 329, 1987.

Acta Physica Hungarica 67 (3–4), pp. 351–357 (1990)

HIGH RESOLUTION SPECTROSCOPY OF THE VAN DER WAALS MOLECULES NaAr AND NaKr*

D. ZIMMERMANN

Institute for Radiation and Nuclear Physics
Technical University Berlin
D-1000 Berlin 12, Germany

(Received 21 December 1988)

The rovibrational structure of the transition $A^2\Pi - X^2\Sigma$ of the van der Waals molecules NaAr and NaKr has been investigated by means of high resolution laser spectroscopy applying the techniques of laser-induced fluorescence and of optical–optical double resonance to the molecules in a supersonic beam. Precise values for the parameters of rotation have been obtained for the $X^2\Sigma$ state of $NaKr^{84}$. By means of an investigation of the spectral distribution of the fluorescence light the repulsive part of the $X\Sigma$-potential of NaKr has been determined. Local perturbations have been detected in the $A^2\Pi$ states of both NaAr and NaKr and a full deperturbation analysis has been performed.

1. Introduction

The interaction potential between an alkali atom and a rare gas atom has been the topic of many investigations, both experimentally and theoretically, for a long time. One of the reasons for this continuous interest is the relative simplicity of the system containing only one electron outside closed shells. Therefore, a useful approach to the theoretical calculation is a treatment as a three-body problem consisting of the valence electron, the core of the alkali ion and the rare gas atom. In this way, pseudo potentials or model potentials have been derived for all combinations of an alkali atom with a rare gas atom. Up to now, experimental information on these systems comes mainly from scattering experiments and from line broadening investigations. However, spectroscopic work on diatomic alkali-rare gas van der Waals molecules is expected to provide more precise information on the interaction potentials.

The present contribution deals with the laserspectroscopic investigation of the molecules NaKr and NaAr. The molecular ground state $X^2\Sigma^+$ is weakly bound with a well-depth of the order of 50 cm^{-1}. The first excited P-state of the sodium atom leads to the two excited molecular states $A^2\Pi_{1/2}$ and $A^2\Pi_{3/2}$ with a well-depth of typically 500 cm^{-1} and to the $B^2\Sigma^+$ state. Up to now, only the transition $A\Pi - X\Sigma$ has been studied in detail. The equilibrium distances in the molecular

*Dedicated to Prof. István Kovács on the occasion of his 75th birthday and presented at the Conference on High Resolution Electronic Spectroscopy of Molecules, held at Tihany in Sept. 88.

ground state and in the $A\Pi$ state are quite different. Therefore, starting from the vibrational ground state $v'' = 0$ one can excite only vibrational levels of the $A\Pi$ state around $v' = 10$ with sufficient intensity due to the Franck–Condon principle.

The intention of the present investigation is to contribute to a precise determination of the $X\Sigma$ and of the $A\Pi$ interaction potential. In addition, the results of our investigations may serve as a sensitive test for the accuracy of model potential calculations. As previous results have been published for NaAr [1] and NaKr [2] I restrict myself to the presentation of some new and unpublished material. This work has been performed in cooperation with my coworkers Dr. E. Zanger, Dipl.-Phys. A. Nunnemann, N. Ahr, I. Kapetanakis and V. Schmatloch.

2. Experimental observation and rotational analysis

The van der Waals molecules were produced by supersonic expansion of a mixture of rare gas and sodium vapour through a nozzle into a vacuum. The molecular beam was crossed by the light beam of a tunable single-mode cw dye laser under right angle. The fluorescence light of the molecules was observed in the direction perpendicular to the laser beam and to the jet. The dye laser was electronically scanned under computer control over a wavenumber range of 1 cm^{-1}. The relative frequency of the laser was determined by a Fabry–Perot interferometer, the absolute wavenumber was obtained by recording the well-known absorption lines of the iodine molecule. The intensity of the fluorescence light and the transmitted intensities of the Fabry–Perot interferometer and the iodine cell were read by the computer and stored in proper files on the disk for further analysis.

The largest amount of information comes from an investigation of the rovibrational structure of the absorption spectrum of the molecules due to the transition $A\Pi$–$X\Sigma$ where the total intensity of the laser-induced fluorescence is detected. The molecular ground state $X^2\Sigma^+$ is a Hund's coupling case b whereas the $A\Pi$ state is dominantly case a. The small amount of decoupling in the $A\Pi$ state for higher rotational quantum numbers has been taken into account in our analysis. The spin–rotation splitting in the $X\Sigma$ state seems to be smaller than the resolution of our apparatus and could not be observed. Therefore, the rotational structure of each vibrational transition consists of 4 instead of 6 branches: P_1, Q_1, R_1, P_{12} with relative intensities of approximately 3:3:1:1 for $A\Pi_{1/2}$–$X\Sigma$, and P_2, Q_2, R_2, R_{21} with relative intensities of 1:3:3:1 for $A\Pi_{3/2}$–$X\Sigma$. As the hyperfine structure of the sodium atom in its ground state is transferred to the molecular $X\Sigma$ state without change in our case, each rovibrational molecular line appears as a doublet with intensity ratio 5:3 and a splitting of 0.059 cm^{-1}.

Fig. 1 shows as an example one high-resolution scan of the absorption spectrum of NaKr. Due to the strong overlapping of different vibrational bands and due to the presence of several Kr-isotopes in natural mixture the observed absorption spectrum turned out to be highly congested. An assignment of rotational branches and rotational quantum numbers to the numerous absorption lines seems to be very difficult or even impossible without additional experimental information.

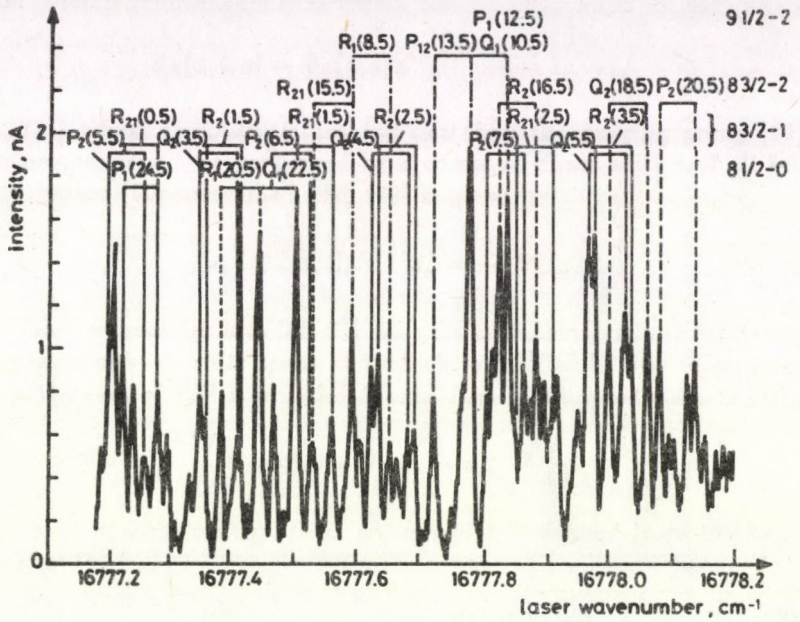

Fig. 1. Part of the high resolution absorption spectrum of NaKr with rotational assignment $P_1(J'')$, $Q_1(J'')$.... The vibrational assignment in the right upper corner is $v'\Omega - v''$ with $\Omega = 1/2$ and $3/2$ for $A\Pi_{1/2}$ and $A\Pi_{3/2}$ resp.

Therefore, we have applied the method of optical–optical double resonance (OODR) using two tunable single-mode dye lasers of about equal intensity. The frequency of laser B is tuned to a certain rovibronic transition of NaKr while the frequency of laser A is scanned. Both laser beams are chopped with different frequencies f_A and f_B. Our detection scheme for OODR essentially corresponds to an observation of the part of the fluorescence light being modulated with frequency $f_A + f_B$. Under these conditions we can observe OODR signals if, for instance, the two rovibrational transitions induced by the two lasers share a common lower level. Therefore, the OODR spectrum is much simpler than the absorption spectrum. It consists of only four lines for each vibrational band, it is isotope-selective and essentially Doppler-free. However, the OODR lines are power-broadened due to the high laser intensities necessary for obtaining the signals. Using the measured frequency separation $Q(J) - P(J)$ and $R(J) - Q(J)$ of the OODR spectrum the value of J and an approximate value of the rotational constant of the upper state may easily be deduced. By performing OODR investigations for different common lower levels we could successfully assign rotational quantum numbers and branches to the numerous lines of the absorption spectrum as indicated in Fig. 1.

Another source of experimental information on the interatomic potential is an investigation of the spectral distribution of the fluorescence light. The frequency of

the exciting laser is fixed to a proper transition. The fluorescence light is focussed onto the entrance slit of a grating monochromator which is scanned under computer

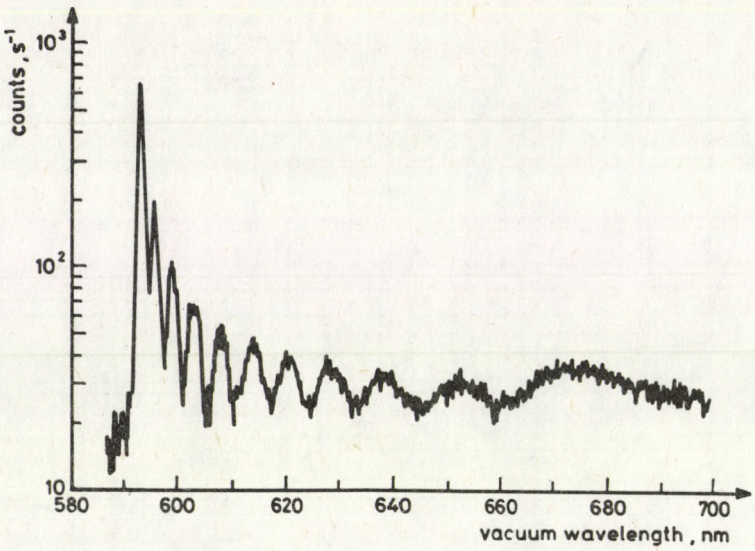

Fig. 2. Spectral intensity distribution of fluorescence light. The laser was tuned to a wavenumber of 16 862.43 cm^{-1} exciting the hfs component $G = 2$ of the $Q_2(9.5)$ line of the transition $X^2\Sigma v'' = 0 \rightarrow A^2\Pi_{3/2} v' = 10$ of $NaKr^{84}$

control by means of a step motor. The result of our measurement in Fig. 2 obtained with an apparatus width of 1 nm shows a pattern with several peaks extending over a wavelength range of about 100 nm. The first peak at low wavelength contains all transitions to bound levels of the molecular ground state, whereas the remaining part of the spectrum is due to bound-free transitions ending on the repulsive part of the interatomic potential of the ground state. The whole pattern shows a clear reflection structure "reflecting" the radial probability distribution of the vibrational wave function of the upper bound state into the observed spectrum. A simple counting of the number of peaks yields then the vibrational quantum number of the upper state.

3. Results

For the case of NaKr our previous investigation of the absorption spectrum of the $A\Pi - X\Sigma$ transition covered the range of wavenumbers between 16 858 and 16 950 cm^{-1}. The present work deals with an extension of this investigation to lower wavenumbers down to 16 758 cm^{-1}. Up to now, our analysis is restricted to the most abundant krypton isotope Kr^{84} with a relative abundance of 57% in

natural mixture of isotopes. We were able to assign rotational quantum numbers and rotational branches to about 700 additional absorption lines of the molecule $NaKr^{84}$. These lines belong to transitions between vibrational levels $v' = 8...10$ of the $A\Pi$ state and $v'' = 0..2$ of the $X\Sigma$ state. The measured frequency positions of these lines were fitted to the proper molecular Hamiltonian together with our previous results in one global fit in order to determine the molecular parameters of rotation, vibration, fine-structure splitting and λ-type doubling.

For the $X\Sigma$ state we obtained for the first time rotationally resolved spectra for the vibrational levels $v'' = 1$ and 2. Our results compiled in Table I allow us a

Table I

Rotational constants and energy differences of vibrational levels of the $X\Sigma$ state of $NaKr^{84}$

v''	$B_{v''}[GHz]$	$D_{v''}[10^{-5}$ GHz]	$H_{v''}[10^{-9}$ GHz]	$(E_{v''+1} - E_{v''})[$ GHz]
0	1.1285(2)	3.29(4)	−2.2(2)	396.91(2)
1	1.0645(3)	3.76(7)	−3.8(6)	348.26(2)
2	1.9940(4)	4.38(18)	−7.7(2.6)	

more precise determination of the bound part of the $X\Sigma$ potential than before [2]. This part of the potential may be represented to a good approximation by a Morse potential with an equilibrium distance of 0.4917(2) nm, a well-depth of 68.1(3) cm^{-1} and with $\beta a_0 = 0.493(2)$ (a_0 Bohr radius). Expanding the experimental values of $B_{v''}$ of Table I into a power series with respect to $v'' + 1/2$ the coefficient of the linear term turns out to be $\alpha_e = 0.0576(8)$ GHz. From the Morse potential given above we deduce a value of $\alpha_e = 0.0647$ GHz which is in satisfactory agreement with the experimental results. According to the Morse approximation altogether 9 vibrational levels $v'' = 0...8$ are expected to be bound within the well of the $X\Sigma$ potential.

For the excited $A\Pi$ states we have determined the parameters of rotation, of fine structure splitting and of λ-type doubling for the vibrational levels $v' = 8, 9$ and 10 for the first time. Parts of our results are compiled in Table II. As can be seen

Table II

Fine structure splitting constant A, rotational constant B, and energy value of vibrational levels of the $A^2\Pi$ state of $NaKr^{84}$

v'	A [GHz]	B [GHz]	$(T_{v'} - T_0)$ [cm^{-1}]
8	938.79(2)	2.1087(3)	16 774.611(4)
9	877.37(2)	1.9974(2)	16 812.721(4)
10	818.26(2)	1.8849(2)	16 846.774(4)

from Table II the fine structure splitting constant increases with decreasing v' and is much higher than the value of 345 GHz expected for a Hund's coupling case a from the fine structure splitting of the 3^2P state of the sodium atom. The interatomic potential of the $A^2\Pi_{1/2}$ and the $A^2\Pi_{3/2}$ state has been obtained in tabulated form by means of the usual RKR procedure using all our data for the vibrational levels

$v' = 8..14$. In comparison with the results of recent model potential calculations [3] our RKR potential curve is of similar shape, but is shifted by about 0.02 nm to higher internuclear separations.

As already mentioned, the fluorescence spectrum of Fig. 2 is useful in order to obtain information on the repulsive part of the $X\Sigma$ potential. We have used a computer program solving the Schrödinger equation for the upper bound state and for the lower continuum states for a given tabulated $A\Pi$ and $X\Sigma$ potential, resp. and calculating the intensity of the fluorescence light as a function of the wavelength. Using the results of the model potential calculations of Düren et al [3] for the $A\Pi$ and the $X\Sigma$ potential we found considerable discrepancies between the calculated pattern and the experimental curve, the experimental maxima occuring consistently at lower wavelengths than in the calculated curve. Therefore, we changed the repulsive part of the $X\Sigma$ model potential by means of a simple two-parameter polynomial in R (R internuclear separation). Setting the coefficients of the polynomial to proper values we obtained better agreement between experiment and calculation. As can be seen from our preliminary results in Table III the repulsive part of the $X\Sigma$ model potential has to be lowered consirably. However,

Table III

Preliminary results for the repulsive part V of the $X\Sigma$ potential as a function of R in comparison with the result V_{mod} of the model potential calculation [3]

R [nm]	V [cm^{-1}]	V_{mod} [cm^{-1}]
0.265	1484	2192
0.291	712	1284
0.330	399	653
0.370	218	270
0.410	52	53

we could not obtain full agreement between experiment and calculation with this simple modification and a more refined analysis is certainly necessary.

4. Local perturbation

For increasing vibrational quantum number v' in the $A\Pi$ state the energy values of the levels v' of the $A\Pi_{3/2}$ and $v'+1$ of $A\Pi_{1/2}$ approach each other. Due to the different rotational constants in both levels we get a crossing of the two rotational ladders at a certain non-integer value of the rotational quantum number. The energy values of the rovibrational levels near the crossing point are considerably shifted by the non-diagonal part of the rotational Hamiltonian proportional to the operator $J_+S_- + J_-S_+$ ($\vec{J}$, $\vec{S}$ operator of total and spin angular momentum, resp.). This operator connects the rovibrational levels v', J' of the $A\Pi_{3/2}$ state and $v'+1, J'$ of the $A\Pi_{1/2}$ state. However, its effect is only important close to the crossing and may be neglected far away from the crossing. In the experimental absorption

spectrum the local perturbation shows up as a shift of the corresponding absorption lines from their regular positions.

A full deperturbation analysis has already been performed for the local perturbation between $v' = 11$, $\Omega = 3/2$ and $v' = 12$, $\Omega = 1/2$ as well as between $v' = 12$, $\Omega = 3/2$ and $v' = 13$, $\Omega = 1/2$ in NaKr [2]. Therefore, I restrict myself to our new results for the case of NaAr. A local perturbation occurs between the levels $v' = 11$, $\Omega = 3/2$ and $v' = 12$, $\Omega = 1/2$ around $J' = 11.5$. In order to get a rotational assignment for the molecular absorption lines near the local perturbation where the spectrum is highly congested it was necessary to perform OODR investigations. By means of these investigations we were able to determine the positions of about 30 absorption lines with known assignment near the local perturbation and to deduce preliminary values of the perturbation parameter $B(v', v' + 1)$. Using this preliminary result we could identify about 70 molecular absorption lines in the absorption spectrum due to the transitions $A\Pi_{3/2}$, $v' = 11 - X\Sigma v'' = 0$ and $A\Pi_{1/2}$, $v' = 12 - X\Sigma v'' = 0$ with J'' - values ranging up to 17.5.

Finally, we performed successfully a deperturbation analysis using the same procedure as described in [2]. The rotational perturbation parameter was determined to be $B_{11/12} = 0.474(3)$ GHz for the $A\Pi$ state of NaAr. The perturbation is slightly different for e and f levels. This effect may be taken into account by introducing a second phenomenological parameter $q(v', v' + 1)$ into the Hamilton operator of the perturbation [2]. For the case of the $A\Pi$ state of NaAr we obtain $q_{11/12} = 0.021(5)$ GHz. Our experimental results for $B_{11/12}$ may be compared to the theoretical prediction which is proportional to the matrix element of $1/R^2$ between the two vibrational states. The vibrational wavefunctions have been calculated by solving the Schrödinger equation of molecular vibration using the model potential of Düren et al [3] for the interatomic potential of the $A\Pi$ state. The result of this calculation is $B_{11/12} = 0.505$ GHz which is in very good agreement with the experimental value.

References

1. G. Aepfelbach, A. Nunnemann and D. Zimmermann, Chem. Phys. Lett., *96*, 311, 1983.
2. E. Zanger, V. Schmatloch and D. Zimmermann, J. Chem. Phys., *88*, 5396, 1988.
3. R. Düren, E. Hasselbrink and G. Moritz, Z. f. Physik, *A307*, 1, 1982; R. Düren and E. Hasselbrink, private communication, 1981.

Acta Physica Hungarica 67 (3–4), pp. 359–362 (1990)

A THEORY OF MASSIVE PHOTONS AND MONOPOLES

G. CALLEGARI, P. FORTINI

Physics Institute, University of Ferrara
Ferrara, Italy
Sez. I. N. F. N Ferrara, Italy

and

D. TARTARI

Physics Institute, University of Ferrara
Ferrara, Italy

(Received 6 February 1989)

A unified theory of massive photons and monopoles is proposed and compared with the measurement of the magnetic field of the earth.

Introduction

In this paper we propose a theory both of massive photons and Dirac's monopoles in order to account for the radial component of the magnetic field of the earth and to give a new method for measuring the mass of the photons.

Beside the interpretation of this radial component our theory allows for giving an upper limit for the total magnetic charge of the planet.

Laboratory experiments based on Coulomb's law have set a very small upper limit for the photon mass [1, 2, 3]. Another upper limit for the photon mass can be obtained from the measurement of the magnetic field of the earth.

The usual dipole expression for a magnetic field is

$$\mathbf{H} = \frac{m}{r^3}\left[3(\hat{\mathbf{z}}\cdot\hat{\mathbf{r}})\hat{\mathbf{r}} - \hat{\mathbf{z}}\right], \tag{1}$$

where $\mathbf{m}$ is the magnetic moment and $\hat{\mathbf{z}}$ is a unit vector in the direction of the dipole axis.

If a massive photon is assumed from Proca's theory the former expression is modified as [4]

$$\mathbf{H}_P = \frac{m}{r^3}e^{-\mu r}\left[(1+\mu r+\frac{1}{3}\mu^2 r^2)(3(\hat{\mathbf{r}}\hat{\mathbf{z}})\hat{\mathbf{r}} - \hat{\mathbf{z}}) - \frac{2}{3}\mu^2 r^2\hat{\mathbf{z}}\right], \tag{2}$$

where μ is the inverse Compton wavelength of the photon. The last term in (2) looks like a constant magnetic field H_{EXT} for fixed r which adds to the classical case. On the earth surface at the equator the ratio between H_{EST} and the classical dipole field is

$$\frac{H_{EST}}{H_{EQ}} = \frac{\frac{2}{3}\mu^2 R^2}{1 + \mu R + \frac{1}{3}\mu^2 R^2}.$$

Measurement of the ratio fixes for the photon mass an upper limit of $4 \cdot 10^{-51} \div 8 \cdot 10^{-52}$ kg [4, 5].

In this paper we show that our theory is compatible with these data.

1. A unitary theory of massive photons and monopoles

In order to give a coherent theory of massive photons and monopoles we start from the formulation of Cabibbo and Ferrari [6]. The electromagnetic tensor is expressed by means of two potentials A^μ and B^μ by

$$F^{\mu\nu} = \partial^\mu A^\nu - \partial^\nu A^\mu - \epsilon^{\mu\nu\rho\sigma}\partial_\rho B_\sigma. \tag{3}$$

This allows to overcome the conceptual difficulties of the Dirac's strings [7, 8]. Our theory starts from the Lagrangian

$$\mathcal{L} = -\frac{1}{16\pi} F^{\mu\nu} - \frac{1}{c} J_\nu A^\nu + \frac{1}{c} K_\nu B^\nu + \frac{\mu^2}{8\pi} A^\mu A_\mu - \frac{\sigma^2}{8\pi} B_\mu A^\mu. \tag{4}$$

when J^μ is the "electrical current" and K^μ is the "magnetic current". As can be seen from (4) our theory allows two photon masses μ and σ. The above expression comes from two assumptions:

1) Terms like $\mu^2 A_\mu B^\mu$ which would mix up the potentials the field equations are omitted.
2) The field sources interact only with their own potentials.

From (4) there follow the field equations:

$$\begin{aligned} \partial^\mu F_{\mu\nu} + \mu^2 A_\nu &= \frac{4\pi}{c} J_\nu, \\ \partial_\mu \tilde{F}_{\mu\nu} + \sigma^2 B_\nu &= \frac{4\pi}{c} K_\nu, \end{aligned} \tag{5}$$

where $\tilde{F}_{\mu\nu}$ is the dual of $F_{\mu\nu}$.

From (5) it turns out that for $\nu \longrightarrow 0$ and $\sigma \longrightarrow 0$ one gets the equations for the Dirac monopoles while in absence of magnetic charges one gets back Proca's equations and the usual definition of $F_{\mu\nu}$.

Obviously for $\mu = \sigma = 0$ and $B_\mu = 0$ one gets the Maxwell equations.

We can therefore say that (5) are the natural extension of classical theory to the case of massive photons and monopoles.

In this theory the field E and H are:

$$\mathbf{E} = -\nabla\Phi - \frac{1}{c}\frac{\partial}{\partial t}\mathbf{A} - \nabla \wedge \mathbf{B}, \tag{6}$$

$$\mathbf{H} = -\nabla\Omega - \frac{1}{c}\frac{\partial}{\partial t}\mathbf{B} + \nabla \wedge \mathbf{A}, \tag{7}$$

where $A^\mu = (\Phi, \mathbf{A})$ and $B^\mu = (\Omega, \mathbf{B})$ are the two four potentials; the free equations are the very complicated expression

$$\Box\,\mathbf{E} = \mu^2\left(\nabla\Phi + \frac{1}{c}\frac{\partial}{\partial t}\mathbf{A}\right) + \sigma^2\nabla \wedge \mathbf{B}, \tag{8}$$

$$\Box\,\mathbf{H} = \sigma^2\left(\nabla\Omega + \frac{1}{c}\frac{\partial}{\partial t}\mathbf{B}\right) - \mu^2\nabla \wedge \mathbf{A}. \tag{9}$$

However, if one puts $\mu = \sigma$ we get instead of (8), (9) the very simple equations

$$(\Box + \mu^2)\,\mathbf{E} = 0, \tag{10}$$

$$(\Box + \sigma^2)\,\mathbf{H} = 0. \tag{11}$$

2. Calculation of the magnetic field of the earth

For a static field we get from (7)

$$\mathbf{H} = -\nabla\Omega + \nabla \wedge \mathbf{A}. \tag{12}$$

Developing the scalar potential Ω and the vector potential A in the multipole series, the scalar potential gives a monopoles term:

$$\Omega(\mathbf{r}) = g\,\frac{\mathrm{e}^{-\mu r}}{r} \tag{13}$$

and a dipole term

$$\Omega(\mathbf{r}) = -\mathbf{P}_m \cdot \nabla\left(\frac{\mathrm{e}^{-\mu r}}{r}\right), \tag{14}$$

where

$$\mathbf{P}_m = \int \mathbf{x}'\rho_m(\mathbf{x}')\,d^3x' \tag{15}$$

is the dipole moment due to the distribution of magnetic charge ρ_m. The vector potential A does not give any monopole term as in the classical case but a dipole term generated by the electric current:

$$\mathbf{A}(\mathbf{x}) = \frac{\mathbf{m} \wedge \mathbf{x}}{|\mathbf{x}|^3}, \tag{16}$$

where

$$\mathbf{m} = \frac{1}{2c} \int \mathbf{x}' \wedge \mathbf{J}(\mathbf{x}')\, d^3x' \tag{17}$$

is the magnetic moment.

After lengthy calculations we have

$$\begin{aligned} \mathbf{H} = & g \frac{e^{-\mu r}}{r^3} (1+\mu r)\mathbf{r} + \\ & + \frac{me^{-\mu r}}{r^3} \left[(1+\mu r + \frac{1}{3}\mu^2 r^2)(3(\hat{\mathbf{m}} \cdot \hat{\mathbf{r}})\hat{\mathbf{r}} - \hat{\mathbf{m}}) - \frac{2}{3}\mu^2 r^2 \hat{\mathbf{m}} \right] + \\ & + \frac{P_m e^{-\mu r}}{r^3} \left[(1+\mu r + \frac{1}{3}\mu^2 r^2)(3(\hat{\mathbf{r}} \cdot \hat{\mathbf{p}})\hat{\mathbf{r}} - \hat{\mathbf{p}}) - \frac{1}{3}\mu^2 r^2 \hat{\mathbf{p}} \right]. \end{aligned} \tag{18}$$

Conclusions

Our formula (18) does not give any further support for the measurement of the photon mass as it is essentially due to the measurement of the external field $2/3r^2\mu^2$ which is proportional to μ^2. A second external field is introduced through $1/3Pr^2\mu^2$ anywhere the external smallness of a magnetic charge distribution is such that this term is much below the instrumental sensitivity.

On the contrary our formula allows to give an upper limit on the magnetic charge of the earth. Experimental evidence supports that the possible radial component of the earth magnetic field is not greater than 10 γ.

From Dirac's quantisation conditions the elementary charge of the monopole is of the order 10^{-15} MKS unit. From the first term of (18) with r taken as the earth radius and with $m_r = 10^{-51}$ kg we get that the total maximum magnetic charge of the planet must be less than 10^8 monopoles. Such density corresponds to 1 monopole every 10^{43} nucleons which does not affect in any way the cosmological critical density.

References

1. S. J. Plimpton and W. E. Lawton, Phys. Rev., *50*, 1066, 1936.
2. D. F. Bartlett, P. E. Goldhagen and E. A. Phillips, Phys. Rev., *D2*, 438, 1970.
3. E. R. Williams, J. E. Faller and H. Hill, Phys. Rev. Lett., *26*, 721, 1972.
4. A. S. Goldhaber and M. M. Nieto, Rev. Mod. Phys., *43*, 277, 1971.
5. L. Davis Jr., A. S. Goldhaber and M. M. Nieto, Phys. Rev. Lett., *35*, 1402, 1975.
6. N. Cabibbo and E. Ferrari, Nuovo Cim., *23*, 1147, 1962.
7. F. Rohrlich, Phys. Rev., *150*, 1104, 1966.
8. E. Ferrari, in "Tachions, Monopoles and Related Topics", p. 203, Ed. Recami, North-Holland, N. Y., 1978.

Acta Physica Hungarica 67 (3–4), pp. 363–366 (1990)

AN APPROACH TO SPHERICALLY SYMMETRIC PERFECT FLUID SOLUTION IN GENERAL RELATIVITY USING THIN LAYERS*

P. KROLL

Physics Section, Friedrich Schiller University Jena
Jena 6900 GDR

(Received 9 February 1989)

The system of Einstein's field equations for a spherically symmetric perfect fluid is integrable in the event of constant mass density. Using this result we consider thin layers with the same symmetric properties. From the fitting conditions and by reducing the thickness of the layers to zero we obtain a new system of differential equations of the former constants of integration.

1. Introduction

From the Einstein's field equations

$$R_{ab} - \frac{1}{2} R g_{ab} = \kappa T_{ab}, \tag{1}$$

(R_{ab} denotes the Ricci tensor, R the curvature invariant, g_{ab} the metric tensor, κ Einstein's gravitational constant and T_{ab} the energy-momentum tensor) using the spherically symmetric metric

$$ds^2 = e^{\lambda(r)} dr^2 + r^2 (d\vartheta^2 + \sin^2 \vartheta \, d\varphi^2) - e^{\nu(r)} c^2 \, dt^2 \tag{2}$$

one obtains for a perfect fluid

$$T^{ab} = \left(\mu + \frac{p}{c^2}\right) u^a u^b + p g^{ab} \tag{3}$$

(μ is the mass density, p is pressure and u^a is the 4-velocity) the following system of differential equations

$$\kappa p = e^{-\lambda} \left[\frac{\nu'}{r} + \frac{1}{r^2}\right] - \frac{1}{r^2}, \tag{4}$$

$$\kappa p = e^{-\lambda} \left[\frac{\nu''}{2} + \frac{\nu'^2}{2} - \frac{\nu'\lambda'}{4} + \frac{\nu' - \lambda'}{2r}\right], \tag{5}$$

$$\kappa \mu c = e^{-\lambda} \left[\frac{\lambda'}{r} - \frac{1}{r^2}\right] + \frac{1}{r^2}, \tag{6}$$

*Dedicated to Professor E. Schmutzer (Jena) on the occasion of his 60th birthday

(bar denotes the derivative with respect to r) and the condition of integrability

$$p' = -\frac{\nu'}{2}\,[p + \mu c^2] \tag{7}$$

(see [1], [2]).

We will use Eq. (7) instead of Eq. (5). For the case $\mu = \text{const}$ it is possible to integrate the above system. The solution is

$$e^{-\lambda(r)} = 1 - Ar^2 + \frac{C}{r}, \tag{8}$$

$$p(r) = B\,e^{-\nu(r)/2} - \frac{3}{\kappa}\,A, \tag{9}$$

$$e^{\nu(r)/2} = \frac{\kappa B}{2A} - D\sqrt{1 - Ar^2} \tag{10}$$

with

$$A := \frac{1}{3}\,\kappa\mu c^2 = \text{constant}, \tag{11}$$

and C, B, D as the constants of integration.

Because of the fact that the metrical functions must be regular we have to set $C = 0$ in (8).

2. The method of thin layers

We are able to treat the system (4)–(7) for any function of $\mu(r)$ (resp. $A(r)$) in the following manner.

We divide the model in thin layers (shells) as shown in the Figure.

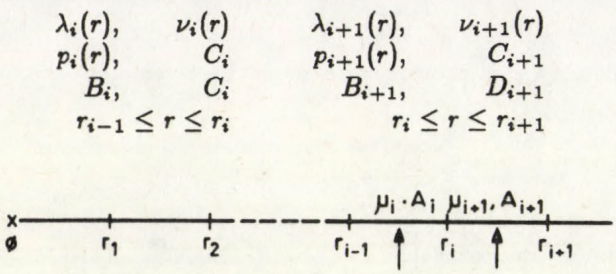

Fig. 1. Model divided into thin layers

In each layer the mass density μ (resp. A) should be constant. The spherical symmetry is not broken. Therefore equations (4)–(7) are valid. We obtain for each layer

$$e^{-\lambda_i(r)} = 1 - A_i r^2 + \frac{C_i}{r}, \tag{12}$$

$$p_i(r) = B_i\, e^{-\nu_i(r)/2} - \frac{3}{\kappa} A_i, \tag{13}$$

$$e^{\nu_i(r)/2} = \left(1 - A_i r^2 + \frac{C_i}{r}\right)^{1/2} \cdot \left[\frac{\kappa B_i}{2} \int_{r_{i-1}}^{r} \frac{r\, dr}{(1 - A_i r^2 + C_i/r)^{3/2}} + D_i\right], \tag{14}$$

$$(r_{i-1} \le r \le r_{i+1}),$$

(i denotes the number of layers). Furthermore we demand fitting conditions for λ, p and ν at the points r_i

$$\lambda_i(r_i) = \lambda_{i+1}(r_i), \tag{15}$$

$$p_i(r_i) = p_{i+1}(r_i), \tag{16}$$

$$\nu_i(r_i) = \nu_{i+1}(r_i). \tag{17}$$

We obtain

$$C_{i+1} - C_i = r_i^3 (A_{i+1} - A_i), \tag{18}$$

$$B_{i+1} - B_i = \frac{3}{\kappa}(A_{i+1} - A_i)\left(1 - A_i r^2 + \frac{C_i}{r_i}\right)^{1/2} D_{i+1}, \tag{19}$$

$$D_{i+1} - D_i = \frac{\kappa B_i}{2} \int_{r_{i-1}}^{r_i} \frac{r\, dr}{(1 - A_i r^2 + C_i/r)^{3/2}}. \tag{20}$$

With the thickness of the layers tending to zero we receive A (resp. μ) as a function of r, furthermore

$$C(r) = A(r) r^3 - 3 \int_0^r A(r) r^2\, dr + C_0, \qquad (C_0 \equiv 0) \tag{21}$$

and a system of differential equations of the former constants of integration

$$B'(r) = \frac{3}{\kappa} A'(r) \left[1 - \frac{3}{r} \int_0^r A(r) r^2\, dr\right]^{1/2} D(r), \tag{22}$$

$$D'(r) = \frac{\kappa}{2} r \left[1 - \frac{3}{r} \int_0^r A(r) r^2\, dr\right]^{-3/2} B(r). \tag{23}$$

Finally the complete result has the form

$$e^{-\lambda} = F^2, \tag{24}$$

$$e^{\nu} = D^2 F^2, \tag{25}$$

$$p = \frac{B}{DF} - \frac{3}{\kappa} A, \tag{26}$$

$$B' = \frac{3}{\kappa} A' F D, \tag{27}$$

$$D' = \frac{\kappa r}{2F^3} B, \tag{28}$$

where

$$F := \left[1 - \frac{3}{r} \int_0^r A(r) r^2 \, dr\right]^{1/2}. \tag{29}$$

That means that for any function $A(r)$ (resp. $\mu(r)$) we have to solve the equations (27) and (28) to obtain the exact solution of the field equations (4)–(7).

Furthermore we are able to formulate a differential equation of Riccati type

$$G' = \frac{3}{\kappa} A' F - \frac{\kappa r}{2F^3} G^2, \tag{30}$$

where

$$G := \frac{B}{D}. \tag{31}$$

3. Problems

The remaining problem is the more complicated treatment of the above system (24)–(28) for a given equation of state

$$p = p(\mu) \tag{32}$$

and not for any given function $\mu(r)$.

Acknowledgement

I want to thank Dr. Z. Perjés of the KFKI – Institute of the Hungarian Academy of Sciences, Budapest, for suggesting the investigation, Dr. G. Neugebauer and Dr. H. Stephani of Friedrich-Schiller University Jena, GDR, for many helpful discussions.

References

1. D. Kramer, H. Stephani, M. MacCallum and E. Herlt, Exact solutions of Einstein's field equations, VEB Deutscher Verlag der Wissenschaften, Berlin, 1980.
2. H. Stephani, Allgemeine Relativitätstheorie, VEB Deutscher Verlag der Wissenschaften, Berlin, 1988.

Acta Physica Hungarica 67 (3–4), pp. 367–379 (1990)

DEPENDENCE OF THE INTERACTION POTENTIAL AND FUSION CROSS-SECTION ON TEMPERATURE

A. OSMAN and S. S. ABDEL-AZIZ

Physics Department, Faculty of Science, Cairo University
Cairo, Egypt

(Received 14 February 1989)

The theory of nuclear fusion of two heavy ions is considered. This fusion process is one of the most dissipative processes since the two ions combine together forming a single excited systems. The fusion process occurs when the system is trapped into a pocket of the potential energy surfaces. The interaction potential is calculated making use of the Thomas–Fermi model. The calculated interaction potential helps in reproducing the fusion barrier by introducing the energy density formalism. Neglecting the temperature, previous calculations show that the fusion of two heavy ions cannot occur if $Z_1 Z_2 \geq 2500$. In the present work, the effects of including the temperature in the interaction potential and on the fusion cross-section are investigated for several two heavy ions using a modified Thomas–Fermi model. In the present calculations, taking the temperature into account, the fusion process of two heavy nuclei is found to occur for all values of $Z_1 Z_2$ to 3000. This result is a generalized modified result for the previously obtained condition. Simple static calculations of the fusion cross-sections are performed using hot potentials. The present calculations show that the barrier of the fusion cross-section is not sensitive at low bombarding energies; while at higher bombarding energies, the inclusion of the temperature increases the fusion cross-section.

1. Introduction

The kinetic energy of the relative motion of two heavy nuclei [1] is converted into two types of energy. The first type of energy is the collective kinetic and potential energy, while the other type is the internal single-particle excitation energy. The first type of the energy (the collective energy) may be reconverted into other collective modes of energy and then consequently it does not represent any true dissipations. In contrast, the coupling of the transfer process of the initial kinetic energy into internal energy is an irreversible process on a macroscopic scale; and consequently it is considered as representing a dissipation. A strong connection between current and dissipation is investigated [2] leading to a friction form factor which is the basic importance in the dynamical description of dissipative heavy ion collisions. The connection between the calculated flux and the imaginary part of the optical potential is also investigated [2]. These techniques have been used in obtaining the particle jetting appearing in the early stages of high energy heavy ion reactions. No previous distinction has been introduced between collective and internal energy.

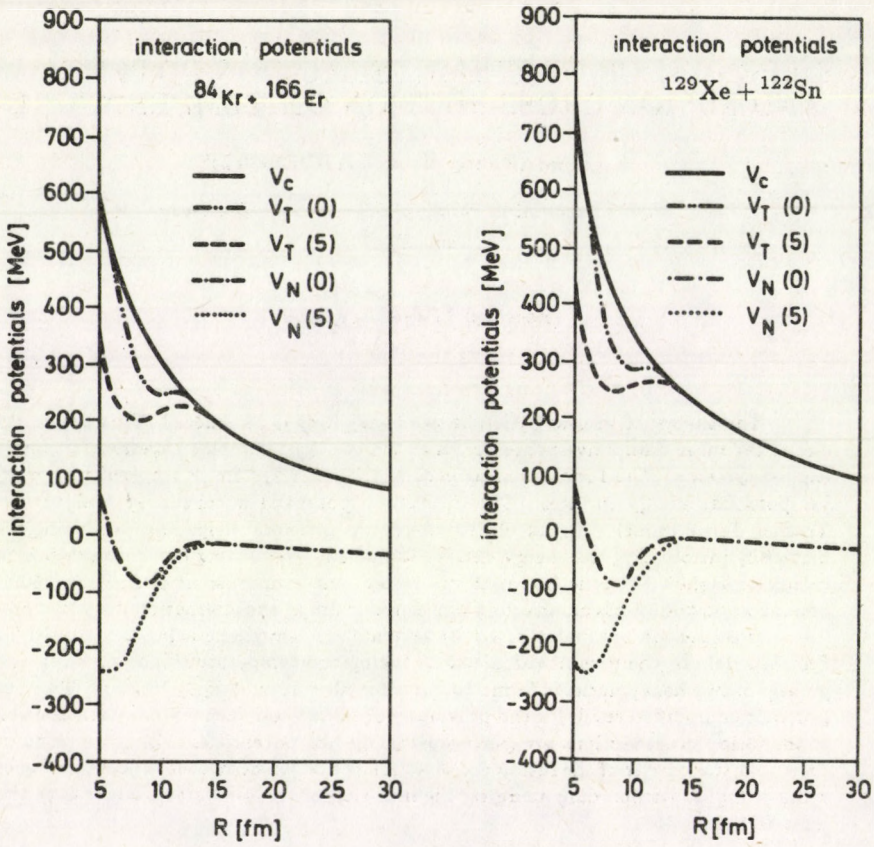

Fig. 1. Interaction energies of the two heavy ions $^{84}Kr + ^{166}Er$ as a function of their relative distance. $V_N(0)$ is the nuclear part of the potential at temperature 0 MeV, V_C is the Coulomb part and $V(0)$ is the total interaction potential at 0 MeV. $V_N(5)$ is the nuclear potential at $T =$ 5 MeV and $V_T(5)$ is the total interaction potential at 5 MeV

Fig. 2. Interaction energies of the two heavy ions $^{129}Xe + ^{122}Sn$ as a function of their relative distance. $V_N(0)$ is the nuclear part of the potential at temperature 0 MeV, V_C is the Coulomb part and $V(0)$ is the total interaction potential at 0 MeV. $V_N(5)$ is the nuclear potential at $T =$ 5 MeV and $V_T(5)$ is the total interaction potential at 5 MeV

The interaction potential between the two heavy ions at bombarding energies smaller than 10 MeV/A has been found to reveal the existence of dissipative phenomena [3]. In that respect two kinds of dissipative collisions have been investigated, namely, the fusion and the deep inelastic reactions. The fusion reactions are certainly the most dissipative ones since the two ions merge into a single system of excited nucleons. Then the fused system subsequently proceeds either to a compound nucleus or, in some special cases, to fast fission [4]. Meanwhile, the deep inelastic processes are introduced [5] in terms of few collective degrees of freedom in treating their evaluation towards the equilibrium. This equilibrium is not necessarily reached since, in

some cases, the interaction time is shorter than the relaxation time of the collective motion under consideration. In these studies the dissipation process is basically treated by means of a friction force acting on the collective motions. Several models [3, 6, 7] have been proposed to explain the dissipative characters of heavy ion reactions. One of the most interesting is the interaction potential in the sudden approximation by which a large number of systems [8, 9] has been calculated. In this model the basic statement is the generalized Thomas–Fermi function [10, 11], from which the parameters were determined by solving the variational problem. The nuclear densities generated in that approach do not exhibit a good tail behaviour, however, the Hartree–Fock densities [13] are used instead of it. One of the main problems in using the interaction potential model [3, 6, 7] is that the Hartree–Fock densities are needed as an input for the calculation. This leads to rather tedious computations and simplifications are necessarily needed.

The fusion process at which the system remains trapped into a pocket of the potential energy surface is investigated by Thomasi et al [14]. In their investigation, they found [15] that the pocket of the interaction potential disappears in two cases. The first case is that when the orbital angular momentum is sufficiently large due to the centrifugal force and being repulsive [16]. Therefore, for $\ell = 100$ it is found that the pocket disappears and can no longer trap the system. The second case of fusion process is that which comes from the repulsive Coulomb field between the two incident ions being very large for two very heavy nuclei. Therefore, the Coulomb force for a very heavy system cannot be counteracted any more by the nuclear force. The properties of dissipative heavy ion collisions are determined at the early stages of the reaction, before the system reaches the closest distance of approach. This case is applicable for instance for fusion process. Therefore, the fusion cross-sections can be obtained with a reasonable description by using the dynamical calculations using the sudden interaction potentials. However, other properties like the total kinetic energy of the deep inelastic fragments are mainly determined in the exit channel. In the case of using sudden potential, there is no quantitative effect if the two nuclei are assumed to remain spherical during the whole collision process.

The importance of conversion of relative motion kinetic energy into collective energy is shown by Nix et al [17] by calculating the compound nucleus cross-section for zero dissipation which provides an important background for subsequent calculations with any type of dissipation. These cross-section calculations are based on the criteria that the dynamical trajectory of the fusion system must pass inside the fusing saddle point in a multidimensional space to form a compound nucleus. Swiatecki [18–20] and Bjornholm [21] developed a model based on the chaotic regime dynamic in which the liquid-drop potential energy plus one-body dissipation [19] is used. In their calculations, a necking degree of freedom is allowed but the finite range of the nuclear forces is disregarded and so the nuclei remain spherical during the neck formation. In an interesting approach, Gross et al [22] and Fröbrich [23, 24] take into account the oblate, prolate and quadrupole deformations using nuclear forces within a single folding potential where the neck formation is excluded and therefore the dissipation is described within the surface friction model. A very strong phenomenological dissipation is assumed by considering [25] two spher-

ical nuclei interacting within a sudden potential derived from the energy density formalism. The overlap of the two spheres is possible but is limited to a small penetration. The necking degree of freedom and the nuclear proximity energy are taken into account [26] to explain the fusion cross-section profile and the barrier heights for heavy systems independent of temperature. Two parameter families are used with shapes which simply allow them to follow the fusion path leading from the two separated spherical nuclei to the spherical compound nucleus. The obtained calculations have been compared with different models. In these calculations it has been found that for very heavy nuclei systems for which $Z_1Z_2 \geq 2100 \pm 100$, a dynamical fusion barrier exists which is significantly higher than the static one and therefore is in close agreement with the experimental data.

The simple dissipative dynamical model [14], in a semi-quantitative way, leads to an increase of the fusion cross-section at higher bombarding energies. With this model, it is possible to investigate the effect of the temperature on the interaction potential between two heavy nuclei. Therefore, this potential can be calculated assuming that the projectile and target nuclei have zero temperature. However, it is obvious that heating a nucleus will change its density distribution which will introduce in turn some modifications to the potential between the interacting nuclei. These modifications have been already investigated [27] by using a double folding model. They studied the $(\alpha + {}^{208}\mathrm{Pb})$ and $({}^{12}\mathrm{C} + {}^{208}\mathrm{Pb})$ systems by using the densities obtained from the thermal Hartree–Fock calculations.

In the present work, the theory of the fusion process is reconsidered. We study the effect of the temperature on both of the interaction potentials and the fusion cross-sections. Numerical calculations for the interaction potentials and fusion cross-sections obtained from heavy ion reaction are carried out. The interaction potentials at finite temperatures are calculated for the ${}^{129}\mathrm{Xe} + {}^{122}\mathrm{Sn}$ and ${}^{84}\mathrm{Kr} + {}^{166}\mathrm{Er}$ systems. The fusion cross-sections are also calculated at finite temperatures for the ${}^{86}\mathrm{Kr}$ (${}^{70}\mathrm{Ge}$, ${}^{76}\mathrm{Ge}$, ${}^{92}\mathrm{Mo}$, ${}^{100}\mathrm{Mo}$, ${}^{99}\mathrm{Ru}$, ${}^{104}\mathrm{Ru}$), $({}^{84}\mathrm{Kr} + {}^{166}\mathrm{Er})$ and $({}^{129}\mathrm{Xe} + {}^{122}\mathrm{Sn})$ systems, where good agreements between the present calculations and the experimental data [28] are obtained. Then the influence of the temperature on the fusion of two heavy nuclei for systems considered here for which $Z_1Z_2 > 2500 - 3000$, can be obtained from the comparison between the present calculations and the experimental data.

In Section 2, we introduce the mathematical and theoretical expressions for the nuclear density distribution together with the interaction potential and fusion cross-section at finite temperatures. In Section 3, the numerical calculations and results are given. Discussion and conclusions are introduced in Section 4.

2. Nuclear density distribution at finite temperature

The hot Thomas–Fermi model has been found by Barranco et al [29, 30] to be a useful tool in investigating the nuclear density distributions at finite temperatures. These calculations are introduced as a general extension of the Brueckner et al [31] calculations of the model at zero temperature. At a point distance defined by r,

the energy density $\varepsilon(r)$ is defined as

$$\varepsilon(r) = \varepsilon\{\rho_n(r), \rho_p(r)\}. \tag{1}$$

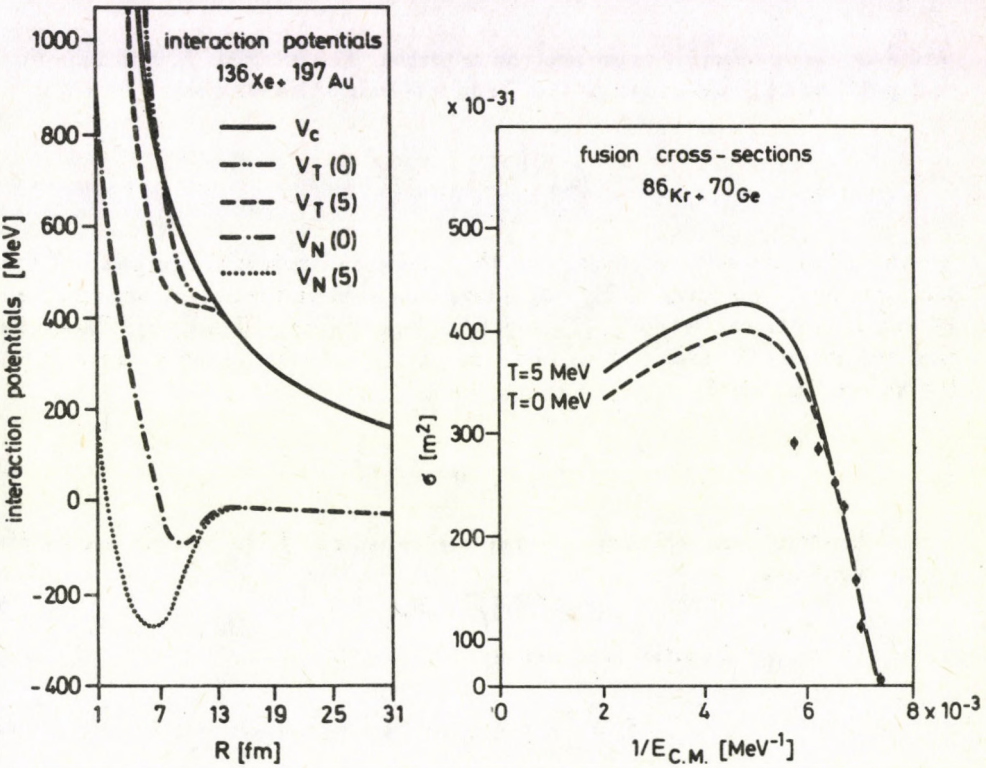

Fig. 3. Interaction energies of the two heavy ions $^{136}Xe + {}^{197}Au$ as a function of their relative distance. $V_N(0)$ is the nuclear part of the potential at temperature 0 MeV, V_C is the Coulomb part and $V(0)$ is the total interaction potential at 0 MeV. $V_N(5)$ is the nuclear potential at $T =$ 5 MeV and $V_T(5)$ is the total interaction potential at 5 MeV

Fig. 4. Fusion cross-sections calculated for the ($^{86}Kr + {}^{70}Ge$) system at a zero temperature interaction potential (dashed line), with a temperature dependent interaction potential (full line) as a function of the inverse of C. M. energy ($1/E_{CM}$). The experimental points are taken from reference [28]

Equation (1) means that the energy density is dependent only on the local one body densities for proton and neutron. In addition to the Coulomb and nuclear potential terms, it includes also the kinetic energy density term τ_i which is related (for a uniform Fermi gas) to the densities ρ_i by the following set of relations

$$\tau_i = \frac{1}{2\pi^2}\left(\frac{2m}{h^2}\right)^{3/2} T^{5/2} J_{3/2}(\eta_i^0) \tag{2}$$

and

$$\rho_i = \frac{1}{2\pi}\left(\frac{2mT}{h^2}\right)^{3/2} J_{1/2}(\eta_i^0), \tag{3}$$

where $i = n$ or p referring to the neutron or proton. The integrals J_ν which appeared in Eqs (2) and (3) are known as the Fermi integrals. Also we have

$$\eta = \eta_0 \left\{1 - k^2\left(\frac{N-Z}{A}\right)^2\right\}, \tag{4}$$

where η_0 and k are the coefficients of the kinetic and potential energies. At fixed temperature T for a given ρ_i, Eq. (3) is inverted to obtain the degeneracy parameter η_i^0 and is introduced into Eq. (2) to get the kinetic energy density τ_i. Then when the temperature T tends to zero, the relationship between ρ_i and τ_i is reduced to the known Thomas–Fermi expression given as

$$\tau_i = \frac{3}{5}\frac{h}{2m_i}(2\pi^2)^{3/2}\rho_i^{\frac{5}{3}}. \tag{5}$$

Therefore, it is necessary to define the free energy $f(r)$. The free energy $f(r)$ can be written as

$$f(r) = \varepsilon(r) - T(S_n + S_p), \tag{6}$$

where the entropy densities are given by

$$S_i = \frac{5}{3}\frac{1}{T}\tau_i - \eta_i^0\rho_i, \quad i = n, p. \tag{7}$$

Then, the total free energy F can be obtained by integrating over the whole space.

2.1. Interaction potentials at finite temperatures

The interaction potential $V(R)$ between two heavy ions is given by

$$V(R) = \int dr\,\{\varepsilon(\rho_{1n} + \rho_{2n}, \rho_{1p} + \rho_{2p}) - \varepsilon(\rho_{1n}, \rho_{1p}) - \varepsilon(\rho_{2n}, \rho_{2p})\} \tag{8}$$

In Eq. (8), the energy densities $\varepsilon(r)$ have the generalized hot Thomas–Fermi expression where ρ_{1n}, ρ_{1p} and ρ_{2n}, ρ_{2p} are the neutron and proton densities of the two incident heavy ions. Also R is the distance separating the two centers of mass of two heavy ions. This potential as given by Eq. (8) is separated into two parts; namely nuclear part and Coulomb part. Therefore, the interaction potential can be written as

$$V(R) = V_N(R) + V_C(R), \tag{9}$$

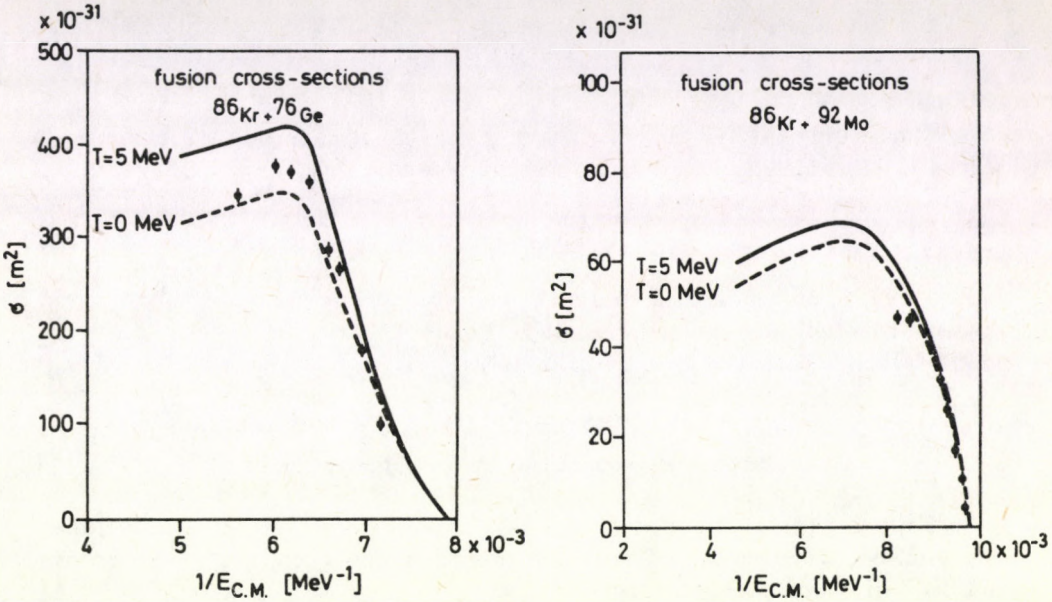

Fig. 5. Fusion cross-sections calculated for the (^{86}Kr + ^{76}Ge) system at a zero temperature interaction potential (dashed line), with a temperature dependent interaction potential (full line) as a function of the inverse of C. M. energy ($1/E_{\mathrm{CM}}$). The experimental data points are taken from reference [28]

Fig. 6. Fusion cross-sections calculated for the (^{86}Kr + ^{92}Mo) system at a zero temperature interaction potential (dashed line), with a temperature dependent interaction potential (full line) as a function of the inverse of C. M. energy ($1/E_{\mathrm{CM}}$). The experimental data points are taken from reference [28]

where $V_N(R)$ is the nuclear part of the interaction potential. This nuclear part of the potential is temperature dependent [31] and has been factorized to be written in the form

$$V_N(S) = \frac{A_1^{1/3} A_2^{1/3}}{A_1^{1/3} + A_2^{1/3}} U_N(S,T), \tag{10}$$

where

$$U(S,T) = \begin{cases} a(T)\exp\left(-b(T)S^2\right) & S \geq 0, \\ a(T) + CS^2 & S < 0. \end{cases} \tag{11}$$

The different variables which appear in Eq. (11) have the form as

$$S = R - \bar{r}\left(A_1^{1/3} + A_2^{1/3}\right), \tag{12}$$

$$\bar{r} = 0.86 - 0.0119\,T^2, \tag{13}$$

$$a(T) = -36 - 2.55\,T^2 \tag{14}$$

and

$$b(T) = 0.2135 - 0.05088T + 0.00382T^2, \tag{15}$$

with the value of $C = 4.82$.

Considering the two colliding heavy ions as point charges, the Coulomb potential $V_C(R)$ which appeared in Eq. (9) can be written as

$$V_C(R) = 1.44 Z_1 Z_2 / R. \tag{16}$$

In Eq. (16), Z_1 and Z_2 are the charges of the two colliding heavy ions and R is the distance between their centers of mass. In Eq. (16), R is given in fermi units and so the Coulomb potential V_C is given in MeV.

2.2. Fusion cross-section at finite temperatures

Following the critical distance model [32, 33], two expressions for the fusion cross-sections are given according to the energy. At low energies the fusion cross-section is given by an expression as

$$\sigma_{\text{fus}} = \pi R_B^2 \left(1 - \frac{V_B(R_B)}{E_{CM}}\right), \tag{17}$$

while at high energies the fusion cross-section is given by the expression

$$\sigma_{\text{fus}} = \pi R_C^2 \left(1 - \frac{V_C(R_C)}{E_{CM}}\right). \tag{18}$$

In Eq. (17), R_B is the barrier radius and V_B is the conservation potential at the barrier radius R_B. In Eq. (18) R_C is the critical distance and V_C is the conservative potential at the critical distance. E_{CM} in both equations (17) and (18) is the center of mass energy. The value of the barrier radius R_B is given as

$$R_B = 1.4\left(A_1^{1/3} + A_2^{1/3}\right). \tag{19}$$

Also the critical distance R_C is given by

$$R_C = 1.0\left(A_1^{1/3} + A_2^{1/3}\right). \tag{20}$$

Introducing the temperature dependent interaction potential in Eqs (17) and (18), we get expressions for the fusion cross-sections at both low and high energies. At low energies, the fusion cross-section is given by the expression

$$\sigma(T) = \pi R_B^2 \left(1 - \frac{V_B(T)}{E_{CM}}\right). \tag{21}$$

Also, at high energies, the fusion cross-section is given by

$$\sigma(T) = \pi R_c^2 \left(1 - \frac{V_C(T)}{E_{CM}}\right). \tag{22}$$

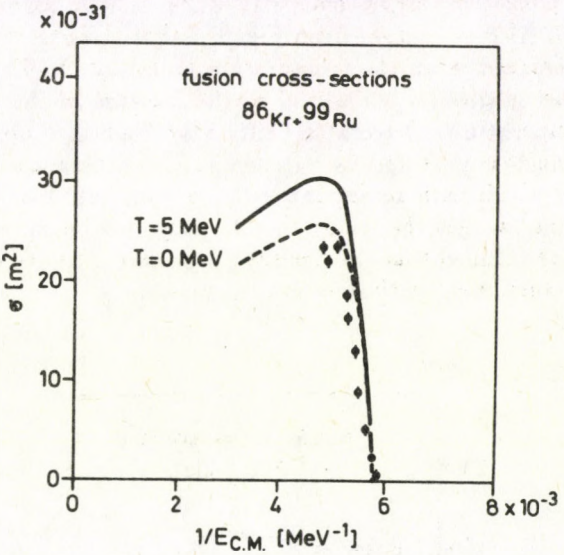

Fig. 7. Fusion cross-sections calculated for the (^{86}Kr + ^{99}Ru) system at a zero temperature interaction potential (dashed line) with a temperature dependent interaction potential (full line) as a function of the inverse of C. M. energy ($1/E_{CM}$). The experimental data points are taken from reference [28]

3. Numerical calculations and results

In the present work, we introduce a theoretical study for the interaction potential and the fusion cross-section between several two heavy ions. The inclusion of the temperature in both expressions for the interaction potential and fusion cross-section are introduced in the preceding Section 2. Numerical calculations of the present expression for the interaction potentials obtained on the basis of the hot Thomas–Fermi model and including the temperature are carried out for both of the systems ^{84}Kr + ^{166}Er and ^{129}Xe + ^{122}Sn at 12.5 MeV/u and for the system ^{136}Xe + ^{197}Au. These three systems are specially considered in the present work since we have for the first system $Z_1 Z_2 < 2500$, while for the second two systems we have $Z_1 Z_2 > 2500$. The present theoretical calculations are shown in Figs 1–3. From the obtained present theoretical calculations introduced in Figs 1–3, we see that the influence of temperature at 5 MeV on the interaction potentials between the two heavy nuclei is that it creates clear pockets for two of the three systems

with $Z_1Z_2 < 2500$, as well as for the systems with $Z_1Z_2 > 2500$. This result is very important, since it has been assumed from previous calculations [31] that the pocket does not appear for a system with $Z_1Z_2 > 2500$, and it appears only for systems for which $Z_1Z_2 < 2500$. Therefore, the results obtained here are a generalization of the previous calculations and so, the present calculations allow for the formation of the pocket for all systems with $Z_1Z_2 < 2500$ as well as for systems with $Z_1Z_2 > 2500$. Also we can see from Figs 1–3 that the observed nuclear energy part is clearly decreased when the temperature is increased. This decrease in the nuclear energy part is directly connected to the increase of the diffuseness of the densities with temperature. Detectable shifts have been also obtained on both of the depth of the nuclear part and its location at lower distances by increasing the temperature. This result is in agreement with previous calculations [14]. From the present calculations, we get the result that for any two heavy nuclei to fuse, the condition should be fulfilled that the fissility parameter must be less than or equal to 47, which is in agreement with previous calculations [15].

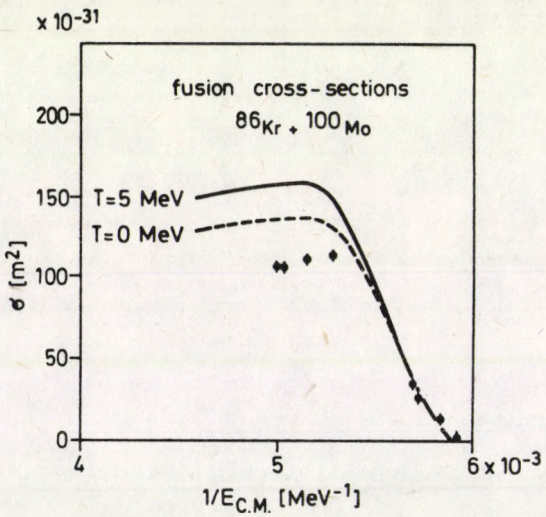

Fig. 8. Fusion cross-sections calculated for the (^{86}Kr + ^{100}Mo) system at a zero temperature interaction potential (dashed line) with a temperature dependent interaction potential (full line) as a function of the inverse of C. M. energy ($1/E_{CM}$). The experimental data points are taken from reference [28]

The influence of the inclusions of the temperature on the fusion cross-section for the fusion of two heavy ions are also investigated. We carried out numerical calculations for the fusion cross-sections of the systems ^{86}Kr (^{70}Ge, ^{76}Ge, ^{92}Mo, ^{99}Ru, ^{100}Mo, ^{104}Ru), (^{84}Kr + ^{166}Er) and also (^{129}Xe + ^{122}Sn), by using statistical model calculations and by including the temperature. The present calculations of the fusion cross-sections are compared with the experimental data [28]. The present

calculations of the fusion cross-sections with the comparisons with the experimental data are shown in Figs 4–11. The present theoretical calculations including the temperature are shown by solid curves, while the experimental measurements are denoted by points. Also, we introduced the theoretical calculations of these reactions without including the temperature and they are shown in Figs 4–11 by dashed curves. From Figs 4–11, we can distinguish between two different effects due to the inclusion of the temperature in the fusion cross-section in both cases of low and high bombarding energies. We see from Figs 4–11 that the barrier height of the fusion cross-section is not sensitive at low bombarding energies above the barrier. However, for the cases at higher bombarding energies, the calculated fusion cross-section is increased when the temperature is included in the interaction potential. Therefore, we see from Figs 4–11 that, our present theoretically calculated fusion cross-sections including the temperature are in agreement with previous calculations [14] for both cases of low and high energies.

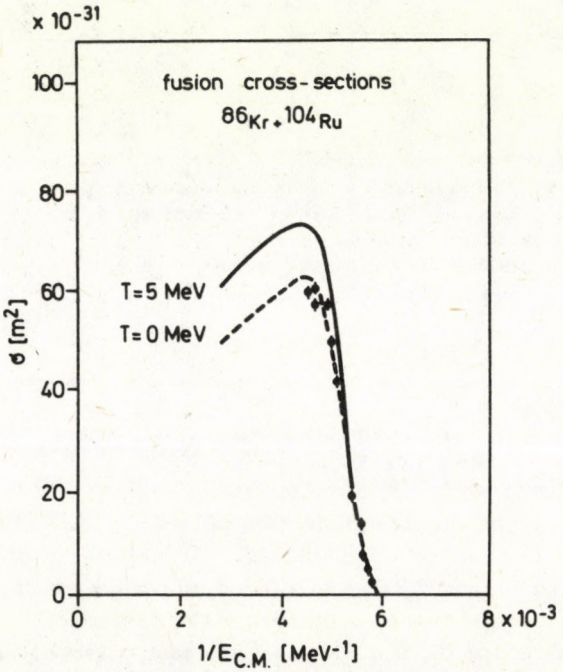

Fig. 9. Fusion cross-sections calculated for the (^{86}Kr + ^{104}Ru) system at a zero temperature interaction potential (dashed line) with a temperature dependent interaction potential (full line) as a function of the inverse of C. M. energy ($1/E_{CM}$). The experimental data points are taken from reference [28]

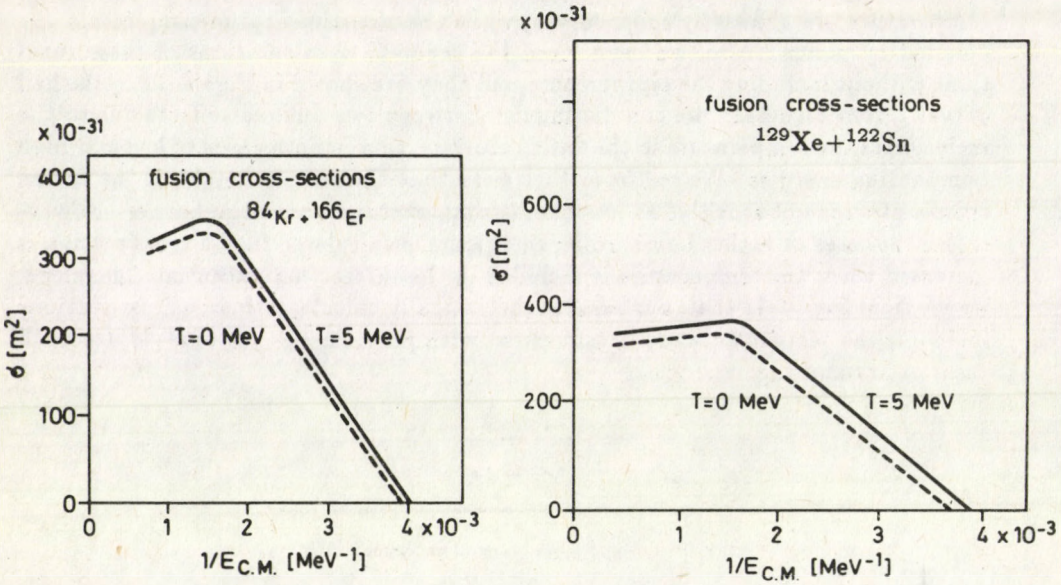

Fig. 10. Fusion cross-sections calculated for the (^{84}Kr + ^{166}Er) system at a zero temperature interaction potential (dashed line) with a temperature dependent interaction potential (full line) as a function of the inverse of C. M. energy ($1/E_{CM}$)

Fig. 11. Fusion cross-sections calculated for the (^{129}Xe + ^{122}Sn) system at a zero temperature interaction potential (dashed line) with a temperature dependent interaction potential (full line) as a function of the inverse of C. M. energy ($1/E_{CM}$)

4. Discussion and conclusions

In the present work, we introduce an investigation of the effect of including the temperature on both of the interaction potential and the fusion cross-section of two heavy ions. The interaction potentials are calculated for different two heavy ion systems for which $Z_1Z_2 < 2500$ as well as for which $Z_1Z_2 > 2500$. From the present calculations we found that a clear pocket for the interaction potential energy exists at finite temperature of about 5.0 MeV. It has been observed also that a decrease in the nuclear part of the interaction potential is obtained by increasing the temperature. Thus, our present calculations lead to the result that the fusion process occurs for any two heavy ions even that for which $Z_1Z_2 > 2500$. This result is a generalization for previous calculations and is breaking down their limiting condition [31]. Meanwhile, the present result is in agreement with previous calculation [15]. Also, very good agreement is obtained between the present theoretically calculated fusion cross-sections and the experimental data for the different two heavy ion system as shown in Figs 4–11.

Thus, we conclude that the inclusion of the temperature increases the fusion cross-sections at higher bombarding energies, while at low bombarding energies the barrier heights of the fusion cross-sections are not sensitive.

References

1. J. R. Nix and A. J. Sierk, Phys. Rev., *C15*, 2072, 1977.
2. M. Barranco, M. Pi, X. Vinas, G. Larana, S. Leray, C. Ngô and E. Tomasi, Nucl. Phys., *A428*, 239, 1984.
3. M. Lefort and C. Ngô, Ann. de Phys., *3*, 5, 1978.
4. C. Gregoire, C. Ngô and B. Remaud, Phys. Lett., *99B*, 17, 1981.
5. C. Gregoire, C. Ngô and B. Remaud, Nucl. Phys., *A383*, 392, 1982.
6. W. Nörenberg and H. A. Weidenmüller, Lecture Notes in Physics, *51*, 1976.
7. W. Schröder and J. Huizenga, Ann. Rev. Nucl. Sci., *27*, 465, 1977.
8. C. Ngô, B. Tamain, J. Galin, M. Beiner and R. J. Lombard, Nucl. Phys., *A240*, 353, 1975.
9. C. Ngô, B. Tamain, M. Beiner, R. J. Lombard, D. Mass and H. M. Deubler, Nucl. Phys., *A252*, 237, 1975.
10. K. A. Brueckner, J. R. Buchler, S. Jorna and R. J. Lombard, Phys. Rev., *171*, 1188, 1968.
11. K. A. Brueckner, J. R. Buchler, R. C. Clark and R. J. Lombard, Phys. Rev., *181*, 1543, 1969.
12. R. J. Lombard, Ann. Phys. (N. Y.), *77*, 380, 1973.
13. M. Beiner and R. J. Lombard, Ann. Phys. (N. Y.), *86*, 262, 1974.
14. E. Tomasi, X. S. Chen, S. Leray, C. Ngô, M. Barranco, X. Vinas and H. Ngô, Nucl. Phys., *A389*, 69, 1982.
15. C. Ngô, C. Gregoire, B. Rem and E. Tomasi, Nucl. Phys., *A400*, 259, 1983.
16. C. Gregoire, R. Lucas, C. Ngô, B. Schürman and H. Ngô, Nucl. Phys., *A361*, 443, 1981.
17. J. R. Nix and A. J. Sierk, Phys. Rev., *C15*, 2072, 1977.
18. W. J. Swiatecki, Phys. Scripta, *24*, 113, 1981.
19. W. J. Swiatecki, Nucl. Phys., *A376*, 275, 1982.
20. J. Blocki, Y. Bonek, J. R. Nix, J. Randrup, M. Robel, A. J. Sierk and W. J. Swiatecki, Ann. Phys. (N. Y.), *113*, 330, 1978.
21. S. Bjønholm, Nucl. Phys., *A387*, 51c, 1982.
22. D. H. E. Gross and L. Stapathy, Phys. Lett., *110B*, 31, 1982.
23. P. Fröbrich, Phys. Lett., *122B*, 338, 1983.
24. P. Fröbrich, Phys. Reports, *116*, 337, 1984.
25. T. Wuomijarvi, R. Lucas, C. Ngo, E. Tomasi, D. Dalil and J. Matusjek, Nuovo Cimento, *82A*, 51, 1984.
26. G. Royer and B. Remaud, Nucl. Phys., *A444*, 477, 1985.
27. J. Fleckner, G. Sauer and U. Mosel, Phys. Lett., *65B*, 316, 1976.
28. W. Reisdorf, F. P. Hessberger, K. D. Hildenbrand, S. Hofmann, G. Munjenberg, K. H. Schmidt, W. F. W. Schmeider, K. Summerer, G. Wirth, J. V. Kratd, K. Schlitt and C. C. Sahm, Nucl. Phys., *A444*, 154, 1985.
29. M. Barranco and J. R. Buchler, Phys. Rev., *C24*, 1191, 1981.
30. M. Barranco and J. Treiner, Nucl. Phys., *A351*, 269, 1981.
31. H. Ngô and C. Ngô, Nucl. Phys., *A348*, 140, 1980.
32. D. Glass and U. Mosel, Phys. Rev., *C10*, 2620, 1974.
33. D. Glass and U. Mosel, Nucl. Phys., *A337*, 429, 1975.

Acta Physica Hungarica 67 (3–4), pp. 381–386 (1990)

APPLICATIONS OF THE STOCHASTIC QUANTIZATION METHOD

J. BALAKRISHNAN, S. N. BISWAS, A. GOYAL and S. K. SONI

Department of Physics, University of Delhi
Delhi 110 007, India

(Received 16 February 1989)

We enumerate the advantages of using the stochastic quantization method over the standard methods and as an example use it to quantize para-Fermi fields obeying trilinear quantum conditions. Finally chiral anomaly for spinor fields is obtained directly from the c-number Langevin equation which forms the basis of the stochastic approach for field quantization.

1. Introduction

Ever since the introduction of the stochastic quantization method by Parisi and Wu [1] in 1981, this method has been applied to a wide variety of physical systems [2] which leaves no doubt about its viability as an alternative to the standard approaches to quantum theory, namely the canonical and the path-integral quantization. This new method of field quantization is based on the equation of motion rather than the Hamiltonian and as such bypasses many of the difficulties associated with the other approaches. For example this method enables us to quantize Abelian gauge fields without gauge-fixing terms [3]. For the nonabelian gauge fields the stochastic quantization method produces the effect of Faddeev–Popov ghosts in a natural way [4]. In addition to the above remarkable features the stochastic method being based on stochastic differential equation(s) (Langevin equation(s)) facilitates the numerical simulation of correlation functions [5] similar to the Monte-Carlo method in the path-integral approach. Other than these the usefulness of the stochastic quantization method has been amply demonstrated in quantizing scalar fields and has also been extended to include fermion fields by Sakita [6]. In the framework of stochastic quantization of fermions, calculation of the chiral anomaly turns out to be much simpler as has been shown by many authors [7]. The quantization of para-Fermi fields which obey trilinear quantum conditions [7] becomes extremely involved in the standard canonical quantization. We show here that para-Fermi field quantization obtains a much simpler procedure within the context of the stochastic quantization method. Finally, to show the further usefulness of the c-number Langevin equation which forms the basis of the stochastic quantization scheme we obtain the chiral anomaly in an obvious way. In the next Section we demonstrate the use of the stochastic quantization scheme to calculate the Green function for para-Fermi fields and in the final Section we obtain the chiral anomaly based on the Langevin equations for spinor fields.

2. Stochastic quantization of para-Fermi field

The specific formalism suitable for the calculation of the two-point Green function for para-Fermi field is described below. This is then utilized to calculate the same when the order of statistics p is different from 2.

In the Euclidean field theory the propagator of a para-Fermi field [9] is given by the well-known path integral formula

$$G(x-y) = \frac{\int d\psi d\overline{\psi}\psi(x)\overline{\psi}(y)e^{-S[\psi,\overline{\psi}]}}{\int d\psi d\overline{\psi}e^{-S[\psi,\overline{\psi}]}}. \tag{2.1}$$

Here ψ and $\overline{\psi}$ are paragrassmannian variables, and x, y are 4-dimensional Euclidean co-ordinates, and $S[\psi\overline{\psi}]$ denotes the Euclidean action in bilinear form. The stochastic quantization method provides us with a simple procedure to evaluate G which is based on the Langevin equations:

$$\begin{aligned}\partial_t\psi(x,t) &= -G^+\frac{\delta S}{\delta\overline{\psi}(x,t)} + G^+\eta(x,t),\\ \partial_t\overline{\psi}(x,t) &= G^{+T}\frac{\delta S}{\delta\psi(x,t)} + \overline{\eta}(x,t).\end{aligned} \tag{2.2}$$

Here $\psi(x,t)$ and $\overline{\psi}(x,t)$ are independent para-Grassmann fields satisfying:

$$\begin{aligned}[\psi(x,t),[\psi(x',t'),\psi(x'',t'')]] &= 0,\\ [\overline{\psi}(x,t),[\psi(x',t'),\psi(x'',t'')]] &= 0,\\ [\psi(x,t),[\overline{\psi}(x',t'),\psi(x'',t'')]] &= 0,\\ [\overline{\psi}(x,t),[\overline{\psi}(x',t'),\overline{\psi}(x'',t'')]] &= 0\end{aligned} \tag{2.3}$$

and G stands for a suitably chosen operator which may be chosen unity or a Dirac operator denoted by K which enters the expression for S:

$$S = \int d^4x\frac{1}{2}[\overline{\psi}(x), K\psi(x)]. \tag{2.4}$$

When the order of parastatistics p obeyed by the para-Fermi field is greater than 2, (2.4) gives the most general form for S [9]. We shall comment on the $p = 2$ case at the end of this Section. The statistical properties of independent para-Grassmann white-noise sources η and $\overline{\eta}$ are summarized in (2.14) and (2.15).

Since (2.2) provides solutions of ψ and $\overline{\psi}$ as a function of η and $\overline{\eta}$, the two-point Green function is obtained by the following $\eta\overline{\eta}$-averaging procedure

$$G(x,t;x',t') = \langle\psi(x,t)\overline{\psi}(x',t')\rangle_{\eta\overline{\eta}}. \tag{2.5}$$

Here $\langle f \rangle_{\eta\overline{\eta}}$ means the average over η and $\overline{\eta}$ given by

$$\langle f(\eta\overline{\eta}) \rangle_{\eta\overline{\eta}} = \frac{\int d\eta d\overline{\eta} f(\eta\overline{\eta}) \exp\left\{(-\frac{1}{2}) \int d^4x dt[\eta(x,t)\overline{\eta}(x,t)]\right\}}{\int d\eta d\overline{\eta} \exp\left\{(-\frac{1}{2}) \int d^4x dt[\eta(x,t)\overline{\eta}(x,t)]\right\}}. \tag{2.6}$$

Using the fact that the equivalent Fokker–Planck equation corresponding to (2.2) leads us to stationary distribution $\exp(-S[\psi, \overline{\psi}])$ in the steady state limit $t \to \infty$ we find

$$G(x,y) = \underset{t\to\infty}{\mathrm{Lt}}\, G(x,t;y,t). \tag{2.7}$$

When the action for the parafield is taken to be of the form given in (2.4), it is very convenient to decompose ψ and $\overline{\psi}$ in terms of Green components

$$\begin{aligned} \psi(x) &= \sum_{a=1}^{p} \psi^a(x), \\ \overline{\psi}(x) &= \sum_{a=1}^{p} \overline{\psi}^a(x), \end{aligned} \tag{2.8}$$

where the Green components satisfy normal anti-commutation relations for equal Green indices

$$[\psi^a(x), \psi^a(x')]_+ = [\psi^a(x), \overline{\psi}^a(x')]_+ = [\overline{\psi}^a(x), \overline{\psi}^a(x')]_+ = 0 \tag{2.9}$$

and anomalous commutation relations for unequal Green indices

$$[\psi^a(x), \psi^b(x')]_- = [\psi^a(x), \overline{\psi}^b(x')]_- = [\overline{\psi}^a(x), \overline{\psi}^b(x')] = 0. \tag{2.10}$$

In terms of Green components the action (2.4) becomes

$$S = \sum_a \int dx \overline{\psi}^a(x) K \psi^a(x). \tag{2.11}$$

The appropriate Hamiltonian for the Fokker–Planck equation

$$\begin{aligned} H_{FP} = \sum_a \int dx \frac{\delta}{\delta\psi^a(x)} G^+ \left[\frac{\delta}{\delta\overline{\psi}^a(x)} + \frac{\delta S}{\delta\overline{\psi}^a(x)}\right] - \\ - \frac{\delta}{\delta\overline{\psi}^a(x)} G^{+^T} \left[\frac{\delta}{\delta\psi^a(x)} + \frac{\delta S}{\delta\psi^a(x)}\right] \end{aligned} \tag{2.12}$$

corresponds to the following Langevin equations

$$\partial_t \psi^a(x,t) = -G^+ \frac{\delta S}{\delta\overline{\psi}^a(x,t)} + G^+ \eta^a(x,t), \tag{2.13a}$$

$$\partial_t \overline{\psi}^a(x,t) = G^{+^T} \frac{\delta S}{\delta\psi^a(x,t)} + \overline{\eta}^a(x,t). \tag{2.13b}$$

For a straightforward proof of this assertion we refer the reader to our earlier work [10]. In (2.13a) and (2.13b) the noise sources η^a and $\overline{\eta}^a$ which act as sources for ψ^a and $\overline{\psi}^a$ satisfy the stochastic properties given by

$$\begin{aligned}
\langle \eta^a(x,t)\rangle &= \langle \overline{\eta}^a(x,t)\rangle = 0, \\
\langle \eta^a(x,t)\overline{\eta}^a(x',t')\rangle &= -\langle \overline{\eta}^a(x',t')\eta^a(x,t)\rangle = 2\delta(x-x')\delta(t-t'), \\
\langle \eta^a(x,t)\eta^a(x',t')\rangle &= -\langle \eta^a(x',t')\eta^a(x,t)\rangle = 0, \quad \text{etc.}
\end{aligned} \tag{2.14}$$

for equal Green indices, and

$$\begin{aligned}
\langle \eta^a(x,t)\overline{\eta}^b(x',t')\rangle &= \langle \overline{\eta}^b(x',t'(\eta^a(x,t)\rangle = 0, \\
\langle \eta^a(x,t)\eta^b(x',t')\rangle &= \langle \eta^b(x',t')\eta^a(x,t)\rangle = 0, \quad \text{etc.}
\end{aligned} \tag{2.15}$$

for unequal Green indices.

In order to obtain the stochastic average of $\psi(x,t)\overline{\psi}(y,t')$ we write this in terms of Green components, i. e.

$$\langle \psi(x,t)\overline{\psi}(y,t')\rangle_{\eta\overline{\eta}} = \sum_{\alpha,\beta=1}^{p} \langle \psi^\alpha(x,t)\overline{\psi}^\beta(y,t')\rangle_{\eta\overline{\eta}}$$

and evaluate this average using the solutions of ψ^a and $\overline{\psi}^a$ from (2.13a) and (2.13b)

$$\langle \psi(x,t)\overline{\psi}(y,t)\rangle_{\eta\overline{\eta}} = pK^{-1}\left(1+O(e^{-2mt})\right) \tag{2.16}$$

whose steady state limit yields the free para-Fermi field propagator for $p>2$ which is equal to p times the well-known propagator for Fermi field.

The action for the $p=2$ case which has been discussed in [9] may also be treated along similar lines. It is better, however, in this case to make a Klein transformation which reduces the action to the direct sum of two Fermionic actions with different masses m_+ and m_-. The resulting parafield propagator is the sum of two fermionic propagators corresponding to masses m_+ and m_-. Here $m_\pm = m \pm \kappa$ where m and κ are coefficients in the mass matrix which for $p=2$ case is given by $\frac{1}{2}m[\overline{\psi},\psi]_- + \frac{\kappa}{2}[\overline{\psi},\psi]_+$. Note that in the limit $\kappa \to 0$ the expression for parafield propagator reduces to twice the fermionic propagator.

3. Chiral anomaly based on Langevin equation

In the previous Section we pointed out the computational ease with which the correlation function for an Euclidean quantum field theory may be calculated by $\eta\overline{\eta}$-averaging. An even more interesting application of the stochastic differential equations (2.2) is the calculation of chiral anomaly in a direct manner which does not even require a solution of the equations of the stochastic formalism. In this way

we rederive the results of our earlier work [11] in a much simpler way. Using the spinor equations of motion we arrive at the following identity

$$\partial_\mu \left(\sum_a \overline{\psi}^a \gamma_5 \gamma_\mu \psi^a \right) + 2m \sum_a \overline{\psi}^a \gamma_5 \psi^a =$$

$$= \sum_a \overline{\psi}^a \gamma_5 (\gamma_\mu \overrightarrow{\partial_\mu} + m)\psi^a + \sum_a \overline{\psi}^a (-\gamma_\mu \overleftarrow{\partial_\mu} + m)\gamma_5 \psi^a =$$

$$= \sum_a \overline{\psi}^a \gamma_5 (\gamma_\mu \overrightarrow{\partial_\mu} - ig\gamma_\mu A_\mu + m)\psi^a + \sum_a \overline{\psi}^a (-\gamma_\mu \overleftarrow{\partial_\mu} - ig\gamma_\mu A_\mu + m)\gamma_5 \psi^a =$$

$$= -\sum_a \overline{\psi}^a \gamma_5 \partial_t \psi^a - \sum_a \partial_t \overline{\psi}^a \gamma_5 \psi^a + \sum_a \overline{\psi}^a \gamma_5 \eta^a + \sum_a \overline{\eta}^a \gamma_5 \psi^a. \tag{3.1}$$

The spinor equations of motion used here are

$$\partial_t \psi^a = -\left[\gamma_\mu (\overrightarrow{\partial_\mu} - igA_\mu) + m \right] \psi^a + \eta^a, \tag{3.2a}$$

$$\partial_t \overline{\psi}^a = -\overline{\psi}^a \left[\gamma_\mu (-\overleftarrow{\partial_\mu} - igA_\mu) + m \right] + \overline{\eta}^a, \tag{3.2b}$$

which follow from (2.13) on setting $G = 1$ for simplicity's sake.

Thus we have finally on taking the $\eta\overline{\eta}$ average

$$\partial_\mu \langle \left(\sum_a \overline{\psi}^a \gamma_5 \gamma_\mu \psi^a \right) \rangle + 2m \langle \sum_a \overline{\psi}^a \gamma_5 \psi^a \rangle = -\partial_t \langle \sum_a \overline{\psi}^a \gamma_5 \psi^a \rangle -$$

$$- 2pTr(\delta^4(0)\gamma_5), \tag{3.3}$$

where the last term is obtained through Novikov's theorem. The right-hand side in (3.3) consists of the sum of two terms: the first term is t-dependent and goes to zero exponentially as t increases (see below) and the second term is clearly t-independent. In the limit $t \to \infty$ only the last term survives and the above identity reduces to the anomalous Ward identity of the equivalent quantum field theory. This is our procedure for deriving chiral anomaly from the equations of motion. In the more general case when G is taken to be different from unity the following identity is still true:

$$\partial_\mu \langle \sum_a \overline{\psi}^a \gamma_5 \gamma_m u \psi^a \rangle + 2m \langle \sum_a \overline{\psi}^a \gamma_5 \gamma_\mu \psi^a \rangle + 2m \langle \sum_a \overline{\psi}^a \gamma_5 \psi^a \rangle = -\partial_t \langle F(\overline{\psi}, \psi) \rangle -$$

$$- 2pTr(\delta^4(0)\gamma_5), \tag{3.4}$$

where $F(\psi\overline{\psi})$ is a bilinear in $\overline{\psi}(x,t)$ and $\psi(x,t)$ whose form depends on the choice of G. Now

$$\langle F(\overline{\psi}, \psi) \rangle = \int d\psi d\overline{\psi} F(\overline{\psi}, \psi) P(\overline{\psi}, \psi, t), \tag{3.5}$$

where $P(\overline{\psi}, \psi, t)$ is the Fokker–Planck distribution function which satisfies the Schrödinger type equation

$$\partial_t P(\overline{\psi}, \psi, t) = -H_{FP} P(\overline{\psi}, \psi, t). \tag{3.6}$$

Thus we have

$$\partial_t \langle F(\overline{\psi}, \psi) \rangle = -\int d\psi d\overline{\psi} F(\overline{\psi}, \psi) H_{FP} P(\overline{\psi}, \psi, t). \tag{3.7}$$

In the steady-state limit $t \to \infty$ the right-hand side of (3.7) approaches zero. Hence the left-hand side of (3.7) relaxes to zero and the anomalous conservation law follows directly. The procedure we have outlined is quite similar in spirit to the derivation of chiral anomaly given by Namiki et al [12]. In contrast to our approach based on the general results given by Novikov's theorem, the latter approach is based on the elegant Ito calculus. However, the two approaches are equivalent.

Acknowledgement

One of us (J. B.) acknowledges financial support from the Council for Scientific and Industrial Research, New Delhi.

References

1. G. Parisi and Y. S. Wu, Sci. Sin., *24*, 483, 1981.
2. Stochastic Quantization, by P. H. Damgaard and H. Huffel, Phys. Rep., *152C*, 228, 1987. In addition to reviewing the basic concepts of the stochastic approach, this review also contains a broad selection of preprints on its applications to gauge fields, large N field theories, lattice gauge theories, gravity, quantization of fermions, etc.
3. M. Namiki, I. Ohba, K. Okano and Y. Yamanaka, Prog. Theor. Phys., *69*, 1580, 1983; E. Gozzi, Phys. Rev., *D31*, 1349, 1985.
4. D. Zwanziger, Nucl. Phys., *B192*, 259, 1981; L. Baulieu and D. Zwanziger, Nucl. Phys., *B193*, 163, 1981; H. Nakagoshi, M. Namiki, I. Ohba and K. Okano, Prog. Theor. Phys., *70*, 326, 1983; E. Floratos, J. Iliopoulos and D. Zwanziger, Nucl. Phys., *B241*, 221, 1984.
5. G. Parisi, Nucl. Phys., *B180*, 378, 1984. G. Parisi, in: "Progress in Gauge Field Theory", eds. G.'t Hooft et al, Plenum Press, New York, 1984.
6. B. Sakita, in 7th John Hopkins Workshop, eds. G. Domokos and S. Kovesi-Domokos, World Scientific, Singapore, 1983.
7. J. Alfaro and M. B. Gavela, Phys. Lett., *158B*, 473, 1985; M. B. Gavela and N. Parga, Phys. Lett., *B171*, 319, 1986. For more references see Ref [11].
8. H. S. Green, Phys. Rev., *90*, 270, 1953.
9. S. Kamefuchi and Y. Ohnuki, Quantum Field Theory and Parastatistics, Univ. of Tokyo Press, Springer Verlag, Tokyo, 1982.
10. J. Balakrishnan, S. N. Biswas, A. Goyal and S. K. Soni, to be published in the Journal of Mathematical Physics.
11. J. Balakrishnan, S. N. Biswas, A. Goyal and S. K. Soni, Phys. Rev., *D37*, 571, 1988.
12. M. Namiki, I. Ohba, S. Tanaka, and D. Yanga, Phys. Lett., *B194*, 530, 1987.

Acta Physica Hungarica 67 (3–4), pp. 387–400 (1990)

PERTURBATION THEORETICAL VS SUPERMOLECULE CALCULATIONS ON INTERMOLECULAR INTERACTIONS

P. R. SURJÁN,* P. CSÁSZÁR, R. A. POIRIER

Department of Chemistry
Memorial University of Newfoundland
St. John's, Newfoundland, Canada A1B 3X7

and

J.-H. VAN LENTHE

Theoretical Chemistry Group
University of Utrecht
De Uithof
Utrecht, The Netherlands

(Received in revised form 18 April 1989)

Perturbation theoretical and variational supermolecule calculations are performed for some model systems, such as **He**...**He**, $\mathbf{H}_2 \ldots \mathbf{H}_2$, and water–water dimers. The symmetry adapted second order **PT** calculations used in this paper are free of basis set superposition error, but the **PT** results are sensitive to the basis set and may show wrong $\mathbf{R} \to 0$ asymptotics. Supermolecule calculations can only be compared to the **PT** results at the *long range*, where the latter involve less approximation and are inherently free from BSSE.

1. Introduction

The most straightforward way of calculating intermolecular interaction energies by quantum chemical methods is the supermolecule approach. It is well known [1] that supermolecular calculations with a finite basis set usually overestimate the interaction energy due to the basis set superposition errors (BSSE). There is a continuous interest in developing methods avoiding or correcting for BSSE [2], but no unique, widely accepted scheme has emerged. The most controversial point is (see e. g. [3] and [4]), whether the original Boys–Bernardi scheme [5], or the "virtual only" counterpoise method [6] is more generally applicable. (In both methods, the monomer energies are calculated with an extended set of basis orbitals; in the Boys–Bernardi scheme within the full dimer basis set, while in the latter case only the virtuals of the other molecule are used as "ghost orbitals".) Introducing a proper criterion for measuring BSSE is not trivial because it is a difficult concept. This point will be discussed in Section 2.

*Present and permanent address: CHINOIN Research Centre, H-1325 Budapest, P. O. B. 110, Hungary

2. Criteria for a BSSE-free energy

2.1. Comparison with experiments

Calculated interaction energies can be compared to experimental results if the latter are available. Unfortunately, this comparison can only be done for a limited number of cases when the calculation and the experiment refers to the same situation (geometrical arrangement, three-body interactions, temperature, etc.). An additional problem is that the BSSE is usually *not the only systematic error* in the calculation, so one cannot really judge its extent simply from the difference between experimental and theoretical results. Moreover, the theoretical errors have a tendency to compensate each other to some extent, which suggests to *retain* BSSE (i. e. not to correct for it) in order to reach acceptable agreement between theory and experiment. This is the case, for example, if the water–water interaction is studied in a minimal STO-3G basis. The uncorrected SCF calculation predicts a surprisingly accurate potential curve, while the interaction completely disappears if the Boys–Bernardi counterpoise correction is used [7, 8]. In other cases, the "virtual only" scheme was found to give the best agreement with experiment [9], while sometimes the Boys–Bernardi method is the best in this sense.

The results of this criterion, therefore are, not at all unique; they are strongly affected by the basis set chosen and the nature of the system under consideration. It is to be emphasized that we are focusing on a reliable method for correcting BSSE, and not on a method for fitting the theory to particular experimental data.

2.2. The stability of the results

Some general conclusions can be drawn by investigating the stability of the predicted interaction energies with respect to changes in the basis set. This criterion has been used, for example, in [10]. Practically all results confirm that interaction energies obtained by the full *Boys–Bernardi counterpoise scheme are the less basis set dependent.*

There is no question that this kind of stability in the results is a very important feature. However, from the purely theoretical point of view, one cannot expect the "true" interaction energies in a finite basis set to be independent of the basis. This criterion measures not only the BSSE, but the overall effect of the basis set change on the interaction energy. It is, therefore, desirable to look for other criteria, which are based on more sound theoretical grounds.

2.3. Analysis of energy partitioning

Several authors have found that, if the Boys–Bernardi counterpoise scheme is applied, some parts of the interaction energy, such as the polarization and delocalization contribution, become positive [11]. This is contrary to the physical meaning

of these terms because these interactions are attractive. This observation, however, does not imply that the Boys–Bernardi scheme is wrong, but simply that the definition of the polarization and delocalization terms is rather ambiguous. One can avoid this problem by a more suitable definition of the energy terms [3, 4, 12].

2.4. Perturbation theoretical calculations

The predicted intermolecular interaction energies may suffer from two types of errors: (i) the lack of some part of the interaction due to the finiteness of the basis, and (ii) the BSSE. Both (i) and (ii) disappear at the limit of the complete basis. In an incomplete basis, however, error (i) usually tends to decrease the apparent interaction energy, while due to error (ii) the interaction is overestimated. One possible way of separating these two effects at the theoretical level is given by perturbation theory (PT). In practice, two approaches are widely used:
(1) PT calculations using the L_2 form of the interaction Hamiltonian, which, for two interacting monomers A and B is written as usual:

$$W_{AB} = \hat{H} - \hat{H}_A - \hat{H}_B = -\sum_{\substack{a\in A\\ i\in B}} Z_a/R_{ia} - \sum_{\substack{a\in B\\ i\in A}} Z_a/R_{ia} + \sum_{\substack{j\in A\\ i\in B}} 1/r_{ij} \qquad (1)$$

with obvious notations. No BSSE is expected if the perturbation energy corrections are evaluated by means of matrix elements of this Hamiltonian. The problem, however, is not trivial due to symmetry adaptation [13]. An elegant formulation of this PT was given by Kochanski and Gouyet [14], who expressed the energy corrections in orbital form using biorthogonal molecular orbitals (MOs).
(2) In another branch of PT approaches, one starts with the finite basis representation of the Hamiltonians $\hat{H}, H_A$ and H_B, the latter two being obtained by an appropriate partitioning of the former in the orbital basis. To be specific, one- and two-electron integrals over orbitals of A are assigned to H_A, (similarly for B), while integrals connecting orbitals on A to those on B are considered to form the interaction Hamiltonian. This problem is, again, non trivial if the two systems overlap. Moreover, the interaction energies obtained in this way suffer from BSSE [6].

The essential difference between approaches (1) and (2) is well illustrated by the role of the kinetic energy operator: it is absent from the L_2-space interaction Hamiltonian of Eq. (1), but *enters the interaction part of the finite basis Hamiltonian* within the second scheme given above.

A careful analysis of the structure of the finite basis Hamiltonian, however, permits one to pick out the terms in the interaction part of $\hat{H}$ not related to BSSE. This analysis was done by Mayer in his chemical Hamiltonian approach (CHA) [15]. First, it turns out from CHA that the *intermolecular kinetic energy matrix elements do not contribute to the physical part of the interaction*, but should be considered merely as giving rise to BSSE — in full agreement with the L_2 space partitioning given by Eq. (1). A perturbation theoretical formalism for calculating

intermolecular interactions based on CHA has been introduced subsequently [16]. The results for first- and second-order energy corrections were found to be essentially the same as in the theory by Kochanski and Gouyet [14], provided that all terms are considered in the latter and that the antisymmetrization is carried out correctly. These results, either because they are based on the L_2 space interaction Hamiltonian, or since they are based on CHA, are free from BSSE, as it has been demonstrated in [8]. Unfortunately, the perturbation theoretical calculations at low orders are usually less accurate than variational ones, which makes these methods less advantageous. The difficulties, as it will be demonstrated in this paper, can sometimes be rather serious, but usually small at the long range. Being free from BSSE, the long range PT results can therefore be more favourable than variational calculations which require some kind of counterpoise correction. However, the BSSE also becomes negligible in the variational calculation at the very long range. Thus the PT method can be appropriate in judging the extent of BSSE only at the beginning of the long range, provided that they are accurate enough to be compared to a variational result. We note that the benefits of the PT approach in connection with BSSE have also been utilized in [17].

An important theoretical argument favouring BSSE-free PT calculations to counterpoise-corrected variational ones is the following. When we solve the problem of molecule A including (some of) the orbitals centred on B, we destroy the symmetry of the molecule. This shortcoming may be manifested even in a wrong (broken-symmetry) solution of A, leading to unrealistic interaction energies [18]. This argument, which is equally valid against the Boys–Bernardi or the "virtual only" counterpoise scheme, rarely causes serious errors in practice. On the other hand, BSSE-free PT calculations are not subject to this danger.

We note also that some simple methods for evaluating only the electrostatic and inductive part of the interaction energy [19], based essentially on McWeeny's group function formalism [20], are also inherently free from BSSE. Both SCF calculations and the post Hartree–Fock methods using properly localized orbitals can be free, too [21, 22]. In practice, however, the localization of the MO's is never complete and is basis set (method) dependent and so are the interaction energies calculated with these methods. The dominant part of BSSE can, however, be eliminated using localized SCF or CI schemes.

Owing to the importance of PT calculations, in Section 4 we are going to report some more extensive applications of the BSSE-free PT developed in [16], discussing the particular problems connected to the PT. The results will be compared to variational supermolecule calculations (Section 3) suffering from BSSE. The aim of the calculations reported is not to obtain quantitatively accurate potential curves, but to analyse the applicability and defects of various procedures in qualitative terms.

3. Supermolecule calculations

For the sake of comparison, supermolecule calculations in various basis sets

were performed for He ... He and H_2O ... H_2O. In the case of the former one a satisfactory account of electron correlation is required, thus the following methods have been used: CEPA1 and CEPA2 [23], CI-SD [24] applying Davidson's correction [25], second order MBPT*, and approximate coupled cluster (ACCD) [26]. Full CI calculations have also been performed in two moderate basis sets. The basis sets chosen are described in Table I. For the water dimer, an SCF calculation is performed in the standard 3-21G split valence shell basis set [27]. To estimate BSSE, the Boys–Bernardi counterpoise method was applied in each case. The numerical results have been obtained by the program TEXAS [28], by the ATMOL program system [29], and by the MONSTERGAUSS program [30] which is an extensively modified version of GAUSSIAN80 [31]. The present version of the MONSTERGAUSS program performs automatically the full (Boys–Bernardi) counterpoise correction in a supermolecule calculation, and also contains a new link for evaluating PT corrections between two closed shell molecules [32].

Table I
Basis sets (for He)

No.	Basis	Ref.	Description
(1)	3-21G	[25]	Standard (used for H_2O and H_2)
(2)	[3*s*1*p*]	[37]	Standard 6-311G*
(3)	[3*s*1*p*1*d*]		Standard 6-311G*, augmented by a single set of 5*d* orbitals with exponent 0.1
(4)	[4*s*2*p*]	[38]	Contracted from (7*s*2*p*)
(5)	[4*s*2*p*1*d*]		Same as 4, augmented with a *d* function of exponent 0.1
(6)	CR2×DS4	[39]	(15*s*4*p*3*d*1*f*1*g*) → [7*s*4*p*3*d*1*f*1*g*]

4. Perturbation theoretical calculations

As mentioned above, the application of PT to the intermolecular interactions is not straightforward. We have used the second order approach outlined in [8] and [16], which is very similar to the method by Kochanski and Gouyet [14].

The derivation of interaction terms for the case of two interacting molecules was given in [16].

The first order results read:

$$E^1 = \sum_{i \in B} H^A_{\tilde{i}\tilde{i}} + \sum_{i \in A} H^B_{\tilde{i}\tilde{i}} + \sum_{\substack{i \in A \\ k \in B}} (\tilde{i}i||\tilde{k}k), \tag{2}$$

*Note that only the correlation part is treated by PT, thus this approach is, though non variational, also a supermolecule one.

where

$$H_{\tilde{i}k}^{X} = \langle \tilde{i} \left| -\sum_{a \in X} Z_a / r_a \right| k \rangle, \quad X = A \text{ or } B$$

is the matrix element of core–electron attraction operator for the molecule A or B, respectively, and $(\tilde{i}i\|\tilde{k}k) = (\tilde{i}i|\tilde{k}k) - (\tilde{i}k|\tilde{k}i)$ is the two electron integral with exchange component in the
(11‖22) convention. The tildes (~) on the orbitals indicate that the orbital in question refers to the biorthogonal set obtained by a linear transformation with the inverse of the overlap matrix.

At the second order we have:

$$E^2 = E^2_{\mathrm{POL}}(A) + E^2_{\mathrm{POL}}(B) + E^2_{\mathrm{DEL}}(A \to B) + E^2_{\mathrm{DEL}}(B \to A) + E^2_{\mathrm{DISP}}, \tag{3}$$

where

$$E^2_{\mathrm{POL}}(A) = - \sum_{\substack{i \in A \\ j^* \in A}} \left[\sum_{k \in B} (\tilde{i}j^* \| \tilde{k}k) + H^B_{\tilde{i}j^*} \right] \left[\sum_{k \in B} (\tilde{j}^* i \| \tilde{k}k) + H^B_{\tilde{j}^* i} \right] / (\epsilon^A_{j^*} - \epsilon^A_i), \tag{4}$$

$$E^2_{\mathrm{DEL}}(A \to B) = - \sum_{\substack{i \in A \\ j^* \in B}} \left[\sum_{k \in A} (\tilde{i}j^* \| \tilde{k}k) + H^A_{\tilde{i}j^*} \right] \left[\sum_{k \in B} (\tilde{j}^* i \| \tilde{k}k) + H^B_{\tilde{j}^* i} \right] / (\epsilon^B_{j^*} - \epsilon^A_i) \tag{5}$$

and

$$E^2_{\mathrm{DISP}} = - \sum_{i,k,j^*,l^*} \frac{(\tilde{i}j^* \| \tilde{k}l^*)(\tilde{j}^* i \| \tilde{l}^* k)}{\epsilon_{j^*} + \epsilon_{l^*} - \epsilon_k - \epsilon_i}, \tag{6}$$

$$(i, j^* \in A, \quad k, l^* \in B)$$

while the terms $E^2_{\mathrm{POL}}(B)$ and $E^2_{\mathrm{DEL}}(B \to A)$ are obtained from Eqs (4) and (5) by interchanging A and B. In the above equations the orbital indices without an asterisk refer to the occupied set of MOs, and with an asterisk to the virtual set. All the orbitals are molecular spin orbitals of the system A or B, so the integrations are understood to contain also summations over spin variables. The ϵ_i-s are the orbital energies, and the two-electron integrals are in the (11|22) convention. The interaction energies as obtained by this method are free from BSSE [16], but the results suffer only from the following two sources of errors:
(i) the finite basis approximation;
(ii) the truncation of the PT series at the second order.

In general, the result of (i) is a slight underestimation of the interaction, which, however, is usually overcompensated by an exaggeration of the interaction due to (ii). These two effects are very much coupled, because in our working formulae (1–6) all integrals are transformed in their bra-indices by the inverse of the

overlap matrix. As a result, a change of the basis set, e.g. adding a new function, changes all elements of the S^{-1} matrix, thus rearranges the orders of the PT. With respect to the choice of the orbital basis, we investigated two possibilities:

(1) Usually, we took the occupied and virtual orbitals directly from the separate MO calculation. As a consequence, all the occupied and virtual orbitals of molecule B overlap with those of A.

(2) In some cases, we projected out (that is, Schmidt-orthogonalized) the virtuals from the occupied space before forming the S^{-1} matrix by the formula

$$\psi_{i^*}^{\mathrm{proj}} = [1 - \hat{P}]\psi_{i^*}, \tag{7}$$

where

$$\hat{P} = \sum_{ik}^{\mathrm{occ}} |\psi_i > \overline{S}_{ik}^{-1} < \psi_k|, \tag{8}$$

where $\overline{S}^{-1}$ is the inverse of the occupied–occupied block of the overlap matrix. As a result, the biorthogonal formulation does not mix virtual components to occupied orbitals if version (2) is applied. It does mix, however, the orbitals of A and B. A similar type of projection was discussed earlier by Gouyet [33].

5. Results and discussion

BSSE in small basis. First, we investigate the role of BSSE for $(He)_2$ in the rather small basis sets termed (2) and (3) (cf. Table I). The two basis sets differ only in the use of a diffuse d function with an exponent of 0.1. The long range interaction is plotted in Fig. 1, where the CI-SD curves are compared to the perturbational ones. The Boys–Bernardi counterpoise correction shifts the CI curves significantly, the change for basis (3) is the more pronounced. In fact, the CI curve in basis (3) is very poor if BSSE is not taken into account. After performing the counterpoise correction the two CI curves corresponding to the basis (2) and (3) (the two dotted lines in Fig. 1), become very similar. This clearly indicates that the extremely large difference between the uncorrected CI curves (the two dashed lines) is not a true basis set effect, but dominantly a BSSE related to the diffuse d orbitals. On the other hand, the PT curves (solid lines) are not seriously affected by the inclusion of the d orbitals, because they are free from BSSE.

The instability of the PT results. The situation is not always so fortunate with respect to the PT results, especially in larger basis sets. It was already observed by Gouyet [33] and Kochanski [34], and by Hayes and Stone [35], that the biorthogonal formulation may result in "instability" of the results with respect to the basis set change. We encountered this problem when the two molecules A and B are brought very close to each other. This is understandable because, using the same set of orbitals on A and B, at $R \to 0$ the basis set becomes overcomplete. Of course, this feature may also result in an instability of the results with respect to the basis set change at small R, but the primary problem is the wrong $R \to 0$ asymptotics.

This point is illustrated in Table II which presents $H_2 \ldots H_2$ interaction energies in a split valence shell basis set. The results given in the first column show an artefact maximum at around 3×10^{-10}m, while for smaller R the interaction energy becomes more negative instead of turning to positive due to exchange repulsion. This indicates a complete breakdown of the PT series for small R. This finding is in agreement with the analysis by Gouyet [33] and with the basic assumption of any PT theory.

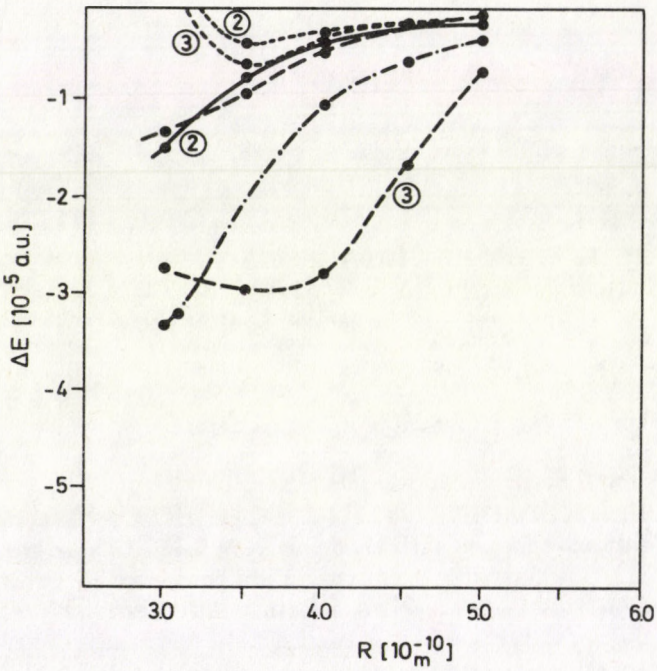

Fig. 1. Long range potential curves for the He ... He interaction as obtained by Davidson-corrected CI-SD without (----) and with (.....) correction for BSSE, and the second order PT (———). The experimental result (.-.-.-.) taken from [40] is indicated for comparison. The figures in the circles refer to the basis set (cf. Table I)

However, if the virtuals are projected out from the occupied space before forming the S^{-1} matrix (cf. Eqs 7–8), the results become meaningful as it is shown by the second column of Table II. The maximum disappears and the interaction becomes repulsive at small R.

Unfortunately, the projecting out of the virtuals does not solve the above problem for the general case. Sometimes the qualitatively acceptable curves become meaningless upon projecting out the virtuals. Such an example was found for He ... He in basis set (5). Without plotting the result, we note that the projecting out of the virtuals *improved* the potential curve if using basis (3).

Table II

Second order $H_2 \ldots H_2$ interaction energies [10^{-6} a.u.] for a T-form geometrical arrangement. R is the distance between the centroid of A and the closest H atom of B. Basis set 1 is used

R[10^{-10}m]	Unprojected virtuals	Projected virtuals
2.5	−45	+530
3.0	−11	+37
3.5	−12	−6

Formally, it is possible to ensure a strong exchange repulsion within the perturbational treatment, avoiding in this manner the pathologically improper potential curves at $R \to 0$ asymptotics. Namely, if we apply the Taylor expansion (with I the unit matrix)

$$S^{-1} = (I + s)^{-1} = I - s + s^2 - \ldots \tag{9}$$

to obtain S^{-1}, and truncate it after the linear term*, we always get strong repulsion (positive interaction) at $R \to 0$, as we checked numerically. The corresponding approach accounts for overlap effects only approximately. Such a method, introduced in a different manner, was used e. g. by Chang and Weinstein [36]. A similar "expanded formalism" was found to be superior to the biorthogonal treatment for describing interbond (intramolecular) interactions [37]. In the present case, however, this first order expansion is not recommended, because it strongly exaggerates the overlap repulsion and the attractive part of the interaction tends to diminish. For example, using basis (3), the He...He interaction at 3A was found to be attractive when using the biorthogonal formulation, but became repulsive if using the first order expansion.

BSSE in larger basis sets. In the light of the above discussion, it is the supermolecule approach from which we can expect a more reliable estimation of interaction energies, especially in larger basis sets where the PT methods run into difficulties in accounting for intermolecular overlap effects. Unfortunately, supermolecule calculations are not only more expensive, but as we shall see below, the proper correction for BSSE is essential even for large basis sets.

First we report He...He interaction energies and superposition errors as obtained by the Boys–Bernardi counterpoise scheme, using various methods to describe electron correlation in the medium-sized basis sets denoted (4) and (5) in Table I. The results are presented in Table III. It can be seen that the second-order Moller–Plesset (MP2) method does not give a satisfactory account of correlation energy, and, as a consequence, the MP2 interaction energies are too small. This finding is in agreement with literature results; it is known that the MP2 method underestimates the dispersion energy by a significant amount (cf. [2]). Moreover, even in the smaller basis (4) (without d function) half of the predicted interaction is merely BSSE. The third order MBPT (MP3), CEPA and ACCD approaches

*Note that the truncation of Eq. (9) after the zeroth order term corresponds to the "classical PT" where the overlap between the two molecules is completely neglected. This approach is, of course, incapable of describing any exchange repulsion [8].

yield nearly the same result. In the smaller basis set, they predict an interaction of $\sim 2.0 \times 10^{-5}$ a.u., of which $\sim 0.8 \times 10^{-5}$ a.u. is BSSE leading to a significantly underestimated interaction energy. The full CI interaction energy, in basis (4), both before and after counterpoise correction, is slightly larger than those obtained by various approximate methods. The value of BSSE is practically the same ($\sim 0.8 \times 10^{-5}$ a.u.) for the full CI and approximate schemes. When diffuse d orbital is added [basis (5)], the uncorrected energies become too large, a consequence of the increased BSSE due to basis set expansion. (Note that this is opposite to the general trends described in the introduction.) After the BSSE is corrected for, we still have a significant underestimation of the interaction energy relative to the experimental result. When adding the d orbitals, the full CI interaction energy increases from 1.6 to 2.2×10^{-5} a.u., but is still significantly less than the experimental value. In other words, the uncorrected and corrected values sandwich the experiment. The question which arises here is whether the Boys–Bernardi counterpoise scheme overestimates the BSSE, a more refined scheme could bring the results of basis set (5) closer to experiment. As we have discussed in Section 2, this question is not trivial to answer. It should be kept in mind that the attractive part of the interaction, originating from electron correlation, is not accounted for completely by the above calculations. At the same time, the repulsive part originates mainly from the SCF energy and it is described quite accurately even in moderate basis sets. Therefore an effect which gives extra attraction, like BSSE, may give results close to experiment. This fact does not necessarily mean that the Boys–Bernardi scheme overestimates the BSSE. The biorthogonal PT calculations, although they are free from BSSE, cannot be involved here to resolve this problem because they overestimate the interaction at the second order.

Table III

He...He interaction energies $\Delta E[10^{-5}$ a.u.] at $3 \cdot 10^{-10}$m by various supermolecule approaches: second and third order Moller–Plesset PT, CEPA1, CEPA2, "approximate coupled cluster" (ACCD) and full CI approach

Basis	ΔE	MP2	MP3	CEPA1	CEPA2	ACCD	full CI	expt.
(4)	uncorrected	−1.4	−2.1		−2.2	−2.0	−2.4	
	counterpoise corr.	0.7	+0.8		+0.8	+0.8	+0.8	
	corrected	−0.7	−1.3	−1.4	−1.4	−1.2	−1.6	
								−3.3
(5)	uncorrected	−3.6	−4.6		−4.8	−4.6	−5.0	
	counterpoise corr.	+2.5	+2.8		+2.9	+2.9	+2.9	
	corrected	−1.1	−1.8	−1.9	−1.9	−1.7	−2.2	

More insight into the nature of counterpoise correction may be gained by studying a wider range of the potential curve within very large basis sets. Such a result is plotted in Fig 2, where we present CEPA1 curves in basis set (6) containing 100 contracted functions. The corresponding numbers are collected in Table IV. One can see that the BSSE is not negligible, it is in the same order of magnitude as in bases (4) and (5). The uncorrected and the corrected curves again sandwich the

experimental one, although the latter nearly coincides with the *uncorrected* one. This is because there is a small portion of dispersion energy still missing in this basis set which is nearly compensated by the BSSE. The corrected results, in turn, are too high. It is remarkable that

(i) curves (a), (b) and (c) are rather parallel indicating a negligible dependence of BSSE on the interatomic distance in this basis set. This might be due to the fact that the basis has a lot of diffuse functions that change little over the range studied.

(ii) The places of minima of the experimental and *uncorrected* curves are nearly the same, while that of the corrected curve is slightly larger due to a fortuitous cancellation of errors.

(iii) The counterpoise correction predicts nearly the same BSSE in basis sets (5) and (6), although the latter is considerably larger.

Water–water interaction. In [8], we compared the second-order PT calculations to supermolecule SCF ones at the minimal basis level. Here we repeat this comparison using a split valence shell basis [basis (1) in Table I].

The energies have been calculated for the linear-perpendicular arrangement of the molecules in which the atoms O– –H...O are collinear, and the planes of the two molecules are perpendicular to each other. This arrangement was found to be energetically the most favourable [38].

Table IV

He...He interaction energies at various inter-atomic distances as obtained by the CEPA2 method in basis (6)

$R_{He...He}[10^{-10}m]$	Interaction energy $[10^{-5}$ a.u.] uncorrected	counterpoise corrected
2.50	7.73	8.92
2.75	−2.13	−1.24
2.86	−3.23	−2.46
2.96	−3.54	−2.88
3.07	−3.45	−2.90
3.18	−3.16	−2.71
3.50	−2.06	−1.83

The potential curves are plotted in Fig. 3, where the 2nd order PT result neglecting the dispersion term (Eq. 8) is also given, allowing a better comparison to the SCF curve which does not contain any dispersion effect. We see from the two PT curves that the dispersion contribution to the water dimerization energy is not negligible, but does not change the qualitative features of the potential curve. The SCF method without counterpoise correction predicts a deeper minimum than the dispersionless PT calculation. Considering the fact that in the latter the interaction is very probably overestimated, the SCF method must suffer from significant BSSE. In fact, after performing the Boys–Bernardi counterpoise correction, the SCF curve shifts up to a very large extent. At the long range, the BSSE-free PT calculation and the counterpoise-corrected SCF method predict similar interaction energies, while the uncorrected SCF results are too deep. Accordingly, the counterpoise correction

does not seem to overestimate the BSSE in the present case.

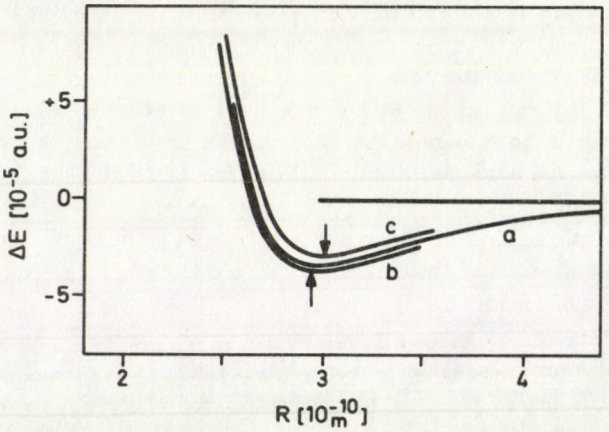

Fig. 2. Experimental (a) and CEPA2 potential curves in basis (6) without (b) and with (c) Boys–Bernardi counterpoise correction. Equilibrium distances are indicated by arrows

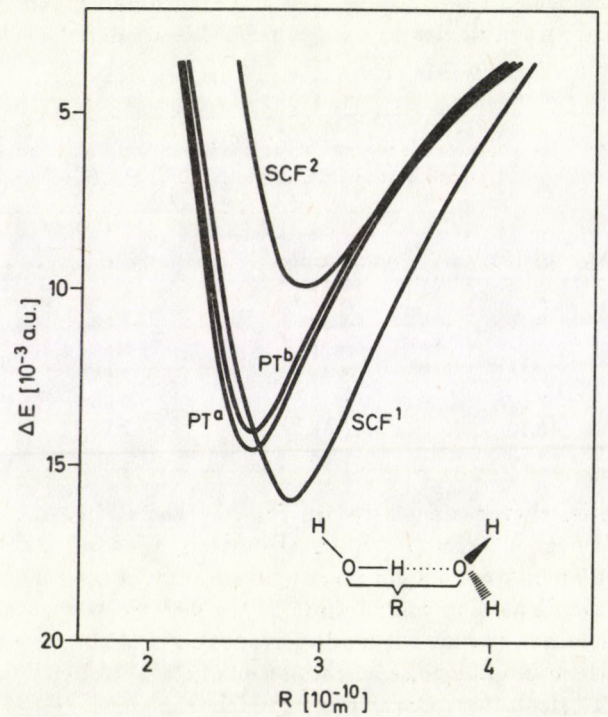

Fig. 3. Water–water interaction in a "linear-perpendicular" geometrical arrangement in 3–21G basis set, as obtained by supermolecule SCF calculations without (1) and with (2) counterpoise correction, and by second order PT method with (a) and without (b) dispersion contribution

6. Conclusion

We have to realize that it is very difficult to draw general conclusions from the presented calculations, no unique picture has emerged. Our findings can be summarized as follows:

(i) Second order PT calculations using a biorthogonal formalism can be reliable only in moderate basis sets and large R. In larger bases, the PT results are sometimes acceptable but they can also be sometimes completely meaningless. Owing to this problem, one has to be very careful in applying this method. More reliable results can only be expected at the third and higher orders of PT — the derivation and programming of these is now in progress.

(ii) Interaction energies obtained by supermolecule calculations and the Boys–Bernardi counterpoise scheme are more stable with respect to the basis set change, but usually (though not always) predict a weaker interaction than BSSE-free PT calculations do — (this comparison, of course, is meaningful only if the latter are reliable, e. g. at the long range).

(iii) Equilibrium bond distances predicted by counterpoise-corrected curves are usually too large, while those of PT calculations are mostly too small.

The latter two points, as it was emphasized throughout this paper, do not indicate directly that the Boys–Bernardi scheme slightly overcorrects for BSSE. The final answer to this question is yet to be established.

Note added in proof: Recent investigations show that wrong PT curves are not consequences of the biorthogonal formulation, but of an improper partitioning of the many-body Hamiltonian (P. R. Surján and I. Mayer, to be published).

References

1. N. R. Kestner, J. Chem. Phys., *48*, 252, 1968.
2. For a recent review, see J. H. van Lenthe, J. G. C. M. van Duijneveldt-van de Rijdt, and F. B. van Duijneveldt, Adv. Chem. Phys., *69*, 521, 1987; Sh. K. Loushin, S. Liu and C. E. Dykstra, J. Chem. Phys., *84*, 2720, 1986; see also [4].
3. M. Gutowski, F. B. van Duijneveldt, G. Chalasinski and L. Piela, Chem. Phys. Letters, *129*, 325, 1986.
4. J. R. Collins and G. A. Gallup, Chem. Phys. Letters, *129*, 329, 1986.
5. S. F. Boys and F. Bernardi, Mol. Phys., *19*, 553, 1970.
6. J. P. Daudey, P. Claverie and J.-P. Malrieu, Intern. J. Quant. Chem., *8*, 1, 1974, J. P. Daudey, J.-P. Malrieu and O. Rojas, *ibid.*, *8*, 17, 1974.
7. A. Johansson, P. Kollman, and S. Rothenberg, Theor. Chim. Acta, *29* 167, 1973; P. Carsky and M. Urban, Ab initio calculations, Lecture Note in Chemistry No. 16, Springer, Berlin, 1980, p. 177.
8. P. R. Surján and R. A. Poirier, Chem. Phys. Letters, *123*, 358, 1986.
9. J. H. van Lenthe, T. van Dam, F. B. van Duijneveldt and L. M. T. Kroon–Batenburg, Faraday Symp., *19*, 125, 1984.
10. R. Osman, S. Topiol and H. Weinstein, J. Comput. Chem., *2*, 73, 1981.
11. P. H. Smit, J. L. Derissen and F. B. van Duijneveldt, Mol. Phys., *37*, 501, 1979; E. Kochanski and D. R. Flower, Chem. Phys., *57*, 217, 1981; J. R. Collins and G. A. Gallup, Chem. Phys. Letters, *123*, 56, 1986.
12. W. A. Sokalski, P. C. Hariharan and J. J. Kaufman, J. Comput. Chem., *4*, 506, 1983.

13. A. Van der Avoird, Chem. Phys. Lett., *1*, 429, 1967, A. T. Amos and J. I. Musher, Chem. Phys. Lett., *1*, 149, 1967; J. O. Hirshfelder, Chem. Phys. Lett., *1*, 363, 1967; J. N. Murrell and G. Shaw, J. Chem. Phys., *46*, 1768, 1967; K. Salewicz and B. Jeziorski, Mol. Phys., *38*, 191, 1979.
14. E. Kochanski and J. F. Gouyet, Theor. Chim. Acta, *39*, 329, 1975; Mol. Phys., *29*, 693, 1975; J. F. Gouyet, J. Chem Phys., *59*, 4637, 1975; E. Kochanski in: Intermolecular Forces, Proc. 14th Jerusalem Symp., 1981, Ed. B. Pullman, p. 15; E. Kochanski, J. Chem. Phys., *58*, 5223, 1973.
15. I. Mayer, Int. J. Quant. Chem., *23*, 341, 1983.
16. P. R. Surján, I. Mayer and L. Lukovits, Chem. Phys. Letters, *119*, 538, 1985.
17. M. Gutowski, J. H. van Lenthe, T. Verbeck, F. B. van Duijneveldt and G. Calasinski, Chem. Phys. Letters, *124*, 370, 1986.
18. D. B. Cook, Mol. Phys., *53*, 645, 1984.
19. (a): P. Otto and J. Ladik, Chem. Phys., *8*., 192, 1975; *19*, 209, 1977; (b): P. Otto, Int. J. Quant. Chem., *28*, 895, 1985; (c): H. Weinstein, J. E. Eilers and S.-Y. Chang, Chem. Phys. Letters, *51*, 534, 1977.
20. R. McWeeny, Proc. Roy. Soc. London, *A523*, 242, 1959.
21. S. Saebo and P. Pulay, Chem. Phys. Letts., *113*, 13, 1985.
22. G. Stollhoff and P. Vasilopoulos, J. Chem. Phys., *84*, 2744, 1986.
23. C. Zirz and R. Ahlrichs, in: Proceedings of the Daresbury Study Weekend on Correlation, Daresbury, November 1979, eds. M. F. Guest and S. Wilson, Science Research Council DL/SCI/R14 (1980); R. Ahlrichs, in: Methods in computational molecular physics, eds. G. H. F. Diercksen and S. Wilson, Reidel, Dordrecht, 1983; W. Meyer, J. Chem. Phys., *58*, 1017, 1972; Intern. J. Quantum Chem., *55*, 341, 1971; P. Pulay, Intern. J. Quantum Chem. Symp., *17*, 257, 1983; P. Pulay and S. Saebo, Chem. Phys. Letters, *117*, 37, 1985.
24. N. C. Handy, J. D. Goddard and H. F. Schaefer III, J. Chem. Phys., *71*, 426, 1979.
25. S. R. Langhoff and E. R. Davidson, Int. J. Quant. Chem., *8*, 61, 1974.
26. R. A. Chiles and L. E. Dykstra, J. Chem. Phys., *74*, 4544, 1981; Chem. Phys. Letts., *80*, 69, 1981.
27. J. S. Binkley, J. A. Pople, and W. J. Hehre, J. Am. Chem. Soc., *102*, 939, 1980.
28. P. Pulay, Theoret. Chim. Acta (Berlin), *50*, 299, 1979.
29. V. R. Saunders and M. F. Guest, ATMOL3/ATMOL-4 program system, 1976, 1982, 1985; J. H. van Lenthe, Supercomputer, *5*, 33, 1985.
30. MONSTERGAUSS (MUN version): M. R. Peterson and R. A. Poirier, Department of Chemistry, University of Toronto, Ontario and Chemistry Department, Memorial University of Newfoundland, St. John's, Newfoundland, Canada A1B 3X7.
31. GAUSSIAN80: J. S. Binkley, R. Whiteside, R. Krishnan, H. B. Schlegel, D. J. Defrees, J. A. Pople, QCPE, *13*, 406, 1981.
32. PROGRAM INTERMOL: P. R. Surján, Department of Chemistry, Memorial University of Newfoundland, St. John's, Newfoundland, Canada A1B 3X7.
33. J. F. Gouyet, unpublished results, 1976.
34. E. Kochanski, personal communication.
35. I. C. Hayes and A. J. Stone, Mol. Phys., *53*, 83, 1984.
36. S-Y. Chang and H. Weinstein, Int. J. Quant. Chem., *14*, 801, 1978.
37. I. Mayer and P. R. Surján, J. Chem. Phys., *80*, J649, 1984.
38. G. H. F. Diercksen, Theor. Chim. Acta, *21*, 335, 1971; see also [29b].
39. R. Krishan, J. S. Binkley, R. Seeger and J. A. Pople, J. Chem. Phys., *72*, 650, 1980.
40. F. B. Brown, D. W. Schwenke and D. G. Truhlar, Theoret. Chim. Acta (Berlin), *68*, 23, 1985.
41. M. Gutowski, J.-H. van Lenthe, J. Verbeek, J. G. C. M. van Duijneveldt-van de Rijdt and F. B. van Duijneveldt, to be published.
42. R. Feltgen, H. Kirst, K. A. Kohler and H. Pauly, J. Chem. Phys., *76*, 2360, 1982.

Acta Physica Hungarica 67 (3–4), pp. 401–405 (1990)

SHORT COMMUNICATIONS

ON THE SATURATED CORONA PROFILES AT GROUND SURFACE AND UNDERNEATH HVDC LINES

SALAH ABDEL-SATTAR

Electrical Engineering Department
Assiut University
Assiut, Egypt

(Received 19 December 1986)

Introduction

Recent advances in the development of the HV terminal equipment have increased the feasibility of high voltage direct current (HVDC) transmission. HVDC overhead lines operating at voltages up to ±600 kV are in operation or under construction and lines at high voltages are under study [1].

One of the main problems associated with HVDC lines is the corona occurring on them and the environmental impact associated with it. Corona on HVDC lines forms space charges which fill the interelectrode region contrary to that in AC ones where the space charges are constrained to the vicinity of the HV subconductors due to the periodic reversal of the electric field. This increases the importance of analyzing the DC ionized field, thus calculating the lateral distribution of the current density and field intensity over the ground surface.

Physical models of HVDC lines would make it convenient to determine the performance of full scale transmission lines by means of laboratory tests with smaller dimensions and lower voltages. Modeling of HVDC lines accounting for the line geometry is much more complicated [2]. The problem can be solved exactly only in the electrostatic and the saturated corona ones.

Zaffanella [1] developed a technique which allows the evaluation of the electric field and ion densities. This technique is based on small scale model tests with voltages several times greater than the corona inception voltage of the wires of the model (saturated case). From model data electric field and ion densities for the full-scale line in saturated corona conditions were calculated [1].

In this paper the author describes a simple mathematical model to calculate the saturated corona profiles (field intensity, current density and then charge density) over the ground surface and underneath HVDC monopolar lines. The relations between these saturated values and the length of the field lines are given. The present results are compared with the experimental ones.

Method of analysis

Measurements [3] show that the field intensity (E) after corona onset value can be represented by:

$$E = A + BV \tag{1}$$

where V is the applied voltage, A and B are constants depending on the measuring position (X) and onset field value.

For saturated corona, the onset voltage and then the onset field is zero and Eq. (1) can be rewritten in the form:

$$E = BV. \tag{2}$$

On the other hand, calculations [4, 5] show the same relation as shown in Fig. 1. The field intensity at ground surface and underneath monopolar practical HVDC line is calculated [4, 5] for very low onset voltage which can be considered negligible with respect to the applied voltage. The field intensity versus applied voltage at constant position (X) (it means at constant field line length (L)) is shown in Fig. 1.

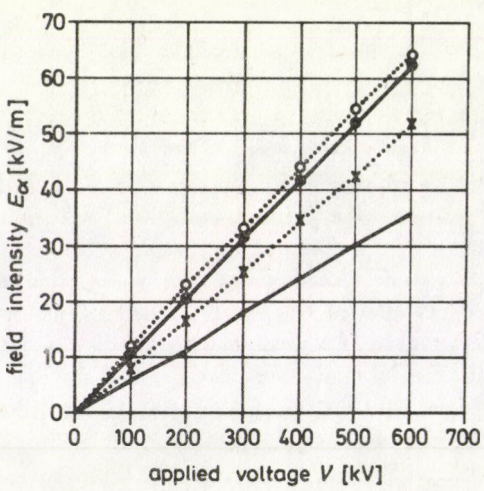

Fig. 1. Calculated field intensity over the ground surface versus applied voltages at different position X and field line length L

o - - - o L =10.8m and X =0.3m
•—— • L =11.9m and X =4.4m
X - - - X L =14.5m and X =8.2m
—— L =20.3m and X =14.0m

The higher the distance X, the longer the field length L [6], the lower the field intensity (Fig. 1). This means that the field intensity E proportional inversely to

L (i. e. $E \propto \frac{1}{L}$) at constant applied voltage V. This can be satisfied by assuming B, in Eq. (2), to equal K_1/L. Then, Eq. (2) is:

$$E = K_1 V/L, \tag{3a}$$

where K_1 is a constant depending on the measuring position X.

For saturated corona where the conductor charge density is very small and by integrating Poisson's equation ($\nabla \cdot E = \rho/\varepsilon_0$), one can find the charge density (ρ) as:

$$\rho = K_2 \varepsilon_0 V/L^2, \tag{4a}$$

where ε_0 is the air permittivity, K_2 is a constant depending on the measuring position. The constants K_1 and K_2 are chosen 1.21 and 0.86, respectively, to fit the previous calculations [4, 5]. Then, Eqs. (3a) and (4a) are rewritten as

$$E = 1.21V/L, \tag{3b}$$

$$\rho = 0.86\varepsilon_0 V/L^2. \tag{4b}$$

The current density (J) at ground surface is given by:

$$J = K\rho E, \tag{5}$$

where K is the ion mobility. Substituting from Eqs (3b) and (4b) in (5):

$$J = 1.04K\varepsilon_0 V^2/L^3. \tag{6}$$

Results and discussion

In this paper the saturated corona profiles over the ground surface and underneath monopolar HVDC lines are calculated according to Eqs (3b) and (6) for the indoor test model [2]. The length of the field lines was precalculated [6] and assumed that the ions move to ground surface through them. This test model [2] consisted of steel wire (stainless steel fibers twisted into thin strands with a surface like a yarn) having corona inception voltage of about -2 kV (negative polarity) and $+3$ kV (positive polarity), practically independent of the distance to ground. The calculated values are compared with those measured experimentally.

Table I shows the calculated lengths of field lines emanating from the wire of the monopolar model at different heights (H) [6]. The distance (X) between the intersection of each field line with the ground surface and the line of symmetry (at which the length of the field line equals the wire height above the ground surface, i. e. $L = H$ and the emanating angle of the field line from the wire surface $\Psi = 0$ or 180°) is also shown. The emanating angle Ψ increases clockwise.

Table I

The length (L) of field lines emanating from the monopolar line at angle Ψ and terminating to the ground surface at distance (X)

Ψ	H = 0.914m		H = 1.22m	
(...°)	X (m)	L (m)	X (m)	L (m)
75	1.190	1.740	–	–
105	0.700	1.240	0.93	1.65
135	0.380	1.020	0.51	1.36
165	0.120	0.924	0.16	1.23

Tables II and III show the calculated and measured values of the saturated field intensity (E) and current density (J) over the ground surface and at different position (X). The applied voltage is kept constant at 40 kV and the wire height above the ground surface is changed.

Table II

Calculated and measured saturated corona field intensity (E) and current density (J) over the ground surface and underneath HVDC monopolar model at H = 0.914m

X (m)	E (kV/m)		J (μA/m^2)	
	Calculated	Measured	Calculated	Measured
1.19	27.8	23	0.42	0.31
0.70	39	35	1.14	0.97
0.38	47.5	45	2.08	2.05
0.12	52.4	52	2.79	2.92

Table III

Calculated and measured saturated corona field intensity (E) and current density (J) over the ground surface and underneath HVDC monopolar model at H = 1.22m

X (m)	E (kV/m)		J (μA/m^2)	
	Calculated	Measured	Calculated	Measured
0.93	23.3	26.0	0.49	0.36
0.51	35.6	34.0	0.87	0.79
0.16	39.3	37.0	1.19	1.15

It is shown that the calculated values of the field intensity fit reasonably the measured ones while the calculated values of the current density fit the measured ones with a certain small error.

The author attributes this discrepancy to the fact that the ions drift along flux lines other than the field lines. This means that the using of Deutsch's assumption for calculating the saturated corona profiles has an error. This error is higher in calculating current density profiles than that in field intensity profile, (Tables II and III), in agreement with previous investigation [7].

Conclusions

On the basis of the analysis presented, the following conclusions can be drawn concerning saturated monopolar corona:

1. The saturated corona profiles over the ground surface and underneath HVDC monopolar lines are calculated using simple expressions.
2. Relations between the saturated values at certain positions and the length of the field line emanating from the wire and terminating to that position are given.
3. The calculated values fit reasonably the measured ones.

References

1. L. E. Zaffanella, Space Charge Effects of HVDC Transmission Line Corona-Full Scale and Model Line Tests, Proceedings of the 1984 Japan-US Science Seminar, Oct. 13–16, 1984 Japan, pp. 109–122.
2. Electric Power Research Institute, DC Conductor Development, Final Report, Project RP 1514, Feb. 1982 (EPRI EL-2257).
3. M. Hara et al, IEEE Trans., Vol. PAS-*101*, 803, 1982.
4. M. Abdel-Salam, M. Farghally and S. Abdel-Sattar, IEEE Trans., Vol. PAS-*101*, 4079, 1982.
5. M. Abdel-Salam, M. Farghally and S. Abdel-Sattar, Acta Phys. Hung., *54*, 313, 1983.
6. S. Abdel-Sattar, Flux Lines Emanating from or Terminating to HVDC Transmission Lines with Bundle Conductors, Modelling, Simulation and Control, A, AMSE Press, Vol. 18, N° 3, pp. 45–54, 1988.
7. W. Janischewskyj and G. Gela, Computation of Electric Fields Surrounding HVDC Transmission Lines in Corona, Proceedings of the 1984 Japan–US Science Seminar, Oct. 13–16, 1984, Japan, pp. 167–181.

Acta Physica Hungarica 67 (3–4), pp. 407–410 (1990)

ON THE THERMOELECTRIC POWER IN GAPLESS SEMICONDUCTORS

K. P. GHATAK

Department of Electronics and Telecommunication Engineering
Faculty of Engineering and Technology
University of Jadavpur, Calcutta-700032, India

(Received 15 August 1988)

In recent years there has been considerable interest in studying the different electronic properties of degenerate materials because of their importance in device technology [1, 2]. Though considerable work has been done, there still remain scopes in the investigations made while the interest for further research of the different other aspects of such small-gap semiconductors is becoming increasingly important. One such useful parameter is the thermoelectric power of the electrons in the presence of a classically large magnetic field (hereafter referred to as TPM) which has also been studied in [3–7] under various physical conditions. The TPM is remarkable for its independence of the scattering processes, depending only on the dispersion relation [3]. Incidentally, it appears from the literature that the TPM in gapless semiconductors has yet to be derived. This is very important since the electronic properties of zero gap semiconductors are currently the subject of intensive investigations and also since the special features of these semiconductors have recently been reported [8–11]. In what follows, we shall study the doping dependence of the TPM in gapless materials taking n-HgTe as an example.

The TPM of the electrons can, in general, be expressed [3] as

$$S_{\infty} = \frac{k_B}{e}\left[\frac{\langle Z\rangle}{\langle I\rangle} - \eta\right], \tag{1}$$

where k_B is the Boltzmann constant, e is the electron charge, $\eta \equiv E_F/k_BT$, E_F is the Fermi energy as measured from the edge of the conduction band, T is temperature, $Z \equiv E/k_BT$, E is the electron energy as measured from the edge of the conduction band,

$$\langle Z\rangle \equiv -(3/4\pi)\int_0^{\infty}\left[\frac{\partial f_0}{\partial E}\right]V(E)ZdE,$$

$f_0 \equiv \left[1+\exp\left(\frac{E-E_F}{k_BT}\right)\right]^{-1}$ and $V(E)$ is the volume of $\mathbf{k}$-space. It appears then that the determination of TPM using (1) requires an expression of $V(E)$ which in turn is determined by the $E-\mathbf{k}$ dispersion relation. The electron energy spectrum in gapless semiconductors can be written [8–11] as

$$E = Ak^2 + B_0k, \tag{2}$$

where $A = \frac{\hbar^2}{2m^*}$, $\hbar \equiv h/2\pi$, $\hbar$ is Planck's constant, m^* is the effective electron mass at the edge of the conduction band, $B_0 = \frac{3e^2}{128\epsilon_s}$ and ϵ_s is the semiconductor permittivity.

From (2) we get

$$V(E) = \frac{4\pi}{3}(2A)^{-3}\left[-B_0 + \sqrt{B_0^2 + 4AE}\right]^3. \tag{3}$$

Combining (1) and (3) we get

$$S_\infty = \frac{1}{eT}\left[\{P(E_F) + Q(E_F)\}\{R(E_F) + \delta(E_F)\}^{-1} - E_F\right], \tag{4}$$

where

$$P(E_F) \equiv E_F R(E_F), \qquad R(E_F) \equiv \left[-B_0 + \sqrt{B_0^2 + 4AE_F}\right]^3,$$

$$Q(E_F) \equiv \sum_{r=1}^{l} \nabla_r [P(E_F)], \qquad \nabla_r \equiv 2(k_B T)^{2r}(1 - 2^{1-2r})\varsigma(2r)\frac{d^{2r}}{dE_F^{2r}},$$

r is the set of real positive integers, $\varsigma(2r)$ is the zeta function of order $2r$ [12] and

$$\delta(E_F) \equiv \sum_{r=1}^{l} \nabla_r [R(E_F)].$$

The evaluation of TPM from (4) as a function of carrier degeneracy requires an expression of electron statistics which, in turn, can be expressed as

$$n_0 = (3\pi^2)^{-1}[R(E_F) + \delta(E_F)]. \tag{5}$$

For $B_0 \to 0$, as for parabolic energy bands, (4) and (5) get simplified into the well-known forms [4, 13] as

$$S_\infty = \frac{k_B}{e}\left[\frac{5}{2}F_{\frac{3}{2}}(\eta)\left\{F_{\frac{1}{2}}(\eta)\right\}^{-1} - \eta\right] \tag{6}$$

and

$$n_0 = N_C F_{\frac{1}{2}}(\eta), \tag{7}$$

where $F_j(\eta)$ is the Fermi–Dirac integral of order j as defined by Blakemore [13] and $N_c = 2(2m^* k_B T/h^2)^{3/2}$.

Using (4) and (5) and taking the parameters [14] $m^* = 0.025m_0$, $\epsilon_{sc} = 20\epsilon_0$ and $T = 4.2$ K as appropriate for n-HgTe we have plotted S_∞ versus n_0 as shown in Fig. 1 in which the same dependence is also plotted by taking $B_0 = 0$

for the purpose of comparison. It appears from Fig. 1 that according to both cases, the TPM decreases with increasing concentration. For relatively low values of electron concentration, the effect of the electron–electron interaction term decreases whereas the influence of the same term becomes rather prominent for relatively higher values of the carrier degeneracy. The term B_0 enhances the values of the TPM as compared to that corresponding to $B_0 = 0$ at a given value of n_0 in the whole range of the concentrations considered. It may finally be noted that the basic purpose of the present work is not solely to demonstrate the effect of carrier degeneracy on the TPM in gapless semiconductors, but also to formulate the electron concentration in the same since the various electron transport and the derivation of the expressions of many physical parameters are based on the temperature dependent electron statistics in such materials.

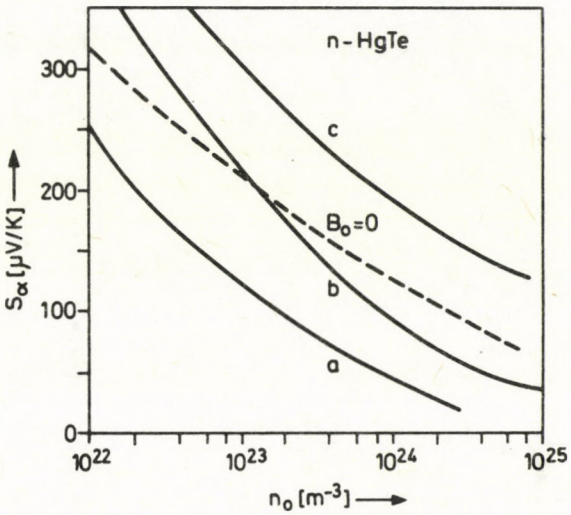

Fig. 1. Plot *c* shows the TPM as a function of electron concentration at 4.2 K in n-Hg.Te. The dotted plot corresponds to $B_0 = 0$ at 2.4 K. The plot b corresponds to 77 K. The plot a ($B_0 = 0$) corresponds to 77 K. From this graph we can assess the influence of temperature on the TPM

Acknowledgement

The author is grateful to Dr. M. Mondal for helpful discussion and computer programming.

References

1. F. Stern, J. Appl. Phys., *47*, 5382, 1976.
2. R. W. Dixon, Bell Syst. Tech. Journal, *55*, 973, 1976.
3. W. Zawadzki, 11th Int. Conf. Phys. of Semicond., *1*, p. 87, Elsevier Publishing Company, Netherlands, 1972.

4. I. M. Tsidilkovski, Band Structure of Semiconductors, Pergamon Press, Oxford, 1982, p. 313 and the references cited therein.
5. W. Zawadzki, Adv. Phys., *23*, 435, 1974 and the references cited therein.
6. S. P. Zelenin, A. S. Kondratev and A. I. Kuchma, Sov. Phys. Semicond., *16*, 355, 1982 and the references cited therein.
7. K. P. Ghatak and M. Mondal, Phys. Stat. Sol. (b), *135*, 819, 1986.
8. V. A. Yakovlev, Sov. Phys. Semicond., *13*, 692, 1979.
9. B. I. Halperin and T. M. Rice, Rev. Mod. Phys., *40*, 755, 1968.
10. A. N. Chakravarti, K. P. Ghatak, G. B. Rao and K. K. Ghosh, Phys. Stat. Sol. (b), *112*, 75, 1982.
11. M. Mondal and K. P. Ghatak, Phys. Stat. Sol. (b), *122*, K93, 1984.
12. M. Abramovitz and I. A. Stegun, Handbook of Mathematical Functions, Washington, 1964.
13. J. S. Blakemore, Semiconductor Statistics, Pergamon Press, London, 1962.
14. M. Neuberger, Hdb. Electronic Materials, *2*, IFI/Plenum Data Corporation, New York, 1971.

Acta Physica Hungarica 67 (3–4), pp. 411–414 (1990)

BOOK REVIEWS

KLARA KISS: *Problem solving with microbeam analysis*

Akadémiai Kiadó, Budapest, 1988, p. 409

In the first of two main parts, the book introduces some of the numerous surface analysis methods. The principles and characteristics of these techniques are described, as well as typical experimental apparatus. In Section 9, a table is presented comparing the characteristic parameters of the main surface analysis methods (AES, RBS, XPS, ISS, SIMS) and a complex apparatus is described which allows the simultaneous use of such techniques. The closing Section of the first part can especially be recommended to engineers and industrial researchers. This Section provides a guide regarding the possible questions which can be raised in connection with a given technological problem and gives the optimal choice of experimental methods to supply the answers to those questions.

Part II contains the description of a wide range of fields of applications, like polymers, microelectronics, metallurgy, corrosion, catalysis, etc. Solving real problems, the author emphasizes the advantages of using combined techniques.

J. Giber

Discussion meeting: "Intramolecular Processes"

Bunsen-Gesellschaft für Physikalische Chemie, August 17–20, 1987. Edited by Edward Schlag, Berichte der Bunsen-Gesellschaft für Physikalische Chemie; Vol. 92, No. 3, March 1988, Frankfurt am Main, West Germany

The contribution described here is not a book, it is a special number of an international journal of physical chemistry issued by the Deutsche Bunsen-Gesellschaft für Physikalische Chemie e. V. It covers the material (240 pages) of a special meeting devoted to the studies of the motion of energy within molecules; mainly intra-molecular vibrational relaxation.

The topic is central to modern photochemical and photo-physical studies of small molecules in the gaseous phase. Therefore very little is mentioned about condensed phase processes. Intra-molecular vibrational and rotational dynamic studies are common for many fundamental research disciplines such as laser-induced physical and chemical processes. This special journal edition is then extremely important for molecular spectroscopists, photophysicists and photochemists alike. There are 46 papers in the collection and a good portion of them deals directly with unimolecular processes. The most important of these are listed below.

R. A. Marcus (California Institute of Technology, U. S. A.) reported on intramolecular dynamics and unimolecular reactions, Moshe Shapiro (Weizmann Institute of Science, Israel) gave considerations on classical and quantum chaos, while R. D. Levine (Hebrew University, Jerusalem, Israel) discussed quantum fluctuations in unimolecular rate processes. Stuart Rice and S. H. Tersigni (The University of Chicago, U. S. A.) investigated the role of bottlenecks in unimolecular fragmentation. J. Troe (Universität Göttingen, F. R. G.) talked about 'ab initio' quantum chemical calculations of potential surfaces and their significance in understanding unimolecular reaction dynamics.

Another large group of very interesting papers were more spectroscopic in their approach to dissociation dynamics. Topics covered were vibrational predissociation of van der Waals complexes, the mechanism of photodissociation of polyatomic molecules, vector correlations in photodissociation and the behaviour of highly vibrationally excited molecules. Other papers touched upon classical and quantum

mechanical features of the photodissociation process.

The present reviewer (who is a spectroscopist himself) is prejudiced to call attention to a very interesting "new" approach of treating complex molecular spectra. The idea is taken from early nuclear spectroscopic work and is centred on the statistical evaluation of complex energy level patterns. Whenever there are strong correlations among the levels through some kind of intramolecular mechanism (such as Coriolis or Fermi interactions) energy level density fluctuations and first-neighbour spacings change characteristically from the uncorrelated level system case. The method is useful to find strong perturbations leading to the destruction of the "goodness" of various quantum numbers until the only good quantum number remaining is the energy itself. The result is a chaotic appearance of the energy levels (of the spectrum) that cannot be handled through the use of classical spectroscopic procedures, but is rather characterized by particular statistics, as e. g. the so-called Wigner distribution.

This journal volume provides the interested reader with a great number of highly specialized interdisciplinary papers and is to prove very helpful in this modern and flourishing field of molecular photophysics and photochemistry. The reviewer strongly recommends anybody who is fundamentally interested in molecular photoprocesses to buy this special issue.

The Berichte der Bunsen-Gesellschaft is a nicely typeset journal and reading of the papers is easy. The only point that may deserve a bit of attention in future issues is a fair number of misspellings in the English.

L. Nemes

Low Temperature Detectors for Neutrinos and Dark Matter

Workshop on neutrino detection held in Ringberg Castle (Tegernsee, F. R. G.) May 1987. Edited by K. Pretzl, N. Schmitz and L. Stodolsky, Springer, Berlin, 160 pp, 94 figs.

In recent years, particle physics has become closely connected with astrophysics and cosmology and these fields are overlapping more and more. One of the most important common areas — and perhaps the most important one — is neutrino physics. The neutrino not only represents a bizarre type of elementary particle but it could help to solve a number of problems in astrophysics and cosmology. A few examples of these problems are: What happens to the neutrinos, having been produced in the interior of the sun, during their flight before reaching the earth? What is the dark matter that seems to be contained by the universe? Is it formed by neutrinos of minute yet finite mass? One of the most recent and sensational events of astrophysics was the supernova explosion in February 1987 when — for the first time in the history of science — neutrinos of such origin could be detected.

One of the most characteristic features of the neutrino is its very low probability of interaction with matter. This, on the one hand, enables us to receive messages from remote parts of the universe or from the interior of the sun, or even "to X-ray" the earth. At the same time, however, neutrino detection is an extremely difficult problem for experimentalists — due to precisely the same characteristic feature. How can a neutrino be caught if it barely reacts on meeting matter (thus also the matter of a detector). Quite a number of neutrino detectors have already been developed, utilizing different operating principles. The present book reports on completely new principles of neutrino detection and on the possibilities of their realization.

One of the detection methods is based on superconductivity. Namely, if a neutrino interaction takes place inside a small granule which is superconductive then the amount of energy released by this interaction warms up the granule and the latter loses its superconductivity — which, in turn, can be detected by an external coil. In one version of the realization of this idea the collision of a neutrino with a nucleus is utilized. This method has the advantage that it provides a relatively large effective cross section, so a detector whose mass is only a few kilograms is sufficient. Another advantage is that this method is equally suitable for the detection of all kinds of neutrinos, i. e. electron-, muon- and tau-neutrinos as well. The basic problem with this technique is that the energies released during the interaction are very low, in the order of about 1 eV. Generally Sn granules are used with a diameter of $2\mu m$ which have to be cooled to 50mK.

In another method, indium granules and the so-called inverse beta decay are em-

ployed. The advantages and difficulties involved in this are just the opposite of the above: the energy values are much higher, in the order of about 100 keV, but a corresponding detector would weigh tons because of the about thousand times smaller cross section — and such a detector arrangement would need to be maintained at the temperature of superconductivity.

A somewhat different technique is bolometry, where the impact electron from elastic neutrino-electron scattering is calorimetrically detected. The detector material is liquid helium, the necessary amount is about 1 ton. In most cases, the backscattering energy of the electrons appears as a roton. These are long-lived excitations that proceed ballistically at low temperatures and result in the evaporation of He atoms from the free surface of the liquid. The evaporated He atoms can be detected on the surface of the liquid helium by using a bolometer.

In addition to the above, further, theoretically possible methods have also been reported such as the measurement of superconductive tunnel junctions and detection using ballistic phonons or superfluid helium. One of the reports (by a Hungarian physicist — György Vesztergombi) relates to a novel idea for detecting neutrinos that has not been tested up till now.

To sum up, the Proceedings report on exciting new approaches to neutrino detection utilizing low temperature and solid state physical phenomena. These methods are generally not yet beyond trials; there are cases where only the bare idea exists. For the time being, the sensitivity of such detectors is by orders of magnitude below the required level. The necessary cryogenics involved means considerable additional costs. A serious problem to be solved in the future is the treatment of the background due to natural radioactivity and cosmic radiation. Read-out electronics represents another task to be solved. The small granules and tunnel junctions are objects of very small dimensions that will have to be produced in large quantities and operated in a very large detector volume in a reproducible manner. The workshop and the book have shown that the way before us is long and difficult but the new ideas are daringly novel and it is possible that the breakthrough in neutrino detection will take place somewhere along this route.

The book may reckon on the interest of experimental particle physicists and solid state physicists and all those who are engaged in particle detection.

D. Kiss

DALE ENSMINGER: *Ultrasonics: fundamentals, technology, applications*

Second edition, revised and expanded. Marcel Dekker Inc., New York and Basel, 1988. ISBN 0-8247-7659-3

What laser light means for today's research and development in technology and medicine, that same enthusiasm could be observed half a century ago when *ultrasonics* was mentioned. The "magic" flavor surrounding both expressions of these basically different radiation modalities issues from a single common property: both are coherent radiations, and as such, both represent high directivity, high energy concentration and a high tendency for interference.

Until the late 50s, early 60s, the "Bible" of ultrasonic science was the famous book of L. Bergmann: Der Ultraschall in Wissenschaft und Technik, first published in 1937, the 6th edition of which came out in 1954.

Although basic principles do not change, technology and application do, therefore already the first edition of D. Ensminger's Ultrasonics several years ago was an important contribution to placing ultrasound as such in a proper light. The second, revised and expanded edition reviewed here shows clearly how developments in electronics, data processing techniques and even marketing demands may put new emphasis on sometimes practically forgotten ideas and possibilities.

This edition is rather a handbook than a Bible, which means that it is not only a collection of papers but the chapters have a logical sequence, too and, what is perhaps more important, each of them is provided with references to fairly recent publications without going back too far into the past.

Chapter 1 entitled "Ultrasonics — a broad field" is a well written summary of the history of ultrasonic sciences and the first endeavours to use ultrasound for practical purposes.

Chapters 2–5 are concerned with those

fundamentals — wave propagation phenomena, fundamental equations, etc., — which are needed for designing ultrasonic systems starting from transducers and ending with various applicators.

Chapter 6 is an introduction to Chapters 7, 8 and 9 discussing the application of ultrasound in nondestructive testing of both metals and nonmetals, since Chapter 6 deals with the evaluation of materials based on velocity and absorption measurements and the acoustic properties of the materials.

Chapter 10 is devoted to imaging with ultrasound, process control and miscellaneous low-intensity applications. This Chapter is perhaps less informative than the others, and mirrors well that the author in his nearly 40 years of ultrasound experience was not really involved in ultrasonic imaging problems since he was mostly concerned with NDT where the use of B and C scans has been restricted until very recently.

In contrast to the previous Chapter, Chapters 11–13, dealing with the basics and applications of high-intensity ultrasonics, are highly recommended for those interested in solving problems with high intensity ultrasound *on industrial scale*. It namely clearly shows, especially if the reader looks at the dates of references, that high-intensity ultrasound is still a very expensive form of energy, thus, its application in everyday practice is very limited. There is a long way from feasibility studies — most of the references are of this nature — to the economic exploitation of the idea.

The last Chapter is an excellent review on the medical applications of ultrasonic energy for technical people, but it is not intended for those who wish to get deeper knowledge in medical ultrasonics.

P. Greguss

Acta Physica Hungarica 67 (3–4), p. 415 (1990)

CORRIGENDA

M. F. Podlaha: Is the physical space empty?
Acta Phys. Hung., *59*, 451, 1986.

Reference [9] should correctly read:

M. F. Podlaha and E. Navrátil: Ref. Real Acad. Sci. Madrid, *61*, 555, 1967.

Acta Physica Hungarica 67, 1990
Akadémiai Kiadó, Budapest

NOTES TO CONTRIBUTORS

I. PAPERS will be considered for publication in Acta Physica Hungarica only if they have not previously been published or submitted for publication elsewhere. They may be written in English, French, German or Russian.

Papers should be submitted to

Prof. I. Kovács, Editor
Department of Atomic Physics, Technical University
1521 Budapest, Budafoki út 8, Hungary

Papers may be either articles with abstracts or short communications. Both should be as concise as possible, articles in general not exceeding 25 typed pages, short communications 8 typed pages.

II. MANUSCRIPTS

1. Papers should be submitted in three copies.
2. The text of papers must be of high stylistic standard, requiring minor corrections only.
3. Manuscripts should be typed in double spacing on good quality paper, with generous margins.
4. The name of the author(s) and of the institutes where the work was carried out should appear on the first page of the manuscript.
5. Particular care should be taken with mathematical expressions. The following should be clearly distinguished, e.g. by underlining in different colours: special founts (italics, script, bold type, Greek, Gothic, etc.); capital and small letters; subscripts and superscripts, e.g. x^2, x_3; small *l* and l; zero and capital O; in expressions written by hand: *e* and *l*, *n* and *u*, *v* and v, etc.

A List of Symbols on a separate sheet should be attached to each paper.

6. References should be numbered serially and listed at the end of the paper in the following form: J. Ise and W. D. Fretter, Phys. Rev., *76*, 933, 1949.

For books, please give the initials and family name of the author(s), title, name of publisher, place and year of publication, e.g.: J. C. Slater, Quantum Theory of Atomic Structures, I. McGraw-Hill Book Company, Inc., New York, 1960.

References should be given in the text in the following forms: Heisenberg [5] or [5].

7. Captions to illustrations should be listed on a separate sheet, not inserted in the text.
8. In papers submitted to Acta Physica all measures should be expressed in SI units.

III. ILLUSTRATIONS AND TABLES

1. Each paper should be accompanied by three sets of illustrations, one of which must be ready for the blockmaker. The other sets attached to the copies of the manuscript may be rough drawings in pencil or photocopies.
2. Illustrations must not be inserted in the text.
3. All illustrations should be identified in blue pencil by the author's name, abbreviated title of the paper and figure number.
4. Tables should be typed on separate pages and have captions describing their content. Clear wording of column heads is advisable. Tables should be numbered in Roman numerals (I, II, III, etc.).

IV. RETURN OF MATERIAL

Owing to high postage costs, the Editorial Office cannot undertake to return *all* material not accepted for any reason for publication. Of papers to be revised (for not being in conformity with the above Notes or other reasons) only *one* copy will be returned. Material rejected for lack of space or on account of the Referees' opinion will not be returned to authors outside Europe.

Periodicals of the Hungarian Academy of Sciences are obtainable at the following addresses:

AUSTRALIA
C.B.D. LIBRARY AND SUBSCRIPTION SERVICE
Box 4886, G.P.O., *Sydney N.S.W. 2001*
COSMOS BOOKSHOP, 145 Ackland Street
St. Kilda (Melbourne), Victoria 3182

AUSTRIA
GLOBUS, Höchstädtplatz 3, *1206 Wien XX*

BELGIUM
OFFICE INTERNATIONAL DES PERIODIQUES
Avenue Louise, 485, *1050 Bruxelles*
E. STORY-SCIENTIA P.V.B.A.
P. van Duyseplein 8, *9000 Gent*

BULGARIA
HEMUS, Bulvar Ruszki 6, *Sofia*

CANADA
PANNONIA BOOKS, P.O. Box 1017
Postal Station "B", *Toronto, Ont. M5T 2T8*

CHINA
CNPICOR, Periodical Department, P.O. Box 50
Peking

CZECHOSLOVAKIA
MAD'ARSKA KULTURA, Národni třida 22
115 66 Praha
PNS DOVOZ TISKU, Vinohradská 46, *Praha 2*
PNS DOVOZ TLAČE, *Bratislava 2*

DENMARK
EJNAR MUNKSGAARD, 35, Nørre Søgade
1370 Copenhagen K

FEDERAL REPUBLIC OF GERMANY
KUNST UND WISSEN ERICH BIEBER
Postfach 46, *7000 Stuttgart 1*

FINLAND
AKATEEMINEN KIRJAKAUPPA, P.O. Box 128
00101 Helsinki 10

FRANCE
DAWSON-FRANCE S.A., B.P. 40, *91121 Palaiseau*
OFFICE INTERNATIONAL DE DOCUMENTATION ET LIBRAIRIE, 48 rue Gay-Lussac
75240 Paris, Cedex 05

GERMAN DEMOCRATIC REPUBLIC
HAUS DER UNGARISCHEN KULTUR
Karl Liebknecht-Straße 9, *DDR-102 Berlin*

GREAT BRITAIN
BLACKWELL'S PERIODICALS DIVISION
Hythe Bridge Street, *Oxford OX1 2ET*
BUMPUS, HALDANE AND MAXWELL LTD.
Cowper Works, *Olney, Bucks MK46 4BN*
COLLET'S HOLDINGS LTD., Denington Estate,
Wellingborough, Northants NN8 2QT
WM DAWSON AND SONS LTD., Cannon House
Folkstone, Kent CT19 5EE
H. K. LEWIS AND CO., 136 Gower Street
London WC1E 6BS

GREECE
KOSTARAKIS BROTHERS INTERNATIONAL BOOKSELLERS, 2 Hippokratous Street, *Athens-143*

HOLLAND
FAXON EUROPE, P.O. Box 167
1000 AD Amsterdam
MARTINUS NIJHOFF B. V.
Lange Voorhout 9–11, *Den Haag*
SWETS SUBSCRIPTION SERVICE
P.O. Box 830, 2160 Sz Lisse

INDIA
ALLIED PUBLISHING PVT. LTD.
750 Mount Road, *Madras 600002*
CENTRAL NEWS AGENCY PVT. LTD.
Connaught Circus, *New Delhi 110001*
INTERNATIONAL BOOK HOUSE PVT. LTD.
Madame Cama Road, *Bombay 400039*

ITALY
D. E. A., Via Lima 28, *00198 Roma*
INTERSCIENTIA, Via Mazzé 28, *10149 Torino*
LIBRERIA COMMISSIONARIA SANSONI
Via Lamarmora 45, *50121 Firenze*
SANTO VANASIA, Via M. Macchi 58
20124 Milano

JAPAN
KINOKUNIYA COMPANY LTD.
Journal Department, P.O. Box 55
Chitose, *Tokyo 156*
MARUZEN COMPANY LTD., Book Department
P.O. Box 5050 Tokyo International, *Tokyo 100-31*
NAUKA LTD., Import Department
2-30-19 Minami Ikebukuro, Toshima-ku, *Tokyo 171*

KOREA
CHULPANMUL, *Phenjan*

NORWAY
TANUM-TIDSKRIFT-SENTRALEN A.S.
Karl Johansgata 43, *1000 Oslo*

POLAND
WĘGIERSKI INSTYTUT KULTURY
Marszalkowska 80, *00-517 Warszawa*
CKP I W, ul. Towarowa 28, *00-958 Warszawa*

ROUMANIA
D. E. P., *Bucuresti*
ILEXIM, Calea Grivitei 64–66, *Bucuresti*

SOVIET UNION
SOYUZPECHAT — IMPORT, *Moscow*
and the post offices in each town
MEZHDUNARODNAYA KNIGA, *Moscow G-200*

SPAIN
DIAZ DE SANTOS Lagasca 95, *Madrid 6*

SWEDEN
ESSELTE TIDSKRIFTSCENTRALEN
Box 62, *101 20 Stockholm*

SWITZERLAND
KARGER LIBRI AG, Petersgraben 31, *4011 Basel*

USA
EBSCO SUBSCRIPTION SERVICES
P.O. Box 1943, *Birmingham, Alabama 35201*
F. W. FAXON COMPANY, INC.
15 Southwest Park, *Westwood Mass. 02090*
MAJOR SCIENTIFIC SUBSCRIPTIONS
1851 Diplomat, P.O. Box 819074,
Pallas, Tx. 75381-9074
READ-MORE PUBLICATIONS, INC.
140 Cedar Street, *New York, N. Y. 10006*

YUGOSLAVIA
JUGOSLOVENSKA KNJIGA, Terazije 27, *Beograd*
FORUM, Vojvode Mišića 1, *21000 Novi Sad*

Index: 26.022